

Nanostructured semiconductor oxides for the next generation of electronics and functional devices

Properties and applications

Serge Zhuiykov

Nanostructured semiconductor oxides for the next generation of electronics and functional devices

Related titles:

Graphene

(ISBN 978-0-85709-508-4)

Carbon nanotubes and graphene for photonic applications

(ISBN 978-0-85709-417-9)

Introduction to the physics of nanoelectronics

(ISBN 978-0-85709-511-4)

Details of these books and a complete list of titles from Woodhead Publishing can be obtained by:

- visiting our web site at www.woodheadpublishing.com
- contacting Customer Services (e-mail: sales@woodheadpublishing.com; fax: +44 (0) 1223 832819; tel.: +44 (0) 1223 499140 ext. 130; address: Woodhead Publishing Limited, 80, High Street, Sawston, Cambridge CB22 3HJ, UK)
- in North America, contacting our US office (e-mail: usmarketing@woodheadpublishing.com; tel.: (215) 928 9112; address: Woodhead Publishing, 1518 Walnut Street, Suite 1100, Philadelphia, PA 19102-3406, USA)

If you would like e-versions of our content, please visit our online platform: www.woodheadpublishingonline.com. Please recommend it to your librarian so that everyone in your institution can benefit from the wealth of content on the site.

We are always happy to receive suggestions for new books from potential editors. To enquire about contributing to our Electronic and Optical Materials series, please send your name, contact address and details of the topic/s you are interested in to laura.pugh@woodheadpublishing.com. We look forward to hearing from you.

The team responsible for publishing this book:

Commissioning Editor: Laura Pugh

Project Editor: Elizabeth Moss

Editorial and Production Manager: Mary Campbell

Production Editor: Richard Fairclough

Copyeditor: Helen MacFadyen

Proofreader: Trevor Birch

Cover Designer: Terry Callanan

Woodhead Publishing Series in Electronic and Optical Materials:
Number 53

Nanostructured semiconductor oxides for the next generation of electronics and functional devices

Properties and applications

Serge Zhuiykov



Oxford Cambridge Philadelphia New Delhi

Published by Woodhead Publishing Limited,
80 High Street, Sawston, Cambridge CB22 3HJ, UK
www.woodheadpublishing.com
www.woodheadpublishingonline.com

Woodhead Publishing, 1518 Walnut Street, Suite 1100, Philadelphia,
PA 19102-3406, USA

Woodhead Publishing India Private Limited, 303, Vardaan House, 7/28 Ansari Road,
Daryaganj, New Delhi – 110002, India
www.woodheadpublishingindia.com

First published 2014, Woodhead Publishing Limited
© Woodhead Publishing Limited, 2014. The publisher has made every effort to ensure that permission for copyright material has been obtained by authors wishing to use such material. The author and the publisher will be glad to hear from any copyright holder it has not been possible to contact.
The author has asserted his moral rights.

This book contains information obtained from authentic and highly regarded sources. Reprinted material is quoted with permission, and sources are indicated. Reasonable efforts have been made to publish reliable data and information, but the author and the publisher cannot assume responsibility for the validity of all materials. Neither the author nor the publisher, nor anyone else associated with this publication, shall be liable for any loss, damage or liability directly or indirectly caused or alleged to be caused by this book.

Neither this book nor any part may be reproduced or transmitted in any form or by any means, electronic or mechanical, including photocopying, microfilming and recording, or by any information storage or retrieval system, without permission in writing from Woodhead Publishing Limited.

The consent of Woodhead Publishing Limited does not extend to copying for general distribution, for promotion, for creating new works, or for resale. Specific permission must be obtained in writing from Woodhead Publishing Limited for such copying.

Trademark notice: Product or corporate names may be trademarks or registered trademarks, and are used only for identification and explanation, without intent to infringe.

British Library Cataloguing in Publication Data
A catalogue record for this book is available from the British Library.

Library of Congress Control Number: 2013946850

ISBN 978-1-78242-220-4 (print)
ISBN 978-1-78242-224-2 (online)
ISSN 2050-1501 Woodhead Publishing Series in Electronic and Optical Materials (print)
ISSN 2050-151X Woodhead Publishing Series in Electronic and Optical Materials (online)

The publisher's policy is to use permanent paper from mills that operate a sustainable forestry policy, and which has been manufactured from pulp which is processed using acid-free and elemental chlorine-free practices. Furthermore, the publisher ensures that the text paper and cover board used have met acceptable environmental accreditation standards.

Typeset by Toppan Best-set Premedia Limited, Hong Kong
Printed by Lightning Source

Contents

<i>About the author</i>	<i>ix</i>	
<i>Woodhead Publishing Series in Electronic and Optical Materials</i>	<i>xi</i>	
<i>Introduction</i>	<i>xvii</i>	
<i>Acknowledgements</i>	<i>xxi</i>	
1	Electrons and holes in a semiconductor	1
1.1	Order and disorder in semiconductor crystals	1
1.2	Electrical conductivity of semiconductor crystals	6
1.3	Mechanisms of <i>n</i> - and <i>p</i> -type conductivity	12
1.4	The energy spectrum of an electron in an infinite crystal lattice	17
1.5	The energy spectrum of an electron in a finite crystal lattice	24
1.6	Statistics of electrons and holes in semiconductors	31
1.7	Limits of the band theory of semiconductors	39
1.8	State-of-the-art techniques for characterization of nanostructured semiconductors	43
1.9	References	47
2	Structural and chemical modification of semiconductor nanocrystals	50
2.1	Introduction	50
2.2	Vapour-phase material growth	51
2.3	Solution-phase material growth	53
2.4	Vertical and horizontal alignment strategies	55
2.5	Doping of metal oxide semiconductor systems	58
2.6	Energy harvesting based on semiconductor piezoelectric nanostructures	66
2.7	Physical electrochemistry of semiconductor nanocrystals	69
2.8	Structural and electrochemical properties of semiconductor nanocrystals	79
2.9	References	84

3	Electronic devices and functional structures based on nanostructured semiconductors	95
3.1	Introduction to novel nanoscale devices from nanostructured semiconductors	95
3.2	Tunable electronic devices	96
3.3	Optoelectronics based on nanostructured semiconductors	102
3.4	Resonators and cantilevers based on nanostructured semiconductors	114
3.5	Functional structures: carbon nanotubes	118
3.6	Carbon nanotubes for environmental sensors	124
3.7	References	129
4	Two-dimensional semiconductor nanocrystals: new direction in science and technology	139
4.1	Physical and chemical properties of graphene	139
4.2	The impact of these properties on science and industry	140
4.3	Chalcogenide semiconductor nanocrystals	148
4.4	Titanium dioxide nanocrystals	162
4.5	Molybdenum trioxide nanocrystals	167
4.6	Tungsten trioxide nanocrystals	173
4.7	Niobium pentoxide nanocrystals	178
4.8	Tantalum pentoxide nanocrystals	187
4.9	Zinc oxide nanocrystals	191
4.10	Impact of combining two-dimensional semiconductor nanocrystals into three-dimensional structure	196
4.11	References	198
5	Composite graphene/semiconductor nanostructures for energy storage	213
5.1	Performance of graphene in lithium ion batteries	213
5.2	Performance of graphene in electrochemical capacitors	222
5.3	Prospects of using graphene in lithium ion batteries (LIBs) and electrochemical capacitors (ECs)	225
5.4	Composite graphene/semiconductor nanocrystals in LIBs and ECs	229
5.5	Development of three-dimensional conductive networks	237
5.6	Nanostructured thermopower wave sources	247
5.7	References	254
6	Nanostructured semiconductor composites for solar cells	267
6.1	Operating principle of a liquid-junction photovoltaic cell	267

6.2	Nanostructured semiconductors as solar harvesting materials: strategic potential of inorganic semiconductors in photovoltaics	271
6.3	Principles of inorganic solid-state nanostructured solar cells	273
6.4	Structured transparent electron conductors	275
6.5	Semiconductor quantum dot absorbers	286
6.6	Dye-sensitized solar cells (DSSCs)	291
6.7	Future trends in technological development	303
6.8	References	306
7	Nanostructured semiconductor composites for solid oxide fuel cells (SOFCs)	321
7.1	Introduction to materials and designs for solid oxide fuel cells (SOFCs)	321
7.2	Nanostructured cathode materials	324
7.3	Electrolytes for SOFCs	334
7.4	Nanostructured anode materials	338
7.5	Interconnects for SOFCs	340
7.6	Miniaturisation of SOFCs	346
7.7	Low-temperature SOFCs	351
7.8	Toward further performance increase of SOFCs at lower temperatures	355
7.9	Rational SOFC material design: new advances and tools	359
7.10	SOFC applications and markets	363
7.11	References	365
8	Semiconductor nanocrystals in environmental sensors	374
8.1	Solid-state pH sensors	374
8.2	Electrochemical dissolved oxygen (DO) sensors	389
8.3	Conductivity measurements	398
8.4	Antifouling technologies for solid-state water quality sensors	400
8.5	Solid-state turbidity sensors	403
8.6	Solid-state dissolved organic carbon (DOC) sensors	405
8.7	Solid-state dissolved metal ion sensors	409
8.8	Future trends	414
8.9	References	417
	<i>Index</i>	427

About the author



Dr Serge Zhuiykov is a principal research scientist of the Materials Science and Engineering Division of the Commonwealth Scientific and Industrial Research Organisation (CSIRO), Australia. He is a Stream Leader of the Sensors and Sensor Networks Transformation Capability Platform (SSN TCP) of CSIRO. He also leads one of the SSN TCP research projects. As a scientist, he possesses combined academic and industrial experience from working at different universities in Australia, Japan and Europe and in an industrial environment for more than 22 years after the completion of his Ph.D. His research interests include the development of new advanced functional nanocrystals including 2D semiconductor nanostructures for various applications such as photovoltaics, nano-electronics and various environmental nanosensors. As an expert, Dr Zhuiykov has been a member of the Technical Committee of Standards Australia International since 2003 and the official head of the Australian delegation at the International Standards Organisation (ISO) TC-21/SC-8 Technical Committee since 2005. Dr Zhuiykov is a recipient of 2007, 2011, 2013 Australian Academy of

Science and 2010 Australian Government Endeavour Executive Awards for his work on advanced functional nanocrystals and their applications. He is the author and co-author of more than 175 scientific publications, including the monograph *Electrochemistry of Zirconia Gas Sensors* (CRC Press, 2007), six book chapters and 15 international patents. He is also the reviewer of several international scientific journals, and an art lover, painter and passionate collector.

Author contact details:

Commonwealth Scientific Industrial Research Organisation (CSIRO)
Materials Science and Engineering Division
37 Graham Road, Highett, VIC. 3190
Australia

E-mail: Serge.Zhuykov@csiro.au

Woodhead Publishing Series in
Electronic and Optical Materials

- 1 **Circuit analysis**
J. E. Whitehouse
- 2 **Signal processing in electronic communications: For engineers and mathematicians**
M. J. Chapman, D. P. Goodall and N. C. Steele
- 3 **Pattern recognition and image processing**
D. Luo
- 4 **Digital filters and signal processing in electronic engineering: Theory, applications, architecture, code**
S. M. Bozic and R. J. Chance
- 5 **Cable engineering for local area networks**
B. J. Elliott
- 6 **Designing a structured cabling system to ISO 11801: Cross-referenced to European CENELEC and American Standards**
Second edition
B. J. Elliott
- 7 **Microscopy techniques for materials science**
A. Clarke and C. Eberhardt
- 8 **Materials for energy conversion devices**
Edited by C. C. Sorrell, J. Nowotny and S. Sugihara
- 9 **Digital image processing: Mathematical and computational methods**
Second edition
J. M. Blackledge
- 10 **Nanolithography and patterning techniques in microelectronics**
Edited by D. Bucknall

- 11 **Digital signal processing: Mathematical and computational methods, software development and applications**
Second edition
J. M. Blackledge
- 12 **Handbook of advanced dielectric, piezoelectric and ferroelectric materials: Synthesis, properties and applications**
Edited by Z.-G. Ye
- 13 **Materials for fuel cells**
Edited by M. Gasik
- 14 **Solid-state hydrogen storage: Materials and chemistry**
Edited by G. Walker
- 15 **Laser cooling of solids**
S. V. Petrushkin and V. V. Samartsev
- 16 **Polymer electrolytes: Fundamentals and applications**
Edited by C. A. C. Sequeira and D. A. F. Santos
- 17 **Advanced piezoelectric materials: Science and technology**
Edited by K. Uchino
- 18 **Optical switches: Materials and design**
Edited by S. J. Chua and B. Li
- 19 **Advanced adhesives in electronics: Materials, properties and applications**
Edited by M. O. Alam and C. Bailey
- 20 **Thin film growth: Physics, materials science and applications**
Edited by Z. Cao
- 21 **Electromigration in thin films and electronic devices: Materials and reliability**
Edited by C.-U. Kim
- 22 ***In situ* characterization of thin film growth**
Edited by G. Koster and G. Rijnders
- 23 **Silicon-germanium (SiGe) nanostructures: Production, properties and applications in electronics**
Edited by Y. Shiraki and N. Usami
- 24 **High-temperature superconductors**
Edited by X. G. Qiu
- 25 **Introduction to the physics of nanoelectronics**
S. G. Tan and M. B. A. Jalil

- 26 **Printed films: Materials science and applications in sensors, electronics and photonics**
Edited by M. Prudenziati and J. Hormadaly
- 27 **Laser growth and processing of photonic devices**
Edited by N. A. Vainos
- 28 **Quantum optics with semiconductor nanostructures**
Edited by F. Jahnke
- 29 **Ultrasonic transducers: Materials and design for sensors, actuators and medical applications**
Edited by K. Nakamura
- 30 **Waste electrical and electronic equipment (WEEE) handbook**
Edited by V. Goodship and A. Stevels
- 31 **Applications of ATILA FEM software to smart materials: Case studies in designing devices**
Edited by K. Uchino and J.-C. Debus
- 32 **MEMS for automotive and aerospace applications**
Edited by M. Kraft and N. M. White
- 33 **Semiconductor lasers: Fundamentals and applications**
Edited by A. Baranov and E. Tournie
- 34 **Handbook of terahertz technology for imaging, sensing and communications**
Edited by D. Saeedkia
- 35 **Handbook of solid-state lasers: Materials, systems and applications**
Edited by B. Denker and E. Shklovsky
- 36 **Organic light-emitting diodes (OLEDs): Materials, devices and applications**
Edited by A. Buckley
- 37 **Lasers for medical applications: Diagnostics, therapy and surgery**
Edited by H. Jelínková
- 38 **Semiconductor gas sensors**
Edited by R. Jaaniso and O. K. Tan
- 39 **Handbook of organic materials for optical and optoelectronic devices: Properties and applications**
Edited by O. Ostroverkhova

- 40 **Metallic films for electronic, optical and magnetic applications: Structure, processing and properties**
Edited by K. Barmak and K. Coffey
- 41 **Handbook of laser welding technologies**
Edited by S. Katayama
- 42 **Nanolithography: The art of fabricating nanoelectronic and nanophotonic devices and systems**
Edited by M. Feldman
- 43 **Laser spectroscopy for sensing: Fundamentals, techniques and applications**
Edited by M. Baudelet
- 44 **Chalcogenide glasses: Preparation, properties and applications**
Edited by J.-L. Adam and X. Zhang
- 45 **Handbook of MEMS for wireless and mobile applications**
Edited by D. Uttamchandani
- 46 **Subsea optics and imaging**
Edited by J. Watson and O. Zielinski
- 47 **Carbon nanotubes and graphene for photonic applications**
Edited by S. Yamashita, Y. Saito and J. H. Choi
- 48 **Optical biomimetics: Materials and applications**
Edited by M. Large
- 49 **Optical thin films and coatings**
Edited by A. Piegari and F. Flory
- 50 **Computer design of diffractive optics**
Edited by V. A. Soifer
- 51 **Smart sensors and MEMS: Intelligent devices and microsystems for industrial applications**
Edited by S. Nihitjanov and A. Luque
- 52 **Fundamentals of femtosecond optics**
S. A. Kozlov and V. V. Samartsev
- 53 **Nanostructured semiconductor oxides for the next generation of electronics and functional devices: Properties and applications**
S. Zhuiykov

- 54 **Nitride semiconductor light-emitting diodes (LEDs): Materials, performance and applications**
Edited by J. J. Huang, H. C. Kuo and S. C. Shen
- 55 **Sensor technologies for civil infrastructures**
Volume 1: Sensing hardware and data collection for performance assessment
Edited by M. Wang, J. Lynch and H. Sohn
- 56 **Sensor technologies for civil infrastructures**
Volume 2: Applications in structural health monitoring
Edited by M. Wang, J. Lynch and H. Sohn
- 57 **Graphene: Properties, preparation, characterisation and devices**
Edited by V. Skákalová and A. B. Kaiser
- 58 **Handbook of silicon-on-insulator (SOI) technology**
Edited by O. Kononchuk and B.-Y. Nguyen
- 59 **Biological identification: DNA amplification and sequencing, optical sensing, lab-on-chip and portable systems**
Edited by P. Schaudies
- 60 **High performance silicon imaging: Fundamentals and applications of CMOS and CCD sensors**
Edited by D. Durini
- 61 **Nanosensors for chemical and biological applications: Sensing with nanotubes, nanowires and nanoparticles**
Edited by K. C. Honeychurch
- 62 **Composite magnetoelectrics: Materials, structures, and applications**
G. Srinivasan, S. Priya, and N. Sun
- 63 **Quantum information processing with diamond: Principles and applications**
Edited by S. Praver and I. Aharonovich
- 64 **Advances in nonvolatile memory and storage technology**
Edited by Y. Nishi
- 65 **Laser surface engineering: Processes and applications**
Edited by J. Lawrence, C. Dowding, D. Waugh and J. Griffiths

Dear Readers, as I write this book, scientific institutes, universities and industries across the world are undergoing spectacular transformations as new semiconductor nanomaterials emerge, and journals publish cutting-edge research which disrupts established technologies at a pace never seen before. Nanostructured semiconductors and their surface interfaces are attracting increasing interest not only among researchers, but also from industrial communities. In fact, the entire semiconductor industry hinges on tight control of their interfaces and surfaces. The established business titans, such as Intel, Motorola, Sony and Kodak, are being profoundly impacted upon by developments in newly discovered nanomaterials and technologies. These are enabling small ‘start-up’ companies and scientific groups to leverage and capitalise on state-of-the-art results, leaving former Goliaths to be hindered by their multi-billion dollar supply chains and infrastructure. Indeed, we are well and truly in the nanomaterials age!

Nanomaterials are becoming ubiquitous: in medical diagnostics, drug development and delivery within the human body, electronics and wireless communications (a subject for another great book), advanced functional materials and their applications; from fuel and solar cells and super-capacitors up to specific selective sensing electrodes for use in a variety of highly-sensitive detecting devices.

When we look ahead, the transition from one age to the next may not be so obvious, especially for those burdened with inertia from legacy businesses. With hindsight, however, it’s usually obvious. Specifically, nanostructuring of semiconductors and their interfaces can enhance the performance of these important functional materials with a reduction in size conferring upon them unique properties that do not exist in their bulk form. The exceptional qualities of nanostructured semiconductors when compared to their bulk counterparts include:

- increased surface-to-volume ratio, which provides more surface and interface area for both chemical and physical interactions;
- significantly altered surface energies that allow tuning and engineering of the material’s properties, as atomic species near the surface have different bond structures than those embedded in the bulk; and

- quantum confinement effects, due to the inherently small size of nanostructured materials which significantly influences charge transport, electronic band structure and optical properties.

Disruption from new nanomaterials and nanotechnologies is on so many fronts. For example, functional devices based on those nanostructures are more than 10 times faster in their performance than their traditional counterparts. They are cheaper in comparison with conventional devices, owing to the very small quantity of nanomaterials utilized in construction. They are also much more convenient, as they open new capabilities never used before.

Since 2010, substantial progress in the development of a new class of nanostructured semiconductors – two-dimensional (2D) nanocrystals – has been made. 2D semiconductors, which can be obtained by the exfoliation of MoS_2 , MoO_3 , WO_3 and Nb_2O_5 , are of special interest for an enormous number of applications – flexible electronics, electronic circuits, electroactuators, optics, catalysts, super-capacitors, solar cells, fuel cells and chemical and bio-sensors – due to their multifaceted structural and outstanding functional properties. These properties of 2D nanocrystals can be further modified by chemical or molecular doping, by application of strain, shear or pressure, and by intercalation with different types of atoms and molecules. Thus, a new class of 2D artificial materials can be created that do not exist in nature and whose parameters we can and will control. The potential outcome of such development would be a large portfolio of new 2D materials available for a so-called ‘*material-on-demand*’ strategy for novel complex 3D architectures, where the 2D structures with precisely tailored properties will be combined into 3D structures for existing and emerging technological applications.

It’s been said that incumbents do not see disruptive technologies and nanomaterials coming, which is absolutely not the case. For example, Kodak invented the digital camera, yet failed to capitalize on the idea before the eventual shift to digital photography. Why do they fail?

It very well known that large companies and institutions are weighed down by inertia. Their desire to change is stifled by the fact that the newly developed hybrid nanomaterials or composites, technologies and innovations and/or devices based on those innovations generate less revenue. Today, nanomaterials and nanotechnologies are disrupting every industry. Apple Inc. is currently worth more than a few countries combined. The future of many industries is for companies such as Apple, which has embraced new nanostructured functional materials, software, innovations and better business models, to lead innovation by creating new products and services based on nanotechnology. In doing so, they produce technology

that has the potential to improve our wellbeing and also open opportunities for other businesses to follow.

The future of using nanomaterials in everyday functional devices looks bright. The next generation of nano-electronics could produce a new wave of light-weight, extremely high-performance and highly reliable (by virtue of tightly controlled fabrication parameters) devices which could have a very positive impact on our lives. These devices will have useful properties such as reduced power consumption and reduced weight; the miniaturization trend will continue; wearable and flexible electronics will be available; and we will see the integration of electronics into new items such as clothing, glasses and miniaturized healthcare functional devices.

In this book, dear readers, we can find only a glimpse of what semiconductor nanotechnology is being achieved, and what nanostructured semiconductors are capable of in current and future applications.

*Dr Serge Zhuiykov
CSIRO
Melbourne, Australia, 2013*

Acknowledgements

This monograph concentrates on the latest developments in semiconductor nanocrystals and their technologies for various applications. As is common with this type of research, there are many people without whose collaboration, this project would not have moved from a sketched thought to a published book. Perhaps, I should start with my lifelong friend Professor Kourosch Kalantar-Zadeh (RMIT University, Melbourne). He has been a driving force towards the research of a new class of non-stoichiometric semiconductors: two-dimensional (2D) nanocrystals resulting in a successful CSIRO-RMIT collaboration program. He allowed me to unmoor myself from the CSIRO Project Leader responsibilities and adhere to a laptop for more hours than I can dare to count: time I would otherwise have spent performing research work, painting my pictures and living a family life. Kourosch has been the impetus – whether offering sound advice or providing general support, he has always been there when needed.

In addition, I would like to acknowledge the collaboration and help of the great RMIT University associates, including Dr Jian Zhen Ou, Mr Ahmad Sabirin Zoolfakar, Mr Sivacarendran Balendhran (Shiva) and Mr Sumeet Walia, who indirectly contributed to this book with words, ideas and encouragement.

I also want to acknowledge support from the Materials Science and Engineering Division (CMSE) management of the Commonwealth Scientific Industrial Research Organization (CSIRO), Australia and especially from Dr Cathy Foley, Chief of CMSE and Dr Scott Furman, Deputy Chief of CMSE.

My special thanks to two '*men of vision*': former (Dr Michael Brünig) and current (Dr Tim Wark) Research Leader of the CSIRO Sensors and Sensor Networks Transformation Capability Platform, who encouraged the goals of *Nanostructured Semiconductor Oxides for the Next Generation of Electronics and Functional Devices*. Michael is now the Director of the CSIRO ICT Centre. Their help and encouragement have proven invaluable.

At this juncture I would also like to thank Professor Janusz Nowotny from the Centre for Solar Energy Technologies, School of Natural Sciences, University of Western Sydney, my lifelong friend Professor Norio Miura,

KASTEK, Kyushu University, Japan for pointing out the relevant properties of graphene to the properties of 2D semiconductor nanocrystals as an example of the quest for unseen opportunity in nanostructured semiconductors.

Appreciation is extended to CMSE Research Program Leader, Dr Gareth Moorhead, Nanophysics Group Leader and my manager, Dr Tim Davis, as well as to my CSIRO colleagues: Dr Robin Kirkham, Dr Donovan Marney, Dr Ivan Cole, Dr Michael Breedon, Dr Jacek Jasieniak, Dr Louis Kuratzis and Dr Mustafa Musameh. Two special friends are the energetic Dr Radislav A. Potyrailo, GE Research, USA and Dr Vlad Maksutov, Australia. The kindness of Dr Vlad Plachnitsa, Canada who went on to allocate much of his time and generosity in conducting some experiments and providing scientific evidence and facts has been profound. In this respect, I would especially like to thank Mr Eugene Kats, who has given me more assistance than an author could dare hope or ask for.

Anyone who has written a book will know the importance of summarizing the obtained materials and helping to create the finished product. In this regard, help from Ms Laura Pugh, Commissioning Editor of Woodhead Publishing, UK has been greatly appreciated.

Thank goodness for friends who are prepared to give of their time and support: Professor Alexander Pud, Head of Department of Chemistry of Functional Materials, Institute of Bio-organic Chemistry and Petro-chemistry, Ukraine, Professor Andrei Kolmakov, South Illinois University, USA, Mr Alex Marich, ALNIGI Electronics Pty Ltd, Australia, Professor Paulo de Souza, University of Tasmania, Australia, D.Sc. Pavel Shuk, Principal Technologist, Rosemount Analytical, USA, Professor Massod Z. Atashbar, Western Michigan University, USA, Ms Carol Robins, Mr David Kennedy, Mr Boris Rotshtein, Australia.

Appreciation is also extended to my two special Chinese friends: one, as a successful businessman, extended my horizons in respect of Chinese culture, 5000-year-old history, the Thick Face – Black Heart concept and ancient Chinese 36 strategies; the second brought understanding, passion and enthusiasm for imperial Chinese porcelain.

I also wish to express my gratitude to the Fire Protection Association of Australia and to the Standards Australia International for the special honour of representing Australia as a Head of the Australian delegation at the International Standards Organization (ISO) TC21/SC8 Technical Committee.

I bow to the ground to my parents, Alla and Ivan Zhuiykov, for their unconditional support during all my ups and downs in this life.

Finally, very special thanks to my best friend, wife, and partner, Tatiana, who has been, as she always is, the perfect combination of prudence, support and patience, and I am indebted to her and my children for their encourage-

ment and support throughout my career. To her I can only say ‘thank you very much indeed ... люблю тебя, Танюша! ...’ this is for you.

*Dr Serge Zhuiykov
CSIRO, CMSE, Melbourne,
February, 2013*

I dedicate this book to my wife Tatiana.
Serge Zhuiykov

DOI: 10.1533/9781782422242.1

Abstract: The chapter begins with the general theory of semiconductors. It then reviews the science of the mechanism of *n*- and *p*-type conductivity, factors influencing conductivity. It continues with an explanation of electrons and holes in semiconductors. The chapter includes some aspects of band theory and state-of-the-art characterization techniques for nanostructured semiconductors.

Key words: semiconductor, nanostructures, *n*- and *p*-type conductivity, characterization techniques

1.1 Order and disorder in semiconductor crystals

1.1.1 Types of defects

Identification of native (or intrinsic) defects during preparation and/or modification of semiconductor materials is of primary importance since so many electronic and structural properties critically depend on the presence of such defects. On the one hand, it is preferable to use ordered nanocrystalline semiconductors. However, many practical applications, for example, microelectronics technology, use such materials that are weakly or strongly disordered by careful doping. On the other hand, many of the challenging problems within solid-state physics and nanochemistry today are in some way or other connected to disorder. Therefore, all the macroscopic properties of semiconductor crystals can be grouped into two main classes. The first represents all characteristics which are determined by the periodicity of the semiconductor crystal, and for which the small defects accumulated in any real lattice play a negligible role. These properties can be considered as *structure-independent*. The second class contains features determined by local violations of the periodicity of the semiconductor crystal lattice. In this case, the defects are of significant importance, as the functional properties of the semiconductor have been manipulated through deliberate introduction of defect and grain boundaries, as well as through the partitioning of very low concentration of dopant species to these localized regions of semiconductors.^{1,2} These properties are known as *structure-sensitive*. The electrical conductivity of a semiconductor crystal containing small traces of impurities within the moderate temperature range is a clear example of a structure-sensitive aspect. As temperature increases towards the higher

range, the conductivity loses its sensitivity to impurities and structural defects and becomes a structure-independent property (intrinsic conductivity).

Another example is the absorption spectrum of a semiconductor crystal. Absorption bands at relatively low frequencies are structure-sensitive (impurity absorption), while absorption bands in the high-frequency region have proven to be structure-independent (intrinsic absorption).³ Adsorption is always accompanied by a reduction of the free energy ΔG , and therefore it is an exothermal process: $\Delta G = \Delta H - T\Delta S$,⁴ where H is enthalpy (J/mol), T is absolute temperature (K) and S is entropy (J mol⁻¹ K⁻¹). Adsorption continues up to the point when the equilibrium between the gaseous (liquid) phase and the surface of the semiconductor crystal is established. Chemisorptive and catalytic properties of semiconductors constitute another typical example of structure-sensitive properties. They depend on the pre-history of the sample and can be changed by introducing impurities into the lattice.

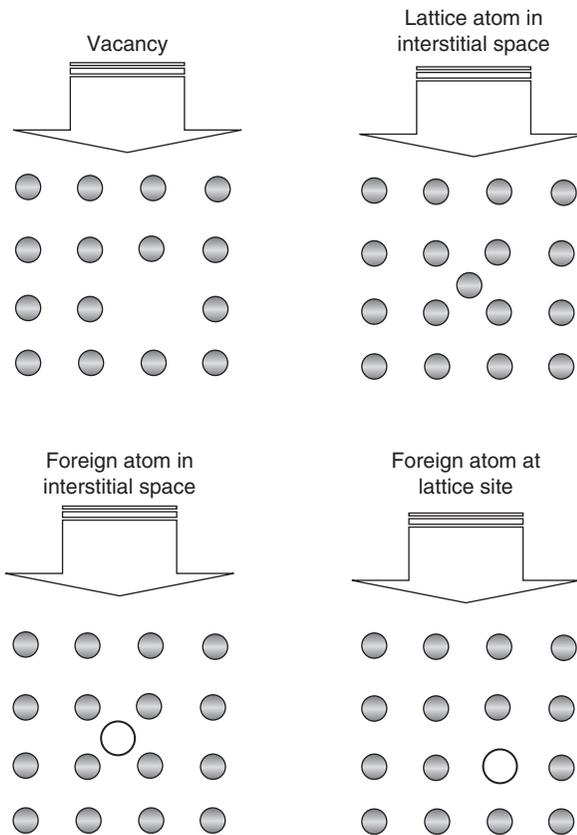
To provide further insight into the interaction between semiconductor lattice and defects, the theoretical interpretation of both the structure-independent and structure-sensitive properties requires various approaches. In the first case, the interpretation can proceed from the theory of the ideal crystal lattice. However, in the second case, the deviations of a real crystal structure from the 'ideal' structure should be taken into account because all structure-sensitive properties retreat completely to the background within the ideal crystal theory. Weak disorder may be defined as a perturbation of the perfect crystalline order. To this category belong defects, vacancies and dislocations which are frequently observed in semiconductors. In polycrystalline materials, the grain boundaries display a more disordered configuration of atoms compared to the grains.

The defects represented in any real semiconductor lattice can be classified as either *macroscopic* or *microscopic*. A macroscopic defect is an imperfection in the periodic structure that involves a region considerably larger than the lattice constant and can cause strong disorder. Strong disorder signifies a marked departure from crystalline order.⁵ Inhomogeneous materials, such as nanocomposites, multiphase nanomaterials and porous semiconductors can be regarded as disordered and homogeneous on sufficiently large length scales, and these inhomogeneities lead to more local strong disorder on mesoscopic (nm– μ m) length scales. As most of the modern semiconductors are nanostructured and their surface morphology usually represents uniformed structures, macroscopic defects will be excluded from further detailed consideration. In contrast, microscopic defects are imperfections whose size in most cases is of the same order of magnitude as an individual cell. Therefore, the main types of such microscopic defects can be divided as follows:

- an unoccupied lattice position (a vacancy) in a semiconductor crystal formed as the result of extracting an atom or ion from the ideal lattice;
- a lattice atom or ion forced into interstitial position;
- a foreign atom placed in interstitial position;
- a foreign atom placed at lattice site, i.e. replacing a lattice atom.

Figure 1.1 graphically displays microscopic defects in semiconductor materials.

The first two types of defects are known as *structural defects*. Usually these flaws do not change the chemical composition of the semiconductor while, in a multicomponent lattice, they may change the stoichiometry. As clearly presented in Fig. 1.1, these defects are presented in a one-component lattice of the crystal (i.e. consist of atoms of only one type). The other two types of defects could be interpreted as *chemical defects*, which usually change the chemical composition in the semiconductor crystal. Chemical



1.1 Microstructural defects in semiconductors.

defects are introduced into the crystal from the outside – in most cases, they occur in the lattice owing to a particular processing of the sample (for example, intercalation by H^+ or Li^+ atoms of the developed nanostructured semiconductor configuration in order to reduce its bandgap).^{6,7} It is important to remember that structural defects may not only be introduced via the different technological processes, but could also appear as a result of heating the lattice.⁸ Larger defect aggregates, clusters and complexes can also be included in the microscopic defect category.

It has long been established that for metal surfaces⁹ the coordination of the surface atoms (the cations and anions in the case of oxides) and the surface chemical reactivity depends upon which crystal planes are exposed to the reactants. Although the surface arrangements can often be deduced from the orientation of the surface plane with respect to the three-dimensional (3D) surface lattice, the influence of surface microscopic defects or even surface reconstruction has not been fully investigated. Most research into the surface reactivity of semiconductor crystals (predominantly oxides) has been undertaken using poly-dispersed samples where several crystal planes may be exposed simultaneously to the reactants. This hinders the identification of active sites. Unlike in the case of metals, where different surfaces can be chosen by cutting the crystal appropriately, this is very difficult to achieve for most of the semiconductors. There is also a lack of spectroscopic data from adsorption on the defined single crystal surfaces of both oxides and chalcogenides.¹⁰ Although several oxides, such as ZnO , TiO_2 , RuO_2 , etc.,^{11–13} were investigated thoroughly in terms of obtaining high-resolution electron energy loss and vibration data, the single crystal phase approach has significantly simplified the interpretation of the spectra obtained.¹⁴ The alternative approach, where the properties of defects and the presence of active sites are taken into account, needs to be investigated.

1.1.2 Properties of defects

Microscopic defects in semiconductors can be point and line defects, surface and volume defects, edge and screw dislocations and planar defects.¹⁵ Considering the general properties of microscopic defects in semiconductors independent of their concrete nature, they can be divided into five groups as follows:

1. When defects interact with each other, they are capable of forming compounds, clusters and various groups, which must be considered as new defects generally possessing completely different properties. For example, impurity atoms in semiconductors and integrated epitaxial structures such as quantum wells (QW) or quantum dots (QD) are regarded as point defects. However, when they react with metalloid and

metallic vacancies in the lattice, leading to the development of new formations having different nature and properties, they should be considered separately. Interactions between adjacent defects may be exothermic or endothermic and can proceed with activation or without, depending on the nature of the reacting defects.

2. In the semiconductor, nanocrystal lattice defects generally serve as attractive centres for free electrons or holes, i.e. they localize these entities near themselves. For instance, dislocations can emit or absorb vacancies and interstitial atoms (native point defects). They can then act as sources or sinks for these defects, respectively. Edge dislocations incorporate point defects at the edge of the extra half-plane. This lowers the energy of the dislocation plus vacancy or interstitial. It creates jogs so dislocation becomes ragged. The emission or absorption of point defects produces 'climb' of the dislocation line up or down out of the slip plane.
3. Defects in which the mobility is temperature-dependent (the mobility increases with a rise in temperature). The system energy of the semiconductor varies periodically, as the defect moves in any direction either along the lattice or inside the different atomically-thin layers – energy minima and maxima alternate. As a result, the motion of the defect is associated with its overcoming potential barriers, whose height depends on the nature of the defect, the structure of the lattice and the direction of the defect's movement. As the transfer of the defect requires a certain activation energy, which is generally dependent on the crystallographic directions, the defects inside a semiconductor crystal may be classified as 'fixed defects' only if the temperature is not too high. Another definition, which has recently been proposed, is thermodynamically reversible (irreversible) defects.¹⁶
4. A general property of microscopic defects is their mutual interaction, which manifests itself more strongly the closer they are to each other. Generally speaking, the energy of the system depends on the adjacent position of the defects, which is evidenced by their interaction.¹⁷
5. Defects of each type given above, taking part in reactions with other defects, may be either created or made to disappear in the process. The certain lifetime for each type of microscopic defect can be assigned only during the equilibrium conditions. However, considering that most of the working conditions for modern nanostructured semiconductors are non-equilibrium, the microscopic defects may be absorbed or created by the lattice. An interesting example of such a process is the dissociation of atoms (or ions) from the lattice sites to interstices. As a result of such dissociation, two types of microscopic defects – interstitial atoms or ions and vacancies – can appear. Another example is the recombination of the interstitial atoms (or ions) with vacancies with disappearance of the defects, as if defects 'absorbed' each other.

Consequently, the presence of a combination of different defects in a semiconductor nanocrystal can be violated in a real crystal. This can be turned into the presence of primitive ‘faulty’ cells in such a crystal. The ratio of faulty cells to the total number of cells is what may be called the *degree of disorder* in the crystal.¹⁸

Generally, the degree of disorder is determined by the pre-history of the semiconductor sample; i.e. it depends on how the sample was manufactured, and to what external stresses it was subjected prior to the experiment. As a rule, it also depends on the manufacturing and working temperature. Increased heating leads to the increased dissociation of lattice atoms (or ions) from sites to interstices and results in additional disorder in the lattice. As a result, the lattice disorder has a two-fold origin: disorder resulting from the semiconductor’s pre-history and thermal disorder. The first type forms the irreversible part of the disorder and the second part is an imposed thermal disorder, which has a temperature-dependent nature.

In some cases, thermal disorder prevails over the first type.¹⁹ It must be stressed that in the vast majority of cases microstructural defects in a semiconductor due to its pre-history can be neglected in comparison with thermal-disorder defects. Due to segregation, the local chemical composition of the planar defect on external surfaces can be completely different from that of the bulk.²⁰ This phenomenon may result in the enrichment of interfaces in a certain type of lattice.¹⁸ It was also reported that in some cases the segregation may even lead to the development of low-dimensional interfacial structures possessing unique properties.²¹ In relation to such semiconductors as TiO₂, these newly developed nanostructures have a considerable influence on both catalytic and photocatalytic properties.²² In other cases, the situation may be quite the opposite. Spatial 3D defects may be formed if one nanostructured semiconductor is heterogeneously doped by another semiconductor at not too high a temperature.^{23–25}

Thus, it must be stressed that each crystal lattice of a nanostructured semiconductor with defects impregnated into it is a single system with properties governed by two competitive factors: order and disorder. The first factor defines all structure-independent properties, whereas the second factor is responsible for most of the structure-sensitive properties of nanocrystals.

1.2 Electrical conductivity of semiconductor crystals

1.2.1 Factors influencing conductivity

In order to understand the operating principle of semiconductor-based devices, the basic mechanism of how currents flow in them must be understood. In this section, attention will be given to certain peculiarities of

nanostructured semiconductors that distinguish them on the one hand from dielectrics and on the other hand from metals. In most cases, semiconductors constitute a broad group of solids occupying an intermediate position between metals and dielectrics. The difference lies primarily in the electrical conductivity σ ($\Omega^{-1}\text{m}^{-1}$). It is well-known that the electrical conductivity σ for metals is within 10^6 – 10^4 m Ω /cm, σ for semiconductors is within 10^2 – 10^{-10} m Ω /cm and σ for dielectrics is within 10^{-14} – 10^{-16} m Ω /cm.¹⁵

However, the difference between metals, semiconductors and dielectrics is not only quantitative but also qualitative. This implies that the electrical conductivity of the three above-mentioned groups of solids reacts differently to the following factors:

- temperature;
- impurities;
- electric field;
- light.

All the above factors can change the electrical conductivity σ of a semiconductor within an extremely wide range. For instance, in different conditions, the electrical conductivity varies by several orders of magnitude for the same semiconductor. In order to establish the influence of each factor independently, they will be considered separately as outlined below:

Temperature

Semiconductor nanocrystals are said to be *intrinsic* if they are not contaminated with impurity atoms. As a rule, more electron–hole pairs are generated at higher temperatures, which leads to a higher concentration of charge carriers. The conductivity of intrinsic semiconductors increases with increasing temperature. Thus, electrons experience a force of attraction towards the positive terminal and holes experience a force of attraction towards the negative terminal of the battery. As a result, there is a net movement of a particular type of charge carriers in a particular direction. This is called *drift*. The electrons drift in the conduction band whereas the holes drift in the valence band. Hence, both electrons and holes have drift velocities.²⁶ In many cases, drift velocity grows with temperature according to an exponential law

$$\sigma = A \exp(-B/kT) \quad [1.1]$$

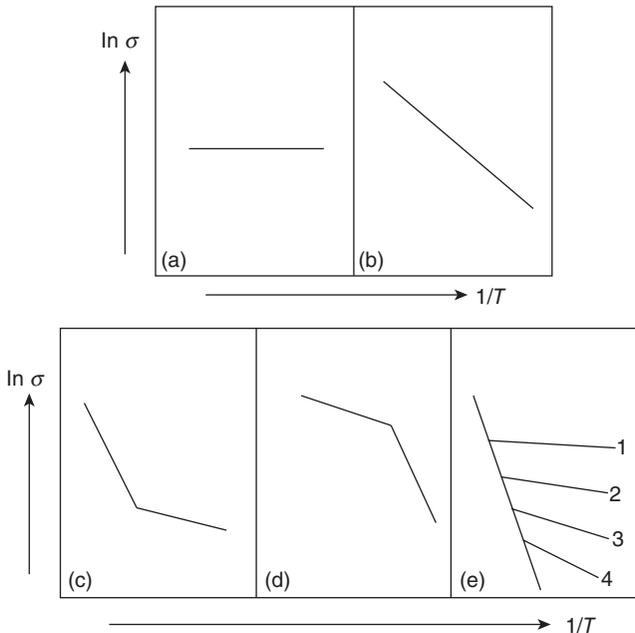
where T is the absolute temperature and coefficients A and B may vary in different temperature intervals. These coefficients are strictly dependent on the degree of impurity concentration in the semiconductor crystal. In some cases, for example in metals, the conductivity can gradually decrease with temperature.²⁷

Considering (1.1), the temperature dependence of electrical conductivity for all semiconductors has an exponential form at high temperatures. Both parameters A and B in (1.1) can be independent of dopant concentration and thus may be considered constant characteristics of the material.

The influence of temperature on the conductivity in a semiconductor can be different, and this is illustrated schematically in Fig. 1.2. However, as impurity concentration increases in a semiconductor lattice, its temperature-dependent influence can vary, as presented in Fig. 1.2e.

Impurities

The conductivity of semiconductors may easily be modified by introducing impurities into their lattice. The process of adding controlled impurities to a semiconductor is known as *doping*.²⁷ The amount of impurity, or dopant, added to an intrinsic semiconductor varies according to its level of conductivity. Doped semiconductors are referred to as *extrinsic*. By adding an impurity to pure semiconductors, the electrical conductivity may be varied by factors of thousands or millions.¹⁶ For example, a 1 cm^3 specimen of a



1.2 Types of the temperature dependence of electrical conductivity: (a) σ constant; (b) slowly varying σ ; (c), (d) varying σ and different A and B in various temperature intervals; (e) different σ vs $1/T$ dependences for different impurity concentrations.

metal or semiconductor has of the order of 10^{22} atoms. In a metal, every atom donates at least one free electron for conduction, thus 1 cm^3 of metal contains on the order of 10^{22} free electrons, whereas a 1 cm^3 sample of pure Ge at 20°C contains about 4.2×10^{22} atoms but only 2.5×10^{13} free electrons and 2.5×10^{13} holes. The addition of only 0.001 % of As donates an extra 10^{17} free electrons in the same volume and the electrical conductivity is increased by a factor of 10000.

It should be noted that at relatively high temperatures most semiconductors become insensitive to impurities.²⁸ The temperature at which this process commences is critical, and it very much depends on the nature of the semiconductor and the number of impurity atoms.

Often the nature of the impurity determines the type of conductance in a semiconductor. For instance, semiconductors that are binary compounds, such as metal oxides or chalcogenides, where the metal is stoichiometrically in excess, are *n*-type, while semiconductors where the metalloid is stoichiometrically in excess are *p*-type.²⁹ Both *n*- and *p*-type semiconductors will be discussed in the following sections.

Let's consider, for example, how the concentration of impurities changes the energy levels in the gap in a photoconductive semiconductor. In this case, the kinetics of electronic transactions may be described by the following set of equations:

$$\frac{dn}{dt} = \sum q_k m_k J + \sum \gamma_k m_k n_{ck} - n \sum \gamma_k p_k \quad [1.2]$$

$$\frac{dm_k}{dt} = -q_k m_k J - \gamma_k m_k n_{ck} + \gamma_k n p_k \quad [1.3]$$

$$n + \sum m_k = N = \text{const} \quad [1.4]$$

where the constant value N is equal to the sum of all electrons at local states in the gap, as well as the number of electrons in the conduction band at the absolute zero temperature, J is impurity light intensity, γ_k is recombination factor at *k*-type level, n_{ck} is electron concentration in the conductivity band at *k*-type level, m_k is electron concentration at *k*-type level, p_k is the holes concentration, q_k is the cross-section of the photon capturing by electron at *k*-type level and t is time.

Electric field

It is necessary to have strong electric fields in order to establish the dependence of the electrical conductivity of a semiconductor on the field strength F . Below a critical value, the conductivity does not depend on F ; in other words, Ohm's law is valid at $\sigma = \text{const}$. The instability region appears above

the critical field strength where, within certain intervals of F , the electrical conductivity becomes negative ($\sigma < 0$) and the volt–current (V – I) characteristic has either an N or an S shape. In stronger fields, conductivity rapidly grows with F , and consequently it can be expressed by the so-called Poole's law¹⁵

$$\sigma = a \exp(bF) \quad [1.5]$$

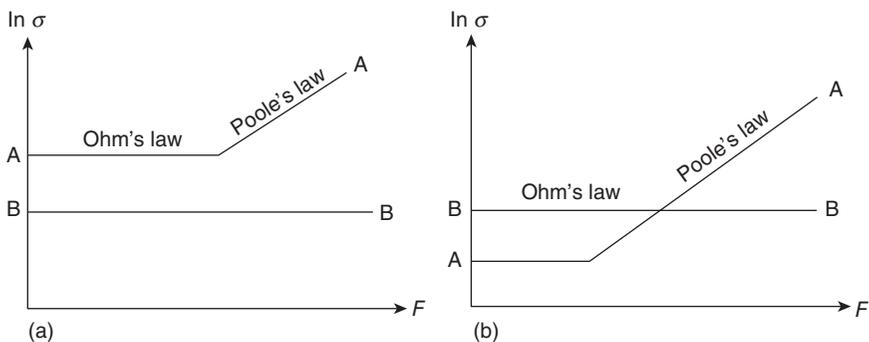
The field strength dependences of electrical conductivity in both semiconductors and dielectrics are graphically explained in Fig. 1.3. This law is valid for many semiconductors including oxides and chalcogenides at sufficiently strong fields. It is also valid for dielectrics.²⁷

Light

It is well-known that the electrical conductivity of most semiconductors is very sensitive to light, just as in the case of dielectrics.^{15,28} Light absorption affects the conductivity of the semiconductor, thus, conductivity in the presence of light differs significantly from conductivity that is without light, all other conditions being equal. The complexity of the photoconductivity in semiconductors and its kinetics are presented above in (1.2)–(1.4). In some cases, when the light does not affect the electrical conductivity (photoelectric non-active light absorption), the so-called normal photoconductive effect is present.

1.2.2 Types of electrical conductivity

As a rule, for most non-metallic nanostructured semiconductor crystals (oxides, chalcogenides, nitrides), the nature of the electrical conductivity can be either *ionic* or *electronic*. Semiconductors are covalently bonded



1.3 Field strength dependence of conductivity: (a) in semiconductors; (b) in dielectrics.

materials for which heat energy is sufficient to promote electrons from bonding energy levels to delocalized energy levels. As was mentioned above, the conductivity of semiconductors is a sensitive function of impurity content (the substitution of semiconductor atoms by atoms with one fewer or more valence electrons) introducing positive (hole) or negative charge carriers into the material.

For electronic conductivity, the observable Hall effect is a sufficient, but not necessary, criterion, whereas for ionic conductivity, the Faraday effect is a necessary and sufficient condition.²⁹ Ionic conductivity in most semiconductors is provided by interstitial ions (the Frenkel mechanism) or vacancies in the ionic crystal (the Schottky mechanism).³⁰ On the other hand, electronic conductivity is normally provided by free electrons (purely *n*-type conduction) or free holes, i.e. electronic vacancies (*p*-type conduction).^{15,27}

To some extent, all types of conduction mechanisms are present in electrical conductivity of nanostructured solids. However, these proportions depend on certain conditions. The role of a component can be changed by external actions on the semiconductor lattice. These external changes can be mechanical, thermal, chemical or electrical, where one of the changes can be dominant while others can be ignored. It has to be stressed that the ionic mobility is relatively small compared to the electron mobility. It is worth noting that it is usually the electron component which prevails in semiconductors over the ionic component, even if the number of free electrons is still very small compared to that of free ions.

However, in normal conditions the ionic conductivity is the prevailing mechanism in many dielectrics. This feature can be explained by the fact that the energy required to provide transportation of an electron from a bound state to a free state is much smaller in semiconductors than in dielectrics. In the region of intense electric fields, dielectrics can change their behaviour and the electronic component of the conductivity can become the predominant one. The reason for this is that the ionic component follows Ohm's law (i.e. is independent of the field strength) up to very high fields, while the electronic component in high fields violates Ohm's law but still obeys Poole's law (see 1.5). This fact can also be confirmed graphically (Fig. 1.3), where line A–A' schematically depicts the electronic component as a function of the field strength and line B–B' represents the ionic component. Figure 1.3a refers to semiconductors and Fig. 1.3b to dielectrics. Transition from Ohm's law to Poole's law in dielectrics reaffirms that the physical nature of the electrical conductivity has changed. Thus, this region possesses a much stronger field than in the case of semiconductors.¹⁸

In contrast, in most semiconductors electrons and holes are the charge carriers. Hence, the electrical conductivity consists of electron and hole components. At relatively low temperatures, one component is greater than

the other and prevalence between *n*- and *p*-type semiconductors can be established. The type of semiconductor depends not so much on the nature of the semiconductor material but rather on the nature of the impurity in it. Moreover, or in the case of binary nanostructured semiconductors, the type depends on the way in which the stoichiometry of the sample is distorted (the predominance of a metal or metalloid). It should be noted that the type of semiconductors can be changed by processing the sample in different ways and, consequently, an *n*-type semiconductor can be turned into a *p*-type, or vice versa. As the temperature rises, the contribution of the non-dominant term in the conductivity also increases. Both components are more or less equal in concentration at high temperatures, and this results in so-called mixed conductivity of the crystal.

1.3 Mechanisms of *n*- and *p*-type conductivity

1.3.1 Free electrons, holes and excitons in a lattice

In the previous sections it was considered that two types of impurities are used for doping semiconductors: *donor impurities* and *acceptor impurities*. Typically one impurity atom is added per 10^8 semiconductor atoms. A semiconductor that is doped with a donor impurity is called an *n*-type semiconductor. One that is doped with an acceptor impurity is called a *p*-type semiconductor.^{15,26–29}

An *n*-type semiconductor is produced by adding a donor impurity such as As, Sb, or P to an intrinsic semiconductor. Each donor atom has five valence electrons. When a donor atom replaces an atom in the crystal lattice, only four valence electrons are shared with the surrounding atoms. The fifth valence electron becomes a free electron. The number of free electrons donated by the donor atoms is much greater than the number of free electrons and holes in the intrinsic semiconductor. This makes the conductivity of the *n*-type semiconductor much greater than that of the intrinsic semiconductor. The free electrons are the majority of carriers because the number of free electrons is far greater than the number of holes. The semiconductor is called *n*-type because the majority of carriers have a negative charge.

A *p*-type semiconductor is produced by adding an acceptor impurity such as Ga, B or In to an intrinsic semiconductor. Each acceptor atom has three valence electrons. When an acceptor atom replaces an atom in the crystal lattice, there are only three valence electrons shared with the surrounding atoms. The number of holes created by the acceptor atoms is much greater than the number of free electrons and holes in the intrinsic semiconductor. This makes the conductivity of the *p*-type semiconductor much greater than that of the intrinsic semiconductor. Because the number of holes is far

greater than the number of electrons, the holes are the majority carrier and, consequently, the semiconductor is called *p*-type because the majority carriers have a positive charge.

Let us consider an M_mR_r type lattice where *M* stands for metal and *R* for metalloid. This type consists of metallic ions with charge $+p$ and metalloid ions with charge $-q$ (with $mp = rq$). The presence of a free electron indicates that there is an ion with the anomalous charge $+(p - 1)$ among the metallic ions. Equally, the presence of a free hole means that one of the lattice atoms (or ions) has an excess positive charge that may be transferred either from atom to atom or from ion to ion. In the case of an M_mR_r -type lattice, this may be a metalloid ion with the anomalous charge $-(q - 1)$ or, alternatively, a metallic ion with the anomalous charge $+(p + 1)$. For example, in the lattice of a typical semiconductor ZnO, which possesses an ionic lattice built on Zn^{2+} and O^{2-} ions, the state Zn^+ corresponds to a free electron and the state O^- to a free hole. In another example, for the Cu_2O lattice built on Cu^+ and O^{2-} ions, state Cu corresponds to a free electron and state Cu^{2+} to a free hole, with the electron and hole migrating along the regular ions Cu^+ .

When a single-component lattice is involved, e.g. the Ge lattice built on neutral Ge atoms, the presence of a free electron or free hole means that there is a Ge^- ion or, respectively, a Ge^+ ion among the neutral Ge atoms.

Electrons and holes exist in the nanostructure provided they are far away from each other. Thus, their mutual interaction may be neglected. In this case, each electron or hole behaves as if no other electrons or holes exist around it. However, if an electron and a hole are relatively close to each other (with a separation of just a few lattice constants), they are bound by the Coulomb interaction and, as a whole, constitute an electrically neutral formation. This is the *Mott exciton*, which may move inside the lattice while contributing nil to charge transport.¹⁸ An electron and ion localized at neighbouring lattice ions correspond to a Mott exciton in its ground (normal) state. The various other excited states of the exciton represent other separations.

An exciton in a semiconductor crystal is not long-lived. After it forms in the crystal, sooner or later it disappears. Usually, this process proceeds in two ways: either by annihilation (recombination) of the electron and hole constituting the exciton or, alternatively, by dissociation of the exciton into a free electron and a free hole. In the first case, the destroying of an exciton is accompanied by energy release. In the second case, the process requires expenditure of energy.

In exceptional circumstances where both electron and hole are localized at the same lattice atom or ion, the Mott exciton can turn into the *Frenkel exciton*.²⁷ The atom or ion does not then carry excess charge but is in an excited state, and this state may be transferred to other like atoms or ions and migrate through the lattice.

It is very important to understand the role that these above-mentioned entities play in surface phenomena of semiconductors. A lattice in its ground state contains no free electrons, free holes or excitons. Their presence indicates lattice excitation. An electron and hole may be created at the expense of the inner resources of the lattice when an electron hops from one atom (or ion) to another atom (or ion). This results in the creation of two atoms (or ions), where both have excess charges. The energy required by this process can be denoted as follows:

$$E = E^- + E^+ + \Delta E$$

where E^- is the energy required to introduce an electron into the lattice, E^+ is the energy required to remove an electron from the lattice (or, in other words, to introduce a hole) and ΔE is the interaction energy between the electron and hole where, in the case of a free electron and hole, $\Delta E = 0$.

Considering the example of an M_mR_r type lattice built on M^+ and R^- ions, where state M corresponds to an electron and state R to a hole, the energy can be expressed as follows:

$$E^- = \frac{e^2}{a}\mu - J, \quad E^+ = \frac{e^2}{a}\mu + A \quad [1.6]$$

where e is the electron charge, a is the smallest possible separation between two oppositely charged ions, μ is the Madelung constant, J is the ionization energy of atom M and A is the electron affinity energy of atom R. The component $e^2\mu/a$ in (1.3) is the energy required to introduce an electron into a metallic site or a hole into a metalloid lattice site. Therefore it represents the interaction energy of the given electron (hole) with all the lattice ions except the one at the given site. If the electron and hole can be localized at neighbouring ions (the exciton in its ground state), then

$$\Delta E = -e^2/a \quad [1.7]$$

However, if these two components are far from each other (free electron and free hole), then

$$\Delta E = 0 \quad [1.8]$$

Thus, the energy needed to create a ground-state exciton, according to (1.6) and (1.7), is

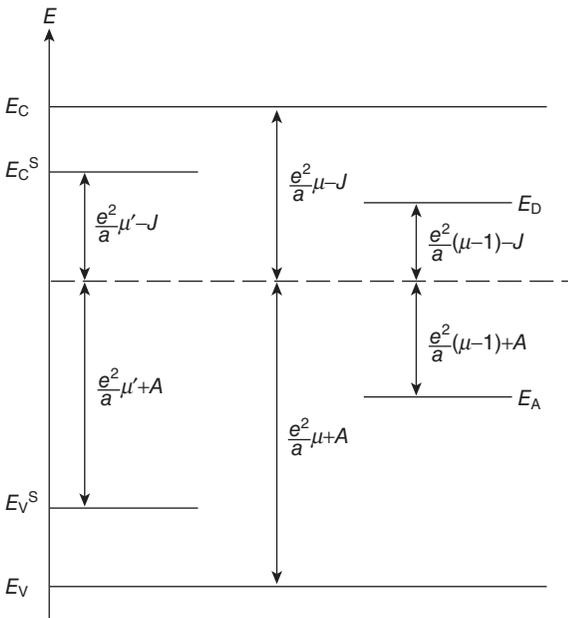
$$E = \frac{e^2}{a}(2\mu - 1) - J + A \quad [1.9]$$

while the energy required to create a free electron and a free hole (a hole-electron pair), according to (1.6) and (1.8), can be expressed as follows:

$$E = \frac{e^2}{a} 2\mu - J + A \tag{1.10}$$

1.3.2 Energy levels of electrons and holes

Although a substantial number of publications has been dedicated to detailed explanations of the electrons' and holes' levels in the oxide semiconductors,^{26-29,31-33} this section will briefly consider what is important to understand about the properties of semiconductors. The formation of energy is a key quantity in the description of the electronic structure and stability of point defects and impurities in oxides. Defects that are present in very low concentrations have a small or negligible impact on conductivity; only those whose concentration exceeds a threshold will have observable effects. Figure 1.4 depicts the energy patterns for the free electron (level E_c) and the free hole (level E_v) in a lattice built on M^+ and R^- ions with the electron energy plotted along the vertical axis upward and the hole energy along the same axis downward. The subscripts c and v stand for 'conduction' and 'valence', respectively.²⁶ In the ground state, the level E_v is occupied by an electron while E_c is vacant. An electron transition from level E_v to E_c means the creation of a pair consisting of a free electron and



1.4 Energy level patterns in M^+ and R^- ions.

a free hole. To illustrate this problem from the quantum mechanical point of view, it can be shown (see Section 1.4) that the two levels spread out into more or less wide energy bands, which are usually called the *conduction* and *valence bands* (they are presented right at the hand side of Fig. 1.4).

Considering that on the surface of a semiconductor crystal the Madelung constant μ' differs from that in the bulk, the following equation should be taken into account instead of (1.3):²⁷

$$E_s^- = \frac{e^2}{a}\mu' - J, \quad E_s^+ = \frac{e^2}{a}\mu' + A \quad [1.11]$$

where $\mu' < \mu$, E_s^- is the energy needed to move an electron from infinity to the ion M^+ on the semiconductor surface, while E_s^+ is the energy required to move an electron from the ion R^- on the surface to infinity.

The corresponding levels, which are schematically presented in Fig 1.4, are denoted by E_c^s and E_v^s . Their common name is the *surface Tamm level (state)*. However, the quantum mechanical effect should not overlap the wave functions. This will be considered in Section 1.5. The electron on the E_c^s level and the hole on the E_v^s can move freely from one atom to another along the crystal surface, but they can only go inside the crystal if they acquire a surplus energy $e^2(\mu' - \mu)/a$.

The surface exciton, which has less energy than a body exciton, can be considered in a very similar way. Therefore, (1.9) can be modified as follows:

$$E_s = \frac{e^2}{a}(2\mu' - 1) - J + A \quad [1.12]$$

This exciton can exist on the surface and freely move along it but cannot go inside the semiconductor crystal.

It should be noted that in real semiconductor crystals not only the regular atoms or ions of the crystal lattice, but also impurities and structural imperfections are present in the crystal. All of these may be sources of free electrons and free holes. As a result, the energy required to create free electrons or free holes in the semiconductor structure may be lower. In this respect, all defects can be divided into two groups: *donors*, which are defects that supply free electrons, and *acceptors*, which are defects that supply free holes. Depending on the specific applications, in the electronic 'household' of a semiconductor, the lattice defects play the main role.²⁹ As an example, the metalloid and metallic vacancies in a MR lattice built on M^+ and R^- ions are equivalent to the presence in the lattice of a positive and negative charge, respectively.

E_D can be denoted as the energy needed to move an electron from infinity to the ion M^+ that is the nearest neighbour of a metalloid vacancy and, respectively, E_A is the energy corresponding to the movement of an electron

to infinity from the ion R^- . Then the Madelung model can be represented as follows:

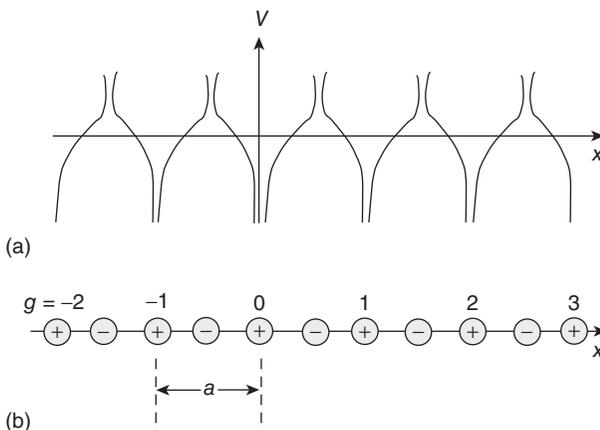
$$E_D = \frac{e^2}{a}(\mu - 1) - J, \quad E_A = \frac{e^2}{a}(\mu - 1) + A$$

The electron on level E_D is localized at the metalloïd vacancy and neutralizes its charge. Such a defect, called an F-centre, is a typical example of a donor. The hole on level E_A is localized at the metallic vacancy and, together with the vacancy, may be considered as an electrically neutral defect. Such a defect, called a V-centre, is a typical example of an acceptor.^{27,28}

1.4 The energy spectrum of an electron in an infinite crystal lattice

1.4.1 Statement of the problem

The behaviour of a free electron in a semiconductor crystal lattice will be considered using an example of the ionic lattice MR consisting of ions M^+ and R^- that are point charges. Let us also assume that the lattice is ‘ideal’, i.e. without imperfections or dislocations, and infinite. To make the problem simpler, only the one-dimensional model, which is an infinite chain of alternating M^+ and R^- ions, will be considered (see Fig. 1.5b). In further discourse all the above-mentioned assumptions will be lifted. Moreover, the interaction of a chosen free electron and all other free electrons and holes will be excluded. It is also assumed that the concentration of free electrons and holes is low in the crystal lattice.



1.5 One-dimensional model of a crystal lattice: (a) periodic lattice potential; (b) (infinite) chain of alternating M^+ and R^- ions.

Let $\psi(x, y, z)$ be the wave function that describes the behaviour of our electron and satisfies the Schrödinger equation²⁷

$$\hat{H}\Psi = E\Psi \quad [1.13]$$

where the Hamiltonian \hat{H} is

$$\hat{H} = -\frac{\hbar^2}{2m}\Delta + V(x, y, z) \quad [1.14]$$

with \hbar being Planck's constant divided by 2π (1.05459×10^{-34} Js) and m the mass of the particle. Here

$$V(x, y, z) = V(x - na, y, z)$$

is the periodic lattice potential depicted in Fig. 1.5a, a is the lattice constant (the distance between neighbouring like ions) and n is an integer.

The next step is to number the metallic ions M^+ in the lattice. Suppose that g is the ion number. Obviously,

$$g = 0, \pm 1, \pm 2, \pm 3, \dots$$

Let us assume that $\varphi_g(x, y, z)$ is the atomic wave function that describes the electron behaviour in an isolated g^{th} metallic atom, with all other M^+ and R^- ions absent. This function, which is assumed to be known, satisfies the Schrödinger equation

$$\hat{H}_g\varphi_g = E_0\varphi_g \quad [1.15]$$

where

$$\hat{H}_g = -\frac{\hbar^2}{2m}\Delta + U_g(x, y, z) \quad [1.16]$$

with

$$\begin{aligned} U_g(x, y, z) &= U_0(x - ga, y, z) \\ \varphi_g(x, y, z) &= \varphi_0(x - ga, y, z) \end{aligned} \quad [1.17]$$

In (1.17) U_g is the potential energy of the electron in the field of the g^{th} isolated metallic ion, the function φ_g is assumed to be non-degenerate (an s function), and the level E_0 is assumed to be sufficiently far from its neighbours.

Eigenfunctions and eigenvalues of (1.13) must be found, assuming that the eigenfunctions and eigenvalues of (1.15) are known. In this regard the function ψ represents a linear combination of atomic functions φ_g ¹⁸

$$\Psi(x, y, z) = \sum_g a_g \varphi_g(x, y, z) \quad [1.18]$$

where the summary should be completed over all lattice ions. The problem is, therefore reduced to finding the expansion coefficients a_g in (1.18). These coefficients must be selected in such a way that the function (1.18) satisfies (1.13). This requirement minimizes the integral

$$J_E = \int \Psi^*(\hat{H} - E)\Psi d\tau \tag{1.19}$$

Integration should be completed over the entire volume where Ψ is normalized. The condition of minimization can be further expressed by a system of the linear equations

$$\frac{\partial J_E}{\partial a_g^*} = 0$$

Then the system can be represented assuming that

$$\hat{H} = \hat{H}_g + V - U_g$$

which can follow from (1.14) and (1.16), and introducing the following notations:

$$S_{gg'} = \int \varphi_g \varphi_{g'} d\tau, \quad P_{gg'} = \int \varphi_g (V - V_{g'}) \varphi_{g'} d\tau \tag{1.20}$$

Consequently, the summary can be expressed as follows:

$$\sum_{g'} \{ (E_0 - E) S_{gg'} + P_{gg'} \} a_{g'} = 0 \tag{1.21}$$

which is an infinite system of linear homogeneous equations with a infinite number of unknowns, a_g .

1.4.2 Eigenfunctions and eigenvalues

Considering that φ_g , being an s function, is spherically symmetric and, assuming that the overlap integral of the wave functions of two neighbouring atoms is small, $S_{gg'}$ can be represented as follows:

$$S_{gg'} = \begin{cases} 1 & \text{if } g' = g \\ 0 & \text{if } g \neq g' \end{cases} \quad P_{gg'} = \begin{cases} \alpha & \text{if } g' = g \\ \beta & \text{if } g' = g \pm 1 \\ 0 & \text{otherwise} \end{cases} \tag{1.22}$$

In view of (1.22), the system of equations (1.21) takes the form

$$(E_0 - E + \alpha)a_g + \beta(a_{g-1} + a_{g+1}) = 0 \tag{1.23}$$

for all g s. The solution of this system of equations can be expressed as

$$a_g = a_0 \exp(i\lambda g) \text{ or } a_g = A \exp(i\lambda g) + B \exp(-i\lambda g) \tag{1.24}$$

with λ any number (generally complex), and A and B arbitrary coefficients. Substituting (1.24) into (1.23) and (1.18), the following system emerges:

$$E = E_0 + \alpha + 2\beta \cos \lambda \tag{1.25}$$

$$\psi(x, y, z) = a_0 \sum_g \exp(i\lambda g) \varphi_g(x, y, z) \tag{1.26}$$

The parameter λ can be taken as a quantum number, since it completely defines eigenfunction (1.26) and the appropriate eigenvalue (1.25). In the case of an infinite lattice, the number λ must be real, since otherwise the function (1.26) becomes infinite at infinity.

It should be also noted that (1.26) is periodic in λ with a period of 2π . This implies that the value of λ can be restricted to an interval 2π , e.g.

$$-\pi \leq \lambda \leq +\pi \tag{1.27}$$

The Born–von Karman condition¹⁸ can be imposed on function ψ , conceiving the infinite crystal as an infinite repetition of the same crystal

$$\psi(x + L, y, z) = \psi(x, y, z) \tag{1.28}$$

where $L = aN$, with N a large positive integer. If (1.26) can be substituted into Eq. (1.28), the λ parameter takes discrete values

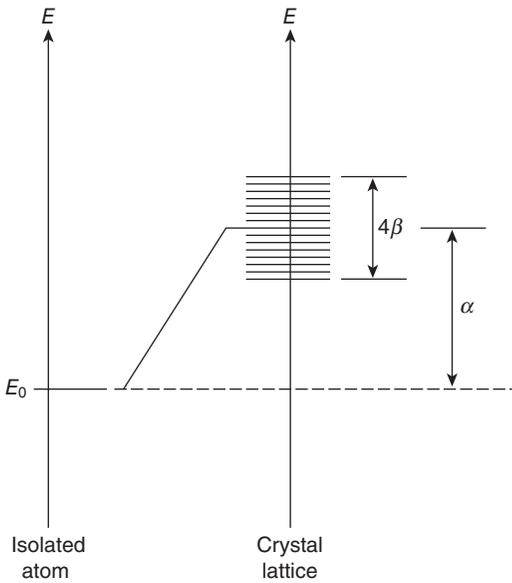
$$\lambda = \frac{2\pi a}{L} j \tag{1.29}$$

where, according to (1.27), $j = 0, \pm 1, \pm 2, \dots$, with $|j| \leq N/2$

Equation (1.25) shows that when we go over from an isolated atom M to a lattice, the level E_0 is shifted by α and broadens out into a band, as schematically shown in Fig. 1.6. We have

top of band($\lambda = 0$)	$E_{\max} = E_0 + \alpha + 2\beta,$	[1.30]
middle of band($\lambda = \pm\pi/2$)	$E_{\text{mid}} = E_0 + \alpha,$	
bottom of band($\lambda = \pm\pi$)	$E_{\min} = E_0 + \alpha - 2\beta,$	
band width	$E_{\max} - E_{\min} = 4\beta$	

since in our case β is positive. The wider the band is the greater is β , which is the overlap integral of the functions φ_g and $\varphi_{g\pm 1}$ of two neighbouring atoms. This integral is greater the closer the lattice atoms are to each other (the smaller a is) and, for a given position of these atoms, the higher E_0 lies. If parameter λ is continuous, so is the band but, if this parameter is discrete (for example, the Born–von Karman condition (1.28), the band splits into a system of levels lying close together and condensing toward the top and bottom of the band. The j in (1.19) can serve as the number of a level in the band, while the total number of states contained in the band is N , i.e. the number of ions M^+ lying in the interval L .



1.6 Energy level broadening in a crystal lattice.

Under an external force, an electron in the periodic lattice field behaves like a classical particle but with an effective mass m^* instead of its true mass $m^{34,35}$

$$m^* = \left(\frac{h}{2a}\right)^2 \left(\frac{d^2 E}{d\lambda^2}\right)^{-1} \tag{1.31}$$

This combined with (1.25) yields

$$m^* = \frac{h^2}{8a^2 \beta \cos \lambda}$$

Thus, the effective mass of the electron very much depends on what level the electron is on in the band. As can be observed from (1.31), the absolute value is smaller the wider the band. The effective mass of the electron is positive in the lower half of the band ($\pi \geq |\lambda| > \pi/2$), negative in the upper half ($\pi/2 > |\lambda| \geq 0$), and becomes infinite in the middle ($|\lambda| = \pi/2$). In the upper half of the band, the electron behaves in a very peculiar manner: it accelerates in the direction opposite to the acting force. However, near the lower edge of the band (when λ is close to $\pm n$) and near the upper edge (when λ is close to zero) m^* can be expressed as follows:

$$m^* = \mp \frac{h^2}{8a^2 \beta} \tag{1.32}$$

where the minus corresponds to the upper edge and the plus to the lower edge.

1.4.3 A three-dimensional lattice

As an interpretation of the one-dimensional model of a semiconductor crystal completed in the previous section, the characterization of the 3D cubic lattice will be provided below. Instead of one integer g describing the position of a metallic ion M^+ in the lattice, three integers, g_1 , g_2 and g_3 , will be needed

$$g_1, g_2, g_3 = 0, \pm 1, \pm 2, \pm 3, \dots$$

as the components of a vector g . Consequently, (1.21) can be transformed as follows:

$$\psi(x, y, z) = a_0 \sum_g \exp(i\lambda g) \varphi_g(x, y, z) \quad [1.33]$$

where λ is a vector with components λ_1 , λ_2 and λ_3 , which serve as three quantum numbers. We can also consider

$$-\pi \leq \lambda_i \leq +\pi$$

where $i = 1, 2, 3$. Summation in (1.33) is over all values of g_1 , g_2 and g_3 . Then instead of (1.25) we have

$$E = E_0 + \alpha + 2\beta(\cos \lambda_1 + \cos \lambda_2 + \cos \lambda_3) \quad [1.34]$$

Here

$$\alpha = \int \varphi_g(V - U_g) \varphi_g d\tau, \quad \beta = \int \varphi_g(V - U_g) \varphi_{g'} d\tau \quad [1.35]$$

where g and g' are the 'number' of neighbouring metallic ions. If the Born-von Karman conditions can be applied, the parameters λ_1 , λ_2 and λ_3 become discrete:

$$\lambda_i = \frac{2\pi a}{L} j_i$$

where $j_i = 0, \pm 1, \pm 2, \pm 3, \dots$, with $|j| \leq N/2$ and $i = 1, 2, 3$.

In (1.34) parameters E_0 and α have a simple physical meaning. Obviously,

$$E_0 = -J$$

where J is the ionization potential of atom M , while α is the potential energy of the electron belonging to the g^{th} metallic atom in the field of all other ions, i.e. except the g^{th} ion. The electron is taken to be smeared out with a density $\varphi_g^* \varphi_g$. Assuming that the electron belonging to the g^{th} metallic

atom is point-like and was localized at the g^{th} metallic site, the quantum-mechanical parameter α becomes a classical quantity

$$\alpha \rightarrow \frac{e^2}{a}\mu$$

as $\beta \rightarrow 0$, and (1.34) takes the form (1.6)

$$E = \frac{e^2}{a}\mu - J$$

If the atomic wave functions φ_g are not s functions, but rather p functions, i.e. three-fold degenerate, then instead of one energy band (1.34), the three bands are superimposed on each other (in other words, a complex band with three times as many states as in the case of s -states).^{36,37} In the case of d functions, which are five-fold degenerate, five superimposed bands can appear.³⁸ Considering that in all these cases only cubic lattices have been assumed, the dependence of E on the quantum numbers λ_1 , λ_2 and λ_3 is confirmed to be more complex than in (1.34). However, in all cases E is a periodic function of λ_1 , λ_2 and λ_3 with a period of 2π . As a result, the energy spectrum (a system of bands corresponding to the levels of an isolated metallic atom) has been exhibited for a free electron in a lattice. The lowest band is well-known as the *conduction band*.^{27,29} These bands usually overlap somewhat, so that we are dealing practically with a continuous spectrum.

1.4.4 The energy spectrum of a hole

Everything that has been considered above about an electron can be repeated for a hole. In addition, an energy spectrum was used in the form of bands. If the holes are fixed *a priori* at negative metalloids of the lattice, these bands correspond to the levels of an isolated metalloid atom. The electron and hole spectra can be depicted in one picture if they are plotted in different directions, as in Fig. 1.4, since introducing a hole is equivalent to extracting an electron. The highest of all hole bands is known as the *valence band*.^{27,29} For the energy spectrum of a hole, it can be assumed that the presence of a free hole in a lattice means that one of the metalloid ions is neutralized. This neutral metalloid atom may be in either its ground state or one of its excited states, depending on whether the hole is in the valence band or one of the lower lying hole bands.¹⁸

The energy bands of a hole may be considered as bands ‘filled’ by electrons, i.e. bands that can be used as a source of electrons. In this sense electron energy bands are ‘empty’, i.e. electrons can be introduced into the bands. As long as the energy bands of a hole contain no holes and the electron energy bands no electrons, our lattice is an ideal dielectric (insulator). To create electrical conduction, electrons must be provided for the

conduction band (*n*-type conduction) or holes must be provided for the valence band (*p*-type conduction) or do both (mixed conduction).

In the energy spectrum, the highest of the hole bands is located below the lowest of the electron bands; i.e. the valence band is below the conduction band. Indeed, if this condition were not present, the electrons from the valence band would move to the conduction band, which would mean that the initial idea of a lattice built on M^+ and R^- ions was wrong. This would simply mean that such a lattice structure is not energetically advantageous.

It is worth noting that the energy bands have been introduced without any reference to the *collective electron method* (Bloch's method), and therefore the preceding explanation is free from all deficiencies and restrictions inherent in that method.¹ The band picture of the energy spectrum of an electron or a hole can be extended in certain conditions from the ionic lattice. The only difference is that, instead of the electrons of the lattice atoms, either the excess electron on the specific atom or the hole, produced by extracting an electron from the atom, have to be considered. The limits of the band picture will be further discussed in Section 1.6.

It can be concluded that in the real material's lattice, various nanodefects can be present, which would influence its energy spectrum. These nanodefects have corresponded to so-called *local* electron and hole levels (acceptors and donors, respectively) positioning in the forbidden gap between the conduction and valence bands. While the levels lying inside the energy bands have appropriate wave functions, the local levels have wave functions with pronounced maxima at the defects and that more or less rapidly disappear as the distance from the defects increases. An electron or a hole in an energy band is spread out over the entire crystal, while an electron or a hole in the local level is localized in the nanodefect. The position of a local level in the spectrum is determined by the nature of the defect, while the extent to which an electron or a hole is localized on such a level is determined by its position in the spectrum – the closer the electron (acceptor) level located to the conduction band or, alternatively, the hole (donor) level to the valence band, the lower the degree of localization of the electron or the hole on the respective level. Consequently, in *n*-type semiconductors the donor levels, particularly the ones of practical interest, are often positioned near the conduction band while in *p*-type semiconductors the acceptor levels lie near the valence band.

1.5 The energy spectrum of an electron in a finite crystal lattice

1.5.1 Statement of the problem

The behaviour of a free electron in a semi-infinite crystal has been established, i.e. a lattice limited on one side. Similarly to the analysis made in the

previous section, an MR lattice built on M^+ and R^- ions will be considered again. In this case, the one-dimensional model will be used. A chain of unlimited ions from the right but limited from the left (Fig. 1.7b) is applied. It makes no difference whether the first ion in the chain is metallic (as presented in Fig. 1.7b) or metalloid. What is important is that in the first potential well we allow for the distortion introduced by the termination of the chain. Assuming that g is the number of the metallic ion and has the values $g = 0, 1, 2, 3, \dots$, the Schrödinger equation for the electron of such a lattice is

$$\hat{H}\Psi = E\Psi \tag{1.36}$$

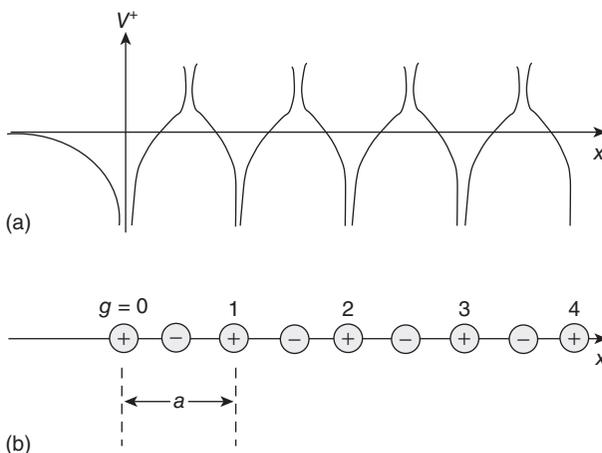
where

$$\hat{H}_g = -\frac{\hbar^2}{2m}\Delta + V^*(x, y, z)$$

Parameter V^* is the summary of potentials of all ions M^+ and R^- in the lattice and certainly does not represent a periodic function of x . It may be considered periodic only approximately at large values of x . However, it can be expressed as

$$V^*(x, y, z) = V(x, y, z) - V'(x, y, z)$$

where V is a periodic potential corresponding to an ideal unlimited crystal lattice and V' is an addition that distorts the periodicity and is affected by the presence of a boundary. At $x \rightarrow \infty, V' \rightarrow 0$. Assuming that V' has non-zero value only near the first ion ($g = 0$), the second ion ($g = 1$)



1.7 Behaviour of a free electron in a semi-infinite crystal: (a) periodic lattice potential; (b) (semi-infinite) chain of alternating M^+ and R^- ions.

is affected by the boundary. In other words, our approximation is depicted in Fig. 1.7a and is as follows:

$$V = \begin{cases} V & \text{for } x > a \\ V - V' & \text{for } x \leq a \end{cases} \quad [1.37]$$

The solution of (1.36) is in the form

$$\Psi(x, y, z) = \sum_{g=0}^{\infty} a_g \varphi_g(x, y, z) \quad [1.38]$$

where φ_g is the atomic wave function corresponding to the g^{th} metallic atom, taking into account that this is an s function. Equation (1.38) satisfies (1.15) and possesses the property (1.17). Similarly to Section 1.4, the system of equations can be as follows:

$$\sum_{g'} \{(E_0 - E)S_{gg'} + P_{gg'}\} a_{g'} = 0 \quad [1.39]$$

which can be used to find the unknown coefficients a_g in the expansion (1.38). In (1.39), just as in (1.16), the summary should be done over all values of g' (in our case $g' = 1, 2, 3, \dots$), while the parameters $S_{gg'}$ and $P_{gg'}$ are given, in contrast to (1.20), by the formulas

$$S_{gg'} = \int \varphi_g \varphi_{g'} d\tau, \quad P_{gg'} = \int \varphi_g (V^* - U_{g'}) \varphi_{g'} d\tau \quad [1.40]$$

1.5.2 Eigenfunctions and eigenvalues

Let us investigate the integrals (1.40). Considering that φ_g are spherically symmetric and their overlap integrals are small, the approximation (1.37) can be used:

$$S_{gg'} = \begin{cases} 1 & \text{if } g' = g \\ 0 & \text{if } g \neq g' \end{cases}, \quad P_{gg'} = \begin{cases} \alpha' & \text{if } g' = g = 0 \\ \alpha & \text{if } g' = g > 0 \\ \beta & \text{if } g' = g \pm 1 \\ 0 & \text{otherwise} \end{cases} \quad [1.41]$$

Then (1.39) takes the form

$$\begin{aligned} (E_0 - E + \alpha')a_0 + \beta a_1 &= 0 & \text{for } g = 0 \\ (E_0 - E + \alpha)a_g + \beta(a_{g-1} + a_{g+1}) &= 0 & \text{for } g > 0 \end{aligned} \quad [1.42]$$

The solution to this system will be in the following form:

$$a_g = A \exp(i\lambda g) + B \exp(-i\lambda g) \quad [1.43]$$

where A and B are arbitrary coefficients and λ is any complex number. Two following cases are from (1.43): (1) both A and B in (1.43) are non-zero, and (2) one of them is equal to zero. In the first case, we arrive at the notion of an energy band, while in the second, which is of special interest, we arrive at the notion of a discrete surface level. Let us consider both cases in detail.

(1) As has been stated, $A \neq 0$ and $B \neq 0$. Then parameter λ must be real. Alternatively, the function ψ at infinity would become infinite, as was already established from (1.38) and (1.43). The second equation in (1.42) yields (1.25). The energy band is exactly the same as for an infinite lattice (see Section 1.4). Substituting (1.43) and (1.25) into the first equation in (1.42), the following equation appears:

$$A \exp(i\lambda)[\alpha' - \alpha - \beta \exp(-i\lambda)] + B \exp(-i\lambda)[\alpha' - \alpha - \beta \exp(i\lambda)] = 0$$

In (1.43) parameters A and B proved to be coupled. In the meantime, for an infinite crystal these parameters are independent (as shown in Section 1.4).

(2) This is an assumption that either A or B is equal to zero. For the sake of definiteness, we consider the case where $A \neq 0$ and $B = 0$. The parameter λ then does not have to be a real value for the function ψ to be finite everywhere. In this regard, a finite lattice differs from an infinite. Thus, the finiteness of ψ is ensured by the fact that

$$\lambda = n\pi + i\lambda' \quad [1.44]$$

where n is an integer and λ' is positive. The second equation in (1.42) transforms one more time into (1.25), while the first equation in (1.42) yields

$$E - E_0 + \alpha' + \beta \exp(i\lambda) = 0 \quad [1.45]$$

and by substituting (1.25) into (1.45), we have

$$\exp(i\lambda) = \frac{\beta}{\alpha' - \alpha} \quad [1.46]$$

Since α , α' and β are real numbers, (1.46) is valid only if λ is expressed via (1.44). Therefore, substitution of (1.44) into (1.46) yields

$$(-1)^n \exp(-\lambda') = \frac{\beta}{\alpha' - \alpha}$$

with n odd, since in our case $\beta > 0$ and $\alpha > \alpha' > 0$.

According to both (1.46) and (1.43), the wave function (1.38) takes the following form:

$$\psi = A \sum_{g=0}^{\infty} \left(\frac{\beta}{\alpha - \alpha'} \right)^g \varphi_g \quad [1.47]$$

The finiteness of the wave function is ensured only if

$$\frac{\beta}{\alpha - \alpha'} < 1, \quad \text{i.e. } \lambda' > 0 \quad [1.48]$$

a fact noted earlier. The wave function (1.47), which decays in the bulk of the crystal, corresponds to a local level, whose position in the energy spectrum may be found by substituting (1.44) into (1.25):

$$E = E_0 + \alpha - 2\beta \cos \lambda' \quad [1.49]$$

Considering that

$$\exp(-\lambda') = \frac{\beta}{\alpha - \alpha'} < 1 \quad [1.50]$$

then substitution of (1.50) into (1.49) yields

$$E = E_0 + \alpha' \quad [1.51]$$

This results in the level positioning below the conduction band.

It should be noted that the numerator of the right-hand side in (1.46) is the band half-width, while the denominator is the distance between the band centre and the surface level. Hence, according to (1.47), the closer the surface level is to the band, the more slowly its wave function disappears in the bulk of the crystal. If we assume that the electron is point-like, parameter α' turns into its classical analogy

$$\alpha' \rightarrow \frac{e^2}{a} \mu$$

and, if $E_0 = -J$, (1.51) transforms into (1.6) (see Section 1.3):

$$E = \frac{e^2}{a} \mu - J$$

The same transformation can be successfully repeated for the case $A = 0$ and $B' \neq 0$. The finiteness of ψ is provided by the fact that

$$\lambda = n\pi - i\lambda'$$

where n is an odd integer, as has been considered above, and λ' is positive. Consequently, the same eigenfunction (1.47) and (1.51) will be obtained.

However, if

$$\frac{\beta}{\alpha - \alpha'} > 1$$

then the level is located inside the band. In this case, both coefficients A and B in (1.43) must be taken to be non-zero.

1.5.3 Tamm and Shockley surface levels

Understanding of surface states naturally emerged from studying the band theory of confined crystals. In a discussion of the nature of surface states, one generally distinguishes between Tamm surface states, arising due to the termination of the crystal lattice at the boundary, and Shockley states, localized at impurities or defects on the surface or in the oxide layer covering the surface. Tamm states are formed by allowed energy bands separated by forbidden bands. Surface allowed bands can be located at energies corresponding to both forbidden and allowed bulk bands.³⁹ In 1932, Tamm, while considering a simple one-dimensional model of a semi-infinite crystal as a sequence of delta potential barriers limited by a potential wall, came to a fundamental conclusion about the possible existence of states whose wave functions are localized to the crystal surface.

In 1939, a fundamentally different approach to dealing with surface states than that proposed by Tamm was proposed by Shockley.⁴⁰ He considered the electron energy levels in a chain of eight atoms. The calculation showed that forbidden bands appear in the spectrum of electron energy and, within each of those, there are two states related to the fact that there are two edge atoms at the ends of the linear chain. The electrons in these two atoms are in the same unique position as the electrons of atoms near the surface of a 3D crystal where, according to Shockley, one can also expect surface states.

In a real crystal, surface electronic states correspond to the coordinatively unsaturated surface atoms. Usually, their emergence results in alteration, surface reconstruction, i.e. the displacement of surface atoms both in a plane tangent to the surface and normal to it, which creates a surface structure with a period equal to several periods of the 3D lattice or incommensurable with them. The character of the reconstruction depends on the crystallographic orientation of the surface, the method of its preparation, as well as the type and concentration of adsorbed impurities, or the presence of the oxide layer on it.⁴¹

Interest in the electronic surface states is associated not only with the desire to understand the physics of surface phenomena, but also with vital technological needs. Surface states act as recombination centres for electrons and holes, thereby reducing the number of carriers and degrading characteristics of diodes, transistors, solar cells and other semiconductor-based functional devices.

In the case of a 3D crystal lattice, the discrete Tamm level (level E_c^s in Fig. 1.4) spreads out into a more or less wide surface energy band (the surface conduction band). Introducing the periodicity condition (1.28) into the wave function in directions parallel to the surface, the band can be split into a set of closely positioned discrete levels. The number of states in the surface band is equal to the number of atoms on the surface (about 10^{15} cm^{-2}).

The squared modulus of the wave function corresponding to a level in the surface band is periodic in directions parallel to the surface (the period is that of the lattice), while in the perpendicular direction it disappears with distance from the surface. This means that an electron belonging to the surface band can move freely along the surface but cannot go inside the crystal or leave it. Electrons in the surface band lead to surface electron conductivity of the crystal and may impart a negative charge to the surface with respect to the bulk.¹⁸

Exactly the same transformation can be successfully repeated for the holes. When the transformation from a one-dimensional crystal goes to the 3D, the hole surface level (level E_V^S in the Fig. 1.4) spreads out into a hole surface band (the *surface valence band*). Holes in this band lead to the surface hole conductivity and may impart an excess positive charge to the surface with respect to the bulk. The fact that there is a potential difference between the surface and the bulk in the crystal leads to important consequences, which will be considered below.

Tamm surface states may not appear in a limited crystal lattice. This depends on certain conditions being fulfilled [e.g. condition (1.48)]. The surface levels may prove to be absorbed by the wide 'bulk' bands which, for example, were clearly demonstrated by (1.48). The wave functions corresponding to these levels lose their damped nature and, hence, do not constitute the surface states.

Therefore, it can be concluded that, along with the Tamm states, which exist due to the finiteness of the crystal, certain other conditions may also appear. The so-called Shockley surface states and their nature are quite different. Shockley⁴⁰ described a one-dimensional crystal lattice limited on both sides, and studied the behaviour of the wave function and the energy spectrum of an electron as the lattice constant a drops from infinity (the case of isolated atoms) to small finite values. In the process, the energy bands, which grow out of the levels of the isolated atoms, broaden, then overlap, but after a becomes smaller than a certain value, gaps appear in the continuous spectrum (forbidden sections). In these gaps one finds discrete levels (one from each band), each of which has a corresponding wave function that disappears as we depart from the crystal boundaries (Shockley surface states). In contrast to the Tamm states, these states appear only at small values of a when the energy bands overlap.

Both Tamm and Shockley levels are characteristic of an ideal surface, where the potential is strictly periodic along the surface. A real surface differs significantly from the ideal by the presence of surface defects, which cause local violations of this periodicity. This leads to an emergence of the surface local levels with wave functions that have maxima near the defect (i.e. in surface plane or near it) but fall off as the distance from the defect increases.

1.6 Statistics of electrons and holes in semiconductors

1.6.1 The Fermi–Dirac distribution function

Electrons are an example of a type of particle called a *fermion*. Other fermions include protons and neutrons. In addition to their charge and mass, electrons have another fundamental property called *spin*. A particle with spin behaves as though it has some intrinsic angular momentum. This causes each electron to have a small magnetic dipole. The spin quantum number is the projection along an arbitrary axis (usually referred to in textbooks as the z -axis) of the spin of a particle expressed in units of h . Electrons have spin $\frac{1}{2}$, which can be aligned in two possible ways, usually referred to as ‘spin up’ or ‘spin down’.

All fermions have half-integer spin. A particle that has integer spin is called a boson. Photons, which have spin 1, are examples of bosons. A consequence of the half-integer spin of fermions is that this imposes a constraint on the behaviour of a system containing more than one fermion. This constraint is the Pauli exclusion principle, which states that no two fermions can have the exact same set of quantum numbers. It is for this reason that only two electrons can occupy each electron energy level – one electron can have spin up and the other can have spin down, so that they have different spin quantum numbers, even though the electrons have the same energy.

However, it should be noted that all results that will be discussed below can also be applicable to the case where this interaction is taken into account by the *self-consistent field method*. In this method, the interaction of the given electron (hole) with all the other electrons and holes is substituted by an effective field produced by the evenly distributed charge of all electrons and holes in the system. In our case the electron (hole) is then presumed to be moving in this effective (self-consistent) force field.⁴²

It is also important that this self-consistent field possesses the same periodicity as the crystal lattice and that even with the interaction taken into account by the self-consistent field method the problem remains a one-electron one.

With the energy gas spectrum of the electron or hole given, the distribution of the entire assembly over the levels of this spectrum must be found. In other words: what is the probability of a given level E being occupied by an electron or remaining unoccupied (i.e. occupied by a hole)? We denote these probabilities by $f_n(E)$ and $f_p(E)$:¹⁸

$$f_n(E) = \frac{n(E)}{Z(E)}, \quad f_p(E) = \frac{p(E)}{Z(E)}$$

where $n(E)$ and $p(E)$ are the number of electrons and holes with an energy E and $Z(E)$ is the total number of states corresponding to E or, in other words, the multiplicity of degeneracy of level E (per unit volume), with

$$n(E) + p(E) = Z$$

and, hence

$$f_n(E) + f_p(E) = 1$$

Based on the fact that both electrons and holes obey the Fermi–Dirac statistics, in equilibrium^{27,29}

$$f_n(E) = \frac{1}{1 + \exp \frac{E - E_F}{kT}}, \quad f_p(E) = \frac{1}{1 + \exp \frac{E_F - E}{kT}} \quad [1.52]$$

where energy E is reckoned with respect to an arbitrary (but fixed) reference point. The parameter E_F in (1.52) has the dimensionality of energy and is known as the *Fermi energy* or *Fermi level*. This quantity is a regulator of all chemisorptive and catalytic properties of semiconductor crystals. The distribution describes the occupation probability for a quantum state of energy E at a temperature T . If the energies of the available electron states and the degeneracy of the states (the number of electron energy states that have the same energy) are both known, this distribution can be used to calculate thermodynamic properties of systems of electrons.

The Fermi–Dirac distribution functions $f_n(E)$ and $f_p(E)$ are schematically depicted in Figs 1.8a and 1.8b, where the electron energy is indicated on the vertical axis upward and the hole energy on the same axis downward. The line in Fig. 1.8a represents the case of absolute zero ($T = 0$). From (1.52) it follows that at $T = 0$

$$f_n(E) = 1, \quad f_p(E) = 0 \quad \text{for } E < E_F$$

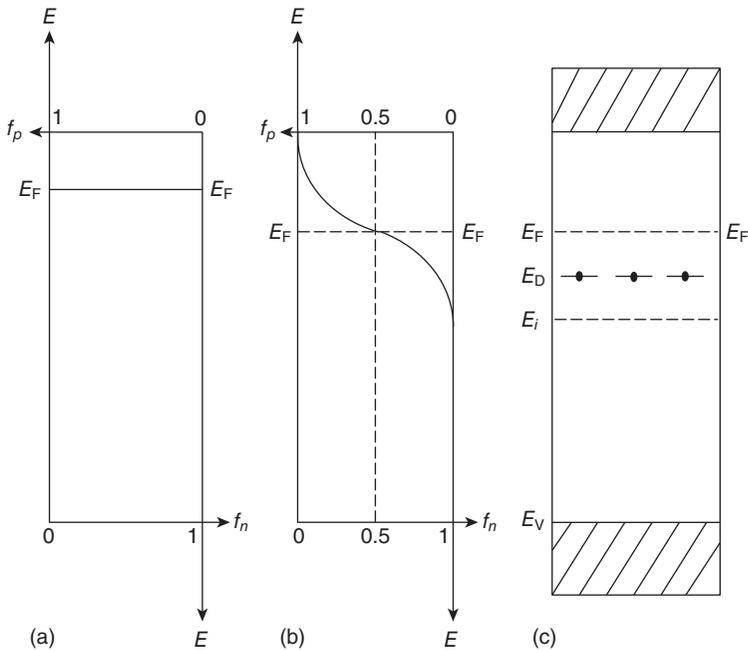
$$f_n(E) = 0, \quad f_p(E) = 1 \quad \text{for } E > E_F$$

i.e. all levels *below* the Fermi level are occupied by electrons (i.e. contain no holes), while all levels *above* the Fermi level are empty (i.e. contain no electrons).

The smooth curve in Fig. 1.8b represents the case when $T \neq 0$ and is symmetric with respect to point $E = E_F$. From (1.52) it follows that

$$f_n(E_F + \Delta E) = f_p(E_F - \Delta E), \quad f_n(E_F) = f_p(E_F) = 1/2$$

Consequently, the Fermi level is one that is populated to an equal degree by electrons and holes. In some respects, this statement may serve as a definition of the Fermi level. From (1.52) it follows that



1.8 Fermi–Dirac distribution functions $f_n(E)$ and $f_p(E)$ and the energy spectrum of a semiconductor with one type of defect at (a) $T = 0$, (b) $T \neq 0$. (c) The energy spectrum.

$$\begin{aligned}
 f_n(E) &= \exp\left(-\frac{E - E_F}{kT}\right) \quad \text{for} \quad \exp\left(-\frac{E - E_F}{kT}\right) < 1, \\
 f_p(E) &= \exp\left(-\frac{E_F - E}{kT}\right) \quad \text{for} \quad \exp\left(-\frac{E_F - E}{kT}\right) < 1
 \end{aligned}
 \tag{1.53}$$

i.e. the Fermi–Dirac distribution turns into the Maxwell–Boltzmann distribution. For electrons, this happens when the energies are considerably *higher* than the Fermi level, while for holes it happens when the energies are much *lower* than the Fermi level. In both cases the electron or hole gas is said to be *non-degenerate*.

Figure 1.8c depicts the energy spectrum of a semiconductor with one type of defect. The extent to which the energy levels in Fig. 1.8c are filled with electrons and holes is given by the curves in Figs 1.8a and 1.8b, which correspond to the fixed position of the Fermi level. Nevertheless this position changes with temperature.

1.6.2 n - and p -type semiconductors

Based on the previous investigations, the electron population of the conduction band and the hole population of the valence band have to be found. In other words, the main concern is in the semiconductor's charge carrier concentrations, which can be denoted by n and p , respectively. According to (1.53)

$$n = \int f_n(E)Z_n(E)dE, \quad p = \int f_p(E)Z_p(E)dE \quad [1.54]$$

where $Z_n(E)dE$ and $Z_p(E)dE$ are the number of states inside the conduction band and valence band, respectively, in the energy range from E to $E + dE$ (per unit volume). In the formula for n the integration is carried over all the levels in the conduction band, and in the formula for p over all the levels in the valence band.

If we assume the electron and hole gases to be non-degenerate [see (1.53)], Eqs (1.54) yield

$$n = N_n \exp\left(-\frac{E_c - E_F}{kT}\right), \quad p = N_p \exp\left(-\frac{E_F - E_v}{kT}\right) \quad [1.55]$$

Here E_c is the bottom of the conduction band and E_v the top of the valence band. The coefficients N_n and N_p depend on the nature of the bands: in the simplest case of an s -band (i.e. the band resulting from the s -level of an isolated atom) we have

$$N_n = 2\left(\frac{m_n kT}{2\pi\hbar^2}\right)^{3/2}, \quad N_p = 2\left(\frac{m_p kT}{2\pi\hbar^2}\right)^{3/2}$$

where m_n and m_p are the effective masses of the electron at the bottom of the conduction band and of the hole at the top of the valence band, respectively.¹⁸ In order of magnitude

$$N_n \sim N_p \sim 10^{19} \text{ cm}^{-3}$$

Equations (1.55) remain valid as long as

$$\exp\left(-\frac{E_c - E_F}{kT}\right) < 1 \quad \text{and} \quad \exp\left(-\frac{E_F - E_v}{kT}\right) < 1 \quad [1.56]$$

i.e. as long as the Fermi level is located deep under the conduction band and high above the valence band. Then the conduction band can be considered as a discrete level coinciding with its bottom and N_n -fold degenerate, while the valence band can be taken as a discrete level coinciding with its top and N_p -fold degenerate.^{18,27,29}

A semiconductor crystal with $n = p$ is called an *i-type semiconductor* (intrinsic semiconductor).^{27,29,33} The position of the Fermi level for such a

semiconductor can be denoted by E_i and the electron (or hole) concentration by n_i . According to (1.55)

$$n_i = N_n \exp\left(-\frac{E_c - E_i}{kT}\right) = N_p \exp\left(-\frac{E_i - E_v}{kT}\right) \quad [1.57]$$

and, hence

$$E_i = \frac{1}{2}(E_c + E_v) - kT \ln \frac{N_n}{N_p} \quad [1.58]$$

It should be noted that the Fermi level of a semiconductor at absolute zero ($T = 0$), or at any other temperature assuming that $N_p = N_n$ (as a rule, $N_p \neq N_n$), is located exactly in the middle of the forbidden section between the bands.

Equations (1.55) can be rewritten on the basis of (1.57) as

$$n = n_i \exp \frac{E_F - E_i}{kT}, \quad p = n_i \exp \frac{E_i - E_F}{kT}$$

It is quite obvious that, if $E_F > E_i$, we are dealing with the n -type semiconductor ($n > p$). On the other hand, if $E_F < E_i$, then semiconductor is a p -type ($p > n$).

As the Fermi level changes upward, the electron concentration in the conduction band increases, as (1.55) implies, while the hole concentration in the valence band decreases:

$$np = n_i^2 = N_n N_p \exp\left(-\frac{E_c - E_v}{kT}\right) \quad [1.59]$$

1.6.3 Statistics of local states

Let us investigate the population of local levels by electrons and holes. In the energy spectrum, these levels represent lattice imperfections (defects). Two types of local levels (corresponding to two types of defects) can be distinguished: *donor levels* and *acceptor levels*. We deal with a donor or with an acceptor depending on whether the defect, being in an electrically neutral state, is depicted by a local level occupied by an electron or a hole. A donor may be either in the neutral state or (freeing itself of an electron) in the positively charged state, while an acceptor may be either in the neutral state or (accepting an electron) in the negatively charged state.

Let us consider that a semiconductor crystal has X donors and Y acceptors of a definite type per unit volume. Taking into account that X^0 and X^+ are the concentrations of neutral and charged donors the Y^0 and Y^- are the concentrations of neutral and charged acceptors. Therefore

$$X = X^0 + X^+, Y = Y^0 + Y^-$$

Then we have for donors

$$n = X^0 = Xf_n, p = X^+ = Xf_p \quad [1.60a]$$

and for acceptors

$$n = Y^- = Yf_n, p = Y^0 = Yf_p \quad [1.60b]$$

where now

$$f_n = \frac{1}{1 + \frac{g_p}{g_n} \exp \frac{E - E_F}{kT}}, \quad f_p = \frac{1}{1 + \frac{g_n}{g_p} \exp \frac{E_F - E}{kT}} \quad [1.61]$$

Here E denotes the position of the local level in the spectrum, and g_n and g_p are the statistical weights of the states occupied by an electron and a hole, respectively, i.e. the number of ways in which these states may be realized (if degeneracy is due only to the electron spin, then $g_n = 2$ and $g_p = 1$).

Comparing (1.61) with (1.52), it can be observed that the local and band states have somewhat different statistics. The reason is not difficult to explain assuming that an energy level is a g -fold degenerate. If this level is positioned inside a band, it can take on g electrons, which may be considered independent: for each electron, there is the same probability of being on this level. However, if an electron appears on a local level, all other electrons are excluded from it. In this case, the interaction between the electrons cannot be neglected. In the final analysis, the difference lies in the corresponding wave functions.

From the practical point of view, the difference between (1.61) and (1.52) is insignificant, and consequently (1.52) can be used instead of (1.61). We can then reduce (1.52) to (1.61) if we substitute E^* for E in (1.52)

$$E^* = E + kT \ln(g_p/g_n)$$

Hence, if we apply the Fermi–Dirac statistics to local levels, these levels shift by $\Delta E = kT \ln(g_p/g_n)$.

In this section we will not discuss the often encountered case where one defect may take on several electrons or holes, i.e. an acceptor or donor capable of multiple ionizations. Nor will we discuss the case (which can be reduced to the above one) where a defect can take on both an electron and a hole, i.e. act as an acceptor and donor simultaneously. Strictly speaking, such defects (just as excitations) cannot be depicted within the band picture, which is built on the one-electron approximation. To do this, we would have to assume that local level population leads to another local level in the spectrum; i.e. each defect would have not one but several alternative levels.

1.6.4 The position of the Fermi level

The position of the Fermi level fixes the charge carrier concentration (the charge carriers are free electrons and holes) and the extent to which the defects in the semiconductor are ionized. It depends on two important factors:^{18,27,29}

1. the nature and concentration of the impurity in the semiconductor;
2. the temperature.

These two factors make the Fermi level moveable within the energy spectrum. Introduction of a donor impurity shifts the Fermi level up, while introduction of an acceptor impurity moves it down. Usually the Fermi level is found from the electrical neutrality of the crystal or, if the crystal is charged, from charge conservation.

Let us find the position of the Fermi level for a neutral semiconductor with one type of donor as an impurity. We denote by n and p , just as we did in the previous sections, the electron concentration in the conduction band and the hole concentration in the valence band, respectively, while X^0 and X^+ will be considered as the concentrations of the neutral and charged donors.

The electrical neutrality condition is simply that

$$n = p + X^+ \quad [1.62]$$

This means that $n \geq p$ and, hence, $E_F \geq E_i$. According to (1.60) and (1.61)

$$X^+ = \frac{X}{1 + \exp\left(\frac{E_F - E_D}{kT}\right)} \quad [1.63]$$

where E_D is donor level [we have assumed that $E_D > (E_c + E_v)/2$; see Fig. 1.8c]. Substituting (1.63) and (1.55) into (1.62), we obtain a third-degree equation for $\exp[(E_c - E_F)/kT]$ or $\exp[(E_F - E_v)/kT]$. There are three cases for which we can easily solve this equation:

1. When the temperature is sufficiently low, so that

$$\frac{N_p}{X} \exp\left(-\frac{E_F - E_v}{kT}\right) < \exp\left(-\frac{E_F - E_D}{kT}\right) < 1$$

(1.62) yields

$$E_F = \frac{1}{2}(E_c + E_D) - kT \ln \frac{N_n}{X} \quad [1.64]$$

and hence, substitution of (1.64) into (1.55) yields

$$n = \sqrt{N_n X} \exp\left(-\frac{E_c - E_D}{2kT}\right) \quad [1.65]$$

It is clearly visible that at $T = 0$ the Fermi level is in the middle of the forbidden gap between the conduction band and the donor levels and, as the temperature grows, the Fermi level shifts down, and the greater X is, the slower it moves.

2. When the temperature is intermediate, so that

$$\frac{N_p}{X} \exp\left(-\frac{E_F - E_v}{kT}\right) < 1 < \exp\left(-\frac{E_F - E_D}{kT}\right)$$

Eq. (1.62) yields

$$E_F = E_c - kT \ln \frac{N_n}{X} \quad [1.66]$$

and, hence, substitution of (1.64) into (1.55) yields

$$n = X \quad [1.67]$$

We can see that in this case the free electron concentration is temperature-independent, and the Fermi level proves to be under the donor levels and continues to move down as the temperature grows.

3. When the temperature is high, so that

$$\frac{N_p}{X} \exp\left(-\frac{E_F - E_v}{kT}\right) < \exp\left(-\frac{E_F - E_D}{kT}\right)$$

(1.62) yields

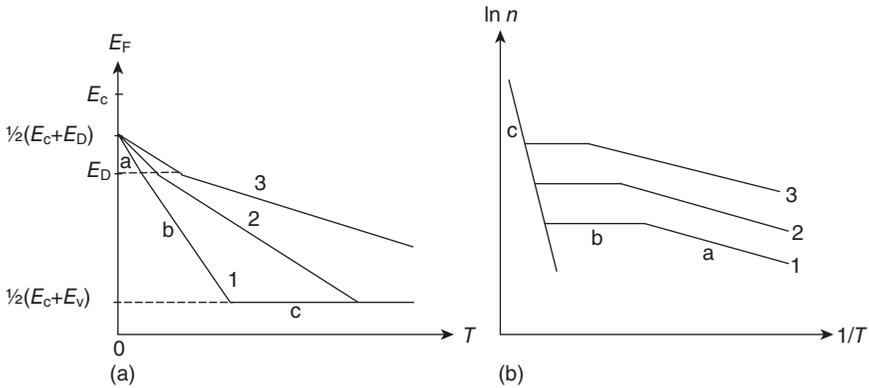
$$E_F = E_i = \frac{1}{2}(E_c + E_v) + \frac{1}{2}kT \ln \frac{N_p}{N_n} \quad [1.68]$$

and

$$n = n_i = \sqrt{N_n N_p} \exp\left(-\frac{E_c - E_v}{2kT}\right) \quad [1.69]$$

i.e. the semiconductor crystal becomes an *i*-type semiconductor [see (1.58) and (1.59)].

Following (1.64), (1.66) and (1.68), we can depict the temperature-dependence of E_F under the assumption that $N_p = N_n$ (see Fig. 1.9a). In Fig. 1.9b we depict the dependence of $\ln n$ on $1/T$. The various curves in Figs 1.9a and 1.9b correspond to different values of X (the numbers indicate an increase in X).



1.9 Temperature dependence of position of Fermi level and electron concentration for a semiconductor: (a) $N_p = N_n$; (b) $\ln n$ vs $1/T$ dependence.

Consequently, the position of the Fermi level and its motion within the local levels with variations of temperature can be determined in a very similar manner for any semiconductor and in any system.

1.7 Limits of the band theory of semiconductors

1.7.1 Characteristic features of the band theory

Basically, the subject matter of all previous explanations of the behaviour of electrons and holes in a semiconductor crystal was within the scope of the *band theory of solids*. Although the band theory is very convenient and pictorial, there are only a few cases when we have to go beyond the limits of this theory. Let us briefly examine the limits of the band theory. First we note some of its characteristic features.

Strictly speaking, the electrons populating a semiconductor can be considered as a system of interacting particles, and the problem is basically many-electron. The band theory makes this many-electron problem a one-electron problem. This is achieved by either neglecting the interaction or accounting for it via the self-consistent field method (Section 1.6) characteristic of the band theory.

Moreover, the band theory is the theory of the behaviour of a single electron. It gives the researcher the right to speak of the behaviour of each electron separately and to ascribe to each electron an individual wave function and individual energy. Within the band theory, each electron lives its own life and pays no attention to the other electrons as if they did not exist. The only reminder of the other electrons is the Pauli principle, which

forbids this electron from taking up quantum states already occupied by the others. This is one characteristic feature of the band theory.

Another feature is the assumption that the force field in which a single electron moves is periodic. The exact form of this field is unimportant to the band theory: it is only essential that the potential is periodic with a period equal to that of the lattice. The characteristic band picture of the energy spectrum, i.e. allowed energy bands generally alternating with forbidden sections, is the result of this periodicity. Hence, the band picture positions in the very prerequisites of the theory the assumption that the potential is periodic. The band theory ignores energy exchange between electron and lattice and the effect of lattice vibrations on the electron energy spectrum.

An important drawback to the band theory is the fact that it takes no account of the tendency of electrons to stay far away from each other. Indeed, if we think of electrons as ignoring each other, there is a possibility of several gathering at one atom (or ion). It may so happen that several concentrate at one atom (or ion) simultaneously. Such states, characterized by overconcentration of electrons at one point, have an equal status with other states in the band theory.

This situation is well known from molecular theory, which uses a method equivalent to Bloch's method^{18,27} in the band theory. This is the method of molecular orbitals (MO method), or the Mulliken–Hund method.⁴³ If we use this method to solve the problem of the hydrogen molecule, we obtain, with non-polar states, polar states, i.e. states in which both electrons gather at one of the two nuclei in the hydrogen molecule while the other nucleus is stripped of its electron. As a result, the hydrogen molecule becomes hetero-polar. In the MO method, such hetero-polar states have the same statistical weight as the homo-polar states and correspond to the same values of energy. If we apply Bloch's method to the crystal lattice, we arrive at the same results.

1.7.2 The validity of the band theory

The limits of the band theory were formulated a long time ago.¹⁸ Based on extensive investigations carried out by many prominent physicists in 20th century, the summary of the conditions for the band theory to be valid is as follows:

- Each atom (or ion) in a crystal lattice has its normal set of electrons. To be precise, the band theory does not work when applied to these 'proper' electrons belonging to the atoms or ions of the crystal lattice. In other words, remaining within the framework of the band theory, we cannot give a correct description of such electrons. However, aside from proper

electrons, an atom or ion in the lattice may hold an additional electron. In the case of an atomic lattice, this additional electron placed on a neutral atom makes it a negative ion, while with ionic lattices such additional electrons produce ions with anomalous charge. These additional electrons may be introduced into the lattice from outside or borrowed from the lattice in the process of shifting electrons from the atom (or ion) to another. When we state that the band theory is able to describe the behaviour of lattice electrons, we actually mean these additional electrons.

- The band theory provides an adequate description of the behaviour of the additional (excess) electrons as long as the concentration of such electrons is low. Consequently, in order for the band theory to be valid, the number of atoms (ions) with an excess charge must be small compared to the overall number of atoms (ions) in the lattice.
- The band theory can be applied to the excess electrons only if such an electron does not change the state of the inner electrons of the atom (ion) that holds such an electron. This is the case when, for example, the inner electrons of an atom (ion) form a closed shell.
- Assuming that all the previous conditions are satisfied, the band theory still ceases to be valid if the interaction between two or more of the excess electrons becomes significant. In other words, the band theory does not work for problems in which two atoms (or ions) are carrying excess charges, i.e. when two such atoms (ions) happen to be close and interact.

As a result, it can be concluded that while the band theory (Bloch's method) works when describing the behaviour of a free electron, i.e. an electron in the conduction band, when we try to describe electrons that fill (partially or completely) the valence band, we immediately run into difficulties with Bloch's method. Indeed, the electrons that fill the valence band cannot claim to have individual wave functions. Their behaviour is essentially a many-electron problem that cannot be reduced to a series of independent one-electron problems.

1.7.3 The valence band

Let us assume that the valence band contains a hole. The electrons in the valence band constitute a family whose behaviour is described by a collective wave function that cannot be presented in the form of products of individual wave functions and depends on the position of all the electrons. By electrons we mean all 'proper' electrons of the lattice atoms (ions) except one electron whose absence is equivalent to the hole. The position coordinates of this electron are not present in the collective wave

function. We can thereby say that this function describes the behaviour of the hole.³⁴

As a result, when describing an electron in the conduction band, we stay within the one-electron approximation while, when describing a hole in the valence band, we are not dealing with a one-hole problem.

The valence band, therefore, has a different meaning from the conduction band. The conduction band constitutes a system of *electron* levels and the valence band is effectively a system of *hole* levels. The relationship between the two is the same as between the optical terms of a one-electron atom and the X-ray terms of a many-electron atom (X-ray terms correspond to removal of an electron from an electron shell). For an atom, we have a whole series of X-ray terms, i.e. the energy of the system depends on which electron is absent in the system. Figures in textbooks on atomic theory usually present electron levels with the energy increasing upward and hole (X-ray) levels with the energy increasing downward. The same is done in the band picture of a crystal, the only difference being that both the electron and the hole levels are combined in one figure.

Such an interpretation of the valence band differs from the Bloch interpretation. In Bloch's method, the 'proper' electrons have an equal status with the excess: valence band electrons are considered as independent as the conduction band electrons, and each is described by an individual wave function. This is as incorrect as trying to build a many-electron atom with n electrons by taking the system of hydrogen levels and placing the n electrons one after another on these levels, allowing only for the Pauli principle. For this reason, from the viewpoint of solid-state theory, the method widely used in theoretical studies of heterogeneous catalysis in which the so-called *d*-electrons (i.e. electrons from the *d*-band) are considered as Bloch electrons, can be considered as unjustified.

Usually when we speak of the valence band of a semiconductor, we do not mean the behaviour of separate and independent electrons. We mean the behaviour of the independent holes. In other words, we do not reduce the many-electron problem to a one-electron but rather to a one-hole problem. As has been mentioned above, the band theory cannot adequately describe the ground state of a system, when the conduction band holds no free electrons and the valence band no free holes. However, it can be used to describe the excited states characterized by the presence of electrons in the conduction band and holes in the valence band.

It has been well-known that the excited states of a system can quantum-mechanically be considered as an ideal gas of so-called quasi-particles, *elementary excitations*. The system energy then splits into the ground state energy and the energies of individual elementary excitations. Free electrons and holes, with which the electron theory of solids is concerned, is nothing more than an example of such elementary excitations.

In conclusion, it must be noted that there is a broad group of problems in solid-state theory relevant to semiconductors that can be solved by the energy band approach. This method, if understood correctly, has every right to be further developed to explain ever more experimental data. However, the solid-state theory also has problems that go beyond the scope of the band theory. The recombination of a free electron with a free hole, a process that in the band theory is described as the drop of an electron from the conduction band to the valence band, is an example of such a problem. Here the band theory gives the initial and final states but is unable to disclose the mechanism of the process in which the hole and electron interact. The same certainly applies to the inverse process of ionization (i.e. creation of a free electron and a free hole), where the band theory again gives only the initial and final states. Intermediate states, which are excitonic states, cannot be explained by the band theory.

1.8 State-of-the-art techniques for characterization of nanostructured semiconductors

Today the vast majority of semiconductors employed in modern electronic devices are nanostructured and the average grain size is within 5–50 nm. Many of them were intercalated by either H^+ or ions of different metals in order to improve their conductivity.⁴⁴ This has resulted not only in the miniaturization of most of the electronic components of devices, but also in an enhancement of their functionality, which relies on the fact that the concentration of free charge carriers has been enhanced in atomically-thin semiconductors compared to their bulk counterparts.⁴⁵ These newly-discovered properties of the quasi-2D semiconductors have already opened new opportunities in new families of devices such as photovoltaic devices, sensors capable of single molecule detection, various optical devices, etc.^{46–49}

As the size of nanoparticles used in quasi-2D layers of functional nanomaterials decreases, the demand for accurate analysis and precise characterization of these nanolayers increases. Sometimes the newly developed semiconductor nanostructures can be as thin as few nm,⁵⁰ and therefore special techniques are required for their analysis and characterization. Modern state-of-the-art techniques involve the use of ions, electrons or photons (e.g. X-rays or infrared light) to probe nanostructured semiconductors, in order to investigate their composition, structure and physical and electrochemical properties. These analyses can: determine the chemical composition and phase of the composite; detect the presence (or absence) of contaminants or dopants; and investigate the physical structure or appearance of the sample of interest. This detailed information is highly useful feedback to scientists, as they can readjust nanotechnology, develop

Table 1.1 Review of analytical techniques with their typical applications and detection limits applicable for analysis of various nanostructured semiconductors

Analytical technique	Typical applications	Detection limits	Imaging/ mapping	Lateral resolution/ probe size
Accelerator Techniques				
Rutherford backscattering	Thin film composition/thickness, quantitative dose measurements, quantitation without standards, hydrogen in thin films, defects and lattice locations	RBS 0.001–10 at% (Z dependent) NRA > 1×10^{15} at/ sm ² HFS 0.1 at%	No	≥ 1 mm
Spectrometry				
Nuclear reaction analysis				
Hydrogen forward scattering Spectrometry				
Channeling				
AFM				
Atomic force microscopy	Roughness, 3D imaging of surfaces, magnetic field, grain size	n/a	Yes	1.5–5 nm
Auger				
Auger electron spectroscopy	Surface, particle, defect analysis, and large and small area depth profiling	0.1–1 at% submonolayer	Yes	≥ 10 nm (field emission) 50 nm–1 μm
EBIC				
Electron beam induced current	Junction location, electrically active crystal defects, depletion layer widths, minority carrier diffusion length	n/a	Yes	
EBSD				
Electron backscatter diffraction	Grain size, grain orientation, grain misalignment, % crystallinity	n/a	Yes	1 nm imaging; ~80 nm minimum grain size
FIB/SEM Imaging				
Dual-beam and single-beam	<i>In situ</i> cross-section preparation and imaging	n/a	Yes	1 nm
FTIR				
Fourier transform infrared spectroscopy	Identification of polymers and organics, contamination identification, particles	0.1–1 wt%	No	≥ 15 μm
GC-MS				
Gas chromatography–mass spectrometry	Identification and quantification of volatile organic compounds in mixtures, outgassing, residual solvents, liquid or gas injection	400 ng (full scan) 10 ng (outgassing)	n/a	n/a
GDMS				
Glow discharge mass spectrometry	Bulk analysis, trace and ultra-trace elemental survey analysis, depth profiling	10 ppt wt – 100%	No	5–5 mm

ICP-OES Inductively coupled plasma optical emission spectroscopy	Bulk composition analysis	10 ppt wt – 100%	n/a	n/a
IGA Instrumental gas analysis (combustion and fusion gas analysis)	Bulk analysis of H, C, N, O and S fractional gas analysis	0.1 ppm – 50%	n/a	n/a
LA-ICPMS and ICPMS Laser ablation inductively coupled plasma mass spectrometry	Bulk composition, trace and ultra-trace elemental analysis, impurity distribution mapping	10 ppb wt – 100%	Yes	5 μ m
LEXES Low-energy X-ray emission spectrometry	Dosimetry /mapping of ion implants, thin film characterization	5×10^{13} at/cm ²	Yes	30 μ m
OP Optical profilometry	Non-contact 3D imaging of surface topography	n/a	Yes	435 nm
Raman Raman spectroscopy	Identification of organics and inorganics, particle identification, stress measurement, carbon phase identification	≥ 1 wt %	Yes	$\geq 1 \mu$ m
SEM (with EDS) Scanning electron microscopy energy dispersive X-ray spectroscopy	Imaging, elemental identification	0.1%	Yes	1 nm imaging 0.5 μ m EDS
SIMS Secondary ion mass spectrometry	Dopant and impurity depth profiling, surface, bulk and microanalysis, insulating films, ultra-low energy/ ultra-shallow depth profiling	10^{12} – 10^{16} at/cm ³	Yes	$\geq 20 \mu$ m (depth profiling) 1–5 μ m (imaging mode) 0.25 nm
STEM (with EDS and EELS) Scanning transmission electron microscopy Energy dispersive X-ray spectroscopy Electron energy loss spectroscopy	Imaging, Z-contrast, elemental mapping elemental identification, EELS line scans, lattice imaging, bright field and dark field imaging	1%	Yes	

Continued

Table 1.1 Continued

Analytical technique	Typical applications	Detection limits	Imaging/ mapping	Lateral resolution/ probe size
TEM (with EDS and EELS)				
Transmission electron microscopy	Imaging, elemental identification, crystallographic information, lattice imaging	0.5%	Yes	0.19 nm
Energy dispersive X-ray spectroscopy				
Electron energy loss spectroscopy	Thermal stability and composition of organic/ inorganic composite materials, glass transition, crystallization, melting, clustering, curing, chemisorption, etc.	0.01–200 °C/min; 20–1100 °C; 40.1 mg–4200 mg; 42.5 μV–42500 μV	n/a	n/a
TGA/DTA/DSC				
Thermogravimetric analysis	Surface microanalysis of organic and inorganic materials, chemical mapping	10^7 – 10^{10} at/cm ² sub-monolayer	Yes	≥0.20 μm
Differential thermal analysis				
Differential scanning calorimetry				
TOF-SIMS				
Time-of-flight secondary ion mass spectrometry				
TXRF				
Total reflection X-ray fluorescence spectroscopy	Metallic surface contamination on semiconductor wafers, non-destructive	10^9 – 10^{12} at/cm ²	Yes	~10 mm
XPS/ESCA				
X-ray photoelectron spectroscopy	Surface analysis of organic and inorganic materials, depth profiling	0.01–1 at% Sub-monolayer	Yes	10 μm–2 mm
Electron spectroscopy for chemical analysis				
XRD				
X-ray diffraction	Identification of crystal phases, crystal orientation and crystal quality, % crystallinity	1 at%	No	50 μm
XRR				
X-ray reflectivity	Determination of film density, roughness and thickness	n/a	Yes	5 mm
XRF				
X-ray fluorescence	Composition and impurities in thick films and bulk materials, wafer mapping	10 ppm	Yes	75 μm

other similar nanomaterials for various products, or optimize a new manufacturing process. Plate I (see colour section between pages 232 and 233) summarizes typical techniques for analysis of nanomaterials depending on the depth of their impact on analysing nanostructure.

A review of such techniques allows researchers to choose the best possible approach and selection of suitable methods depending on the thickness of the samples obtained. By careful selection of these methods, such structural parameters as dopant and impurity depth profiling, nanofilm coating, bulk composition and impurity identification, materials characterization, characterization of nanoparticles, nanodefects and residues, crystal structure determination, roughness measurement and investigation of the thermal properties may be analysed and optimized. Table 1.1 provides an overview of the modern state-of-the-art analytical techniques with their detection limits and possible applications to nanostructured semiconductors.

1.9 References

1. H.J. Queisser, E.E. Haller, Defects in semiconductors: Some fatal, some vital, *Science*, 281 (1998) 945–950.
2. J. Simon, V. Protasenko, C.X. Lian, H.L. Xing, D. Jena, Polarization-induced hole doping in wide-band-gap uniaxial semiconductor heterostructures. *Science*, 327 (2010) 60–64.
3. A. Davydov, *Molecular Spectroscopy of Oxide Catalysts Surfaces*, 2003, Wiley, Chichester, 669p.
4. F.A. Cotton, G. Wilkinson, *Advanced Inorganic Chemistry*, 5th ed., 1997, Wiley, New York, 396p.
5. W. Walukiewicz, Amphoteric native defects in semiconductors, *Appl. Phys. Lett.*, 54 (1989) 2094–2096.
6. D.D. Yao, J.Z. Ou, K. Latham, S. Zhuiykov, A.P. O’Mullane, K. Kalantar-zadeh, Electrodeposited α - and β -phase MoO₃ films and investigation of their gasochromic properties, *Cryst. Growth Des.*, 12 (2012) 1865–1870.
7. N.C. Cates, R. Gysel, Z. Beiley, C.E. Miller, M.F. Toney, M. Heeney, I. McCulloch, M.D. McGehee, Tuning the properties of polymer bulk heterojunction solar cells by adjusting fullerene size to control intercalation, *Nano Lett.*, 9 (2009) 4153–4157.
8. S. Balendhran, J.Z. Ou, M. Bhaskaran, S. Sriram, S. Ippolito, Z. Vasic, E. Kats, S. Bhargava, S. Zhuiykov, K. Kalantar-zadeh, Atomically thin layers of MoS₂ via a two step thermal evaporation – exfoliation method, *Nanoscale*, 4 (2012) 461–466.
9. G.A. Somorjai, *Chemistry of Two Dimensions: Surfaces*, 1981, Cornell University Press, Ithaka, NY, 367p.
10. T.H. Etsell, S.N. Flenders, The electrical properties of solid oxide electrolytes, *Chem. Rev.*, 70 (1970) 339–376.
11. G. Ertl, H. Knozinger, J. Weitkamp, *Handbook of Heterogeneous Catalysis*, v. 2, 1997, Wiley-VCH, Weinheim, 380p.

12. A. Zecchina, D. Scarano, S. Bordiga, G. Ricchiardi, G. Spoto, F. Geobaldo, IR studies of CO and NO adsorbed on well characterized oxide single microcrystals, *Catal. Today*, 27 (1996) 403–435.
13. S. Zhuiykov, In-situ FTIR study of oxygen adsorption on nanostructured RuO₂ thin-film electrode, *Ionics*, 15 (2009) 507–512.
14. J.L.G. Fierro, *Spectroscopic Characterization of Heterogeneous Catalysis, Part A: methods of surface analysis, Part B: Chemisorption of probe-molecules*, 1990, Elsevier, Amsterdam, 498p.
15. D.B. Holt, B.G. Yacobi, *Extended Defects in Semiconductors: Electronic Properties, Device Effects and Structures*, 2007, Cambridge University Press, Cambridge, 644p.
16. H.H. Kung, *Transition Metal Oxides: Surface chemistry and catalysis*, 1989, Elsevier, NY, 497p.
17. J. Nowotny, *Oxide Semiconductors for Solar Energy Conversion*, 2012, CRC Press, Boca Raton, 392p.
18. T. Wolkenstein, *Electronic Processes on Semiconductor Surfaces During Chemisorption*, 1990, Plenum Publishing, New York, 445p.
19. J. Nowotny, T. Bak, C.C. Sorell, Charge transfer at the oxygen/zirconia interface at elevated temperatures. Part 7: Effect of surface processing, *Adv. Appl. Ceram.*, 104 (2005) 195–199.
20. J. Cabane, F. Cabane, Equilibrium segregation at interfaces, in: *Interface Segregation and Related Processes in Materials*, J. Nowotny, Ed., 1991, Trans. Tech. Publications, Zurich, 1–159p.
21. J. Nowotny, Interface defect chemistry and its impact on properties of oxide ceramic materials, in: *Science of Ceramic Interfaces*, J. Nowotny, Ed., 1991, Elsevier, Amsterdam, 79–204p.
22. M.K. Nowotny, L. Sheppard, T. Bak, J. Nowotny, Defect chemistry of titanium dioxide. Application of defect engineering in processing of TiO₂-based photocatalysts, *J. Phys. Chem. C*, 112 (2008) 5275–5230.
23. S. Zhuiykov, D. Marney, E. Kats, Investigation electrochemical properties of La₂O₃-RuO₂ thin-film sensing electrode used in sensors for analysis of complex solutions, *Int. J. Appl. Ceram. Tec.*, 8 (2011) 1192–1200.
24. M. Breedon, S. Zhuiykov, N. Miura, The synthesis and gas sensitivity of CuO micro-dimensional structures featuring a stepped morphology, *Mater. Lett.*, 83 (2012) 51–53.
25. S. Zhuiykov, E. Kats, D. Marney, Potentiometric sensor using sub-micron Cu₂O-doped RuO₂ sensing electrode with improved antifouling resistance, *Talanta*, 82 (2010) 502–507.
26. B.P. Singh, R. Singh, *Electronic Devices and Integrated Circuits*, 2006, Pearson Education, Delhi, 958p.
27. P.Y. Yu, M. Cardona, *Fundamentals of Semiconductors: Physics and materials properties*, 2010, Springer, Berlin, 780p.
28. G.S. May, S.M. Sze, *Fundamentals of Semiconductor Fabrication*, 2003, Wiley, New York, 320p.
29. R.F. Pierret, *Advanced Semiconductor Fundamentals*, 2nd ed., 2002, Prentice Hall, Englewood Cliffs, 221p.
30. S. Zhuiykov, *Electrochemistry of Zirconia Gas Sensors*, 2007, CRC Press, Boca Raton, 297p.

31. J. Wu, J. Cao, W.-Q. Han, A. Janotti, H.-C. Kim, *Functional Metal Oxide Nanostructures*, 2012, Springer, New York, 368p.
32. M.D. McCluskey, S.J. Jokela, Sources of *n*-type conductivity in ZnO, *Phys. B*, 401–402 (2007) 355–360.
33. S. Samson, C.G. Fonstad, Defect structure and electronic donor levels in stannic oxide crystals, *J. Appl. Phys.*, 44 (1973) 4618–4623.
34. A.I. Anselm, *An Introduction to Semiconductor Theory*, 1981, Mir Publishing, Moscow, 356p.
35. N.F. Mott, W. Jones, *The Theory of Properties of Metals and Alloys*, 1958, Oxford University Press, Oxford, 279p.
36. J. Baik, M. Zielke, M.H. Kim, K.L. Turner, A.M. Wodtke, M. Moskovits, Tin-oxide-nanowire-based electronic nose using heterogeneous catalysis as a functionalization strategy, *ACS Nano*, 4 (2010) 3117–3121.
37. G. Brouwer, A general asymptotic solution of reaction equations common in solid-state chemistry, *Phillips Res. Rep.*, 9 (1954) 366–371.
38. N.W. Ashcroft, N.D. Mermin, *Solid State Physics*, 1976, Brooks Cole, NY, 409p.
39. S.G. Davison, M. Steslicka, *Basic Theory of Surface States*, 1993, Oxford Science Publications, Clarendon, 220p.
40. W. Shockley, On the surface states associated with a periodic potential, *Phys. Rev.*, 56 (1939) 317–323.
41. S.G. Davison, A.T. Amos, Spin polarized orbitals for localized states in crystals, *J. Chem. Phys.*, 43 (1965) 2223–2233.
42. L. Pauling, E.B. Wilson, *Introduction to Quantum Mechanics with Applications to Chemistry*, 1985, General Publishing Corp., Toronto, 468p.
43. F.O. Ellison, H. Shull, Molecular calculations. I. LCAO MO self-consistent field treatment of the ground state of H₂O, *J. Chem. Phys.*, 23 (1955) 2348–2358.
44. J.Z. Ou, S. Balendhran, M.A. Field, D.G. McCulloch, A.S. Zoofakar, R.A. Rani, S. Zhuiykov, A.P. O'Mullane, K. Kalantar-zadeh, The anodized crystalline WO₃ nanoporous network with enhanced electrochromic properties, *Nanoscale*, 4 (2012) 5980–5988.
45. J.Z. Ou, R.A. Rani, M.H. Ham, Y. Zhang, H. Zheng, S. Sriram, M. Bhaskaran, K. Latham, S. Zhuiykov, R.B. Kaner, K. Kalantar-Zadeh, Elevated temperature anodized Nb₂O₅ – a photoanode material with exceptionally large photoconversion, *ASC Nano*, 6 (2012) 4045–4053.
46. S. Balendhran, J. Deng, J.Z. Ou, J. Scott, J. Tang, K. Wang, M.S. Field, S. Russo, S. Zhuiykov, M. Strano, N. Medhekar, S. Sriram, M. Bhaskaran, K. Kalantar-zadeh, Enhanced change carrier mobility in two-dimensional high dielectric molybdenum oxide, *Adv. Mater.*, 25 (2013) 109–114.
47. J.J. Jasieniak, J. Seiffter, J. Jo, T. Mates, A.J. Heeger, A solution-processed MoO_x anode interlayer for use within organic photovoltaic devices, *Adv. Funct. Mater.*, 22 (2012) 2594–2605.
48. M.J. Allen, V.C. Tung, R.B. Kaner, Honeycomb carbon: A review of graphene, *Chem. Rev.*, 110 (2010) 132–145.
49. H. Zeng, J. Dai, W. Yao, D. Xiao, X. Cui, Valley polarization in MoS₂ monolayers by optical pumping, *Nature Nanotechnol.*, 7 (2012) 490–493.
50. C. Lee, H. Yan, L.E. Brus, T.F. Heinz, J. Hone, S. Ryu, Anomalous lattice vibrations of single- and few-layer MoS₂, *ACS Nano*, 4 (2010) 2695–2700.

Structural and chemical modification of semiconductor nanocrystals

DOI: 10.1533/978178242242.50

Abstract: The chapter begins by reviewing the modern deposition techniques for semiconductor nanocrystals, doping of semiconductors using an example of ZnO nanowires and the development of nanoscale semiconductor hetero-structures. The chapter then discusses physical electrochemistry and structural and electrochemical properties of semiconductor nanocrystals.

Key words: doping of oxide semiconductors, surface stoichiometry, vapour-phase growth, solution-phase growth

2.1 Introduction

Since the beginning of the 21st century, there has been an unprecedented growth in demand for portable electronic devices and wireless data transmitters including mobile phones, as the internet has opened completely new possibilities for science, business and commerce. These past few years have witnessed a remarkable increase in interest in the development of new nanostructured semiconductors with modified and, sometimes, completely new and unpredictable structural and electrochemical properties, caused either by new hetero-junction interfaces or advanced nanotechnologies.¹⁻¹⁰ One of the important factors driving the current interest in nanostructured semiconductors is their properties at the nanoscale, which can be successfully utilized in various applications. Recent advances in the field of nanotechnology have led to the synthesis and characterization of an assortment of embodiments of metal oxide semiconductors in nanowires (NWs), nanobelts (NBs), nanorods (NRs), nanotubes and other configurations. In-depth physical and electrochemical property characterization has already demonstrated them to be promising candidates for the next generation of electronics, optoelectronics and sensing devices. Nanostructured metal oxide semiconductors stand out as one of the most versatile nanomaterials, owing to their diverse properties and functionalities. These can be achieved by careful selection of appropriate manufacturing technologies and deposition techniques, which will be discussed in detail in the following sections. Based on the synthesis environment, these can be divided into two major categories: vapour-phase growth and liquid (solution)-phase growth.¹¹ Most of the metal oxide nanostructures are grown via the well-developed

vapour-phase technique, which is based on the reaction between metal vapour and oxygen in a gaseous environment. The governing mechanisms are the vapour–liquid–solid process (VLS) and vapour–solid (VS) process. On the other hand, solution-phase growth methods provide a more flexible synthesis process as an alternative to achieve lower costs.

2.2 Vapour-phase material growth

High-temperature vapour-phase growth assisted by a thermal furnace is a relatively straightforward approach that controls the reaction between a metal vapour source and oxygen gas. In order to control the dimensions of nanoparticles, their aspect ratio, morphology and crystallinity, the following diverse fabricating techniques have been extensively employed during preparation of advanced semiconductors:

- thermal chemical vapour deposition (CVD);^{1,12}
- direct thermal evaporation;¹³
- pulsed laser deposition (PLD);^{14–16}
- metal–organic chemical vapour deposition (MOCVD).^{17–19}

These manufacturing techniques are based on two mechanisms: VLS and VS.

The VLS mechanism was first proposed by Wagner and Ellis in 1964²⁰ while observing the growth of Si whiskers.²¹ Basically, VLS is a catalyst-assisted growth technique which uses metal nanoclusters or nanoparticles as the nucleation seeds. These nucleation seeds determine the interfacial energy, growth direction and diameter of the nanostructure. Therefore, a proper choice of catalyst is critical. In the case of growing semiconductor metal oxides, the VLS process is initiated by the formation of a liquid alloy droplet which contains both a catalyst and a source metal. Precipitation occurs when the liquid droplet becomes supersaturated with the source metal. Under the flow of oxygen, semiconductor metal oxide nanocrystals are created.²² Normally the resulting crystal is grown along one particular crystallographic orientation which corresponds to the minimum atomic stacking energy, leading to the structural development. This type of growth is epitaxial; thus it results in high crystalline quality. Real-time *in-situ* transmission electron microscope observations can provide direct evidence of VLS growth and depict a vivid dynamic insight for the better understanding of such microscopic chemical processes.²³

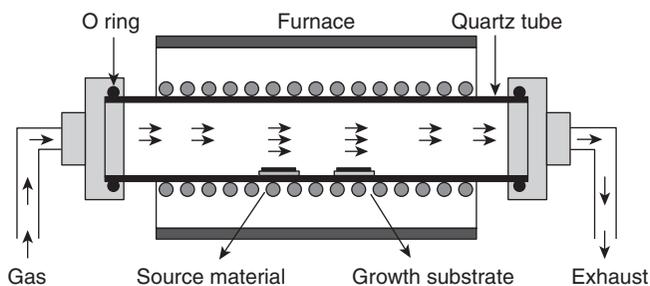
During recent years, successful reports have been published in relation to sintering of the following semiconductor oxide NWs by the VLS technique: TiO₂,²⁴ SnO₂,²⁵ ZnO,²⁶ CdO,⁸ In₂O₃,²⁷ MgO²⁸ and Ga₂O₃.²⁹ Based on the VLS mechanism, several approaches have also been developed. For instance, the thermal CVD synthesis process can be utilized in a thermal

furnace to vaporize the metal source. The applicable amount of oxygen gas is introduced in the next step through the mass flow controller. Both the metal and the oxygen vapour can be supplied by different means, such as carbothermal or hydrogen reduction of metal oxide source material^{30,31} and flowing water vapour instead of oxygen.^{32,33}

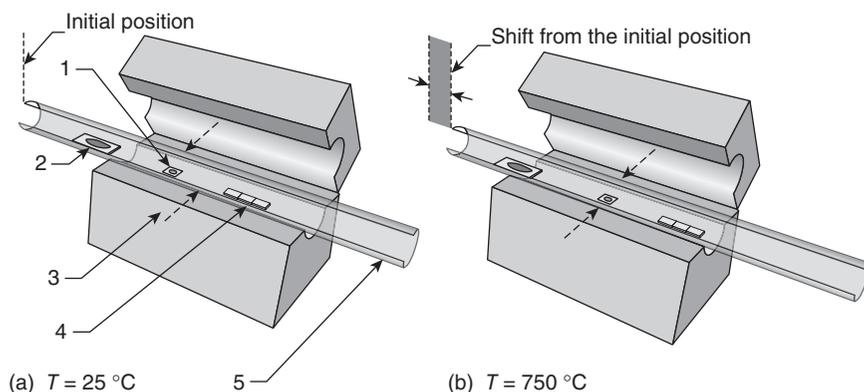
Figure 2.1 graphically depicts a typical thermal CVD set-up consisting of a horizontal quartz tube and a resistive heating furnace.¹¹ Metal source material is positioned inside the quartz tube. Another substrate (SiO_2 , sapphire, etc.) is deposited with catalyst nanoparticles and placed downstream for nanostructure growth.

A VS mechanism occurs in many catalyst-free growth processes.^{34–40} It must be admitted that, despite the substantial use of VS operations in the development of oxide nanostructures, we still lack fundamental understanding of the process. Several experimental and theoretical works have suggested that the minimization of surface free energy primarily governs the VS process.^{37–40} Under high-temperature conditions, source materials are vaporized and then directly condensed on the substrate which is situated in the low-temperature region. Once the condensation stage is reached, the initially condensed molecules form seed crystals serving as nucleation sites. As a consequence of this, they facilitate directional growth to minimize the surface energy. This self-catalytic growth associated with many thermodynamic parameters is a relatively complicated procedure that needs quantitative modelling.

A very interesting modification of the CVD technique has recently been reported,⁴¹ where atomically-thin MoS_2 was prepared at a temperature less than 830°C by a two-step method schematically presented in Fig. 2.2. Interest in the development of two-dimensional (2D) semiconductors has been steadily growing during the last few years due to their unique physical and electrochemical properties compared to the in bulk counterparts. Fabrication of 2D materials is generally a process consisting of two



2.1 Schematic of a thermal furnace synthesis system used in vapour phase growth methods including CVD, thermal evaporation and PLD. (Reprinted from Ref. 11 with permission from Elsevier Science)



2.2 Experimental set-up: (a) initially at room temperature, the centre of the tube is offset from the centre of the furnace; (b) at $750\text{ }^{\circ}\text{C}$, the tube is pushed inside the furnace aligning the centre of the tube with the centre of the furnace. [Legend: (1) MoO_3 nanopowder; (2) sulphur powder; (3) horizontal furnace; (4) quartz substrates for deposition; (5) quartz tube] (Reprinted from Ref. 41 with permission from The Royal Society of Chemistry)

phases: synthesis of the layered bulk material followed by a mechanical exfoliation process.⁴² Although a wide range of controlled methods of synthesis is available to produce different morphologies of MoS_2 , the fabrication of layered MoS_2 is a topic that is yet to be widely explored. A few known approaches to layered MoS_2 synthesis are thermal decomposition of ammonium thiomolybdate precursors and chemical reactions between S- and Mo- based compounds.⁴³ These schemes consist of highly controlled parameters (pressure, temperature, etc.) and also require complex chemical experimental apparatus (a three-zone furnace, autoclave set-ups, etc.).^{44,45} In addition, some of these methods involve hazardous materials such as H_2S and CS_2 and are conducted over a long period of time, features which render them less desirable.⁴⁴ The thermal evaporation procedure developed for the fabrication of layered MoS_2 involved CVD of MoO_3 nanopowder in a horizontal furnace along with excess sulphur, overcoming the direct evaporation barrier with MoS_2 .⁴¹

2.3 Solution-phase material growth

Fabrication of various NWs, NRs and nanoneedles of semiconductors in solution phase has been successfully achieved. This growth method is usually carried out at ambient temperature which considerably reduces the complexity and cost of fabrication. To develop strategies that can guide and confine the growth direction to form 1D, 2D and other nanostructures, researchers have used a number of approaches which may be grouped as follows:

- *Template-assisted synthesis.*^{46,47} Large-area patterning of 1D metal oxide NW arrays assisted by templates can be achieved by using a periodic structured template, such as anodic aluminium oxide (AAO), molecular sieves or polymer membranes, whereby nanostructures can form inside the confined channels. For instance, AAO membranes have embedded hexagonally-ordered nanochannels. These are prepared via the anodization of pure Al in acidic solution.⁴⁷ The indicated pores can be filled to form different nanostructures using electro-deposition and sol-gel deposition methods. Because the diameter of these nanochannels and the inter-channel distance are easily controlled by the anodization voltage, this provides a convenient means to manipulate the aspect ratio and the area density of the developing nanostructures.
- *Electrochemical deposition (ED).*^{48–52} ED has been widely used to fabricate metallic NWs in porous structures. This method has also been very reliable for sintering metal oxide nanostructures. In fact, there are both direct and indirect approaches to the fabrication as quasi-1D metal oxides using ED. By using a direct method and with careful choice of the electrolyte, nanostructured ZnO,⁴⁸ Fe₂O₃,⁴⁹ Cu₂O⁵⁰ and NiO⁵¹ have been successfully synthesized. By using an indirect approach, SnO₂ NWs⁵² and ZnO NWs⁵³ have been fabricated.
- *Sol-gel technique.*^{54–59} This procedure has been widely used for the development of various nanostructures. In general, the sol-gel process is associated with a gel composed of sol particles. As the first step, colloidal (sol) suspension of the desired particles is prepared from a solution of precursor molecules. An AAO template will be immersed into the sol suspension, so that the sol will aggregate on the AAO template surface. With an appropriate deposition time, sol particles can fill the channels and form structures with high aspect ratio. The final product will be obtained after a thermal annealing to remove the gel. Nanostructures of ZnO⁵⁴ MnO₂,⁵⁵ ZrO₂,⁵⁶ and TiO₂⁵⁷ were obtained by utilizing the sol-gel method. There were also reports that various multi-compound oxide NRs^{58,59} had also been synthesized.
- *Surfactant-assisted growth.*^{60–65} Surfactant-promoted anisotropic nanocrystal growth has been considered as a convenient way to synthesize oxide NWs. This anisotropic growth is often carried out in a micro-emulsion system composed of three phases: oil, surfactant and aqueous. In the emulsion system, these surfactants serve as micro-reactors to confine the crystal growth. To obtain the desired nanomaterials, both species of precursor, the surfactants and also other parameters such as temperature, pH value and concentration of the reactants must be very carefully selected. As a result, the surfactant-assisted system is a trial-and-error-based procedure which requires much endeavour to choose the proper capping agents and reaction environment. Recent reports

have highlighted that ZnO,⁶⁰ SnO₂,⁶¹ NiO⁶² NRs have been sintered by this method. Moreover, PbO₂,⁶³ PbCrO₄, CuCrO₄, BaCrO₄⁶⁴ and CeO₂⁶⁵ NRs have also been fabricated.

- *Sonochemical method.*^{66–71} The sonochemical procedure uses an ultrasonic wave to acoustically agitate or alter the reaction environment. As a result, it modifies the crystal growth. The sonication process is based on the acoustic cavitation phenomenon which involves the formation, growth and collapse of many bubbles in the aqueous solution.⁶⁶ Extreme reaction conditions can be created at localized spots. Assisted by the extreme parameters, for example, at very high temperatures and pressures larger than 500 atm, and a cooling rate higher than 10¹⁰ K/s, nanostructures of metal oxides can be fabricated via chemical reactions. There are reports regarding the development of metal oxide NRs by this method: Fe₃O₄⁶⁷ and ZnO.⁶⁸ More recently, other nanocomposites have been grown by applying this technique: ZnO NR/CdS nanoparticle (core/shell) composites,⁶⁹ Eu₂O₃ NRs⁷⁰ and CeO₂ nanotubes.⁷¹
- *Hydrothermal technique.*^{72–80} The hydrothermal process has been used to produce crystalline structures since the 1970s. This mechanism begins with an aqueous mixture of soluble metal salt (metal and/or metal–organic) of the precursor materials. Usually, the mixed solution is placed in an autoclave under elevated temperature and relatively high-pressure conditions. Typically, the temperature ranges between 100 and 300 °C and the pressure exceeds 1 atm. ZnO NRs have been sintered by using wet-chemical hydrothermal approaches.^{72–74} Other nanostructured metal oxides such as, such as CuO,⁷⁵ Ga₂O₃,⁷⁶ MnO₂ nanotubes,⁷⁷ Fe₃O₄,⁷⁸ CeO₂,⁷⁹ TiO₂⁸⁰ and In₂O₃²⁷ have also been developed.

2.4 Vertical and horizontal alignment strategies

It is well-known that in most cases metal oxide nanofilms deposited using various technologies are agglomerated.¹ In this context, it becomes clear that during comparative analysis of the different characteristics of the metal nano-oxides it is necessary to consider first the size of agglomerates and their porosity; and only after that the grain size and film thickness. Consequently, when applying structural engineering methodology¹ for fabrication processes, the following geometric parameters of metal oxide nanostructures should be controlled in order to achieve the desired properties:⁸¹

- grain size;
- agglomeration;
- area of inter-grain and inter-agglomerate contacts;
- thickness;

- porosity;
- dominant orientation and faceting of crystallites.

However, it is necessary to note that the indicated parameters are only a part of the metal oxide matrix guidelines which can influence properties of nano-oxides. Without a doubt, besides the geometric framework, the following physical chemical specifications of the nanocomposite matrix must also be taken into account:

- chemical and phase composition;
- type of conductivity of additives;
- the bulk and surface oxygen vacancy concentrations (stoichiometry);
- size and density of both metal catalyst particles and single atoms on the surface of metal oxides;
- surface architecture;
- type and concentration of uncontrolled impurities, and so on.

This is because even a slight variation in these parameters can drastically affect the electrophysical, electrochemical, adsorption and catalytic properties of metal nano-oxides. In order to fully take advantage of the geometric anisotropy of 1D and 2D nanostructures for integrated device applications, the control of their location, orientation and packing density is also very important. Since these nanostructures can be grown from catalytic seeds via the VLS process, one route to reach this objective is to simply control the locations of the catalysts. In fact, both lithographic (top-down) and non-lithographic (bottom-up) techniques have been employed to achieve defined growth of semiconductor nanostructures. Based on these capabilities, vertical as well as horizontal alignment of metal oxide nanostructures has been accomplished. In many cases, an epitaxial substrate/layer is utilized to assist the directional growth of nanostructures. In addition, alignment using a template or external field has also been achieved. Several procedures which are applied for the manipulation, orientation and alignment of semiconductor metal oxide NWs will be described in the following sections.

2.4.1 Catalyst patterning

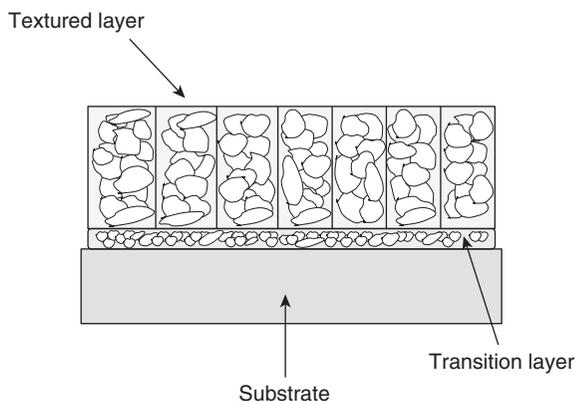
A simple route leading to the growth of NWs at the desired location is by catalyst patterning. Lithography and nano-imprint⁸² techniques have been widely used to achieve this objective. In general, they refer to photolithography, electron beam lithography and masking methods. By utilizing standard UV exposure, catalyst patterns are easily defined by photolithography with a resolution limit of $\sim 1\ \mu\text{m}$.¹¹ It has been demonstrated that square and hexagonal catalyst pattern arrays were generated on sapphire substrate, and

ZnO NWs were grown from the patterned catalysts via a VLS process.³⁰ On the other hand, due to the high resolution of electron beams, electron beam lithography can achieve more precision in defining the catalyst pattern, yielding highly-ordered and high-density NW arrays. Another approach is to imprint a mask or to take a ready-to-use patterned structure to serve as a shadow mask. This method has attracted interest owing to its low cost and simple implementation. For instance a transmission electron microscopy (TEM) copper grid has been used as a mask to directly generate patterns for Au catalyst deposition, which results in the growth of ZnO NW arrays.⁸³

2.4.2 Substrate lattice matching

One of the essential prerequisites for successful deposition of semiconductor oxide NWs and NRs is careful selection of the appropriate substrate. There are a great many platforms suitable for deposition of NWs and NRs, such as various dielectric polycrystalline Al_2O_3 -based substrates; Si, MgO, ZrO, Al_2O_3 single crystals with specific crystallographic orientation; glass ceramics; and so on.

It has been reported that during analysis of the structure of SnO_2 and In_2O_3 nanofilms, deposited by spray pyrolysis on Si, SiO_2 and Al_2O_3 substrates, these films were mechanically strained.^{84,85} Even in the case of high texture between the substrate and the film, they contain a transitional layer with a thickness $\sim 10\text{--}20\text{ nm}$, consisting of randomly-oriented crystallites. The simplified structure of such films is presented in Fig. 2.3. It has been reported that the mechanical strains in SnO_2 nanofilms deposited by spray pyrolysis on Si substrates have not been reduced after post-deposition



2.3 Oversimplified view of metal oxide film with transition layer.

thermal treatments.⁸⁴ It was therefore concluded that the above-mentioned strains were conditioned by the difference in thermal expansion coefficients between the substrate and the deposited film.⁸⁵

In order to overcome such substrate–lattice mismatching, semiconductor oxide nanostructures can be grown epitaxially from the substrate due to the lattice matching between the crystal and the substrate. A good example for consideration is ZnO. In order to grow directional ZnO NWs, several types of epitaxial substrates have been used, including sapphire,^{30,31} GaN,^{86–88} SiC,⁸⁹ Si^{90–92} and ZnO film coated substrates.⁹³ Among them, the most commonly utilized epitaxial substrate is sapphire. However, from the lattice matching aspect, GaN may be an even better candidate since it has the same crystal system and lattice parameters similar to ZnO.⁸⁷ This report highlighted that NWs grown on a GaN epilayer have better vertical alignment than those grown on sapphire. One additional advantage of applying GaN as the epilayer lies in the fact that GaN is much easier to dope with *p*-type dopants. As a result, it was concluded that creating nanoscale light-emitting devices by using *n*-ZnO/*p*-GaN hetero-junctions is technically more feasible than it is by using *n*-ZnO/*p*-ZnO homo-junctions.⁸⁶

2.4.3 Template alignment

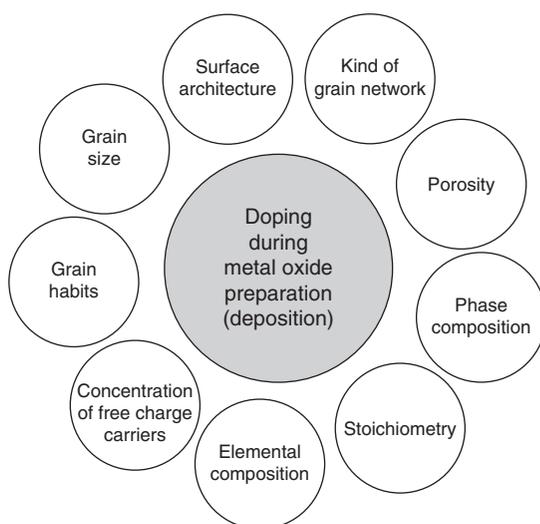
In addition to vertical alignment by lattice matching, an alternative template alignment technique has been reported.⁹⁴ Integration of nanostructures can be easily achieved if the template is precisely designed. A commonly used template is anodic Al₂O₃ membrane where the channel density can exceed 10⁹ cm⁻² by controlling the membrane fabrication procedure which in essence is a self-organizing process. Therefore, there are no costly and complicated lithographic procedures involved. As has been described above, the solution-phase-based method has been utilized to assemble oxide NWs into AAO by using ED or the sol–gel process. Lately, a high-density vertical aligned ZnO NW array in an AAO template was successfully fabricated by combining electrochemical deposition and laser ablation-assisted CVD methods. In this operation, a Sn catalyst is deposited first in AAO using pulsed ED, followed by a CVD approach to synthesize the ZnO NWs.⁹⁴

2.5 Doping of metal oxide semiconductor systems

In order to meet the demands of potential applications offered by metal nano-oxides, high-quality *n*- and *p*-type materials are both indispensable. Therefore, in order to control doping with intrinsic or extrinsic elements it is essential to harmonize and adjust their electrical, electrochemical, optical and magnetic properties.

At the end of the 20th century, doping of semiconductor structures was originally carried out in randomly doped samples. Various technologies were employed for this process because doping the base semiconductor with noble metal nanoparticles^{95–98} and/or by other oxide nanocrystals^{99,100} has been established as a very successful method of changing the physical and, more importantly, the chemical and electrochemical properties of the modified material. However, nanotechnology has been progressing very rapidly since the beginning of the 21st century, and new properties of atomically-thin nanostructures have been obtained. The development of top-down doped semiconductor oxide devices has been greatly enhanced by investigation of the physics of individual atoms embedded into semiconductor nanostructures. Figure 2.4 schematically overviews the parameters which may be changed as a result of metal oxide doping during their preparation (deposition).¹

Dopant atoms are used to control the properties of semiconductors in most electronic devices. For example, in chemical gas sensors, doping enhances the sensitivity and selectivity of the sensor and at the same time suppresses undesirable properties, such as interference with other gaseous elements in the measurement environment,¹⁰¹ slow response/recovery time,¹ etc. For instance, in water quality sensors, doping provides built-in antifouling resistance for the sensing electrode, maintaining a high level of sensitivity to the measuring parameter.¹⁰² All improvements achieved so far testify



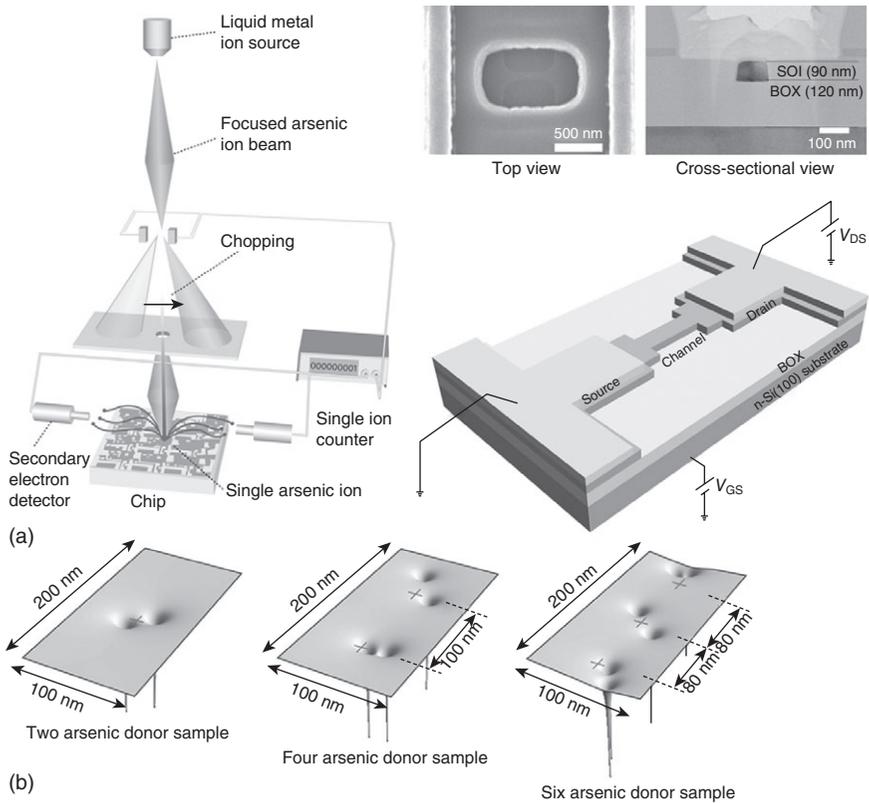
2.4 Parameters which may be changed as a result of metal oxide doping during their preparation (deposition). (Reprinted from Ref. 1 with permission from Elsevier Science)

that doping has become more selective, optimized and able to target specific semiconductor crystal properties.

Recent advances in single-ion implantation^{103–106} have allowed the precise positioning of single dopants in semiconductors, as well as the fabrication of single-atom transistors,^{107,108} representing steps forward in the realization of quantum circuits.^{109–112} Hybrid nanostructures combining doped semiconductors and graphene are being developed for applications such as fuel cells, photovoltaics and various sensors.^{113,114} However, the absence of a bandgap in graphene has restricted the electrical and optical characteristics of these hybrids, particularly their emissive properties. On the other hand, the interactions between dopant atoms have only been studied in systems containing a large number of dopants. Therefore, it was not possible to explore fundamental phenomena such as the Anderson–Mott transition between conduction by sequential tunnelling through isolated dopant atoms, and conduction through thermally activated impurity Hubbard bands.¹¹⁵ The incorporation of donors into a semiconductor's lattice may lead to an increase or a decrease in the Fermi level (E_F) in oxide semiconductors. For example, the effect of defect disorder on the Fermi level of TiO_2 has been comprehensively presented in a recent monograph.¹¹⁶ In this book, it was clearly shown that if the donor can be, for instance Nb, then the E_F is closer to the E_c level and, alternatively, the incorporation of acceptors will shift the E_F toward the E_v level (subscripts c and v standing for conduction and valence level, respectively). As a result of such manipulations, defect engineering can be successfully employed to change the chemical potential of electrons in the doped TiO_2 compared to the undoped nanocrystal. This, in turn, can modify the charge transfer between the surface of the nanostructured TiO_2 and the adsorbed molecule. However, information relating to the effect of local surface properties on the reactivity of metal oxides, which are closely related to the presence of point defects, is limited, and further research is necessary for the utilization of the defect disorder method in practical doping of various oxide semiconductors. One interesting approach to the development of single-ion-implanted devices has recently been demonstrated,¹¹³ which is graphically displayed in Fig. 2.5.

2.5.1 Doping of ZnO nanowires

Environmentally-friendly, multifunctional ZnO is one of the most important II–VI semiconductor materials with a wide direct bandgap of 3.37 eV. Interest in this semiconductor is fuelled and fanned by its prospects in optoelectronics due to its direct wide bandgap and large exciton binding energy of 60 meV at room temperature.¹¹⁷ The existence of various 1D and 2D forms of ZnO has provided further opportunity for its use in energy harvesting, including photovoltaic and sensor applications.¹¹⁸



2.5 Experimental devices and calculated potential distributions in the channel regions. (a) Left: illustration of the device structure for controlling transport by controlling the dopant number and position via single-ion implantation (nominal channel length, 200 nm; channel width, 100 nm; channel thickness, 90 nm). Top right: a top view of the channel of a device similar to those measured. The channel is visible through the aperture required for single-ion implantation. The 90 nm Si channel on the 125 nm buried oxide (BOX) of the silicon-on-insulator (SOI) substrate is shown in the cross-sectional view. Bottom right: a schematic of the measurement set-up. The drain of the device is controlled by applying a drain voltage V_{DS} while the source is connected to ground. The gate voltage V_{GS} is applied to the back gate. (b) Idealized representation of the potential distributions in the two, four and six arsenic donor samples. Crosses indicate target positions. (Reprinted from Ref. 113 with permission from Nature Publishing)

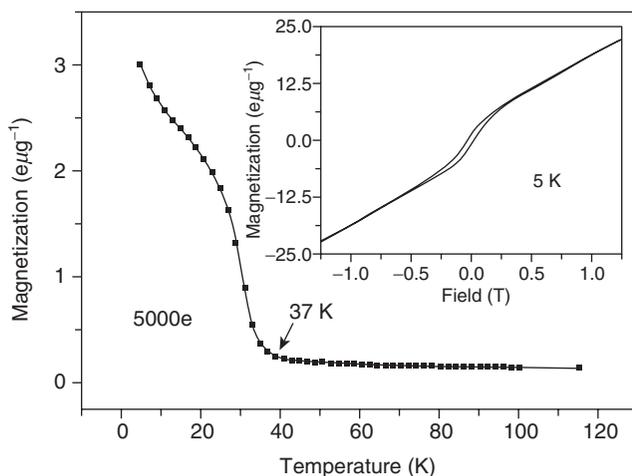
Due to the presence of intrinsic defects such as oxygen vacancies and Zn interstitials in ZnO, it has been considered as a natural *n*-type semiconductor. Those defects form shallow donor levels with an ionization energy of about 30–60 meV. It has also been suggested that the *n*-type conductivity is due to the hydrogen impurity introduced during fabrication.^{119,120} To date,

various types of dopants, such as group-III (Al,^{121,122} Ga,^{122–124} In¹²⁴), group-IV (Sn^{124,125}), group-V (N,^{121,122} P,¹²⁶ As,^{125,126} Sb¹²⁷), group-VI (S^{26,128}) and transition metals (Co,¹²⁹ Fe,¹³⁰ Ni,^{129,131} Mn¹³²) have been implanted into ZnO nanostructures. Doping group-III and -IV elements into ZnO has been proved to enhance its *n*-type conductivity. In contrast, *p*-type ZnO has been investigated by incorporating group-V elements. Additionally, co-doping N with group-III elements was found to enhance the incorporation of N acceptors in *p*-ZnO by forming N–III–N complex in ZnO.^{121,122}

The *n*-type ZnO is easily realized via substituting group-III and -IV elements or incorporating excess Zn. It has been shown that the electrical properties of ZnO NWs can be fine-tuned by adjusting synthesis conditions to generate oxygen vacancy and Zn interstitials.¹³³ By using a ‘so-called’ vapour trapping configuration, a small quartz vial is used in the CVD system to trap the metal vapour, thus creating a high vapour concentration gradient in the vial. NWs were observed to display a variety of morphology at different positions on the growth chip due to the change in the Zn and O₂ vapour pressure ratio. It was found that those ZnO NWs grown inside the vial with a higher Zn/O₂ pressure ratio possessed enhanced carrier concentration. Consequently, the vapour trapping method is a very effective doping process, which can be used to adjust carrier concentration.¹¹

Although considerable effort has been invested to achieve *p*-type doping of ZnO, reliable and reproducible *p*-type conductivity has not yet been achieved. The difficulties arise from several causes. One is the compensation of dopants by energetically favourable native defects such as zinc interstitials or oxygen vacancies. Dopant solubility is another obstacle. Recently, an intra-molecular *p*–*n* junction on ZnO NWs has been reported.⁹⁴ In this work, an anodic Al membrane was used as a porous template with an average pore size of around 40 nm. A two-step vapour transport growth was applied and boron was introduced as the *p*-type dopant. As a result, the current–voltage (*I*–*V*) characteristics demonstrated rectifying behaviour due to the *p*–*n* junction within the NW. Furthermore, by doping ZnO NWs to *p*-type in order to fabricate intra-NW *p*–*n* junction, light emission from the *p*–*n* hetero-junctions composed of *n*-ZnO and *p*-GaN has been achieved.⁸⁶ In that work, a vertically aligned ZnO NR array was epitaxially grown on a *p*-type GaN substrate.

ZnO is emerging as a promising dilute magnetic semiconductor (DMS material). DMS is attracting tremendous research interest because it is predicted to have a high Curie temperature, and can also enhance polarized spin injection into semiconductor systems. Room temperature hole-mediated ferromagnetism in ZnO by introducing Mn as dopant has been predicted theoretically and reported experimentally in ZnO thin film.¹³⁴ An attempt at growing ferromagnetic Zn_{1–*x*}Mn_{*x*}O (*x* = 0.13) NWs with a Curie temperature of 37 K has also been recently reported.¹³⁵ Figure 2.6 displays



2.6 Temperature-dependent magnetization curve of $\text{Zn}_{1-x}\text{Mn}_x\text{O}$ ($x = 0.13$) NW at 500 Oe shows Curie temperature of 37 K. Inset: magnetization-field hysteresis loop obtained at 5 K. (Reprinted from Ref. 11 with permission from Elsevier Science)

the temperature-dependent magnetization curve of a $\text{Zn}_{1-x}\text{Mn}_x\text{O}$ ($x = 0.13$) NW.^{11,135}

Another successful approach to doping ZnO NBs with Mn has also been reported.¹³⁴ Moreover, ferromagnetism in ZnO NRs was observed with Co impurities. Anisotropic ferromagnetic behaviour of Co- and Ni-doped ZnO NWs at room temperature has been demonstrated.¹²⁹ Owing to its wide bandgap, ferromagnetic ZnO is regarded as an excellent potential nanomaterial for short-wavelength magneto-optical devices. These studies enable potential applications of ZnO NWs as nanoscale spin-based devices.

2.5.2 Doping of other oxide nanowires

Although ZnO NW is probably the most widely investigated nanostructure to date, doping of other oxide NWs has been a subject of interest in the years since 2000. There have been several reported methods dedicated to the development of doped NWs. For example, doping of Ga_2O_3 NW affects its transport properties.²⁹ Before doping, the electron transport measurements demonstrate poor conductivity at room temperature ($10^{-9} \Omega^{-1} \text{cm}^{-1}$). Specifically, a thermal diffusion doping process was utilized to substitute Ga^{3+} ions with Zn^{2+} . The resulting conductivity improves by orders of magnitude.

An alternative report highlighted configurable changes in the properties of $\alpha\text{-Fe}_2\text{O}_3$ nanostructures through doping procedures: quasi-1D (Q1D)

α -Fe₂O₃ NBs were doped with elemental Zn to control their electrical properties.¹³⁶ It was shown that α -Fe₂O₃ NBs can be successfully modified to be either *p*-type or *n*-type with enhanced conductivity and electron mobility, depending on the doping conditions.¹³⁶

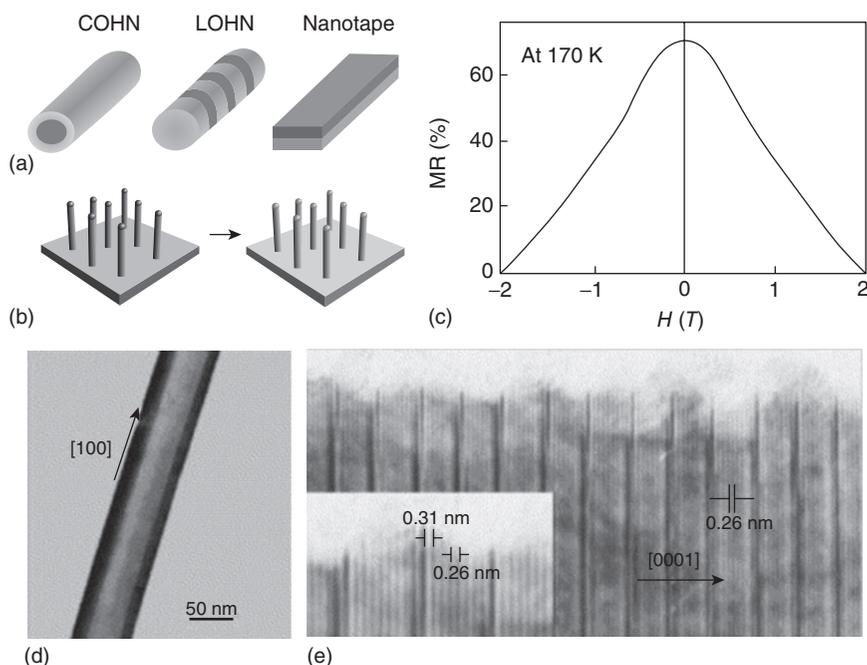
In₂O₃ NWs can also be doped with either Ga¹³⁷ or native defects.¹³⁸ In this case, doping changed the carrier concentration which was ultimately reflected during optimization of the electrical transport and gas sensing properties.^{138,139} Moreover, it has also been reported that In₂O₃ NWs were doped with Sn, resulting in indium tin oxide (ITO) NWs.^{140,141} Among other recent reports, it is worth mentioning that SnO₂ NWs can also be doped with In via epitaxial directional growth with the In concentration at ~5 % atomic ratio.¹⁴²

2.5.3 Construction of nanoscale metal oxide heterostructures

The previous section overviewed the basic methods and techniques which have been successfully applied for the growth of various metal oxide semiconductor NWs, NRs and other nanostructures. However, recent reports have also shown that in some cases the developed 1D and 2D metal oxide nanostructures themselves can function as templates for growing novel hetero-structured materials. These materials can be mainly classified into three configurations: coaxial core/shell NWs, longitudinal super-lattice NWs and layered nanotapes.^{11,143–145} Graphical interpretation of this classification is illustrated in Fig. 2.7a.

Core/shell nanowires

The core–shell configuration of semiconductor NWs^{146,147} permits the development of hetero-junctions within the nanostructure, yielding reliable, fast-processing and efficient devices, such as highly efficient light-emitting diodes.¹⁴⁸ So far several types of core/shell structures have been synthesized and reported.^{146–154} These include semiconductor/oxide,¹⁴⁹ metal/oxide,¹⁵⁰ oxide/oxide,^{151,152,153} oxide/polymer,¹⁵⁴ etc. The unique hetero-junctions formed at the core/shell interfaces render promising the prospect of making versatile functional devices with enhanced electrochemical properties. For instance, amorphous alumina was grown by atomic layer deposition on ZnO NWs to form a ZnO/Al₂O₃ core/shell configuration. An individual amorphous Al₂O₃ nanotube was then obtained after wet etching the core ZnO material. By selecting an appropriate core material, epitaxial shell growth can be realized instead of amorphous deposition.^{144,152} Another report concluded that vertically aligned single-crystalline MgO NWs as a 1D template can be used to produce a variety of transition metal oxide core/shell



2.7 (a) Three different types of hetero-structures using 1D NW as template: core-shell hetero-structured NW (COHN), a longitudinal hetero-structured superlattice NW (LOHN) and a nanotape. (b) Schematic illustration of vertically aligned Fe_3O_4 shell coated on MgO core NW. (c) Magnetoresistance measured at 170 K with a magnetic field swept from -2 T to 2 T . (d) TEM image of such core-shell Fe_3O_4 NW. (e) HRTEM image of an individual $\text{In}_2\text{O}_3/\text{ZnO}$ NW with longitudinal superlattice structure. (Reprinted from Ref. 11 with permission from Elsevier Science)

structured NWs (graphically displayed in Fig. 2.7b), including $\text{YBa}_2\text{Cu}_3\text{O}_{6.66}$ (YBCO), $\text{La}_{0.67}\text{Ca}_{0.33}\text{MnO}_3$ (LCMO), $\text{PbZr}_{0.58}\text{Ti}_{0.42}\text{O}_3$ (PZT) and Fe_3O_4 .¹⁴⁴ A significant achievement of 70 % magnetoresistance (MR) was observed in a MgO/LCMO NW system at 170 K (Fig. 2.7c),¹⁴⁴ and 1.2 % MR at room temperature in $\text{Fe}_3\text{O}_4/\text{MgO}$ NWs (Fig. 2.7d) with the presence of antiphase boundaries has been reported.¹⁵⁵ Furthermore, an investigation dedicated to the sophisticated optimization of a $\text{ZnO}/\text{Mg}_{0.2}\text{Zn}_{0.8}\text{O}$ multi-shell structure for radial direction quantum confinement has been published.¹⁵⁶ In this work, the dominant excitonic emissions in the photoluminescence spectra showed a blue shift which depends on the ZnO shell layer thickness. Moreover, near-field scanning optical microscopy demonstrated sharp photoluminescence peaks corresponding to the sub-band levels of the individual NR quantum structures.

Longitudinal super-lattice nanowires

An alternative type of metal oxide hetero-junctions is longitudinal super-lattice NWs. They can be grown along the Q1D structure by periodically controlling the conditions of the synthesis process. For example, recent reports have confirmed the development of longitudinal composition modulated semiconductor NWs such as GaAs/GaP,¹⁵⁷ Si/SiGe¹⁵⁸ and InAs/InP.¹⁵⁹ Single or multiple $p-n$ junctions of these commonly used semiconductors have been fabricated and characterized. In addition, an In₂O₃/ZnO super-lattice structure has recently been reported.¹⁴⁵ In that work, a ZnO, In₂O₃ and Co₂O₃ mixture was thermally evaporated resulting in the super-lattice In₂O₃(ZnO) m , as presented in Fig. 2.7e. The recorded lattice parameters were as follows: In₂O₃(ZnO)₅ ($a = 0.3327$ nm, $c = 5.811$ nm) and In₂O₃(ZnO)₄ ($a = 0.3339$ nm, $c = 3.352$ nm).¹⁶⁰ The as-fabricated superlattices were comparable with the pristine ZnO NWs in their structure, composition and optical properties. Electrical measurement of the intra-NW $p-n$ junctions exhibited rectifying behaviour.¹⁵⁷ More importantly, polarized electroluminescence was observed, demonstrating their application as nanoscale light-emitting devices.¹⁵⁷

2.6 Energy harvesting based on semiconductor piezoelectric nanostructures

Recent advances in the development of 1D and 2D semiconductor oxide nanostructures have provided an opportunity for a new generation of functional devices not only in optoelectronics and chemical sensors, but also in energy-harvesting photovoltaics.¹⁶¹ This is because variations of semiconductor nanostructures and their combinations in complex electrodes have led to new functionalities in electronic devices. For example, ZnO has already been fabricated in different nanoforms such as 1D NWs, NRs, NBs, nanotubes and other complex nano-architectures. The number of applications for this variety of nano-shaped ZnO complexes has increased enormously and now nanostructures of ZnO are considered as one of the premium materials for energy harvesting.¹¹⁸

Energy harvesting has been proven as a feasible approach for powering micro- and nanodevices and mobile electronics due to their small size, lower power consumption and special working environment. The type of energy harvesting depends on the application. For mobile, implantable and personal electronics, solar energy may not be the best choice, as it may not be readily available. Alternatively, mechanical energy, including vibrations, air flow and human physical motion, which is called random energy with irregular amplitudes and frequencies, is accessible when required. Piezoelectricity is a novel approach that has been developed for harvesting

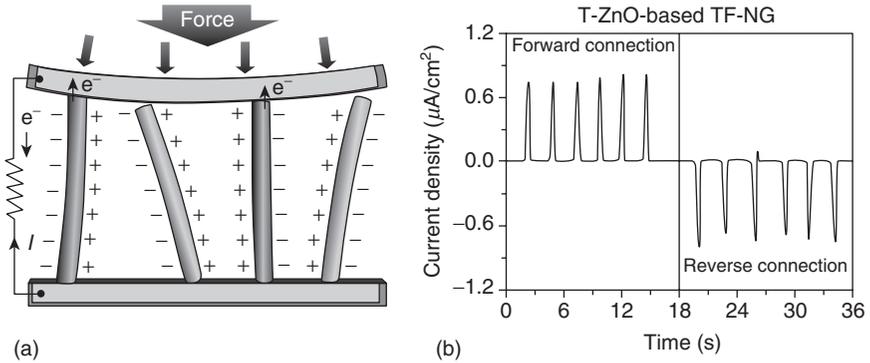
these types of mechanical and biomechanical energies using piezoelectric materials.¹⁶²

Considering that ZnO possesses piezoelectric properties and is biologically safe and environment friendly, it can be used in mechanical energy-harvesting systems to generate electricity for self-powered electronics devices.¹⁶² The main intention for mechanical energy harvesting through nanogenerators is to replace or supplement the current battery systems.

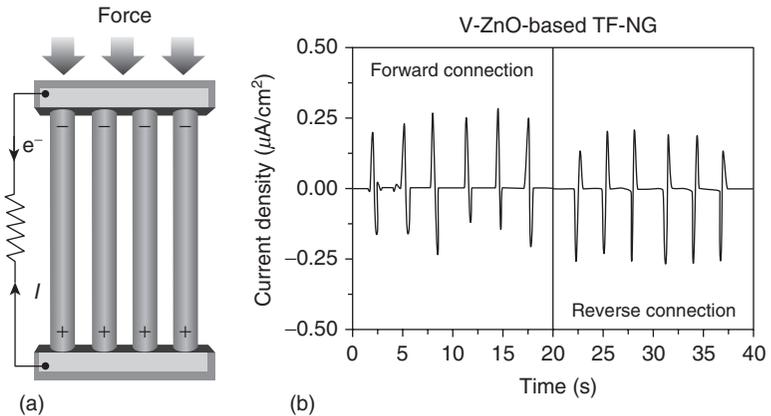
The working principles of nanogenerators can be explained for alternating current (AC) and direct current (DC) power generation. The mechanism of the power generation behaviour of nanogenerators fabricated from piezoelectric semiconductor materials relies on coupled semiconducting and piezoelectric properties. Power generation from piezoelectric semiconductor nanomaterial-based nanogenerators varies with the direction of the exerted force, viz. perpendicular or parallel to the axis of the NW, and can be referred to as AC and DC power generation.¹⁶³ When piezoelectric semiconducting NWs are subjected to an external force, a piezoelectric potential is generated in the NW, due to the relative displacement of the cations with respect to the anions. If the piezoelectric potential generated in the NW is sufficient to drive the piezoelectric-induced electrons from the top or bottom electrode to the bottom or top electrode, respectively, through an external circuit, voltage and current pulses can be recorded by applying and releasing the force.¹¹⁸

It has been reported that the AC and DC power generation modes can be controlled by integrating nanogenerators with vertical and tilted ZnO NRs.¹⁶⁴ Figure 2.8 demonstrates the mode transition of charge generation between DC and AC from transparent flexible piezoelectric nanogenerators (TF-NG), which is dependent solely on the morphology of the ZnO NRs without the use of an AC/DC converter. DC-type output charge generation is based on the coupled effects of the semiconducting and piezoelectric properties of ZnO. When tilted ZnO (T-ZnO) NRs are subjected to an external force, they are bent and generate a piezoelectric potential, due to the charges induced via the polarization created by the ionic charges of the lattice ions along the width of the NRs. A positive potential is produced on the stretched side of the NR and a negative potential is induced on the compressed side, as displayed in Fig. 2.8a. Since the tilted NRs are easily deformed by an external pushing force (under a load of 0.9 kgf), the piezoelectric potential is formed along the width of the T-ZnO NRs. Consequently, the piezopotential-induced charges follow the DC-type behaviour of the nanogenerator along the internal and external circuit (as presented in Fig. 2.8b).

The AC-type charge generation mechanism and the AC output current generated by a nanogenerator fabricated with vertical ZnO (V-ZnO) NRs are exhibited in Figs. 2.9a and 2.9b, respectively.¹¹⁸ The AC-type current



2.8 (a) Schematic diagrams showing DC-type output charge generation from T-ZnO NRs. When the ZnO NRs are brought into contact with the top ITO electrode by applying an external force, electrons flow from the compressed sides of the ZnO NRs to the top electrode. (b) T-ZnO-based nanogenerator showing DC-type charge generation. (Reprinted from Ref. 118 with permission from Elsevier Science)



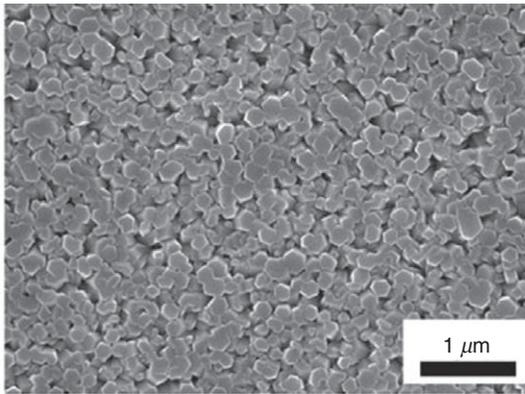
2.9 (a) Proposed mechanism for AC-type charge generation in V-ZnO-based nanogenerators. The electrons flow from the electrode in contact with the sides of the NRs having a negative potential to the opposite electrode in contact with the sides of the NRs having a positive potential through the external circuit under a compressive force. (b) V-ZnO-based nanogenerator that presents AC-type charge generation. The switching polarity tests (forward and reverse connections) demonstrate that the output signals are from the nanogenerators rather than the instruments. (Reprinted from Ref. 118 with permission from Elsevier Science)

behaviour is attributed to the direct compression of the ZnO NRs by the external force (under a load of 0.9 kgf). Considering the geometry of the V-ZnO, the vertically well-aligned NRs are easily compressed by the external pushing force in the direction of the NR length rather than being bent. Hence, a piezoelectric potential is generated in the ZnO NR along the *c*-axis under uniaxial strain. Therefore, when an external force results in the uniaxial strain of the V-ZnO NRs, one side of the NRs is subjected to a negative piezoelectric potential and the other side to a positive potential.¹¹⁸

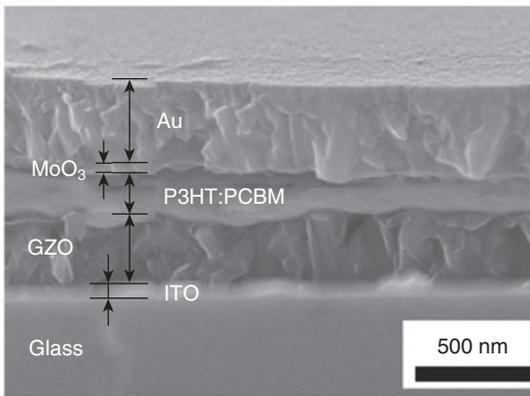
In order to generate a measurable signal above the noise level from nanogenerators, the presence of a Schottky contact at one end of the NRs is essential. The Schottky contact at the sides of the NRs with a negative potential enhances the output signal by preventing the flow of electrons into the ZnO NRs through the interface. The piezopotential-induced electrons are then moved via the external circuit and are accumulated at the interface between the electrode and the side of the NRs with a positive potential. When the external force is removed and the compressive strain is released, the piezoelectric potential inside the NRs instantly disappears and the accumulated electrons flow back via the external circuit, creating a negative electric pulse and, therefore, allowing the current to flow in AC mode from V-ZnO-based nanogenerators. There have been several attempts to increase the power conversion efficiency of inverted organic solar cells using various ZnO nanostructures including Ga-doped ZnO (GZO) with poly(3-hexylthiophene) (P3HT):(6,6)-phenyl-C₇₁-butyric acid methyl ester (PCBM) and poly[2,6-(4,4-bis-(2-ethylhexyl)-4H-cyclopenta[2,1-b;3,4-b'] dithiophene)-alt-4,7(2,1,3-benzothiadiazole)] (PCDBT):PCBM up to 6%.¹¹⁸ The complexity of a modern layered hybrid inverted organic solar cell employing different nanostructured materials is illustrated in Fig. 2.10. This structure offers a more promising concept than those with a regular structure, in terms of their interface stability and device degradation. Stable high-work-function metals are used as the anode to collect holes and a metal oxide such as ITO is employed as the cathode to collect electrons. Nanostructured ZnO is one of the *n*-type semiconductors that can be successfully used in inverted cells to increase their power-conversion efficiency and reliability.

2.7 Physical electrochemistry of semiconductor nanocrystals

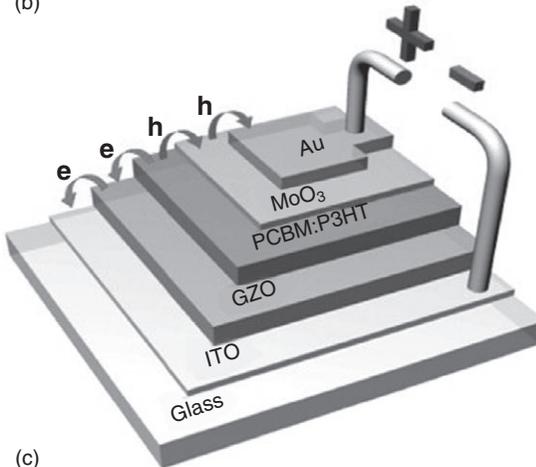
In order to gain insight into the variables of nanostructured complex systems, a broad interdisciplinary approach is needed, both conceptually and experimentally, to bridge solid-state physics, nanotechnologies, solid-state chemistry, surface physics and surface chemistry with electrochemistry.¹⁶⁵



(a)



(b)



(c)

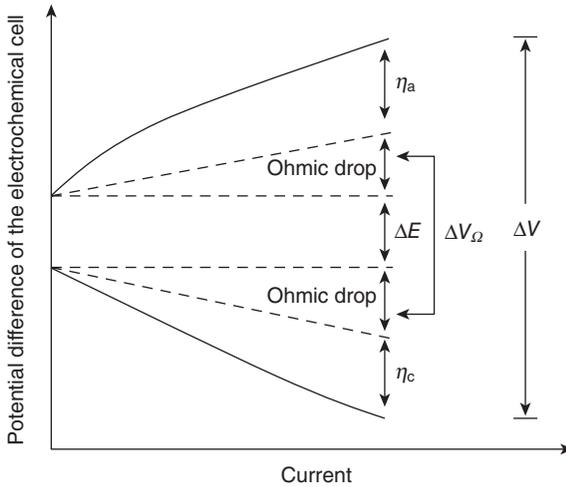
2.10 Schematic illustration of the complexity of inverted layered organic solar cells. (Reprinted from Ref. 118 with permission from Elsevier Science)

Functional nano-oxides have a wide range of applications, including transparent optoelectronics, chemical sensors, piezoelectric transducers, light-emitting devices, etc. The downscaling of the material dimensions not only implies a shrinkage of the active device which leads to higher packing density and lower power consumption, but can also significantly improve the device's performance. In addition, when the dimension reduces to a few nanometers, quantum mechanical effects start to play an important role. Doubtless, a thorough understanding of the fundamental properties of 1D and 2D metal oxide systems is the prerequisite for research and development towards practical applications. In this regard, *electro-catalysis* has been considered as a 'magic' term which is attracting growing interest from both academics and industry. The broad meaning attached to this term is 'the dependence of the electrode reaction rate on the nature of the nano-structured electrode material'. Fundamental and applied researchers consider electro-catalysis to be a link between fundamental and applied problems and, consequently, there is a need to establish a conceptual guide to the selection and, more importantly, the optimization of the design of new nanomaterials.¹⁶⁶ On the other hand, industry looks at electro-catalysis with the hope of being able to improve electrolysis performance (and electric power generation efficiency), thus reducing operational costs.

2.7.1 Technological demand

One way or another, all nanostructured semiconductor metal oxides will be utilized in the electrochemical cell, which can be an essential part of a variety of advanced functional devices. In this electrochemical cell, the applied cell potential difference, ΔV , is often used as a main output signal, and therefore it is imperative from the practical point of view to achieve an applied cell potential difference as close as possible to the thermodynamic value. ΔV can be split into a number of components as graphically presented in Fig. 2.11, some of which depend on the magnitude of the current (I). Thus, the overpotential terms for the anodic (η_a) and cathodic (η_c) reactions increase logarithmically with I while the ohmic drop (IR) rises linearly. This means that ohmic difficulties become more and more important as the electrolysis rate is increased.

Minimizing η_a and η_c is a problem of electro-catalysis, while the ohmic drop is in principle a fundamental difficulty of cell engineering, although these two quantities are often inter-related. The minimum value of ΔV to obtain electrolysis, the equilibrium ΔE , is determined by thermodynamics (Nernst relations) and does not depend on the electrode material.¹⁶⁷ However, since energy saving requires that the magnitude of ΔV should be as small as possible, industry is exploring the possibility of replacing some traditional pairs of electrode reactions entailing large ΔE values with new



2.11 Dependence on current flow of the components of the potential difference applied to an electrolysis cell.

ones (of lower ΔE), where the 'auxiliary' reaction of the unwanted electrode process is appropriately designed. For example, in the process of chlorine production, the electrolytic reactions are chlorine evolution at the anode and, as a rule, hydrogen liberation (from alkaline solution) at the cathode with $\Delta E^\circ = 2.2\text{V}$. If the cathodic reaction is replaced by oxygen reduction (air or oxygen cathode)¹⁶⁵ the nominal ΔE° becomes $<1\text{V}$ with a theoretical reduction of ΔV by $\sim 30\%$ (but η_c will be substantially higher in this case). Therefore, technical and economic issues other than those of electro-catalysis have to be solved in order to follow this route.

It has to be noted that Fig. 2.11 does not reproduce the actual situation in advanced functional devices. Overpotentials and ohmic drops (and also ΔE if the thermodynamic conditions change) may drift with time (in long-term performances), usually increasing the value of ΔV .¹⁶⁵ Thus, a more complete equation is in fact the following:

$$\Delta V = \Delta E + \eta_a + \eta_c + \Delta V_\Omega + \Delta V(t) \quad [2.1]$$

where the last term on the right-hand-side analytically represents what is called 'electrode stability'. $\Delta V(t)$ may be related to the deterioration of the outer surface of the electro-catalyst and/or of the support/active nanolayer interface in the case of coatings. However, electrode wear can also occur without visible electrical effects until the whole catalyst is consumed. In this case, although the electrode is unstable, an increase of ΔV can be observed only as the electrode collapses abruptly. In addition to the cost of the lost material, if precious metals are contained in the

electro-catalyst, maintenance expenses rise due to the need for electrode replacement.

The fact that two reactions on a nanostructured electrode inevitably take place simultaneously in an electrolytic cell also creates reactions which do not give rise to commercially attractive products which may be relevant and important for electro-catalysis. Thus, O_2 evolution accompanies most of the desired inorganic and organic electro-syntheses in aqueous solutions, while H_2 is formed at the cathode of most of the cells where anodic processes are being carried out. Taking into an account the importance *per se* of Cl_2 evolution (one of the largest electrochemical productions), and also of O_2 reduction (especially) in fuel cells and batteries, it can be easily understood why practically the whole of electro-catalytic research is concentrated on Cl_2 and O_2 evolution as anodic reactions (H_2 ionization is far less investigated) and O_2 reduction and H_2 liberation as cathodic reactions.

The importance of O_2 electro-catalysis is also related to the fact that, beyond the possibility of an unwanted anodic reaction, it is a secondary reaction in some of the anodic processes taking place around or above the potential range of oxygen evolution. The most typical example is provided by the chlor-alkali process. On a thermodynamic basis, O_2 evolution would be preferred over Cl_2 formation even in chloride media. However, η_{O_2} is rather high while η_{Cl_2} is negligible at practical current densities.¹⁶⁵ However, selectivity problems may arise, requiring a specific research strategy to tackle them.

Considering the analysis provided in the above section as well as existing fabricating technologies of semiconductor nano-oxides, current trends in applied electro-catalytic research relevant to semiconductor nano-oxides can be summarized as follows:¹⁶⁵

- stabilization of electrode nanomaterials towards wear;
- improvement of electro-catalytic activity for wanted reactions;
- depression (reduction) of electro-catalytic activity for unwanted reactions;
- replacement of materials containing precious metals with (cheaper) materials or composite materials based on non-precious metals or oxides;
- finding substitutes for polluting materials.

Although the current level of development of nanostructured materials provides confidence that such materials satisfying all of the above requirements can be found, it is very hard to develop nanomaterials for which all the needs can be optimized simultaneously. Nevertheless, several classes of transitional metal nano-oxides have been found to give performances superior to the parent metals traditionally used in industrial electrodes.¹⁶⁶ They can be grouped into three main classes as follows:

1. rutile-type metal oxides (dioxides);
2. spinel-type metal oxides;
3. perovskite-type metal oxides.

Most of the above-mentioned metal nano-oxides can be prepared in various ways as has been described in the previous sections. Up to now, one of the most widely used technologies involves thermal decomposition of appropriate precursors dissolved in suitable solvents and spread on the appropriate substrate. This procedure results in non-stoichiometric, structurally defective nano-oxides, whose parameters and physical and electrochemical properties at first approximation depend on the temperature and procedure of preparation. In order to analyse, characterize and eventually improve the surfaces and electro-catalytic properties obtained, correlation between changes of the structural parameters and obtained characteristics of the developed nano-oxides should be established. Bulk, surface, physical and chemical analyses provide outstanding pieces of information that are essential in interpreting electro-catalysis and stability performances. The most widely used characterization techniques are summarized in Table 2.1.

Table 2.1 Physical/chemical characterization of nanostructured metal oxides

Thermal decomposition	Thermogravimetric analysis (TGA), differential thermal analysis (DTA)
Lattice structure Crystallinity Crystallite size	X-ray diffraction
Surface area Electronic structure	Brunauer-Emmett-Teller analysis (BET), ion adsorption Electrical conduction
Chemical composition [Bulk surface profile	Rutherford back scattering (RBS), auger electron spectroscopy (AES), X-ray photoelectron spectroscopy (XPS), secondary ion mass spectrometry (SIMS), time-domain spectroscopy (TDS)
Hydration	Tritium exchange Immersion heat Nuclear techniques
Acid-base properties Point of zero charge Surface charge	Potentiometric titration Electrophoretic mobility
Electrochemical surface spectrum Electrochemical surface charge	Cyclic voltammetry Impedance measurements Chronocoulometry

2.7.2 The role of the crystallographic structure of metal nano-oxides

Crystal shape

At present, the effect that grain shape and faceting of crystallites has on electro-catalysis in various applications is not subject to comprehensive analysis. However, there are reasons to conclude that the role of these parameters is understated. The following statements can be made based on recent results:^{1,81,84,85,161,165–171}

- Each crystallographic crystal form has its own combination of crystallographic planes, framing the nanocrystal. Every crystallographic plane has its own combination of surface electron parameters, which include surface state density, energetic position of the levels, induced by adsorbed species, adsorption and desorption energies of interacted molecules, concentration of adsorption surface states, the energetic position of surface Fermi level, activation energy of native point defects, and so on.
- The external planes of nanocrystals participate in interactions with the surrounding (measuring) environment, and therefore these very planes determine the electrochemical and catalytic properties of nanostructured materials. Even spherulites have micro-planes and facets. The nanocrystal shape may determine parameters such as crystallographic planes, inter-grain contacts, area of inter-grain contacts, gas permeability and so on. This implies that the chemisorption characteristics change noticeably from one crystal surface orientation to another. Thus, there is a large surface dependence at the atomic level for chemical bonding of the adsorbed or chemisorbed particles.
- Adsorption/desorption being chemical processes, have activation energies. The parameters controlling these processes are orientation- and grain-size-dependent. The decrease in crystal size in the nm range notably strengthens the influence of crystallite shape on the adsorption properties. Both the shape and the size of nanocrystals have a profound influence on the concentration of adsorbed species and on the type of bonding to the surface that takes place. It is known that, depending on the type of bonding, some chemical species may have preferred adsorption on either the edge/corner sites or on the plane surface.¹⁷¹ For example, it has been reported that mono-dentate adsorption on MgO and CaO is preferred on the edge/corner sites, whereas bi-dentate adsorption is favoured by smooth planes.¹⁷²

Consequently, depending on the external form of the nanocrystallites, a developed matrix of nano-oxide will have a unique combination of structural, electronic and electrochemical parameters.

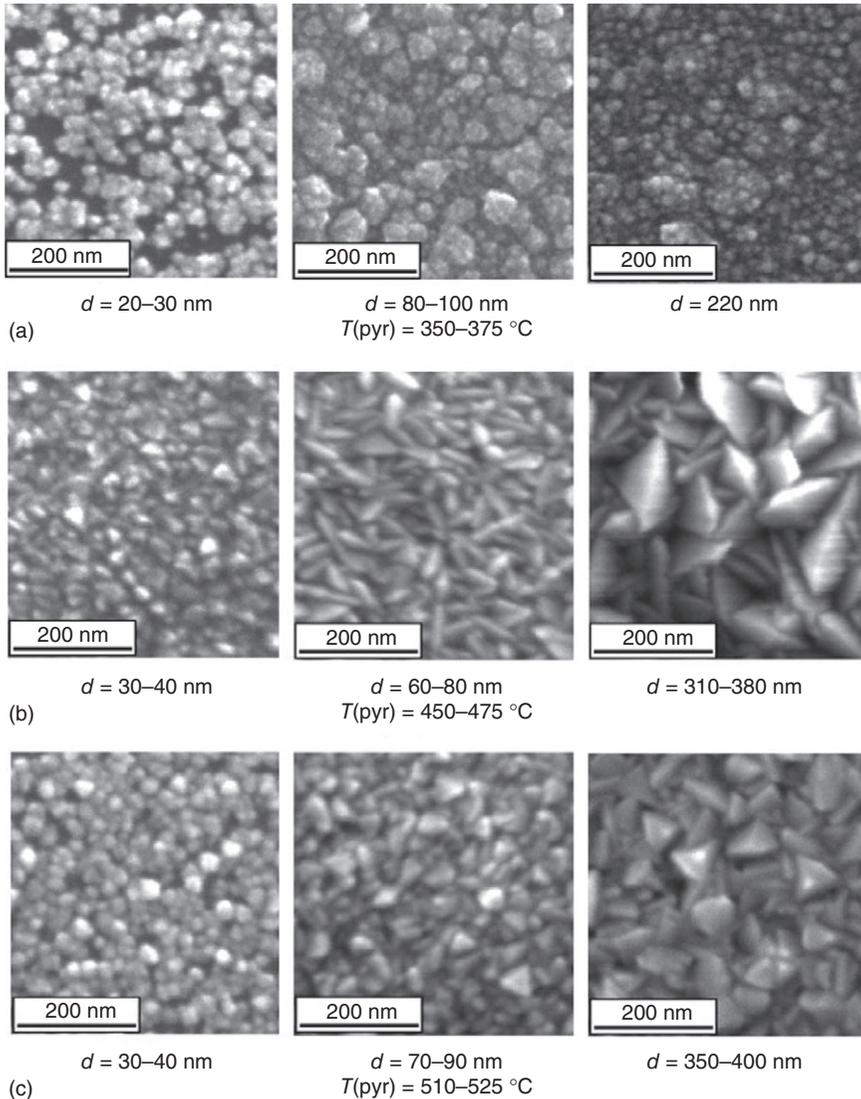
One of the examples of utilization of fabricated nano-oxides and complex nano-oxides in sensing electrode materials is chemical gas sensors. Let's consider SnO₂ nanocrystals, most widely used as a material for sensing electrodes in various semiconductor gas sensors. Detailed studies conducted on SnO₂ films deposited by a spray pyrolysis method confirmed the appropriateness of modification of the crystal shapes and sizes for optimization of gas-sensing properties.^{1,81,85,171} For example, it has been established that the growth of grains, especially in the range from nm to μm, during which the transition from spherulites to nanocrystallites and from nanocrystallites to nanocrystals and crystals takes place, is accompanied by changes in both the size and the external shape of the crystallites. Possible morphologies of SnO₂ films deposited by spray pyrolysis are presented in Fig. 2.12.¹⁷¹

There is no doubt that the preparation of polycrystalline metal nano-oxides with necessary grain faceting is difficult to control. However, it is achievable for 1D metal nano-oxide and, therefore, semiconductor 1D gas sensors can be considered as the evidence of this.¹⁷¹ 1D structures are crystallographically perfect and have clear faceting with a fixed set of planes. As a result, this research area must have a higher priority in further development of chemical gas sensors. Furthermore, it is necessary to note that semiconductor 1D nano-oxide structures with well-defined geometry and perfect crystallinity could represent a perfect model–material family for systematic experimental study and theoretical understanding of the fundamentals of gas-sensing mechanisms in semiconductor metal oxides.

In analysing the potential practical applications of Q1D structures of various types, it is noteworthy that NBs (nanoribbons) probably could be one of the most in-demand Q1D structures for different applications. NBs do not possess the mechanical strength of nanotubes.^{173–175} However, they do have structural homogeneity and crystallographic perfection. It is well-known that crystallographic defects may destroy quantum-size effects. Because of the zero-defects of NBs, structural defects will not be a problem as observed for NW-type structures. It is necessary to emphasize that suitable geometry (see Fig. 2.13¹⁷¹), high homogeneity of the structure and long length are important advantages of NBs for mass manufacturing of gas sensors. Moreover, NBs have flexible structures and, therefore, they could be curved up to 180° without being damaged. It is known that nanotubes do not have such properties. This fact gives additional advantages to NBs for different electrochemical sensor designs.

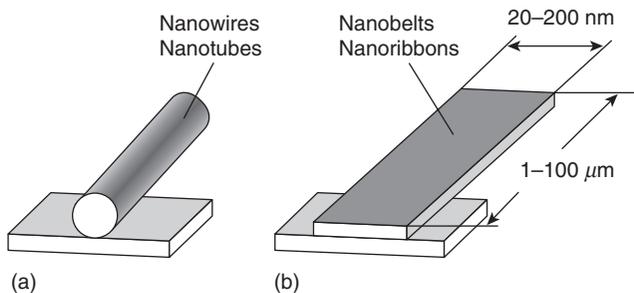
Surface stoichiometry (disordering)

Surface stoichiometry (disordering) of the metal oxide grains may be as important a parameter in gas-sensing and photovoltaics as film thickness



2.12 SEM images of SnO_2 films deposited by spray pyrolysis using different technological parameters. (Reprinted from Ref. 171 with permission from Elsevier Science)

and grain size. This criterion determines the adsorption ability and the surface charge through the number of oxygen vacancies and, as a result, controls the initial surface band bending (eVs) of the metal oxide and the change of eVs at the replacement of the surrounding gas. Considering that stoichiometry has a direct impact on such functional device characteristics



2.13 Schematic illustration of the positions of (a) NWs and (b) NBs on bonding pad and typical sizes of NBs used in chemical gas sensor design. (Reprinted from Ref. 171 with permission from Elsevier Science)

as sensitivity, selectivity (gas sensing) and reproducibility of electrochemical reactions, it must be accurately controlled.

It is known that excessive lattice disordering of the surface layer could be accompanied by a significant growth of native surface states.¹¹⁶ Theoretical studies have indicated that an increase in these surface defects may lead to pinning of the surface Fermi level position, and correspondingly to a drop in the response of gas sensors.^{1,85,171} This means that if the operation of solid-state gas sensors is to be effectively maintained, the concentration of those states as well as the lattice disordering of the surface layer of metal oxide grains should be minimized. However, in this case the surface Fermi level will not be pinned, because the charge of native surface states becomes comparable to or less than the charge of chemisorbed particles. This surface property creates a condition for modulation of surface band bending of semiconductors with the change of the surrounding atmosphere. Therefore change in the surface stoichiometry of metal oxide films may result from changes in deposition and annealing temperature.^{161,171}

A recent report has shown that the surface stoichiometry of metal oxides can be controlled through a charge transfer-induced diffusion mechanism for O_2 molecules adsorbed on a metal oxide surface.¹⁷⁶ Time-resolved scanning tunnelling microscopy of the TiO_2 ¹¹⁰ surface has shown that the O_2 hopping rate depended on the number of surface donors (oxygen vacancies), which determines the density of conduction band electrons. The assumption was that the metal oxides act as reservoirs for oxygen and the O_2 diffusion may be a rate-limiting step in oxidation processes on these metal oxides.¹⁷⁶ Diffusion of oxygen molecules on a metal oxide surface plays a vital role in adsorption/desorption effects and therefore those results may have implications for the understanding of their nature. This mechanism is expected to be an important one for reducible oxides such as TiO_2 ,

Fe_2O_3 , SnO_2 and ZnO , where shallow donor states enable increase to a high density of electrons in the conduction band.

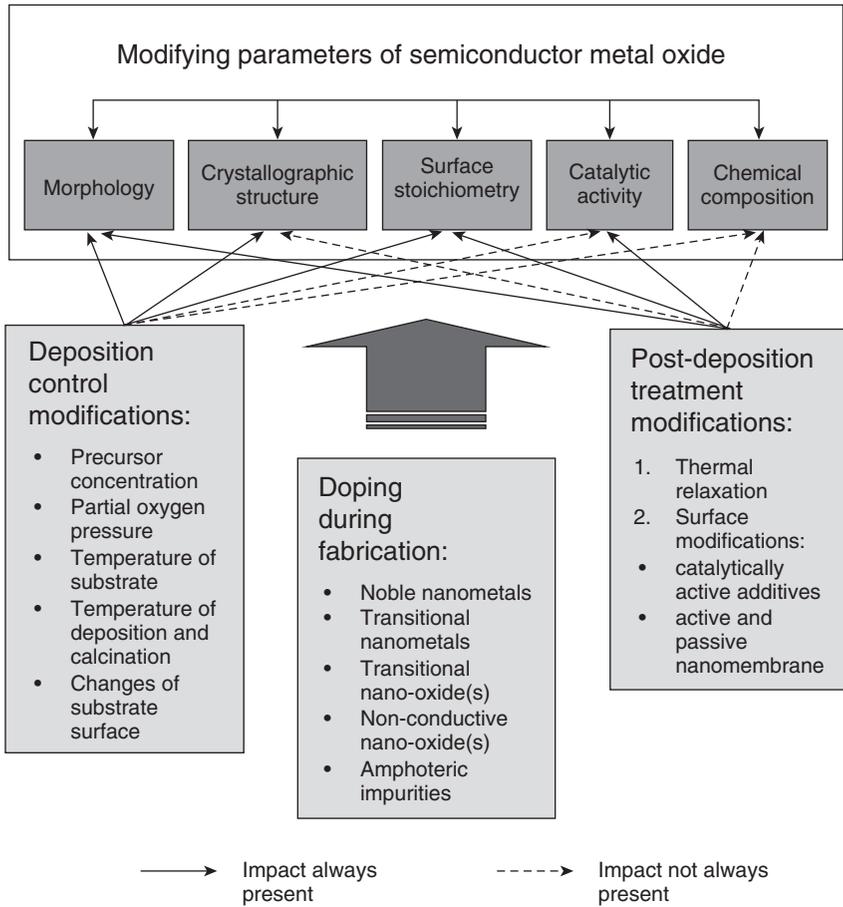
The presence of an unstoichiometric surface layer can also be responsible for a strong interaction between noble metals and metal oxides. The role and activity of noble metal catalysts incorporated on solid-state sensors are determined by either their chemical state, aggregation form or the interaction with the metal oxide.^{171,177}

2.8 Structural and electrochemical properties of semiconductor nanocrystals

It is well-known that semiconductor nano-oxides, especially doped ones, are very complicated substances for research, because the electroconductivity, adsorption–desorption and catalytic characteristics of those materials depend on a variety of influencing factors. Therefore, to specify the optimal fabricating methods and techniques for achieving ‘*perfect*’ nanostructures with a set of desired properties, it is necessary to expand our understanding of electrochemical reaction mechanisms in nano-oxides beyond our existing knowledge. For instance, it is vital to establish the role of morphology, crystallographic structure, surface geometry, surface stoichiometry (disordering) and other parameters, including their interactions in nano-oxides, because there is a lack of genuine, detailed and integrated research reports establishing a connection between the structural parameters of nano-oxides and the properties of functional devices based on these nanostructures. There has perhaps been only one relatively recent attempt to summarize variations in properties and characteristics of nanostructured TiO_2 from the defect-stoichiometry point of view.¹¹⁶ However, this study was focused only on TiO_2 and just confirmed the complexity of correlation between changes of the structural parameters and obtained characteristics of the developed devices. It is therefore necessary to admit that the methods of structural engineering employed during fabrication of 1D and 2D nanostructured semiconductors can drastically alter all relevant parameters controlling the desired properties of nano-oxides. For example, Fig. 2.14 represents a complex approach focusing on summarizing the different structural engineering methods applicable for optimization of semiconductor nano-oxides.

Based on this approach, there are five main modifying parameters of semiconductor nano-oxides, which can be changed in various proportions and ratios during the fabrication process. They are as follows:

1. morphology
2. crystallographic structure
3. surface stoichiometry



2.14 Diagram illustrating how the methods of structural engineering can be utilized and implemented for optimization of parameters of semiconductor nano-oxides.

4. catalytic activity
5. chemical composition.

All of these are inter-connected with each other: changes in just one parameter immediately influence the others and, consequently, the properties of the oxide nanostructure. A detailed analysis of the deposition control modifications, presented in Fig. 2.14, shows that some of the adjustments always impact the parameters of the developing semiconductor nano-oxides, such as morphology, crystal structure and surface stoichiometry, whereas other criteria, such as catalytic activity and chemical composition, may or may not be affected.

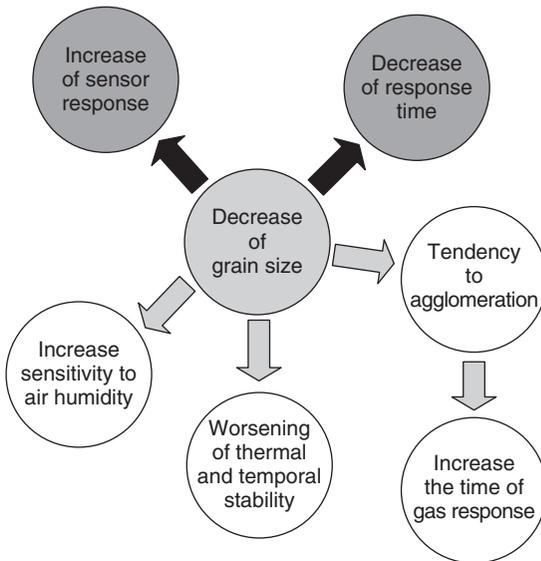
The second widely-used method for the structural engineering of semiconductor nano-oxide is doping.^{1,84,95–99,102,123,124,134,136,160} During nanofabrication, this process has always impacted on all specifications and has resulted in modified and/or optimized properties. Sometimes doping has been expressed in the development of completely new complex nano-oxides with unexpected and unpredictable properties.^{45,69,100,114,122,129,141,142} This is specifically related to the various sensor applications where nanostructured semiconductor oxides were used in the development of a sensing electrode (element) of the functional device.

On the other hand, post-deposition treatment modifications can also have an impact on the morphology, surface stoichiometry and catalytic activity of the nano-oxide. At the same time, the parameters of the fabricated semiconductor nano-oxides, such as crystallographic structure and chemical composition, may or may not be changed.

It has to be noted that in addition to the methods schematically presented in Fig. 2.14, other possible effects of metal nano-oxide doping include the development of *p–n* junctions, the appearance of transitional layers and hetero-junctions acting as catalytic filters, changes in the valency of the metal state and so on.^{1,94}

The existence of such a large number of factors influencing the potential structural changes that impact on the main characteristics of the functional devices is the major reason for the observed high diversity of device performance parameters between units fabricated in various laboratories and conditions. This fact confirms the indisputable difficulty in reproducing the results obtained by other developers.

Taking into account the complexity of the factors affecting the structural properties of semiconductor nano-oxides, elaboration of nanostructures with optimal characteristics must be completed through careful optimization of all the parameters of the developing nano-oxides. Difficulties may arise because one imprudent technological decision could induce the opposite results between various parameters of a nanostructure. As a result, improvement in one parameter may be accompanied by an adverse alteration of other characteristics. A typical example of this is environmental chemical gas sensors based on semiconductor nano-oxides.^{1,81,85,166,171} For example, thin-film sensors possess a maximum rate of response, but along with that they might have very high sheet resistance, which can complicate their compatibility with peripheral measuring devices. Sensitivity and stability are interconnected parameters. As a rule, the smaller the crystallite size, the higher the sensor response but, at the same time, the stability of gas sensors with finely dispersed grains is often decreased. The ambiguity of the effect of grain size decrease on parameters of solid state gas sensors is presented in Fig. 2.15.¹⁷¹

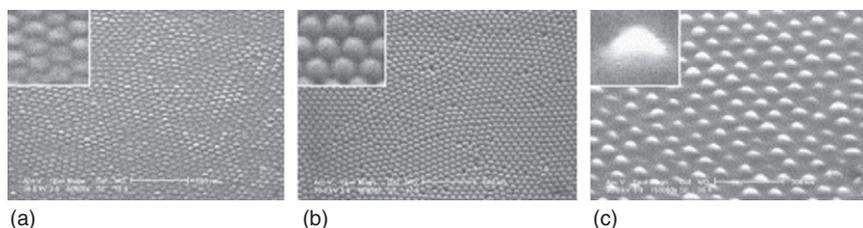


2.15 Diagram illustrating influence of grain size decrease on the sensor parameters. (Reprinted from Ref. 171 with permission from Elsevier Science)

Nano-sized oxide particles are one of the main building blocks of functional nanodevices. In the application of nanoparticles to fields such as optical and electronic devices, it is usually desirable to fabricate ordered arrays of nanoparticles on substrates in order to improve the controllability and performance of the nanodevices. Ultrathin alumina mask (UTAM) nanopatterning has recently been recognized as a suitable method for fabricating ordered nanoparticle arrays on substrates with controllable structural parameters and, more importantly, tunable properties.¹⁷⁸ For any nanofabricating technique described in the previous sections, the ability to tune the structural parameters such as shape and size is vital since, at the nanoscale, many new phenomena and physical properties are closely related to the shape and size of the structures.^{1,85,171} Thus, the ability to adjust these parameters is key to realizing nanostructures with novel properties. Anisotropic optical and magnetic properties have been found in metallic NRs,¹⁷⁹ nanoparticles^{180,181} and nanodisks.¹⁸² Another report has indicated that the luminescence of semiconductor NRs is strongly related to their shape.¹⁸³ Furthermore, size is often a crucial nanostructure parameter, as mentioned and described in previous sections. Therefore, for these reasons, good control of the shape and size of nanostructures has become one of the challenges in nanotechnology and nanofabrication.

For the UTAM nanopatterning approach, the size of the surface nanostructures can be adjusted in order to achieve controllable structural parameters and tunable properties. This is because the pore diameters of UTAMs can be controlled within limits of about 10–200 nm.¹⁷⁸ Moreover, using the pore-widening process, the pore diameter can be regulated within the cell size of the pores. Thus, it is possible to control the spacing of the nanoparticles at the same periodicity (equal to the cell size of the UTAM pores). Most nanoparticles fabricated using UTAM nanopatterning are prepared using UTAMs anodized in 0.3 M oxalic acid solution at 40 V. The cell size of this UTAM is about 105 nm, while the pore diameter is usually modified in the range of 50–80 nm, resulting in nanoparticles with similar sizes, as presented in Fig. 2.16.¹⁷⁸ Specifically, Fig. 2.16c shows that the smallest nanoparticles obtained in the process had a diameter as small as 20 nm. Recently, UTAMs prepared in sulphuric acid solutions with lesser cell size and pore diameters of about 65 and 45 nm were used and arrayed nanoparticles with smaller pore size and period were successfully fabricated.¹⁷⁹

In conclusion, it is necessary to note that the vast majority of studies reported to date relevant to the structural and electrochemical properties of semiconductor nano-oxides have been focused on resolving routine applied problems without comprehensive investigation of the observed effects. Consequently, there has not been a coordinated study in such adjacent areas as heterogeneous catalysis, surface science of semiconductor nano-oxides and adsorption/desorption behaviour. Therefore, if researchers need to accelerate progress towards a better understanding of the nature of effects which can serve as the basis for the design of advanced functional devices, the direction of research in this scientific area should be changed.



2.16 Ordered nanoparticles with small size (CdSe): nanodisks (a), nanohemisphere (b) and nanoconics (c). The UTAMs used in (a), (b) and (c), which were prepared in 0.3 M sulphuric acid solution at 0°C and anodization voltage of 27 V, have the same pore diameter and cell size of about 45 and 66 nm, respectively. The aspect ratios of the apertures of the UTAMs are different, being about 1:3 (a), 1:4 (b) and 1:10 (c). The diameters of the nanoparticles are about 45 (a), 40 (b) and 20–40 nm (c). (Reprinted from Ref. 178 with permission from Elsevier Science)

Nevertheless, the results obtained in relation to improvement of the properties of 1D and 2D nanostructures give us hope that a broadening of research into 1D and 2D structures would promote this challenging process.

2.9 References

1. G. Korotcenkov, Gas response control through structural and chemical modification of metal oxide films: state of the art and approaches, *Sens. Actuat. B-Chem.*, 107 (2005) 209–232.
2. T. Shinada, S. Okamoto, T. Kobayashi, I. Ohdomari, Enhancing semiconductor device performance using ordered dopant arrays, *Nature*, 437 (2005) 1128–1131.
3. D.I. Son, B.W. Kwon, D.H. Park, W.S. Sero, Y. Yi, B. Angadi, C.L. Lee, W.K. Choi, Emissive ZnO-graphene quantum dots for white-light-emitting diodes, *Nature Nanotechnol.*, 7 (2012) 465–471.
4. G. Leti, E. Prati, M. Belli, G. Petretto, M. Fanciulli, M. Vinet, R. Wacquez, M. Sanquer, Switching quantum transport in a three donors silicon fin-field effect transistor, *Appl. Phys. Lett.*, 99 (2011) 242102.
5. J. Rossmeisl, Z.W. Qu, H. Zhu, G.J. Kroes, J.K. Nørskov, Electrolysis of water on oxide surfaces, *J. Electroanal. Chem.*, 607 (2007) 83–89.
6. S.K. Deb, Opportunities and challenges in science and thechnology of WO₃ for electrochromic and related applications, *Sol. Energ. Mater. Sol. Cells*, 92 (2008) 245–258.
7. A.D. Franklin, M. Luisier, S.J. Han, G. Tulevski, C.M. Breslin, L. Gignac, M.S. Lundstrom, W. Haensch, Sub-10 nm carbon nanotube transistor, *Nano Lett.*, 12 (2012) 758–762.
8. P.S. Peercy, The drive to miniaturization, *Nature*, 406 (2000) 1023–1026.
9. W. Liu, X. Yan, G. Chen, Z. Ren, Recent advances in thermoelectric nanocomposites, *Nano Energy*, 1 (2012) 42–56.
10. D.J. Mowbray, J.I. Martinez, F. Calle-Vallejo, J. Rossmeisl, K.S. Thygesen, K.W. Jacobsen, J.K. Nørskov, Trends in metal oxide stability for nanorods, nanotubes and surfaces, *J. Phys. Chem. C*, 115 (2011) 2244–2252.
11. J.G. Lu, P. Chang, Z. Fan, Quasi-one-dimensional metal oxide materials – Synthesis, properties and applications, *Mater. Sci. Eng. R*, 52 (2006) 49–91.
12. C.N.R. Rao, F.L. Deepak, G. Gundiah, A. Govindaraj, Inorganic nanowires, *Prog. Solid State Chem.*, 31 (2003) 5–147.
13. Z.R. Dai, Z.W. Pan, Z.L. Wang, Novel nanostructures of functional oxides synthesized by thermal evaporation, *Adv. Funct. Mater.*, 13 (2003) 9–24.
14. D.H. Zhang, C. Li, S. Han *et al.*, Electronic transport studies of single-crystalline In₂O₃ nanowires, *Appl. Phys. Lett.*, 82 (2003) 112–114.
15. Z.Q. Liu, D.H. Zhang, S. Han *et al.*, Laser ablation synthesis and electron transport studies of tin oxide nanowires, *Adv. Mater.*, 15 (2003) 1754–1757.
16. X. Liu, C. Li, S. Han, J. Han, C.W. Zhou, Synthesis and electronic transport studies of CdO nanoneedles, *Appl. Phys. Lett.*, 82 (2003) 1950–1952.
17. W.I. Park, D.H. Kim, S.W. Jung, G.C. Yi, Metalorganic vapor-phase epitaxial growth of vertically well-aligned ZnO nanorods, *Appl. Phys. Lett.*, 80 (2002) 4232–4234.

18. G. Malandrino, S.T. Finocchiaro, R. Lo Nigro, C. Bongiorno, C. Spinella, I.L. Fragala, Free-standing copper(II) oxide nanotube arrays through an MOCVD template process, *Chem. Mater.*, 16 (2004) 5559–5561.
19. H.W. Kim, N.H. Kim, Synthesis of beta-Ga₂O₃ nanowires by an MOCVD approach, *Appl. Phys. A Mater. Sci. Process.*, 81 (2005) 763–765.
20. R.S. Wagner, W.C. Ellis, Vapor–liquid–solid mechanism of single crystal growth (new method growth catalysis from impurity whisker epitaxial + large crystals Si E), *Appl. Phys. Lett.*, 4 (1964) 89–90.
21. R.S. Wagner, W.C. Ellis, S.M. Arnold, K.A. Jackson, Study of filamentary growth of silicon crystals from vapour, *J. Appl. Phys.*, 35 (1964) 2993–3000.
22. X. Liu, X.H. Wu, H. Cao, R.P.H. Chang, Growth mechanism and properties of ZnO nanorods synthesized by plasma-enhanced chemical vapor deposition, *J. Appl. Phys.*, 95 (2004) 3141–3147.
23. Y.Y. Wu, P.D. Yang, Direct observation of vapor–liquid–solid nanowire growth, *J. Am. Chem. Soc.*, 123 (2001) 3165–3166.
24. J.M. Wu, H.C. Shih, W.T. Wu, Y.K. Tseng, I.C. Chen, Thermal evaporation growth and the luminescence property of TiO₂ nanowires, *J. Cryst. Growth*, 281 (2005) 384–390.
25. Z.R. Dai, J.L. Gole, J.D. Stout, Z.L. Wang, Tin oxide nanowires, nanoribbons, and nanotubes, *J. Phys. Chem. B*, 106 (2002) 1274–1279.
26. S.Y. Bae, H.W. Seo, J.H. Park, Vertically aligned sulfur-doped ZnO nanowires synthesized via chemical vapor deposition, *J. Phys. Chem. B*, 108 (2004) 5206–5210.
27. L. Dai, X.L. Chen, J.K. Jian, M. He, T. Zhou, B.Q. Hu, Fabrication and characterization of In₂O₃ nanowires, *Appl. Phys. A Mater. Sci. Process.*, 75 (2002) 687–689.
28. Y.J. Chen, J.B. Li, Y.S. Han, X.Z. Yang, J.H. Dai, The effect of Mg vapor source on the formation of MgO whiskers and sheets, *J. Cryst. Growth*, 245 (2002) 163–170.
29. P.C. Chang, Z. Y. Fan, W.Y. Tseng, A. Rajagopal, J.G. Lu, beta-Ga₂O₃ nanowires: synthesis, characterization, and *p*-channel field-effect transistor, *Appl. Phys. Lett.*, 87 (2005) 222102–222104.
30. P.D. Yang, H.Q. Yan, S. Mao *et al.*, Controlled growth of ZnO nanowires and their optical properties, *Adv. Funct. Mater.*, 12 (2002) 323–331.
31. X.D. Wang, C.J. Summers, Z.L. Wang, Large-scale hexagonal-patterned growth of aligned ZnO nanorods for nano-optoelectronics and nanosensor arrays, *Nano Lett.*, 4 (2004) 423–426.
32. Y.K. Tseng, I.N. Lin, K.S. Liu, T.S. Lin, I.C. Chen, Low-temperature growth of ZnO nanowires, *J. Mater. Res.*, 18 (2003) 714–718.
33. H.B. Huang, S.G. Yang, J.F. Gong *et al.*, Controllable assembly of aligned ZnO nanowires/belts arrays, *J. Phys. Chem. B*, 109 (2005) 20746–20750.
34. A. Sekar, S.H. Kim, A. Umar, Y.B. Hahn, Catalyst-free synthesis of ZnO nanowires on Si by oxidation of Zn powders, *J. Cryst. Growth*, 277 (2005) 471–478.
35. Q. Zhao, X. Xu, H. Zhang, Y. Chen, J. Xu, D. Yu, Catalyst-free growth of single-crystalline alumina nanowire arrays, *Appl. Phys. A Mater. Sci. Process.*, 79 (2004) 1721–1724.

36. Y. Sun, G.M. Fuge, M.N.R. Ashfold, Growth mechanisms for ZnO nanorods formed by pulsed laser deposition, *Superlattices Microstruct.*, 39 (2006) 33–48.
37. A. Umar, S.H. Kim, Y.S. Lee, K.S. Nahm, Y.B. Hahn, Catalyst-free large-quantity synthesis of ZnO nanorods by a vapor–solid growth mechanism: structural and optical properties, *J. Cryst. Growth*, 282 (2005) 131–136.
38. N. Cabrera, W.K. Burton, Crystal growth and surface structure. Part II, *Discuss. Faraday Soc.*, 5 (1949) 40–48.
39. J.M. Blakely, K.A. Jackson, Growth of crystal whiskers, *J. Chem. Phys.*, 37 (1962) 428–430.
40. G.W. Sears, A mechanism of whisker growth, *Acta Metallurgica*, 3 (1955) 367–369.
41. S. Balendhran, J.Z. Ou, M. Bhaskaran, S. Sriram, S. Ippolito, Z. Vasic, E. Kats, S. Bhargava, S. Zhuiykov, K. Kalantar-zadeh, Atomically thin layers of MoS₂ via a two step thermal evaporation – exfoliation method, *Nanoscale*, 4 (2012) 461–466.
42. K. Kalantar-zadeh, J.S. Tang, M.S. Wang, K.L. Wang, A. Shailos, K. Galatsis, R. Kojima, V. Strong, A. Lech, W. Wlodarski, R.B. Kaner, Synthesis of nanometre-thick MoO₃ Sheets, *Nanoscale*, 2 (2010) 429–433.
43. P.A. Lieberzeit, A. Afzal, A. Rehman, F.L. Dickert, Nanoparticles for detecting pollutants and degradation processes with mass-sensitive sensors, *Sens. Actuat. B-Chem.*, 127 (2007) 132–136.
44. X.Y. Chen, X. Wang, Z.H. Wang, W.C. Yu, Y.T. Qian, Direct sulfidization synthesis of high-quality binary sulfides (WS₂, MoS₂, and V₅S₈) from the respective oxides, *Mater. Chem. Phys.*, 87 (2004) 327–331.
45. G.W. Li, C.S. Li, H. Tang, K.S. Cao, J.A. Chen, F.F. Wang, Y.J. Jin, Synthesis and characterization of hollow MoS₂ microspheres grown from MoO₃ precursors, *J. Alloys Compounds*, 501 (2010) 275–281.
46. J.C. Hulthen, C.R. Martin, A general template-based method for the preparation of nanomaterials, *J. Mater. Chem.*, 7 (1997) 1075–1087.
47. D.S. Xue, L.Y. Zhang, A.B. Gui, X.F. Xu, Fe₃O₄ nanowire arrays synthesized in AAO templates, *Appl. Phys. A Mater. Sci. Process.*, 80 (2005) 439–442.
48. M.J. Zheng, L.D. Zhang, G.H. Li, W.Z. Shen, Fabrication and optical properties of large-scale uniform zinc oxide nanowire arrays by one-step electrochemical deposition technique, *Chem. Phys. Lett.*, 363 (2002) 123–128.
49. K.Y. Shi, B.F. Xin, Y.J. Chi, H.G. Fu, Assembling porous Fe₂O₃ nanowire arrays by electrochemical deposition in mesoporous silica SBA-16 films, *Acta Chim. Sin.*, 62 (2004) 1859–1861.
50. X.M. Liu, Y.C. Zhou, Electrochemical deposition and characterization of Cu₂O nanowires, *Appl. Phys. A Mater. Sci. Process.*, 81 (2005) 685–689.
51. T.S. Mintz, Y.V. Bhargava, S.A. Thorne *et al.*, Electrochemical synthesis of functionalized nickel oxide nanowires, *Electrochem. Solid State Lett.*, 8 (2005) D26–D30.
52. Y.H. Chen, X.T. Zhang, Z.H. Xue, Z.L. Du, T.J. Li, Preparation of SnO₂ nanowires by AC electrodeposition in anodic alumina template and its deposition conditions, *J. Inorg. Mater.*, 20 (2005) 59–60.
53. Y. Li, G.S. Cheng, L.D. Zhang, Fabrication of highly ordered ZnO nanowire arrays in anodic alumina membranes, *J. Mater. Res.*, 15 (2000) 2305–2308.

54. Y.W. Chen, Y.C. Liu, S.X. Lu *et al.*, Optical properties of ZnO and ZnO: In nanorods assembled by sol-gel method, *J. Chem. Phys.*, 123 (2005) 134701–134705.
55. X.Y. Wang, X.Y. Wang, W.G. Huang, P.J. Sebastian, S. Gamboa, Sol-gel template synthesis of highly ordered MnO₂ nanowire arrays, *J. Power Sources*, 140 (2005) 211–215.
56. H. Xu, D.H. Qin, Z. Yang, H.L. Li, Fabrication and characterization of highly ordered zirconia nanowire arrays by sol-gel template method, *Mater. Chem. Phys.*, 80 (2003) 524–528.
57. M. Zhang, Y. Bando, K. Wada, Sol-gel template preparation of TiO₂ nanotubes and nanorods, *J. Mater. Sci. Lett.*, 20 (2001) 167–170.
58. Y.K. Zhou, H.L. Li, Sol-gel template synthesis and structural properties of a highly ordered LiNi_{0.5}Mn_{0.5}O₂ nanowire array, *J. Mater. Chem.*, 12 (2002) 681–686.
59. Z. Yang, Y. Huang, B. Dong, H.L. Li, Fabrication and structural properties of LaFeO₃ nanowires by an ethanol-ammonia-based sol-gel template route, *Appl. Phys. A Mater. Sci. Process.*, 81 (2005) 453–457.
60. C.K. Xu, G.D. Xu, Y.K. Liu, G.H. Wang, A simple and novel route for the preparation of ZnO nanorods, *Solid State Commun.*, 122 (2002) 175–179.
61. C.K. Xu, X.L. Zhao, S. Liu, G.H. Wang, Large-scale synthesis of rutile SnO₂ nanorods, *Solid State Commun.*, 125 (2003) 301–304.
62. C.K. Xu, G.D. Xu, G.H. Wang, Preparation and characterization of NiO nanorods by thermal decomposition of NiC₂O₄ precursor, *J. Mater. Sci.*, 38 (2003) 779–782.
63. Y.L. Cao, D.Z. Jia, L. Liu, J.M. Luo, Rapid synthesis of lead oxide nanorods by one-step solid-state chemical reaction at room temperature, *Chin. J. Chem.*, 22 (2004) 1288–1290.
64. J.H. Liang, C. Peng, X. Wang *et al.*, Chromate nanorods/nanobelts: general synthesis, characterization, and properties, *Inorg. Chem.*, 44 (2005) 9405–9415.
65. A. Vantomme, Z.Y. Yuan, G.H. Du, B.L. Su, Surfactant-assisted large-scale preparation of crystalline CeO₂ nanorods, *Langmuir*, 21 (2005) 1132–1135.
66. L.H. Thompson, L.K. Doraiswamy, Sonochemistry: science and engineering, *Ind. Eng. Chem. Res.*, 38 (1999) 1215–1249.
67. R.V. Kumar, Y. Kolytyn, X.N. Xu, Y. Yeshurun, A. Gedanken, I. Felner, Fabrication of magnetite nanorods by ultrasound irradiation, *J. Appl. Phys.*, 89 (2001) 6324–6328.
68. X.L. Hu, Y.J. Zhu, S.W. Wang, Sonochemical and microwave-assisted synthesis of linked single-crystalline ZnO rods, *Mater. Chem. Phys.*, 88 (2004) 421–426.
69. T. Gao, Q.H. Li, T.H. Wang, Sonochemical synthesis, optical properties, and electrical properties of core/shell-type ZnO nanorod/CdS nanoparticle composites, *Chem. Mater.*, 17 (2005) 887–892.
70. V.G. Pol, O. Palchik, A. Gedanken, I. Felner, Synthesis of europium oxide nanorods by ultrasound irradiation, *J. Phys. Chem. B*, 106 (2002) 9737–9743.
71. J.J. Miao, H. Wang, Y.R. Li, J.M. Zhu, J.J. Zhu, Ultrasonic-induced synthesis of CeO₂ nanotubes, *J. Cryst. Growth*, 281 (2005) 525–529.
72. B. Liu, H.C. Zeng, Hydrothermal synthesis of ZnO nanorods in the diameter regime of 50 nm, *J. Am. Chem. Soc.*, 125 (2003) 4430–4431.

73. J.M. Wang, L. Gao, Wet chemical synthesis of ultralong and straight single-crystalline ZnO nanowires and their excellent UV emission properties, *J. Mater. Chem.*, 13 (2003) 2551–2554.
74. M. Guo, P. Diao, S.M. Cai, Hydrothermal growth of well-aligned ZnO nanorod arrays: dependence of morphology and alignment ordering upon preparing conditions, *J. Solid State Chem.*, 178 (2005) 1864–1873.
75. M.H. Cao, Y.H. Wang, C.X. Guo, Y.J. Qi, C.W. Hu, E.B. Wang, A simple route towards CuO nanowires and nanorods, *J. Nanosci. Nanotechnol.*, 4 (2004) 824–828.
76. J. Zhang, Z.G. Liu, C.K. Lin, J. Lin, A simple method to synthesize beta-Ga₂O₃ nanorods and their photoluminescence properties, *J. Cryst. Growth*, 280 (2005) 99–106.
77. D.S. Zheng, S.X. Sun, W.L. Fan *et al.*, One-step preparation of single-crystalline beta-MnO₂ nanotubes, *J. Phys. Chem. B*, 109 (2005) 16439–16443.
78. D.L. Zhu, H. Zhu, Y.H. Zhang, Microstructure and magnetization of single-crystal perovskite manganese nanowires prepared by hydrothermal method, *J. Cryst. Growth*, 249 (2003) 172–175.
79. K.B. Zhou, X. Wang, X.M. Sun, Q. Peng, Y.D. Li, Enhanced catalytic activity of ceria nanorods from well-defined reactive crystal planes, *J. Catal.*, 229 (2005) 206–212.
80. Z.Y. Yuan, B.L. Su, Titanium oxide nanotubes, nanofibers and nanowires, *Colloids Surf. A Physicochem. Eng. Aspects*, 241 (2004) 173–183.
81. V. Brynzari, G. Korotchenkov, S. Dmitriev, Theoretical study of semiconductor thin film gas sensitivity: attempt to consistent approach, *J. Electron. Technol.*, 33 (2000) 225–235.
82. T. Martensson, P. Carlberg, M. Borgstrom, L. Montelius, W. Seifert, L. Samuelson, Nanowire arrays defined by nanoimprint lithography, *Nano Lett.*, 4 (2004) 699–702.
83. X.C. Jiang, T. Herricks, Y.N. Xia, CuO nanowires can be synthesized by heating copper substrates in air, *Nano Lett.*, 2 (2002) 1333–1338.
84. G. Korotcenkov, V. Brinzari, M. Ivanov, A. Cerneavschi, J. Rodriguez, A. Cirera, A. Cornet, J. Morante, Structural stability of In₂O₃ films deposited by spray pyrolysis during thermal annealing, *Thin Solid Films*, 479 (2004) 38–51.
85. G. Korotcenkov, M. DiBattista, J. Schwank, V. Brinzari, Structural characterization of SnO₂ gas sensing films deposited by spray pyrolysis, *J. Mater. Sci. Eng. B*, 77 (2000) 33–39.
86. W.I. Park, G.C. Yi, Electroluminescence in *n*-ZnO nanorod arrays vertically grown on *p*-GaN, *Adv. Mater.*, 16 (2004) 87–90.
87. H.J. Fan, F. Bertram, A. Dadgar, J. Christen, A. Krost, M. Zacharias, Self-assembly of ZnO nanowires and the spatial resolved characterization of their luminescence, *Nanotechnology*, 15 (2004) 1401–1404.
88. Y.K. Tseng, C.T. Chia, C.Y. Tsay *et al.*, Growth of epitaxial needle like ZnO nanowires on GaN films, *J. Electrochem. Soc.*, 152 (2005) G95–G98.
89. H.T. Ng, J. Han, T. Yamada, P. Nguyen, Y.P. Chen, M. Meyyappan, Single crystal nanowire vertical surround-gate field-effect transistor, *Nano Lett.*, 4 (2004) 1247–1252.
90. C.Y. Geng, Y. Jiang, Y. Yao *et al.*, Well-aligned ZnO nanowire arrays fabricated on silicon substrates, *Adv. Funct. Mater.*, 14 (2004) 589–594.

91. Y. Zhang, H.B. Jia, R.M. Wang *et al.*, Low-temperature growth and Raman scattering study of vertically aligned ZnO nanowires on Si substrate, *Appl. Phys. Lett.*, 83 (2003) 4631–4633.
92. J. Park, H.H. Choi, K. Siebein, R.K. Singh, Two-step evaporation process for formation of aligned zinc oxide nanowires, *J. Cryst. Growth*, 258 (2003) 342–348.
93. S.Y. Li, P. Lin, C.Y. Lee, M.S. Ho, T.Y. Tseng, Fabrication of vertical ZnO nanowires on silicon (100) with epitaxial ZnO buffer layer, *J. Nanosci. Nanotechnol.*, 4 (2004) 968–971.
94. C.H. Liu, W.C. Yiu, F.C.K. Au, J.X. Ding, C.S. Lee, S.T. Lee, Electrical properties of zinc oxide nanowires and intramolecular *p-n* junctions, *Appl. Phys. Lett.*, 83 (2003) 3168–3170.
95. S. Zhuiykov, Morphology of Pt-doped RuO₂ nanocomposites and their application in water quality monitoring sensors, *Sens. Actuat. B-Chem.*, 136 (2009) 248–256.
96. S. Zhuiykov, Carbon monoxide detection at low temperatures by semiconductor sensor with nanostructured Au-doped CoOOH films, *Sens. Actuat. B-Chem.*, 129 (2008) 431–441.
97. C. Carrara, J. Munera, E.A. Lombardo, L.M. Cornaglia, Kinetic and stability studies of Ru/La₂O₃ used in the dry reforming of methane, *Top. Catal.*, 51 (2008) 98–106.
98. S.Y. Li, P. Lin, C.Y. Lee, T.Y. Tseng, C.J. Huang, Effect of Sn dopant on the properties of ZnO nanowires, *J. Phys. D Appl. Phys.*, 37 (2004) 2274–2282.
99. J. Ribeiro, F.L.S. Purgato, K.B. Kokoh, J.M. Leger, A.R. de Andrade, Application of Ti/RuO₂-Ta₂O₅ electrodes in the electrooxidation of ethanol and derivatives: reactivity versus electrocatalytic efficiency, *Electrochim. Acta*, 53 (2008) 7845–7851.
100. T. Yamamoto, H. Katayama-Yoshida, Solution using a codoping method to unipolarity for the fabrication of *p*-type ZnO, *Jpn J. Appl. Phys. Part 2 Lett.*, 38 (1999) L166–L169.
101. P.M. Koenraad, M.E. Flatté, Single dopants in semiconductors, *Nature Mater.*, 10 (2011) 91–100.
102. S. Zhuiykov, E. Kats, D. Marney, K. Kalantar-zadeh, Improved antifouling resistance of electrochemical water quality sensors based on Cu₂O-doped RuO₂ sensing electrode, *Prog. Org. Coat.*, 70 (2011) 67–73.
103. K.Y. Tan, K.W. Chan, M. Möttönen, A. Morello, C. Yang, J. Van Donkelaar, A. Alves, J.M. Pirkkalainen, D.N. Jamieson, R.G. Clark, A.S. Dzurak, Transport spectroscopy of single phosphorus donors in a silicon nanoscale transistor, *Nano Lett.*, 10 (2010) 11–15.
104. A. Persaud, S.J. Park, J.A. Liddle, T. Schenkel, J. Bokor, I.W. Rangelow, Integration of scanning probes and ion beams, *Nano Lett.*, 5 (2005) 1087–1091.
105. T. Shinada, T. Kurosawa, H. Nakayama, Y. Zhu, M. Hori, I. Ohdomari, A reliable method for the counting and control of single ions for single-dopant controlled devices, *Nanotechnology*, 19 (2008) 345202.
106. M. Hori, T. Shinada, K. Taira, A. Komatsubara, Y. Ono, T. Tanii, T. Endoh, I. Ohdomari, Enhancing single-ion detection efficiency by applying substrate

- bias voltage for deterministic single-ion doping, *Appl. Phys. Exp.*, 4 (2011) 046501–04502.
107. M. Pierre, R. Wacquez, X. Jehl, M. Sanquer, M. Vinet, O. Cueto, Single-donor ionization energies in nanoscale CMOS channel, *Nature Nanotechnol.*, 5 (2010) 133–137.
 108. A Morello, *et al.*, Single-shot readout of an electron spin in silicon, *Nature*, 467 (2010) 687–691.
 109. L.C.L. Hollenberg, A.D. Greentree, A.G. Fowler, C.J. Wellard, Two-dimensional architectures for donor-based quantum computing, *Phys. Rev. B*, 74 (2006) 045311.
 110. R. Rahman, S. Park, J. Cole, A. Greentree, R. Muller, G. Klimeck, L. Hollenberg, Atomistic simulations of adiabatic coherent electron transport in triple donor systems, *Phys. Rev. B*, 80 (2009) 035302.
 111. E. Prati, Valley blockage quantum switching in silicon nanostructures, *J. Nanosci. Nanotechnol.*, 11 (2011) 8522–8526.
 112. M. Klein, J.A. Mol, J. Verduijn, G.P. Lansbergen, S. Rogge, R.D. Levine, F. Remacle, Ternary logic implemented on a single dopant atom field effect silicon transistor, *Appl. Phys. Lett.*, 96 (2010) 043107.
 113. E. Prati, M. Hori, F. Guagliardo, G. Ferrari, T. Shinada, Anderson-Mott transition in arrays of a few dopant atoms in a silicon transistor, *Nature Nanotechnol.*, 7 (2012) 443–447.
 114. S. Zhuiykov, K. Kalantar-zadeh, Development of antifouling of electrochemical solid-state DO sensors based on nanostructured $\text{Cu}_{0.4}\text{Ru}_{3.4}\text{O}_7+\text{RuO}_2$ sensing electrodes, *Electrochim. Acta*, 73 (2012) 105–111.
 115. M. Fuechle, J.A. Miwa, S. Mahapatra, H. Ryu, S. Lee, O. Warschkow, L.C.L. Hollenberg, G. Klimeck, M.Y. Simmons, A single atom transistor, *Nature Nanotechnol.*, 7 (2012) 242–246.
 116. J. Nowotny, *Oxide Semiconductors for Solar Energy Conversion: Titanium dioxide*, 2012, CRC Press, Boca Raton, 393p.
 117. M.-P. Lu, M.-Y. Lu, L.-J. Chen, p-Type ZnO nanowires: From synthesis to nanoenergy, *Nano Energy*, 1 (2012) 247–258.
 118. B. Kumar, S.W. Kim, Energy harvesting based on semiconducting piezoelectric ZnO nanostructures, *Nano Energy*, 1 (2012) 342–355.
 119. C.G. Van de Walle, S. Limpijumng, J. Neugebauer, First-principles studies of beryllium doping of GaN, *Phys. Rev. B*, 6324 (2001) 2452051–2452057.
 120. F.J. Cox, E.A. Davis, S.P. Cottrell *et al.*, Experimental confirmation of the predicted shallow donor hydrogen state in zinc oxide, *Phys. Rev. Lett.*, 86 (2001) 2601–2604.
 121. J.G. Lu, L.P. Zhu, Z.Z. Ye *et al.*, Reproducibility and stability of N–Al codoped p-type ZnO thin films, *J. Mater. Sci.*, 41 (2006) 467–470.
 122. J. Zhong, S. Muthukumar, Y. Chen *et al.*, Ga-doped ZnO single-crystal nanotips grown on fused silica by metal organic chemical vapor deposition, *Appl. Phys. Lett.*, 83 (2003) 3401–3403.
 123. S.Y. Bae, C.W. Na, J.H. Kang, J. Park, Comparative structure and optical properties of Ga-, In-, and Sn-doped ZnO nanowires synthesized via thermal evaporation, *J. Phys. Chem. B*, 109 (2005) 2526–2531.
 124. D.K. Hwang, H.S. Kim, J.H. Lim *et al.*, Study of the photoluminescence of phosphorus-doped p-type ZnO thin films grown by radio-frequency magnetron sputtering, *Appl. Phys. Lett.*, 86 (2005) 151917–151919.

125. W. Lee, M.C. Jeong, S.W. Joo, J.M. Myoung, Arsenic doping of ZnO nanowires by post-annealing treatment, *Nanotechnology*, 16 (2005) 764–768.
126. W. Lee, M.C. Jeong, J.M. Myoung, Optical characteristics of arsenic-doped ZnO nanowires, *Appl. Phys. Lett.*, 85 (2004) 6167–6169.
127. D.W. Zeng, C.S. Xie, B.L. Zhu *et al.*, Controlled growth of ZnO nanomaterials via doping Sb, *J. Cryst. Growth*, 266 (2004) 511–518.
128. G.Z. Shen, J.H. Cho, J.K. Yoo, G.C. Yi, C.J. Lee, Synthesis and optical properties of S-doped ZnO nanostructures: nanonails and nanowires, *J. Phys. Chem. B*, 109 (2005) 5491–5496.
129. J.B. Cui, U.J. Gibson, Electrodeposition and room temperature ferromagnetic anisotropy of Co and Ni-doped ZnO nanowire arrays, *Appl. Phys. Lett.*, 87 (2005) 133108–133110.
130. C.X. Xu, X.W. Sun, Z.L. Dong, M.B. Yu, Y.Z. Xiong, J.S. Chen, Magnetic nanobelts of iron-doped zinc oxide, *Appl. Phys. Lett.*, 86 (2005) 173110–173112.
131. D.A. Schwartz, K.R. Kittilstved, D.R. Gamelin, Above-room-temperature ferromagnetic Ni²⁺-doped ZnO thin films prepared from colloidal diluted magnetic semiconductor quantum dots, *Appl. Phys. Lett.*, 85 (2004) 1395–1397.
132. C. Ronning, P.X. Gao, Y. Ding, Z.L. Wang, D. Schwen, Manganese-doped ZnO nanobelts for spintronics, *Appl. Phys. Lett.*, 84 (2004) 783–785.
133. P.C. Chang, Z.Y. Fan, D.W. Wang *et al.*, ZnO nanowires synthesized by vapor trapping CVD method, *Chem. Mater.*, 16 (2004) 5133–5137.
134. P. Sharma, A. Gupta, K.V. Rao *et al.*, Ferromagnetism above room temperature in bulk and transparent thin films of Mn-doped ZnO, *Nature Mater.*, 2 (2003) 673–677.
135. Y.Q. Chang, D.B. Wang, X.H. Luo *et al.*, Synthesis, optical, and magnetic properties of diluted magnetic semiconductor Zn_{1-x}Mn_xO nanowires via vapor phase growth, *Appl. Phys. Lett.*, 83 (2003) 4020–4022.
136. Z.Y. Fan, X.G. Wen, S.H. Yang, J.G. Lu, Controlled *p*- and *n*-type doping of Fe₂O₃ nanobelt field effect transistors, *Appl. Phys. Lett.*, 87 (2005) 013113–013115.
137. H.J. Chun, Y.S. Choi, S.Y. Bae, H.C. Choi, J. Park, Single-crystalline gallium-doped indium oxide nanowires, *Appl. Phys. Lett.*, 85 (2004) 461–464.
138. C. Li, D.H. Zhang, B. Lei, S. Han, X.L. Liu, C.W. Zhou, Surface treatment and doping dependence of In₂O₃ nanowires as ammonia sensors, *J. Phys. Chem. B*, 107 (2003) 12451–12455.
139. D.J. Zhang, C. Li, X.L. Liu, S. Han, T. Tang, C.W. Zhou, Doping dependent NH₃ sensing of indium oxide nanowires, *Appl. Phys. Lett.*, 83 (2003) 1845–1847.
140. X.S. Peng, G.W. Meng, X.F. Wang *et al.*, Synthesis of oxygen-deficient indium-tin-oxide (ITO) nanofibers, *Chem. Mater.*, 14 (2002) 4490–4493.
141. Q. Wan, Z.T. Song, S.L. Feng, T.H. Wang, Single-crystalline tin-doped indium oxide whiskers: synthesis and characterization, *Appl. Phys. Lett.*, 85 (2004) 4759–4761.
142. P. Nguyen, H.T. Ng, J. Kong *et al.*, Epitaxial directional growth of indium-doped tin oxide nanowire arrays, *Nano Lett.*, 3 (2003) 925–928.
143. P.D. Yang, The chemistry and physics of semiconductor nanowires, *MRS Bull.*, 30 (2005) 85–91.

144. S. Han, C. Li, Z.Q. Liu *et al.*, Transition metal oxide core-shell nanowires: generic synthesis and transport studies, *Nano Lett.*, 4 (2004) 1241–1246.
145. J.S. Jie, G.Z. Wang, X.H. Han, J.G. Hou, Synthesis and characterization of ZnO: In nanowires with superlattice structure, *J. Phys. Chem. B*, 108 (2004) 17027–17031.
146. L.J. Lauhon, M.S. Gudiksen, C.L. Wang, C.M. Lieber, Epitaxial core-shell and core-multi shell nanowire heterostructures, *Nature*, 420 (2002) 57–61.
147. W. Lu, J. Xiang, B.P. Timko, Y. Wu, C.M. Lieber, One-dimensional hole gas in germanium/silicon nanowire heterostructures, *Proc. Natl Acad. Sci. USA*, 102 (2005) 10046–10051.
148. F. Qian, S. Gradecak, Y. Li, C.Y. Wen, C.M. Lieber, Core/multishell nanowire heterostructures as multicolor, high-efficiency light-emitting diodes, *Nano Lett.*, 5 (2005) 2287–2291.
149. H.F. Zhang, C.M. Wang, L.S. Wang, Helical crystalline SiC/SiO₂ core-shell nanowires, *Nano Lett.*, 2 (2002) 941–944.
150. Y.H. Wong, Q. Li, Study of the crystallinity of ZnO in the Zn/ZnO nanocable heterostructures, *J. Mater. Chem.*, 14 (2004) 1413–1418.
151. J. Hwang, B.D. Min, J.S. Lee *et al.*, Al₂O₃ nanotubes fabricated by wet etching of ZnO/Al₂O₃ core/shell nanofibers, *Adv. Mater.*, 16 (2004) 422–425.
152. K.W. Chang, J.J. Wu, Formation of well-aligned ZnGa₂O₄ nanowires from Ga₂O₃/ZnO core-shell nanowires via a Ga₂O₃/ZnGa₂O₄ epitaxial relationship, *J. Phys. Chem. B*, 109 (2005) 13572–13577.
153. C.W. Lai, J.Y. Dai, X.Y. Zhang *et al.*, In situ synthesis and phase transformation of In₂O₃/Sb core-shell nanostructures, *J. Cryst. Growth*, 282 (2005) 383–388.
154. J. Xu, X.L. Li, J.F. Liu, X. Wang, Q. Peng, Y.D. Li, Solution route to inorganic nanobelt-conducting organic polymer core-shell nanocomposites, *J. Polym. Sci. Part A Polym. Chem.*, 43 (2005) 2892–2900.
155. D.H. Zhang, Z.Q. Liu, S. Han *et al.*, Magnetite (Fe₃O₄) core-shell nanowires: synthesis and magnetoresistance, *Nano Lett.*, 4 (2004) 2151–2155.
156. E.S. Jang, J.Y. Bae, J. Yoo *et al.*, Quantum confinement effect in ZnO/Mg_{0.2}Zn_{0.8}O multishell nanorod heterostructures, *Appl. Phys. Lett.*, 88 (2006) 023102–023104.
157. M.S. Gudiksen, L.J. Lauhon, J. Wang, D.C. Smith, C.M. Lieber, Growth of nanowire superlattice structures for nanoscale photonics and electronics, *Nature*, 415 (2002) 617–620.
158. Y.Y. Wu, R. Fan, P.D. Yang, Block-by-block growth of single-crystalline Si/SiGe superlattice nanowires, *Nano Lett.*, 2 (2002) 83–86.
159. M.T. Bjork, B.J. Ohlsson, T. Sass *et al.*, One-dimensional heterostructures in semiconductor nanowhiskers, *Appl. Phys. Lett.*, 80 (2002) 1058–1060.
160. C.W. Na, S.Y. Bae, J. Park, Short-period superlattice structure of Sn-doped In₂O₃(ZnO)(4) and In₂O₃(ZnO)(5) nanowires, *J. Phys. Chem. B*, 109 (2005) 12785–12790.
161. I.M. Tiginyanu, O. Lupan, V.V. Ursaki, L. Chow, M. Enachi, Nanostructures of metal oxides, in P.K. Bhattacharya, R. Fornani, S. Mahajan, H. Kamimura (eds) *Comprehensive Semiconductor Science and Technology*, 3, 2011, Elsevier Science, Amsterdam, 396–479.

162. X.D. Wang, J.H. Song, J. Liu, Z.L. Wang, DC nanogenerator driven by ultrasonic wave, *Science*, 316 (2007) 102–105.
163. B. Kumar, S.W. Kim, Recent advances in power generation through piezoelectric nanogenerators, *J. Mater. Chem.*, 21 (2011) 18946–18958.
164. H.-K. Park, K.Y. Lee, J.-S. Seo, J.-A. Jeong, H.-K. Kim, D. Choi, S.-W. Kim, Charge-generating mode control in high-performance transparent flexible piezoelectric nanogenerators, *Adv. Funct. Mater.*, 21 (2011) 1187–1193.
165. S. Trasatti, Physical electrochemistry of ceramic oxides, *Electrochim. Acta*, 36 (1991) 225–241.
166. Z.W. Chen, Z. Jiao, M.H. Wu, C.H. Shek, C.M.L. Wu, J.K.L. Lai, Microstructural evolution of oxide and semiconductor thin films, *Prog. Mater. Sci.*, 56 (2011) 901–1029.
167. S. Zhuiykov, *Electrochemistry of Zirconia Gas Sensors*, 2007, CRC Press, Boca Raton, 292p.
168. D.J. Mowbray *et al.*, Trends in metal oxide stability for nanorods, nanotubes and surfaces, *J. Phys. Chem. C*, 115 (2011) 2244–2252.
169. O. Harnack, C. Pacholski, H. Weller, A. Yasuda, J.M. Wessels, Rectifying behaviour of electrically aligned ZnO nanorods, *Nano Lett.*, 3 (2003) 1097–1101.
170. S. Kumar, S. Rajaraman, R.A. Gerhardt, Z.L. Wang, P.J. Hesketh, Tin oxide nanosensor fabrication, using AC dielectrophoretic manipulation of nanobelts, *Electrochim. Acta*, 51 (2005) 943–951.
171. G. Korotcenkov, The role of morphology and crystallographic structure of metal oxides in response of conductometric-type gas sensors, *Mater. Sci. Eng. R*, 61 (2008) 1–39.
172. E. Lucas, S. Decker, A. Khaleel, A. Seitz, A. Fultz, S. Fultz, A. Ponce, W. Li, C. Carnes, K. Klabunde, Nanocrystalline metal oxides as unique chemical reagents/sorbents, *Chem. Europ. J.*, 12 (2001) 2505–2510.
173. O. Englander, D. Christensen, L.W. Lin, Local synthesis of silicon nanowires and carbon nanotubes on microbridges, *Appl. Phys. Lett.*, 82 (2003) 4797–4799.
174. A. Ural, Y.M. Li, H.J. Dai, Electric-field-aligned growth of single-walled carbon nanotubes on surfaces, *Appl. Phys. Lett.*, 81 (2002) 3464–3466.
175. S. Dittmer, J. Svensson, E.E.B. Campbell, Electric field aligned growth of single-walled carbon nanotubes, *Curr. Appl. Phys.*, 4 (2004) 595–598.
176. E. Wahlstrom, E.K. Vestergaard, R. Schaub, A. Ronnau, M. Vestergaard, E. Lagsgaard, I. Stensgaard, F. Besenbacher, Electron transfer-induced dynamics of oxygen molecules on the TiO₂(110) surface, *Science*, 303 (2004) 511–513.
177. L. Castañeda, Effects of palladium coatings on oxygen sensors of titanium dioxide thin films, *Mater. Sci. Eng. B*, 139 (2–3) (2007) 149–154.
178. Y. Lei, W. Cai, G. Wilde, Highly ordered nanostructures with tunable size, shape and properties: A new way to surface nano-patterning using ultra-thin alumina masks, *Prog. Mater. Sci.*, 52 (2007) 465–539.
179. Y.Y. Yu, S.S. Chang, C.L. Lee, C.R.C. Wang, Gold nanorods: electrochemical synthesis and optical properties, *J. Phys. Chem. B*, 101 (1997) 6661–6664.
180. M. Porto, Relative significance of particle anisotropy in systems of ultrafine ferromagnetic particles, *J. Appl. Phys.*, 92 (2002) 6057–6061.

181. X. Battle, A. Labarta, Finite-size effects in fine particles: magnetic and transport properties, *J. Phys. D*, 35 (2002) R15–R42.
182. M. Maillard, S. Giorgio, M.P. Pileni, Silver nanodisks, *Adv. Mater.*, 14 (2002) 1084–1086.
183. J. Hu, L.S. Li, W. Yang, L. Manna, L. Wang, A.P. Alivisatos, Linearly polarized emission from colloidal semiconductor quantum rods, *Science*, 292 (2001) 2060–2063.

Electronic devices and functional structures based on nanostructured semiconductors

DOI: 10.1533/9781782422242.95

Abstract: The chapter provides an overview of the majority of the novel nanoscale devices based on nanostructured semiconductors: from tunable electronic devices and optoelectronic devices to resonators and cantilevers. It then describes the functional structures, such as carbon nanotubes, which have been used in various electronic devices including environmental sensors.

Key words: nanoscale functional structures, tunable electronic devices, optoelectronic devices, resonators, carbon nanotubes (CNT)

3.1 Introduction to novel nanoscale devices from nanostructured semiconductors

If electronics maintains its development in accordance with Moore's law,¹ in the early part of the 21st century, the number of transistors per chip will double every two years. Based on this law, microprocessor architecture will soon reach over a billion transistors per chip, operating at clock rates exceeding 10 GHz. This trend towards device miniaturization will not only be hindered by the existing fabrication technology, but will also result in dramatically increased power consumption. Moreover, the length of the projected channel in a CMOS field-effect transistor will reach about ~20 nm in 2014² and the gate oxide thickness will decrease to approximately two mono-layers.³ As a result, the associated tunnelling-induced leakage current and dielectric breakdown will lead to device failure.

Consequently, the development of new nanostructured materials with thickness of less than 10 nm will be able to address the challenge and thus offer exciting new possibilities. This supports Richard Feynman's speech back in 1959, when he described a vision – 'to synthesize nanoscale building blocks with precisely controlled size and composition, and assemble them into larger structures with unique properties and functions'.⁴ This revelation still sparks the imagination of a new generation of scientists.

One class of nanostructured materials which has attracted tremendous attention is the quasi-two-dimensional (Q2D) structures enabled by the revolutionary discovery of carbon nanotubes (CNT) in 1991.⁵ Enormous progress has been achieved during the last few years in the synthesis, characterization and functional application of 2D semiconductors. These semiconductors within the size of two coordinates, i.e. with a thickness of less

than 7–10 nm, offer completely different properties, higher integration density and lower power consumption.^{6–9} They also possess large surface-to-volume ratio and a Debye length consistent with their small size, which makes them very attractive in ultra-high-sensitive chemical and biological sensors. Furthermore, their size confinement enables a tunable bandgap, higher optical gain and faster operation speed, features which establish this class of nanomaterials in the superior position for a variety of functional structures and devices based on such structures.¹⁰

Considering their in-depth physical and chemical properties, 1D and 2D structures have been demonstrated to be promising candidates for the next generation of electronic, sensing and optoelectronic devices. Due to their diverse physical or chemical properties and functionalities, the 2D metal oxides stand out among other semiconductors as one of the most versatile classes of materials.^{5,11–15} Their 2D structures have not only inherited the fascinating qualities and characteristics of their bulk structures, but also created unique properties associated with their highly anisotropic geometry and size confinement.^{5,11,16} Plate IIa (see colour section between pages 232 and 233) illustrates a SEM image of a thermodynamically stable layered α - MoO_3 nanostructure.¹⁰ As clearly shown in this picture, the α - MoO_3 structure comprises perfect planar crystals, held together by Van der Waals forces, which also offers the possibility of obtaining 2D structures. Advantageously, the electronic properties, in particular the bandgap, of such 2D semiconductor oxides can be largely manoeuvred using well-known chemical and physical approaches.¹⁷ Such manipulations, which impose their effects on the 2D environment, categorize these materials as excellent templates for achieving the optimum quantum parameters required for target applications. Moreover, the combination of several 2D nanomaterials into sandwich structures (made up of two, three, four or more different layers of such materials, see Plate IIb) can offer even greater scope. These 2D-based sandwich heterostructures^{18,19} can be tailored with atomic precision, and individual layers of very different character can be combined together in the sandwich structure. Consequently, the properties of these sandwich structures can be tuned to fit an enormous range of possible applications. Furthermore, the functionality of hetero-structure stacks is ‘embedded’ in their design.¹¹ The first designs have already been reported;²⁰ vertical tunnelling transistors based on this type of hetero-structure have recently been demonstrated and showed very promising characteristics.

3.2 Tunable electronic devices

3.2.1 Field-effect transistor

Both 1D and 2D structures can be fabricated into field-effect transistors (FETs) to serve as the fundamental building blocks of electronic devices

such as logic gates, computing circuits and chemical sensors. To date, there have been few reports showing that various semiconductor metal oxides such as ZnO,²¹ Fe₂O₃,²² In₂O₃,²³ SnO₂,²⁴ Ga₂O₃,²⁵ V₂O₅²⁶ and CdO²⁷ have been configured into FETs. In brief, the manufacturing process can be described as follows: nanowires (NWs) are first dispersed in a solvent, usually isopropanol alcohol or ethanol to form a suspension phase, and then deposited onto a SiO₂/Si substrate. The bottom substrate underneath the SiO₂ layer is degenerately doped (p^{++} or n^{++}), serving as the back gate. Photolithography or ebeam-lithography is utilized to define the contact electrode pattern. Assuming a cylindrical wire of radius r and length L , the capacitance per unit length with respect to the back gate may be simply represented as:

$$\frac{C}{L} = \frac{2\pi\epsilon\epsilon_0}{\ln(2h/r)} \quad [3.1]$$

where ϵ is the dielectric constant of the gate oxide and h is the thickness of the oxide layer. The carrier mobility in an atomically-thin layer is calculated using $\mu = e/m^*\langle\tau\rangle$ in which e is the point charge and τ is the transport relaxation rate of momentum in the plane. Using the Born approximation, the transport relaxation time is calculated using:²⁸

$$\frac{1}{\tau} = \frac{2\pi}{\hbar} \sum_{k_z} \sum_{\mu} \int_{-\infty}^{+\infty} N_i^{(\mu)}(z) dz |V_{k-k_z}^{(\mu)}(z)|^2 \times f(k, k_z) \quad [3.2]$$

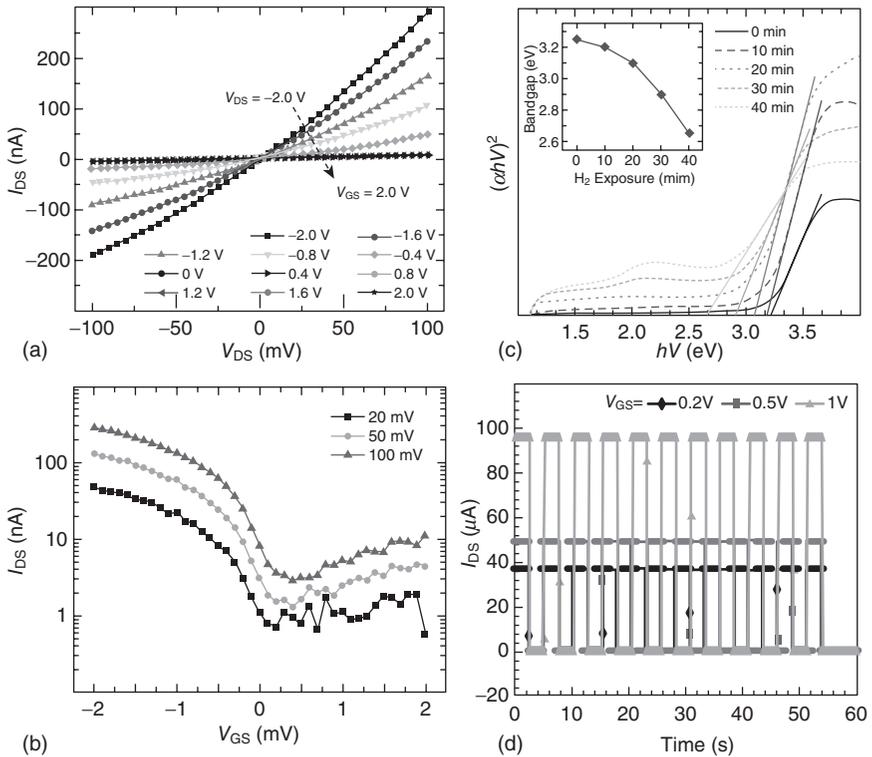
in which $N_i^{(\mu)}(z) dx dy dz$ is the concentration of the μ^{th} kind of Coulomb charge centre within the volume $dx dy dz$ and $f(k, k_z)$ is a function of k and k_z vectors. $V_{k-k_z}^{(\mu)}(z)$ is a potential function showing the intensity of the scattering effects on free charges, and reducing it is important if large carrier mobilities are to be obtained. In accordance with (3.2), in materials of high relative dielectric constants, such as α -MoO₃, the overall effect of Coulomb charges on $V_{k-k_z}^{(\mu)}(z)$ is reduced and the scattering effect is dominated by the optical and acoustic phonons. For example, in the case of a 2D material with a relative dielectric constant of ~ 5 and a thickness of 10 nm, the exhibited mobility is approximately $\sim 550 \text{ cm}^2/\text{Vs}$, while for a higher dielectric material of ~ 500 this number advantageously increases to $\sim 62000 \text{ cm}^2/\text{Vs}$.¹⁰ Also favourably, the structure of α -MoO₃ is made of perfect planar crystals (Plate IIa), which also offers the possibility of obtaining 2D structures using various exfoliation methods. At a level of a few layers, the dielectric value can be reduced in comparison to its bulk counterpart. However, this reduced value has a negligible effect on the overall charge mobility of the device, as acoustic scattering still remains the main limiting factor at and above room temperature.

Current–voltage (I – V) characteristics of the FETs based on α -MoO₃ were obtained for a range of back-gate voltages as shown in Figs 3.1a and

3.1b. The carrier mobility of the device was calculated using the following equation:²⁹

$$\mu = \frac{\Delta I_{DS}}{\Delta V_{GS}} \times \frac{l}{C \times w \times V_{DS}} \quad [3.3]$$

where $\Delta I_{DS}/\Delta V_{GS}$ is the trans-conductance defined by the drain–source current (I_{DS}) and the gate–source voltage (V_{GS}), $l = 800\text{nm}$ is the channel length, $w = 80\text{nm}$ is the channel width, $C = 1.15 \times 10^{-8}\text{F cm}^{-2}$ is capacitance per unit area of the gate dielectric material and $V_{DS} = 20\text{mV}$ is the drain–

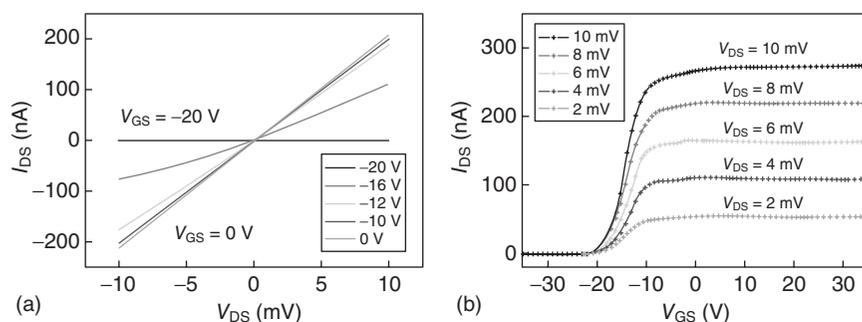


3.1 (a) Drain current (I_{DS}) vs drain voltage and (b) gate voltage (V_{GS}) characteristics of the transistor based on 2D $\text{MoO}_{(3-x)}/\text{MoO}_3$ heterostructure. (c) Photon energy vs $(\alpha h\nu)^2$ curves derived from the absorbance spectrum of a MoO_3 flake with progression of catalysed H^+ intercalation. Intersection is the linear fit with the x-axis indicating the bandgap energy used to depict the change in estimated optical bandgap with progression of the intercalation process (inset). The measurement for (c) was performed by intercalating thicker flakes in order to observe changes in the absorption spectra. (d) Transistor on/off function for various V_{GS} values for a constant V_{DS} of 1V and pulsed laser deposition.

source voltage. The carrier mobility was calculated from the I - V curves to be $>1100\text{cm}^2\text{V}^{-1}\text{s}^{-1}$. In this device, the surface charge density was also estimated to be $1.73 \times 10^{-8}\text{Ccm}^{-2}$.¹⁰ It is important to note that the FETs could not be completely switched off. The intercalation process caused the top layer to become nearly metallic, effectively reducing the on/off ratio to $<10^3$ (Fig. 3.1b). This near-metallic layer proved to be very effective for the injection of excess electrons, similar to high electron mobility transistor structures. The gate modulation seems significant under a small range of gate bias (from -2 to 2V),³⁰ considering that a very thick gate dielectric layer (300nm of SiO_2) was used in experiments.

Temperature-dependent mobility studies were conducted in the range of 20 – 100°C and compared to the theoretical calculations. The experimental values follow the theoretical trend.¹⁰ Figure 3.1c shows that the bandgap can be successfully reduced from 3.25 to 2.65eV after exposure to H_2 gas and even to values less than 2eV afterwards. Collectively, these results confirm the presence of sub-stoichiometric $\text{MoO}_{(3-x)}$ and the ability to reduce bandgap as a function of x .¹⁰ In this work, the aforementioned process is adopted to reduce stoichiometry in thin layers of MoO_3 , in order to produce a 2D layer with reduced bandgap and large electron concentration, hence making it suitable for FET applications. The transistor on/off function for various gate voltage V_{GS} values for a constant drain voltage V_{DS} of 1V has also been demonstrated on the developed $\text{MoO}_{(3-x)}$ with reduced bandgap (see Fig. 3.1d).

Single ZnO NWs and nanobelts (NBs) have been very intensively studied and fabricated into FETs for electrical transport measurements, and similar plots of drain–source I_{DS} - V_{DS} characteristics have been obtained (Fig. 3.2a). In this FET structure, the ZnO contacted by Ti/Au electrodes has exhibited



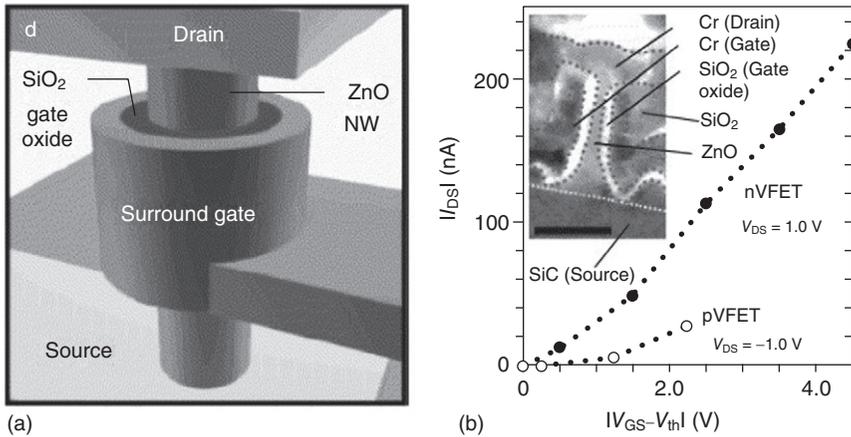
3.2 (A) Current vs bias voltage (I - V) shows n -type behaviour of a FET based on ZnO NW. Increasing gate voltage (V_{GS}) contributes to higher conductivity of NW. (b) Typical FET current vs gate voltage (I - V_{GS}) data shows high-performance device behaviour. (Reprinted from Ref. 4 with permission from Elsevier Science)

high conductance, excellent gate dependence and high on/off ratio.³¹ It is noteworthy that the CVD-grown ZnO nanostructures are single crystalline, endowing them with superior electrical properties compared to polycrystalline thin film. For example, an electron field-effect mobility of $7\text{ cm}^2/\text{Vs}$ is regarded as high for ZnO thin-film transistors.⁴ However, in an alternative report, an electron mobility of $1000\text{ cm}^2/\text{Vs}$ was obtained after coating the NWs with a polyimide (PI) passivation layer to reduce the electron scattering and trapping at the surface.³² It has also been demonstrated that, after coating the ZnO NW with a layer of SiO_2 followed by Si_3N_4 to passivate the surface states, the field-effect mobility is dramatically improved and exceeds $4000\text{ cm}^2/\text{Vs}$ (as illustrated in Fig. 3.2^{4,33}). These results have confirmed that devices based on 1D ZnO structures have exceptional potential for high-speed electronics applications.³³

3.2.2 Vertical electronic device

A number of different approaches have been used to build vertical FETs, which can utilize the increased integration density of nanoscaled devices and fully exploit the nanoscaling advantages. One of the first reports highlighting the benefits of vertical surround-gate NW FETs was published in 2004.³⁴ In this work, the positions of NWs were controlled via a lithographic patterning technique. Vertically aligned ZnO NWs were observed to grow from lithographically patterned Au spots. These vertical NWs were then surrounded with SiO_2 and Cr which function as the gate oxide and electrode, respectively, as depicted in Fig. 3.3a.⁴ The drain–source current versus absolute deviation of the gate voltage (V_{GS}) from the threshold voltage (V_{th}) for both *n*-channel and *p*-channel vertical surrounding gate (VSG)-FETs are presented in Fig. 3.3b. It has been shown that the *n*-channel VSG-FET exhibited a linear dependence, while the *p*-channel showed strong non-linearity. This is because in the *n*-channel the variation of gate-induced charge involves essentially electrons that are mobile in the channel; in contrast, in the *p*-channel, the gate-induced charge involves both holes and ionized impurities in the depletion region, and the hole concentration governs conduction and increases with the gate deviation.⁴

Another report published by the same research group has also demonstrated variations of the vertical FET based on aligned In_2O_3 NWs.³⁵ In this design, conductive SiC substrate was employed and direct electrical contact was generated by a self-assembled underlying In_2O_3 buffer layer. This buffer layer was fabricated during the synthesis process right on the top of the non-conductive sapphire substrate. This depletion mode *n*-type In_2O_3 NW vertical FET architecture used a top-gate configuration which placed the gate dielectric capping on the Pt electrode. These first successful reports on the fabrication of vertical nanodevices confirmed that it is possible to



3.3 (a) 3D schematic illustration of the critical components of a V_{SG} -FET. (b) I - V characteristics for two n - and p -channel VSG-FETs. The inset shows a cross-sectional image of a VSG-FET with a channel length about 200 nm. Scale bar: 200 nm. (Reprinted from Ref. 4 with permission from Elsevier Science)

combine the integration of electronic and optoelectronic devices into one package with high packing density, design flexibility and function modularity.

3.2.3 Field emission tip

By definition, field emission is an electron escape process from the surface of a material in the presence of a sufficiently large electric field.³⁶ The emitting material/electrode is called a cathode, and it is usually of low electron affinity. Since the discovery of the excellent field-emission (FE) properties of carbon nanotubes (CNTs) in the 1990s, there has been constantly growing interest in studying the field emission of Q1D structures for potential FE applications owing to their high aspect ratio. Moreover, during the last few years, semiconductor 1D materials have started to attract considerable interest for their unique FE properties. Theoretical modelling has elucidated their advantages³⁶ such as well-controlled electronic properties and low electron affinity.

One of the first breakthroughs in the development of FE aspects using metal oxide NWs was reported in 2002, where an aligned ZnO NW field emitter demonstrated a turn-on voltage of $6.0\text{V}/\mu\text{m}$ at a current density of $0.1\mu\text{Acm}^{-2}$.³⁷ The emission current density from the ZnO NWs reached $1\mu\text{Acm}^{-2}$ at a bias field of $11.0\text{V}/\mu\text{m}$, which is sufficiently bright for flat panel display application. Since vertically aligned NWs present lower field threshold (turn-on) with better performance, a combination of aligned

metal oxide Q1D structures, including IrO_2 ,³⁸ RuO_2 ,³⁹ SnO_2 ,⁴⁰ In_2O_3 ,⁴¹ WO_3 ,⁴² TiO_2 ,⁴³ CuO ,⁴⁴ etc., have been investigated for their FE properties.

Generally, the patterning and alignment techniques used must be suitable for fabrication of NW FE devices.^{38,41} In fact, apart from the above-mentioned techniques, other methods, such as surface coating and doping, have also been proposed to enhance the performance and efficiency of their field-emission property. FE current density was reported to be increased and the threshold electric field reduced by coating a layer of low work function materials such as amorphous carbon and carbon nitride.⁴⁵ Sn ⁴⁶ and Ga ⁴⁷ doped ZnO have also demonstrated lower turn-on electric field. Consequently, since the surface defect states (stoichiometry), which trap charge carriers and form a high potential barrier, are a drawback of using metal oxide materials for field emission, a thermal annealing process was used to improve the crystal stoichiometry.^{39,48}

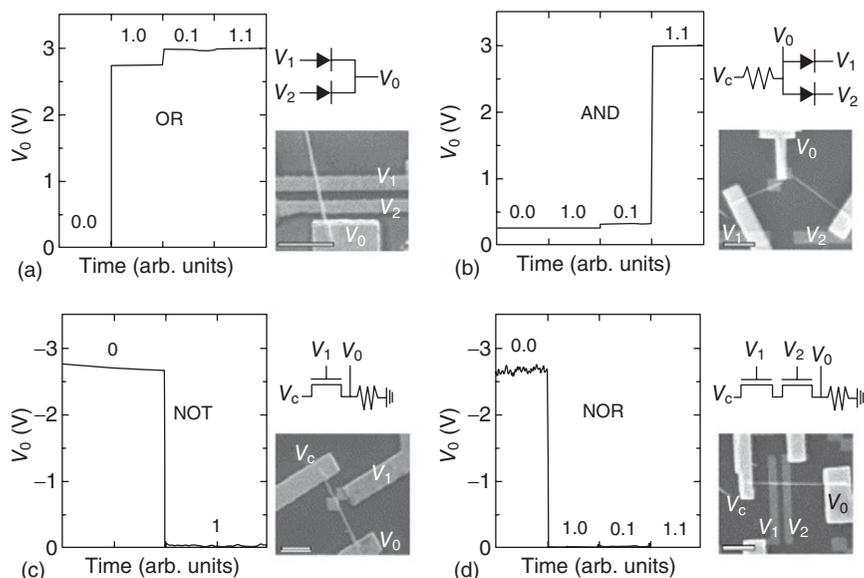
3.2.4 Logic gate

Diodes and FETs with electrically controlled ‘on’ and ‘off’ switching function are the fundamental elements to construct and develop higher level circuits, for instance logic gates, which are the key components in modern integrated computation circuits. Apart from the confirmed transistor function of the 2D MoO_3 semiconductor (see Fig. 3.1d), a similar transistor function of the 1D metal oxide system has been discovered in electrical transport studies.⁴⁹ In this report, logic units such as ‘OR’, ‘AND’, ‘NOT’ and ‘NOR’ have been designed and fabricated using *n*-type ZnO nanorods. These gates are built upon a combination of metal–semiconductor Schottky junction diodes or FETs, as shown in Fig. 3.4.

3.3 Optoelectronics based on nanostructured semiconductors

3.3.1 Emitter, laser and waveguide

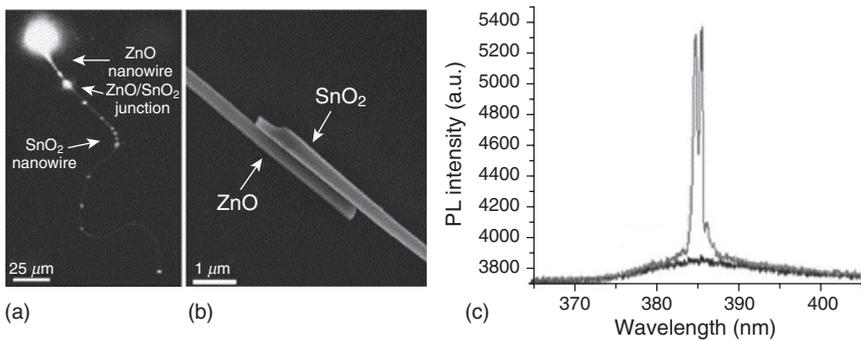
Although many of the 1D and 2D metal oxide semiconductors are attractive to various electronic and optoelectronic devices (lasers,⁵⁰ electro-optical modulators,⁵¹ photodetectors⁵² and waveguides⁵³) owing to their versatile properties, up to now their successful implementation in such practical applications has been rather limited. This is partly due to the limitations of existing technologies and to the challenges of coupling a suitable probe light into a NW waveguide. However, NWs that possess a direct bandgap such as ZnO , GaN , CdSe and CdS , in particular, are attractive because of their tunable electric field confinement and strong coupling between electron–hole pairs (excitons) and the light field.^{54,55} Specifically,



3.4 ZnO nanorod logic devices. (a) Schematic, SEM image and device characteristic of an OR logic gate fabricated using two Schottky diodes based on a single nanorod. Output voltage (V_o) vs the logic input configurations (V_1, V_2): (0, 0), (1, 0), (0, 1) and (1, 1). Logic input 0 is 0V and logic input 1 is 3V. (b) AND logic device fabricated using two Schottky diodes based on two ZnO nanorods. For this measurement, V_c is biased at 3V. (c) a NOT logic gate constructed using a FET based on a single nanorod. The output voltage (V_o) vs the logic inputs (V_i) of 0 and 1, where logic inputs 0 and 1 are 0V and -3 V, respectively. V_c is biased at -3 V. (d) a NOR gate using two FETs fabricated on a ZnO nanorod. Voltage bias is the same as for the NOT gate. Scale bars are $2\mu\text{m}$. (Reprinted from Ref. 4 with permission from Elsevier Science)

ZnO NW, owing to its large energy bandgap and exciton binding energy, is especially suitable for short-wavelength optoelectronic applications. The excitonic recombination provides an efficient radiative process and facilitates a low-threshold stimulated emission. Photoluminescence spectra studies have shown that ZnO NW is a promising material for ultraviolet emission and lasing.⁴ Another advantage of the ZnO NW is its near-cylindrical geometry and large refractive index (~ 2.0), making it a natural candidate for optical waveguides.⁵⁶

Figure 3.5a depicts how optically pumped light emission is guided by a ZnO NW and coupled into a SnO_2 nanoribbon (Fig. 3.5b).⁴ Figure 3.5c illustrates the stimulated emission (typical lasing peak) of a ZnO NW laser cavity.⁵⁷ In addition, the well-faceted NWs form ideal optical resonance cavities which facilitate highly directional lasing at a room temperature in



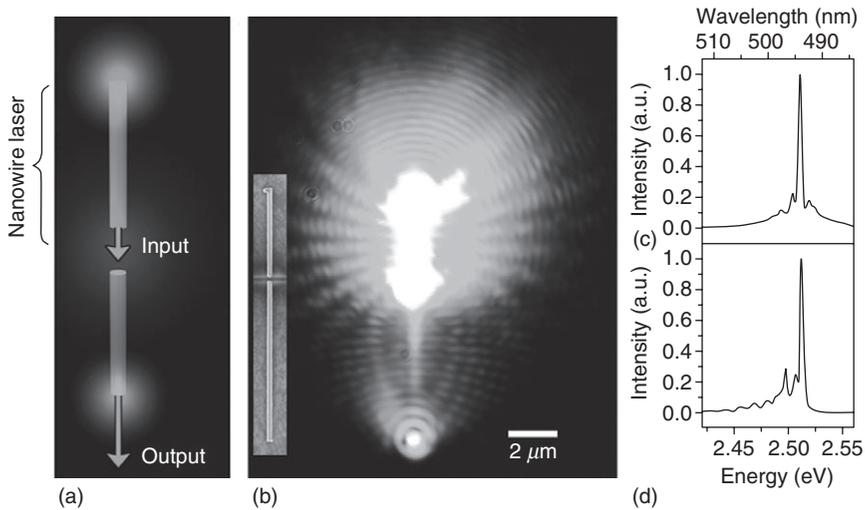
3.5 (a) An optical microscope image of a ZnO NW guiding light into a SnO₂ nanoribbon and (b) an SEM image displaying the NW–nanoribbon junction. (c) Stimulated emission of ZnO NW laser cavity was observed. (Reprinted from Ref. 4 with permission from Elsevier Science)

well-aligned ZnO NWs.⁵⁸ To reveal the dynamics underlying the lasing phenomenon, time-resolved second-harmonic generation (TRSHG) and transient photoluminescence spectroscopy were used to probe the creation and relaxation of excited carriers, and successfully described the radiative and non-radiative recombinations.⁵⁹ In this paper, a lasing power threshold of 40–100 kW cm⁻² was reported, and it was suggested that higher crystal quality renders lower threshold. The additional advantage of lasers based on ZnO NW is that the size confinement yields a substantial density of states at the band edge, thus enhancing optical gain.

Recently, CdS NW has been successfully used in all-optical active switching devices,⁵⁵ exploiting the strong light–matter coupling present in such NWs. The reported design fulfils the critical functions of two structurally isolated optical waveguides, and simultaneously provides efficient optical coupling between waveguides to inject the probe light generated by one segment into another via butt coupling, as presented in Fig. 3.6.⁵⁵ The on-chip all-optical switching using individual CdS NWs described has leveraged the concept into a working all-optical semiconductor NW NAND gate. The study underscored the potential of strong light–matter coupling in compound semiconductor nanostructures and emphasized the importance of further development of such all-optical active switching, as it can open new opportunities for comparable silicon-based dielectric contrast⁶⁰ and photonic crystal⁶¹ devices in the near future.

3.3.2 Light-emitting diode

Previous sections have briefly described how metal oxide NW arrays have demonstrated unique UV emission and even lasing behaviour under the

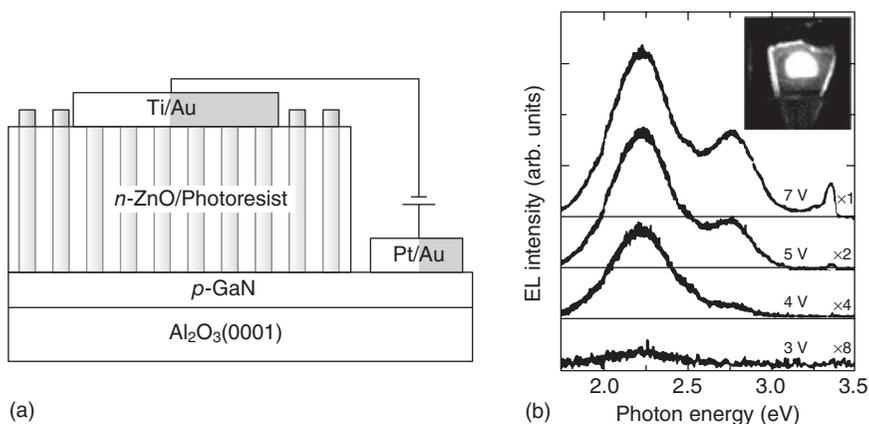


3.6 (a) Illustration of the switching device concept with a single CdS NW cut in two by a focused Ga ion beam, resulting in two nanowires of identical diameters aligned end to end, structurally isolated from one another and separated by a distance of 5–500 nm. A frequency-doubled Ti:sapphire laser at 458 nm is used to optically pump the upper portion to lasing conditions, and the resultant on-chip laser light emitted by the nanowire is then transmitted through the gap and waveguided to the bottom end facet. (b) True colour optical microscope image of a 10.9 μm long, 205 nm diameter CdS NW device at 77 K under the conditions explained in (a). Note the strong interference fringes emanating from both portions of the NW indicating successful transmission of laser light across the 160 nm wide ion-milled gap. Inset: SEM image of the NW-based device. Scale bar applies to both images. (c,d) Photoluminescence spectra collected using a position-sensitive photodetector positioned at the top (c) and bottom (d) end facets. Other than minor changes due to Fabry–Pérot resonances in the lower portion and attenuation of short wavelengths, the two spectra are similar and the laser peak at 2.510 eV remains intact. (Reprinted from Ref. 55 with permission from Nature Publishing)

excitation of an external laser source. However, from the practical device application point of view, electrically-driven light emitting and lasing are of more technical importance. To achieve this objective, both electrons and holes need to be injected into the metal oxide nanostructure to facilitate electron–hole pair recombination. This picture is quite alluring but, in the case of ZnO, the fabrication of *p–n* junctions is rather difficult.⁴ Although *p*-type ZnO doping still represents a challenge, progress has been achieved on thin-film ZnO *p–n* junctions by introducing nitrogen as the *p*-type dopant for light-emitting diodes (LEDs).^{62,63} Recently, it has been reported that intra-molecular *p–n* junctions were fabricated using ZnO NWs.⁶⁴

However, light emission has not been achieved. As an alternative solution, light emission from p - n hetero-junctions composed of n -ZnO and p -GaN has been proposed.⁶⁵ In this report, a vertically aligned ZnO nanorod array was epitaxially grown on a p -type GaN substrate as schematically illustrated in Fig. 3.7a. The electroluminescence (EL) was measured at room temperature, as presented in Fig. 3.7b. Similar results were reported for p - n hetero-junctions developed between ZnO NWs and p -type poly(3,4-ethylene-dioxythiophene) poly(styrenesulphonate) (PEDOTIPSS).⁶⁶ Their EL spectrum showed excitonic luminescence at around 380 nm.

Another approach to developing efficient LEDs is to combine the properties of graphene and ZnO quantum dots (QDs).⁶⁷ White emission was achieved by combining the QDs with other emissive materials in a multi-layer LED. In general, QDs represent a huge potential in nanoscale device applications such as next-generation electronic and optoelectronic devices (including LEDs and solar cells) owing to their unique properties, which arise due to the quantum confinement effect.⁶⁸ The potential use of hybrid nanocomposites to develop and fabricate functional optoelectronic devices with a simple solution process recently suggested the feasibility of transferring this technique to plastic substrates, an achievement that would offer many attractive advantages, including flexibility, light weight, shock resistance, softness and transparency.^{69,70} The implementation of this approach has resulted in carbon nanomaterial-based electronic and optoelectronic devices such as thin film transistors and LEDs.^{71,72}

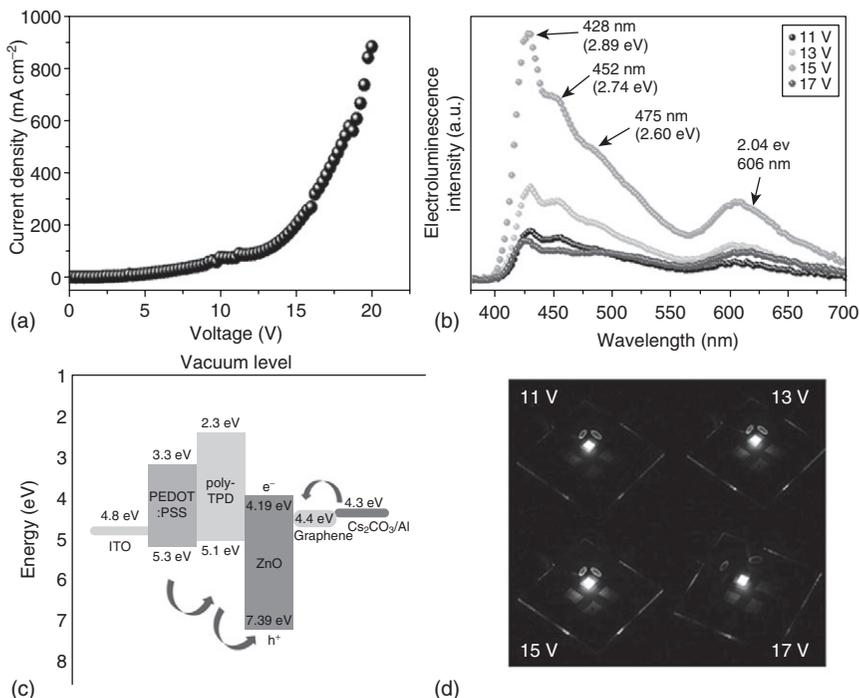


3.7 (a) Schematic diagram of the p -GaN/ n -ZnO nanorod hetero-junction device. (b) Room-temperature EL spectra of a p -GaN/ n -ZnO hetero-junction device at different reverse-bias. The inset is a photograph of light emission at a 5V reverse-bias. (Reprinted from Ref. 4 with permission from Elsevier Science)

A novelty in these types of approaches has also been reflected in a simple and facile technique for the synthesis of ZnO–graphene quasi-core–shell QDs.⁶⁷ Plate III (see colour section between pages 232 and 233) graphically summarizes the chemical synthesis process for the ZnO–graphene quasi-core–shell structure QDs. In this configuration, graphite oxide (GO) is first prepared by surface treatment of natural graphite powder with a mixed acid of H₂SO₄ and HNO₃ (Plate IIIa). Consequently, in a mixture of zinc acetate dihydrate and GO in dimethyl formamide (DMF), embryo ZnO QDs are preferentially formed, growing to ~10.6 nm in diameter.⁶⁷ At the outermost edges of the embryo ZnO QDs, it is probable that two chemical reactions then occur, as schematically encapsulated in Plate IIIb. In one reaction, Zn²⁺ ions chemisorbed on the embryo ZnO QDs (denoted Zn²⁺(ZnO)) react with functional groups on the GO,⁷³ leading to the local creation of Zn–O–C bonding. On the other hand, Zn²⁺ ions bonded on GO (denoted Zn²⁺(GO)) in another reaction to form Zn–O bonding and then combined with embryo ZnO QDs. Plate IIIc shows that the ZnO QDs are not entirely encircled by the graphene. Nevertheless, during this reaction, sections of graphene detach from the GO layers through a layer-by-layer chemical peel-off process (chemical exfoliation), then partially encircle the ZnO QDs to form quasi-core–shell nanoparticles with a diameter of ~15.8 nm, as shown in the high-resolution transmission electron microscopy (HRTEM) image presented in Plate III d.

In order to demonstrate the potential applications of these ZnO–graphene quasi-core–shell QDs to optoelectronic devices, a hybrid polymer–quantum dot LED device with a multilayer structure has been fabricated and evaluated.⁶⁷ Figure 3.8a displays the *J*–*V* characteristic curve of a ZnO–graphene quasi-core–shell QD LED with the applied voltage varying up to 17 V. With increasing applied voltage, the current density *J* remains approximately constant (increasing slightly) up to ~11–12 V, then increases drastically, corresponding to the turn-on voltage of the LED. In addition, Fig. 3.8b shows the electroluminescence at different applied voltages. Four distinctive emissions appear at ~428 nm (2.89 eV), 452 nm (2.74 eV), 475 nm (2.60 eV) and 606 nm (2.04 eV), the peak positions of which differ slightly from those of the photoluminescence. In the energy band diagrams for the ZnO–graphene QD LED (Fig. 3.8c), Cs₂CO₃ (with the lowest work function, 2.8 eV) is utilized as both an electron-injection layer (EIL) and a hole-blocking layer (HBL) rather than the widely used thermally evaporated LiF.⁷⁴ Electrons were injected from the Cs₂CO₃ to the LUMO and LUMO + 2 excited MOs of the G–O_{epoxy} conjugated with the ZnO QD rather than to the conduction band of the ZnO, because the 4.4 eV energy level of graphene⁷⁵ is lower than the 4.19 eV conduction band of ZnO.

In the creation of the LUMO and LUMO + 2 MOs of G–O_{epoxy}, the first two emissions – 428 nm (2.89 eV) and 452 nm (2.74 eV) – can be easily



3.8 (a) Current density–voltage (J – V) characteristics for the fabricated LED device. (b) Electroluminescence spectra of the fabricated ZnO–graphene quasi-QD LED device with applied voltages from 11 to 17 V. (c) Band diagram of the fabricated LED device. The HOMO and LUMO (highest and lowest unoccupied molecular orbital, respectively) levels of PEDOT:PSS, poly-TPD (poly(4-butylphenyl-diphenyl-amine), graphene and ZnO are taken from Ref. 67. The pathways of holes and electrons are indicated by arrows. (d) Photograph of light emission at 11, 13, 15 and 17 V applied bias. (Reprinted from Ref. 67 with permission from Nature Publishing)

ascribed to excitonic recombination of injected electrons on the unoccupied LUMO and LUMO + 2 MOs of G–O_{epoxy} and holes in the valence band of ZnO. Under forward bias, electrons injected from the Cs₂CO₃/Al electrode result in a net carrier doping, that is, an upward shift of the Fermi energy (E_F) of the graphene. This means that the valence band of ZnO has to be slightly lifted to align the Fermi level of ZnO with that of G–O_{epoxy}. Accordingly, the energy differences between the unoccupied LUMO and LUMO + 2 MOs of G–O_{epoxy} and the valence band of ZnO are reduced, so that the peak positions of the two emissions shift towards longer wavelengths (red-shift).⁶⁷ The applied voltage V changes the charge-carrier density n in graphene ($n = \alpha V$), and therefore shifts the Fermi level E_F , where $\Delta E_F = \hbar v_F (\pi n)^{1/2}$. Here, positive (negative) n corresponds to electron (hole) doping, v_F is the

Fermi velocity ($0.8 \times 10^6 \text{ ms}^{-1}$) and $\alpha \approx 7 \times 10^{10} \text{ cm}^{-2} \text{ V}^{-1}$ (estimated from a simple capacitor model).⁷⁶

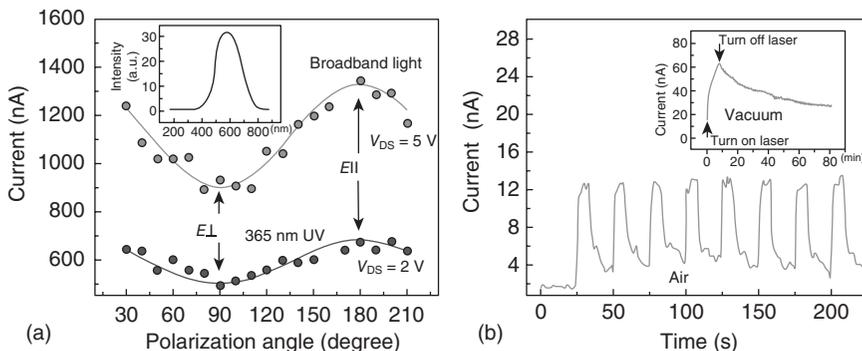
The shift in E_F to align with that of graphene affects the positions of the valence and conduction bands of ZnO. For an applied voltage of $V \approx 11\text{--}15 \text{ V}$, the calculated ΔE_F is as much as $\sim 82\text{--}95 \text{ meV}$ and the Fermi level of graphene is elevated to the same level. If ΔE_F is assumed to be 95 meV for $V = 15 \text{ V}$, the transition energies of electroluminescence are expected at 2.95 eV and 2.80 eV . Because these agree well with the observed 2.89 eV (428 nm) and 2.74 eV (452 nm) electroluminescence values, qualitatively we can attribute the change in the peak position of electroluminescence to the shift of E_F due to the injection of electrons. In this way, we have found a new way to tune the centre of the electroluminescence of a metal oxide semiconductor by conjugation with graphene, the Fermi level of which is located between the conduction and valence bands of the metal oxide QDs.

Figure 3.8d shows a photograph of the light emission from the fabricated LED for applied biases of 11, 13, 15 and 17 V. The ZnO–graphene QD layer LED pixels appear uniformly luminescent and appear bluish-white to the naked eye due to the combination of a series of blue emissions ($428, 452$ and 475 nm) and yellow emission (606 nm), with CIE coordinates $(0.23, 0.20)$, $(0.28, 0.24)$ and $(0.31, 0.26)$ for 13, 15 and 17 V applied biases, respectively. At 15 V applied bias and with optimal CIE coordinates $(0.23, 0.20)$, the maximum brightness reaches $\sim 798.1 \text{ cd m}^{-2}$. The external quantum efficiencies of the fabricated LEDs were measured to be 0.18, 0.04 and 0.02 % for 13, 15 and 17 V applied biases, respectively.⁶⁷

Consequently, all the above-mentioned studies confirmed that the wavelength of excitonic emission of metal oxide semiconductor QDs can be modulated by conjugation with graphene in the form of a consolidated layered structure (Plate IV, see colour section between pages 232 and 233). Graphene is the obvious material choice for this application, offering high intrinsic electrical conductivity, an accessible and defined pore structure, good resistance to oxidative processes and high temperature stability.¹¹

3.3.3 Polarization-dependent photodetector

Another type of functional optoelectronic device based on nanostructured semiconductors is polarization-dependent photodetectors. ZnO NWs^{77,78} and SnO₂ NWs⁷⁹ have been intensively investigated for their UV emission, lasing and photodetection properties. Polarized photodetection in In₂O₃ NWs has also been observed.⁸⁰ Photoconductance is found to be proportional to $\cos^2 \theta$, where θ is the angle between the polarization of incident light and the long axis of the NW. It is at a maximum when the electric field component of the incident light is polarized parallel to the NW long axis as graphically presented in Fig. 3.9a.⁴ Since a NW's diameter is much smaller



3.9 (a) Polarized photodetection of both UV (365 nm) and visible light (spectrum shown in the inset) show that NW conductance is maximized when the electric field component of the incident light is polarized parallel to the NW axis. (b) NW photoresponse to 633 nm laser in air compared to that in vacuum (inset). (Reprinted from Ref. 4 with permission from Elsevier Science)

than the light wavelength, the electric field component of light normal to the NW axis is effectively attenuated inside the NW. This interesting property can lead to promising applications for Q1D polarization-dependent photodetectors and optically gated switches. In some of the recent reports dedicated to the investigation of photoconductivity measurements of ZnO NWs, it was found that the environment has a crucial effect on the photoresponse.^{77,81,82} For example, surface chemical adsorption on the NWs could significantly expedite the photocurrent relaxation time. Figure 3.9b presents the results of ZnO NW photoresponse to 633 nm laser in air, compared to vacuum (presented as an insert). As is clearly shown in this figure, the photocurrent relaxation time is approximately 8 s in air but represents hours in vacuum. This is because in air, photogenerated holes discharge surface chemisorbed ions upon illumination, while the photogenerated electrons significantly increase the conductivity. When the illumination is switched off, oxidizing gas (mainly O₂) molecules in the air re-adsorb onto the surface and reduce the conductivity. This sensitivity to surface chemisorption is vital for chemical sensor applications, which will be discussed in detail below.

The existence of a wide bandgap in metal oxides has been extensively exploited for blue-UV range optoelectronic applications. However, some metal oxides also exhibit infrared (IR) photodetection due to indirect bandgaps. For example, CdO has a small indirect bandgap of 0.55 eV. Recently, photoconductivity measurements of a CdO-based FET with IR light illumination have been presented.⁷⁹ The IR detection on/off ratio is about 8.6 at 1.2 K and the relaxation time constant is estimated to be 8.6 s.

3.3.4 Flexible molecular-scale electronic devices

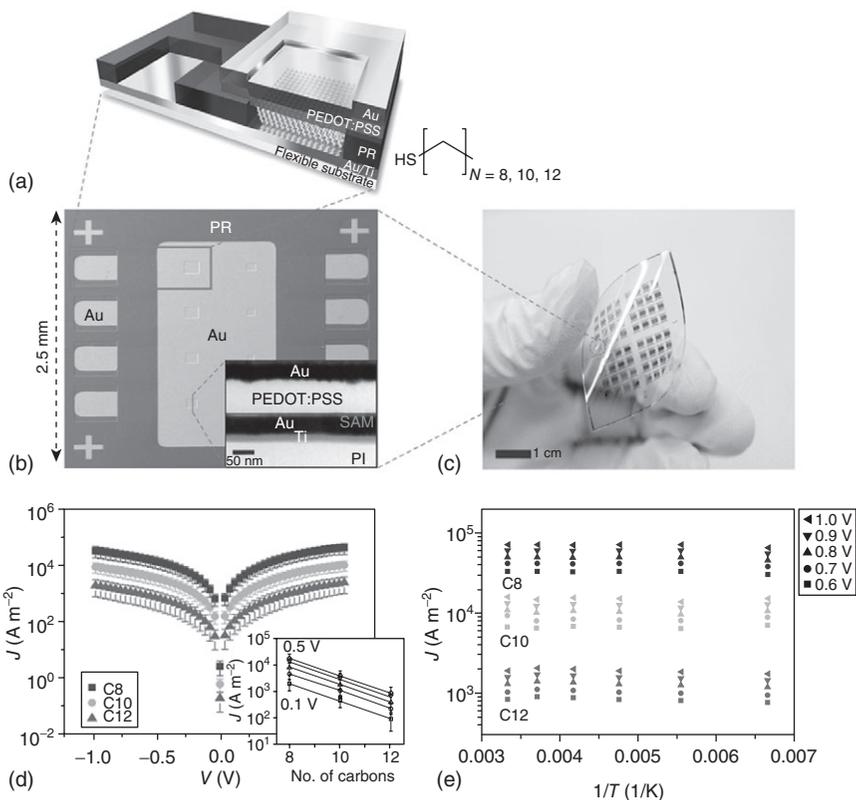
Large-area devices containing extremely thin films of molecular materials represent the ultimate scaling of flexible devices based on organic materials.^{83,84} However, for long-term stability, the influence of bending and twisting on the electrical and mechanical stability of such devices has to be preserved. The latest advances in nanotechnology and nanostructured semiconductor materials have allowed the employment of these materials and devices in flexible electronic circuits,^{85,86} memory devices,⁸⁷ various sensors,^{88,89} displays⁹⁰ and bio-electronic devices.⁹¹ In this regard, nanoscaled elements such as thin films,^{92,93} NWs,⁹⁴ NTs⁹⁵ and nanoparticles⁸⁷ can also be incorporated into the active films of mechanically flexible devices. In all the above-mentioned flexible devices and instruments, bending stability is a critical factor affecting the suitability of molecular devices for applications in flexible electronic systems. One excellent recent report has highlighted improvements in such bending stability and detailed fabrication and characterization of two-terminal electronic devices based on self-assembled monolayers of alkyl or aromatic thiol molecules on flexible substrates.⁹⁶

In order to investigate how the performance of flexible molecular-scale electronic devices changes in response to mechanical deformation, a two-terminal configuration, schematically presented in Fig. 3.10a, was chosen.⁹⁶ PI was used as the flexible substrate for two reasons:

1. Compared with other flexible substrates, it has a relatively high thermal stability (up to 520 K), which prevents substrate deformation during the thermal treatment used to make the isolating layer (photoresist) insoluble in ethanol for the self-assembly process performed on the bottom gold electrode.⁸³
2. The low surface roughness of PI reduces the defect density of the self-assembled monolayer (SAM) molecules in the junction. Indeed, atomic force microscopy revealed that the root-mean-square roughness of a $2.5\ \mu\text{m} \times 2.5\ \mu\text{m}$ region of the surface was $\sim 1.9\ \text{\AA}$. In total 512 devices on $3\ \text{cm} \times 3\ \text{cm}$ units were fabricated (Fig. 3.10c).

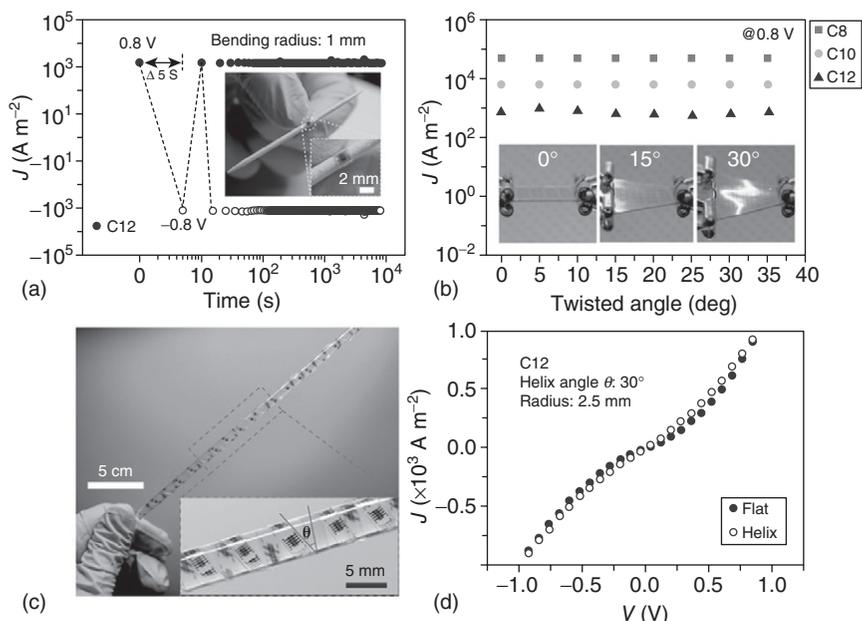
To ensure a practical device platform, the stability and design lifetime of the molecular junctions must be determined.⁸³ Two voltage step conditions with short time intervals ($\Delta t = 10\ \text{s}$) were also applied to test the retention of a C12 molecular junction.⁹⁷ The J values were measured at 0.8 V and $-0.8\ \text{V}$ for $1 \times 10^4\ \text{s}$ at $\Delta t = 10\ \text{s}$, and were retained without significant degradation. The reported results demonstrate that the developed molecular device has exhibited an outstanding operational stability and durability.⁹⁶

Figure 3.11 represents excellent achieved retention characteristics under severe bending conditions. As displayed in Fig. 3.11a, the J values of the flexible molecular devices were maintained when bent over a toothpick



3.10 (a) Schematic of a flexible molecular device. The layers (from bottom to top) are a flexible substrate, a bottom Au/Ti electrode, a molecular layer or photoresist (PR) for electrical isolation, a PEDOT:PSS layer and a top Au electrode. (b) SEM image of a molecular device. The junctions are square-shaped and have sides with lengths ranging from 30 to 100 μm in increments of 10 μm . Inset: high-resolution cross-sectional TEM image of a molecular device. (c) Photograph of completed device. (d) Current density J (on a log scale) versus voltage V for C8, C10 and C12 molecular devices under flat conditions at 300 K. Inset: J (on a log scale) vs number of carbon atoms. Error bars denote standard deviation of individual measurements for several devices. (e) Arrhenius plot (J vs inverse temperature) for C8, C10 and C12 molecular devices at different temperatures (from 150 to 300 K) and five different voltages. (Reprinted from Ref. 96 with permission from Nature Publishing)

(bending radius ≈ 1 mm) for 1×10^4 s, indicating superb durability and operational stability under extreme bending conditions. These results also suggested that there were no significant changes in the structure and phase of SAM molecules in the molecular junctions when the device was bent severely. The measured the J - V characteristics of the flexible molecular



3.11 (a) Current density J vs time (both on log scales) for a C12 device being bent around a toothpick (bending radius, $r \approx 1$ mm, shown in inset). The voltage was stepped between +0.8 V and -0.8 V and J was measured every 5 s for 10 000 s. (b) Values of J measured at 0.8 V for C8, C10 and C12 devices as a function of twist angle. Insets: photographs taken at three different angles. (c) Photograph of flexible devices rolled over a tube (radius, 2.5 mm; $\theta = 30^\circ$) under helical structural conditions. (d) Plot of J (on a linear scale) vs V for a C12 device under flat (solid circles) and helical (open circles) conditions. (Reprinted from Ref. 96 with permission from Nature Publishing)

devices under various bending configurations are depicted in Fig. 3.11b,⁹⁶ which represents the J - V characteristics and operational stability of C8, C10 and C12 flexible molecular devices under twist conditions. Noticeable degradation was not observed as the twist angle was varied from 0 to 35° (in steps of 5°). Figure 3.11c shows a photographic image of the investigated flexible molecular device (a strip with dimensions of $0.25 \text{ cm} \times 40 \text{ cm}$ containing 1024 molecular junctions) rolled over a tube (radius, 2.5 mm) in a helical configuration ($\theta = 30^\circ$). The J - V characteristics of a C12 device under helical and flat conditions are shown in Fig. 3.11d. Pronounced changes in these characteristics were not observed under helical structural conditions.

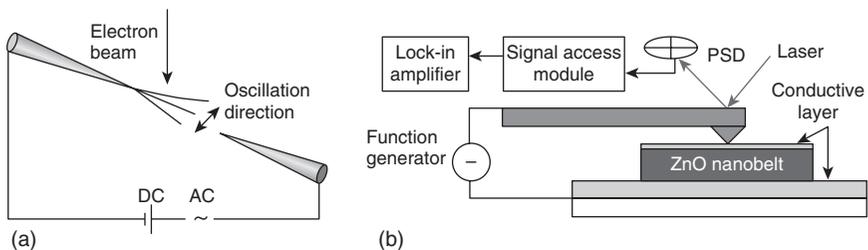
All the reported results have demonstrated that ultrathin molecular-monolayer-based devices can operate reliably when bent, twisted or

deformed into helical structures, and that their performance can be explained by molecular modelling. These observations and data also suggested that it should be possible to make large-area flexible devices in which the active layer is a single layer of molecules.

3.4 Resonators and cantilevers based on nanostructured semiconductors

3.4.1 Nanoresonator

Typical characterizations of NW mechanical properties such as Young's modulus and resonant frequency are not easily performed due to the sophisticated instrumentation necessary for such testing. Although theoretical modelling can assist and support in this exercise,⁹⁸ it is not always easy to have all constants for precise and accurate modelling. There have been several pioneering works dedicated to the characterization of nanoscale mechanical properties, the measurement of the bending modulus and the piezoelectric properties of various nanostructures,^{99–103} including employment of *in-situ* TEM.¹⁰⁰ In this work, electric-field-induced excitation was applied to drive the harmonic resonances of a Q1D structure. ZnO NB,¹⁰⁰ SiO₂/SiC composite⁹⁹ and CNT¹⁰⁴ have been tested for potential nanoresonator applications. Another recent report has presented SEM and electric field excitation techniques to characterize the Young's modulus of β -Ga₂O₃ NW⁴ and amorphous SiO₂ NW.¹⁰⁵ A schematic experimental set-up for these measurements is presented in Fig. 3.12a. In addition, the thermally driven mechanical deflection of ZrOx/SiOx and TiOx/ZnOx hybrid NWs to electrically-driven resonance was also reported.¹⁰⁶



3.12 (a) Schematic of experimental set-up showing a resonating Ga₂O₃ NW under applied DC bias and AC driving signal. (b) Piezo-response force microscope analysis is performed in contact mode with the addition of a function generator, a lock-in amplifier and a signal access module. (Reprinted from Ref. 4 with permission from Elsevier Science)

3.4.2 Piezoelectric properties

Due to the great efforts of researchers in the years since 2000 working on the development of advanced methods utilizing contact mode atomic force microscopy (AFM), it has been possible to measure the piezoelectric properties of ZnO NBs¹⁰¹ and the elastic characteristics of vertically standing ZnO NWs.¹⁰² The elastic moduli of individual NWs were derived by simultaneously recording the topography and lateral force image while the AFM tip was scanning across the NW.¹⁰² This principle originates from the dependence of the change of lateral force on NW bending. Moreover, a piezoresponse force microscope (PFM) technique evolved from AFM, graphically displayed in Fig. 3.12b, was used to investigate the ferroelectric and piezoelectric properties of Q1D metal oxide nanostructures including ZnO NBs,¹⁰¹ KNbO₃ (KN) NRs¹⁰⁷ and Pb(Zr_{0.53}Ti_{0.47})O₃ (PZT)¹⁰⁸ NWs. The PFM technique is based on detecting local mechanical deformation induced by an AC signal applied across the conductive AFM tip and the bottom electrode of the sample. In the recorded data, the amplitude of the piezoelectric response indicates the extent of the local piezoelectric phenomenon, and the phase related to the applied AC signal reveals the polarization direction of different ferroelectric domains.

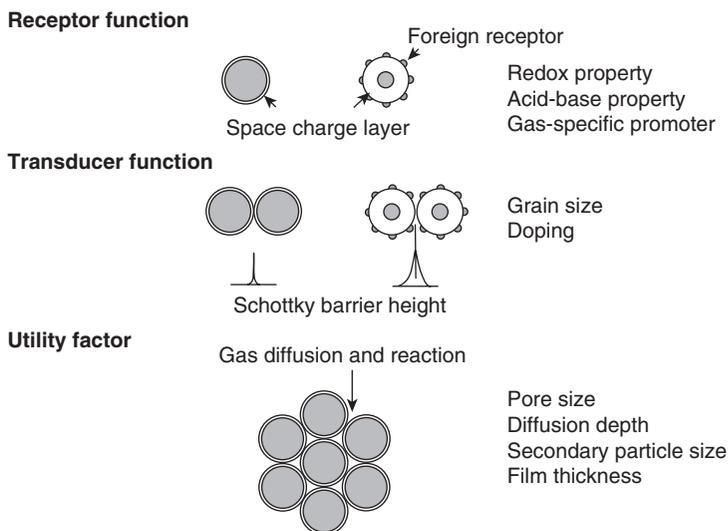
3.4.3 Chemical sensors

Sensing behaviour has been one of the most important and well-known properties of nanostructured metal oxide semiconductors. In addition to their sensitivity to light and pressure, which was mentioned in previous sections, metal oxide nanoparticles have shown high sensitivity to the surrounding environment. This is a very big class of sensors – *semiconductor chemical sensors* – capable of measuring various parameters in gaseous and aqueous environments.¹⁰⁹ Recently, electronic noses (*e-noses*) and electronic tongues (*e-tongues*) have emerged in the sensors community.¹¹⁰ These are similar in a sense to the human olfactory senses.

However, modern applications of semiconductor chemical sensors still face problems of high cross-sensitivity to gases, i.e. low selectivity, high sensitivity to humidity in the measuring environment and long-term stability problems, resulting in gradual drift of the sensing characteristics related to oxygen bulk diffusion and transformation of the crystal nanostructures, especially if the measurements are taken at high temperatures.¹¹¹ Moreover, the basic science of the semiconductor chemical sensors still remains far from being satisfactorily elucidated. It is evident that interfaces between the chemically sensitive nanostructures and the transducers used to convert the chemical and biological information into electronic signals play the key role in optimizing such devices towards long-term stability and reliability.

With the capability of being doped by a foreign receptor to improve and increase sensitivity and selectivity,^{112–114} and operated in harsh environments, semiconductor chemical sensors surpass other chemical sensors in their sensitivity, reliability and durability. The advantages of using 1D and 2D metal oxide nanostructures for chemical sensing are manifold. With a large surface-to-volume ratio and a Debye length comparable to the NW radius, the electronic properties of NWs are strongly influenced by surface processes, yielding superior sensitivity compared to their thin-film counterparts. In order to achieve maximum sensitivity, thin-film gas sensors are often operated at elevated temperatures.^{115,116} This indicates that a single sensing device needs to incorporate a temperature control unit, which will increase the complexity of the sensor design and the power consumption. Fortunately, metal oxide NW-based gas sensors have demonstrated significantly higher sensitivity at room temperature. Surface catalytic properties, including oxygen adsorptive, redox or acid-base properties, are design factors in relation to the receptor function, while nanograin size as well as levels and densities of intrinsic and extrinsic donors in the lattice are the factors relevant to the transducer function. Typical key factors and related design functions in semiconductor gas sensors are schematically shown in Fig. 3.13.¹¹³

Apart from the factors mentioned above, other aspects must also be considered during design of semiconductor sensors based on nanostruc-



3.13 Key factors and related design factors in semiconductor gas sensors. (Reprinted from Ref. 113 with permission from Elsevier Science)

tured metal oxides. For example, flammable gases diffuse in the porous sensing body (and assembly of nanograins) while reacting with the adsorbed oxygen in such a way that the gas concentration decreases as the gas penetrates inside, because the nanocrystal bilayer can act as a tandem catalyst.¹¹⁷ The utility factor takes into account the attenuation of the gas response due to this diffusion–reaction effect. The sizes and distribution of pores and the length of the gas diffusion path (the thickness or radius of secondary particles of nanograins) are design considerations in this respect. None of the factors presented in Fig. 3.13 is free from assumptions which have not so far been verified, one such being that the double Schottky barrier dominates the transducer function.

The sensing mechanism of semiconductor metal oxides is mainly governed by the fact that the oxygen vacancies on the oxide surfaces are electrically and chemically active. In this case, two types of the following sensing responses have been observed and reported:

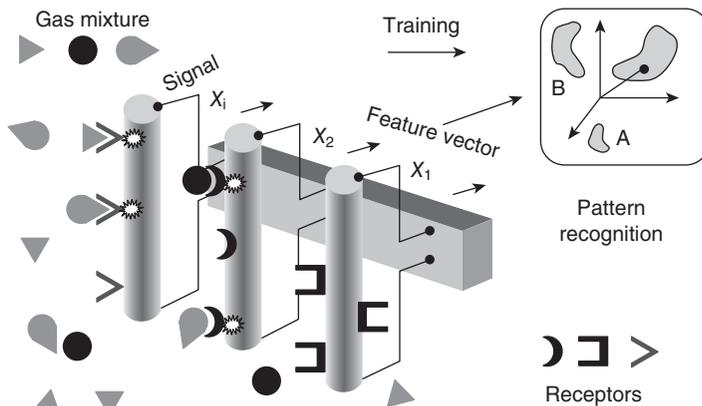
1. Upon adsorption of charge accepting molecules, such as NO_2 and O_2 , at the vacancy sites, electrons are withdrawn and effectively depleted from the conduction band, leading to a reduction in conductivity.
2. On the other hand, in an oxygen-rich environment, gas molecules, for example CO and H_2 , could react with the surface adsorbed oxygen and consequently release the captured electrons back to the channel, resulting in an increase in conductance.

In conclusion, if one categorizes such redox sensing responses into reducing and oxidizing, which manifests as an increase or a decrease in the channel conductance, the sensing responses can be represented using two examples:

1. reducing response:¹¹⁸ $\text{CO} + \text{O} \rightarrow \text{CO}_2 + \text{e}^-$
2. oxidizing response:¹¹⁹ $\text{NO} + \text{e}^- \rightarrow \text{NO}^-$

In the context of studying metal oxide NW field-effect sensors, it has been discovered that the transverse electrical field induced by the back gate can be utilized to distinguish between different chemical gases.¹²⁰ Considering that the ultimate goal is to develop e-nose systems that mimic the mammalian olfactory system, this can be achieved by assembling multicomponent sensing modules integrated with signal processing and pattern recognition functions. This concept is graphically illustrated in Fig. 3.14.⁴

So far, practical implementation of the above concept has resulted in nanostructured semiconductor metal oxide sensors accurately measuring gas species such as CO , CO_2 , CH_4 , $\text{C}_2\text{H}_5\text{OH}$, C_3H_8 , H_2 , H_2S , NH_3 , NO , NO_2 , O_2 , O_3 , SO_2 , acetone, humidity, etc.^{121,122} In the past few years, there has been a surge of research focusing on chemical sensing based on metal oxide NWs,



3.14 A proposed NW-based E-nose system. The NW surfaces may be functionalized with molecule-selective receptors. The operation is based on molecular selective bonding, signal transduction and chemical detection through complex pattern recognition. (Reprinted from Ref. 4 with permission from Elsevier Science)

such as ZnO, SnO₂, In₂O₃, WO₃ and V₂O₅ and others towards environmentally hazardous gases.¹²³

In summary, it can be stated with confidence that recent progress in the methods used to synthesize 1D and 2D structures enables their potential employment in various applications where they have not been previously used. These newly-developed fabricating technologies have produced advanced functional semiconductors in an assortment of NWs, NBs and other nanoforms. Further improvements in the fabrication of functionalized forms of 1D and 2D materials can provide an arena for fundamental studies as well as technological developments. For example, enormous effort has been dedicated so far to device applications utilizing crystalline 1D nanostructure in nanolasers, FETs, cantilevers and chemical sensors. As a whole, the research based on individual metal oxide nanostructures has been successful, and the alignment of these nanostructures towards device integration has also achieved considerable progress. Therefore, further studies will pave the way for the practical applications of the 1D and 2D metal oxides in integrated nano-electronics and sensing devices.

3.5 Functional structures: carbon nanotubes

Three recently-developed carbon-based materials, which can be called ‘nanocarbon’, have lately attracted a lot of interest from the scientific and industrial communities: graphene, CNT and fullerenes. Like graphite, they are composed entirely of sp^2 orbitals; however, fullerenes contain 12

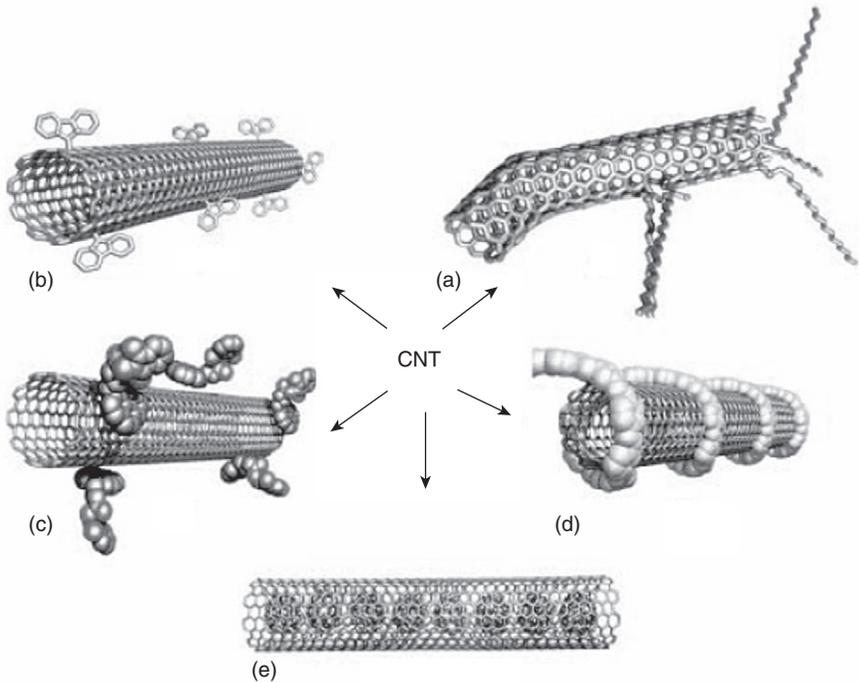
pentagons and have some sp^3 characteristics. The physical and chemical properties of graphene as well as potential graphene-based applications will be discussed in detail in Chapters 4 and 5, respectively. Rolling up graphene into the smallest possible tube makes a single-walled CNT. CNTs were initially discovered in Japan in 1991¹²⁴ and, since then, owing to their remarkable electrical, mechanical, chemical and structural properties, they have been employed as a building-block nanomaterial for various applications.¹²⁵ Apart from these single-wall CNTs, multi-walled CNTs can be composed of several graphene nanosheets with diameters ranging from 5–50 nm.¹²⁶ There are several methods of fabricating CNTs, including laser evaporation, chemical vapour deposition, etc., allowing CNTs to be available in commercial quantities at relatively low cost. Based on their geometry, CNTs can display metallic, semiconducting and superconducting electron transport properties, which were comprehensively described in a recent review.¹²⁷ Due to development of defects on the surface and at the ends of their structure, including pentagons, carboxylic and hydroxyl groups, CNTs can be tailored for various functionalities, and consequently can be employed for a number of different applications. Some functionalization schemes of CNTs are schematically presented in Fig. 3.15.¹²⁵

There are plenty of different publications dedicated to direct and indirect usage, modification and improvement of physical and chemical properties of CNTs and/or composite nanomaterials based on CNTs. The role of CNTs in electro-analytical chemistry and their potential applications can be summarized as follows:¹²⁸

- Enzyme bio-sensors:
 - CNT–polymer composite-based bio-sensors;
 - CNT–metal nanoparticle-based bio-sensors;
 - bio-sensors involving other CNT composites.
- Geno-sensors and immuno-sensors.
- Electrochemical sensors based on CNTs:
 - CNT-modified electrodes as redox mediators;
 - CNT-modified electrodes.
- Hybrid materials:
 - CNT–conducting polymer composites;
 - CNT–nanoparticle composites;
 - other nano-composites involving CNTs.

Although plasma-enhanced chemical vapour deposition has been proven to be one of the most successful fabrication techniques for CNTs, problems with the current CNT preparation methods remain as follows:

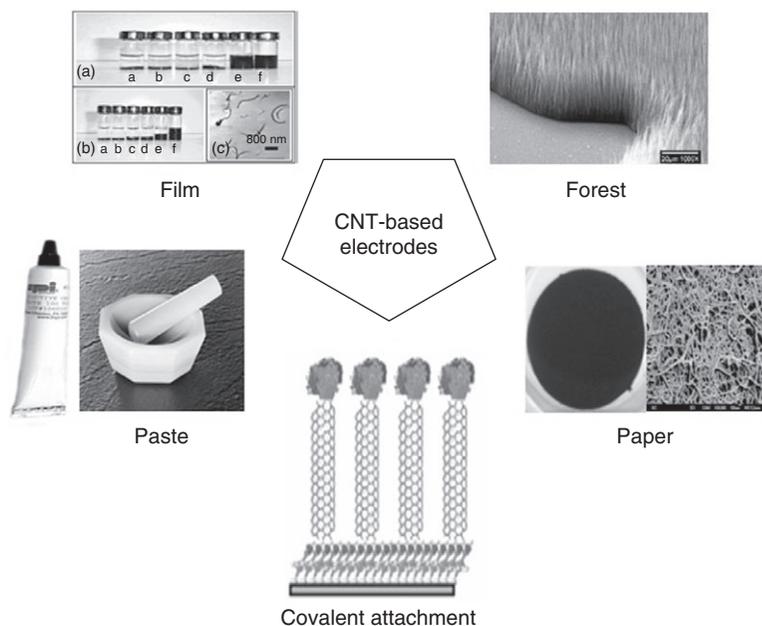
- lengthy preparation;
- mostly dealing with short CNTs;



3.15 Possible functionalization schemes for CNTs: (a) defect-group functionalization; (b) covalent sidewall functionalization; (c) non-covalent exohedral functionalization with surfactants; (d) non-covalent exohedral functionalization with polymers; and (e) endohedral functionalization with, for example, C60. (Reprinted from Ref. 125 with permission from the Taylor & Francis Group)

- loss of original CNT structure;
- chemical, physical and mechanical properties are altered;
- mechanical stability;
- reproducibility;
- purity.

Figure 3.16 graphically represents various existing types of CNT-based electrodes: film,¹²⁹ paste,¹³⁰ covalent attachment,¹³¹ paper¹³² and forest.¹³³ Among these CNT-based electrodes, CNT webs are a novel form of CNT produced by drawing nanotubes away from the front face of specially grown ‘forests’ of aligned CNTs.¹³⁴ CNTs are drawn as a continuous pure CNT ‘web’ of around 20 μm thickness with high porosity (optical transmission ~ 80 %). It has been reported that those webs can adhere to a solid surface and can be densified to about 50 nm thickness by wetting in a solvent and drying.¹³⁴ CNT webs mainly comprise highly pure and well-aligned CNTs,

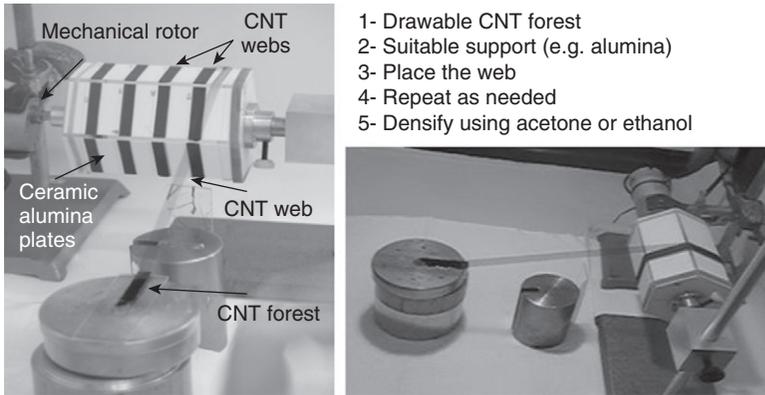


3.16 Representation of the existing types of CNT-based electrodes: film, paste, covalent attachment, paper and forest.

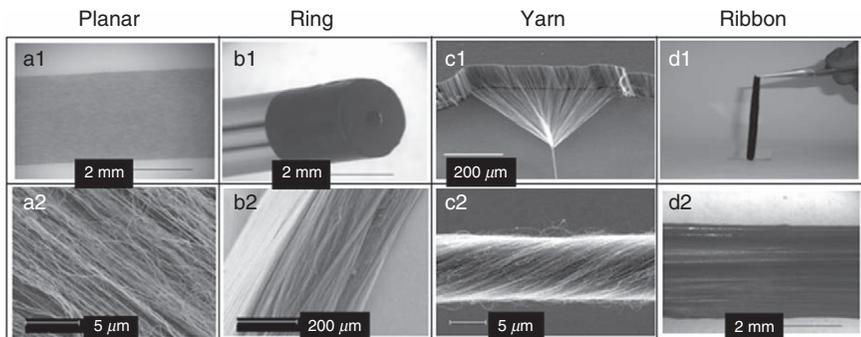
with some occasional cross fibres (mean diameter ≈ 10 nm), and they are electrically conductive.¹³⁵

One of the most promising techniques for fabricating CNTs has recently been developed at CSIRO.¹³⁶ It represents CNT web formation from a CNT forest, as schematically illustrated in Fig. 3.17. This fabricating method has been refined and expanded for making CNTs specifically for sensor and bio-sensor applications. The electrodes formed have exhibited excellent electrical conductivities in comparison with other forms of CNT-based electrodes, such as CNT networks,¹³⁷ with improved chemical and mechanical properties.

In this technique, CNT webs are applied directly on several Al_2O_3 sensor substrates with different controlled thickness. The sensor substrates are in the fixed position on the rotating base. The high degree of flexibility of CNT webs enables the design of electrodes with different geometries such as planar, yarn, ring and ribbon, as shown in Fig. 3.18.¹³⁶ The simplest configuration is the planar electrode. This design can be readily adapted for the mass production of CNT-based electrodes. The amount of CNT can be regulated either by controlling the number of CNT web layers or by manipulating the electrode electro-active surface area of the electrode. It is evident from Fig. 3.18a and 3.18b that CNT webs possess a high degree



3.17 Representation of a new method of development and production of CNT-based electrochemical sensors using CNT webs without the need for binder.



3.18 (a) SEM images of 10 CNT web layers placed on alumina substrate. (b) Optical images of 50 CNT web layers supported on a glass rod and side view of the CNT forest. (c) A twisting of single layer of a CNT web. (d) 50 CNT web layers after densification and peeling off a glass substrate and densification. (Reprinted from Ref. 136 with permission from Wiley Publishing)

of alignment with occasional cross CNT fibres in between. Each single CNT within the web is made of an average of seven inner walls (multi-walled) about $450\mu\text{m}$ long and approximately 10nm in diameter.

The second geometry is the ring electrode (Fig. 3.18b), prepared by wrapping the CNT web continuously around a cylindrical support such as a glass or Teflon rod. This type of design is very practical for the preparation of a multi-electrode system configuration, for electrode miniaturization, and for applications involving rotating ring electrodes. CNT web ring electrodes are

very useful for energy storage applications due to their high flexibility, mechanical stability and electrical conductivity.

The third possible design using CNT webs is the yarn, which can be formed by twisting the CNT web during the spinning process as illustrated in Fig. 3.18c. CNT web yarns or fibres are highly electrically conductive ($\approx 300 \text{ S cm}^{-1}$ for $10 \mu\text{m}$ diameter) with strengths greater than 460 MPa .¹³⁶ Yarns with different diameters can be prepared by adjusting the width of the CNT web and by combining more fibres together to form larger bundles. CNT web yarns are very useful in fabricating nano- and microelectrodes.

The fourth possible geometry for CNT webs is the ribbon design (Fig. 3.18d). This design can be described as a free-standing CNT web that comprises a large number of CNT web layers (usually > 50) to maintain the required mechanical stability in order to remain intact. The fabrication technique for the CNT web ribbon is similar to the procedure for planar electrodes and is followed by the removal of the thick CNT web layers from the support. The CNT web ribbon has proven to be very attractive in the design of chemical and biological reactors owing to its relatively large active surface area and high affinity to bio-recognition elements such as enzymes and antibodies. Moreover, it can also be used as a strong adsorbent for many hydrophobic compounds. It is also possible to use the ribbon-based material as a flow-through electrochemical detector due to its high porosity.¹³⁶

In many practical applications, most of the above-mentioned designs have been used as unique structures themselves as well as incorporating other nanomaterials to bring in new operations. In this regard, doping of CNTs has been considered as one of the most effective techniques to achieve the desired functionality and further performance improvement.^{127,138} For instance, *n*-type doping of semiconducting CNTs is required for complementary circuit applications. For transparent and conductive films, doping CNTs increases the charge carrier number for high electrical conductivity. For thin film transistors with a high on/off ratio, elimination of metallic CNTs can significantly decrease the off current.¹²⁷

In practice, CNTs can be doped in various ways,¹³⁹ including intercalation of electron donors or acceptors, substitutional doping, encapsulation in the interior spacing, molecular absorption and covalent sidewall functionalization. Studies of the doped CNTs include electrical measurement of individual CNTs on devices, spectral studies of doped CNTs in solution, and thin-film properties such as transport and optical properties.

For CNT thin films, *p*-type doping can substantially enhance the conductivity, as the charge transfer between dopants and the CNTs increases the number of charge carriers along the CNTs and improves the conductivity. The reported *p*-type dopants for CNTs include acids, for example HNO_3 , gases such as O_2 , NO_2 and Br_2 , molecules such as SOCl_2 and F_4TCNQ , polymers and transitional nanometals.¹⁴⁰⁻¹⁴⁴ This particular doping process has

been proven to be quite useful for enhancing the performance of a CNT thin-film transparent electrode. For gaseous dopants, the absorption and desorption dynamics depend on the binding energy, temperature and concentration of the gaseous species and CNTs.¹⁴⁵ The outlook for doping CNTs will be based on the very challenging task of finding a stable dopant that has sufficiently high binding energy. However, at the same time, this should not affect the electronic and transport properties of CNTs.

3.6 Carbon nanotubes for environmental sensors

Due to their unique and attractive properties and the existence of a number of CNT designs as described in the previous section, CNTs have been successfully employed in the development of different enzyme-based biosensors.^{146–149} Measurement by bio-sensors based on CNTs involves direct adsorption, polymer entrapment, covalent attachment and layer-by-layer deposition. Moreover, the ability of CNTs to interact with the redox center of enzymes enables direct electron transfer between the enzyme centre and the electrode surface, eliminating the need for co-factors and mediators. Different oxidase- and dehydrogenase-based enzymes, such as glucose and alcohol oxidase and dehydrogenase, were used along with CNTs for the detection of glucose and ethanol.¹⁵⁰ In the same review, other enzyme-CNT-based biosensors, used for the detection of important compounds such as lactate, polyphenol, ascorbic and uric acids were described.¹⁵⁰ Most of the CNT-based bio-sensors can be employed for the detection of organophosphate (OP) pesticides, organophosphorous hydrolase (OPH) and a cetylcholinesterase (AChE). Various designs of these bio-sensors have been reported, mainly monitoring pesticides in conjunction with electrochemical and optical detection, using the enzyme and non-enzymatic methods.

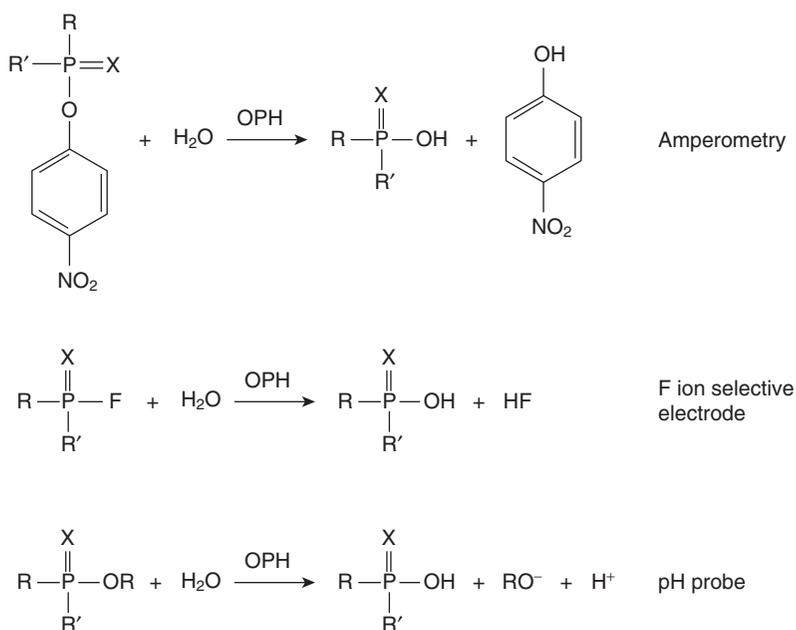
3.6.1 OP and OPH pesticides detection

OP pesticides are among the most toxic substances and have been widely employed in different parts of the world as insecticides in agriculture. Although they are effective against several types of pests, their long-term toxicity on human health and the ecosystem is becoming an issue worldwide. OP pesticides (as well as sarin and VX [O-ethyl-S-2-diisopropylaminoethyl methylphosphonothioate] nerve agent) irreversibly deactivate the enzyme AChE, which is essential to nerve function in insects, humans and many other animals. Early detection of OP neurotoxins is vital for protecting water resources and food supplies, in the defence against terrorist activity and for monitoring detoxification processes. Accordingly, there are growing demands for field-deployable devices for reliable on-site monitoring of OP compounds.^{151,152} The detection and sensing of these toxins in a

timely manner and at very low levels is a priority. Traditional methods, such as gas chromatography (GC), high-performance liquid chromatography (HPLC), and mass spectroscopy, and biological methods, such as immunoassay, can be used for the analysis of OPs. However, such analyses are generally laboratory-based, time-consuming and require expensive analytical instruments. Therefore there is an urgent need for fast, sensitive and accurate, field deployable, compact and relatively inexpensive sensors for on-site monitoring of OP compounds. CNT-based amperometric bio-sensors for field screening of OPs can be successfully utilized as practical measuring devices. They greatly benefit from the ability of CNT-based transducers to promote the electro-transfer reactions of enzymatically generated species.¹⁵³

A preferred direct bio-sensing route for detecting OP neurotoxins involves the bio-catalytic activity of OPH.¹⁵⁴ Several OPH-based amperometric, potentiometric or optical bio-sensing devices have been investigated and reported.¹⁴⁹ A direct bio-sensing protocol that is suitable for fast and accurate field testing of OP substances is schematically illustrated in Fig. 3.19.¹²⁵

Amperometric OPH electrodes commonly rely on monitoring the oxidation of the *p*-nitrophenol product of the enzyme reaction. Improved anodic



3.19 Detection of OPs using OPH. (Reprinted from Ref. 125 with permission from the Taylor & Francis Group)

detection of the *p*-nitrophenol is highly desirable in order to address the high-overvoltage and surface-fouling limitations associated with such transduction reaction. The ability of CNT-modified electrodes to promote the oxidation of phenolic compounds (including the *p*-nitrophenol product of the OPH reaction) and to minimize surface fouling paves the way for new OPH–CNT amperometric bio-sensors.¹⁴⁹ Alternatively, sensors that do not rely on enzymes or antibodies have also been developed using molecular imprint technologies with high selectivity toward specific OP species.¹⁵⁵ During the fabrication of CNT-based biosensors for pesticide detection, various shapes of nanostructured materials have been used, which have offered advantages over the traditional analytical methods.¹⁵⁶

3.6.2 The AChE enzyme

AChE is an important enzyme present in the synaptic clefts of the central nervous system of living organisms. It degrades (through its hydrolytic activity) the neurotransmitter acetylcholine, producing choline and an acetate group. It is mainly found at neuromuscular junctions and cholinergic synapses in the central nervous system, where its activity serves to terminate synaptic transmission. AChE has a very high catalytic activity where each molecule of AChE degrades about 25000 molecules of acetylcholine per second.¹³⁶ The major role of AChE includes the transmission of the nerve impulses to the cholinergic synapses, involved with memory and Alzheimer's disease. Therefore, AChE has been the subject of detailed studies in the past.¹⁴⁷ Those studies revealed that AChE activity could be significantly inhibited by OP pesticides used in agriculture, medicine, industry and chemical warfare agents. The enzyme inhibition mechanism proceeds through the formation of a stable complex through reversible and irreversible reactions of OP pesticides with the active site of AChE.¹²⁵ As a result, acetylcholine largely accumulates in the muscular tissues and leads to severe muscular paralysis. Thus, the acetylcholine level significantly depends on the availability of active AChE. This ultimately corroborates the requirement for accurate detection of OP pesticides in the environment.

In most AChE sensors, OP detection is mainly based on the irreversible inhibition of AChE activity by OP pesticides.¹⁴⁶ The degree of inhibition has been calculated by comparing the residual activity of the enzyme with the initial activity. In the past, AChE was added directly to solutions to carry out inhibition studies. Although satisfactory results were obtained in such conditions, significant advances occurred when AChE was immobilized on modified electrode matrices. However, the enzyme immobilization technique remains rather complicated and often involves very complex matrices. Moreover, the incorporation of AChE into certain mediator complexes also lowered the stability of the enzyme and reduced reproducibility after

spiked river water samples. SAMs of single-walled CNTs were used to modify the gold electrode after wrapping by thiol-terminated single-stranded oligonucleotide (ssDNA). A thin film of PANI was electrochemically deposited on the CNT. AChE was then immobilized after cross-linking with glutaraldehyde. The dynamic range for the determination of methyl parathion and chlorpyrifos was found to be 1.0×10^{-11} – 1.0×10^{-6} M ($0.6 < SD < 3.5$) with good reproducibility and stability and a detection limit of 1 pM. The incorporation of the conductive polymer PANI onto CNT played an important role in signal amplification. In addition to the time needed for the enzyme to incubate with the OP, further enhancement of response was due to an additional incubation of PANI with ATC which resulted in further protonation of the polymer and hence better sensitivity. This protocol enables the use of a very small amount of the enzyme and, at the same time, produces a higher response to the addition of ATC which is important for monitoring the inhibition effect of the OP at trace levels.¹²⁵ With regard to the electrode material, it mainly relies on casting films of pure CNT or a mixture of CNT with other binders and additives such as polymers, surfactants, and metals. Different polymers, for example Nafion™, Chitosan and PANI, have been employed for these applications, providing extra enzyme stabilization, selectivity and sensitivity based on their structure.

Plate Va (see colour section between pages 232 and 233) shows some of the examples of the CSIRO-developed portable planar CNT-based biosensors with their appropriate CV characteristics depending on the number of CNT layers. Field tests have revealed that these CNT-based biosensors displayed a sensitivity of ~ 1 nM RSD $< 5\%$ (eight electrodes) and extended storage stability up to one month (with daily testing against substrate). Sensor electrodes, which consisted of 10 and fewer CNT web layers, have exhibited high resistance ($> 500 \Omega$) and low capacitance ($< 30 \mu\text{F}$). Therefore, increasing the number of CNT web layers beyond ten resulted in a lower resistance (40–100 Ω) and appropriate higher capacitance (50–500 μF). Thus the decrease in resistance and increase in capacitance is mainly attributed to the increase in the electro-active surface area, which results in an increase in current density and surface charge.¹³⁶

Plate Vb correlates the obtained CV measurements for different numbers of CNT web layers using 10 mM $\text{K}_3[\text{Fe}(\text{CN})_6]$. Electrodes made of ten and fewer CNT web layers displayed poorly defined and negligible CV responses. On the other hand, electrodes modified with more than ten CNT web layers provided improved electron transport rates and better reversibility. The peak-shaped CV response indicates an overlap of the diffusion layers of adjacent CNT sites that leads to an improved diffusion flux. The CV ferri-cyanide anodic peak currents increased almost linearly with up to 30 CNT web layers. Anodic peak potentials also shifted to smaller values as the number of CNT webs increased, indicating better electron transfer rates.

Nearly identical peak separations (ΔE_p) of $\approx 0.25\text{V}$ were observed upon raising the number of CNT web layers to between 20 and 30.¹²⁵ Consequently, sensor electrodes made of CNT webs efficiently promoted electro-catalytic activity towards analytes with a sluggish redox process.

Noteworthy in relation to the modern sensor and bio-sensor applications, CNTs have provided an excellent electro-catalytic activity, high surface-to-volume ratio, chemical and physical stability, surface functionalities and noteworthy antifouling resistance. Despite of all these advances and improvements in sensitivity, detection limits, response time and stability of CNT-based biosensors for pesticides monitoring reported to date, several issues still need to be addressed before the full potential of such bio-sensors will be realized and adopted. They are as follows:

1. More robust forms of CNTs and/or CNTs-based composite materials are highly desirable that would resist harsh environment such as sea water.
2. The stability of CNT-modified surfaces must be refined.
3. Improvement in long-term stability can be achieved by solving the bio-fouling problem. That can lead to substantial increase in the sensor's lifespan.
4. Sample preparation and the need for pre-oxidation of some OPs to enhance the sensitivity should be replaced by dual catalytic systems for oxidation and detection of OPs.
5. The selectivity of CNT-based bio-sensors must be improved. This can be achieved by incorporating other more specific bio-recognition elements such as antibodies and engineered forms of enzymes: mutant AChE and OPH.
6. Synthesis of CNTs with higher electro-catalytic activity and enhanced structural and functional properties is required, which would lead to improved enzyme stabilization and, consequently, to higher detection limits.

3.7 References

1. G.E. Moore, Cramming more components onto integrated circuit, *Electronics*, 38 (1965) 114–117.
2. P.S. Peercy, The drive to miniaturization, *Nature*, 406 (2000) 1023–1026.
3. E. Regis, *Nano: the Emerging Science and Technology – remarking the world-molecule by molecule*, 1995, Little Brown and Company, Boston.
4. J.G. Lu, P. Chang, Z. Fan, Quasi-one-dimensional metal oxide materials – Synthesis, properties and applications, *Mater. Sci. Eng. R*, 52 (2006) 49–91.
5. A.H. Castro Neto, K. Novoselov, New directions in science and technology: two-dimensional crystals, *Rep. Prog. Phys.*, 74 (2011) 082501 (9pp).
6. X. Miao, S. Tongay, M.K. Petterson, K. Berke, A.G. Rinzler, B.R. Appleton, A.F. Hebard, High efficiency graphene solar cells by chemical doping, *Nano Lett.*, 12 (2012) 2745–2750.

7. J.Z. Ou, S. Balendhran, M.R. Field, D.G. McCulloch, A.S. Zoofakar, R.A. Rani, S. Zhuiykov, A.P. O'Mullane, K. Kalantar-zadeh, The anodized crystalline WO₃ nanoporous network with enhanced electrochromic properties, *Nanoscale*, 4 (2012) 5980–5988.
8. D.D. Yao, J.Z. Ou, K. Latham, S. Zhuiykov, A.P. O'Mullane, K. Kalantar-zadeh, Electrodeposited α - and β -phase MoO₃ films and investigation of their gasochromic properties, *Cryst. Growth Des.*, 12 (2012) 1865–1870.
9. S. Balendhran, J.Z. Ou, M. Bhaskaran, S. Sriram, S. Ippolito, Z. Vasic, E. Kats, S. Bhargava, S. Zhuiykov, K. Kalantar-zadeh, Atomically thin layers of MoS₂ via a two step thermal evaporation – exfoliation method, *Nanoscale*, 4 (2012) 461–466.
10. S. Balendhran, D. Deng, J.Z. Ou, S. Sriram, M. Bhaskaran, J. Scott, S. Russo, S. Zhuiykov, M.S. Strano, N. Medhekar, K. Kalantar-zadeh, Large carrier mobility in high-*k* two-dimensional metal oxides, *Adv. Mater.*, 25 (2013) 109–114.
11. K.S. Novoselov, V.I. Fal'ko, L. Colombo, P.R. Gellert, M.G. Schwab, K. Kim, A roadmap for graphene, *Nature*, 490 (2012) 192–200.
12. S. Zhuiykov, E. Kats, Atomically-thin two-dimensional semiconductor nanocrystals: A review, *Ionics*, 19 (2013) 825–865.
13. J.Z. Ou, R.A. Rani, M.H. Ham, Y. Zhang, H. Zheng, S. Sriram, M. Bhaskaran, K. Latham, S. Zhuiykov, R.B. Kaner, K. Kalantar-zadeh, Elevated temperature anodized Nb₂O₅ – a photoanode material with exceptionally large photoconversion, *ASC Nano*, 6 (2012) 4045–4053.
14. B. Radisavljevic, A. Radenovic, J. Brivio, V. Giacometti, A. Kis, Single-layer MoS₂ transistors, *Nature Nanotechnol.*, 6 (2011) 147–150.
15. Z. Yin, H. Li, Hong Li, L. Jiang, Y. Sun, G. Lu, Q. Zhang, X. Chen, H. Zhang, Single-layer MoS₂ phototransistors, *ACS Nano*, 6 (2012) 74–80.
16. J.N. Coleman *et al.*, Two-dimensional nano-sheets produced by liquid exfoliation of layered materials, *Science*, 331 (2011) 568–571.
17. M. Osada, T. Sasaki, Two-dimensional dielectric nanosheets: novel nanoelectronics from nanocrystal building blocks, *Adv. Mater.*, 24 (2012) 210–228.
18. A.K. Geim, Nobel lecture. Random walk of graphene, *Rev. Mod. Phys.*, 83 (2011) 851–862.
19. K.S. Novoselov, Nobel lecture. Graphene: materials in the flatland, *Rev. Mod. Phys.*, 83 (2011) 837–849.
20. L. Britnell *et al.*, Field-effect tunnelling transistor based on vertical graphene heterostructures, *Science*, 335 (2012) 947–950.
21. Z.Y. Fan, D.W. Wang, P.C. Chang, W.Y. Tseng, J.G. Lu, ZnO nanowire field-effect transistor and oxygen sensing property, *Appl. Phys. Lett.*, 85 (2004) 5923–5925.
22. Z.Y. Fan, X.G. Wen, S.H. Yang, J.G. Lu, Controlled *p*- and *n*-type doping of Fe₂O₃ nanobelt field effect transistors, *Appl. Phys. Lett.*, 87 (2005) 013113–013115.
23. D.H. Zhang, C. Li, S. Han, X. Liu, T. Tang, W. Jin, C. Zhou, Electronic transport studies of single-crystalline In₂O₃ nanowires, *Appl. Phys. Lett.*, 82 (2003) 112–114.
24. Z.Q. Liu, D.H. Zhang, S. Han, C. Li, T. Tang, W. Jin, X.L. Liu, B. Lei, C.W. Zhou, Laser ablation synthesis and electron transport studies of tin oxide nanowires, *Adv. Mater.*, 15 (2003) 1754–1757.

25. P.C. Chang, Z.Y. Fan, W.Y. Tseng, A. Rajagopal, J.G. Lu, Beta-Ga₂O₃ nanowires: synthesis, characterization, and *p*-channel field-effect transistor, *Appl. Phys. Lett.*, 87 (2005) 222102.
26. J. Muster, G.T. Kim, V. Krstic, J.G. Park, Y.W. Park, S. Roth, M. Burghard, Electrical transport through individual vanadium pentoxide nanowires, *Adv. Mater.*, 12 (2000) 420–424.
27. X. Liu, C. Li, S. Han, J. Han, C.W. Zhou, Synthesis and electronic transport studies of CdO nanoneedles, *Appl. Phys. Lett.*, 82 (2003) 1950–1952.
28. E.H. Hwang, S. Das Sarma, Gate-tunable quantum transport in double-layer graphene, *Phys. Rev. B*, 77 (2008) 235437.
29. D.K. Schroder, *Semiconductor Material and Device Characterisation*, 1990, Wiley, New York.
30. L.T. Liu, S.B. Kumar, Y. Ouyang, J. Guo, Performance limits of monolayer transition metal dichalcogenide transistors, *IEEE Trans. Electron Devices*, 58 (2011) 3042–3047.
31. F.M. Hossain, J. Nishii, S. Takagi *et al.*, Modeling of grain boundary barrier modulation in ZnO invisible thin film transistors, *Phys. E Low-Dimensional Syst. Nanostruct.*, 21 (2004) 911–915.
32. W.I. Park, J.S. Kim, G.C. Yi, M.H. Bae, H.J. Lee, Fabrication and electrical characteristics of high-performance ZnO nanorod field-effect transistors, *Appl. Phys. Lett.*, 85 (2004) 5052–5054.
33. P.C. Chang, Z.Y. Fan, J.G. Lu, High-performance ZnO nanowire field effect transistors, *Appl. Phys. Lett.*, 89 (2006) 133113–133115.
34. H.T. Ng, J. Han, T. Yamada, P. Nguyen, Y.P. Chen, M. Meyyappan, Single crystal nanowire vertical surround-gate field-effect transistor, *Nano Lett.*, 4 (2004) 1247–1252.
35. P. Nguyen, H.T. Ng, T. Yamada *et al.*, Direct integration of metal oxide nanowire in vertical field-effect transistor, *Nano Lett.*, 4 (2004) 651–657.
36. T. Marinov, A. Buldum, C.B. Clemons, K.L. Kreider, G.W. Young, S.I. Hariharan, Field emission from coated nanowires, *J. Appl. Phys.*, 98 (2005) 044314.
37. C.J. Lee, T.J. Lee, S.C. Lyu, Y. Zhang, H. Ruh, H.J. Lee, Field emission from well-aligned zinc oxide nanowires grown at low temperature, *Appl. Phys. Lett.*, 81 (2002) 3648–3650.
38. R.S. Chen, Y.S. Huang, Y.M. Liang, C.S. Hsieh, D.S. Tsai, K.K. Tiong, Field emission from vertically aligned conductive IrO₂ nanorods, *Appl. Phys. Lett.*, 84 (2004) 1552–1554.
39. C.S. Hsieh, G. Wang, D.S. Tsai, R.S. Chen, Y.S. Huang, Field emission characteristics of ruthenium dioxide nanorods, *Nanotechnology*, 16 (2005) 1885–1891.
40. H.S. Jang, D.H. Kim, H.R. Lee, S.Y. Lee, Field emission from cone-like single crystalline indium tin oxide nanorods, *Mater. Lett.*, 59 (2005) 1526–1529.
41. S.Q. Li, Y.X. Liang, T.H. Wang, Electric-field-aligned vertical growth and field emission properties of In₂O₃ nanowires, *Appl. Phys. Lett.*, 87 (2005) 143104–143106.
42. J.G. Liu, Z.J. Zhang, Y. Zhao, X. Su, S. Liu, E.G. Wang, Tuning the field-emission properties of tungsten oxide nanorods, *Small*, 1 (2005) 310–313.

43. J.M. Wu, H.C. Shih, W.T. Wu, Electron field emission from single crystalline TiO₂ nanowires prepared by thermal evaporation, *Chem. Phys. Lett.*, 413 (2005) 490–494.
44. J. Chen, N.Y. Huang, S.Z. Deng *et al.*, Effects of light illumination on field emission from CuO nanobelt arrays, *Appl. Phys. Lett.*, 86 (2005) 151107–151109.
45. L. Liao, J.C. Li, D.F. Wang *et al.*, Field emission property improvement of ZnO nanowires coated with amorphous carbon and carbon nitride films, *Nanotechnology*, 16 (2005) 985–989.
46. S.Y. Li, P. Lin, C.Y. Lee, T.Y. Tseng, C.J. Huang, Effect of Sn dopant on the properties of ZnO nanowires, *J. Phys. D Appl. Phys.*, 37 (2004) 2274–2282.
47. C.X. Xu, X.W. Sun, B.J. Chen, Field emission from gallium-doped zinc oxide nanofiber array, *Appl. Phys. Lett.*, 84 (2004) 1540–1542.
48. J. Nowotny, *Oxide Semiconductors for Solar Energy Conversion: Titanium dioxide*, 2012, CRC Press, Boca Raton, 393p.
49. W.I. Park, J.S. Kim, G.C. Yi, H.J. Lee, ZnO nanorod logic circuits, *Adv. Mater.*, 17 (2005) 1393–1398.
50. X. Duan, Y. Huang, R. Agarwal, C.M. Lieber, Single-nanowire electrically driven lasers, *Nature*, 421 (2003) 241–245.
51. A.B. Greytak, C.J. Barrelet, Y. Li, C.M. Lieber, Semiconductor nanowire laser and nanowire waveguide electro-optic modulators, *Appl. Phys. Lett.*, 87 (2005) 15103.
52. O. Hayden, R. Agarwal, C.M. Lieber, Nanoscale avalanche photodiodes for highly sensitive and spatially resolved photon detection, *Nature Mater.*, 5 (2006) 352–356.
53. B. Paccione, L.K. van Vugt, R. Agarwal, Propagation loss spectroscopy on single nanowire active waveguides, *Nano Lett.*, 10 (2010) 2251–2256.
54. L.K. Van Vugt, B. Piccione, C.H. Cho, P. Nukala, R. Agarwal, One-dimensional polaritons with size-tunable and enhanced coupling strengths in semiconducting nanowires, *Proc. Natl Acad. Sci. USA*, 108 (2011) 10050–10055.
55. B. Piccione, C.H. Cho, L.K. van Vugt, R. Agarwal, All-optical active switching in individual semiconductor nanowires, *Nature Nanotechnol.*, 7 (2012) 640–645.
56. M. Law, D.J. Sirbully, J.C. Johnson, J. Goldberger, R.J. Saykally, P.D. Yang, Nanoribbon waveguides for subwavelength photonics integration, *Science*, 305 (2004) 1269–1273.
57. J.C. Johnson, H.Q. Yan, P.D. Yang, R.J. Saykally, Optical cavity effects in ZnO nanowire lasers and waveguides, *J. Phys. Chem. B*, 107 (2003) 8816–8828.
58. P.D. Yang, H.Q. Yan, S. Mao *et al.*, Controlled growth of ZnO nanowires and their optical properties, *Adv. Funct. Mater.*, 12 (2002) 323–331.
59. Y. Zhang, H.B. Jia, R.M. Wang *et al.*, Low-temperature growth and Raman scattering study of vertically aligned ZnO nanowires on Si substrate, *Appl. Phys. Lett.*, 83 (2003) 4631–4633.
60. Q. Xu, M. Lipson, All-optical logic based on silicon micro-ring resonators, *Opt. Express*, 15 (2007) 924–929.
61. T. Tanabe, M. Notomi, S. Mitsugi, A. Shinya, E. Kuramochi, All-optical switches on a silicon chip realized using photonic crystal nanocavities, *Appl. Phys. Lett.*, 87 (2005) 151112–151113.

62. D.K. Hwang, S.H. Kang, J.H. Lim *et al.*, *p*-ZnO/*n*-GaN heterostructure ZnO light-emitting diodes, *Appl. Phys. Lett.*, 86 (2005) 222101–222103.
63. S.J. Jiao, Z.Z. Zhang, Y.M. Lu *et al.*, ZnO *p*-*n* junction light-emitting diodes fabricated on sapphire substrates, *Appl. Phys. Lett.*, 88 (2006) 031911–031913.
64. C.H. Liu, W.C. Yiu, F.C.K. Au, J.X. Ding, C.S. Lee, S.T. Lee, Electrical properties of zinc oxide nanowires and intramolecular *p*-*n* junctions, *Appl. Phys. Lett.*, 83 (2003) 3168–3170.
65. W.I. Park, G.C. Yi, Electroluminescence in *n*-ZnO nanorod arrays vertically grown on *p*-GaN, *Adv. Mater.*, 16 (2004) 87–90.
66. R. Konenkamp, R.C. Word, C. Schlegel, Vertical nanowire light-emitting diode, *Appl. Phys. Lett.*, 85 (2004) 6004–6006.
67. D.I. Son *et al.*, Emissive ZnO-graphene quantum dots for white-light-emitting diodes, *Nature Nanotechnol.*, 7 (2012) 465–471.
68. J.M. Caruge, J.E. Halpert, V. Wood, V. Bulovic, M.G. Bawendi, Colloidal quantum-dot light-emitting diodes with metal-oxide charge transport layers, *Nature Photonics*, 2 (2008) 247–250.
69. D.I. Son *et al.*, Bistable organic memory device with gold nanoparticles embedded in a conducting poly(*n*-vinylcarbazole) colloids hybrid, *J. Phys. Chem. C*, 115 (2011) 2341–2348.
70. M.C. McAlpine, H. Ahmad, D. Wang, J.R. Heath, Highly ordered nanowire arrays on plastic substrate for ultrasensitive flexible chemical sensors, *Nature Mater.*, 6 (2007) 379–384.
71. M. Terrones *et al.*, Graphene and graphite nanoribbons: morphology, properties, synthesis, defects and applications, *Nano Today*, 5 (2010) 351–372.
72. D.I. Son *et al.*, Polymer-ultrathin graphite sheet-polymer composite structured flexible non-volatile organic memory devices, *Nanotechnology*, 22 (2011) 295203.
73. S. Niyogi *et al.*, Solution properties of graphite and graphene, *J. Am. Chem. Soc.*, 128 (2006) 7720–7721.
74. J. Huang, Z. Xu, Y. Yang, Low-work-function surface formed by solution-processed and thermally deposited nanoscale layers of cesium carbonate, *Adv. Funct. Mater.*, 17 (2007) 1966–1973.
75. H.Y. Yang, D.I. Son, T.W. Kim, J.M. Lee, W.I. Park, Enhancement of the photocurrent in ultraviolet photodetectors fabricated utilizing hybrid polymer-ZnO quantum dot nanocomposites due to an embedded graphene layer, *Org. Electron.*, 11 (2010) 1313–1317.
76. F. Wang *et al.*, Gate-variable optical transitions in graphene, *Science*, 320 (2008) 206–208.
77. H. Kind, H.Q. Yan, B. Messer, M. Law, P.D. Yang, Nanowire ultraviolet photodetectors and optical switches, *Adv. Mater.*, 14 (2002) 158–160.
78. Z.Y. Fan, P.C. Chang, J.G. Lu *et al.*, Photoluminescence and polarized photodetection of single ZnO nanowires, *Appl. Phys. Lett.*, 85 (2004) 6128–6130.
79. Z.Q. Liu, D.H. Zhang, S. Han *et al.*, Laser ablation synthesis and electron transport studies of tin oxide nanowires, *Adv. Mater.*, 15 (2003) 1754–1757.
80. D. Zhang, C. Li, S. Han *et al.*, Ultraviolet photodetection properties of indium oxide nanowires, *Appl. Phys. A Mater. Sci. Process.*, 77 (2003) 163–166.

81. Y.W. Heo, L.C. Tien, D.P. Norton *et al.*, Electrical transport properties of single ZnO nanorods, *Appl. Phys. Lett.*, 85 (2004) 2002–2004.
82. K. Keem, H. Kim, G.T. Kim *et al.*, Photocurrent in ZnO nanowires grown from Au electrodes, *Appl. Phys. Lett.*, 84 (2004) 4376–4378.
83. H.B. Akkerman, P.W.M. Blom, D.M. de Leeuw, B. de Boer, Towards molecular electronics with large-area molecular junctions, *Nature*, 441(2006) 69–72.
84. P.A. Van Hal *et al.*, Upscaling, integration and electrical characterization of molecular junctions, *Nature Nanotechnol.*, 3 (2008) 749–754.
85. H. Klauk, U. Zschieschang, J. Pfau, M. Halik, Ultralow-power organic complementary circuits, *Nature*, 445 (2007) 745–748.
86. T. Sekitani, U. Zschieschang, H. Klauk, T. Someya, Flexible organic transistors and circuits with extreme bending stability, *Nature Mater.*, 9 (2010) 1015–1022.
87. S.J. Kim, J.S. Lee, Flexible organic transistor memory devices, *Nano Lett.*, 10 (2010) 2884–2890.
88. T. Sekitani *et al.*, Organic nonvolatile memory transistors for flexible sensor arrays, *Science*, 326 (2009) 1516–1519.
89. S.C.B. Mannsfeld *et al.*, Highly sensitive flexible pressure sensors with microstructured rubber dielectric layers, *Nature Mater.*, 9 (2010) 859–864.
90. G.H. Gelinck *et al.*, Flexible active-matrix displays and shift registers based on solution-processed organic transistors, *Nature Mater.*, 3 (2004) 106–110.
91. D-H. Kim *et al.*, Dissolvable films of silk fibroin for ultrathin conformal bio-integrated electronics, *Nature Mater.*, 9 (2010) 511–517.
92. S. Bae *et al.*, Roll-to-roll production of 30-inch graphene films for transparent electrodes, *Nature Nanotechnol.*, 5 (2010) 574–578.
93. Y. Zhu, Z.Z. Sun, Z. Yan, Z. Jin, J.M. Tour, Rational design of hybrid graphene films for high-performance transparent electrodes, *ACS Nano*, 5 (2011) 6472–6479.
94. K. Takei *et al.*, Nanowire active-matrix circuitry for low-voltage macroscale artificial skin, *Nature Mater.*, 9 (2010) 821–826.
95. D-M. Sun *et al.*, Flexible high-performance carbon nanotube integrated circuits. *Nature Nanotechnol.*, 6 (2011) 156–161.
96. S. Park *et al.*, Flexible molecular-scale electronic devices, *Nature Nanotechnol.*, 7 (2012) 438–442.
97. Y. Kim *et al.*, Conductance and vibrational states of single-molecule junctions controlled by mechanical stretching and material variation, *Phys. Rev. Lett.*, 106 (2011) 196804.
98. P.J. Michalski, N. Sai, E.J. Mele, Continuum theory for nanotube piezoelectricity, *Phys. Rev. Lett.*, 95 (2005) 116803.
99. Z.L. Wang, Z.R. Dai, R.P. Gao, J.L. Gole, Measuring the Young's modulus of solid nanowires by in situ TEM, *J. Electron. Microscop.*, 51 (2002) S79–S85.
100. Z.L. Wang, New developments in transmission electron microscopy for nanotechnology, *Adv. Mater.*, 15 (2003) 1497–1514.
101. M.H. Zhao, Z.L. Wang, S.X. Mao, Piezoelectric characterization of individual zinc oxide nanobelt probed by piezoresponse force microscope, *Nano Lett.*, 4 (2004) 587–590.
102. Z.L. Wang, Properties of nanobelts and nanotubes measured by in situ TEM, *Microsc. Microanal.*, 10 (2004) 158–166.

103. J.H. Song, X.D. Wang, E. Riedo, Z.L. Wang, Elastic property of vertically aligned nanowires, *Nano Lett.*, 5 (2005) 1954–1958.
104. Z.L. Wang, R.P. Gao, Z.W. Pan, Z.R. Dai, Nano-scale mechanics of nanotubes, nanowires, and nanobelts, *Adv. Eng. Mater.*, 3 (2001) 657–661.
105. D.A. Dikin, X. Chen, W. Ding, G. Wagner, R.S. Ruoff, Resonance vibration of amorphous SiO₂ nanowires driven by mechanical or electrical field excitation, *J. Appl. Phys.*, 93 (2003) 226–230.
106. T. Ikuno, S. Honda, T. Yasuda *et al.*, Thermally driven nanomechanical deflection of hybrid nanowires, *Appl. Phys. Lett.*, 87 (2005) 213104–213106.
107. G. Suyal, E. Colla, R. Gysel, M. Cantoni, N. Setter, Piezoelectric response and polarization switching in small anisotropic perovskite particles, *Nano Lett.*, 4 (2004) 1339–1342.
108. X.Y. Zhang, X. Zhao, C.W. Lai, J. Wang, X.G. Tang, J.Y. Dai, Synthesis and piezoresponse of highly ordered Pb(Zr_{0.53}Ti_{0.47})O₃ nanowire arrays, *Appl. Phys. Lett.*, 85 (2004) 4190–4192.
109. S. Zhuiykov, *Electrochemistry of Zirconia Gas Sensors*, 2007, CRC Press, Boca Raton, 297p.
110. P.R. Hauptmann, Selected examples of intelligent (micro) sensor systems: state-of-the-art and tendencies, *Meas. Sci. Technol.*, 17 (2006) 459–466.
111. G. Korotcenkov, Gas response control through structural and chemical modification of metal oxide films: state of the art and approaches, *Sens. Actuators B: Chem.*, 107 (2005) 209–232.
112. S. Zhuiykov, Carbon monoxide detection at low temperatures by semiconductor sensor with nanostructured Au-doped CoOOH films, *Sens. Actuators B: Chem.*, 129 (2008) 431–441.
113. N. Yamazoe, K. Shimano, C. Sawada, Contribution of electron tunnelling transport in semiconductor gas sensor, *Thin Solid Films*, 515 (2007) 8302–8309.
114. S. Zhuiykov, Morphology of Pt-doped RuO₂ nanocomposites and their application in water quality monitoring sensors, *Sens. Actuators B: Chem.*, 136 (2009) 248–256.
115. S.T. Shishiyanu, T.S. Shishiyanu, O.I. Lupan, Sensing characteristics of tin-doped ZnO thin films as NO₂ gas sensor, *Sens. Actuators B Chem.*, 107 (2005) 379–386.
116. R. Ramamoorthy, P.K. Dutta, S.A. Akbar, Oxygen sensors: materials, methods, designs and applications, *J. Mater. Sci.*, 38 (2003) 4271–4282.
117. Y. Yamada *et al.*, Nanocrystal bilayer for tandem catalysis, *Nature Chem.*, 3 (2011) 372–376.
118. A. Kolmakov, Y.X. Zhang, G.S. Cheng, M. Moskovits, Detection of CO and O₂ using tin oxide nanowire sensors, *Adv. Mater.*, 15 (2003) 997–1000.
119. C. Baratto, E. Comini, G. Faglia, G. Sberveglieri, M. Zha, A. Zappettini, Metal oxide nanocrystals for gas sensing, *Sens. Actuators B Chem.*, 109 (2005) 2–6.
120. Y. Zhang, A. Kolmakov, S. Chretien, H. Metiu, M. Moskovits, Control of catalytic reactions at the surface of a metal oxide nanowire by manipulating electron density inside it, *Nano Lett.*, 4 (2004) 403–407.
121. A.M. Azad, S.A. Akbar, S.G. Mhaisalkar, L.D. Birkefeld, K.S. Goto, Solid-state gas sensors – a review, *J. Electrochem. Soc.*, 139 (1992) 3690–3704.

122. G. Eranna, B.C. Joshi, D.P. Runthala, R.P. Gupta, Oxide materials for development of integrated gas sensors—a comprehensive review, *Crit. Rev. Solid State Mater. Sci.*, 29 (2004) 111–118.
123. K. Wetchakun, T. Samerjai, N. Tamaekong, C. Liewhiran, C. Siritwong, V. Kruefu, A. Wisitsoraat, A. Tuantranont, S. Phanichphant, Semiconductor metal oxides as sensors for environmentally hazardous gases, *Sens Actuators B: Chem.*, 160 (2011) 580–591.
124. C.N.R. Rao *et al.*, Nanotubes, *Chem. Physchem.*, 2 (2001) 78–105.
125. M.M. Musameh, Y. Gao, M. Hickey, I.L. Kyratzis, Application of carbon nanotubes in the extraction and electrochemical detection of organophosphate pesticides: A review, *Anal. Lett.*, 45 (2012) 783–803.
126. F. Pei, E.A. Laird, G.A. Steele, L. Kouwenhoven, Valley-spin blockade and spin resonance in carbon nanotubes, *Nature Nanotechnol.*, 7 (2012) 630–634.
127. L. Hu, D.S. Hecht, G. Gruner, carbon nanotube thin films: fabrication, properties and application, *Chem. Rev.*, 110 (2010) 5790–5844.
128. L. Agui, P. Yanez-Sedeno, J.M. Pingarron, Role of carbon nanotubes in electro-analytical chemistry: a review, *Anal. Chim. Acta*, 622 (2008) 11–47.
129. J. Wang, M. Musameh, Y.H. Lin, Solubilization of carbon nanotubes by nafion toward the preparation of amperometric biosensors. *J. Am. Chem. Soc.*, 125 (2003) 2408–2409.
130. M.D. Rubianes, G.A. Rivas, Carbon nanotubes paste electrode, *Electrochem. Commun.*, 5 (2003) 689–694.
131. J.J. Gooding, R. Wibowo, J. Liu, W. Yang, D. Losic, S. Orbons, F.J. Mearns, J.G. Shapter, D.B. Hibbert, Protein electrochemistry using aligned carbon nanotubes electrode arrays, *J. Am. Chem. Soc.*, 125 (2003) 9006–9007.
132. J.N. Barisci, G.G. Wallace, D. Chattopadhyay, F. Papadimitrakopoulos, R.H. Baughman, Electrochemical properties of single-wall carbon nanotube electrodes, *J. Electrochem. Soc.*, 150(2003) E409–E415.
133. G. Liu, Y. Lin, Y. Tu, Z. Ren, Ultrasensitive voltammetric detection of trace heavy metal ions using carbon nanotube nanoelectrode array, *Analyst*, 130 (2005) 1098–1101.
134. M. Zhang, S. Fang, A.A. Zakhidov, S.B. Lee, A.E. Aliev, C.D. Williams, K.R. Atkinson, R.H. Baughman, R.H. Baughman, Strong, transparent, multifunctional, carbon nanotube sheets, *Science*, 309 (2005) 1215–1219.
135. M. Zhang, K.R. Atkinson, R.H. Baughman, Multifunctional carbon nanotube yarns by downsizing an ancient technology, *Science*, 304 (2004) 1358–1361.
136. M. Musameh, M. Redrado Notivoli, M. Hickey, I.L. Kyratzis, Y. Gao, C. Huynh, S.C. Hawkins, Carbon nanotube webs: a novel material for sensor applications, *Adv. Mater.*, 23 (2011) 906–910.
137. T.M. Day, N.R. Wilson, J.V. Macpherson, Electrochemical and conductivity measurements of single-wall carbon nanotube network electrodes, *J. Am. Chem. Soc.*, 126 (2004) 16724–16725.
138. S. Viswanathan, H. Radecka, J. Radecki, Electrochemical biosensor for pesticides based on acetylcholinesterase immobilized on polyaniline deposited on vertically assembled carbon nanotubes wrapped with ssDNA, *Biosens. Bioelectron.*, 24 (2009) 2772–2777.
139. S.H. Jhi, S.G. Lourie, M.L. Cohen, Electronic properties of oxidized carbon nanotubes, *Phys. Rev. Lett.*, 85 (2000) 1710–1713.

140. H.Z. Geng, K.K. Kim, K.P. So, Y.S. Lee, Y. Chang, Y.H. Lee, Effect of acid treatment on carbon nanotube-based flexible transparent conducting films, *J. Am. Chem. Soc.*, 129 (2007) 7758–7759.
141. A. Tselov, M. Woodson, C. Qian, J. Liu, Microwave impedance spectroscopy of dense carbon nanotube bundles, *Nano Lett.*, 8 (2008) 152–156.
142. T.W. Tombler, C. Zhou, L. Alexseyev, J. Kong, H. Dai, L. Liu, C.S. Jayanthi, M. Tang, S.-Y. Wu, Reversible electromechanical characteristics of carbon nanotubes under local-probe manipulation, *Nature*, 405 (2000) 769–772.
143. S. Kazaoui, N. Minami, N. Matsuda, H. Kataura, Y. Achiba, Electrochemical tuning of electronic states in single-wall carbon nanotubes studied by *in situ* absorption spectroscopy and ac resistance, *Appl. Phys. Lett.*, 78 (2001) 3433–3435.
144. S. Banerjee, T. Hemraj-Benny, S.S. Wong, Covalent surface chemistry of single-walled carbon nanotubes, *Adv. Mater.*, 17 (2005) 17–29.
145. H. Ulbricht, G. Moos, T. Hertel, Physisorption of molecular oxygen on single-wall carbon nanotube bundles and graphite, *Phys. Rev. B*, 66 (2002) 075404–075410.
146. S. Liu, L. Yuan, Z. Zheng, Z. Tang, Recent advances in nanosensors for organophosphate pesticide detection, *Adv. Powder Technol.*, 19 (2008) 419–441.
147. A.P. Periasamy, Y. Umasankar, S.M. Chen, Nanomaterials – acetylcholinesterase enzyme matrices for organophosphorus pesticides electrochemical sensors: a review, *Sensors*, 9 (2009) 4034–4055.
148. G. Liu, Y. Lin, Biosensor based on self-assembling acetylcholinesterase on carbon nanotubes for flow injection/amperometric detection of organophosphate pesticides and nerve agents, *Anal. Chem.*, 78 (2006) 835–843.
149. R.P. Deo *et al.*, Determination of organophosphate pesticides at a carbon nanotube/organophosphorus hydrolase electrochemical biosensor, *Anal. Chim. Acta*, 530 (2005) 185–189.
150. J. Wang, Carbon-nanotube based electrochemical biosensors: A review. *Electroanal.*, 17 (2005) 7–14.
151. C. Cremisini, S. Disario, J. Mela, R. Pilloton, G. Palleschi, Evaluation of the use of free and immobilized acetylcholinesterase for paraoxon detection with an amperometric choline oxidase based biosensor, *Anal. Chim. Acta*, 311 (1995) 273–280.
152. S. Zhang, H. Zhao, R. John, Development of a quantitative relationship between inhibition percentage and both incubation time and inhibitor concentration for inhibition biosensors – theoretical and practical considerations, *Biosens. Bioelectron.*, 16 (2001) 1119–1126.
153. J.M. Gong, L.Y. Wang, L.Z. Zhang, Electrochemical biosensing of methyl parathion pesticide based on acetylcholinesterase immobilized onto Au-polypyrrole interlaced network-like nanocomposite, *Biosens. Bioelectron.*, 24 (2009) 2285–2288.
154. A. Mulchandani, W. Chen, P. Mulchandani, J. Wang, K. Rogers, Biosensors for direct determination of organophosphate pesticides, *Biosens. Bioelectron.*, 16 (2001) 225–230.
155. E. Turiel, A. Martin-Esteban, P. Fernandez, C. Perez-Conde, C. Camara, Molecular recognition in a propazine-imprinted polymer and its application

- to the determination of triazines in environmental samples, *Anal. Chem.*, 73 (2001) 5133–5141.
156. S.Q. Liu, L. Yuan, X.L. Yue, Z.Z. Zheng, Z.Y. Tang, Recent advances in nanosensors for organophosphate pesticide detection, *Adv. Powder Technol.*, 19 (2008) 419–441.
 157. Y. Gao, I. Kyratzis, R. Taylor, C. Huynh, M. Hickey, Immobilization of acetylcholinesterase onto carbon nanotubes utilizing streptavidin-biotin interaction for the construction of amperometric biosensors for pesticides, *Anal. Lett.*, 42 (2009) 2711–2727.
 158. G.D. Liu, Y.H. Lin, Biosensor based on self-assembling acetylcholinesterase on carbon nanotubes for flow injection/amperometric detection of organophosphate pesticides and nerve agents, *Anal. Chem.*, 78 (2006) 835–843.

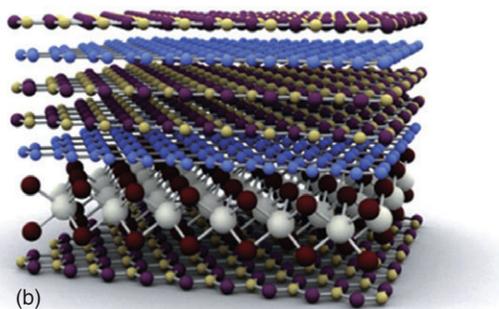
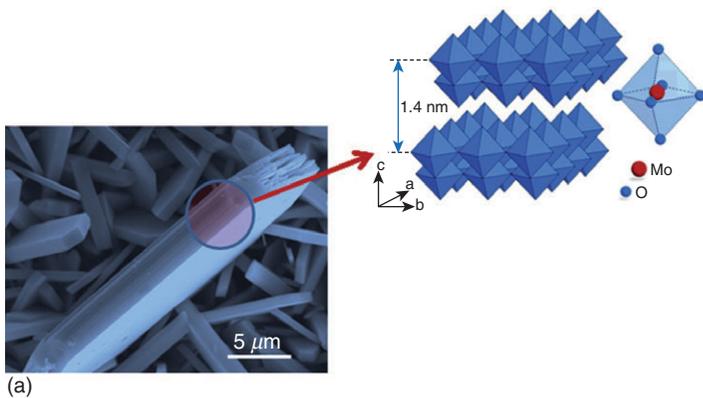


Plate II (Chapter 3) (a) SEM image of layered MoO_3 (false coloured) with structure of thermodynamically stable $\alpha\text{-MoO}_3$. (b) Example of 2D-based hetero-structure.

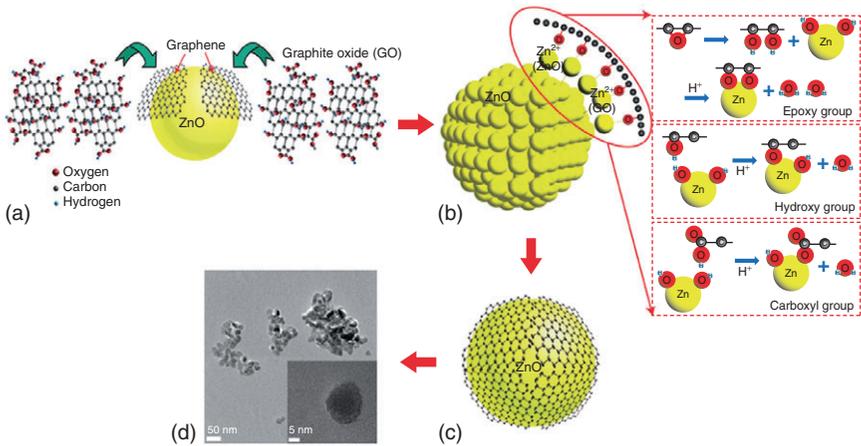


Plate III (Chapter 3) (a) Schematic of chemical exfoliation of graphene sheets from GO. (b) Synthesis of ZnO-graphene QDs from GO and zinc acetate dihydrate. The QDs are synthesized via chemical reaction between three kinds of functional groups (carboxyl ($-\text{COOH}$), hydroxy ($-\text{OH}$) and epoxy), of GO and Zn^{2+} . The magnified image shows chemical bonding between the functional groups and Zn^{2+} . (c,d) Schematic of graphene-covered ZnO QDs (c) and TEM image (d). Inset to (d) enlarged HRTEM image of the ZnO-graphene QDs. (Reprinted from Ref. 67 with permission from Nature Publishing)

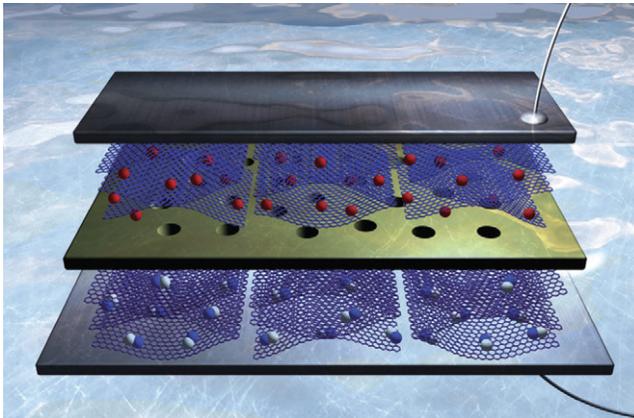
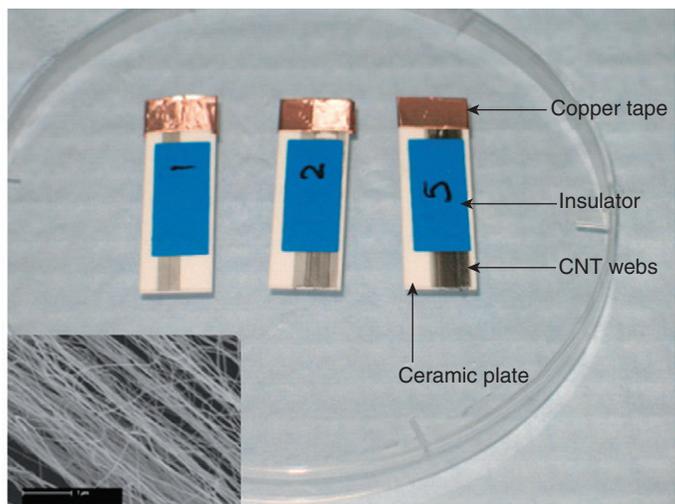
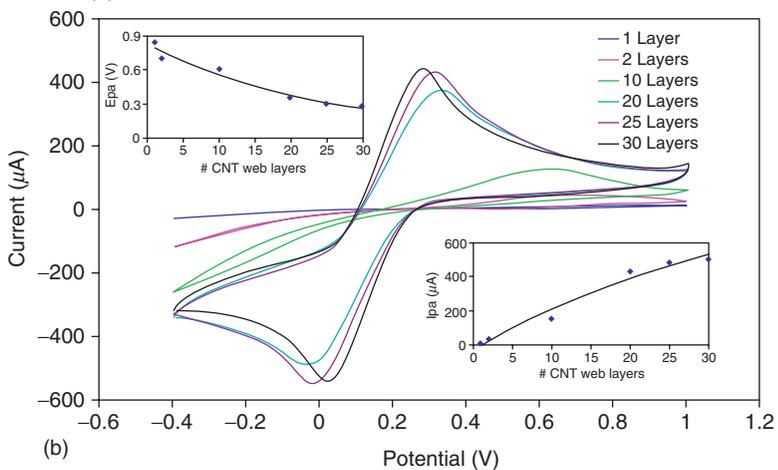


Plate IV (Chapter 3) Design of the planar sandwich nanostructure of the device based on graphene nanosheets doped by various QDs. (Reprinted from Ref. 11 with permission from Nature Publishing)



(a)



(b)

Plate V (Chapter 3) (a) Samples of the CNT-based planar bio-sensors developed by CSIRO for pesticide control. Inset: CNT web. (b) CV measurements using electrodes with different CNT web layers in 10 mM $K_3[Fe(CN)_6]$ and the effect on the anodic peak potential (top inset) and anodic peak current (bottom inset). (Reprinted from Ref. 136 with permission from Wiley Publishing)

Two-dimensional semiconductor nanocrystals: new direction in science and technology

DOI: 10.1533/9781782422242.139

Abstract: This chapter discusses various two-dimensional (2D) semiconductor nanocrystals as a new direction in modern science and technology. The chapter begins with a review of the physicochemical properties of graphene and its impact on science and industry. It then reviews other 2D nanocrystals: chalcogenides, titanium dioxide (TiO_2), molybdenum trioxide (MoO_3), tungsten trioxide (WO_3), niobium pentoxide (Nb_2O_5), tantalum pentoxide (Ta_2O_5) and zinc oxide (ZnO). The chapter concludes by discussing the future impact of the combination of the 2D semiconductor nanocrystals into 3D structures.

Key words: two-dimensional (2D) nano-crystals, graphene, 2D chalcogenide and oxide nanostructures

4.1 Physical and chemical properties of graphene

Although atomically-thin carbon network, better known as graphene, has been under development in the years since 2000, the shift to its exploration as a potentially excellent nanomaterial for such applications as nano-electronics, nano-architectures, hydrogen production and storage, polymer composites for nano-optics, catalysis and photovoltaics has taken place only after the award of Nobel price in physics in 2010 to scientists working in the field.¹⁻⁹ From the viewpoint of its electronic properties, graphene presents itself as a zero-gap nanocrystal with unique electronic properties originating from the fact that the charge carriers in graphene are described by a Dirac-like equation, rather than the usual Schrödinger equation.² Owing to its perfect crystal structure and low-energy quasi-particles, it is obeying a linear dispersion relation, similar to mass-less relativistic particles. Consequently, there have been many observations of peculiar electronic properties^{3,5,8-11} including ballistic transport, pseudo-spin chirality based on the ‘Berry phase’, a room-temperature half-integer ‘chiral’ quantum Hall effect, and conductivity without charge carriers. This has inspired extensive research into using graphene as an electronic material, a material for sensing electrodes and an interconnect material. For example, from the point of view of sensors development, incorporation of catalyst particles into individual graphene sheets can provide greater versatility in

carrying out selective measurements or catalytic processes.⁹ Up to now, graphene has exhibited electron mobility of up to $\sim 15\,000\text{ cm}^2\text{ V}^{-1}\text{ cm}^{-1}$ or $10^6\ \Omega\text{ cm}$ (lower than Ag), a super-high portability of temperature-independent charge carriers of $200\,000\text{ cm}^2\text{ V}^{-1}\text{ s}^{-1}$ (200 times higher than Si) and an effective Fermi velocity of 10^6 m s^{-1} at room temperature, similar to the speed of light. More importantly, in addition to its unique electronic properties, graphene possesses excellent mechanical, optical, thermal and electrochemical properties which are superior to other carbon allotropes, such as graphite, diamond, fullerene and carbon nanotubes (CNTs), as shown in Table 4.1.^{5,6,12-19} Single-layer graphene has distinctive mechanical properties with a Young's modulus of 1.0 TPa and a stiffness of 130 GPa, optical transmittance of $\sim 97.7\%$ (absorbing 2.3% of white light) and superior thermal conductivity of $5000\text{ W m}^{-1}\text{ K}^{-1}$ (about 100 times that of Cu). It also has a high theoretical specific surface area of $2620\text{ m}^2\text{ g}^{-1}$, extreme electrical conductivity and desirable flexibility. Furthermore, there has been some speculation that, due to its particular properties, graphene could possibly out-perform CNTs, graphite, metals and semiconductors where it is used as an individual substance or as a component in a hybrid or composite nanomaterial.

4.2 The impact of these properties on science and industry

4.2.1 Synthesis of graphene

A number of different graphene synthesis methods have been developed over the last few years. However, despite great efforts, they have failed to deliver a commercially valuable technology, and mechanical exfoliation^{16,17} has remained as one of the most reliable approaches for the development of atomically-thin sheets of graphene since 2004. The fact of the matter is that the mechanical exfoliation technique yields graphene sheets which are virtually free from crystal defects, having therefore a very high concentration of carrier mobilities. A typical example of such a graphene structure is shown in Fig. 4.1. Another approach to mechanical exfoliation of graphene is based on the concept of anodic bonding.⁸ In this approach, bulk graphite was bonded onto borosilicate glass at a particular temperature and voltage and then peeled away leaving behind a single-layer or a few-layer sheet of graphene on the substrate.¹⁸

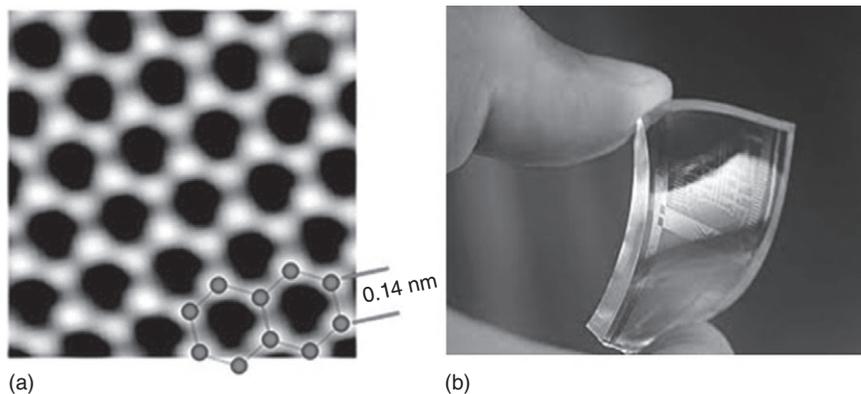
Unfortunately, during the last few years these graphene fabrication techniques have proved to be difficult to upscale to mass production. In addition to mechanical exfoliation, current strategies of interest for producing single-layer graphene nanosheets can be summarized into the following eight groups:¹⁹

Table 4.1 Properties of graphene and other carbon allotropes¹⁹

Carbon allotropes	Graphite	Diamond	Fullerene (C ₆₀)	Carbon nanotube	Graphene
Hybridized form	sp ²	sp ³	Mainly sp ²	Mainly sp ²	sp ²
Crystal system	Hexagonal	Octahedral	Tetragonal	Icosahedral	Hexagonal
Dimension	Three	Three	Zero	One	Two
Experimental specific surface area (m ² g ⁻¹)	~10–20	20–160	80–90	~1300	~1500
Density (g cm ⁻³)	2.09–2.23	3.5–3.53	1.72	>1	>1
Optical properties	Uniaxial	Isotropic	Non-linear optical response	Structure-dependent properties	97.7% of optical transmittance
Thermal conductivity (W m ⁻¹ K ⁻¹)	1500–2000 ^a , 5–10	900–2320	0.4	3500	4840–5300
Hardness	High	Ultrahigh	High	High	Highest (single layer)
Tenacity	Flexible non-elastic	–	Elastic	Flexible elastic	Flexible elastic
Electronic properties	Electrical conductor	Insulator, semi-conductor	Insulator	Metallic and semiconducting	Semi-metal, zero-gap semiconductor
Electrical conductivity (S cm ⁻¹)	Anisotropic, 2–3 × 10 ^{10a} , 6 ^b	–	10 ⁻¹⁰	Structure-dependent	2000

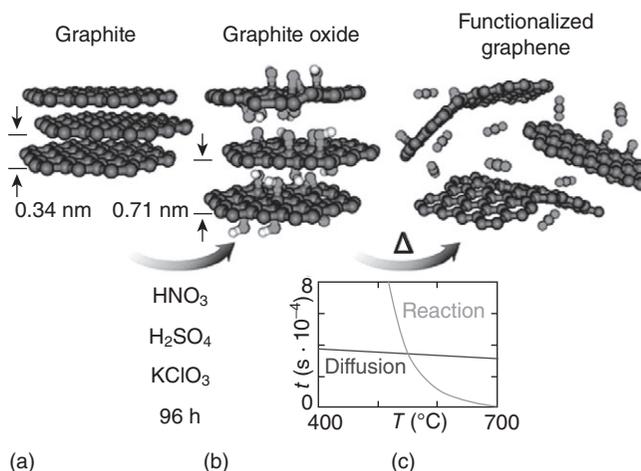
^a a-direction.

^b c-direction.



4.1 (a) An atomic-resolution image (TEAM 0.5) of a clean and structurally perfect synthesized graphene sheet. Individual carbon atoms appear white in the image. (Reprinted from Ref. 1 with permission from The Royal Society of Chemistry) (b) Graphene image showing transparency and flexibility of the material.

1. Chemical exfoliation of graphitic materials. This approach involves oxidation, intercalation, exfoliation and/or reduction of graphite, graphite oxide, expandable graphite, CNTs and graphite fluoride.^{20–23} To produce graphene sheets by this method, sufficient oxidation of graphite is required during acid treatment and adequate pressure during thermal heat treatment. This method is schematically presented in Fig. 4.2, and a more detailed understanding of the mechanism of thermal exfoliation is provided by McAllister *et al.*²³ Further development of chemical exfoliation can yield a large quantity of reduced graphene oxide, which can be produced at a relatively low cost.
2. Chemical vapour deposition (CVD) of graphene from the decomposition of hydrocarbons at high temperatures on either metallic substrates or metal oxide. CVD processes can be thermally- or plasma-enhanced, producing uniform, large-area, high-quality graphene on Ni, Cu or Pt.^{24–26} However, despite all its advantages, this process is still power-consuming and relatively expensive and so requires further substantial improvement.
3. Epitaxial growth of graphene on SiC^{27,28} and metal (Ru, Pt)²⁹ single-crystal substrates at high temperature and under ultra-high vacuum. With this approach, graphene is produced on the Si-terminated face of single-crystal H-SiC by thermal desorption of Si, which leaves behind a two- to three-layer thick graphene sheet. Unfortunately, this method requires high-vacuum conditions, high-cost fabrication systems and is not yet adapted to prepare atomically-thin graphene. Moreover, achiev-



4.2 Graphene sheets developed by the thermal reduction methods: a – graphite; b – strong oxidation of graphite leads to formation of oxygen containing functional groups within the interlayer; c – exfoliation takes place once the rate of decomposition of the functional group is higher than that of the gas diffusion. (Reprinted from Ref. 23 with permission from The American Chemical Society)

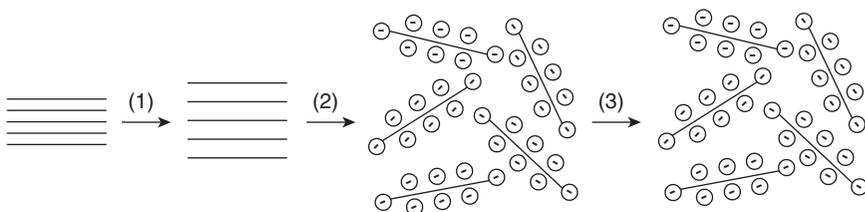
ing large graphene domains with uniform thickness remains a challenge.

4. Ultrasonic cleavage of graphene.^{30,31} In this method, graphene precursors are suspended in water or organic solvents and then ultrasonic agitation is applied to provide the energy to cleave the graphene precursors. The idea is conceptually similar to mechanical exfoliation and is based on the experimental observation that CNTs can be successfully exfoliated in solvents such as N-methylpyrrolidone.³² The success of ultrasonic cleavage depends on the appropriate choice of solvents and surfactants, as well as the sonication frequency, time and amplitude.^{33,34}
5. Graphene synthesis from organic compounds. This is used to synthesize nano/micrographene and graphene-based materials from structurally defined precursors, such as polycyclic aromatic hydrocarbons. This technique can precisely control the formation of molecular graphene (<5 nm), nanographene (5–500 nm) and integrated macrographene (>500 nm) with well-defined structures and high processability.³⁵ However, the production rate of this method is relatively low.³⁶
6. Graphene sheets can be generated by unrolling CNTs.^{37–39} In this process, NH_3 -solvated Li^+ is electrostatically attracted into negatively charged multi-walled CNTs (MWCNTs). Simultaneous intercalation of Li and NH_3 into MWCNTs can increase the interlayer distances from 3.35 to 6.62 Å, allowing the exfoliation to follow.³⁷ Another variation of this

approach is based on strong oxidizing agents, such as KMnO_4 , to cut along the longitudinal direction of MWCNTs.³⁸ The exfoliation process can then be executed at room temperature. Another modification of this method utilizes Ar plasma etching to unzip MWCNTs, producing graphene nanoribbons.⁴⁰

7. An important alternative scheme for preparing graphene is the chemical reduction method.^{41–43} This mechanism involves the complete exfoliation of graphene oxide into individual graphene oxide sheets followed by the *in situ* reduction of these layers to produce individual graphene-like sheets.⁴⁴ Figure 4.3 schematically illustrates the main stages of this method. Successful reduction of the exfoliated graphene oxide requires careful selection of the reducing agent, solvent and/or surfactant to maintain a stable suspension. It has been determined that hydrazine hydrate is the optimum reducing agent for producing very thin graphene-like sheets.⁴⁵ The two steps of reduction and sulphonation of the graphene oxide can increase the concentration of graphene produced to a reasonable value (2 mg mL^{-1}).⁴⁶
8. Graphene can also be grown from solid-state carbon,⁴⁷ by direct arc discharge of graphite,⁴⁸ reduction of ethanol by sodium metal⁴⁹ and the thermal splitting of SiC granules.⁵⁰ All of these methods have their advantages and disadvantages in terms of both the scalability of the method and the quality of the graphene produced.^{15,51,52}

The chemical exfoliation method is considered to be the most reliable technique for low-cost production of graphene in large quantities.²⁰ It involves the oxidation of well-stacked graphite to graphite oxide,⁵³ which is then followed either by chemical reduction of graphene oxide to obtain reduced graphene oxide⁴⁵ or by thermal exfoliation of graphite oxide^{54–57} to produce graphene. Generally, oxidation results in an increase of the *d*-spacing and intercalation between adjacent graphene layers, thus weakening the interaction between adjacent sheets, finally leading to the delamination



4.3 Chemical reduction routine: (1) graphite is oxidized to graphite oxide; (2) exfoliation of graphite oxide yields graphene oxide suspended on solution; (3) chemical reduction of graphene oxide yields the conducting graphene. (Reprinted from Ref. 1 with permission from The Royal Society of Chemistry)

of graphene oxide in an aqueous solution. It has been found that the higher the heating rate, the greater both the exfoliation and de-oxygenation degrees of graphite oxide. High annealing temperature is considered to be an essential factor in eliminating any structural defects. Consequently, the development of a hydrogen arc discharge exfoliation method ($>2000^{\circ}\text{C}$) for the synthesis of high-quality graphene nanosheets from graphite oxide with excellent electrical conductivity ($\sim 2 \times 10^3 \text{ S cm}^{-1}$) and good thermal stability ($\sim 601^{\circ}\text{C}$) has been reported.⁵⁷ Complete exfoliation and considerable de-oxygenation of graphite oxide and defect omission can be simultaneously achieved during the hydrogen arc discharge exfoliation process.

In addition to easy bulk synthesis, a major advantage of both graphene oxide and reduced graphene oxide is the controlled attachment of oxygen species on the edges and surfaces of the graphene sheets. This enables the formation of stable graphene oxide dispersions and easy functionalization in aqueous and organic solvents,⁵⁸ hence offering a variety of opportunities for the simple processing of structure-dependent functionalized graphene-based materials.⁵⁹ It is evident that future progress in development of methods for the mass-production of graphene will be focused on innovation in its low-cost, large-area, large-scale production for various applications.

4.2.2 Potential applications of graphene

Since the discovery of its unique outstanding properties, graphene has been utilized in a large number of applications, either as an individual material or as a component in a hybrid or composite material. It should be stressed that the field of graphene-based applications is expanding very fast and obviously the impact of graphene on the increased functionality of many applications is enormous. Some of the recently published material^{15,51,60–64} provides detailed descriptions of physical, chemical and electrical properties of graphene which are relevant to its synthesis and applications. This chapter, therefore, provides only an overview of recent progress in graphene/metal oxide composites as advanced electrodes for high-performance systems, emphasizing the importance of synergistic effects between graphene and metal oxides in the composites and the improvement of their electrochemical properties, including high capacity/capacitance, increased rate capability, excellent cyclic stability and high energy density and power density. It should be clearly stated that in order to achieve the desired functionality of graphene-based devices, graphene has to be nano-engineered, i.e. structural defects or impurities must be introduced within the graphene structure. The study of the influence of intrinsic defects on the electronic properties of graphene is still in its infancy, and experimental data relating defect concentration to changes in electronic and optical characteristics are urgently needed. On the other hand, it is clear that extrinsic

defects such as foreign atoms on different positions have a strong influence on electron–electron interaction and, consequently, the charge distribution and band structure of graphene.⁶⁴

It is expected that the following applications of graphene may be considered as breakthroughs in the near future:

- Graphene-based electronics and optoelectronics, partially replacing conventional silicon-based electronics. Graphene possesses ultrafast THz electron mobility that is favourable for building smaller, faster, cheaper electronic devices such as ballistic transistors,⁶⁵ spintronics,⁶⁶ field-effect transistors (FETs),⁶⁷ and optoelectronics.^{3,68}
- Graphene-filled polymer composites with high electrical and thermal conductivity, good mechanical strength and low percolation threshold which, in combination with low-cost and large-scale production, allow a variety of performance-enhanced multifunctional uses in electrically conductive composites and thermal interface materials.^{69,70}
- CVD-grown graphene on Cu substrate for devices designed to energy harvest from water flow.⁷¹ There are two reasons why power generation from water flow over graphene is superior to CNTs: (i) in a bulk single-walled CNT only one-third of CNTs are metallic and the rest are semi-conducting,⁷² (ii) interfaces in CNT networks are lossy.⁷³
- Large-area CVD-grown graphene that is suitable to replace indium tin oxide (ITO) as cheaper, transparent conducting electrodes in various display applications such as touch screens.^{3,74,75}
- Graphene-based electrochemical storage energy devices.⁷⁶
- Graphene-based chemical and electrochemical sensors,^{13,60} dye-sensitized solar cells,^{77–79} organic solar cells,⁸⁰ field emission devices,⁸¹ catalysts,⁸² photocatalysts,⁸³ nanogenerators⁸⁴ and hydrogen storage.⁸⁵

There is no doubt that structurally modified graphene will offer additional and sometimes unexpected advantageous properties that will outperform those of CNT and graphite, resulting in the development of new and emerging applications. Future research may open completely new possibilities for graphene due to its unique properties, such as high surface area, ultra-thin thickness, excellent electrical and thermal conductivity, mechanical flexibility and high chemical functionality. All of these properties are relevant, for example, to further development of graphene/semiconductor and graphene/metal in composite nanomaterials. As a result, graphene can be utilized as an ideal 2D support for growing or assembling very small nanoparticles with well-defined structures, creating various graphene-based nanomaterials with excellent enhanced properties.^{86,87} Recent advances in the development of graphene/metal oxide composites, presented in Plate VI (see colour section between pages 232 and 233),¹⁹ suggest that, by employing such wet-chemical strategies as chemical *in situ* deposition,

sol–gel technology and hydrothermal synthesis in graphene/metal oxide nanocomposites, it is possible to create functional networks for a number of applications.

Plate VI highlights the synergistic effects of graphene/metal oxide composites, which can be briefly summarized as follows:

- Graphene is a novel 2D support for uniformly nucleating, growing or assembling metal oxides with well-defined size, shape, and crystallinity.
- Metal oxide nanoparticles between the layers of graphene can efficiently suppress the restacking of graphene.
- Graphene can act as a 2D conductive template for building a 3D interconnected conductive sensing platform to improve the electrical conductivity and charge transport of pure oxides as well as their sensitivity to the measuring parameters.⁸⁸ This advance increases sensitivity up to ~224 % compared to the similar graphene-based 2D sensing platform.
- Graphene can suppress the volume change and particle agglomeration of metal oxides during the charge–discharge process.
- Oxygen-containing functional groups on graphene ensure good interfacial interactions and electrical contacts between graphene and metal oxides.

Despite the short period of research, the greatly improved electrochemical performance, increased capacity/capacitance, advanced rate capability and cycling stability, and increased energy and power densities of graphene/metal oxide composites with anchored, wrapped, encapsulated, layered, sandwich and mixed structures have already been confirmed. However, notwithstanding the great achievements of the last few years in the development of graphene/metal oxide composites, several important challenges still urgently need to be addressed.¹⁹ These are as follows:

- Graphene/metal oxides interface control. A better understanding of the surface chemistry of graphene/metal oxides interfaces is critical for achieving a well-defined uniform structure on graphene, in particular by modifying the surface chemistry using covalent or non-covalent techniques to increase the charge transfer. Unfortunately, most graphene/metal oxide materials reported to date are synthesized simply by mixing or dispersing their inorganic components with graphene, and these materials exhibit poor interfacial interactions.
- Rational design and control of the morphology and phase composition of metal oxides deposited on graphene, thus ensuring better reproducibility and understanding of the structure–property relationships.
- Shift in development of reliable graphene/metal oxide composites towards miniature, lightweight, inexpensive and even flexible energy storage devices for advanced thin and wearable electronics. In this respect, graphene with its unique properties of being ultrathin,

lightweight (offering much higher power and energy with less device mass) and flexible (working well even under twisting and bending conditions) will open up enormous opportunities for the fabrication of thin and flexible electrodes for more delicate and fine but high-power and high-energy applications.

- New approaches to fabrication of graphene-based composites must be orientated towards controlled synthesis and device-performance of newly created composite materials with optimized properties and functionalities. This is essential to improve the overall performance of such graphene-based devices as energy storage, fuel cells and organic electronics.
- With respect to final industrial implementation, the successful application of graphene/metal oxide composites requires a comprehensive improvement in methodology and performance and better compatibility of the composite materials.
- Less complex and more cost-effective large-scale production of graphene remains the most important challenge to overcome.
- Clarification of the effects of anisotropy on the physical and electrochemical properties of the structure of graphene and other 2D functional nanosheets attached to it. This is particularly important for superior understanding of the relationship between Li storage and defects, layer number, sizes and surface chemistry. Further research should be focused on control of the size, morphology, quantity and distribution of the functional components and on improving the interfacial interactions between graphene and functional building blocks. It has been envisaged that in the near future graphene/metal oxide composite materials with continuous modifications will fulfil increasing demand in such practical applications as personal electronics, wireless communications, ultra-high sensitive and selective measuring devices, portable tools, hybrid electric vehicles, etc.

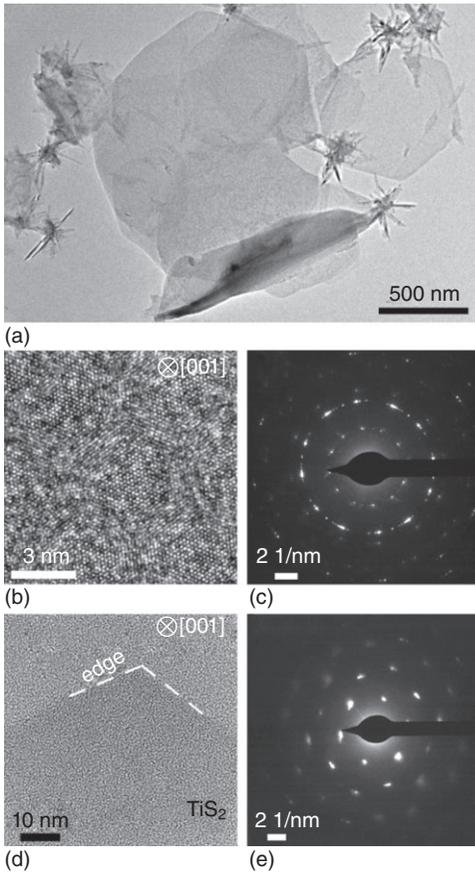
4.3 Chalcogenide semiconductor nano-crystals

As the thickness of the atomically-thin nanomaterials can be reduced down to the nanoscale, their already anisotropic physical, chemical and electrochemical properties can also be changed and modified,^{89–93} and this has been considered as one of their great advantages.⁹² However, it has to be admitted that up to now this particular emerging class of 2D or quasi-2D (Q2D) nanocrystals has been overlooked. The real technology-push strategy was definitely provided only after the award of the 2010 Nobel Prize in Physics for graphene. This recognition of the unique properties of 2D nanomaterials has opened up new opportunities for utilizing their discovered properties in physical, chemical, optical and electrochemical systems beyond

graphene.⁹⁴ The first reported class of atomically-thin 2D materials is layered dichalcogenides (XY_2 , where $X = \text{Mo, Ti}$ and $Y = \text{S, Se}$ and Te), which has been extensively investigated during 2011–2012.^{89–98} The results obtained so far have confirmed that chalcogenide semiconductors have sizeable differences in 2D and bulk conductivities ($\sigma_1/\sigma_2 \sim 10^2\text{--}10^3$).⁹⁵ This and other anisotropies arise from the presence of strong, interlayer $X\text{--}Y$ bonding, which is in contrast to the weak Van der Waals interactions between layers.⁹³ For example, TiS_2 crystallizes in a hexagonal layered structure, where one hexagonally packed sheet of Ti atoms is sandwiched between two hexagonal sheets of sulphur for each monolayer.⁹⁷

Conventional TiS_2 thin films can be prepared using the CVD technique.⁹⁸ It has recently been reported that a colloidal wet chemical approach has also been attempted as a first successful step in producing nanostructured TiS_2 .^{97,99–101} The TiS_2 nanosheets obtained are presented in Fig. 4.4. They were prepared by facile wet-chemical synthesis, which involved dissolving a slight molar excess of elemental sulphur in oleylamine, followed by the introduction of (TiCl_4) at room temperature in nitrogen. The reaction mixture was subsequently heat-treated to the final temperature of 300°C , where it was kept for 3 h. More details of this technique are given by Plashnitsa *et al.*⁹⁷ As a result, the captured TiS_2 nanoflakes were from 500–650 nm in dimensions with average thickness between 4 and 6 nm. Although many of these TiS_2 nanoflakes were bundled up during preparation, it has been verified that, by using this technique, single ultrathin TiS_2 nanosheets can be produced. This suggests that the post-synthesis exfoliation technique requires further optimization in order to be able to acquire high-quality TiS_2 nanoflakes in the future. Figure 4.4 shows low- (a) and high-resolution (Figs 4.4a and 4.4d) transmission electron microscope (TEM) images together with selected area electron diffraction patterns of TiS_2 nanosheets (Figs 4.4c and 4.4e). As clearly shown in Fig. 4.5b, the developed TiS_2 nanosheets have a high degree of crystallinity. This arises from the underlying hexagonal lattice characteristic of TiS_2 . This was also confirmed by the excellent relationship between experimental (100) and (110) d -spacings of 0.290 ± 0.008 and 0.170 ± 0.002 nm compared to the published values of 0.295 and 0.170, respectively.¹⁰²

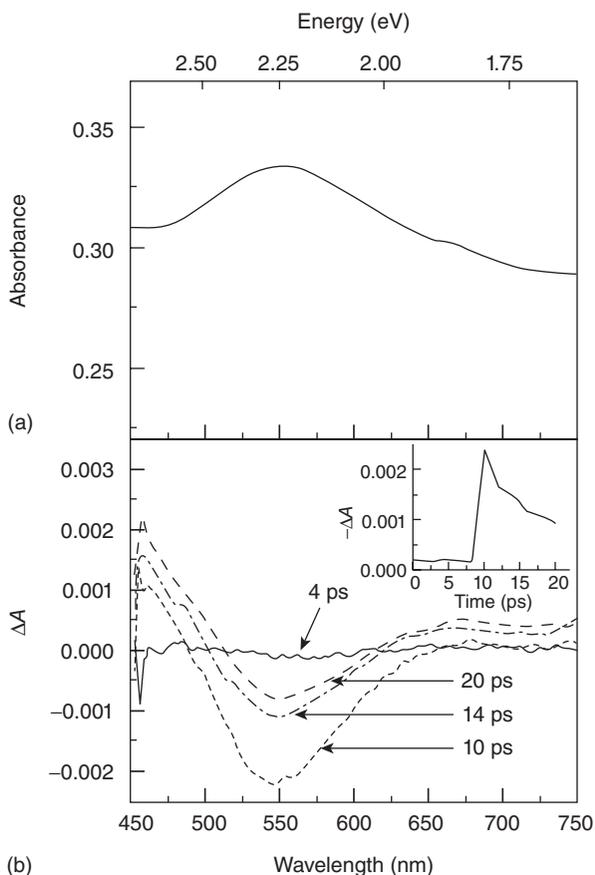
Previous theoretical investigations of nanostructured TiS_2 have outlined that the decrease in thickness of TiS_2 may lead to semimetal-to-semiconductor transition.^{103–105} Molecular dynamics and functional density theory simulations suggested that the bandgap (E_g) of nanostructured TiS_2 can be tuned from 1.25 (992 nm) to 1.65 eV (752 nm) once its morphology changes from that of nanotubes^{103,104} to single-sheet monolayers.¹⁰⁴ Calculated E_g values showed that the semiconductor TiS_2 nanosheets should be optically active in the visible range. Therefore, they can potentially be used for applications such as solar cells and photochemical water splitting



4.4 (a) Low- and (b) high-resolution TEM images of TiS_2 nanosheets. (c) AED pattern of TiS_2 nanosheets stacked atop each other. (d) High-resolution TEM image showing the edge of a single TiS_2 . (e) SAED pattern of a single TiS_2 nanosheet. (Reprinted from Ref. 97 with permission from The American Chemical Society)

cells. Thus the structural and optical properties of the developed TiS_2 nanocrystals determined experimentally were consistent with thin TiS_2 nanosheets possessing bulk-like electronic structure.

Experimentally obtained optical properties of the developed TiS_2 nanosheets are shown in Fig. 4.5. Figure 4.5a highlights the rapid carrier cooling that occurs following excitation (inset, Fig. 4.5b). Subsequent bleach recovery occurs on a slower ~ 15 ps timescale.⁹⁷ The delayed bleach recovery as well as strong linear absorption at ~ 550 nm suggest that this feature is the direct $M_2^- \rightarrow M_1^+$ transition of TiS_2 .^{106,107} The developed TiS_2 nanosheets were also able to absorb across the near-infrared spectra, confirming the



4.5 (a) Linear absorption and (b) corresponding transient differential absorption (TDA) spectra of TiS_2 nanosheets suspended in toluene (inset: kinetic trace of the bleach growth/recovery taken at 550 nm). (Reprinted from Ref. 97 with permission from The American Chemical Society)

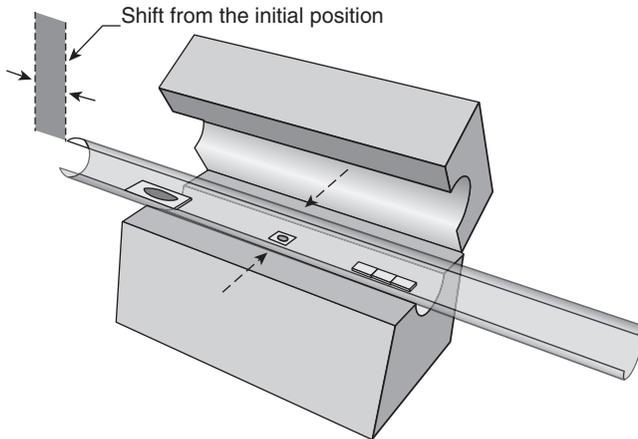
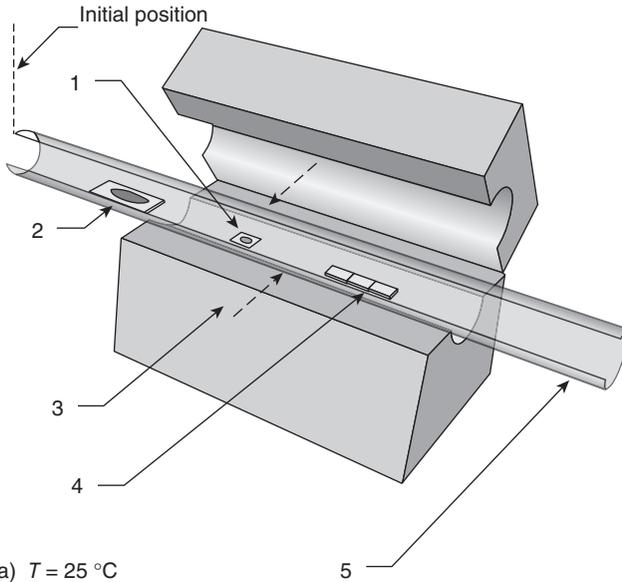
absence of a sizable band gap. All obtained optical properties of TiS_2 nanosheets proved that, despite their narrow thickness of 4–6 nm, they possess bulk-like optical properties.⁹⁷ Therefore, optimized synthesis of the large surface area of TiS_2 nanosheets may in turn lead to the eventual production of semiconductor TiS_2 having advanced electron affinities for potential solar-driven energy applications.

It has also been reported that wet-chemical techniques can be employed to break down less-ordered materials into more-ordered structures by meddling with molecular forces such as Van der Waals interactions. For instance, solvent liquid-exfoliation has been employed to produce single- or

multilayered 2D crystals of some dichalcogenides such as WS_2 , MoTe_2 , Bi_2Te_3 ¹⁰⁸ and MoS_2 .^{89,90,94,96} As an example, the atomic structure of MoS_2 can be visualized as presented in Plate VII (see colour section between pages 232 and 233). The figure shows a 3D atomic force microscopy (AFM) image of a MoS_2 nanosheet with an average thickness of ~ 11 nm deposited on Si substrate and a graphical interpretation of this structure. It is clear from this presentation that the developed MoS_2 nanosheets possess a multi-layered structure with a corresponding distance of ~ 0.65 nm between the MoS_2 layers.

Similarly to graphene, most of the above-mentioned dichalcogenides are naturally layered materials. Thus they can be dispersed as thin nanosheets by using the liquid-exfoliation method employing appropriate solvents or other developed state-of-the-art techniques. Eventually, these dichalcogenides can be manufactured as thin-film nanocomposites with tuned-up electronic, thermal and/or mechanical properties. However, diversification of the manufacturing techniques and methods and controlling the single-crystalline structure of formed 2D crystals are among the biggest existing challenges. In order to overcome these challenges and make appropriate nanostructures for various applications, it is vital to control the number of stacked layers on the substrate or the graphene surface. This can be achieved by manipulation of nanosheets or a two-step thermal evaporation approach⁹⁴ before exfoliation takes place. The reported combination of two-step thermal evaporation and exfoliation methods may offer a new opportunity, as it has already been demonstrated that layered hexagonal MoS_2 can be successfully sintered at temperatures less than 830°C , which is significantly less than the sintering temperature required for direct evaporation of MoS_2 .⁹⁰ The experimental set-up for this method is shown in Fig. 4.6.⁹⁴

The key advance in the thermal evaporation technique was a set-up in a horizontal furnace incorporating a quartz tube in an argon environment at a flow rate of $\sim 200\text{cm}^3/\text{min}$. To produce suitable MoO_3 nanostructures for further exfoliation, MoO_3 nanopowder was placed on a quartz substrate located in the centre of the furnace tube. Sulphur powder was placed upstream relative to the gas flow direction, 20 cm from the MoO_3 powder. Quartz substrates were placed along the downstream side for the MoS_2 deposition. The deposition process was conducted by simultaneously evaporating both the sulphur powder and the MoO_3 nanoparticles in an argon environment.⁹⁴ Further annealing was carried out in a sulphur-rich environment to enhance the presence of MoS_2 . Initially, the centre of the quartz tube was offset from the centre of the furnace and was heated at a rate of $20^\circ\text{C}/\text{min}$ (Fig. 4.6a). As soon as the centre of the furnace reached 750°C , the quartz tube was pushed in (Fig. 4.6b), placing the centre of the tube at the centre of the furnace. This procedure allows the MoO_3 and the sulphur to evaporate simultaneously. Subsequently, the set-up was held at the set



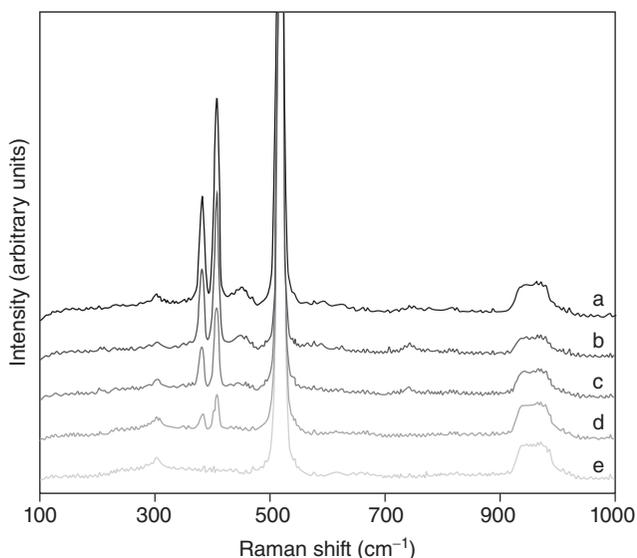
4.6 Experimental set-up: (a) initially at room temperature, the centre of the tube is offset from the center of the furnace and in (b) at $750\text{ }^{\circ}\text{C}$, the tube is pushed inside the furnace aligning the center of the tube with the centre of the furnace. [1 – MoO_3 nanopowder; 2 – sulphur powder; 3 – horizontal furnace; 4 – quartz substrates for deposition; 5 – quartz tube] (Reprinted from Ref. 94 with permission from The Royal Society of Chemistry)

temperature for the experimental annealing duration. The thermal evaporation process was performed at different temperatures and durations in order to determine the optimal experimental conditions for layered MoS₂ deposition. Three annealing conditions were explored: 775 °C for 60 min, 830 °C for 60 min and 830 °C for 180 min.⁹⁴ A sintering temperature of 830 °C for 180 min was found to be optimal for the development of MoS₂ nanostructures. At the end of the process, the temperature was ramped down at 20 °C/min until room temperature was reached.⁹⁴

In order to obtain thin-layered MoS₂, a known mechanical exfoliation method has been applied for deposition of exfoliated nanoflakes onto silica on silicon (SiO₂/Si) substrates.^{109,110} AFM results confirmed that the developed exfoliated flakes were indeed layered, as shown in Plate VIII (see colour section between pages 232 and 233). Steps of ~0.6 nm were seen on both flakes, corresponding to the approximate thickness of a single atomic layer of MoS₂, as was presented in Plate VII. Plate VIIIa illustrates a random MoS₂ flakes consisting of a base of seven fundamental atomic layers with a few more stacked on top.

Raman spectroscopy has proved to be an excellent tool for the assessment and confirmation of the developed 2D materials obtained via the exfoliation method and, more importantly, the difference in properties between the bulk and 2D nanosheets.^{109,110} Raman spectra of randomly exfoliated MoS₂ nanoflakes of different thicknesses were obtained in order to determine their composition.⁹⁴ Figure 4.7 represents the Raman spectra of exfoliated MoS₂ nanoflakes with thickness reducing from 50 to 5 nm. The Raman spectra obtained revealed that the vibration modes for the MoS₂ nanoflakes are identical to the as-deposited MoS₂ films with no MoO₂ contamination with reducing thickness. This fact suggested that the top surface of the synthesized films is predominantly MoS₂ and the observed MoO₂ contribution in the X-ray diffractograms is mainly from the bottom of the films. The strong peak at 521 cm⁻¹ in all the spectra corresponds to the Si substrate, and is verified by a background spectral measurement (Fig. 4.7e).

Raman spectroscopy can also be successfully employed to characterize the effect of Li⁺ intercalation for various exfoliated flakes of different thicknesses. For example, Fig. 4.8 shows the Raman spectrum obtained before and after Li⁺ exposure of two randomly targeted MoS₂ nanoflakes. The shift of the Raman peaks for E_{2g}¹ and A_{1g} at a level of few atomic layers in comparison with the bulk material has been previously reported.¹¹¹ The spectra for MoS₂ nanoflakes in Fig. 4.8a (thin flake ~10 nm) and in Fig. 4.8b (thick flake > 20 nm) both show a shift in E_{2g}¹ and A_{1g} modes after intercalation.⁹⁴ For both MoS₂ nanoflakes, after the Li⁺ exposure the peak shift is observed to the right with respect to the initial Raman spectra before the exposure. However, as can be seen, the shift is significantly larger for the thinner flake. This is due to the fact that the Li⁺ ions only affect the surface of the MoS₂ nanoflakes and do not intercalate between the layers.



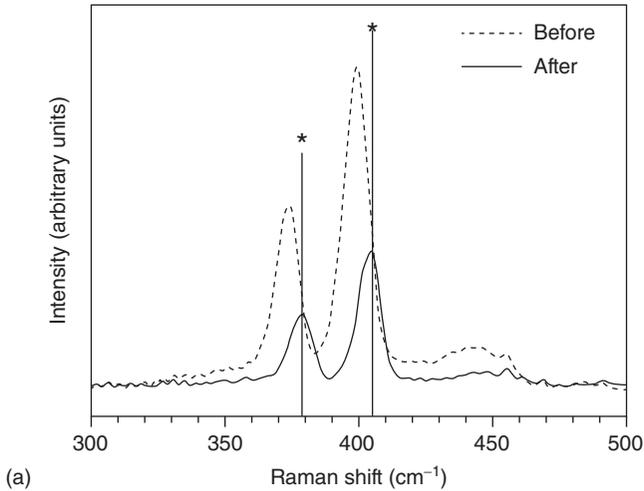
4.7 Raman spectra of (a–d) exfoliated MoS₂ flakes with thickness reducing from (a) to (d) in a range of 50 nm to 5 nm and (e) background substrate SiO₂/Si. (Reprinted from Ref. 94 with permission from The Royal Society of Chemistry)

Consequently, due to the smaller number of layers, the overall observed surface effect is much more enhanced in the thinner MoS₂ nanoflakes.

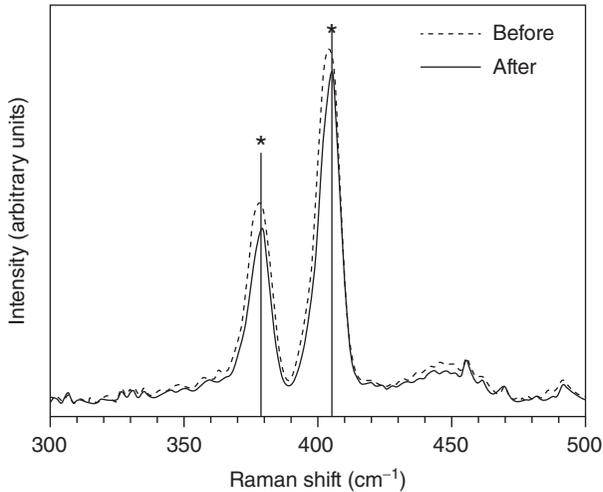
Up to now, MoS₂ has been considered as a more favourable nanomaterial among all the above-mentioned 2D dichalcogenides, as it has a relatively small bandgap of 1.29 eV and 1.90 eV for the bulk material and single layers, respectively.¹¹² Therefore, the combination of two-step thermal evaporation and exfoliation methods offers a new opportunity for the synthesis of such a nanomaterial at much lower temperatures than 2D MoS₂ nanosheets developed by the chemical evaporation technique. These atomically-thin MoS₂ nanocrystals can be utilized in the fabrication of electronic devices of high carrier mobility to pave the way for the next generation of advanced functional electronic devices.

One of the interesting recent applications of 2D MoS₂ nanocrystals is the transistor⁹⁰ and phototransistor⁹⁶ based on a single-layer MoS₂ nanosheet. Structurally, these functional devices are shown in Plate X (see colour section between pages 232 and 233) and Fig. 4.9, respectively.

A transistor based on 2D MoS₂ nanosheets is presented in Plate X. Specifically, a very interesting technical solution was found in compiling the transistor's layers (Plate Xc), as an atomic layer deposition (ALD) of 30 nm HfO₂ was achieved as a high- κ gate dielectric for the local top gate and mobility booster to realize the full potential of the single-layer MoS₂.⁹⁰ HfO₂



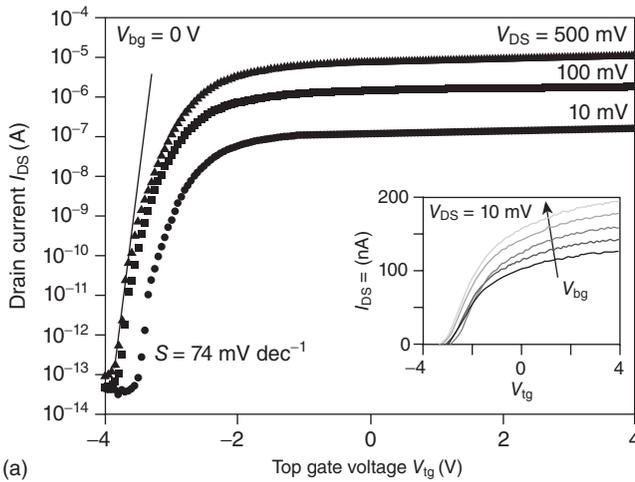
(a)



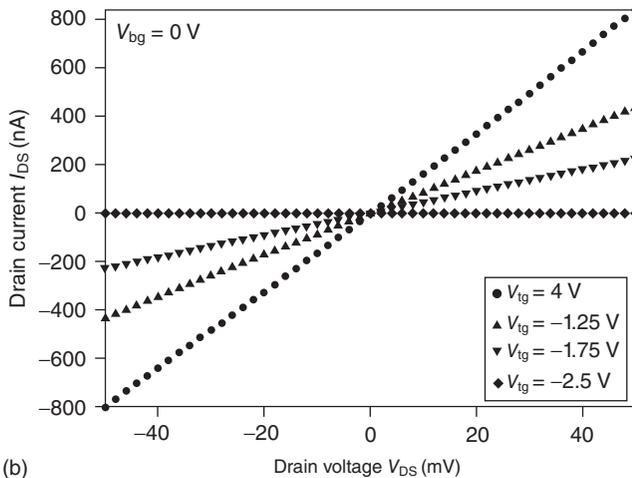
(b)

4.8 Raman spectra acquired before and after Li^+ intercalation of two different MoS_2 flakes: (a) thickness ~ 10 nm and (b) thickness > 20 nm. [*] represents the peak locations corresponding to the bulk MoS_2 deposition. (Reprinted from Ref. 94 with permission from The Royal Society of Chemistry)

was selected due to its high dielectric constant of 25, bandgap of 5.7 eV and the fact that it is commonly used as a gate dielectric by both the research community and the major microprocessor manufacturers.¹¹³ MoS_2 monolayers were deposited on doped Si substrates covered with 270 nm thick SiO_2 (Plate Xa). As a correlation between contrast and thickness for optical detection of single-layer MoS_2 has been established,⁹⁰ electrical contacts



(a)



(b)

4.9 Local gate control of the MoS₂ monolayer transistor. (a) $I_{DS}-V_{tg}$ curve recorded for a bias voltage ranging from 10 to 500 mV. (b) $I_{DS}-V_{DS}$ curve recorded for different values of V_{tg} . The linear dependence of the current on bias voltage for small voltages indicates that the Au contacts are ohmic. (Reprinted from Ref. 90 with permission from Nature Publishing)

were prepared using electron-beam lithography followed by deposition of 50 nm thick Au electrodes. The device was then annealed at 200 °C to remove resist residue¹¹⁴ and decrease contact resistance. At this point the single-layer MoS₂ devices exhibited a typical mobility in the range 0.1–10 cm²V⁻¹s⁻¹, similar to reported values for single layers¹¹⁵ and thin crystals containing more than 10 layers of MoS₂.¹¹⁶ This is lower than the

previously reported phonon-scattering-limited room-temperature mobility in the $200\text{--}500\text{cm}^2\text{V}^{-1}\text{s}^{-1}$ range for bulk MoS_2 .¹¹⁷ The final structure, composed of two FETs connected in series, is shown in Plate Xb. The top-gate width of the device was $4\mu\text{m}$ and the top-gate length, source-gate and gate-drain spacing were approximately 500nm .

It is well-known that the ability to control charge density in a local manner independent of a global back gate is one of the crucial requirements for building integrated circuits based on single MoS_2 layers. It has been executed by applying a voltage V_{tg} to the top gate, separated from the monolayer MoS_2 by 30nm of HfO_2 , while keeping the substrate grounded.⁹⁰ The corresponding transfer characteristic is illustrated in Fig. 4.9a.

For a bias of 10mV an on-current of 150nA ($37\text{nA}\mu\text{m}^{-1}$) has been recorded and current on/off ratio $I_{\text{on}}/I_{\text{off}} > 1 \times 10^6$ for the $\pm 4\text{V}$ range of V_{tg} , an off-state current $< 100\text{fA}$ ($25\text{fA}\mu\text{m}^{-1}$) and a gate leakage $< 2\text{pA}\mu\text{m}^{-2}$. The observed current variation for different values of V_{tg} indicated that the field-effect behaviour of the transistor based on single-layer MoS_2 is dominated by the MoS_2 channel and not the contacts. At the drain source bias $V_{\text{DS}} = 500\text{mV}$, the maximal measured on-current was $10\mu\text{A}$ ($2.5\mu\text{A}\mu\text{m}^{-1}$), with $I_{\text{on}}/I_{\text{off}}$ higher than 1×10^8 for the $\pm 4\text{V}$ range of V_{tg} .⁹⁰ The device transconductance, defined as $g_{\text{m}} = dI_{\text{DS}}/dV_{\text{tg}}$, at $V_{\text{DS}} = 500\text{mV}$ is $\sim 4\mu\text{S}$ ($1\mu\text{S}\mu\text{m}^{-1}$), similar to values obtained for high-performance CdS nanoribbon array transistors ($2.5\mu\text{S}\mu\text{m}^{-1}$ at $V_{\text{DS}} = 1\text{V}$).¹¹⁸ For comparison, high-performance top-gated graphene transistors can have normalized transconductance values as high as $1.27\text{mS}\mu\text{m}^{-1}$.¹¹⁹ Figure 4.9b clearly illustrates the large degree of current control in the single-layer MoS_2 -based transistor, where I_{DS} versus V_{DS} is plotted for different values of voltage applied to the local gate. The sub-threshold slope for the transition between the *on*- and *off*- states was deduced from the channel current dependence on top-gate voltage and was 74mV/dec for a bias $V_{\text{DS}} = 500\text{mV}$.

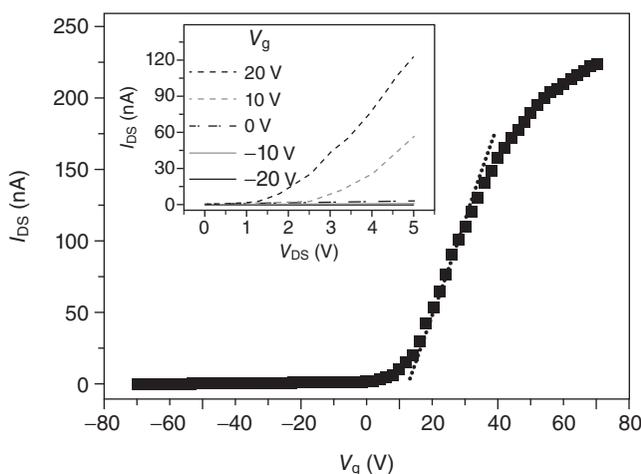
Being a direct gap semiconductor, single layers of MoS_2 offer the intriguing possibility for the realization of an inter-band tunnel FET, which is characterized by a turn-on sharper than the theoretical limit of 60mVdec^{-1} for classical transistors and consequently smaller power dissipation. This feature has remained difficult to achieve in the case of Si, an indirect gap semiconductor, because inter-band transitions there require phonons and recombination centres.¹²⁰

A phototransistor based on a mechanically exfoliated single-layer MoS_2 nanosheet is shown in Plate IX (see colour section between pages 232 and 233) and its light-induced electric properties were recently investigated in detail. It was shown that the photocurrent generated from the phototransistor is solely determined by the illuminated optical power at a constant drain or gate voltage. It should be stressed that the single-layer MoS_2 -based phototransistor exhibited better photoresponsivity compared

to the graphene-based device.⁹⁶ The switching behaviour of photocurrent generation and annihilation could be completely finished within *c.* 50 ms, and it exhibited acceptable stability.

In a typical experimental procedure, single-layer MoS₂ was deposited onto on a Si/SiO₂ (300 nm) substrate using the scotch-tape-based mechanical exfoliation method.^{4,86,90} Plates IXa and IXb represent the optical and AFM images of the obtained single-layer MoS₂ on Si/SiO₂, respectively. The height of the single-layer MoS₂ measured by AFM is *c.* 0.8 nm, which was consistent with the previously published values.^{112,115} The photoluminescence (PL) of a single-layer MoS₂ sheet was measured at room temperature using a 488 nm laser, as shown in Plate IXc. The dominant PL peak at 676 nm arises from the direct intra-band recombination of the photogenerated electron–hole pairs in the single-layer MoS₂, and the weak shoulder peak at *c.* 623 nm is attributed to the energy split of valence band spin–orbital coupling of MoS₂.¹²¹ Raman spectroscopy was used to further confirm the single-layer MoS₂ (inset in Plate IXc). Two peaks at 384 and 400 cm⁻¹ are attributed to the in-plane E_{2g} and out-of-plane A_{1g} vibration of single-layer MoS₂, respectively.¹¹¹ An optical image of the single-layer MoS₂ FET device, where two Ti/Au electrodes and Si were used as the source, drain and back gate, respectively, is presented in Plate IXd.⁹⁶

The developed phototransistor based on a single-layer MoS₂ nanosheet has exhibited *n*-type semiconducting behaviour, as shown in Fig. 4.10, which was consistent with the previous reports.^{112,115} Typical *n*-type doping might



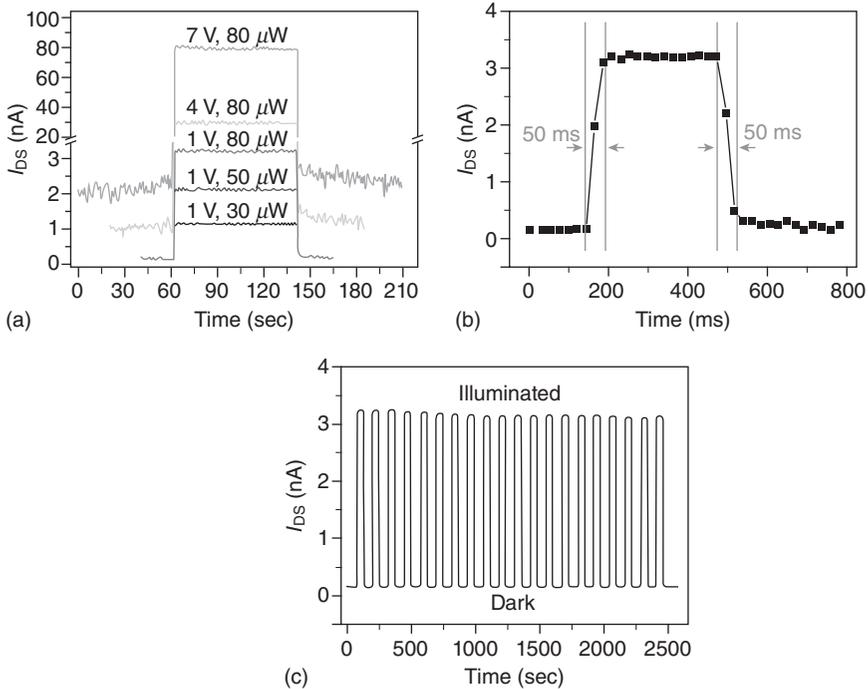
4.10 Room-temperature electrical characteristic of single-layer MoS₂ FET at drain voltage of 3 V. The is used to calculate the channel mobility. Inset: Plot of drain current (I_{DS}) vs voltage (V_{DS}) at different gate voltage (V_g , from -20 to 20 V). (Reprinted from Ref. 96 with permission from The American Chemical Society)

appear from such impurities as halogen (Cl or Br) atoms, which could replace sulphur atoms in the natural MoS₂ crystals or exist as the interstitial atoms in the interlayer gap of MoS₂. This increases the total electron concentration of the host MoS₂ system, resulting in an *n*-type doping for MoS₂.⁹⁶ The field-effect mobility of this single-layer MoS₂ device can be estimated as follows:⁹⁰

$$\mu = \frac{L}{W \times (\epsilon_0 \epsilon_r / d) \times V_{ds}} \times \frac{dI_{ds}}{dV_g} \quad [4.1]$$

where the channel length L is 2.1 μm , the channel width W is 2.6 μm , ϵ_0 is $8.854 \times 10^{-12} \text{Fm}^{-1}$, ϵ_r for SiO₂ is 3.9 and d is the thickness of SiO₂ (300 nm). The calculated mobility of this device is *c.* 0.11 $\text{cm}^2 \text{V}^{-1} \text{s}^{-1}$, which is comparable with the previous results from the bottom-gate FETs reported by other research groups.^{90,112} However, the reported mobility is far lower than the $\sim 200 \text{cm}^2 \text{V}^{-1} \text{s}^{-1}$ obtained from the top-gate device by deposition of the high- κ gate dielectric of HfO₂, used for the device mobility booster, on the top of MoS₂.⁹⁰ The likely reason is that the trap/impurity states exist at the SiO₂ surface in the bottom-gate transistor, and the scattering from these charged impurities degrades the device mobility.^{90,122,123} Reduction of the surface traps/impurities in the bottom-gate dielectric was expected to improve the mobility of such single-layer MoS₂-based bottom-gate FET devices. It has to be noted that the enhanced mobility and on/off ratio from the developed single-layer MoS₂ device were attributed to the thermal annealing treatment after the device fabrication, which could remove the photoresist residue and improve the electrode contact.¹¹⁴

Good stability and excellent photoswitching characteristics for devices based on single-layer MoS₂ nanosheets were obtained at room temperature in air. Figure 4.11a illustrates the photocurrent as a function of time under conditions of alternating darkness and illumination at different optical power and drain voltage. The switching behaviour of the drain current, that is the current ramps to a high value (on state) under illumination and resumes to the low value (off state) under dark, was clearly recorded. The generated photocurrent increased with the incident optical power and drain voltage. For instance, when the optical power was changed from 30 to 80 μW at constant drain voltage of 1V the photocurrent increased, as expected, from 1.0 to 3.1 nA. Note that the photocurrent further increased from 3.1 to 77.5 nA when the drain voltage increased from 1 to 7V at constant optical power of 80 μW .⁹⁶ Such drain voltage-dependent photocurrent generation indicated that some photogenerated charge carriers cannot be converted to the photocurrent when the applied drain voltage is low. This was reasonable since a larger drain voltage can better drive photogenerated charges to electrode, or suppress photogenerated charges from the recombination.



4.11 (a) Photoswitching characteristics of single-layer MoS_2 phototransistor at different optical power (P_{light}) and drain voltage (V_{DS}). (b) Photoswitching rate and (c) stability test of photoswitching behaviour of single-layer MoS_2 phototransistor at $V_{\text{DS}} = 1\text{ V}$, $P_{\text{light}} = 80\ \mu\text{W}$. (Reprinted from Ref. 96 with permission from The American Chemical Society)

Figure 4.11b shows investigation of photoswitching behaviour for a single-layer MoS_2 phototransistor. The measured switching duration for the current rise (from off to on) or decay (from on to off) process was only *c.* 50 ms. Rapid photo-switching behaviour can only be obtained at different V_{ds} or P_{light} . Furthermore, the stability of such switching behaviour was demonstrated by applying multiple illuminations on the device for ~ 50 s. As Fig. 4.11c explains, the on-off switching behaviour can be sustainable even after 20 cycle repeats. However, the photocurrent response rate in our single-layer MoS_2 is still lower than that from graphene (tens of picoseconds), as the carrier transport in graphene is much faster.¹²⁴

Another recent development of applications based on single-layer MoS_2 nanosheets is a transparent top-gate phototransistor with single-, double- and triple-layer MoS_2 nanosheets.¹²⁵ This device was analysed by photoelectric probing equipped with a patterned transparent gate electrode on top of a 50 nm thin oxide dielectric. The device based on triple-layer MoS_2

exhibited improved photodetection capabilities for red light whilst similar devices based on single and double layers were more appropriate for green light detection. This is schematically presented in Plate XI (see colour section between pages 232 and 233). According to the photoelectric probing results obtained from the working nanosheet transistors, single-layer MoS₂ had a significant energy bandgap of 1.82 eV. At the same time, devices based on double- and triple-layer MoS₂ nanosheets showed reduced values of 1.65 and 1.35 eV, respectively. Thus, the electrical and photoelectric properties of the practical phototransistors can be tuned up by appropriate modulation of the thickness of MoS₂ sheets given that the mobility and the optical bandgap can be controlled by the adjustment of MoS₂ layers.

4.4 Titanium dioxide nanocrystals

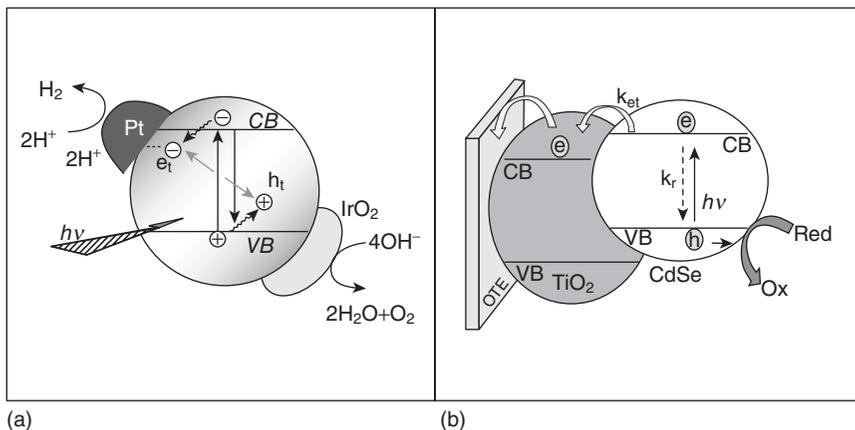
Since early in the 21st century, research into 2D semiconductor oxides has emerged as a new scientific direction independent of the development of 2D dichalcogenides owing to the unique multifaceted, structural and functional properties of these nano-oxides. 2D metal oxides such as TiO₂, MoO₃, WO₃, V₂O₅ and Nb₂O₅ are of special interest in the electronics, optics, catalysts and sensors industries. Most of these semiconductor oxides can be exfoliated. Although the highest carrier mobility observed so far has been in graphene, it has its own drawbacks: zero-bandgap in its pristine form, low affinity and adhesion to the ceramic substrate and tendency to turn into nanotubes. All of the above-mentioned semiconductor oxides are already favoured for their photochromic and thermochromic properties and are widely used as electrochromic materials. WO₃, for example, has been widely accepted in smart windows that change their colour upon request. Most of these semiconductors have also been utilized in the development of electronic displays. It has also been recently shown that, as functional materials, they can be applied in the fabrication of FETs, for generating enhanced electric field emission, solar cells, in batteries, as catalysts and in various gas sensors.

By using these metal oxides in their 2D form, phonons and electrons can be confined. While this confinement reduces electron scattering, it increases phonon scattering. Reduction of electron scattering increases their mobility and, as a result, they can be used for the creation of fast electronic devices. 2D semiconductor nanocrystals can potentially offer a replacement for Si in the electronics industry. Structural devices based on 2D semiconductor oxides have the potential to significantly impact the development of fast, low-dimensional electronics and telecommunications elements such as ultrafast switches, amplifiers with large trans-conductance, ultrafast photo- and electrochromic transducers, highly sensitive detectors and optical modulators. Among the above-mentioned semiconductor oxides, TiO₂ has

probably been the most widely investigated, resulting in more than 13 600 publications in 2010–2011.¹²⁶ It has already been accepted for use in various practical applications, which have been comprehensively reviewed in one of the latest monographs¹²⁷ and recent relevant publications.^{127–139} One of the driving forces behind the improvement in efficiency of the TiO₂-based functional devices has been the need to comply with current clean-energy demands.¹⁴⁰

TiO₂ nanostructures have been very successful in capturing the attention of physical chemists, physicists, materials scientists and engineers in exploring their distinctive semiconductor and catalytic properties. Although TiO₂ (titania) exists in three common crystalline forms, rutile, anatase and brookite,¹²⁷ the most common state is rutile, as this is the only thermodynamically stable structure of TiO₂. All these forms contain six-coordinate Ti. Owing to its high UV absorbance, inertness to the chemical environment and long-term photostability, nanostructured TiO₂ has been widely utilized in a large number of modern applications: paints, pharmaceuticals, sunscreens, solar cells, catalysts and highly-sensitive and selective sensors. Many new properties of TiO₂ have been explored during the last few years as TiO₂ nanostructures of different shapes have been designed to tailor optical and electronic properties. New and advanced capabilities were found in 2D TiO₂ nanosheets with reduced bandgap of this new phase (~2.1 eV).¹⁴¹ However, to produce 2D TiO₂ nanostructures is not as straightforward as it might sound. The long-standing challenge is to produce a stable phase, which can withstand an atmospheric pressure, and therefore can be utilized in photocatalysis. It requires innovation both in the strategies of development of 2D TiO₂ nanosheets and in processing and characterizing the resulting properties of the developed nanostructures. Photocatalytic activation using TiO₂ nanoparticles is schematically presented in Fig. 4.12.¹³⁸

The standard rutile phase of TiO₂ has a large band gap (~3.0 eV) compared to a 2D TiO₂ nanostructure (~2.1 eV). It has been extensively investigated since year 2000 for its super hydrophilicity and has been used in environmental remediation and solar fuel production. As clearly shown in Fig. 4.12a TiO₂ band gap excitation causes charge separation, followed by scavenging of electrons and holes by surface adsorbed species. Alternatively, photocatalytic activity in the visible range can be extended by coupling with a sensitizing dye or short bandgap semiconductor (Fig. 4.12b). In this case, the combination of TiO₂ with semiconductor quantum dots (QDs) (for example, CdS, CdSe, PbS, PbSe) has been successfully adopted.¹⁴⁰ By controlling the surface treatment and medium conditions, it is possible to tune the photocatalytic properties of nanostructured TiO₂ for desired applications. In addition, TiO₂ has been very effective for the mineralization of contaminants from air and is used in commercial products such as self-cleaning glass and ceramic tiles. However, the utilization of TiO₂ in a wide

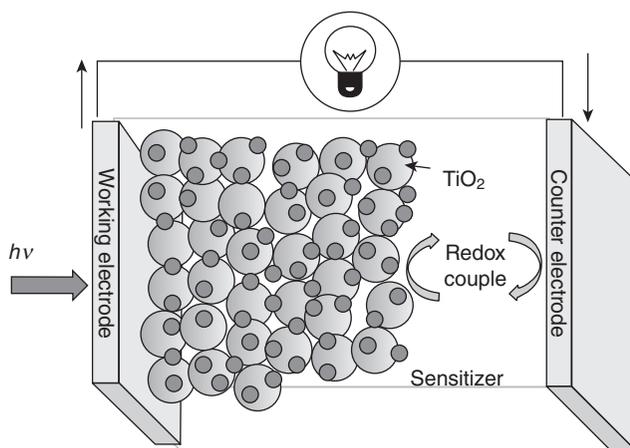


4.12 Photocatalytic activation using TiO_2 nanoparticles: (a) direct bandgap (UV) excitation; (b) sensitized charge injection using a visible light absorber. (Reprinted from Ref. 138 with permission from The American Chemical Society)

range of industrial applications for remediation of chemical contaminants from wastewater remains a difficult task because of adverse catalyst poisoning effects. Challenges remain to extend the photocatalytic response in the visible region. Despite extensive efforts to dope TiO_2 with C, N, S and transition metal ions, so far photocatalytic activity in the visible range has remained quite low.^{142–144}

One of the most advanced applications, where the nanostructured TiO_2 has in fact set a benchmark for industry, is solar cells.^{126,140,145–147} It has also been used in organic photovoltaics,¹⁴⁸ and QD-sensitized solar cells.^{149,150} Mesoscopic TiO_2 film, which has been employed as a substrate in these solar cells, assists in capturing electrons from an excited sensitizer or QD and transports the electrons to the collecting electrode surface, as schematically presented in Fig. 4.13. A quantitative model¹⁵¹ provides an explanation of the photovoltaic response of the dye-sensitized solar cell dependence on the non-linear charge recombination rate ($U_n = k_r n^\beta$, with $\beta < 1$) (where k_r is a simulation constant and n is a free electron concentration) and interprets the diffusion length measurements obtained from various techniques. Different spectroscopy studies have been conducted to probe the ultrafast charge injection from an excited sensitizer into TiO_2 and charge recombination processes to identify the factors that restrict the energy conversion efficiency. However, so far this capability has been only within the range 6–12%.^{152,153}

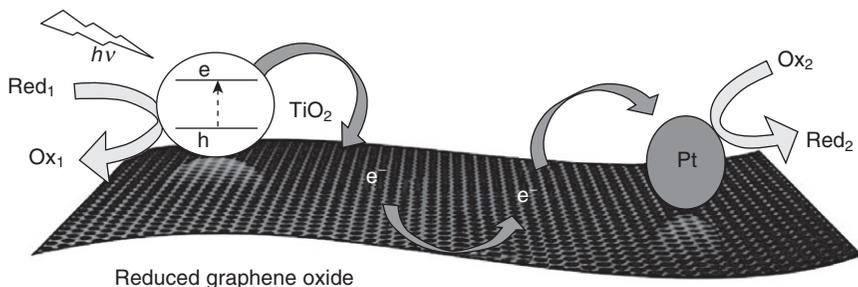
TiO_2 nanostructures of different shapes have also been designed in order to tailor optical and electronic properties.¹⁵⁴ While anodization of Ti foil is a common technique to prepare TiO_2 nanotubes, hydrothermal methods



4.13 Principle of liquid junction dye operation or QD-sensitized solar cell using mesoscopic TiO_2 films. (Reprinted from Ref. 138 with permission from The American Chemical Society)

provide convenient routes to fabricate 1D and 2D nanostructures. The ability to design anatase nanocrystals with the most active [001] facet has enabled researchers to systematically probe the catalytic activity of the phase of TiO_2 .¹⁵⁵

Future development of TiO_2 nanostructures is inseparably connected with tailoring desirable nanostructure architectures. Semiconductor–metal composite nanostructures in core–shell or coupled geometry is one of the approaches designed to enhance photocatalytic activity by facilitating reduction processes.¹⁵⁶ In this regard, electron storage, as well as localized plasmon resonance of metal nanoparticles embedded in the TiO_2 core or placed in close proximity to the TiO_2 nanostructure, have improved both photocatalytic and photovoltaic performances.¹⁵⁷ However, up to now, there have been only limited improvements. On the other hand, extensive tests have been carried out in order to establish a hole transfer process aided by an oxidation catalyst such as IrO_2 .¹⁵⁸ It has been stressed that better understanding of the interfacial charge transfer kinetics is important in designing more efficient photocatalysts for water splitting reactions.¹⁴² The fast development of a graphene-based platform for combination with nanostructured semiconductor oxides has been considered to be another fast-growing emerging area, allowing the design of photocatalysts with tailored properties.¹⁵⁹ For instance, graphene oxide-based TiO_2 composites have shown enhancement in both photocatalytic and photo-electrochemical properties.^{160,161} An illustration of the selective oxidation and reduction processes in the TiO_2 –graphene oxide–metal nanoparticle composite is shown in Fig. 4.14. This scheme encapsulated the essence of the graphene’s ability

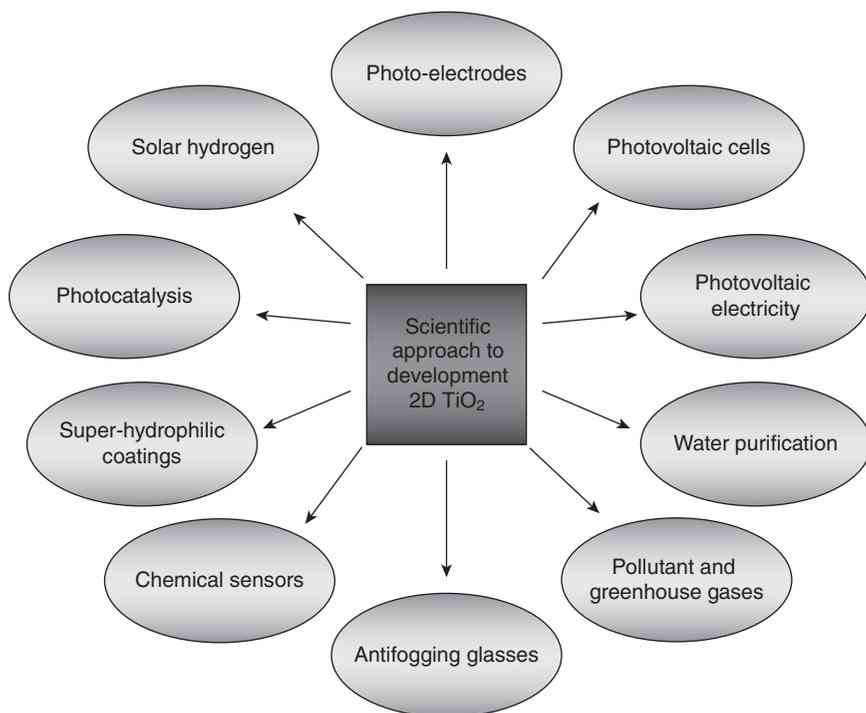


4.14 Illustration of selective oxidation and reduction processes in a TiO₂-graphene oxide-metal nanoparticle composite. (Reprinted from Ref. 138 with permission from The American Chemical Society)

to capture and shuttle electrons, which provides a unique opportunity for the development of a catalyst with multifunctional characteristics.¹⁶²

Consequently, efficient transfer of charges across the semiconductor interface is the key to converting light energy into electricity or fuel. Notwithstanding the recent advances in the development of TiO₂ nanostructures, it has to be admitted that up to now the improvement in the overall efficiency of TiO₂-based devices has been marginal. One of the areas where improvements are expected to take place in near future is in the device applications where nanostructured TiO₂ has been utilized in 2D form.¹⁴¹ The outlook for this development of nanostructured TiO₂ within the next few years will be focused on the additional manipulation of the interfacial charge transfer processes with surface modification and/or with a catalyst. This is because the reactivity of nanostructured semiconductors, including TiO₂, is closely related to their defect disorder.¹²⁶ In contrast to bulk materials, where knowing precisely how many dopant atoms are present is not so critical, doping 2D semiconductors with impurities by using the appropriate dopant in the correct amount has proven to be a very effective way of tuning their physicochemical properties. In fact, this is especially important when the nanomaterials to be doped are 2D nanocrystals, and the number of dopant atoms could be as low as one! The position of the dopant within the 2D nanosheet can also affect its properties; therefore, being able to visualize dopant atoms within such nanosheets is vital for better understanding and, more importantly, for controlling their behaviour.^{163,164}

The doping can enhance such typical defect-related properties as charge transport, electronic structure, surface reactivity and photoreactivity. Therefore, defect chemistry may be adopted in the future development of 2D nanocrystals with controlled features that are requested for specific purposes. A scientific approach to the imposition of specific disorder TiO₂-related characteristics which will be able to tailor these properties for various applications is schematically presented in Fig. 4.15. Thus, both

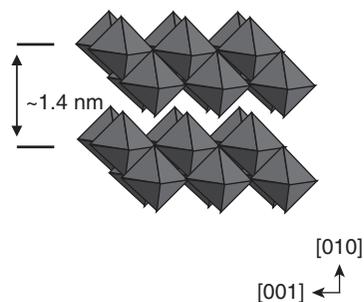


4.15 Schematic illustration of the potential applications of 2D TiO₂. (Reprinted from Ref. 218 with permission from Springer Verlag)

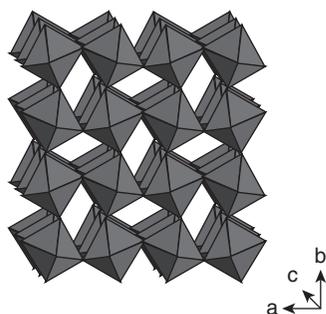
careful selection and controlled manipulation by processing conditions of 2D TiO₂ nanosheets are crucial factors in the further development of 2D nanostructures with selective *built-in* properties.

4.5 Molybdenum trioxide nanocrystals

Interest in the development of nanostructured MoO₃ is based on its multifaceted structural and functional properties. Similar to TiO₂, its thermo-¹⁶⁵ and photochromic¹⁶⁶ properties have attracted the attention of developers of electrochromic materials,¹⁶⁷ batteries,¹⁶⁸ catalysts,¹⁶⁹ photovoltaic cells¹⁶⁷ and highly sensitive and selective gas sensors.¹⁷⁰ Figure 4.16 overviews the two most common crystalline phases of MoO₃: the thermodynamically stable α -phase MoO₃ (Fig. 4.16a) and the metastable monoclinic β -phase MoO₃ (Fig. 4.16b).⁹¹ These phases have completely different crystalline structures, and the transformation of the α -phase into the β -phase of MoO₃ is possible at temperatures over 350 °C.¹⁷¹ The α -phase of MoO₃ possesses a unique layered structure: atomically-thin layers that have a thickness of



(a)



(b)

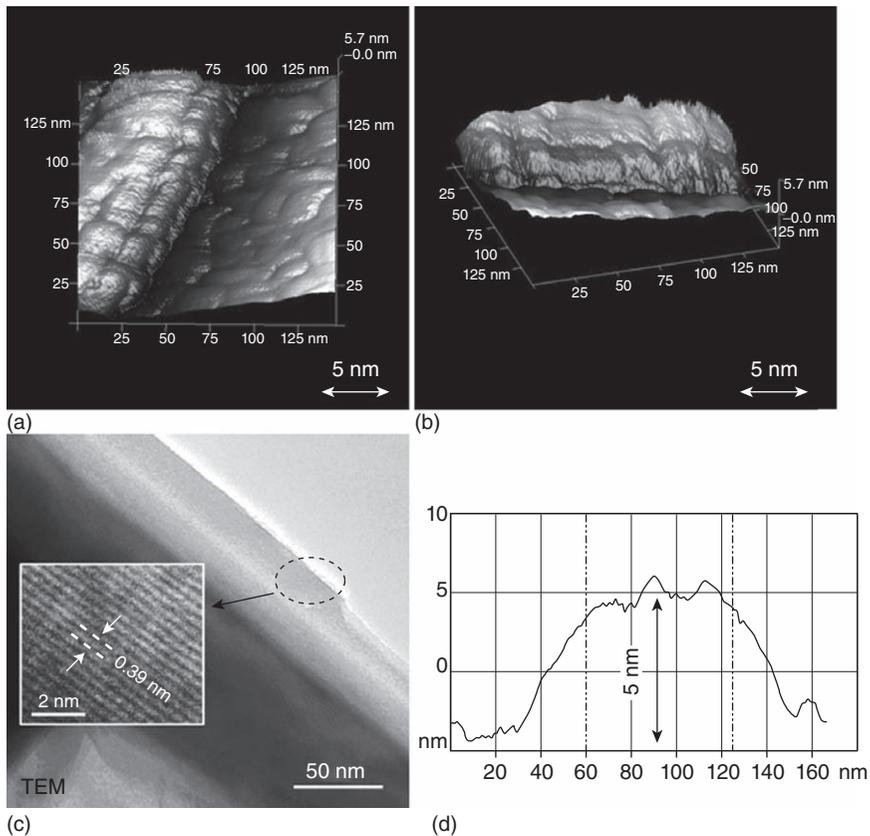
4.16 The two most common crystalline phases of molybdenum trioxide: (a) orthorhombic α - MoO_3 ; (b) monoclinic β - MoO_3 . (Reprinted from Ref. 218 with permission from Springer Verlag)

~ 0.7 nm and exist in double layers of link-distorted MoO_6 octahedra, which then stack up to cast secondary layers of several tens of nanometers.¹⁷² In each double layer, MoO_6 octahedra form corner-sharing rows along the $[100]$ plane and edge-sharing zigzag rows along the $[001]$ plane (Fig. 4.16a). Lamellar formation is made by linking the adjacent layers along the $[010]$ plane only through weak Van der Waals forces,¹⁷¹ while the internal interactions between atoms within the double layers are dominated by strong covalent and ionic bonding.

Several techniques for the development of stratified crystallites of orthorhombic α - MoO_3 have been employed so far. These include pulsed laser deposition,¹⁷³ sol-gel,¹⁷⁴ sputtering,¹⁷⁵ spray pyrolysis,¹⁷⁶ CVD,¹⁷⁷ thermal evaporation,^{178,179} hydrothermal,¹⁸⁰ anodization¹⁸¹ and electrodeposition.¹⁸² Amongst these techniques, electrochemical methods are more preferred, as they are generally easy to carry out and can be adapted to engineer physical and chemical properties of MoO_3 ,¹⁸³ followed by mechanical exfoliation similar to exfoliation of graphene. So far, there have been several scientific reports confirming the successful mechanical exfoliation

of MoO_3 and the development of 2D MoO_3 nanostructures as thin as ~ 5 nm.^{110,184} Figure 4.17 provides typical 3D scanning tunnelling microscope (STM) images (Figs 4.17a and 4.17b) and transmission electron microscope (TEM) image (Fig. 4.17c) of the developed 2D MoO_3 nanosheets with their measured thickness (Fig. 4.17d).

A recent report on atomically-thin MoS_2 nanosheets indicated that it is possible to enhance the mobility values of these MoS_2 nanostructures up to $200 \text{ cm}^2/\text{Vs}$.⁹⁰ However, considering that dichalcogenides generally have smaller relative dielectric constants than semiconductor oxides (e.g. ~ 5 for MoS_2), the mobility values obtained are still not high enough for acceptance of MoS_2 by the electronics industry. Therefore, development of 2D semiconductor oxides with higher dielectric constants offers a possible



4.17 Typical STM (a) and (b) images of exfoliated MoO_3 nanosheets with TEM image (c) and measured thickness (d) of the developed MoO_3 nanosheet. (Reprinted from Ref. 218 with permission from Springer Verlag)

solution.^{172,184} In contrast to dichalcogenides, a semiconductor oxide such as α -MoO₃ has a much higher dielectric constant (>500 for α -MoO₃).¹⁸⁵ The structure of α -MoO₃ comprises perfect planar crystals, held together by Van der Waals forces (Fig. 4.16a), which offers the potential to obtain 2D structures.¹⁷² Bulk MoO₃ in its intrinsic form still has a relatively wide bandgap (>2.7 eV), i.e. a value which is not yet suitable for making electronic devices. Thus, the development 2D α -MoO₃ nanosheet with following intercalation provides a practical alternative in tuning up its properties.

It is known that the reduction of α -MoO₃ results in reduced bandgap MoO_(3-x), and it is possible to tune the energy bandgap from a neutral value to zero.^{186,187} However, in material with low relative dielectric constants, this process increases the number of embedded Coulomb charges and possibly their detrimental effect on electron scattering, which is the main limiting factor in electron mobility. The carrier's motility in a thin layer is calculated using $\mu = e/m^*\langle\tau\rangle$ in which e is the point charge, m^* is the electron effective mass and τ is the transport relaxation rate of momentum in the plane. Using the Born approximation, the transport relaxation time can be calculated as follows.¹⁸⁸

$$\frac{1}{\tau} = \frac{2\pi}{\hbar} \sum_{k_z} \sum_{\mu} \int_{-\infty}^{+\infty} N_i^{(\mu)}(z) dz |V_{k-k_z}^{(\mu)}(z)|^2 \times f(k, k_z) \quad [4.2]$$

where $N_i^{(\mu)}(z)dx dy dz$ is the concentration of the μ^{th} kind of Coulomb charge centre within the volume $dx dy dz$ and $f(k, k_z)$ is a function of k and k_z vectors. $V_{k-k_z}^{(\mu)}(z)$ is a potential function showing the intensity of the scattering effects on free charges, and reducing its importance in obtaining large carrier mobilities. According to (4.2), in materials possessing high relative dielectric constants, such as α -MoO₃, the overall effect of Coulomb charges on $V_{k-k_z}^{(\mu)}(z)$ is reduced and the scattering effect is dominated by the optical and acoustic phonons. For instance, for a 2D material with a relative dielectric constant of ~ 5 and thickness of 10 nm, the mobility is approximately $\sim 550 \text{ cm}^2/\text{Vs}$, while, for higher dielectric materials of 500, this number advantageously increases up to $\sim 62\,000 \text{ cm}^2/\text{Vs}$.

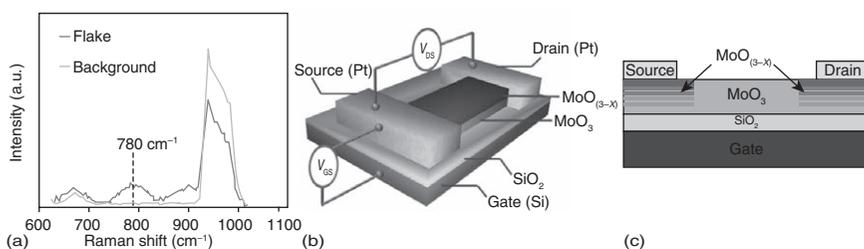
Raman spectra of 2D MoO₃ nanocrystals deposited on quartz substrates at different temperatures (Plate XIIa, see colour section between pages 232 and 233) revealed similar peak features corresponding to that observed in MoO_(3-x).¹⁸⁹ Further H⁺ intercalation of perfectly layered α -MoO₃ planar nanocrystals in liquid showed that both the colour of the MoO₃ nanosheets (Plate XIIb) and the corresponding Raman shift (Plate XIIc) depended on intercalation time. Raman spectra of the same nanosheet show that MoO_(3-x) evolved from the layered α -MoO₃, based on the fact that the sharp peak of MoO₃ at 820 cm^{-1} gradually disappeared and a broad peak at 780 cm^{-1} emerged. The Raman peak shift at 780 cm^{-1} is a strong indication of the

presence and strength of sub-stoichiometric crystal formation.¹⁸⁹ The MoO₃ bandgap was reduced from 3.25 to 2.65 eV under exposure to H₂ gas for 40 min (Plate XIId) and to smaller values (<2 eV) afterwards (which can be interpolated). Consequently, the presence of sub-stoichiometric MoO_(3-x), which displays reduced bandgap energy, was confirmed.¹⁸⁴

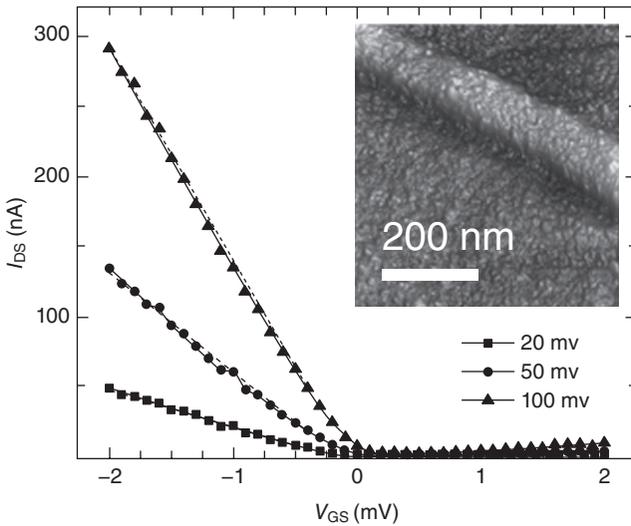
Mechanically exfoliated 2D MoO₃ nanosheets were deposited onto optically smooth 300 nm SiO₂ on highly *p*-doped Si substrates, as well as on Si substrates without the SiO₂ layers. Raman spectra of the 2D layer used in the FET (Fig. 4.18a) show similar peak features corresponding to that observed in MoO_(3-x). The FETs were reduced (Figs 4.18b and 4.18c), generating oxygen vacancies resulting in either the formation of sub-stoichiometric MoO_(3-x) on the top layers of the MoO₃ layer (for thicker layers) or throughout the layer (for thinner layers).

The drain current (I_{DS}) vs gate voltage (V_{GS}) characteristics of a MoO_(3-x) FET with flake dimensions of 800 × 80 × 11 nm are presented in Fig. 4.19. The calculated mobility of charge carriers at room temperature was ~1100 cm²/Vs. The mobility value over a period of five days remained within 10 % of variation.

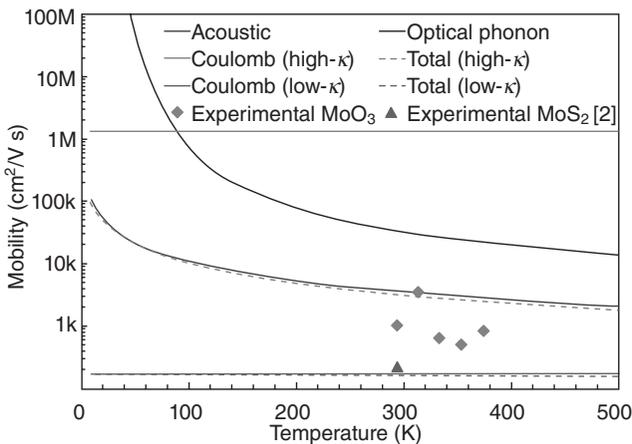
The experimental mobilities and the theoretical behaviour of the movement, calculated using the Born approximation with respect to temperature, are summarized in Fig. 4.20. The overall mobility influenced by coulomb, acoustic and optical phonon scattering mechanisms, presented in this figure for comparison, is calculated using Matthiesen's Rule.¹⁸⁴ Figure 4.20 clearly shows that the acoustic and optical phonon scattering effects are independent of the dielectric value of the material. In a low- κ (~5) material, the coulomb scattering effect seems to be the limiting mechanism of the overall mobility. As a result, the theoretical prediction of the overall mobility is around 170 cm²/Vs and the reported experimental value for 2D MoS₂ nanosheets closely matches this.⁹⁰ In a high- κ (~500) material, the coulomb



4.18 Raman spectra of MoO₃ nanosheet and corresponding background spectral acquisition with the same parameter (a); set-up of a MoO_(3-x)/MoO₃ FET I - V analysis (b) and (c) cross-sectional view of MoO₃ layers of the FET displaying the formation of sub-stoichiometry. (Reprinted from Ref. 184 with permission from Wiley)



4.19 Drain current (I_{DS}) vs gate voltage (V_{GS}) characteristics obtained at room temperature for different drain voltage (V_{DS}) values. Inset: 3D AFM image of the corresponding $\text{MoO}_{(3-x)}$ layer. (Reprinted from Ref. 218 with permission from Springer Verlag)



4.20 Charge carrier mobility dominated by different scattering mechanisms vs temperature characteristics. Theoretical predictions of total mobilities are in agreement with the experimental trend. (Reprinted from Ref. 218 with permission from Springer Verlag)

scattering effect is minimized and the mobility increases by an order of four. Hence, acoustic phonon scattering emerges as the dominant mechanism limiting overall mobility. The experimental transportability observed in the 2D $\text{MoO}_{(3-x)}$ FET was in the same order of magnitude and matches the theoretically predicted trend of the overall mobility.¹⁸⁴

Therefore, in high- κ nanomaterials, such as 2D $\text{MoO}_{(3-x)}$ nanosheets, the enhancement of total carrier mobility is limited by acoustic phonon scattering. The high- κ media advantageously reduce the coulomb scattering effect, which is generally the mechanism dominating overall mobility in low- κ materials. The mobility values observed so far readily exceed those of doped and low-dimensional Si. The relative abundance and the desirable electronic properties of 2D MoO_3 and similar transition semiconductor oxides render them to be suitable building blocks for future electronic applications.

4.6 Tungsten trioxide nanocrystals

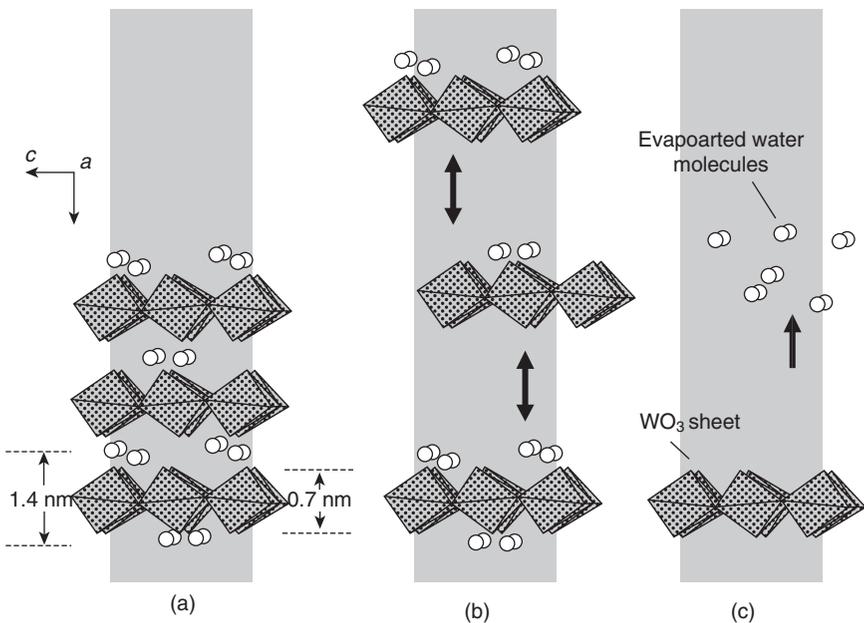
Tungsten trioxide (WO_3) is a transition metal oxide made up of perovskite units, which is well-known for its non-stoichiometric properties.¹⁹⁰ As WO_3 belongs to the same group of elements as MoO_3 , in some respects its structure is similar. Its phase classification is based on the tilting angles and rotation direction of WO_6 octahedra with reference to the 'ideal' structure (ReO_3 type). Crystals are generally formed by corner and edge sharing of WO_6 octahedra. Like other metal oxides, WO_3 crystal phase transitions can take place during annealing and cooling. It has been previously reported that for WO_3 , in bulk form, phase transformation occurs in the following sequence: monoclinic II ($\epsilon\text{-WO}_3$, $<-43^\circ\text{C}$) \rightarrow triclinic ($\delta\text{-WO}_3$, -43°C to 17°C) \rightarrow monoclinic I ($\gamma\text{-WO}_3$, 17°C to 330°C) \rightarrow orthorhombic ($\beta\text{-WO}_3$, 330°C to 740°C) \rightarrow tetragonal ($\alpha\text{-WO}_3$, $>740^\circ\text{C}$).¹⁹¹ The main physico-chemical properties and applications of WO_3 have been comprehensively described in a recent review.¹⁹²

The strong interest in WO_3 on the part of researchers and from various industries has been based on the versatile and exceptional chromic properties of nanocrystalline WO_3 . In comparison to many other semiconductor metal oxides, such as TiO_2 , ZnO , NiO and their sub-stoichiometric forms, investigation of WO_3 chromic properties is much more advanced.¹⁹³ Consequently, nanostructured WO_3 is also a well-studied material for photocatalysis and sensing.¹⁷⁰ Nevertheless, the importance of the development of WO_3 -based nanostructures for electrochromic devices (smart windows and EC displays),¹⁹⁴ dye-sensitized solar cells,¹⁹⁵ optical recording devices¹⁹⁶ and sensing applications¹⁷⁰ cannot be over-estimated. Consequently, new approaches to the synthesis of advanced WO_3 -based nanocrystals have emerged during last few years.^{109,197-199} Among those approaches, synthesis

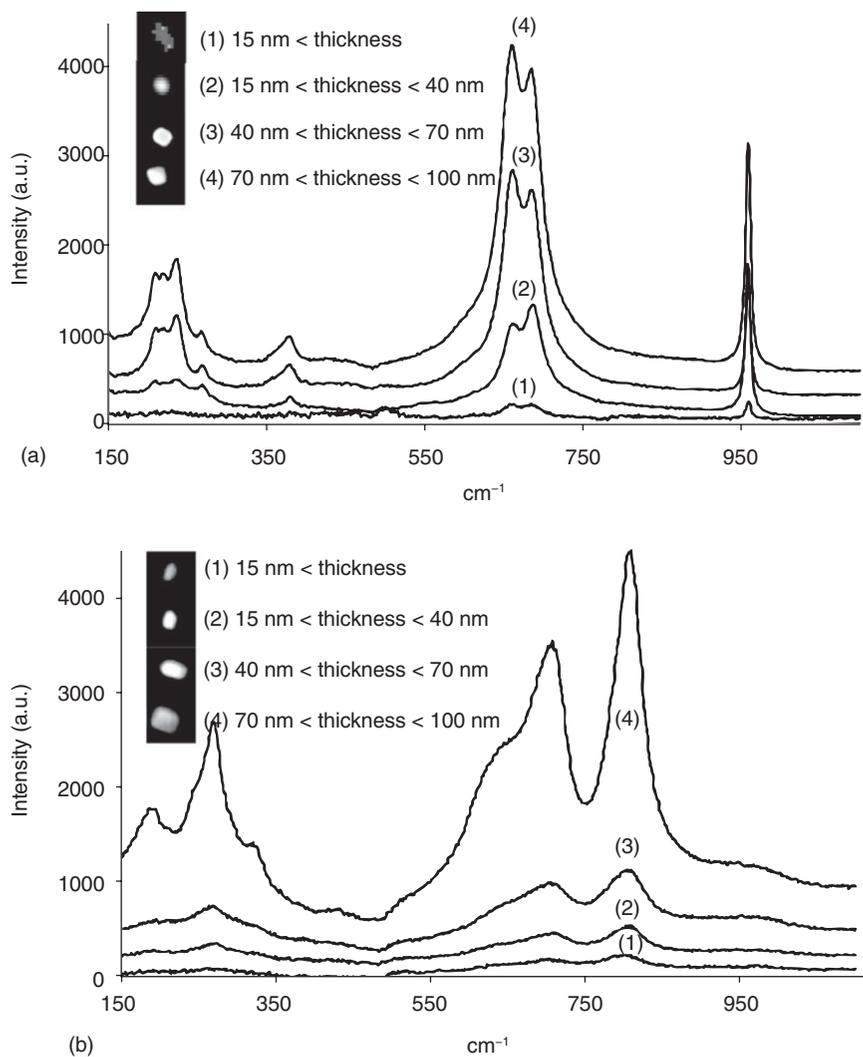
of atomically-thin nanosheets from hydrated WO_3 has proved to be a very effective and efficient method in the development of Q2D WO_3 .^{109,197} Figure 4.21 schematically represents details of the main stages in the development of 2D WO_3 nanosheets.¹⁰⁹

As a result of this new approach, Q2D WO_3 nanosheets with different thicknesses have been obtained. The thinnest nanosheets were less than 15 nm in thickness and had a faint blue appearance. The platelet colours (Fig. 4.22a) changed in the following order as a function of thickness: faint blue (<15 nm), white (15–40 nm), yellow (40–70 nm), orange (70–100 nm) and red (100–150 nm).¹⁰⁹

When the developing semiconductor oxide nanostructure possesses very small dimensions and is very thin, Raman spectroscopy is ideally suited for analysis of the atomically-thin layers of such nanomaterial. Given the low dimensionality of the atomically-thin layers, extracting crystallographic information using conventional methods, such as X-ray diffraction (XRD),



4.21 Schematic of the formation of a single layer of monoclinic WO_3 from layered hydrated WO_3 via an exfoliation process: (a) hydrated WO_3 ($\text{WO}_3 \cdot 2\text{H}_2\text{O}$), which is made of layers of WO_3 with H_2O molecules in between; (b) mechanical exfoliation separates layers at their weakest bonds into 1.4 nm sheets; (c) water molecules are evaporated and WO_3 layers of multiples of 0.7 nm thickness are formed after annealing. (Reprinted from Ref. 109 with permission from The American Chemical Society)



4.22 Raman spectra for $\text{WO}_3 \cdot 2\text{H}_2\text{O}$ for samples with the thickness of several fundamental sheets (less than 15 nm) to 100 nm. Optical images of these samples are shown in the left side: (a) non-annealed samples; (b) annealed at 300 °C. (Reprinted from Ref. 109 with permission from The American Chemical Society)

is largely unsuitable. To assess the influence of both thinning and annealing processes on the Raman vibration signatures, typically manifesting as symmetric features, as well as chemical bonds that occur during annealing, Raman spectroscopy was conducted on WO_3 sheets of different thicknesses. The results for the series of hydrated exfoliated WO_3 of different

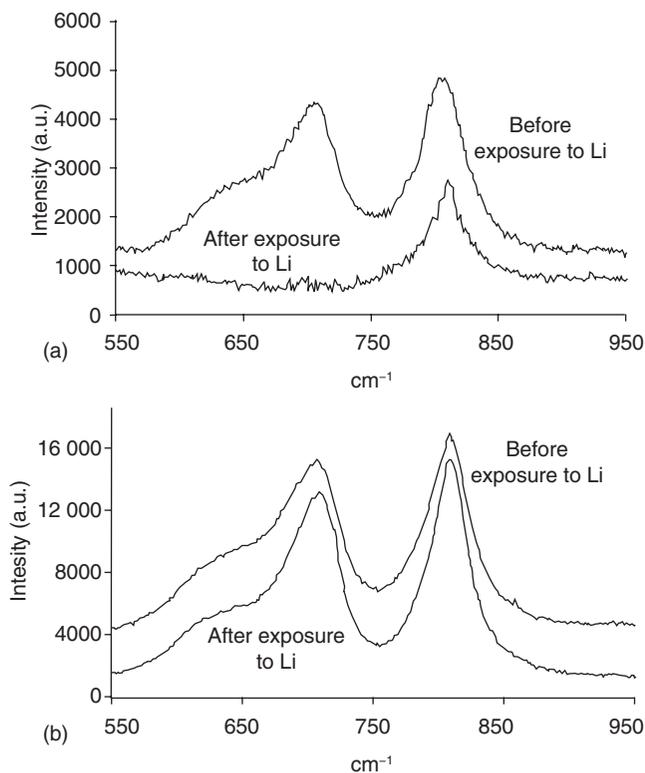
thicknesses have been recently published¹⁰⁹ and are shown in Fig. 4.22a. Both hydrated and dehydrated WO_3 layers have strong Raman modes, which can be matched to the hydration level and crystal phase signatures.

All spectra exhibited features with bands indicative of a hydrous, nanocrystalline $\text{WO}_3 \cdot x\text{H}_2\text{O}$ complex structure.²⁰⁰ The sharp peak at 960 cm^{-1} is attributed to the symmetric stretching mode of the terminal $\text{W}=\text{O}$ bonds. The stretching modes of $\text{O}=\text{W}=\text{O}$ for the bridging oxygens across planes, which occur around 660 cm^{-1} (with bending modes around 230 and 270 cm^{-1}), are expected from the layered and 2D character of $\text{WO}_3 \cdot 2\text{H}_2\text{O}$. They are also suggested to be influenced significantly by the hydration levels, and the 660 cm^{-1} band is used to identify the hydration level. The rest of the modes between 100 and 300 cm^{-1} are attributed to the lattice modes. As can be seen, two bands appear at 660 and 685 cm^{-1} , which indicate that the nano-material is fully hydrated as $\text{WO}_3 \cdot 2\text{H}_2\text{O}$. For fine samples, the intensity of all but the peaks at 660 , 685 and 960 cm^{-1} decreased, indicating that only the strong planar modes survive as a result of thinning.¹⁰⁹

Figure 4.22b clearly shows that the annealing of Q2D WO_3 nanosheets at 300°C has dramatically changed the Raman spectral features of these nanosheets. Two main regions for the $m\text{-WO}_3$ vibrations occur at $900\text{--}600\text{ cm}^{-1}$ and below 300 cm^{-1} , respectively. The terminal $\text{W}=\text{O}$ stretching mode at 960 cm^{-1} is now completely absent and the two peaks of 660 and 685 cm^{-1} have been replaced by two strong bands in the region between 709 and 810 cm^{-1} . In addition to these stretches, a strong peak appears at 272 cm^{-1} and two weaker peaks can be observed at 195 and 320 cm^{-1} . A shoulder peak at 690 cm^{-1} is typically associated with the presence of hexagonal WO_3 .²⁰¹ After the evaporation of the water molecules from the crystal lattice, the volume between WO_3 layers, once occupied by water molecules, decreases and the unit-cell height halves. The annealed WO_3 showed steps of 0.7 nm , which corresponds to unit cells of monoclinic WO_3 without the water molecules.

Li^+ intercalation was performed on the developed Q2D WO_3 nanosheets in order to decrease bandgap and assess the differences between thick and fine WO_3 nanosheets.²⁰² The Li^+ intercalation resulted in changes of the Raman spectra for the thinnest WO_3 nanosheets, whereas thick WO_3 nanosheets (thickness $\geq 50\text{ nm}$) were mostly unaffected.¹⁰⁹ Figure 4.23 shows that for very thin WO_3 nanosheets, the 705 cm^{-1} peak (shifted from 709 cm^{-1}) and its left side shoulder completely vanish. At the same time the Li^+ intercalation did not affect the thicker samples. Disappearance of the 705 cm^{-1} peak was possibly due to the increased vibration symmetry along both axes after the Li^+ intercalation,²⁰³ which was in good agreement with previous results.²⁰²

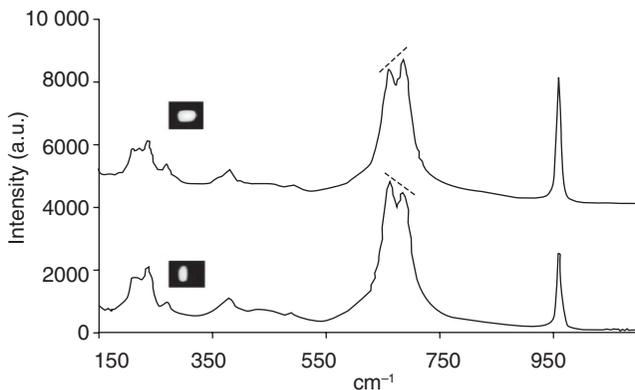
The disappearance of the planar Raman peaks should, however, be carefully evaluated. It was observed that the direction of the planar growth



4.23 Effect of Li^+ intercalation on Raman spectra for (a) thin and (b) thick WO_3 nanosheets. (Reprinted from Ref. 109 with permission from The American Chemical Society)

significantly affects the intensity of peaks in the $600\text{--}900\text{cm}^{-1}$ range of the spectrum, which are assigned to the planar $\text{O}=\text{W}=\text{O}$ stretching modes.¹⁰⁹ Figure 4.24 explains that when horizontal and vertical growth are dominant, this results in a change in the relative intensity of different peaks of the hydrated WO_3 . The same effect was also observed for the planar modes of annealed WO_3 sheets with different degrees of hydration. The absence of any shifts for the 810cm^{-1} peak can suggest that the intercalated Li^+ ions dampen the 705cm^{-1} stretching mode by affecting the WO_3 plane in one direction rather than making the system more symmetric.

Results obtained so far clearly indicate that mechanical exfoliation followed by Li^+ intercalation enabled the tuning of the bandgap of Q2D WO_3 nanosheets within the range $2.5\text{--}2.7\text{eV}$.²⁰⁴ These findings also highlighted that the investigation of atomically-thin WO_3 nanosheets is essential for better understanding of the thinning effect on photon–electron and electron–photon interactions in the developed WO_3 nanostructures. Apart from



4.24 Effect of the growth directions along different unit-cell axes on the planar O-W-O stretching modes intensities. (Reprinted from Ref. 109 with permission from The American Chemical Society)

the new generation of electrochromic devices, such 2D semiconductors can be utilized in the development of a wide variety of devices ranging from perfect insulating dielectric layers to layers with high carrier mobility in 2D for creating transistors with large on/off ratios and transconductance.

4.7 Niobium pentoxide nanocrystals

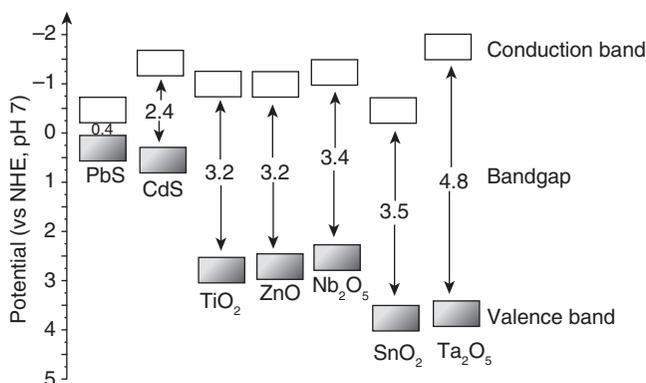
With wide bandgap, Nb_2O_5 is an *n*-type transitional metal semiconductor with an oxygen stoichiometry-dependent bandgap ranging between 3.4 and 4.0 eV and high-*k* (between 33 and 40).^{205,206} Stoichiometric Nb_2O_5 is an insulator (conductivity, $\sigma = \sim 3 \times 10^{-6} \text{ Scm}^{-1}$) and it converts into a semi-conducting state (conductivity, $\sigma = \sim 3 \times 10^{-3} \text{ Scm}^{-1}$) with a decrease in oxygen stoichiometry ($\text{Nb}_2\text{O}_{4.8}$). $\text{H-Nb}_2\text{O}_5$ (pseudo-hexagonal), $\text{O-Nb}_2\text{O}_5$ (orthorhombic), $\text{T-Nb}_2\text{O}_5$ (tetragonal) and $\text{M-Nb}_2\text{O}_5$ (monoclinic) are the most common crystallographic phases.²⁰⁷ Nb_2O_5 is very resistive to thermal shocks and thermocycling, and it possesses a high melting point and a wide working temperature range. So far, both microstructured and nanostructured Nb_2O_5 have been widely used in catalysis (for selective oxidation, hydrocarbon conversion, hydrogenation and hydrotreating), photovoltaics (as a photo-anode material for dye-sensitized solar cells), electrochromic devices, field-emission displays, microelectronics and gas sensors.

The dielectric constant value is somewhat superior to Ta_2O_5 ($\epsilon'_{\text{Nb}_2\text{O}_5} = 41$ vs $\epsilon'_{\text{Ta}_2\text{O}_5} = 27$),²⁰⁷ and it has almost half the density (and higher specific capacitance). These are some of its advantages for passive electronic device components. Due to its acidic character, Nb_2O_5 has attracted a great deal of attention for its applications as a catalyst in electrochemistry,²⁰⁸ in dye-sensitized solar cells,^{93,209,210} in optical devices,²¹¹ in electrochromics²⁰⁷ and in

sensors.^{212,213} However, consideration of Nb_2O_5 for photodegradation of contaminants is not well-explored in the literature.²¹⁴ Given that the bandgap of Nb_2O_5 is similar to that of TiO_2 (Fig. 4.25), with structural modification it can be recognized as an alternative to TiO_2 for dye-sensitized solar cell operations.⁹³ The use of Nb_2O_5 in dye-sensitized solar cells will be further described in Chapter 6.

Although bulk Nb_2O_5 has high bandgap energy (3.4–4.0 eV) (Table 4.2), it can be manufactured as nanobelts²¹⁵ and nanorods.²¹⁶ The mechanism of the development of Nb_2O_5 nanobelts is schematically presented in Fig. 4.26. Based on this mechanism, Nb nanopowder was initially reacted with urea solution under hydrothermal conditions, and the layered structure $\text{NH}_4\text{Nb}_3\text{O}_8$ was formed with interlayer spaces between the $[\text{NbO}_6]$ octahedral sheets. Secondly, the interactions between the layers of $\text{NH}_4\text{Nb}_3\text{O}_8$ were weakened under hydrothermal conditions, the layered structures were gradually exfoliated and nanosheets were formed. The nanosheets do not have an inversion symmetry, i.e. the layer is symmetric, and an intrinsic tension exists that may cause the edges of the nanosheets to roll up. Finally, the nanosheets were spitted to form nanobelts in order to release the strong stress and lower the total energy. Nb_2O_5 nanobelts as thin as ~15 nm have been developed.²¹⁵ Similar models for nanowire formation from layered compounds have also been reported.²¹⁷

However, from a practical point of view, difficulty in adhering the developed nanobelts and nanowires to the substrate limits their use for industrial purposes. Consequently, new approaches have been implemented in order to develop Q2D Nb_2O_5 nanosheets. During the last few years, research in the development of 2D semiconductor oxides has predominantly concentrated on either dichalcogenides or MoO_3 and WO_3 semiconductor



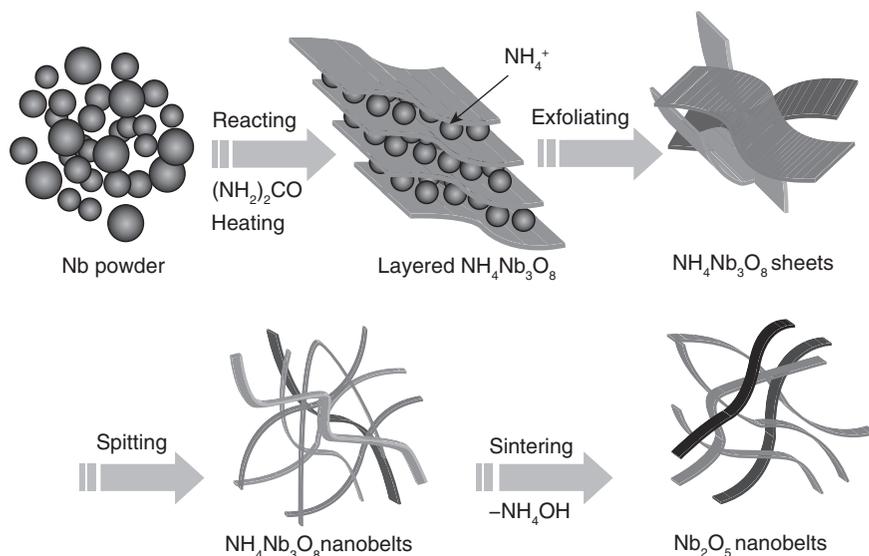
4.25 Position of conduction and valence bands and bandgap values for some semiconductors. (Reprinted from Ref. 205 with permission from Elsevier Science)

Table 4.2 Bandgap energies for various semiconductors²¹⁸

Chalcogenides			Oxides		
N/N	Material	E_G (EV)	N/N	Material	E_G (EV)
1	PbTe	0.275	1	CdO	2.100
2	PbSe	0.400	2	Cu ₂ O	2.100
3	PbS (galena)	0.350	3	FeO	2.400
4	CdTe	1.450	4	WO ₃	2.600
5	CdSe	1.850	5	BaTiO ₃	2.800–3.200
6	CdS	2.420	6	MoO ₃	3.000
				MoO _(3-x) ¹⁸⁴	2.000–2.650
7	ZnSe	2.600	7	Fe ₂ O ₃	3.100
8	ZnS	3.600	8	ZnO	3.200
9	TiS	1.250–1.650	9	TiO ₂ (rutile)	3.000–3.400
				2D TiO ₂ ¹⁴¹	2.100
10	MoS ₂ ¹²⁵	1.290–1.800	10	KNbO ₃	3.300
11	NbSe ₂	1.950–3.600	11	Cr ₂ O ₃	3.300
12	TaS ₂	0.200–1.000	12	SrTiO ₃	3.400
			13	MnO	3.600
			14	MgTiO ₃	3.700
			15	LiTaO ₃	3.800
			16	LiNbO ₃	3.800
			17	NaTaO ₃	3.800
			18	Nb ₂ O ₅	3.400–4.000
			19	CoO	4.000
			20	NiO	4.200
			21	Ta ₂ O ₅	4.200
			22	Ga ₂ O ₃	4.600
			23	SrZrO ₃	5.400
			24	Y ₂ O ₃	5.500
			25	MgO	7.700
			26	SiO ₂	8.300
			27	Al ₂ O ₃	8.800

oxides, as has been shown in previous sections. This research confirmed that these semiconductor oxides can be nanostructured and further exfoliated down to Q2D structures with further tuning of their bandgap down to the level considered acceptable for most electronic applications. The first review of 2D nanomaterials for functional electrodes of electrochemical devices has highlighted the possibility of advances in Q2D Nb₂O₅.²¹⁸ This review also summarized various Nb₂O₅ polymorphic forms that exist today, as presented in Table 4.3, and confirmed a new combined sol–gel/exfoliation approach employed for the development of quasi-2D Nb₂O₅.²¹⁸ This approach is schematically presented in Fig. 4.27.

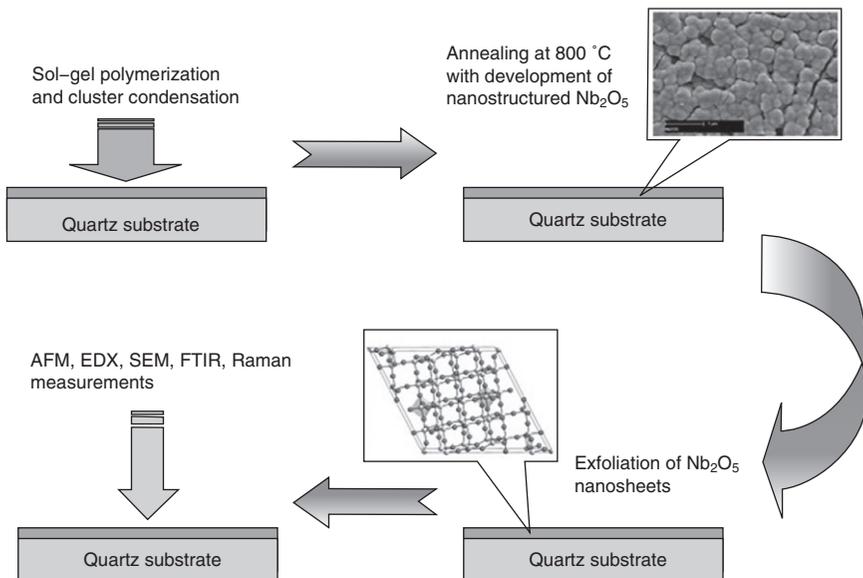
The preparation of Q2D Nb₂O₅ was a three-step process: the deposition method was conducted via spin-coating, followed by annealing at 800 °C, and, in the last step in the sequence, sintered Nb₂O₅ was subjected to



4.26 Mechanism for development of 1D nanostructural Nb_2O_5 nanobelts. (Reprinted from Ref. 211 with permission from Elsevier Science)

Table 4.3 Structural characteristics of several NbO phases²¹⁸

Compound	Structure	Lattice parameters	Space group
NbO	Face-centered cubic	$a = 4.210 \text{ \AA}$	O_h
NbO ₂	Tetragonal	$a = 13.695 \text{ \AA}$ $c = 5.981 \text{ \AA}$	C_{4h}^6
	Rutile	$a = 4.55 \text{ \AA}$ / $a = 4.841 \text{ \AA}$ $c = 2.86 \text{ \AA}$ / $c = 2.992 \text{ \AA}$	D_{4h}^{14}
	Monoclinic	$a = 12.03 \text{ \AA}$ $b = 14.37 \text{ \AA}$ $c = 10.36 \text{ \AA}$ $\beta = 121.17^\circ$	C_{2h}
T-Nb ₂ O ₅	Orthorhombic	$a = 6.175 \text{ \AA}$ / $a = 6.114 \text{ \AA}$ $b = 29.175 \text{ \AA}$ / $b = 29.194 \text{ \AA}$ $c = 3.930 \text{ \AA}$ / $c = 3.940 \text{ \AA}$	D_{2h}^9
B-Nb ₂ O ₅	Monoclinic	$a = 12.73 \text{ \AA}$ $b = 4.88 \text{ \AA}$ $c = 5.56 \text{ \AA}$ $\beta = 105.1^\circ$	C_{2h}^6
H-Nb ₂ O ₅	Monoclinic	$a = 21.153 \text{ \AA}$ / $a = 21.163 \text{ \AA}$ $b = 3.8233 \text{ \AA}$ / $b = 3.824 \text{ \AA}$ $c = 19.356 \text{ \AA}$ / $c = 19.355 \text{ \AA}$ $\beta = 119.80^\circ$	C_{2h}^1
M-Nb ₂ O ₅	Tetragonal	$a = 20.44 \text{ \AA}$ $c = 3.832 \text{ \AA}$	D_{4h}^{17}
N-Nb ₂ O ₅	Monoclinic	$a = 28.51 \text{ \AA}$ $b = 3.830 \text{ \AA}$ $c = 17.48 \text{ \AA}$ $\beta = 120.8^\circ$	C_{2h}^3
	P-Nb ₂ O ₅	Tetragonal	$a = 3.876 \text{ \AA}$ $c = 25.43 \text{ \AA}$
R-Nb ₂ O ₅	Monoclinic	$a = 12.79 \text{ \AA}$ $b = 3.826 \text{ \AA}$ $c = 3.926 \text{ \AA}$ $\beta = 90.75^\circ$	C_{2h}^3
	TT-Nb ₂ O ₅	Pseudo-hexagonal Monoclinic	$a = 3.607 \text{ \AA}$ / $a = 3.600 \text{ \AA}$ $c = 3.925 \text{ \AA}$ / $c = 3.919 \text{ \AA}$ $a = 7.23 \text{ \AA}$ $b = 15.7 \text{ \AA}$ $c = 7.18 \text{ \AA}$ $\beta = 119.08^\circ$

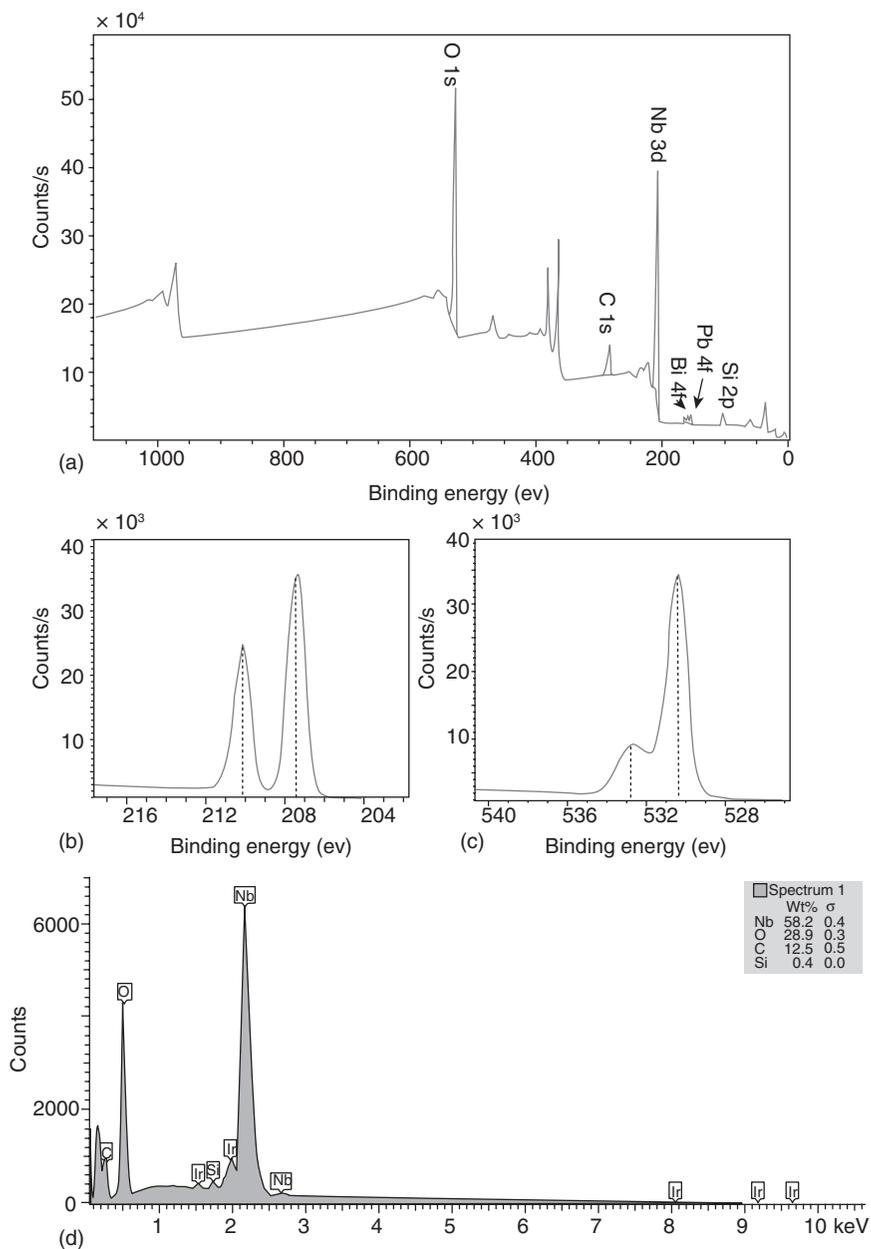


4.27 Schematic interpretation of the sol-gel/exfoliation approach for development of quasi-2D Nb₂O₅ nanostructures.

mechanical exfoliation to achieve super-thin nanolayers. Plate XIII (see colour section between pages 232 and 233) shows topographical AFM measurement of the developed Q2D Nb₂O₅ nanosheets deposited on quartz with height data for individual nanosheets. The exfoliated nanosheets of Nb₂O₅, as is clearly shown in this figure, still comprise a layered structure consisting of three layers of Nb₂O₅ nanoflakes with average measured thickness from 15–25 nm.²¹⁸

The main advantage of these Q2D structures is that their electrochemical properties and morphological characteristics can be significantly improved by two factors: (i) controlling (reducing) the bandgap; and (ii) increasing the mobility by intercalation with H⁺ or Li⁴⁺ ions. The crystalline structures and surface chemistry were examined by energy-dispersive X-ray spectroscopy (EDS) and X-ray photoelectron spectroscopy (XPS) techniques, and the principal results are presented in Fig. 4.28.²¹⁸

XPS analysis was used to examine the surface chemistry of the Nb₂O₅ nanoflake by measuring its elemental composition and both the chemical and the electronic state of Nb and O within the film. XPS analysis of the Nb₂O₅ nanosheets (Figs 4.28a, 4.28b and 4.28c) indicates the characteristic binding energy shape of the core level spectra for Nb 3d shell electrons and O 1s shell electrons. EDS measurement of the Nb₂O₅ nanosheets, presented in Fig. 4.28d, clearly identifies Nb and oxygen as key components of the material. Due to the fact that the nanosheets were not 100% dense, weak



4.28 XPS measurement (a,b,c) and EDS analysis (d) of the developed Q2D Nb₂O₅ nanosheets. (Reprinted from Ref. 218 with permission from Springer Verlag)

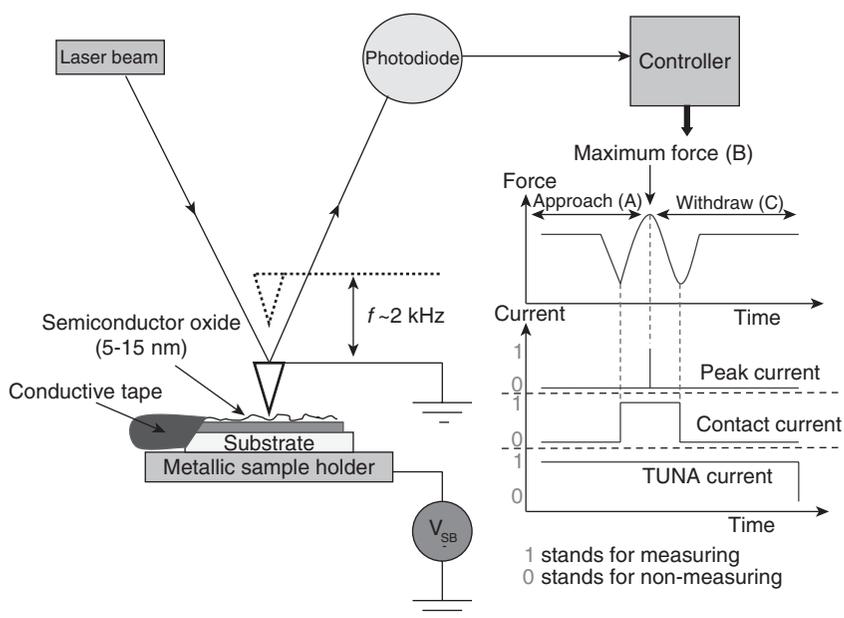
silica peaks are also observed. These signals are most probably because of the silica substrate, which was used as a platform for the entire film. As Ir was applied to coat the sample to improve the image quality, it is also present in the spectrum.

The new approach to mapping the electrical properties of the developed 2D nanostructures below 15 nm scale represents a combination of conductive AFM and a new method that combines the advantages of intermittent contact AFM (IC-AFM), i.e. a spatial resolution approximately 10 nm and no sample damage, and conductive AFM (C-AFM), i.e. very high current sensitivity, and the possibility to record local current–voltage (I – V) curves, allowing the analysis of charge transport properties.²¹⁹ This latest and unique current sensing force spectroscopy AFM (CSFS-AFM, also known as Peak-Force (PF) TUNA™) is based on simultaneous measurement of the topography and the current flowing between the tip of the probe and the sample from real-time analysis of force–distance curves measured for a tip oscillating in the kHz regime, far below the resonance frequency of the cantilever.

CSFS-AFM is an advanced scanning probe approach which integrates the superiority of IC-AFM and the benefits of C-AFM into one powerful and instrumental capability.²¹⁸ It is schematically shown in Fig. 4.29. The concept behind this technique is relatively analogous to IC-AFM, where the tip of the probe and the sample are applied into intercalation at the same time the object is scanned. Nevertheless, there is a significant difference in that the feedback loop controls the applied force on the sample for every individual oscillation cycle, safeguarding the tip and the sample from scan-induced damage. Also direct force control allows each tip–sample contact to be regulated and measured to extract the current values whilst the tip–sample contact area is minimized. The two electrical modules are characterized by a sensitivity of less than 100 fA. The oscillation frequency of the probe is established to be between 0.5 and 2 kHz which allows the recorded current values to have an acceptable signal-to-noise ratio.

As soon as the tip of the probe approaches the surface, the attractive forces strain the cantilever down towards the surface. When the forces overcome the cantilever constraint, the tip is attracted by the surface, resulting in a dip in the approach curve. Next, the force increases until the Z position of the transformation achieves its lowest point and the force at this stage is maintained constant and uniform by the system. Then the tip commences to withdraw from the surface and the force is reduced until it reaches a minimum point on the retract curve. Just as the tip of the probe has been removed from the surface, there is virtually nil force applied to it.

Throughout scanning, a DC bias may be applied between the tip and the sample, resulting in the current passing directly through the sample. As soon a contact is made, the result can be recorded. The peak current is the



4.29 Schematic representation of the sample set-up and the working principle of CSFC-AFM. (Reprinted from Ref. 218 with permission from Springer Verlag)

instantaneous current measured when the tip is located at the lowest point in the approach–retract phase. This could be the maximum current because the limited rise in time can result in a lag in the current response. Likewise, the contact current is the average current throughout the fundamental interaction between the sample and the tip. Lastly, the PF TUNA™ current is the integration of the current during the entire approach–retract phase, averaging the current measured during the contact and additionally taking into the account the zero signal as soon as the probe is retracted.

Bruker, Multi mode 8 scanning probe AFM was employed to image the Q2D Nb_2O_5 nanoflakes and provide topographical information on the samples as seen in Fig. 4.29. The images illustrate that the surface morphology and electrical data are acquired simultaneously and identify the structure and main features of the developed Q2D Nb_2O_5 nanosheets (Plate XV (see colour section between pages 232 and 233)). As far as the next generation of advanced functional devices is concerned, structurally homogeneous 2D Nb_2O_5 nano-oxide is of primary importance in order to comply with the requirements for reliability and long-term stability of these devices.

Plates XVa and XVb illustrate the topography of the developed Q2D Nb_2O_5 and interfaces between several nanoflakes. At the edges between the different regions, an increased Fowler–Nordheim tunnelling current is

represented by the dark areas on the image (Plate XVb). This indicates local structural thinning of the oxide during fabrication, which serves as an insulating area between adjacent active regions. Enhanced current flow is noticeable along the grain boundaries of Nb_2O_5 nanosheet, whereas less current is observed on the individual nanoflakes. The average tunnelling current was much lower, corresponding to changes in Nb_2O_5 nanosheet thickness and small inhomogeneities, as the developed Nb_2O_5 nanosheet consisted of several nanoflakes with different dimensions. A big contrast in colours for current/voltage measurements (Plate XVc) represents local variations in effective electrical thickness. It is noticeable that most often, areas with increased tunnelling current seem to correspond with topographically elevated features. Analysis of the adhesion image (Plate XVd) revealed that the developed Q2D nanosheets had very good adhesion between the tip and nanoflakes (dark areas on nanoflakes, especially on those nanoflakes which are in direct contact with the substrate).

It was possible to imprint STM measurements on the edge of some of the Nb_2O_5 nanoflakes, as depicted in Plate XIV (see colour section between pages 232 and 233). These measurements unambiguously confirmed the typical layered profile of the Nb_2O_5 matrix. In all CSFS-AFM and STM measurements, the tip radius was evaluated to be around 20 nm using the Hertz model for sub-nN contact forces while performing classical C-AFM experiments.²¹⁹

It must be stressed that the combination of CSFS-AFM and STM measurements provides not only simultaneous analysis of the physical and electrical parameters of the developed Nb_2O_5 nanosheets with thickness less than 20 nm, but also mapping of the measured parameters to the specific morphology of analysed Nb_2O_5 nanostructures. Furthermore, the great advantage of this approach can be illustrated by analysis of the grain boundaries of the developed Nb_2O_5 nanosheets, as presented in Plate XVI (see colour section). A 3D AFM image of the grain boundaries between three neighbouring nanosheets (Plate XVIa) appeared to be relatively smooth. The analysed image surface area was 4373 nm^2 while the measured image surface area difference was only 6.81 %. It must be noted that the widest measured distance between two neighbouring Nb_2O_5 nanoflakes was approximately 25 nm (Plates XVIb, c and d), whereas the average distance was ~ 8 nm. Exfoliated Nb_2O_5 nanoflakes appeared to be quite flat with a measured vertical distance of 0.2–0.7 nm (Plate XVI d). Although measured adhesion (Plate XVIe) appeared to be fuzzy, it was confirmed that the grain boundaries have the weakest adhesion to the substrate (other flakes), which was supported by the light colour contrasting with the dark colour of the Nb_2O_5 nanosheets. However, it is interesting that the peak current with maximum intensity was clearly identified and its measured value was 8.3 pA (Plate XVI f). It was also confirmed that the maximum current was on the edges of the Nb_2O_5 flakes, i.e. on the grain boundaries, and dropped to

almost zero above the centre of the nanosheet. The colour code of the current image is defined to be bright yellow for large current values and dark yellow for small current value (dark brown standing for zero).

Raman spectroscopy was employed to determine the vibration and rotational information in relation to chemical bonds and symmetry of molecules in the Nb_2O_5 nanoflakes with particular interest in the finger-print region of the spectrum, as presented in Figs 4.30a and 4.30b.

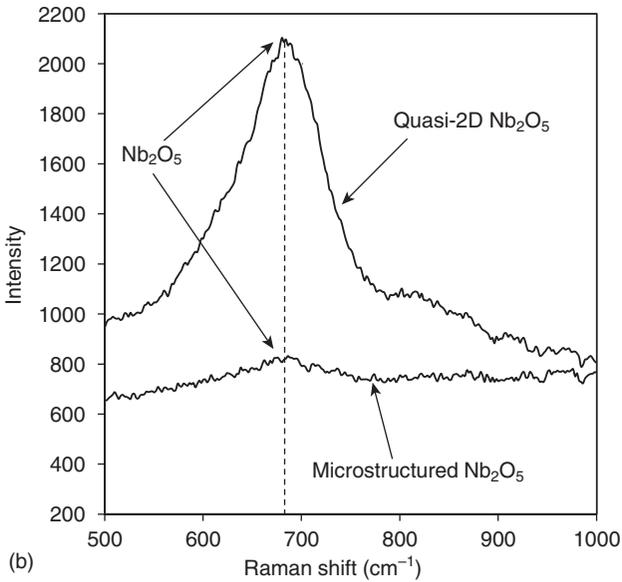
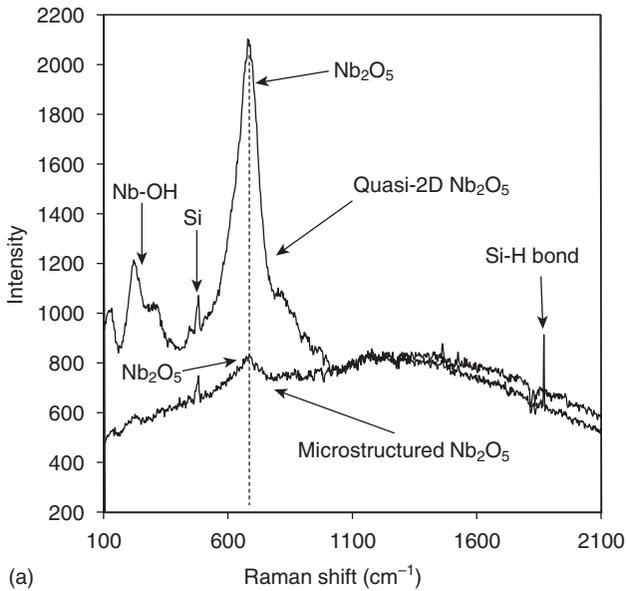
In general terms, the graph not only displays significant peaks in the perturbation area of the spectrum (Fig. 4.30b), but also demonstrates a number of substantial stretches with various magnitudes in the region of $1400\text{--}2000\text{cm}^{-1}$. Two stretches observed at 482cm^{-1} and 1526cm^{-1} correspond to Si and Au, respectively, which are part of the substrate itself. A broad peak detected at 680cm^{-1} confirms the presence of Nb_2O_5 . However, the intensity of this peak for quasi-2D Nb_2O_5 nanosheets was about three times higher than the intensity of the same peak for microstructural Nb_2O_5 . A distinctive peak observed at 1462cm^{-1} confirms the strong existence of C=N bonds. The spike at 228cm^{-1} indicates the presence of a Nb=OH bond. There were no other peaks noted, suggesting that no impurities were present. An analysis of the Raman spectra (Fig. 4.30) revealed that Q2D Nb_2O_5 nanosheets are much more sensitive than microstructural Nb_2O_5 as a component for various plasmonic-based sensing platforms.

In order to increase mobility in the established Q2D Nb_2O_5 nanoflakes, H^+ intercalation was completed by exposing these nanosheets to a gas mixture (97% N_2 + 3% H_2) with controlled flow rate of $200\text{cm}^3/\text{min}$. The samples were mounted inside the chamber and were subjected to synthetic air for 30 min in order to remove any moisture and possible contaminants. Following this initial process, samples were subjected to a H_2 -containing atmosphere for 5 min. After completion of the H^+ intercalation, I - V measurements were performed using PF TUNATM on several points of interest: from the edge to the middle of the Q2D Nb_2O_5 sample, as presented in Plate XVII (see colour section between pages 232 and 233).

Analysis of the results obtained confirmed that the H^+ intercalation had increased the conductivity of the Q2D Nb_2O_5 nanoflakes, particularly on the edges (positions 1 and 3 in Plates XVIIa and XVIIb). However, in the middle of the nanoflake, where the thickness is usually at its maximum, the conductivity had not been increased. This means that either the thickness of the Q2D Nb_2O_5 nanostructures should be further decreased or, alternatively, intensification of the H^+ intercalation is required.

4.8 Tantalum pentoxide nanocrystals

Tantalum pentoxide (Ta_2O_5) is a transitional semiconductor oxide which has a very similar structure to Nb_2O_5 and a wide bandgap of $\sim 4.5\text{eV}$.²²⁰

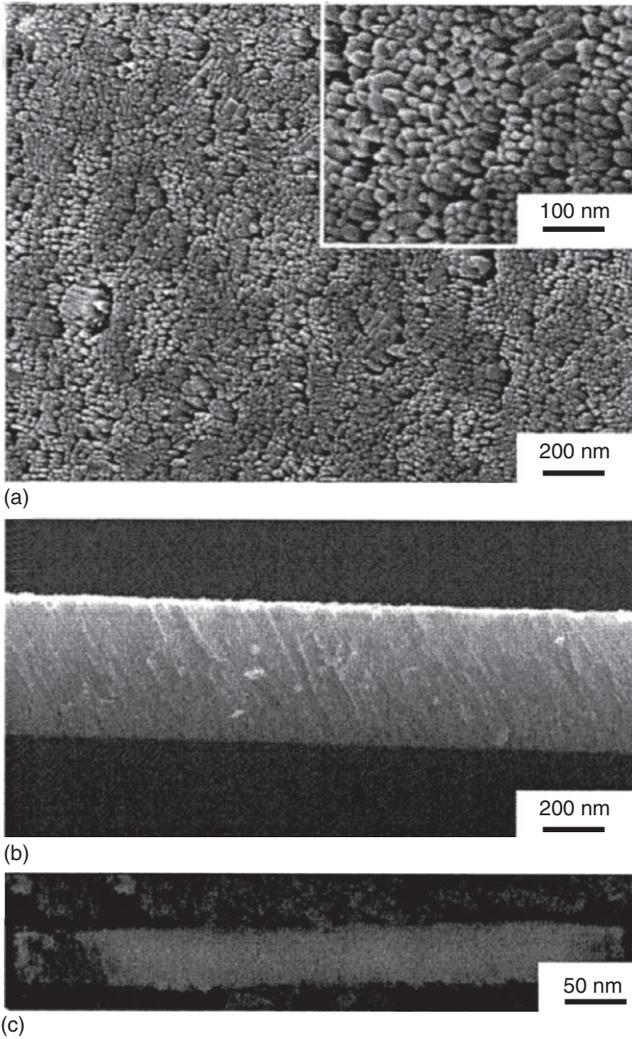


4.30 Raman spectra for microstructured and quasi-2D Nb_2O_5 nanoflakes (a); perturbation region within $500\text{--}1000\text{ cm}^{-1}$ (b).

Although the crystalline structure of Ta_2O_5 is complicated, it is based only on a network of TaO_6 octahedral and TaO_7 pentagonal bipyramids²²¹ with shared oxygen atoms. Specifically, Ta_2O_5 contains only two polyhedral building blocks, TaO_6 octahedral and TaO_7 pentagonal bipyramids. The volatility of oxygen in Ta_2O_5 leads to oxygen vacancies being the most predominant type of defect. Each oxygen vacancy offers dangling bonds and donates two electrons close to the vacancy location. The dangling bonds give rise to electronic states within the bandgap which are able to trap excited electrons, creating many trap levels within the bandgap of Ta_2O_5 . The trap levels correspond to the ionization energies of the oxygen deficiencies and are sufficient to provide visible-light emission.²²² Consequently, the presence of oxygen vacancies is expected to make Ta_2O_5 an *n*-type semiconductor and to play a strong role in the photoluminescence emissions of Ta_2O_5 .

Among wide bandgap hosts, Ta_2O_5 has attracted the attention of researchers owing to its optical, catalytic, dielectric and chemical properties.²²³ Optically active rare earth-doped Ta_2O_5 films have been produced, helping the development of compact sources and amplifiers in telecommunication applications.²²⁴ Moreover, aggressive scaling and the industry drive for faster/more power-efficient/lower-cost integrated circuits requires the use of high-*k* semiconductors as insulating materials in integrated capacitors or gate insulators.^{224,225} Ta_2O_5 films also provide wide-range refractive index adjustment for integrated optical circuits, good anti-reflection properties for solar cells²²⁶ and increased ionic conductivity for electrochromic devices (such as chromogenic glazing in windows and large-scale information displays²²⁴). Ta_2O_5 also has potential for non-linear optical applications, multi-layer interference filters²²⁷ and bio-²²⁸ and water quality sensors.^{229,230} The challenge for Ta_2O_5 is to grow high-performance dielectric nanostructures in order to obtain highly ordered crystalline defect-free Ta_2O_5 nanosheets. In that respect, the development of Q2D or 1D nanostructures would be valuable solutions. So far, there have been several reports outlining the deposition techniques and properties of 1D Ta_2O_5 nanostructures.²²⁰ This development, similar to the other 2D semiconductor oxides, has opened up a new area in nanotechnology, leading to exploration of the dependence of electrical, thermal transport and mechanical properties on dimensionality and size reduction. The structural identity of Ta_2O_5 nanosheets is strongly dependent on processing conditions and impurities.²³¹ One example of the developed 1D Ta_2O_5 structures is shown in Figs 4.31a and 4.31b.²²⁰

It can be clearly seen from this figure that surface morphology of the developed Ta_2O_5 represents large-scale and high-density nanorods. The 1D Ta_2O_5 nanorod array is very compact, containing 1675 nanorods per square micrometer.²²⁰ The high-magnification SEM image (Fig. 4.31c) shows that 1D Ta_2O_5 nanorods can be as small as 50 nm in diameter and about ~550 nm long. The 1D Ta_2O_5 nanorods were able to provide not only green-light,



4.31 SEM images showing the (a) top and (b) side views of a large-area high-density array of 1D Ta_2O_5 nanorods on Si substrate. (c) High-magnification SEM image of single 1D Ta_2O_5 nanorod separated from the array. (Reprinted from Ref. 220 with permission from the IOP Publishing)

yellow-light and red-light emission, but also UV-light and blue-light emission. Blue, red and green are three primary colours widely used in optical transportation and colour display devices.²²⁰ Moreover, the numerous oxygen vacancies make 1D Ta_2O_5 nanorods arranged in a large-scale high-density array a strong candidate for such optoelectronic devices as light-emitting diodes and laser diodes.

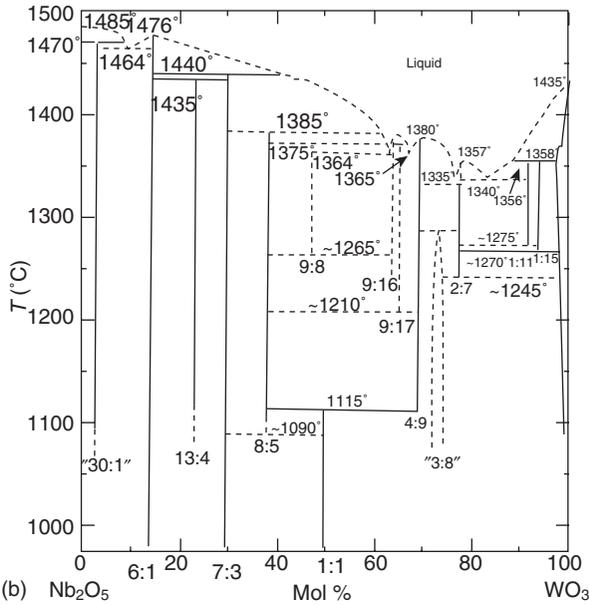
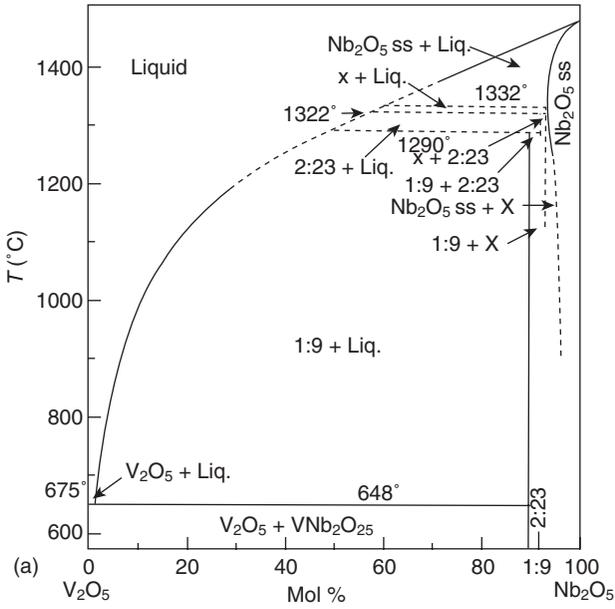
Another exciting and perhaps unknown area in the development of 2D Ta₂O₅ nanocrystals providing fine tuning of their electrical, optical and electrochemical properties is doping of these nanocrystals by another nanostructured semiconductor oxide.²³² With regard to the sensing application, doping is also in favour because tuning of the carrier concentration, electrical transport and sensing properties can also be optimized. Several oxides may be successfully used as dopants in different concentrations. Figure 4.32 gives an overview of just a few phase equilibrium diagrams for Ta₂O₅, Nb₂O₅ and V₂O₅, where their chemical and structural similarities favour the idea of mixing the two nano-oxides together to tune the physical and electrochemical properties of the base nanocrystal.²¹⁸ Alternatively, careful selection of the doping nano-oxide and its molar concentration can vary (increase/decrease) the bandgap of the base semiconductor nano-oxide.

4.9 Zinc oxide nanocrystals

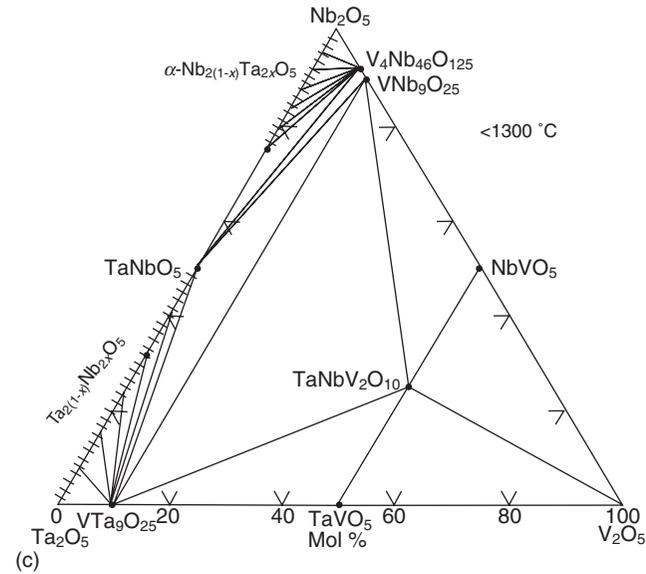
As one of the prominent semiconductors, nanostructured ZnO has been extensively investigated for its versatile physical and electrochemical properties and promising potential for electronics, including optoelectronics and piezoelectric applications. With a wide bandgap (3.4 eV) and a strong binding energy (~60 meV) at room temperature, ZnO has been considered as an excellent material for UV lasers,²³³ sensing applications^{234,235} and dye-sensitized solar cells.²³⁶

The structure of ZnO can be described as a number of alternating planes composed of tetrahedrally coordinated O²⁻ and Zn²⁺ ions, stacked along the *c*-axis. The oppositely charged ions produce positively charged (0 0 0 1)-Zn and negatively charged (0 0 0 -1)-O polar surfaces, resulting in a normal dipole moment and spontaneous polarization along the *c*-axis. The polarization effect induces the formation of a stripe structure (as displayed in Fig. 4.33a-d).⁹² There have been several reports relating to the synthesis of 1D ZnO nanostructures.²³⁷⁻²⁴¹ SEM images of the developed 1D ZnO structures show that in most circumstances, the as-grown 1D ZnO nanostructures are single crystalline and have a well-defined shape with a high aspect ratio. HRTEM images, displayed in Fig. 4.33e, demonstrate the ZnO nanowires obtained by the CVD method.²⁴² Lattice fringes can be clearly distinguished as 0.52 nm, and the growth direction of the nanowire [0 0 0 1] is confirmed by the selected-area electron diffraction (SAED) pattern (Fig. 4.33e, right inset).

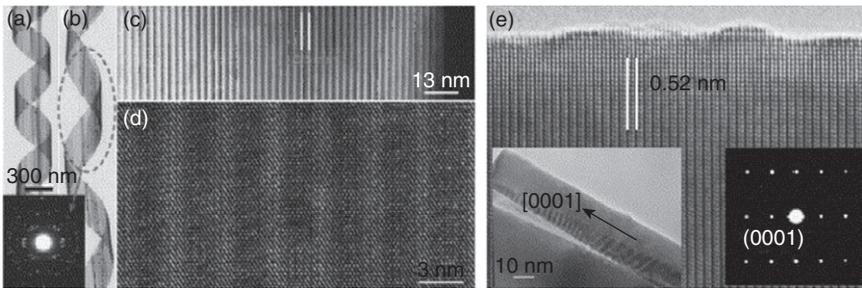
In order to explore the potential of ZnO nanowires as the building blocks for nanoscale electronics, electrical transport properties of these nanowires have been investigated.²³⁷ It was found that ZnO is a typical *n*-type semiconductor which originates from native defects such as oxygen vacancies



4.32 Phase diagrams for $\text{Nb}_2\text{O}_5\text{-V}_2\text{O}_5$ (a), $\text{Nb}_2\text{O}_5\text{-WO}_3$ (b) and $\text{Nb}_2\text{O}_5\text{-V}_2\text{O}_5\text{-Ta}_2\text{O}_5$ (c) systems. (Reprinted from Ref. 218 with permission from Springer Verlag)



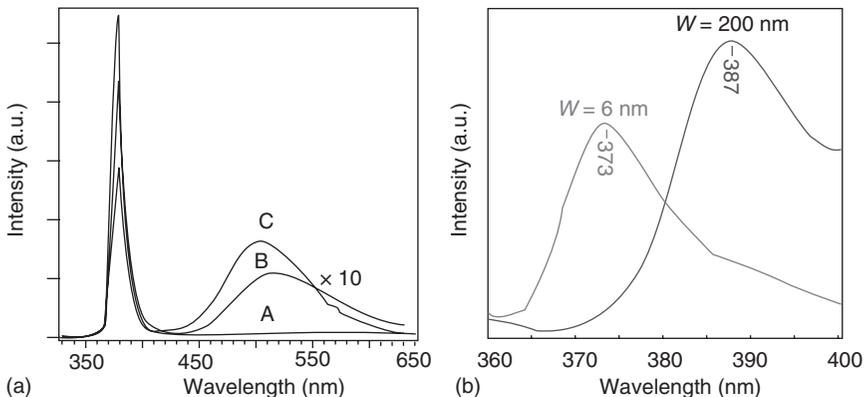
4.32 Continued



4.33 (a) Typical low-magnification TEM image of a ZnO nanohelix, showing its structural uniformity. (b) Low-magnification TEM image of a ZnO nanohelix with a larger pitch-to-diameter ratio. (c) Dark-field TEM image from a segment of a nanohelix, showing that a nanobelt that coils into a helix is composed of alternating distributed stripes at a periodicity of 3.5 nm. (d) HRTEM image shows the lattice structure of the two alternating stripes (reprint permission from Ref. 92). (e) HRTEM image of the edge of the nanowire showing ZnO crystal lattice fringes with spacing of 0.52 nm. The inset is a SAED pattern confirming the growth direction along the [0 0 0 1] *c*-axis. (Reprinted with permission from Ref. 242)

and zinc interstitials. Since the defects are concentrated in the surface region, they have a significant effect on the electrical and optical properties of the 1D structure with a large surface-to-volume ratio.⁹² Electrical transport studies after configuring individual ZnO nanowires as FETs²³⁹ confirm that they exhibit *n*-type behaviour. Typically the field-effect mobility of as-grown nanowires is in the range 20–100 cm²/Vs. However, after surface treatment, the mobility of ZnO nanowires can be dramatically enhanced to exceed 4000 cm²/Vs.²⁴⁰

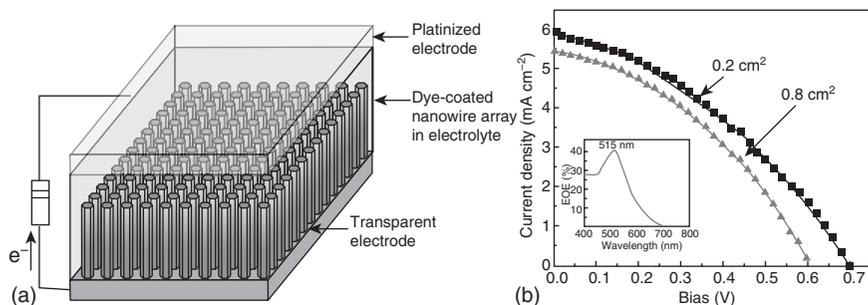
The optical properties of Q1D ZnO nanostructures have been extensively studied because of their promising potential in optoelectronics. Due to its large energy bandgap and exciton binding energy, ZnO is especially suitable for short-wavelength optoelectronic applications. Photoluminescence spectra reveal fundamental optical properties of the material, including band-edge emission, defect characterization and exciton–phonon interaction. Figure 4.34a demonstrates the photoluminescence of ZnO nanowires with diameters of 100 nm, 50 nm and 25 nm.²³⁷ Both band-edge emission at ~380 nm and imperfection state-related green emission centring at ~520 nm have been observed. The progressive increase of the green emission intensity with a decrease of nanowire diameter suggests that the defect level is higher in thinner nanowires due to the increasing surface-to-volume ratio. Continuous reduction of the diameter of ZnO nanowire results in a quantum size effect which manifests itself in the blue shift of band-edge emission in the photoluminescence spectra (as shown in Fig. 4.34b).²⁴⁰ It has also been reported that the exciton binding energy is significantly enhanced due to size confinement in ZnO nanorods with diameters of ~2 nm.²⁴¹



4.34 (a) Photoluminescence of ZnO nanowires with diameters of 100 nm, 50 nm and 25 nm (reprinted with permission from Ref. 237). (b) PL spectra of 6 nm and 200 nm wide ZnO nanobelts showing a blue shift of the emission peak. (Reprinted with permission from Ref. 240)

One of the most interesting applications, where Q1D ZnO nanowires can replace conventional nanoparticle film, is dye-sensitized solar cells (DSSC).²⁴³ Apart from the higher crystallinity and rapid carrier collection rate, the nanowire arrays are also advantageous for cell designs that could use non-standard electrolytes, such as polymer gels or solid inorganic phases, in which the recombination rates are higher than the liquid electrolyte cell.²⁴³ In these DSSC systems, ZnO,²⁴³ TiO₂²⁴⁴ and CuO²⁴⁵ nanowires have been used as the photo-anodes. Figure 4.35a exhibits ZnO nanowire arrays bathed in Ru-based DSSC. At a full sun intensity of $\sim 100 \text{ mW cm}^{-2}$, a conversion efficiency of 1.5% has been reported with a nanowire filling factor of 0.37.²⁴³ Figure 4.35b shows the current density vs bias voltage for two cells with different active areas. The small cell (with area 0.2 cm^2) shows higher short circuit current J_{sc} and open-circuit voltage V_{oc} than the large cell (0.8 cm^2). The external quantum efficiency (EQE) peaks at $\sim 40\%$ near the absorption maximum of the dye. Furthermore, conversion efficiency up to 7% with a denser filling factor of 0.70 based on TiO₂ nanorods was achieved.²⁴⁴ Unlike other *n*-type oxides, CuO is representative of *p*-type semiconducting oxides with a relatively small bandgap energy of 1.2 eV. This implies that CuO nanorods can act as the cathode in the DSSC. It has been reported that the CuO nanorods can be prepared from solution phase using the Cu substrate as the cathode. In addition, an ITO conducting electrode coated with dye-absorbed TiO₂ nanoparticles can be used as the anode. Such a cell composed of ITO/TiO₂/dye/electrolyte/CuO nanorods/Cu was tested and yielded a 0.29% conversion efficiency at 0.17 filling factor.²⁴⁵

Another very interesting application of Q1D ZnO nanowires is in so-called ‘electronic noses’ – chemical sensors with enhanced sensitivity and



4.35 (a) Schematic diagram of the ZnO nanowire array based dye-sensitized cell. Incident light is shone through the bottom transparent electrode. (b) Current density against voltage for two cells. The small cell shows a higher V_{oc} and J_{sc} than the large cell. Inset shows the external quantum efficiency vs wavelength for the large cell. (Reprinted with permission from Ref. 243)

unipolar selectivity. With the capability of being operated in harsh industrial environments, they surpass other chemical sensors in their sensitivity, reliability and durability. The advantage of using 1D and 2D semiconductor oxide nanostructures for chemical sensing is manifold. With a large surface-to-volume ratio and a Debye length comparable to the nanowire radius, the electronic properties of the nanowire are strongly influenced by surface processes, yielding superior sensitivity compared to their thin-film counterparts.²⁴⁶ In order to achieve maximum sensitivity, thin-film gas sensors are often operated at elevated temperatures.²⁴⁷ This indicates that a single sensing device needs to incorporate a temperature control unit, which will certainly increase the complexity of sensor design and the power consumption. However, metal oxide nanowire-based ‘electronic noses’ have demonstrated significantly higher sensitivity at room temperature. For example, room temperature NO₂ sensing with ZnO nanowire shows more than 50 % conductance change under an exposure of 0.6 ppm NO₂.²⁴⁸ In contrast, a NO₂ sensor made of doped ZnO thin film demonstrates less than 2 % conductance change when exposed to an even higher concentration of NO₂ (1.5 ppm).²⁴⁶ These encouraging results manifested the potential of building room temperature operating, highly sensitive gas sensors. In addition, metal oxide nanowires configured as FETs have demonstrated that a transverse electric field can effectively tune the sensing behaviour of the system.^{248,249} The ultimate goal is to develop an ‘electronic nose’ system imitating the mammalian olfactory system by assembling multicomponent sensing modules integrated with signal processing and pattern recognition functions.

Bulk and thin-film metal oxides have been used for sensing gas species such as CO, CO₂, CH₄, C₂H₅OH, C₃H₈, H₂, H₂S, NH₃, NO, NO₂, O₂, O₃, SO₂, acetone, humidity, etc.^{250–252} In the past few years, the research efforts of the sensors community have been focused on chemical sensing based on metal oxide nanostructures, such as ZnO, SnO₂, In₂O₃, Al₂O₃, TiO₂, WO₃, MoO₃ and RuO₂. Environmental sensors based on those nanostructured semiconductor oxides and other doped semiconductor nanocrystals will be described in detail in Chapter 8.

4.10 Impact of combining two-dimensional semiconductor nanocrystals into three-dimensional structure

It is not difficult to explain the increasing worldwide interest in the development of advanced functional nanocrystals, as they have been considered as potential candidates to replace conventional microstructured materials in various applications. The downscaling of microelectronic systems to produce

nano-electronic systems and functional devices such as DSSC, electrochromic and optical devices, batteries with enhanced specific energy capacitance, self-powered integrated circuits and nanosensors requires principally new advanced nanomaterials with prominent energy and power densities, and higher carrier mobility per designated area than can be achieved with the thin-film and MEMS technologies that exist today. Nowadays, conventional applied and industrial sciences are approaching their limits and inevitably seeking new breakthroughs. In this regard, graphene and 1D and/or 2D semiconductor oxides represent the potential building blocks for the next generation of advanced functional electronics and devices with superior properties utilized in much smaller volumes. In this context, Q1D and Q2D nanostructures represent an ideal channel for electrical carrier transport and are suitable for device integration.²⁵³

The most important lesson from the recent progress in the development of Q1D and Q2D nanomaterials is the fact that the results achieved so far are only a very small portion of what can be studied with respect to the universe of 1D and 2D nanocrystals. Each of them has its own unique features, complexity and attractiveness. It is fair to say that the great field of 1D and 2D nanocrystals lies undiscovered before us.

Furthermore, the area of 2D nanocrystals which can be modified and tuned to tailor the desired properties by careful chemical and molecular doping has not been explored at all. Great discoveries are expected in this area in the next few years, which can potentially challenge our perception of the design of advanced functional devices: electro-actuators, flexible electronics, electronic circuits, chemical and biosensors, DSSC, fuel cells, optical devices, photosensors, super-capacitors, infrared filters, to name but a few.⁹²

Completely new functional opportunities can be initiated and launched if the next generation of advanced functional 3D devices can be designed using the process schematically presented in Plate XVIII (see colour section between pages 232 and 233). Outstanding performance of these devices can be achieved through combinatorial multistacking (in analogy with combinatorial chemistry). Considering that each of these 1D and 2D nanocrystals has a different functionality, multifunctional nanomaterials can be created with an enormous economy in terms of energy and volume. It can be envisaged that a library of 1D and 2D nanocrystals and nanosheets will be established. Using this library and advanced robotics, new 3D structures can be efficiently developed at low cost and high speed. For instance, three different types of 1D or 2D nanocrystals could be combined into a single 3D structure: one that can convert light into electrical current, a second one that is conductive and transparent, and finally a third that can store the electricity efficiently.⁸⁷ Putting together superior conversion, transportation and storage of energy, could enable the development of a functional device

that works as an artificial super-economical ‘green plant’. With the help of the constructed library, the outcome would be a ‘nanocrystals-on-demand’ strategy with attached portfolio of novel complex architectures and nanostructures possessing accurately tailored properties for different purposes and practices. From these nanocrystals, new 3D functional nanodevices could be designed.

4.11 References

1. D.A. Bronson, L.J. Munro, D.K. Kampouris, C.E. Banks, Electrochemistry of graphene: not such a beneficial electrode material? *RSC Advances*, 1 (2011) 978–988.
2. K.S. Novoselov, A.K. Geim, S.V. Morozov, D. Jiang, M.I. Katsnelson, I.V. Grigorieva, S.V. Dubonos, A.A. Firsov, Two-dimensional gas of massless Dirac fermions in graphene, *Nature*, 438 (2005) 197–200.
3. J.K. Wassei, R.B. Kaner, Graphene, a promising transparent conductor, *Materials Today*, 13 (2010) 52–59.
4. A. Dimiev, D.V. Kosynkin, A. Sinitskii, A. Slesarev, Z. Sun, J.M. Tour, Layer-by-layer removal of graphene for device patterning, *Science*, 331 (2011) 1168–1172.
5. A.K. Geim, K.S. Novoselov, The rise of graphene, *Nat. Mater.*, 6 (2007) 183–191.
6. A.K. Geim, Graphene: status and prospects, *Science*, 324 (2009) 1530–1534.
7. D.R. Dreyer, R.S. Ruoff, C.W. Bielawski, From conception to realization: an historical account of graphene and some perspectives for its future, *Angew. Chemie Int. Edit.*, 49 (2010) 9336–9344.
8. Q. Cheng, J. Tang, J. Ma, H. Zhang, N. Shinya, L.C. Qin, Graphene and carbon nanotube composite electrodes for supercapacitors and ultra-high energy density, *Phys. Chem. Chem. Phys.*, 13 (2011) 17615–17624.
9. P.V. Kamat, Graphene-based nanoarchitectures. Anchoring semiconductor and metal nanoparticles on a two-dimensional carbon support, *J. Phys. Chem. Lett.*, 1 (2010) 520–527.
10. V.I. Fal’ko, A.K. Geim, Graphene: Emerging matter in two dimensions, *Europ. Phys. J.*, 148 (2007) 1–4.
11. Y. Kopelevich, P. Esquinazi, Graphene physics in graphite, *Adv. Mater.*, 19 (2007) 4559–4563.
12. S. Pisana, M. Lazzeri, C. Casiraghi, K.S. Novoselov, A.K. Geim, A.C. Ferrari, F. Mauri, Breakdown of the adiabatic Born-Oppenheimer approximation in graphene, *Nat. Mater.*, 6 (2007) 198–201.
13. F. Schedin, A.K. Geim, S.V. Morozov, E.W. Hill, P. Blake, M.I. Katsnelson, K.S. Novoselov, Detection of individual gas molecules adsorbed on graphene, *Nat. Mater.*, 6 (2007) 652–655.
14. R.R. Nair, P. Blake, A.N. Grigorenko, K.S. Novoselov, T.J. Booth, T. Stauber, N.M.R. Peres, A.K. Geim, Fine structure constant defines visual transparency of graphene, *Science*, 320 (2008) 1308–1308.
15. C.N.R. Rao, A.K. Sood, K.S. Subrahmanyam, A. Govindaraj, Graphene: the new two-dimensional nanomaterial, *Angew. Chemie Int. Ed.*, 48 (2009) 7752–7777.

16. V.C. Tung, M.J. Allen, Y. Yang, R.B. Kaner, High-throughput solution processing of large-scale graphene, *Nat. Nanotechnol.*, 4 (2009) 25–29.
17. M. Choucair, P. Thordarson, J.A. Stride, Graphene oxide (rGO) sheets has been realized, *Nat. Nanotechnol.*, 4 (2009) 30–34.
18. A. Shukla, *et al.*, Graphene made easy: High quality large-area samples, *Solid State Commun.*, 149 (2009) 718–721.
19. Z.S. Wu, G. Zhou, L.C. Yin, W. Ren, F. Li, H.M. Cheng, Graphene/metal oxide composite electrode materials for energy storage, *Nano Energy*, 1 (2012) 107–131.
20. J.N. Coleman, Liquid-phase exfoliation nanotubes and graphene, *Adv. Funct. Mater.*, 19 (2009) 3680–3695.
21. S. Stankovich, R.D. Piner, X.Q. Chen, N.Q. Wu, S.T. Nguyen, R.S. Ruoff, Stable aqueous dispersions of graphitic nanoplatelets *via* the reduction of exfoliated graphite oxide in the presence of poly(sodium 4-styrenesulfonate), *J. Mater. Chem.*, 16 (2006) 155–158.
22. Z.S. Wu, W.C. Ren, L.B. Gao, B.L. Liu, J.P. Zhao, H.M. Cheng, Efficient synthesis of graphene nanoribbons sonochemically cut from graphene sheets, *Nano Res.*, 3 (2010) 16–22.
23. M.J. McAllister, J.L. Li, D.H. Adamson, H.C. Schniepp, A.A. Abdala, J. Liu, M. Herrera-Alonso, D.L. Milius, R. Car, R.K. Prud'homme, I.A. Aksay, Single sheet functionalized graphene by oxidation and thermal expansion of graphite, *Chem. Mater.*, 19 (2007) 4396–4404.
24. Z.P. Chen, W.C. Ren, L.B. Gao, B.L. Liu, S.F. Pei, H.M. Cheng, CVD growth and applications of graphene with millimetre-size single-crystal grains and three-dimensional interconnected graphene networks, *Nat. Mater.*, 10 (2011) 424–428.
25. X.S. Li, W.W. Cai, J.H. An, S. Kim, J. Nah, D.X. Yang, R. Piner, A. Velamakanni, I. Jung, E. Tutuc, S.K. Banerjee, L. Colombo, R.S. Ruoff, Large-area synthesis of high-quality and uniform graphene films on copper coils, *Science*, 324 (2009) 1312–1314.
26. A. Reina, X.T. Jia, J. Ho, D. Nezich, H.B. Son, V. Bulovic, M.S. Dresselhaus, J. Kong, Large area, few-layer graphene films on arbitrary substrates by chemical vapor deposition, *Nano Lett.*, 9 (2009) 30–35.
27. C. Berger, Z.M. Song, T.B. Li, X.B. Li, A.Y. Ogbazghi, R. Feng, Z.T. Dai, A.N. Marchenkov, E.H. Conrad, P.N. First, W.A. de Heer, Ultrathin epitaxial graphite: 2D electron gas properties and a route toward graphene-based nanoelectronics, *J. Phys. Chem. B*, 108 (2004) 19912–19916.
28. C. Berger, Z.M. Song, X.B. Li, X.S. Wu, N. Brown, C. Naud, D. Mayo, T.B. Li, J. Hass, A.N. Marchenkov, E.H. Conrad, P.N. First, W.A. de Heer, Multidimensional characterization, Landau levels and density of states in epitaxial graphene grown on SiC substrates, *Science*, 312 (2006) 1191–1196.
29. P.W. Sutter, J.I. Flege, E.A. Sutter, Epitaxial graphene on ruthenium, *Nat. Mater.*, 7 (2008) 406–411.
30. Y. Hernandez, V. Nicolosi, M. Lotya, F.M. Blighe, Z. Sun, S. De, I.T. McGovern, B. Holland, M. Byrne, Y.K. Gun'ko, J.J. Boland, P. Niraj, G. Duesberg, S. Krishnamurthy, R. Goodhue, J. Hutchison, V. Scardaci, A.C. Ferrari, J.N. Coleman, High-yield production of graphene by liquid-phase exfoliation of graphite, *Nat. Nanotechnol.*, 3 (2008) 563–568.

31. M. Lotya, Y. Hernandez, P.J. King, R.J. Smith, Valeria Nicolosi, L.S. Karlsson, F.M. Blighe, S. De, Z. Wang, I.T. McGovern, G.S. Duesberg, J.N. Coleman *et al.*, Liquid phase production of graphene by exfoliation of graphite in surfactant/water solutions, *J. Am. Chem. Soc.*, 131 (2009) 3611–3620.
32. C.A. Furtado, U.J. Kim, H.R. Gutierrez, L. Pan, E.C. Dickey, P.C. Eklund, Debundling and dissolution of single-walled carbon nanotubes in amide solvents, *J. Am. Chem. Soc.*, 126 (2004) 6095–6105.
33. U. Khan, A. O'Neill, M. Lotya, S. De, J.N. Coleman, High-concentration solvent exfoliation of graphene, *Small*, 6 (2010) 864–871.
34. C. Schliehe, B.H. Juarez, M. Pelletier, S. Jander, D. Greshnykh, M. Nagel, A. Meyer, S. Foester, A. Kornowski, A. Klinker, Unrathin PbS sheets by two-dimensional oriented attachment, *Science*, 329 (2010) 550–553.
35. L.J. Zhi, K. Müllen, A bottom-up approach from molecular nanographenes to unconventional carbon materials, *J. Mater. Chem.*, 18 (2008) 1472–1484.
36. X.Y. Yang, X. Dou, A. Rouhanipour, L.J. Zhi, H.J. Rader, K. Müllen, Two-dimensional graphene nanoribbons, *J. Am. Chem. Soc.*, 130 (2008) 4216–4217.
37. A.G. Cano-Marquez, F.J. Rodríguez-Macías, J. Campos-Delgado, C.G. Espinosa-González, F. Tristán-López, D. Ramírez-González, D.A. Cullen, D.J. Smith, M. Terrones, Y.I. Vega-Cantú, Ex-MWNTs: Graphene sheets and ribbons produced by lithium intercalation and exfoliation of carbon nanotubes, *Nano Lett.*, 9 (2009) 1527–1533.
38. D.V. Kosynkin, A.L. Higginbotham, A. Sinitskii, J.R. Lomeda, A. Dimiev, B.K. Price, J.M. Tour, Longitudinal unzipping of carbon nanotubes to form graphene nanoribbons, *Nature*, 458 (2009) 872.
39. A. Sinitskii, D.V. Kosynkin, A. Dimiev, and J.M. Tour, Corrugation of chemically converted graphene monolayers on SiO₂, *ACS Nano*, 4 (2010) 3095–3102.
40. L.Y. Jiao, L. Zhang, X. Wang, G. Diankov, H. Dai, Narrow graphene nanoribbons from carbon nanotubes, *Nature*, 458 (2009) 877–880.
41. S. Gilje, S. Han, S. Wang, M. Wang, R.B. Kaner, A chemical route to graphene for device applications, *Nano Lett.*, 7 (2007) 3394–3398.
42. L. Zhang, X. Li, Y. Huang, Y. Ma, X. Wan, Y. Chen, Controlled synthesis of few-layered graphene sheets on a large scale using chemical exfoliation, *Carbon*, 48 (2010) 2367–2371.
43. S. Park, R.S. Ruoff, Chemical methods for the production of graphenes, *Nat. Nanotechnol.*, 4 (2009) 217–224.
44. D. Li, M.B. Müller, S. Gilje, R.B. Kaner, G.G. Wallace, Processable aqueous dispersions of graphene nanosheets, *Nat. Nanotechnol.*, 3 (2008) 101–105.
45. S. Stankovich, D.A. Dikin, R.D. Piner, K.A. Kohlhaas, A. Kleinhammes, Y. Jia, Y. Wu, S.T. Nguyen, R.S. Ruoff, Synthesis of graphene-based nanosheets via chemical reduction of exfoliated graphite oxides, *Carbon*, 45 (2007) 1558–1565.
46. Y. Si, E.T. Samulski, Synthesis of water soluble graphene, *Nano Lett.*, 8 (2008) 1679–1682.
47. Z.Z. Sun, Z. Yan, J. Yao, E. Beitler, Y. Zhu, J.M. Tour, Growth of graphene from solid carbon sources, *Nature*, 468 (2010) 549–552.
48. Y.P. Wu, B. Wang, Y.F. Ma, Y. Huang, N. Li, F. Zhang, Y.S. Chen, Efficient and large-scale synthesis of few-layered graphene using an arc-discharge method and conductivity studies of the resulting films, *Nano Res.*, 3 (2010) 661–669.

49. M. Choucair, P. Thordarson, J.A. Stride, Gram-scale production of graphene based on solvothermal synthesis and sonication, *Nat. Nanotechnol.*, 4 (2009) 30–33.
50. D.H. Deng, X.L. Pan, H. Zhang, Q.A. Fu, D.L. Tan, X.H. Bao, Freestanding graphene by thermal splitting of silicon carbide granules, *Adv. Mater.*, 22 (2010) 2168–2171.
51. Y.W. Zhu, S. Murali, W.W. Cai, X.S. Li, J.W. Suk, J.R. Potts, R.S. Ruoff, Graphene and graphene oxide: synthesis, properties, and applications, *Adv. Mater.*, 22 (2010) 3906–3924.
52. C. Soldano, A. Mahmood, E. Dujardin, Production, properties and potential of graphene, *Carbon*, 48 (2010) 2127–2150.
53. W. Hummers, R. Offman, Preparation of graphitic oxide, *J. Am. Chem. Soc.*, 80 (1958) 1339.
54. H.C. Schniepp, J.L. Li, M.J. McAllister, H. Sai, M. Herrera-Alonso, D.H. Adamson, R.K. Prud'homme, R. Car, D.A. Saville, I.A. Aksay, Functionalized single graphene sheets derived from splitting graphite oxide, *J. Phys. Chem. B*, 110 (2006) 8535–8539.
55. M.J. McAllister, J.L. Li, D.H. Adamson, H.C. Schniepp, A.A. Abdala, J. Liu, M. Herrera-Alonso, D.L. Milius, R. Car, R.K. Prud'homme, I.A. Aksay, Single sheet functionalized graphene by oxidation and thermal expansion of graphite, *Chem. Mater.*, 19 (2007) 4396–4404.
56. Z.S. Wu, W. Ren, L. Gao, B. Liu, C. Jiang, H.M. Cheng, Synthesis of high-quality graphene with a pre-determined number of layers, *Carbon*, 47 (2009) 493–499.
57. Z.S. Wu, W. Ren, L. Gao, J. Zhao, Z. Chen, B. Liu, D. Tang, B. Yu, C. Jiang, H.M. Cheng, Synthesis of graphene sheets with high electrical conductivity and good thermal stability by hydrogen arc discharge exfoliation, *ACS Nano*, 3 (2009) 411–417.
58. J.I. Paredes, S. Villar-Rodil, A. Martinez-Alonso, J.M.D. Tascon, Graphene oxide dispersions in organic solvents, *Langmuir*, 24 (2008) 10560–10564.
59. T. Ramanathan, A.A. Abdala, S. Stankovich, D.A. Dikin, M. Herrera-Alonso, R.D. Piner, D.H. Adamson, H.C. Schniepp, X. Chen, R.S. Ruoff, S.T. Nguyen, I.A. Aksay, R.K. Prud'homme, L.C. Brinson, Functionalized graphene sheets for polymer nanocomposites, *Nat. Nanotechnol.*, 3 (2008) 327–331.
60. M. Pumera, Electrochemistry of graphene: new horizons for sensing and energy storage, *Chem. Rec.*, 9 (2009) 211–223.
61. M. Pumera, Graphene-based nanomaterials and their electrochemistry, *Chem. Soc. Rev.*, 39 (2010) 4146–4157.
62. W. Choi, I. Lahiri, R. Seelaboyina, Y.S. Kang, Synthesis of graphene and its applications: a review, *Crit. Rev. Solid State Mater. Sci.*, 35 (2010) 52–71.
63. D.C. Wei, Y.Q. Liu, Controllable synthesis of graphene and its applications, *Adv. Mater.*, 22 (2010) 3225–3241.
64. F. Banhart, J. Kotakoski, A.V. Krasheninnikov, Structural defects in graphene, *ACS Nano*, 5 (2011) 26–41.
65. G.C. Liang, N. Neophytou, M.S. Lundstrom, D.E. Nikonov, Ballistic graphene nanoribbon metal-oxide-semiconductor field-effect transistors: a full real-space quantum transport simulation, *J. Appl. Phys.*, 102 (2007) 054307.
66. O.V. Yazyev, M.I. Katsnelson, Magnetic correlations at graphene edges: Basis for novel spintronics devices, *Phys. Rev. Lett.*, 100 (2008) 047209.

67. I. Meric, M.Y. Han, A.F. Young, B. Ozyilmaz, P. Kim, K.L. Shepard, Current saturation in zero-bandgap, top-gated graphene field-effect transistors, *Nat. Nanotechnol.*, 3 (2008) 654–659.
68. F. Bonaccorso, Z. Sun, T. Hasan, A.C. Ferrari, Graphene photonics and optoelectronics, *Nat. Photonics*, 4 (2010) 611–622.
69. D.A. Dikin, S. Stankovich, E.J. Zimney, R.D. Piner, G.H.B. Dommett, G. Evmenenko, S.T. Nguyen, R.S. Ruoff, Preparation and characterization of graphene oxide-based paper, *Nature*, 448 (2007) 457–460.
70. S. Stankovich, D.A. Dikin, G.H.B. Dommett, K.M. Kohlhaas, E.J. Zimney, E.A. Stach, R.D. Piner, S.T. Nguyen, R.S. Ruoff, Graphene-based composite materials, *Nature*, 442 (2006) 282–286.
71. P. Dhiman, F. Yavari, X. Mi, H. Gullapalli, Y. Shi, P.M. Ajayan, N. Koratkar, Harvesting energy from water flow over graphene, *Nano Lett.*, 11 (2011) 3123–3127.
72. S. Ghost, A.K. Sood, N. Kumar, Carbon nanotube flow sensors, *Science*, 299 (2003) 1042–1044.
73. P.B. Amama, C. Lan, B.A. Cola, X. Xu, R.G. Reifengerger, T.S. Fisher, Electrical and thermal interface conductance of carbon nanotubes grown under direct bias voltage, *J. Phys. Chem. C*, 112 (2008) 19727–19733.
74. K.S. Kim, Y. Zhao, H. Jang, S.Y. Lee, J.M. Kim, K.S. Kim, J.H. Ahn, P. Kim, J.Y. Choi, B.H. Hong, Large-scale pattern growth of graphene films for stretchable transparent electrodes, *Nature*, 457 (2009) 706–710.
75. S. Bae, H. Kim, Y. Lee, X.F. Xu, J.S. Park, Y. Zheng, J. Balakrishnan, T. Lei, H.R. Kim, Y.I. Song, Y.J. Kim, K.S. Kim, B. Ozyilmaz, J.H. Ahn, B.H. Hong, S. Iijima, Roll-to-roll production of 30-inch graphene films for transparent electrodes, *Nat. Nanotechnol.*, 5 (2010) 574–578.
76. H. Chen, M.B. Müller, K.J. Gilmore, G.G. Wallace, D. Li, Mechanically strong, electrically conductive and biocompatible graphene paper, *Adv. Mater.*, 20 (2008) 3557–3561.
77. X. Wang, L.J. Zhi, K. Müllen, Transparent, conductive graphene electrodes for dye-sensitized solar cells, *Nano Lett.*, 8 (2008) 323–327.
78. Y.Y. Dou, G.R. Li, J. Song, X.P. Gao, Nickel phosphide-embedded graphene as counter electrode for dye-sensitized solar cells, *Phys. Chem. Chem. Phys.*, 14 (2012) 1339–1342.
79. A.Y. Anderson, P.R.F. Barnes, J.R. Durrant, B.C.O. Regan, Quantifying regeneration in dye-sensitized solar cells, *J. Phys. Chem. C*, 115 (2011) 2439–2447.
80. X. Wang, L.J. Zhi, N. Tsao, Z. Tomovic, J.L. Li, K. Müllen, Transparent carbon films as electrodes in organic solar cells, *Angew. Chemie Int. Ed.*, 47 (2008) 2990–2992.
81. Z.S. Wu, S. Pei, W. Ren, D. Tang, L. Gao, B. Liu, F. Li, C. Liu, H.M. Cheng, field emission of single-layer graphene films prepared by electrophoretic deposition, *Adv. Mater.*, 21 (2009) 1756–1760.
82. I.V. Lightcap, T.H. Kosel, P.V. Kamat, Anchoring semiconductor and metal nanoparticles on a two-dimensional catalyst mat. storing and shuttling electrons with reduced graphene oxide, *Nano Lett.*, 10 (2010) 577–583.
83. G. Williams, B. Seger, P.V. Kamat, TiO₂-graphene nanocomposites. UV-assisted photocatalytic reduction of graphene oxide, *ACS Nano*, 2 (2008) 1487–1491.

84. D. Choi, M.Y. Choi, W.M. Choi, H.J. Shin, H.K. Park, J.S. Seo, J. Park, S.M. Yoon, S.J. Chae, Y.H. Lee, S.W. Kim, J.Y. Choi, S.Y. Lee, J.M. Kim, Fully rollable transparent nanogenerators based on graphene electrodes, *Adv. Mater.*, 22 (2010) 2187–2192.
85. L.P. Ma, Z.S. Wu, J. Li, E.D. Wu, W. Ren, H.M. Cheng, Hydrogen adsorption behavior of graphene above critical temperature, *Int. J. Hydr. Energy*, 34 (2009) 2329–2332.
86. D. Gunlycke, P.E. Sheehan, Local peeling of graphene, *Science*, 331 (2011) 1146–1147.
87. A.H. Castro Neto, K. Novoselov, New directions in science and technology: two-dimensional crystals, *Rep. Prog. Phys.*, 74 (2011) 082501.
88. A.E. Rider, S. Kumar, S.A. Furman, K. Ostrikov, Self-organised Au nanoarrays on vertical graphenes: an advanced three-dimensional sensing platform, *Chem. Commun.*, 48 (2012) 2659–2661.
89. B. Nikoobakht, X. Li, Two-dimensional nanomembranes: Can they outperform lower dimensional nanocrystals?, *ACS Nano*, 6 (2012) 1883–1887.
90. B. Radisavljevic, A. Radenovic, J. Brivio, V. Giacometti, A. Kis, Single-layer MoS₂ transistors, *Nat. Nanotechnol.*, 6 (2011) 147–150.
91. D. Di Yao, J. Zhen Ou, K. Latham, S. Zhuiykov, A.P. O'Mullane, K. Kalantar-zadeh, Electrodeposited α - and β -phase MoO₃ films and investigation of their gasochromic properties, *ACS Cryst. Growth Des.*, 12 (2012) 1865–1870.
92. J.G. Lu, P. Chang, Z. Fan, Quasi-one-dimensional metal oxide materials-synthesis, properties and applications, *Mater. Sci. Eng. R*, 52 (2006) 49–91.
93. J.Z. Ou, R.A. Rani, M.H. Ham, Y. Zhang, H. Zheng, S. Sriram, M. Bhaskaran, K. Latham, S. Zhuiykov, R.B. Kaner, K. Kalantar-zadeh, Elevated temperature anodized Nb₂O₅ – a photoanode material with exceptionally large photoconversion, *ACS Nano*, 6 (2012) 4045–4053.
94. S. Balendhran, J.Z. Ou, M. Bhaskaran, S. Sriram, S. Ippolito, Z. Vasic, E. Kats, S. Bhargava, S. Zhuiykov, K. Kalantar-zadeh, Atomically thin layers of MoS₂ via a two step thermal evaporation – exfoliation method, *Nanoscale*, 4 (2012) 461–466.
95. Z. Yin, H. Li, Hong Li, L. Jiang, Y. Sun, G. Lu, Q. Zhang, X. Chen, H. Zhang, Single-layer MoS₂ phototransistors, *ACS Nano*, 6 (2012) 74–80.
96. F.R. Schepherd, P.M. Williams, Photoemission studies of the band structures of transition metal dichalcogenides. I Groups IVA and IVB, *J. Phys. C: Solid State Phys.*, 7 (1974) 4416–4426.
97. V.V. Plashnitsa, F. Vietmeyer, N. Petchsang, P. Tonguing, T.H. Kosel, M. Kuno, Synthetic strategy and structural and optical characterisation of thin highly crystalline titanium disulfide nanosheets, *J. Phys. Chem. Lett.*, 3 (2012) 1554–1558.
98. Y. Zhang, Z. Li, H. Jia, X. Luo, J. Xu, X. Zhang, D. Yu, TiS₂ whisker growth by a simple vapour-deposition method, *J. Cryst. Growth*, 293 (2006) 124–127.
99. K.H. Park, J. Choi, H.J. Kim, D.-H. Oh, J.R. Ahn S.U. Son, Unstable single-layered colloidal TiS₂ nanodisks, *Small*, 4 (2008) 945–950.
100. S. Prabakar, S. Collings, B. Northover, R.D. Tilley, Colloidal synthesis of inorganic fullerene nanoparticles and hollow spheres of titanium disulfide, *Chem. Commun.*, 47 (2011) 439–441.

101. S. Jeong, J.H. Han, J.-T. Jang, J.-W. Seo, J.G. Kim, J. Cheon, Transformative two-dimensional layered TiS_2 nanocrystals, *J. Am. Chem. Soc.*, 133 (2011) 14500–14503.
102. H.E. Swanson, M.C. Morris, E.H. Evans, *Standard X-ray diffraction power patterns*, Natl. Bur. Stand. (US) Monograph 25; U.S. Department of Commerce: Washington, DC, 1966.
103. D. Teich, T. Lorenz, J.-O. Joswig, G. Seifert, D.-B. Zhang, T. Dumitrica, Structural and electronic properties of helical TiS_2 nanotubes studied with objective molecular dynamics, *J. Phys. Chem. C*, 115 (2011) 6392–6296.
104. V.V. Ivanovskaya, G. Seifert, A.L. Ivanovskii, Electronic structure of titanium disulfide nanostructures: monolayers, nanostripes and nanotubes, *Semiconductors*, 39 (2005) 1058–1065.
105. Y.H. Liu, S.H. Porter, J.E. Goldberger, Dimensional reduction of a layered chalcogenide into a 1D near-IR direct band gap semiconductor, *J. Am. Chem. Soc.*, 134 (2012) 5044–5047.
106. H.W. Myron, A.J. Freeman, Electronic structure and optical properties of layered dichalcogenides TiS_2 and TiSe_2 , *Phys. Rev. B*, 9 (1974) 481–486.
107. A.R. Beal, J.C. Knights, W.Y. Liang, Transmission spectra of some transition metal dichalcogenides: I. Group IVA: Octahedral coordination, *J. Phys. C: Solid State Phys.*, 5 (1972) 3531–3539.
108. J.N. Coleman, M. Lotya, A. O'Neill, S.D. Bergin, P.J. King, U. Khan, K. Young, A. Gaucher, S. De, R.J. Smith, I.V. Shvets, S.K. Arora, G. Stanton, H. Kim, K. Lee, G.T. Kim, G.S. Duesberg, T. Hallam, J.J. Boland, J.J. Wang, J.F. Donegan, J.C. Grunlan, G. Moriarty, A. Shmeliov, R.J. Nicholls, J.P. Perkins, E.M. Grieverson, K. Theuwissen, D.W. McComb, P.D. Nellist, V. Nicolosi, Two-dimensional nano-sheets produced by liquid exfoliation of layered materials, *Science*, 331 (2011) 568–571.
109. K. Kalantar-zadeh, A. Vijayaraghavan, M.H. Ham, H.D. Zheng, M. Breedon, M.S. Strano, Synthesis of atomically thin WO_3 sheets from hydrated tungsten trioxide, *Chem. Mater.*, 22 (2010) 5660–5666.
110. K. Kalantar-zadeh, J.S. Tang, M.S. Wang, K.L. Wang, A. Shailos, K. Galatsis, R. Kojima, V. Strong, A. Lech, W. Wlodarski, R.B. Kaner, Synthesis of nanometre-thick MoO_3 sheets, *Nanoscale*, 2 (2010) 429–433.
111. C. Lee, H. Yan, L.E. Brus, T.F. Heinz, J. Hone, S. Ryu, Anomalous lattice vibrations of single- and few-layer MoS_2 , *ACS Nano*, 4 (2010) 2695–2700.
112. K.F. Mak, C. Lee, J. Hone, J. Shan, T.F. Heinz, Atomically thin MoS_2 : a new direct-gap semiconductor, *Phys. Rev. Lett.*, 105 (2010) 136805.
113. M.T. Bohr, R.S. Chau, T. Chani, K. Misty, The high-k solution, *IEEE Spectrum*, 44 (2007) 29–35.
114. M. Ishigami, J.H. Chen, W.G. Cullen, M.S. Fuhrer, E.D. Williams, Atomic structure of graphene on SiO_2 , *Nano Lett.*, 7 (2007) 1643–1648.
115. K.S. Novoselov *et al.*, Two-dimensional atomic crystals, *Proc. Natl Acad. Sci. USA*, 102 (2005) 10451–10453.
116. A. Avari, E. Cobas, O. Ogundadegbe, M.S. Fuhrer, Realisation and electrical characterisation of ultrathin crystals of layered transition-metal dichalcogenides, *J. Appl. Phys.*, 101 (2007) 014507.
117. R. Fivaz, E. Mooser, Mobility of charge carriers in semiconducting layer structures, *Phys. Rev.*, 163 (1967) 743–755.

118. X. Duan, *et al.*, High-performance thin-film transistors using semiconductor nanowires and nanoribbons, *Nature*, 425 (2003) 274–278.
119. L. Liao, *et al.*, High-speed graphene transistors with a self-aligned nanowire gate, *Nature*, 467 (2010) 305–308.
120. A. Castellanos-Gomez, M. Barkelid, A.M. Goossens, V.E. Calado, H.S.J. van der Zant, G.A. Steele, Laser-thinning of MoS₂: On demand generation of a single-layer semiconductor, *Nano Lett.*, 12 (2012) 3187–3192.
121. A. Splendiani, L. Sun, Y.B. Zhang, T.S. Li, J. Kim, C.Y. Chim, G. Galli, F. Wang, Emerging photoluminescence in monolayer MoS₂, *Nano Lett.*, 10 (2010) 1271–1275.
122. S. Ghatak, A.N. Pal, A. Ghosh, Nature of electronic states in atomically thin MoS₂ field-effect transistors, *ACS Nano*, 5 (2011) 7707–7712.
123. J.H. Chen, C. Jang, S. Adam, M.S. Fuhrer, E.D. Williams, M. Ishigami, Charged-impurity scattering in graphene, *Nat. Phys.*, 4 (2008) 377–381.
124. F. Xia, T. Mueller, Y. Lin, A. Valdes-Garcia, P. Avouris, Ultrafast graphene photodetector, *Nat. Nanotechnol.*, 4 (2009) 839–843.
125. H.S. Lee, S.-W. Min, Y.-G. Chang, M.K. Park, T. Nam, H. Kim, J.H. Kim, S. Ryu, S. Im, MoS₂ nanosheet phototransistors with thickness-modulated optical energy gap, *Nano Lett.*, 12 (2012) 3695–3700.
126. P.V. Kamat, TiO₂ nanostructures: recent physical chemistry advances, *J. Phys. Chem. C*, 116 (2012) 11849–11851.
127. J. Nowontny, *Oxide Semiconductors for Solar Energy Conversion: Titanium dioxide*, 2012, CRC Press, New York, 394.
128. A. Fujishima, X. Zhang, D.A. Tryk, TiO₂ photocatalysis and related surface phenomena. *Surf. Sci. Rep.*, 63 (2008) 515–582.
129. W. Choi, A. Termin, M.R. Hoffmann, The role of metal ion dopants in quantum-sized TiO₂: correlation between photoreactivity and charge carrier recombination dynamics. *J. Phys. Chem.*, 98 (1994) 13669–13679.
130. R. Asahi, T. Morikawa, T. Ohwaki, K. Aoki, Y. Taga, Visible-light photocatalysis in nitrogen-doped titanium oxides, *Science*, 293 (2001) 269–271.
131. S.U.M. Khan, M. Al-Shahry, W.B. Jr Ingler, Efficient photochemical water splitting by a chemically modified n-TiO₂, *Science*, 297 (2002) 2243–2245.
132. D.Y. Kim, J.S.D. Almeida, L. KoCi, R. Ahuja, Dynamical stability of the hardest known oxide and the cubic solar material: TiO₂, *Appl. Phys. Lett.*, 90 (2007) 171903.
133. M. Mattesini, J.S. de Almeida, L. Dubrovinsky, N. Dubrovinskaia, B. Johansson, R. Ahuja, Cubic TiO₂ as a potential light absorber in solar-energy conversion, *Phys. Rev. B*, 70 (2004) 115101.
134. H. Ariga, T. Taniike, H. Morikawa, M. Tada, B.K. Min, K. Watanabe, Y. Matsumoto, S. Ikeda, K. Saiki, Y. Iwasawa, Surface-mediated visible-light photo-oxidation on pure TiO₂(001), *J. Am. Chem. Soc.*, 131 (2009) 14670–14672.
135. A.C. Papageorgiou, N.S. Beglitis, C.L. Pang, G. Teobaldi, G. Cabailh, Q. Chen, A.J. Fisher, W.A. Hofer, G. Thornton, Electron traps and their effect on the surface chemistry of TiO₂(110), *Proc. Natl Acad. Sci. USA*, 107 (2010) 2391–2396.
136. U. Diebold, The surface science of titanium dioxide, *Surf. Sci. Rep.*, 48 (2003) 53–229.

137. X. Torrelles, G. Cabailh, R. Lindsay, O. Bikondoa, J. Roy, J. Zegenhagen, G. Teobaldi, W.A. Hofer, G. Thornton, Geometric structure of $\text{TiO}_2(011)(2\times 1)$, *Phys. Rev. Lett.*, 101 (2008) 185501.
138. G.D. Scholes, G.R. Fleming, A. Olaya-Castro, R. van Grondelle, Lessons from nature about solar light harvesting, *Nat. Chem.*, 3 (2011) 763–774.
139. P.V. Kamat, Manipulation of charge transfer across semiconductor interface. A criterion that cannot be ignored in photocatalyst design, *J. Phys. Chem. Lett.*, 3 (2012) 663–672.
140. P.V. Kamat, Capturing hot electrons, *Nat. Chem.*, 2 (2010) 809–810.
141. J. Tao, T. Luttrell, M. Batzill, A two-dimensional phase of TiO_2 with a reduced bandgap, *Nat. Chem.*, 3 (2011) 296–300.
142. K. Maeda, K. Domen, Photocatalytic water splitting: Recent progress and future challenges, *J. Phys. Chem. Lett.*, 1 (2010) 2655–2661.
143. W.Y. Teoh, J.A. Scott, R. Amal, Progress in heterogeneous photocatalysis: from classical radical chemistry to engineering nanomaterials and solar reactors, *J. Phys. Chem. Lett.*, 3 (2012) 629–639.
144. X. Pan, Y. Zhao, S. Liu, C.L. Korzeniewski, S. Wang, Z. Fan, Comparing graphene- TiO_2 nanowire and graphene- TiO_2 nanoparticles composite photocatalysis, *ACS Appl. Mater. Int.*, 4 (2012) 3944–3950.
145. W. Choi, A. Termin, M.R. Hoffman, The role of metal ion dopants in quantum-sized TiO_2 : correlation between photoreactivity and charge carrier recombination dynamics, *J. Phys. Chem.*, 98 (1994) 13669–13679.
146. L.M. Peter, The Gratzel cell: Where next? *J. Phys. Chem. Lett.*, 2 (2011) 1861–1867.
147. T. Miyasaka, Toward printable sensitized mesoscopic solar cells: light-harvesting management with thin TiO_2 films, *J. Phys. Chem. Lett.*, 2 (2011) 262–269.
148. E.L. Ratcliff, B. Zacher, N.R. Armstrong, Selective interlayers and contacts in organic photovoltaic cells, *J. Phys. Chem. Lett.*, 2 (2011) 1337–1350.
149. I. Mora-Sero, J. Bisquert, Breakthroughs in the development of semiconductor-sensitized solar cells, *J. Phys. Chem. Lett.*, 1 (2010) 3046–3052.
150. A. Braga, S. Gimenez, I. Concina, A. Vomiero, I. Mora-Sero, Panchromatic sensitized solar cells based on metal sulfide quantum dots grown directly on nanostructured TiO_2 electrodes, *J. Phys. Chem. Lett.*, 2 (2011) 454–460.
151. J. Bisquert, I. Mora-Sero, Simulation of steady-state characteristics of dye-sensitized solar cells and the interpretation of the diffusion length, *J. Phys. Chem. Lett.*, 1 (2010) 450–456.
152. A.Y. Anderson, P.R.F. Barnes, J.R. Durrant, B.C. O'Regan, Quantifying regeneration in dye-sensitized solar cells, *J. Phys. Chem. C*, 115 (2011) 2439–2447.
153. J.J.H. Pijpers, R. Ulbricht, S. Derossi, J.N.H. Reek, M. Bonn, Picosecond electron injection dynamics in dye-sensitized oxides in the presence of electrolyte, *J. Phys. Chem. C*, 115 (2011) 2578–2584.
154. D.J. Mowbray, J.I. Martinez, F. Calle-Vallejo, J. Rossmeisl, K.S. Thygesen, K.W. Jacobsen, J.K. Nørskov, Trends in metal oxide stability for nanorods, nanotubes, and surfaces, *J. Phys. Chem. C*, 115 (2011) 2244–2252.
155. W.Q. Fang, X.Q. Gong, H.G. Yang, On the unusual properties of anatase TiO_2 exposed by highly reactive facets, *J. Phys. Chem. Lett.*, 2 (2011) 725–734.
156. J.G. Yu, Y. Hai, B. Cheng, Enhanced photocatalytic H₂-production activity of TiO_2 by $\text{Ni}(\text{OH})_2$ cluster modification, *J. Phys. Chem. C*, 115 (2011) 4953–4958.

157. Y. Nishijima, K. Ueno, Y. Yokota, K. Murakoshi, H. Misawa, Plasmon-assisted photocurrent generation from visible to near-infrared wavelength using a Au-nanorods/TiO₂ electrode, *J. Phys. Chem. Lett.*, 1 (2010) 2031–2036.
158. B.H. Meekins, P.V. Kamat, Role of water oxidation catalyst, IrO₂ in shuttling photogenerated holes across TiO₂ interface, *J. Phys. Chem. Lett.*, 2 (2011) 2304–2310.
159. Z.R. Tang, F. Li, Y.H. Zhang, X.Z. Fu, Y.J. Xu, Composites of titanate nanotube and carbon nanotube as photocatalyst with high mineralization ratio for gas-phase degradation of volatile aromatic pollutant, *J. Phys. Chem. C*, 115 (2011) 7880–7886.
160. Y.H. Ng, I.V. Lightcap, K. Goodwin, M. Matsumura, P.V. Kamat, To what extent do graphene scaffolds improve the photovoltaic and photocatalytic response of TiO₂ nanostructured films? *J. Phys. Chem. Lett.*, 1 (2010) 2222–2227.
161. N.J. Bell, H.N. Yun, A.J. Du, H. Coster, S.C. Smith, R. Amal, Understanding the enhancement in photoelectrochemical properties of photocatalytically prepared TiO₂-reduced graphene oxide composite, *J. Phys. Chem. C*, 115 (2011) 6004–6009.
162. P.V. Kamat, Graphene-based nanoarchitectures: Anchoring semiconductor and metal nanoparticles on a two-dimensional carbon support, *J. Phys. Chem. Lett.*, 1 (2010) 520–527.
163. B.R. Matis, J.S. Burgess, F.A. Bulat, A.L. Friedman, B.H. Houston, J.W. Baldwin, Surface doping and band gap tunability in hydrogenated graphene, *ACS Nano*, 6 (2012) 17–22.
164. R. Zan, U. Bangert, Q. Ramasse, K.S. Novoselov, Metal-graphene interaction studied via atomic resolution scanning transmission electron microscopy, *Nano Lett.*, 11 (2011) 1087–1092.
165. J.N. Yao, K. Hashimoto, A. Fujishima, Photochromism induced in an electrolytically pretreated MoO₃ thin film by visible light, *Nature*, 355 (1992) 624–626.
166. M.A. Quevedo-Lopez, R.F. Reidy, R.A. Orozco-Teran, O. Mendoza-Gonzalez, R. Ramirez-Bon, Enhancement of photo and thermochromic properties of molybdenum oxide by a CdS underlayer, *J. Mater. Sci.: Mater. Electron.*, 11 (2000) 151–155.
167. K. Gesheva, A. Szekers, T. Ivanova, Optical properties of chemical vapour deposited thin films of molybdenum and tungsten based metal oxides, *Sol. Energy Mater. Sol. Cells*, 76 (2003) 563–576.
168. L.A. Riley, S.-H. Lee, L. Gedvilias, A.C. Dillon, Optimization of MoO₃ nanoparticles as negative-electrode material in high-energy lithium ion batteries, *J. Power Sources*, 195 (2010) 588–592.
169. A. Bielanski, M. Naibar, V₂O₅-MoO₃ catalysts for benzene oxidation, *Appl. Catal. A*, 157 (1997) 223–261.
170. K. Galatsis, Y.X. Li, W. Wlodarski, K. Kalantar-zadeh, Sol-gel prepared MoO₃ – WO₃ thin films for O₂ gas sensing, *Sens. Actuators B: Chem.*, 77 (2001) 478–483.
171. T.M. McEvoy, K.J. Stevenson, J.T. Hupp, X. Dang, Electrochemical preparation of molybdenum trioxide thin films: effect of sintering on electrochromic and electroinsertion properties, *Langmuir*, 19 (2003) 4316–4326.

172. K. Kalantar-zadeh, J.S. Tang, M.S. Wang, K.L. Wang, A. Shailos, K. Galatsis, R. Kojima, V. Strong, A. Lech, W. Wlodarski, R.B. Kaner, Synthesis of nanometre-thick MoO₃ sheets, *Nanoscale*, 2 (2010) 429–433.
173. C.J. Machiels, W.H. Cheng, U. Chowdhry, W.E. Farneth, F. Hong, E.M. McCarron, A.W. Sleight, The effect of the structure of molybdenum oxides on the selective oxidation of methanol, *Appl. Catal.*, 25 (1986) 249–256.
174. V. Bhosle, A. Tiwari, J. Narayan, Epitaxial growth and properties of MoO_x ($2 < x < 2.75$) films, *J. Appl. Phys.*, 97 (2005) 083539.
175. A.K. Prasad, D.J. Kubinski, P.I. Gouma, Comparison of sol–gel and ion beam deposited MoO₃ thin film gas sensors for selective ammonia detection, *Sens. Actuators B: Chem.*, 93 (2003) 25–30.
176. I. Navas, R. Vinodkumar, K.J. Lethy, A.P. Detty, V. Ganesan, V. Sathe, V.P.M. Pillai, Growth and characterization of molybdenum oxide nanorods by RF magnetron sputtering and subsequent annealing, *J. Phys. D: Appl. Phys.*, 42 (2009) 175305.
177. A. Bouzidi, N. Benramdane, H. Tabet-Derraz, C. Mathieu, B. Khelifa, R. Desfeux, Effect of substrate temperature on the structural and optical properties of MoO₃ thin films prepared by spray pyrolysis technique, *Mater. Sci. Eng. B*, 97 (2003) 5–8.
178. Y.J. Lee, W.T. Nichols, D.G. Kim, Y. Do Kim, Chemical vapour transport synthesis and optical characterization of MoO₃ thin films, *J. Phys. D: Appl. Phys.*, 42 (2009) 115419.
179. T. Siciliano, A. Tepore, E. Filippo, G. Micocci, M. Tepore, Characteristics of molybdenum trioxide nanobelts prepared by thermal evaporation technique, *Mater. Chem. Phys.*, 114 (2009) 687–691.
180. Y.L. Xie, F.C. Cheong, Y.W. Zhu, B. Varghese, R. Tamang, A.A. Bettioli, C.H. Sow, Rainbow-like MoO₃ nanobelts fashioned via afm micromachining, *J. Phys. Chem. C*, 114 (2009) 120–124.
181. S. Wang, Y. Zhang, X. Ma, W. Wang, X. Li, Z. Zhang, Y. Qian, Hydrothermal route to single crystalline α -MoO₃ nanobelts and hierarchical structures, *Solid State Commun.*, 136 (2005) 283–287.
182. A. Guerfi, R.W. Paynter, L.H. Dao, Characterization and stability of electrochromic MoO₃ thin-films prepared by electrodeposition, *J. Electrochem. Soc.*, 142 (1995) 3457–3464.
183. T.M. McEvoy, K.J. Stevenson, Electrochemical quartz crystal microbalance study of the electrodeposition mechanism of molybdenum oxide thin films from peroxo-polymolybdate solution, *Anal. Chim. Acta*, 496 (2003) 39–51.
184. S. Balendhran, J. Deng, J.Z. Ou, J. Scott, J. Tang, K. Wang, M.R. Field, S. Russo, S. Zhuiykov, M. Strano, N. Medhekar, S. Sriram, M. Bhaskaran, K. Kalantar-zadeh, Enhanced charge carrier mobility in two-dimensional high dielectric molybdenum oxide, *Adv. Mater.*, 25 (2013) 109–114.
185. S. Al-Khawaja, M. Kassem, Low-frequency dielectric response in two-dimensional layered MoO₃ system doped with Nb₂O₅ at low temperatures, *Curr. Sci. India*, 102 (2012) 478–484.
186. X.K. Hu, *et al.*, Comparative study on MoO₃ and H_xMoO₃ nanobelts: Structure and electric transport, *Chem. Mater.*, 20 (2008) 1527–1533.
187. X.W. Sha, L. Chen, A.C. Cooper, G.P. Pez, H.S. Cheng, Hydrogen absorption and diffusion in bulk alpha-MoO₃, *J. Phys. Chem. C*, 113 (2009) 11399–11407.

188. T. Ando, A.B. Fowler, F. Stern, Electronic-properties of two-dimensional systems. *Rev. Mod. Phys.*, 54 (1982) 437–672.
189. J.Z. Ou, J.L. Campbell, D. Yao, W. Wlodarski, K. Kalantar-zadeh, In situ Raman spectroscopy of H₂ gas interaction with layered MoO₃, *J. Phys. Chem. C*, 115 (2011) 10757–10763.
190. A. Polaczek, M. Pekala, Z. Obuszko, Re-entrant disordering of colloidal molecular crystals on two-dimensional periodic substrates, *J. Phys. Condens. Mater.*, 6 (1994) 7909–7916.
191. T. Vogt, P.M. Woodward, B.A. Hunter, The high-temperature phases of WO₃, *J. Solid State Chem.*, 144 (1999) 209–215.
192. H. Zheng, J.Z. Ou, M.S. Strano, R.B. Kaner, A. Mitchell, K. Kalantar-zadeh, Nanostructured tungsten oxide – properties, synthesis and applications, *Adv. Funct. Mater.*, 21 (2011) 2175–2196.
193. N. Mukherjee, M. Paulose, O.K. Varghese, G.K. Mor, C.A. Grimes, Fabrication of nanoporous tungsten oxide by galvanostatic anodization, *J. Mater. Res.*, 18 (2003) 2296–2299.
194. R.D. Rauh, Electrochromic windows: An overview, *Electrochim. Acta*, 44 (1999) 3165–3176.
195. H. Zheng, Y. Tachibana, K. Kalantar-zadeh, Dye-sensitized solar cells based on WO₃, *Langmuir*, 26 (2010) 19148.
196. Y. Takeda, N. Kato, T. Fukano, A. Takeichi, T. Motohiro, S. Kawai, WO₃/metal thin-film bilayered structures as optical recording materials, *J. Appl. Phys.*, 96 (2004) 2417–2422.
197. M. Breedon, P. Spizzirri, M. Taylor, J. du Plessis, D. McCulloch, J. Zhu, L. Yu, Z. Hu, C. Rix, W. Wlodarski, K. Kalantar-zadeh, Synthesis of nanostructured tungsten oxide thin films: A simple, controllable, inexpensive, aqueous sol-gel method, *Cryst. Growth Des.*, 10 (2010) 430–439.
198. J. Livage, D. Ganguli, Sol-gel electrochromic coatings and devices: A review, *Sol. Energ. Mater. Sol. C*, 68 (2001) 365–381.
199. C. Balazsi, J. Pfeifer, Development of tungsten oxide hydrate phases during precipitation, room temperature ripening and hydrothermal treatment, *Solid State Ionics*, 151 (2002) 353–358.
200. M. Epifani, T. Andreu, J. Arbiol, R. Diaz, P. Siciliano, J.R. Morante, Chloroalkoxide route to transition metal oxides. Synthesis of WO₃ thin films and powders from a tungsten chloro-methoxide, *Chem. Mater.*, 21 (2009) 5215–5221.
201. S. Balaji, A.S. Albert, Y. Djaoued, R. Bruning, Micro-Raman spectroscopic characterization of a tunable electrochromic device for application in smart windows, *J. Raman Spectrosc.*, 40 (2009) 92–97.
202. S.H. Lee, P. Liu, C.E. Tracy, D.K. Benson, All solid-state rocking chair lithium battery on a flexible Al substrate, *Electrochem. Solid-State Lett.*, 2 (1999) 425–427.
203. S.H. Lee, M.J. Seong, H.M. Cheong, E. Ozkan, E.C. Tracy, S.K. Deb, Effect of crystallinity on electrochromic mechanism of Li_xWO₃ thin films, *Solid State Ionics*, 156 (2003) 447–452.
204. S.K. Deb, Opportunities and challenges in science and technology of WO₃ for electrochromic and related applications, *Sol. Energy Mater. Sol. Cells*, 92 (2008) 245–258.

205. A. Le Viet, M.V. Reddy, R. Jose, B.V.R. Chowdari, S. Ramakrishna, Nanostructured Nb₂O₅ polymorphs by electrospinning for rechargeable lithium batteries, *J. Phys. Chem.*, 114 (2010) 664–671.
206. A.G.S. Prado, L.B. Bolzon, C.P. Pedroso, A.O. Moura, L.L. Costa, Nb₂O₅ as efficient and recyclable photocatalyst for indigo carmine degradation, *Appl. Catal. B: Environmental*, 84 (2008) 219–224.
207. C. Nico, M.R.N. Soares, J. Rodrigues, M. Matos, R. Monteiro, M.P.F. Graça, M.A. Valente, F.M. Costa, T. Monteiro, Sintered NbO powders for electronic device applications, *J. Phys. Chem.*, 115 (2011) 4879–4886.
208. H. Stromer, A. Weber, V. Fischer, E. Ivers-Tiffée, D. Gerthsen, Anodically formed films on niobium: Microstructural and electrical properties, *J. Europ. Ceram. Soc.*, 29 (2009) 1743–1753.
209. J. Xia, N. Masaki, K. Jiang, S. Yanagida, Fabrication and characterization of thin Nb₂O₅ blocking layers for ionic liquid-based dye-sensitized solar cells, *J. Photochem. Photobiol A: Chem.*, 188 (2007) 120–127.
210. G. Hodes, A. Zaban, Nanocrystalline solar cells, *Front. Nanosci.*, 1 (2009) 232–269.
211. X. Xiao, G. Dong, C. Xu, H. He, H. Qi, Z. Fan, J. Shao, Structure and optical properties of sculptured Nb₂O₅ thin films by glancing angle deposition, *Appl. Surf. Sci.*, 255 (2008) 2192–2195.
212. L. Chevallier, E.D. Bartolomeo, M.L. Grilli, M. Mainas, B. White, E.D. Wachsmann, E. Traversa, Non-Nernstian planar sensors based on YSZ with a Nb₂O₅ electrode, *Sens. Actuators B: Chem.*, 129 (2008) 591–598.
213. T. Hyodo, J. Ohoka, Y. Shimizu, M. Egashira, Design of anodically oxidized Nb₂O₅ films as diode-type H₂ sensing material, *Sens. Actuators B: Chem.*, 117 (2006) 359–366.
214. M. Zhang, C. Hu, X. He, B. Wan, Y. Xi, Building nestlike Nb₂O₅:Tb³⁺ for effective catalytic degradation, *Cataly. Commun.*, 11 (2009) 206–209.
215. M. Wei, Z.M. Qi, M. Ichihara, H. Zhou, Synthesis of single-crystal niobium pentoxide nanobelts, *Acta Mater.*, 56 (2008) 2488–2494.
216. M. Wei, K. Wei, M. Ichihara, H. Zhou, Nb₂O₅ nanobelts: A lithium intercalation host with large capacity and high rate capability, *Electrochem. Commun.*, 10 (2008) 980–983.
217. G. Viau, J. Piquemal, M. Esparrica, D. Ung, N. Chakroune, F. Warmont, F. Fiévet, Formation of assembled silver nanowires by reduction of silver thiolate in polyol/toluene medium, *Chem. Commun.*, 17 (2003) 2216–2217.
218. S. Zhuiykov, E. Kats, Atomically-thin two-dimensional materials for functional electrodes of electrochemical devices: A review, *Ionics*, 19 (2013) 825–865.
219. V. Palermo, A. Liscio, M. Palma, M. Surin, R. Lazzaroni, P. Samori, Exploring nanoscale electrical and electronic properties of organic and polymeric functional materials by atomic force microscopy based approaches, *Chem. Commun.*, 9 (2007) 3326–3337.
220. R.S. Devan, W. Ho, C. Chen, H. Shiu, C. Ho, C. Cheng, S.Y. Wu, Y. Liou, Y. Ma, High room-temperature photoluminescence of one-dimensional Ta₂O₅ nanorod arrays, *Nanotechnology*, 20 (2009) 445708.
221. X.Q. Liu, X.D. Han, Z. Zhang, L.F. Ji, Y.J. Jiang, The crystal structure of high temperature phase Ta₂O₅, *Acta Mater.*, 55 (2007) 2385–2396.

222. F.Z. Tepehan, F.E. Ghodsi, N. Ozer, G.G. Tepehan, Optical properties of sol-gel dip-coated Ta₂O₅ films for electrochromic applications, *Sol. Energy Sol. Cells*, 59 (1999) 265–275.
223. C. Bartic, H. Jansen, A. Campitelli, S. Borghs, Ta₂O₅ as gate dielectric material for low-voltage organic thin-film transistor, *Org. Electron.*, 3 (2002) 65–72.
224. L. Pewreira, P. Barquinha, E. Fortunato, R. Martinez, D. Kang, C.J. Kim, H. Lim, I. Song, Y. Park, High *k* dielectrics for low temperature electronics, *Thin Solid Films*, 516 (2008) 1544–1548.
225. E. Atanassova, A. Paskaleva, Challenges of Ta₂O₅ as high-*k* dielectric for nanoscale DRAMs, *Microelectron. Reliab.*, 47 (2007) 913–923.
226. O.A. Azim, M.M. Abdel-Aziz, I.S. Yahia, Structure and optical analysis of Ta₂O₅ deposited on infrasil substrate, *Appl. Surf. Science*, 255 (2009) 4829–4835.
227. M. Audier, B. Chenevier, H. Roussel, L. Vincent, A. Pena, A. Lintanf-Salaun, A very promising piezoelectric property of thin films. I: Monoclinic-trigonal phase transition, *J. Solid State Chem.*, 184 (2011) 2023–2032.
228. D.F. Lu, Z.M. Qi, R.P. Liu, An interferometric biosensor composed of a prism-chamber assembly and a composite waveguide with a Ta₂O₅ nanometric layer, *Sens. Actuators B: Chem.*, 157 (2011) 575–580.
229. L.M. Kalinina, A.V. Linvinov, I.N. Nikolaev, N.N. Samotaev, MIS-Field effect sensors for low concentration H₂S for environment monitoring, *Procedia Engineering*, 5 (2010) 1216–1219.
230. A. Fog, R.P. Buck, Electronic semiconducting oxides as pH sensors, *Sens. Actuators B: Chem.*, 5 (1984) 137–146.
231. E. Atanassova, A. Pakaleva, D. Spassov, Doping of Ta₂O₅ as a way to extend its potential for DRAM applications, *Proc. 27th International conference on Microelectronics (Miel 2010)*, NIS, Serbia, 16–19 May 2010, 427–434.
232. B.Z. Saggiaro, M.R.B. Andreetta, A.C. Hernandez, M. Macatrão, M. Peres, F.M. Costa, T. Monteiro, N. Franco, E. Alves, Effect of Eu₂O₃ doping on Ta₂O₅ crystal growth by the laser-heated pedestal technique, *J. Cryst. Growth*, 313 (2010) 62–67.
233. G. Deng, A. Ding, W. Cheng, X. Zheng, P. Qiu, Two-dimensional zinc oxide nanostructure, *Solid State Commun.*, 134 (2005) 283–286.
234. D-T. Phan, G-S. Chung, Surface acoustic wave hydrogen sensors based on ZnO nanoparticles incorporated with a Pt catalyst, *Sens. Actuators B: Chem.*, 161 (2012) 341–348.
235. S. Ma, R. Li, C. Lv, W. Xu, X. Gou, Facile synthesis of ZnO nanorod arrays and hierarchical nanostructures for photocatalysis and gas sensor applications, *J. Hazard. Mater.*, 192 (2011) 730–740.
236. Y.-T. Kim, J. Park, S. Kim, D.W. Park, J. Choi, Fabrication of hierarchical ZnO nanostructures for dye-sensitized solar cells, *Electrochim. Acta*, 78 (2012) 417–421.
237. P.D. Yang, H.Q. Yan, S. Mao, P. Yang, H. Yan, S. Mao, R. Russo, J. Johnson, R. Saykally, N. Morris, J. Phan, R. He, H.J. Choi, Controlled growth of ZnO nanowires and their optical properties, *Adv. Funct. Mater.*, 12 (2002) 323–331.
238. P.M. Gao, Y. Ding, W.J. Mai, W.L. Hughes, C.S. Lao, Z.L. Wang, Conversion of zinc oxide nanobelts into superlattice-structured nanohelices, *Science*, 309 (2005) 1700–1704

239. Z.Y. Fan, D.W. Wang, P.C. Chang, W.Y. Tseng, J.G. Lu, ZnO nanowire field-effect transistor and oxygen sensing property, *Appl. Phys. Lett.*, 85 (2004) 5923–5925.
240. X.D. Wang, Y. Ding, C.J. Summers, Z.L. Wang, Large-scale synthesis of six-nanometer-wide ZnO nanobelts, *J. Phys. Chem. B*, 108 (2004) 8773–8777.
241. Y. Gu, I.L. Kuskovsky, M. Yin, S. O'Brien, G.F. Neumark, Quantum confinement in ZnO nanorods, *Appl. Phys. Lett.*, 85 (2004) 3833–3835.
242. P.C. Chang, Z.Y. Fan, D.W. Wang, W.Y. Tseng, W.A. Chioi, J. Hong, J.G. Lu, ZnO nanowires synthesized by vapour trapping CVD method, *Chem. Mater.*, 16 (2004) 5133–5137.
243. M. Law, L.E. Greene, J.C. Johnson, R. Saykally, P.D. Yang, Nanowire dye-sensitized solar cells, *Nat. Mater.*, 4 (2005) 455–459.
244. J.T. Jiu, F.M. Wang, S. Isoda, M. Adachi, Highly efficient dye-sensitized solar cells based on single crystalline TiO₂ nanorod film, *Chem. Lett.*, 34 (2005) 1506–1507.
245. S. Anandan, X.G. Wen, S.H. Yang, Room temperature growth of CuO nanorod arrays on copper and their application as a cathode in dye-sensitized solar cells, *Mater. Chem. Phys.*, 93 (2005) 35–40.
246. S.T. Shishiyanu, T.S. Shishiyanu, O.I. Lupan, Sensing characteristics of tin-doped ZnO thin films as NO₂ gas sensor, *Sens. Actuators B Chem.*, 107 (2005) 379–386.
247. R. Ramamoorthy, P.K. Dutta, S.A. Akbar, Oxygen sensors: materials, methods, designs and applications, *J. Mater. Sci.*, 38 (2003) 4271–4282.
248. Z.Y. Fan, J.G. Lu, Gate-refreshable nanowire chemical sensors, *Appl. Phys. Lett.*, 86 (2005) 123510–123513.
249. A. Kolmakov, M. Moskovits, Chemical sensing and catalysis by one-dimensional metal–oxide nanostructures, *Annu. Rev. Mater. Res.*, 34 (2004) 151–180.
250. S. Zhuiykov, N. Miura, Development of zirconia-based potentiometric NO_x sensors for automotive and energy industries in early 21st century: What are the prospects for sensors? *Sens. Actuators B, Chem.*, 121 (2007) 639–651.
251. A.M. Azad, S.A. Akbar, S.G. Mhaisalkar, L.D. Birkefeld, K.S. Goto, Solid-state gas sensors – a review, *J. Electrochem. Soc.*, 139 (1992) 3690–3704.
252. G. Eranna, B.C. Joshi, D.P. Runthala, R.P. Gupta, Oxide materials for development of integrated gas sensors – a comprehensive review, *Crit. Rev. Solid State Mater. Sci.*, 29 (2004) 111–188.
253. E. Orentas, M. Lista, N.T. Lin, N. Sakai, S. Matile, A quantitative model for the transcript of 2D pattern into functional 3D architectures, *Nat. Chem.*, 4 (2012) 746–750.

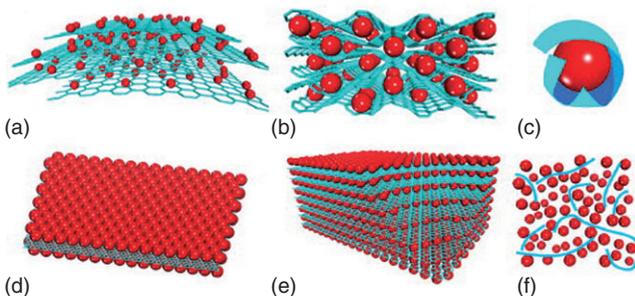


Plate VI (Chapter 4) Schematic of structural models of graphene/metal oxide composites. (a) Anchored model: nanosized oxide particles are anchored on the surface of graphene. (b) Wrapped model: metal oxide particles are wrapped by graphene. (c) Encapsulated model: oxide particles are encapsulated by graphene. (d) Sandwich-like model: graphene serves as a template for the creation of a metal oxide/graphene/metal oxide sandwich-like structure. (e) Layered model: a structure composed of alternating layers of metal oxide nanoparticles and graphene. (f) Mixed model: graphene and metal oxide particles are mechanically mixed and graphene forms a conductive network among the metal oxide particles. Red – metal oxide particles; Blue – graphene sheets. (Reprinted from Ref. 19 with permission from The Royal Society of Chemistry)

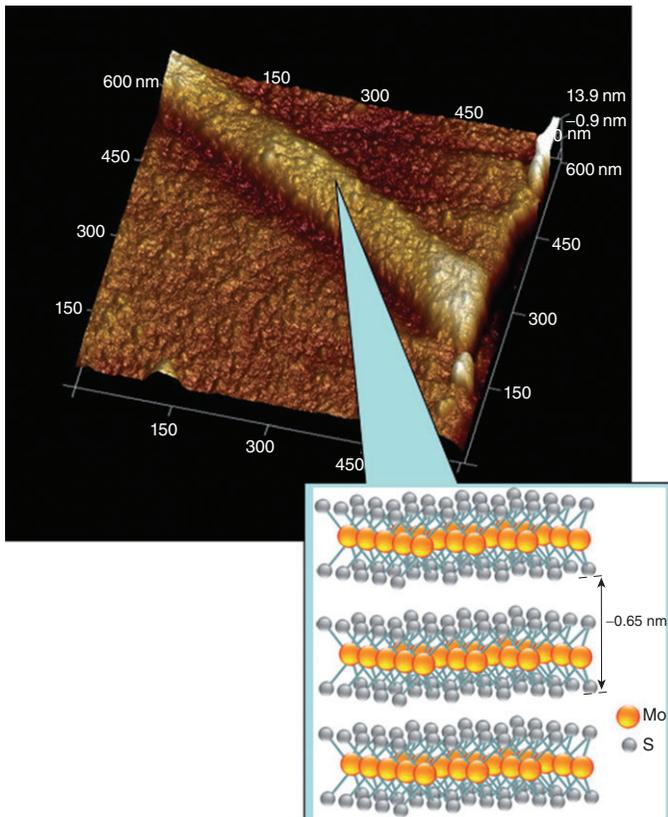
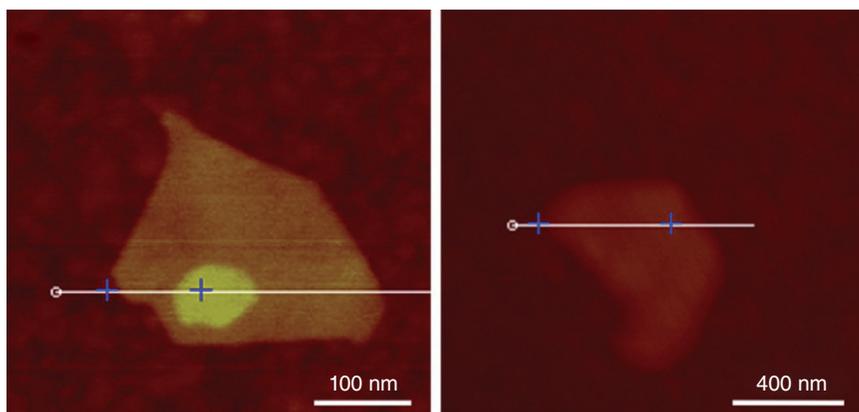


Plate VII (Chapter 4) 3D AFM image and graphical illustration of the developed structure of layered hexagonal MoS₂ with thickness of ~11 nm.



(a)

(b)

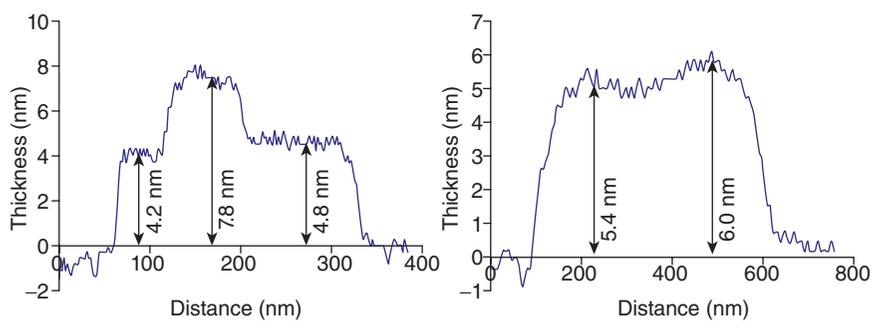
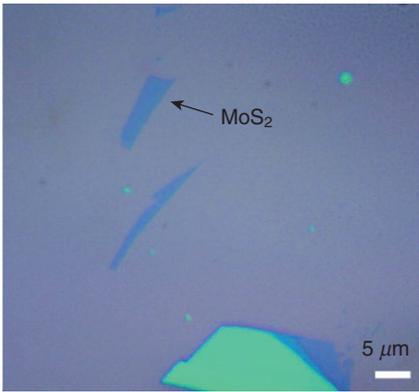
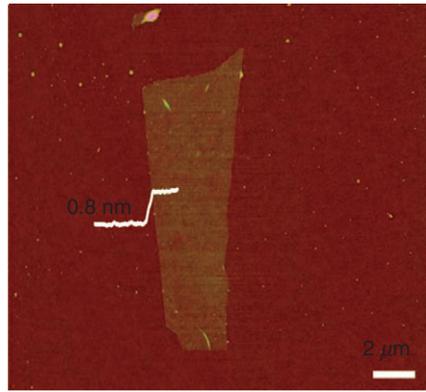


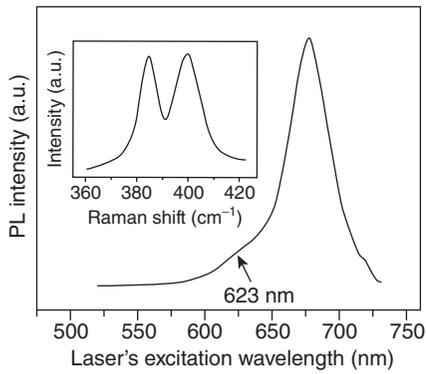
Plate VIII (Chapter 4) AFM images of different MoS₂ nanoflakes (a and b) exfoliated on quartz and their corresponding thicknesses. (Reprinted from Ref. 94 with permission from The Royal Society of Chemistry)



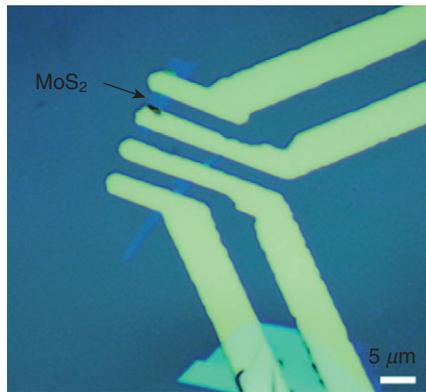
(a)



(b)



(c)



(d)

Plate IX (Chapter 4) (a) Optical microscopy image and (b) AFM image of single-layer MoS₂. (c) PL and Raman (inset) spectra of single-layer MoS₂. (d) Optical image of FET device made by single-layer MoS₂ in (a, b). (Reprinted from Ref. 96 with permission from The American Chemical Society)

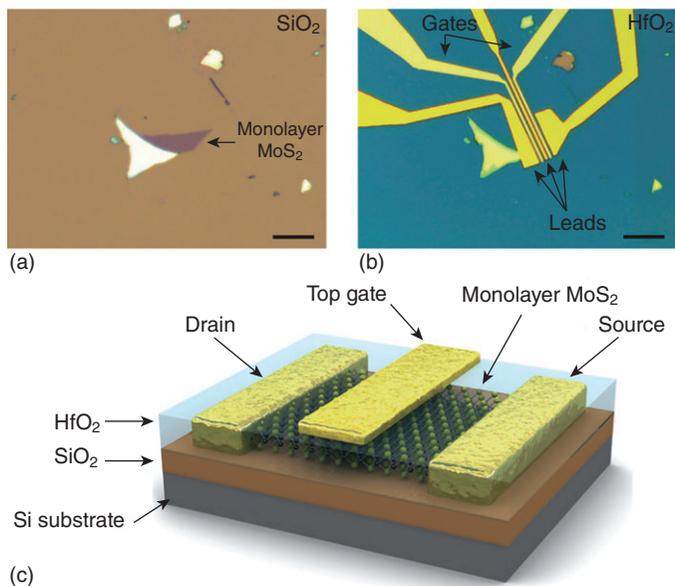


Plate X (Chapter 4) Fabrication of MoS₂ monolayer transistor: (a) optical image of a single layer of MoS₂ (thickness 6.5 Å) deposited on top of a Si substrate with a 270 nm thick SiO₂ layer; (b) optical image of a device based on the flake shown in (a). The device consists of two FETs connected in series and defined by three Au leads that serve as source and drain electrodes for two transistors. Monolayer MoS₂ is covered by 30 nm of ALD-deposited HfO₂ that acts as both a gate dielectric and a mobility booster. Scale bars (a,b), 10 μm. (c) Three-dimensional schematic view of one of the transistors shown in (b). (Reprinted from Ref. 90 with permission from Nature Publishing)

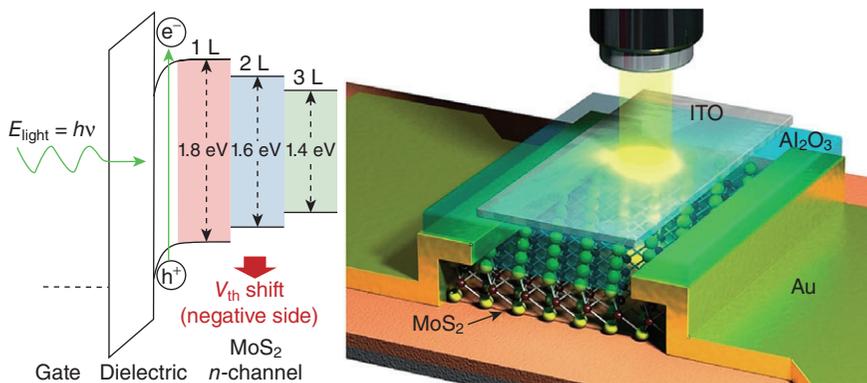


Plate XI (Chapter 4) Thickness-modulated phototransistor based on layered MoS₂ nanosheets. (Reprinted from Ref. 125 with permission from The American Chemical Society)

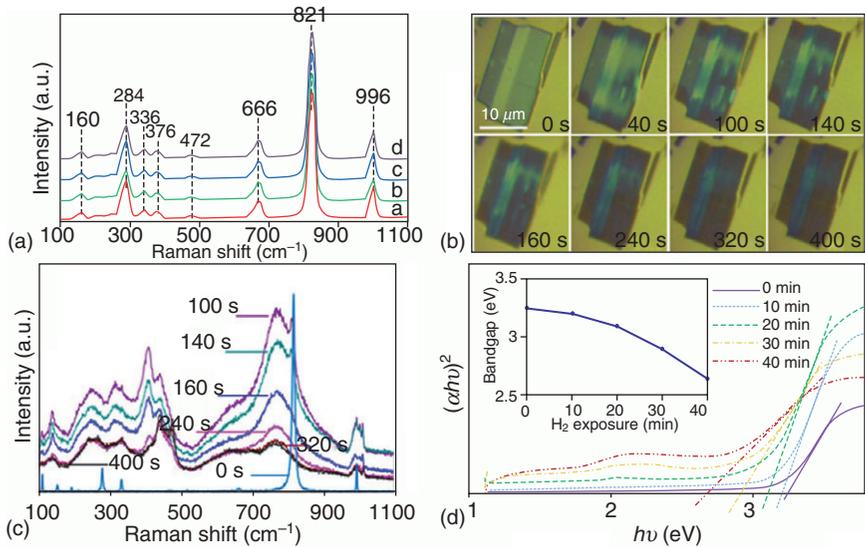


Plate XII (Chapter 4) (a) Raman spectra of MoO₃ thin films deposited on quartz substrates at temperatures of a – 560°C, b – 520°C, c – 460°C and d – 350°C. (b) Influence of H⁺ intercalation time on MoO₃ nanosheet. (c) Corresponding Raman spectral changes of the intercalated nanosheet. The intensity of the reference Raman spectrum (0s) has been scaled down. (d) Photon energy vs $(\alpha h\nu)^2$ curves derived from the absorbance spectrum of a MoO₃ nanosheet in the progression of catalysed H⁺ intercalation. (Reprinted from Ref. 184 with permission from Wiley)

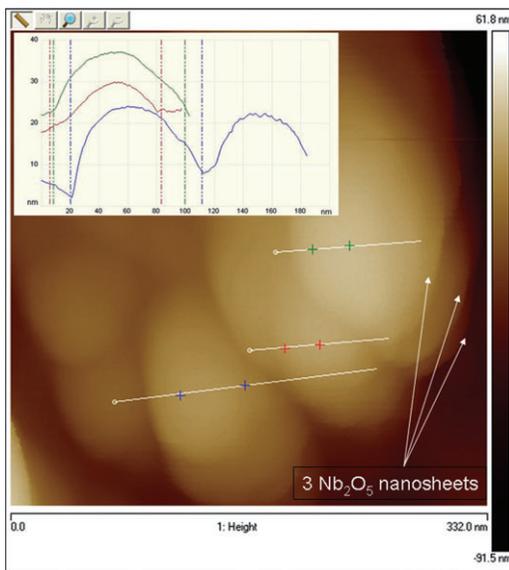
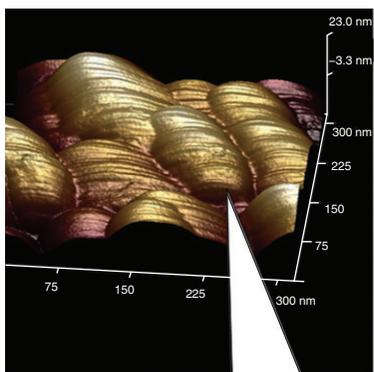
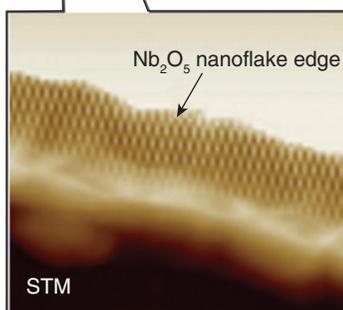


Plate XIII (Chapter 4) AMF measurement of the developed structure of quasi-2D Nb₂O₅ nanosheets deposited on quartz. Inset height measurements of individual Nb₂O₅ nanoflakes. (Reprinted from Ref. 218 with permission from Springer Verlag)



(a)



(b)

Plate XIV (Chapter 4) (a) 3D AFM image of developed structure of quasi-2D Nb₂O₅ nanosheets with (b) STM analysis of the layered matrix on the edge of Nb₂O₅ nanoflake.

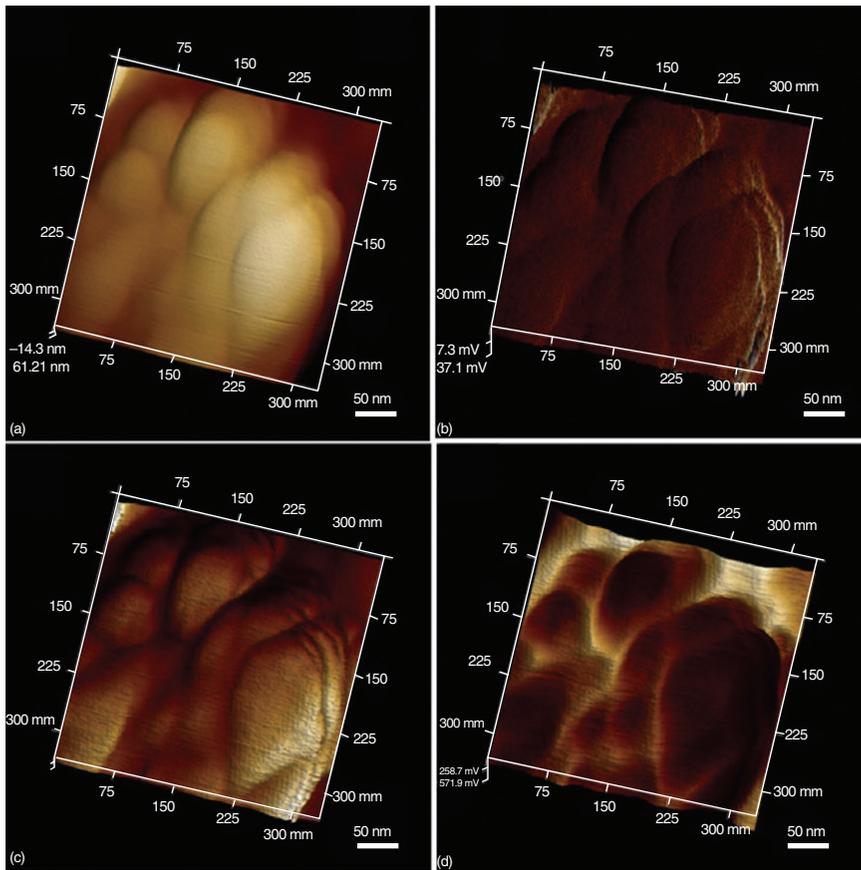


Plate XV (Chapter 4) Topography (a), tunnelling (b), current/voltage (c) and adhesion (d) images obtained on quasi-2D Nb₂O₅ nanosheets deposited on quartz substrate. (Reprinted from Ref. 218 with permission from Springer Verlag)

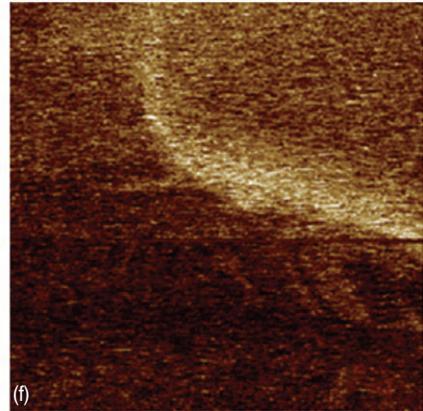
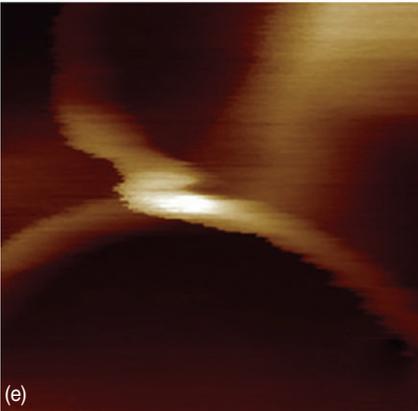
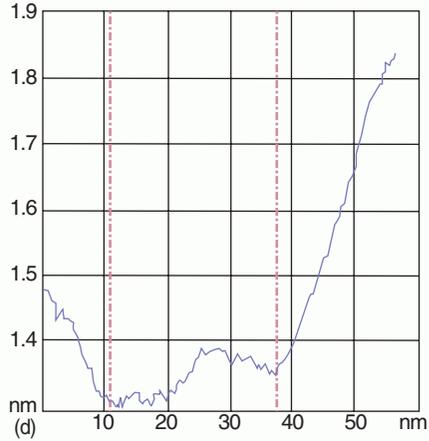
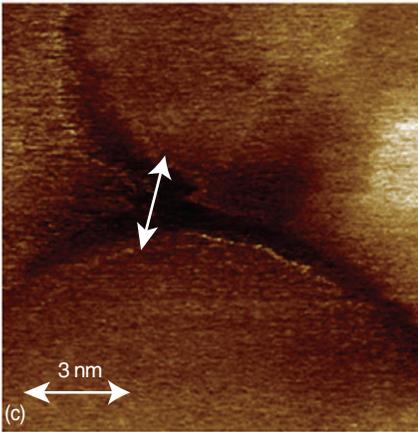
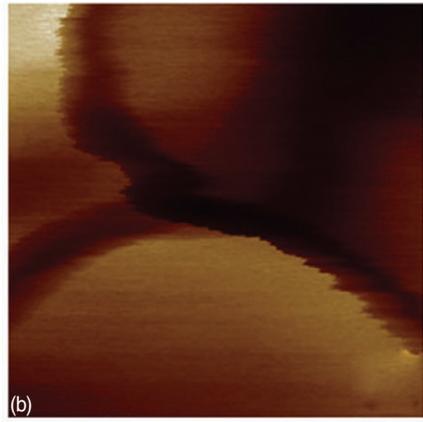
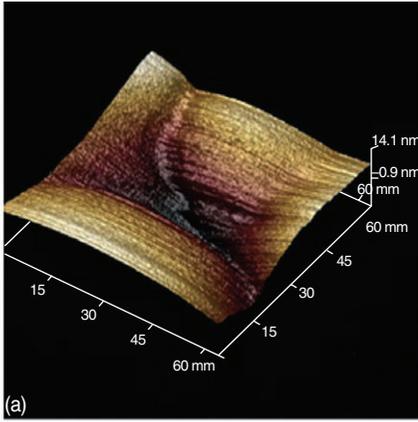


Plate XVI (Chapter 4) 3D AFM image of grain boundaries of Nb_2O_5 nanosheet (a), log DMT modulus (b), deformation of the grain boundaries (c) with measured depth between neighbouring nanosheets (d), adhesion (e) and peak current (f).

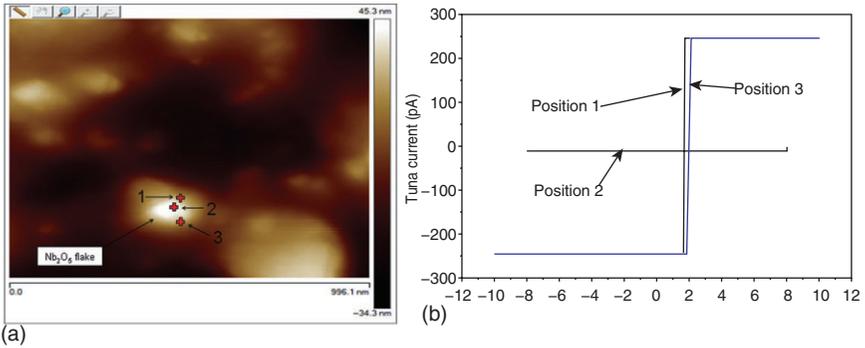


Plate XVII (Chapter 4) PF TUNA™ AFM image for Nb₂O₅ nanoflake at three different positions on the flake (a); I - V graphs for all three positions (b).

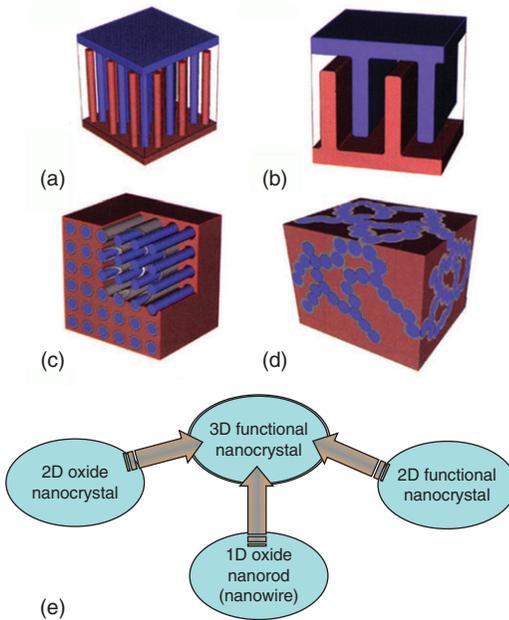


Plate XVIII (Chapter 4) 3D designs of advanced multifunctional nanomaterials: (a) inter-digitated pillar; (b) trenches; (c) concentric; (d) aperiodic. (e) Schematic interpretation of assembly of 1D and 2D oxide nanocrystals into 3D functional element of the designing material's structure. All architectures imply high surface area, high surface-to-volume ratio and minimum pathways for ion (electron) transport. (Reprinted from Ref. 218 with permission from Springer Verlag)

Composite graphene/semiconductor nanostructures for energy storage

DOI: 10.1533/9781782422242.213

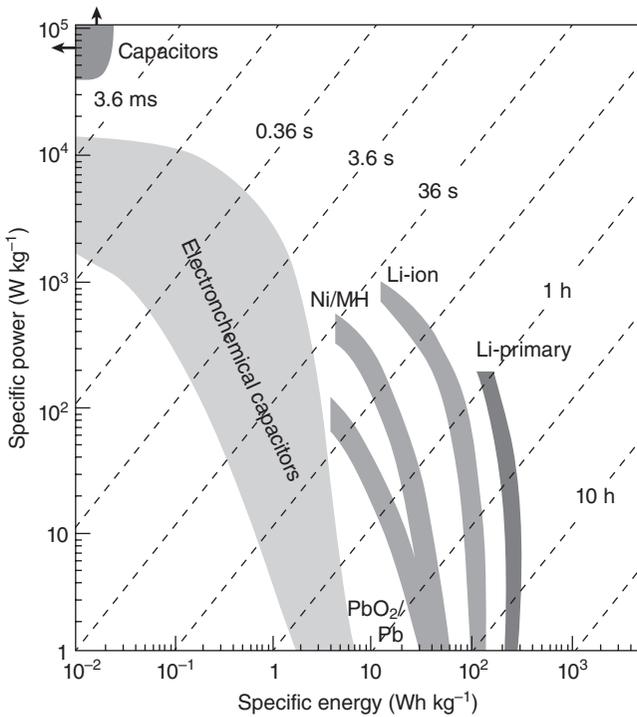
Abstract: This chapter discusses different graphene/semiconductor nanostructures for energy storage, including lithium ion batteries, electrochemical capacitors and graphene-based heterogeneous hybrids. It then reviews structural models of the graphene/semiconductor nanocrystals, three-dimensional conductive networks and nanostructured thermopower wave sources.

Key words: lithium ion batteries, electrochemical capacitors, graphene/semiconductor nanostructures, thermopower wave sources.

5.1 Performance of graphene in lithium ion batteries

Li-based rechargeable batteries were first proposed by Whittingham in 1976 whereby he demonstrated a rapid and highly reversible intercalation reaction between Li (anode) and layered TiS_2 (cathodes).¹ Since that discovery, the Li^+ ion battery (LIB) has been successfully commercialized by the Sony Corporation since the early 1990s. Owing to its high voltage, significant energy density, long cycling life, light weight and favourable environmental compatibility, it has become the most important secondary battery for various portable electronic devices.^{2,3} However, at the beginning of the 21st century LIBs are still restricted to low achievable power densities, as clearly illustrated in Fig. 5.1.⁴

In general, LIBs consist of a negatively charged anode and positively charged cathode and electrolyte (separator) representing an electrochemical storage element based on the intercalation and de-intercalation of Li^+ ions. When charged, the Li^+ ions are extracted from the cathode and introduced into the anode. The opposite occurs during discharge. As a rule, the anode comprises materials that can reversibly store Li^+ ions, such as carbon, transition metal oxides and alloy materials such as Si and Sn. Li-containing metal oxides (LiCoO_2 and LiFePO_4) have usually been employed as the cathode materials. The effect of a carbonaceous electrode structure (ordered, disordered and layered) on the performance of LIBs has been published in a comprehensive review.⁵ Compared with super-capacitors, the requirements for LIB electrodes are much more stringent.⁶ However, with the emergence in recent years of high-capacity carbonaceous nanostructured materials, such as graphene and graphene oxide (GO),^{5,7} carbon nanotubes



5.1 Specific power versus specific energy for various energy storage devices. (Reprinted from Ref. 4 with permission from Nature Publishing group)

(CNTs),⁸ carbon nanofibres,⁹ ordered mesoporous carbons¹⁰ and hierarchically porous carbons,¹¹ excess capacitance has been achieved.

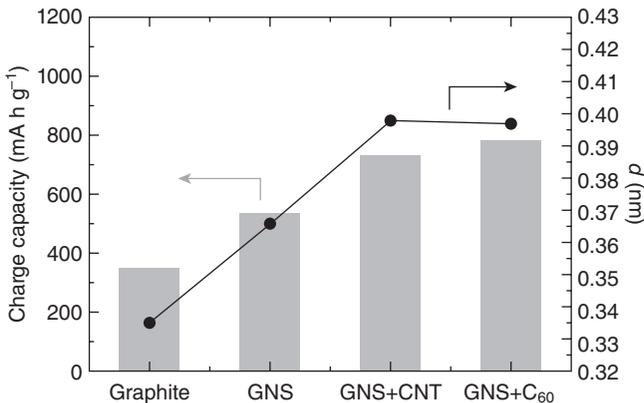
Carbonaceous nanomaterials in general, and graphene in particular, have been attracting great interest from electrochemical storage researchers owing to their large surface area, excellent flexibility, good chemical and thermal stability, rich surface chemistry and exceptional electrical, thermal and mechanical capabilities.^{5,12} All of these properties represent huge potential for its utilization in energy storage and conversion systems. The structure modifications and chemistry of graphene have been covered extensively in recent reviews^{13,14} and in Chapter 4 and are therefore not described in detail here. However, a few important features should be briefly described as they are crucial for understanding the unique properties of graphene and have not been addressed in detail in previous reviews.

Graphene has proved to have some unique advantages in comparison to CNTs in energy storage applications. For example, the theoretical specific surface area of graphene is $2620 \text{ m}^2 \text{ g}^{-1}$, which is much higher than that of

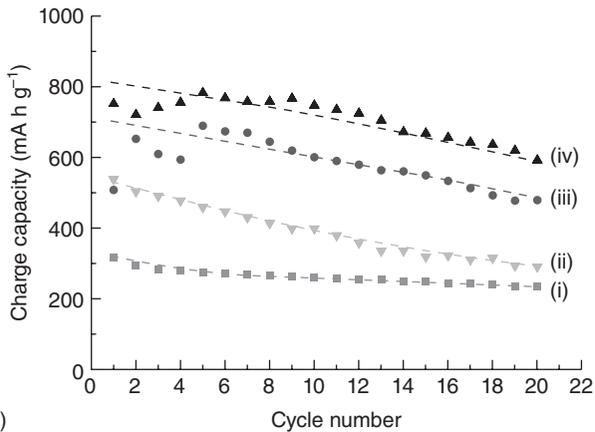
CNTs and graphite, with values of 1300 and 10–20 m² g⁻¹, respectively. The large surface area provides more active sites for the electrochemical reactions involved in the energy storage process. Another distinctive advantage of graphene is its flexibility compared to brittle graphite. This can create an opportunity for designing adjustable energy-storage devices.¹⁵ Graphene also possesses high surface-to-volume ratio, a feature which confers stipulating a significant advantage in fast ion transport, enabling a higher rate capability compared to graphite. Moreover, in a bulk single-walled CNT, only one-third of nanotubes are metallic and the remainder are semiconducting. As a result, the available charge carrier density is suppressed for such a single-walled CNT film as compared to graphene, which behaves as a semi-metal with exceptionally high electron mobilities.¹⁶ In addition, interfaces in CNT networks are lossy.¹⁷ The controllable surface chemical groups of graphene make for easier functioning in versatile applications in comparison to graphite and CNTs. Furthermore, graphene exhibits a key advantage over CNTs in that it precludes the problem of residual metallic impurities, which are difficult to remove, thus hindering many practical applications of CNTs, including energy storage.¹⁵ All the above advantages have encouraged the use of graphene in LIBs in preference to other carbonaceous nanostructured materials.

The specific capacity of graphene could reach 540 mA h g⁻¹, which is much larger than that of graphite.¹⁶ However, higher capacity (730 and 784 mA h g⁻¹) could also be obtained by embedding CNTs or fullerene macromolecules into graphene layers to increase the interlayer distance, which may provide additional sites for the accommodation of Li⁺ ions.¹⁷ Figure 5.2 displays the relationship between the *d*-spacing and charge capacity of graphene nanosheet (GNS) families and graphite.¹⁷

Another report claimed synthesized flower-like GNSs with improved Li storage, where Li⁺ ions could not only adsorb on both surfaces of the GNS, but also be stored on the edges and covalent sites.¹⁸ It has also recently been found that GNSs displayed relatively high reversible capacity of 672 mA h g⁻¹ and reasonable cyclic performance.¹⁹ This improved efficiency can be explained by the presence of a large number of functional groups and the abundance of micropores and/or defects, i.e. the Li⁺ ions could be stored on both sides of the graphene surface.²⁰ One of the highest reported initial capacities (1264 mA h g⁻¹ at a current density of 100 mA g⁻¹) has been demonstrated on high-quality GNSs with ~4 layers and a large specific surface area (492.5 m² g⁻¹).²¹ Such high capacity has been attributed to the fewer layers of graphene with a large surface area, curled morphology and disordered structure, many edge-type sites or nanopores, the reaction of Li⁺ ions with the residual H, and a broad electrochemical window (0.01–3.5 V).²² During GNS preparation, the structural parameters, including surface functional groups, specific surface area, interlayer spacing, defects or degree of



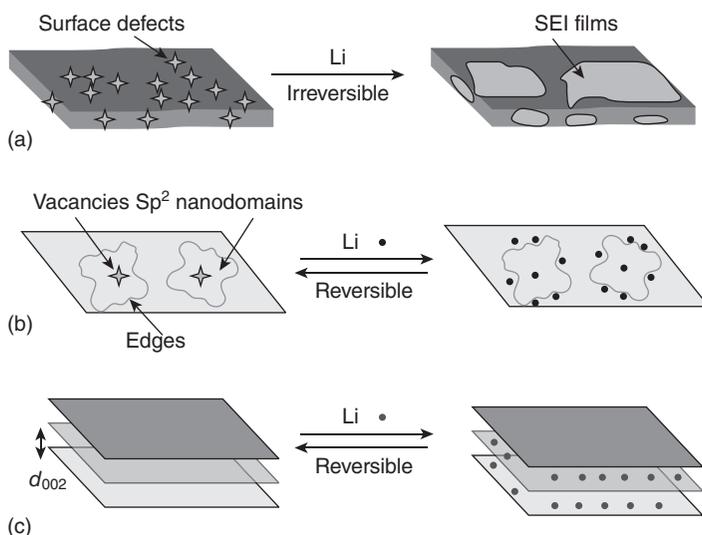
(a)



(b)

5.2 (a) Relationship between the *d*-spacing and the charge capacity of GNS families and graphite. (b) Charge/discharge cycle performance of (i) graphite, (ii) GNS, (iii) GNS+CNT and (iv) GNS+C₆₀. (Reprinted from Ref. 17 with permission from Elsevier Science)

disorder, can be systematically tuned up by using different reduction methods, such as hydrazine reduction, low-temperature pyrolysis and electron beam irradiation, investigating their effects on Li storage properties.²³ By manipulation of these structural parameters, the key criterion for evaluating the reversible capacity and the improved Li storage properties was found to be the intensity ratio of the Raman D band to the G band. Figure 5.3 illustrates different interfaces between GNSs and electrolyte, which can be extended to the edges as additional storage sites. Moreover, it has also been reported that the defects on interfaces are the dominant factors for improving performance.²³



5.3 (a) Irreversible Li storage at the interface between GNS and electrolyte. (b) Reversible Li storage at edge sites and internal defects (vacancies, etc.) of nanodomains embedded in GNS. (c) Reversible Li storage between (002) planes. (Reprinted from Ref. 17 with permission from Elsevier Science)

Graphene-based paper has also been tested as a flexible electrode material. Although the graphene paper is mechanically enduring with a Young's modulus of 41.8 GPa and tensile strength of 293.3 MPa, and shows a high electrical conductivity of 351 Scm^{-1} , its electrochemical performance was not satisfactory, probably owing to the restacking of GNSs.²⁴ One of the promising candidates for large-capacity and super-high-rate anode for high-power and high-energy Li^+ ion batteries under fast charge and discharge conditions can be graphene doped by nitrogen or boron.²⁵ It has been established that the unique 2D structure, disordered surface morphology, hetero-atomic defects, better electrode/electrolyte wettability, increased inter-sheet distance, improved electrical conductivity and thermal stability of the doped graphene are beneficial to rapid surface Li^+ absorption and ultrafast Li^+ diffusion and electron transport.²⁶

Fascinating results have already been achieved and published in the 21st century relating to GNSs as electrode materials for LIBs. However, detailed Li storage mechanisms are still not clear, due to various possible Li^+ ion storage sites in a GNS electrode, such as that (i) Li^+ ions might intercalate few-layer GNS with a LiC_6 intercalation mechanism; (ii) Li^+ ions may be adsorbed and accumulated on both surfaces of a GNS; (iii) Li^+ ions can be stored on the layer edges and covalent sites; (iv) Li^+ ions could be deposited

in the nanopores/cavities and defect sites; (v) Li^+ ions may be accommodated in the interlayer and void spaces of GNS; (vi) Li^+ ions can react with oxygen-containing functional groups or hetero-atoms such as residual hydrogen.^{27–30}

5.1.1 Graphene anodes

Although graphitic carbon has been widely used as an anode material in LIBs, it still exhibits low Li storage capacity (i.e. less than 372 mA h g^{-1}).⁶ The low storage capacity of graphite is ascribed to limited Li^+ ion storage sites within the sp^2 carbon hexahedrons – typically one per hexahedron yielding LiC_6 . Recently, two configurations have been proposed to go beyond the limitation of the LiC_6 composition: one is double layer adsorption³¹ and another is covalent molecule configuration.³² In the latter case, each Li atom is trapped at a covalent site on the benzene ring and therefore the highest Li storage capacity corresponds to LiC_2 and is $\sim 1116 \text{ mA h g}^{-1}$. Therefore, it is obvious that a single layer of graphene in the LiC_6 complex is not a promising insertion material, but attainment of the double-layer or covalent structure could yield attractive performance.

Li^+ ions could be stored between the GNS interlayers if each single GNS could be reassembled with spacers to achieve ‘pseudo-graphite’ with a large interlayer distance. This would lead to a higher proficiency. In fact, it has been reported that the specific capacity of GNS increased from 540 mA h g^{-1} to 730 mA h g^{-1} when GNS was carefully intercalated by CNTs.³³ Further progress can be made if such intercalation can be achieved by C_{60} molecules. In this case, the specific capacity increased to 784 mA h g^{-1} . However, the battery shows poor cyclic performance as the capacity drops from 540 mA h g^{-1} to 290 mA h g^{-1} after only 20 charge–discharge cycles. Nevertheless, the demonstration of graphene as a potential anode material supports the need for further research into other methods for fabricating graphene anodes.

Graphene paper can be prepared by flow-directed vacuum filtration and hydrazine reduction of prefabricated GO paper as one of the alternative methods. The reported distance between the obtained graphene layers was approximately 0.375 nm , larger than that of graphite (0.334 nm).^{34,35} Despite the drastic capacity drop from 680 to 84 mA h g^{-1} after just the first cycle, a comparatively flat discharge plateau existed at 2.20 V in the first discharge curve with a discharge capacity of 582 mA h g^{-1} . This fact highlighted the potential of using graphene paper in a new updated primary battery system.³⁴ The advantage of using graphene paper as an electrode is that it is applicable as a single electrochemically active component without the need for the polymer binders and other additives that are required for the fabrication of conventional electrodes.³⁵

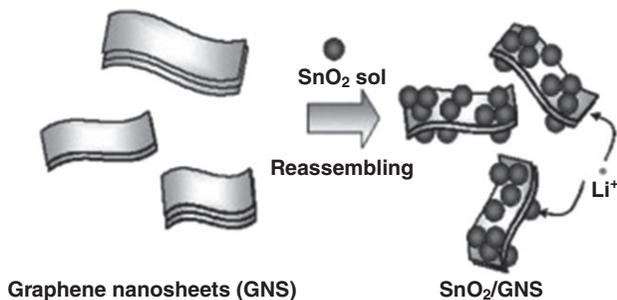
Another approach has been used to control the distance between graphene layers.³⁶ In this method, the GNSs are functionalized by oxalic acid molecules, poly-condensed under the evolution of water via oxalyl bonding and assembled along the tubular axis of templating CNTs, forming layered coaxial tubes. Nevertheless, both insufficient cyclic performance for the graphene-based electrode and the irreversible loss of capacity during the first cycle need to be addressed in the future. These types of material systems are strongly influenced by: the spacing of d (002) within the GNSs; specific surface area; functional groups on the graphene; and defects.³⁷ The increase in capacity has arisen from the use of graphene instead of graphite and the expansion of the interlayer spacing of the GNSs, which improves the insertion storage. In addition, defects in the graphene also contribute, and high reversible capacities (794–1054 mA h g⁻¹) and good cyclic stability have been reported.³⁷ On the other hand, the irreversible capacity loss was attributed to the presence of oxygen-containing functional groups which leads to the formation of a solid electrolyte interface (SEI) film and to the reaction of Li⁺ ions with these groups.³⁸ Modelling work based on density functional theory (DFT) has shown that the introduction of armchair and zigzag edges leads to enhanced adsorption of Li⁺ ions and improved diffusion properties.³⁹ This theoretical research suggests that if a nanoribbon of graphene is used as the anode material, the advantage of enhanced adsorption of Li⁺ ions and their increased diffusion rate can be fully exploited. Another benefit of the use of small graphene sheets such as graphene nanoribbons is that the diffusion distance of Li⁺ ions can be reduced, which makes the reaction rate of intercalation and de-intercalation much faster. GNSs must be oriented in a direction that facilitates Li⁺ ion insertion and extraction in order to fully realize this benefit. Otherwise, nanoholes must exist on the GNSs, which is unlikely, although such nanoholes have been proposed in the basal graphene plane on the round-shaped natural graphite.⁴⁰

5.1.2 Graphene-based heterogeneous hybrids

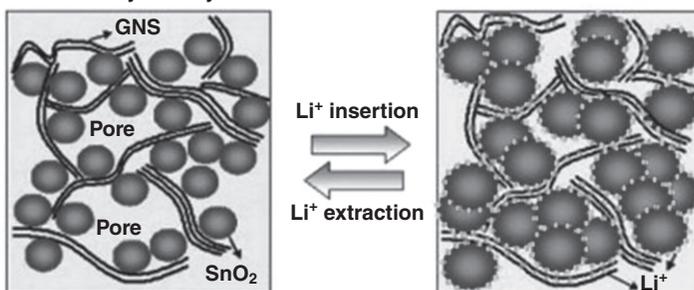
It has been reported that the transition metal oxides can reversibly react with Li⁺ ions and thus can provide Li storage capability.⁴¹ For example, SnO₂ has high theoretical Li storage capacity of 782 mA h g⁻¹, much higher in comparison with graphite. Unfortunately, during charge–discharge cycles, SnO₂ experiences a very large volume change which causes crumbling and cracking of electrodes, resulting in deficient cyclic performance. In order to solve these problems, GNSs in an ethylene glycol solution can be reassembled in the presence of rutile SnO₂ nanoparticles, as schematically presented in Fig. 5.4.

It is clearly shown in this figure that the GNSs were homogeneously distributed between the SnO₂ nanoparticles in such a way that a nanoporous

Increased capacity: Li^+ can be intercalated into both GNS and SnO_2



Enhanced cyclability via 3-D flexible structure



5.4 Schematic structure of hybrids including metal oxides such as SnO_2 and GNSs which enhance the cycle performance of electrodes. (Reprinted from Ref. 41 with permission from Elsevier Science)

structure with a large amount of void space developed. The dimensional confinement of SnO_2 nanoparticles by the surrounding GNS limits the volume expansion upon Li insertion. Consequently, the pores between SnO_2 and the GNSs can be used as buffering spaces during charge–discharge cycles, leading to improved cyclic operations.⁴¹ In another reported approach, Co_3O_4 , owing to its high theoretical capacity (890 mA h g^{-1}), has also been anchored on the GNSs as an advanced anode material.^{42,43} In these hybrid materials, the GNSs not only provided buffering spaces, but also prevented the agglomeration of Co_3O_4 nanoparticles. In addition, the GNSs in the hybrids serve as the electrical conducting network to improve the power density of the electrodes. GNSs themselves have also worked as electrode materials for Li^+ ion storage. Furthermore, the metal oxide nanoparticles between the GNSs effectively prevented agglomeration of GNSs and kept them available for Li insertion and extraction. This final result also maintains a large specific surface area that may have the negative effect of inducing high irreversible capacity loss during the reported first charge–discharge cycle due to the formation of SEI films.³⁶ The net effect on long-term stability

is a subject for further improvement. In addition to the homogeneous GNS/metal oxide mixtures, self-assembly methods using surfactants or polymers have been used to construct ordered metal oxide GNS nanocomposites.⁴⁴ In such layered nanostructures, stable alternating layers of nanocrystalline metal oxides with GNS or graphene stacks are developed.

A general strategy has been demonstrated to achieve improved electrochemical performance by constructing 3D nanocomposite architectures based on the combination of nanosized Sn particles and GNSs.⁴⁵ Electrochemical tests demonstrated the highly reversible nature of the reaction between Li^+ and Sn/GNS nanocomposites. In one of the last reports, Li was stored on both sides of GNS (Li_2C_6) with a theoretical capacity of 744 mA h g^{-1} .⁴⁵ For Si, it has been shown that enhanced cyclic performance can be achieved in electrodes prepared by simple mixing of commercially available nano-sized Si and graphene. After 30 cycles, the mixed Si/graphene composite retained a capacity of approximately 1168 mA h g^{-1} and an average Coulombic efficiency of 93%. Composites consisting of Si nanoparticles and graphene paper have also established high Li^+ ion storage capacities and cycling stability with storage capacity $>2200 \text{ mA h g}^{-1}$ after 50 cycles and $>1500 \text{ mA h g}^{-1}$ after 200 cycles with a decrease rate of $\sim 0.5\%$ per cycle.⁴⁶ From these results, the benefits of using GNS-based hybrids are obvious. However, despite the promising early results, further work is needed to systematically compare the performance of GNS-based materials to other carbonaceous materials and to build a level of understanding that can lead to optimization of the GNS-based composite electrodes.

5.1.3 Electrode additive

Due to their outstanding electrical conductivity, GNSs have been considered as ideal conductive additives to hybrid nanostructured electrodes. For instance, it has been reported that nanostructured TiO_2 GNSs, developed by a self-assembly technique, exhibited significantly enhanced Li-ion insertion/extraction compared with pure TiO_2 .⁴⁴ In contrast to pure TiO_2 , phase-doubled specific capacity and improved capacitance at high charge–discharge rate were obtained. These developments may be attributed to increased electrode conductivity in the presence of a percolated GNS network embedded into the metal oxide electrodes.⁴⁴ Later, this anatase TiO_2 /graphene composite anode was combined with a LiFePO_4 cathode to form a full cell that operated at 1.6V and demonstrated negligible fade even after more than 700 cycles at a one-hour discharge rate.⁴⁷ This battery potentially offers long life and low cost, along with safety, all of which are critical to stationary and vehicle applications. Another composite nanostructure based on a combination of LiFePO_4 /GNSs was prepared by the co-precipitation method, and the capacity and cycle

performances of LiFePO_4 were considerably enhanced.⁴⁸ GNSs have also been shown to stabilize the performance of $\text{Li}_4\text{Ti}_5\text{O}_{12}$ (LTO) anodes for LIBs. While LTO anodes are advantageous owing to their well-known zero-strain characteristics, the electrical conductivity of LTO is intrinsically poor, and GNS can be utilized as an effective additive to increase the surface conductivity of the nanocomposites.⁴⁹

Therefore, all reports published so far have concluded that the use of GNSs as an electrode additive is a very effective way of achieving an overall improvement in the characteristics of the electrodes. Due to its specific surface area and the presence of functional groups, edges and defects, GNS-based electrodes have demonstrated enhanced performance for electrochemical energy devices. Early examples of improvements achieved with GNSs are as follows:

- The interactions between GNS and supported catalyst particles have been shown to improve catalyst durability for fuel cells.
- Hybrids of GNS and metal oxides or GNS and conducting polymers have demonstrated synergic effects for super-capacitor applications.
- Combination of GNS with Li storage materials has yielded increased electrode capacity.

Further work should include pursuing the most suitable techniques for preparing GNSs for electrochemical applications and methods to control the number of layers, the extent of defects and surface functionality. All improvements must be developed and tailored to address requirements for specific applications. Moreover, early successes reported so far warrant continued exploration of the synthesis of GNS-based nanostructured electrode materials with high electrochemical performance, for example, GNS-supported precious or non-precious metals and binary catalysts with high activity and stability that may have application to alcohol oxidation or oxygen reduction.

5.2 Performance of graphene in electrochemical capacitors

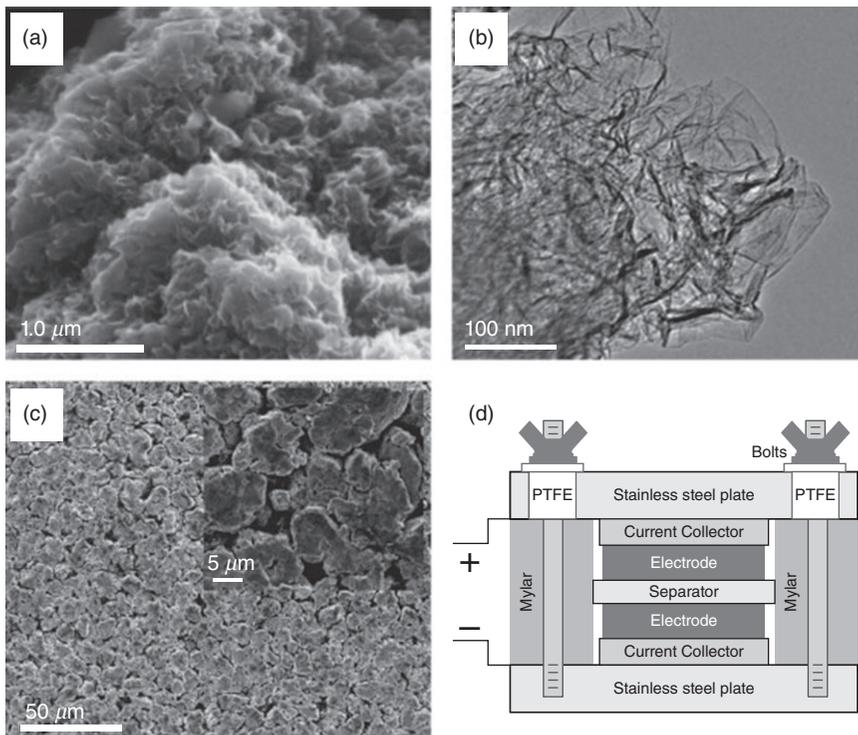
Development of nanostructured composite materials for electrochemical capacitors (ECs) is another important area where nano-sized complex compounds with unique structural variables such as anchored, wrapped, sandwich, layered and mixed nanostructures have demonstrated significant improvement compared to individual constituents.⁴ ECs utilizing graphene/metal oxide combined nanostructures have already established higher energy density compared to conventional physical capacitors, higher charging/discharging rate capability and longer cycle-life than primary/secondary

batteries.⁵⁰ The main energy storage mechanisms include carbon-based electric double layer (EDL) and metal oxide- or polymer-based pseudo-capacitive charge storage. The former depository mode is an electrostatic (physical) process with fast charge adsorption and separation at the interface between electrode and electrolyte. The latter is a chemical process involving redox reactions between electrode materials and electrolyte ions.^{51,52} The two charge storage modes are determined by electrode materials. As a result, much attention has been paid to the exploitation of the electrode materials aimed at increasing specific capacitance as well as high power density. During the last decade graphene, owing to its attractive characteristics, such as large surface area, good flexibility, excellent electrical conductivity, good chemical and thermal stability, has been considered to be a very promising candidate for super-capacitor electrode materials.^{53–57}

Recent reports describing the first generation of graphene-based super-capacitors have shown that they can exhibit excellent performance with a specific capacitance of 75 F g^{-1} together with an energy density of 31.9 Wh kg^{-1} in ionic liquid electrolytes.⁵³ Figure 5.5 displays scanning electron microscope (SEM) and transmission electron microscope (TEM) images of chemically modified graphene and a schematic view of the test assembly obtaining specific capacitance of 135 and 99 F g^{-1} in aqueous and organic electrolytes.⁵⁷

Reduced graphene with a low degree of agglomeration can be achieved by using a gas–solid reduction process.⁵⁵ A maximum specific capacitance of 205 F g^{-1} in an aqueous electrolyte with an energy density of 28.5 Wh kg^{-1} has been observed. Another approach for graphene development is based on exfoliation at a temperature of 200°C and under a high vacuum.⁵⁶ It has been demonstrated that the graphene produced possesses a specific capacitance as high as 260 F g^{-1} at a scanning rate of 10 mV s^{-1} in an aqueous system. With microwave irradiation or direct heating of GO suspensions in propylene carbonate, modified graphene was obtained by exfoliation and reduction of graphite oxide powders simultaneously. Reduced GO was used as electrode material in ECs, and capacitance of 191 F g^{-1} and 120 F g^{-1} was achieved in KOH ⁵⁸ and tetraethylammonium tetrafluoroborate (TEABF_4)⁵⁹ electrolytes, respectively. It has also been reported that the interfacial capacitance of graphene depends on the number of layers, which can be calculated according to the specific surface area.⁶⁰ These results have confirmed the dependence of the space charge layer capacitance of graphene on the number of layers and opened up understanding of the electronic structure of multilayer graphene using an electrochemical approach.

In an alternative report, a GNS-based super-capacitor exhibited a superior energy density of 85.6 Wh kg^{-1} at room temperature and 136 Wh kg^{-1}



5.5 (a) SEM and (b) TEM images of chemically modified graphene. (c) Low and high (inset) magnification SEM images of a chemically modified electrode surface. (d) Schematic view of test assembly. (Reprinted from Ref. 41 with permission from Elsevier Science)

at 80°C, both of which are comparable to a Ni metal hydride battery.⁶¹ These encouraging results were obtained by using environmentally benign ionic liquids which are capable of operating at a high voltage of 4.5V. In addition to this case, directly-grown vertically-oriented GNS on Ni current collectors as electrodes for EDL capacitors efficiently filtered 120Hz current with a resistor–capacitor time constant less than 0.2ms.⁶²

All the above-mentioned works have highlighted that more fundamental understanding of the chemical and physical mechanisms that give rise to the electrochemical properties of graphene-based nanostructures is essential. This effort will require further experimental work to systematically vary surface area, functional groups and defects to explore the resulting effect on properties as well as analytical work to reconcile observations with physical principles.

5.3 Prospects of using graphene in lithium ion batteries (LIBs) and electrochemical capacitors (ECs)

In the field of electrochemical energy conversion and storage, graphene has already shown promise for applications in LIBs and ECs. In relation to further development of LIBs and ECs, its unique properties, summarized previously in Table 4.1 (p. 141), are as follows:

- superior electrical conductivity to graphitic carbon;
- high surface area – the theoretical specific surface area of monolayer graphene is $2620\text{ m}^2\text{ g}^{-1}$;
- a high surface-to-volume ratio, which provides more active sites for ion adsorption and/or electrochemical reactions;
- ultrathin thickness that obviously shortens the diffusion distance of ions;
- structural flexibility that paves the way for constructing flexible electrodes;
- thermal and chemical stability which guarantee its use in harsh environments;
- abundant surface functional groups which make it hydrophilic in aqueous electrolytes and provide binding sites with other atoms or functional groups;
- a broad electrochemical window which is critical for increasing energy density, which is proportional to the square of the window voltage.

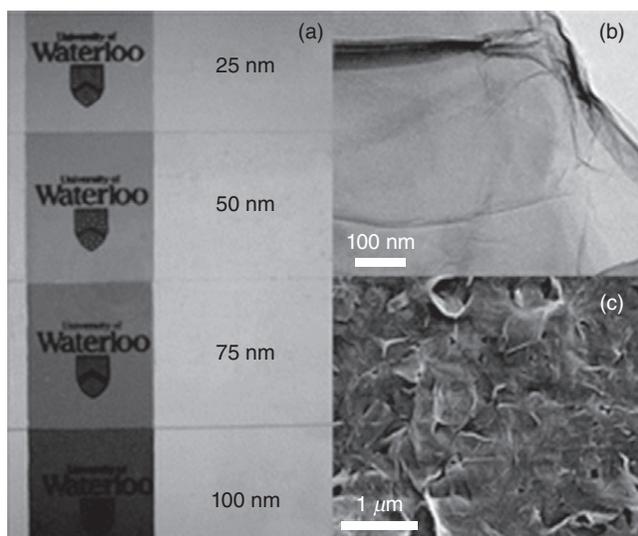
In addition, graphene electrodes used for ECs have a major innovation arising from the fact that they are not like activated carbons which achieve a large surface area because of a rigid porous structure, having rather an intrinsic flexible, open pore system,^{12,55} which offers potential for fast ion transport kinetics. This feature is particularly important for LIBs. However, the development of graphene and GNS-based nanomaterials and their applications in the field of electrochemical energy is still in its infancy and many challenges need to be overcome. Well-controlled methods of synthesis and processing of graphene and GNS-based nanostructures are only beginning to emerge. A better understanding of the correlation between electrochemical performance and the properties of graphene nanostructures and their interactions within hybrids is required. In addition, current electrode designs should be revisited to explore whether graphene and GNS-based nanostructures with their unique structure and properties may enable enhanced performance. For instance, the development of a novel and effective battery electrode, based on nano-sized Li storage materials, may be possible using graphene to create an aligned structure that promotes Li^+ ion insertion and extraction while also facilitating good electrical conductivity within the electrode.

All the above results have indicated that graphene has considerable potential as a new anode material in LIBs and ECs. An important aspect which cannot be ignored is the cost of mass production. The prospect that GNS prepared through chemical exfoliation of graphite in polar solvents or chemical reduction of GO can be produced on a large scale at a relatively low cost, which is important for their practical applications looks promising. However, great challenges for GNS used as electrodes in LIBs and ECs remain and they have to be addressed in near future. They are as follows:¹⁷

- Due to differences in opinions, the Li storage mechanisms in GNS need to be clearly established – for example, a Li_2 covalent molecule model predicting the highest Li storage capacity of 1116 mA h g^{-1} (LiC_2)²³ or absorption of Li on both sides of a GNS resulting in two layers of Li per layer of GNS to give a Li_2C_6 model.⁶³ Relationships between Li storage and defects, oxygen-containing functional groups, number of layers and lateral size of the GNS also need to be elucidated.
- The initial capacity of GNS is much higher than that of graphite-based ones but suffers from large irreversible capacity, low initial Coulombic efficiency and fast capacity fading, features which are mainly owing to the restacking of GNS and side reactions between GNS and electrolytes arising from the abundant functional groups and defects.
- There is no obvious voltage plateau to provide stable potential outputs, and there is a large hysteresis between the charge–discharge curves of GNS which will be a major drawback for their practical use in commercial LIBs. As for ECs, EDL capacitance is limited by the easy agglomeration and restacking of GNS, resulting in a small surface area and low energy density.
- Although effective reduction of GO has been obtained, the electrical conductivity of the resulting reduced GO is usually quite low compared with graphite.

Another direction in the development of graphene for efficient ECs is the manufacture of ultrathin and transparent GNSs as electrodes. Figure 5.6 illustrates examples of both types of GNSs (from 25 nm to 100 nm).^{6,64} The ultrathin and optically transparent GNSs have several advantages:

- allowance for ECs in transparent electronics;
- elimination of the presence of current collectors which leads to a simplified and lightweight architecture;
- flexible and robust GNSs as thin as 25 nm;
- possibility of enabling graphene to be printed out for full integration with printable electronics. The capacitance obtained by using developed ultrathin GNSs for charge–discharge analysis was 135 F g^{-1} in 2M KCl electrolyte for GNS with thickness of 25 nm. These GNSs had transmittance of 70 % at 550 nm.⁶⁴

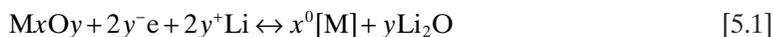


5.6 Morphology of ultrathin and transparent GNSs: (a) photographs of films on glass substrates; (b) TEM images from graphene suspension; (c) SEM images of 100 nm GNDS on glass substrate. (Reprinted from Ref. 6 with permission from The Royal Chemical Society)

Graphene has generally been considered an ideal building block in 2D and 3D composite nanomaterials sandwiched with various metal oxides. So far the sandwich nanostructures obtained have already exhibited exceptional performance in applications such as super-capacitors,^{65,66} batteries,^{17,67} sensors^{15,68} and photovoltaics.^{69–72} It therefore appears that significant synergistic effects are expected between graphene and inorganic nanostructures when combined at the molecular scale, and these may create unexpected properties different from those of each individual component.

In addition to all of the above examples of use of GNSs in LIBs and ECs, much effort has been focused on finding substitutes with larger capacity and slightly more positive intercalation voltage compared to Li/Li⁺, so as to reduce the possible safety problems of Li plating.⁷³ Typically, nanostructured metal oxides can provide a capacity more than two times larger than that of graphite with higher potential.⁷⁴ The electrode reaction mechanism of metal oxides can be typically classified into three groups:^{75–77} (i) conversion reaction; (ii) Li–alloy reaction; and (iii) Li insertion/extraction reaction.

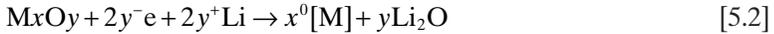
The conversion reaction mechanism is as follows:



where M is a metal such as Sn, Co, Ni, Fe, Cu or Mn, and the final product consists of a homogeneous distribution of metal nanoparticles embedded

in a Li_2O matrix. Nevertheless, their application in practical LIBs is significantly hindered by inadequate cyclic performance caused by substantial volume expansion and severe aggregation of metal oxides during charge–discharge cycle. A further problem is the large voltage hysteresis between charge and discharge together with poor energy efficiency.

The Li–alloy reaction mechanism is as follows:



A good example is a Sn-based oxide initially following the conversions (5.2) and (5.3) forming Li_2O and metallic Sn. Subsequently, the *in situ* formed Sn distributed in Li_2O can store and release Li^+ ions according to Li–Sn alloying/de-alloying reactions up to the theoretical limit of $\text{Li}_{4.4}\text{Sn}$ corresponding to a theoretical reversible capacity of 782 mA h g^{-1} based on the mass of SnO_2 .⁷⁵ However, its poor cyclic performance caused by large volume changes (up to 300 %) during charge–discharge leads to mechanical disintegration and the loss of electrical connection of the active material from current collectors.

The Li insertion/extraction reaction mechanism involves the insertion and extraction of Li^+ into and from the lattice of the metal oxide which can be described as follows:



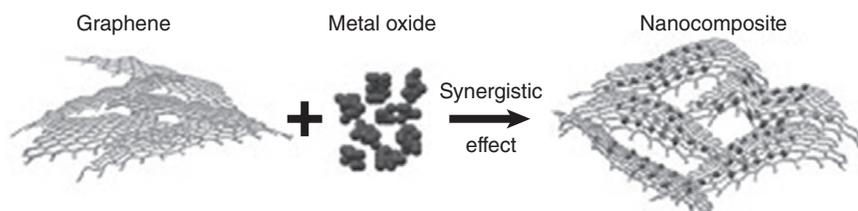
For example, TiO_2 is usually used as an anode material intercalated by Li with a volume change smaller than 4 % in the reaction: $\text{TiO}_2 + x\text{Li}^+ + xe^- \leftrightarrow 4\text{Li}_x\text{TiO}_2$ ($0 \leq x \leq 1$). The Li intercalation and extraction process with a small lattice change ensures its structural stability and cycling life. The Li intercalation potential is about 1.5V, thus intrinsically maintaining the safety of the electrode through the avoidance of electrochemical Li deposition. However, the problem is low specific capacity, poor Li ionic and electronic conductivity and high polarization, resulting from the slow ionic and electronic diffusion of bulk TiO_2 .⁷⁵ In supercapacitors, nanostructured metal oxides provide higher pseudo-capacitance through bulk redox reactions compared with surface charge storage of carbonaceous materials. However, the large volume variation-induced structure change breaks the stability of electrode materials, causing rapid capacity loss during charge–discharge processes. Consequently, Li can react with metallic/semi-metallic elements and metal alloys, such as Si, Sn, Ge, Bi, Cu–Sn and Ni–Sn showing high capacity, while their applications are facing the same challenge as metal oxides, i.e. large volume change during Li alloying/de-alloying processes, which leads to the severe capacity fading.^{75–77}

5.4 Composite graphene/semiconductor nanocrystals in LIBs and ECs

5.4.1 Structural models of graphene/semiconductor nanocrystals

As described above, there are still challenges with respect to the successful use of graphene in LIBs and ECs. These follow from the substantial agglomeration and restacking after the removal of dispersed solutions and drying due to the Van der Waals interactions between GNSs. As a result, the electrochemical performance of GNSs in LIBs and ECs has been lowered. It is well-known that the most notable feature of graphene is a very large electrochemically active surface area. Cyclic voltammetry has exhibited a 13 times higher capacitance on GNSs compared to bare glassy carbon.⁷⁸ To this extent, there are potential advantages of using GNSs in LIBs and ECs. One efficient and relatively simple method is impregnation of metal oxide nanoparticles into GNSs. This fabrication process is schematically presented in Fig. 5.7.¹⁷

The main purpose of this mechanism is to maximize the combined advantages of both GNS and metal oxide nanoparticles as active materials joined together for practical applications. This operation can be utilized for LIB and EC devices, improving the electrochemical energy storage and, to some extent, even solving the current electrode problems of the individual components of graphene or metal oxides as active materials. The GNSs in the nanocomposite provide chemical functionality for metal oxide nanoparticles. Considering that the metal oxide nanoparticles usually stipulate higher capacity, owing to their structure, size and crystalline orientation in the composite nanomaterial, the established nanocomposites should be considered as new nanomaterials possessing their own functional properties. These properties can be tuned up or down depending on specific requirements from the potential applications. This can be carried out mechanically,



5.7 Schematic preparation of graphene/metal oxide nanocomposites with synergistic effects between graphene and metal oxide nanoparticles. (Reprinted from Ref. 17 with permission from Elsevier Science)

chemically and/or electrochemically. Moreover, metal oxide nanoparticles impregnated on GNSs not only suppress the restacking of GNSs, but also increase the electrochemically active surface area of GNSs resulting in high chemical functionality. However, it has to be admitted that anisotropy does exist in GNSs⁷⁹ and, in order to reach a uniform dispersion and the desired controlled morphology of the GNS-based composite, care should be taken during their preparation. Another great advantage of this modified GNS-based nanostructure is the ability to create electron-conductive networks. As a result, the development of new nanostructures based on GNSs with embedded nanoparticles of metal oxides ensures new electrochemical capabilities of the designed nanostructures and suppression of the agglomeration of GNSs. This direction of nanomaterials research has already received a lot of attention from the various groups and resulted in a great many highly-cited publications.^{80–159} The quality of the GNSs produced, and, consequently, their applications can be categorized as follows:

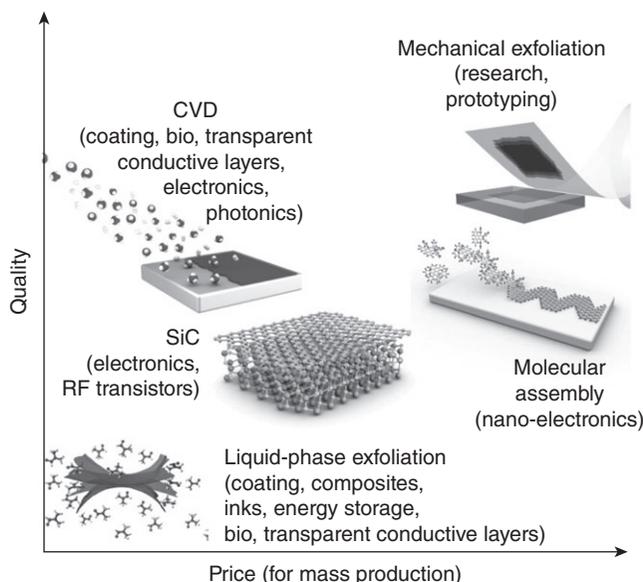
- GNSs or reduced GO flakes for conductive paints, composite materials, etc.;
- planar GNSs for high-performing electronic functional devices;
- planar GNSs for non-active and lower-performing devices.

The properties of the GNSs produced depend significantly on the quality of material, type of defects and substrate and are generally strongly affected by the production method, as graphically presented in Fig. 5.8.⁸⁰

Up to now, the following GNS/metal oxide nanocomposites have been investigated and reported:

- nano-sized oxides anchoring on GNS for LIBs: Co_3O_4 ,^{81–86} TiO_2 ,^{87–89} SnO_2 ,^{90–102} Fe_2O_3 ,^{103,104} Fe_3O_4 ,^{105–111} Mn_3O_4 ,¹¹² MnO ,¹¹³ NiO ,¹¹⁴ MoO_3 ,¹¹⁵ CuO ,^{116–118} Cu_2O ,^{119,120} CeO_2 ,¹²² LiFePO_4 ,^{88,121}
- nano-sized oxides anchoring on GNS for ECs: Co_3O_4 ,^{123,124} RuO_2 ,^{125,126} TiO_2 ,¹²⁶ SnO_2 ,⁹⁰ Fe_3O_4 ,¹²⁶ Mn_3O_4 ,¹³⁶ MnO_2 ,^{127–135} ZnO ,^{137,138}
- GNS-wrapped metal oxide nanoparticles: Fe_3O_4 ,¹³⁹ TiO_2 ,¹⁴⁰ NiO ,¹⁴¹ V_2O_5 ,¹⁴³ MoO_2 ,¹⁴²
- GNS-encapsulated metal oxide nanoparticles for LIBs: Co_3O_4 ,¹⁴⁴ Fe_3O_4 ,^{145,146} Fe_2O_3 ,¹⁰⁴
- 2D sandwich-like model,^{147–149}
- GNS/metal oxides nanoparticles multilayered structures: SnO_2 – NiO – MnO_2 ,¹⁵⁰ TiO_2 ,¹⁵¹ NiO ,¹⁵² MnO_2 ,^{153,154}
- 3D GNS (normally ≤ 10 wt% in composite) conductive networks among metal oxides: $\text{Li}_4\text{Ti}_5\text{O}_{12}$,^{155,156} LiFePO_4 ,¹²⁵ TiO_2 ,¹⁵⁷ $\text{Li}_3\text{V}_2(\text{PO}_4)_3$,¹⁵⁸ Fe_2O_3 .¹⁵⁹

Conclusions from the review of progress in developing such composite nanomaterials can be summarized as follows:



5.8 Combination of approaches to mass-production of graphene, which allow a wide variety of choices of quality, size and potential price for any particular application. (Reprinted from Ref. 80 with permission from Nature Publishing)

1. As a 2D support, GNSs are an ideal supporting structure for uniformly-dispersed metal oxide nanoparticles. Interactions between GNSs and metal oxide nanoparticles have been shown to be dependent on the size, shape and crystallinity of the nanoparticles. The nanocomposites developed have demonstrated synergic effects and advanced electrochemical properties.
2. Restacking of GNSs can be eliminated by using metal oxide nanoparticles. A better understanding of the correlation between the electrochemical performance and structure, properties and interaction within the developed GNS-based nanocomposites is needed.
3. GNSs have been considered as effective 2D building blocks for the progression and advancement of 3D conductive porous networks, improving the poor electrical properties and charge transfer pathways of pure metal oxides.
4. The volume change and agglomeration of metal oxides can be suppressed by employing GNS with embedded metal oxide nanoparticles. However, well-controlled methods of preparation and synthesis of such GNS-based nanocomposites are only beginning to emerge. Further work should be focused on pursuing the most suitable methods addressing the anisotropy issue of GNS.

5. Early success warrants continuing exploration of the synthesis of GNS-based nanocomposites on and between GNSs, ensuring excellent bonding, interfacial interactions and electrical contacts between GNSs and metal nano-oxides.
6. Successful computation of GNS-based nanocomposites remains a problem. When the solid matter is considered, the layered composite nanostructures are so complex that current existing models, as well as the computer's power to model structures which can yield particular properties, run out of steam. Therefore, in order to improve the design and adequately predict both the physical and electrochemical properties of GNS-based nanocomposites, new approaches to modelling are required. Ultimately, researchers will need software which would be able to reveal how a nanomaterial's structural alterations – for example, a change in a nanocomposite crystal's lattice structure – influence its properties and functions.

5.4.2 Multifunctionalities of graphene as a support

Modern nanomaterials have attracted great scientific and industrial interest owing to their size-related unique characteristics and a wide variety of potential applications. Research into their properties has proceeded in several directions. First, design rules are being developed for complex hierarchical nanostructured systems through exploiting the analogy of nanoparticles with molecules.¹⁵⁹ Although robust and reproducible synthesis of relatively simple nanoparticles has been reported,¹⁶⁰ when more complex and composite nanostructures are considered, uncontrolled agglomeration and growth of large particles that often lose their dispersibility and good properties remains a challenge. Moreover, the required physical, chemical and electrochemical properties of the complex nanostructures are dependent upon uniform morphology and good crystallinity, which can only be achieved by the synthesis of nanoparticles with controlled sizes, crystal-orientation and shapes, where the aspect ratio, high dispersion and heterogeneity are known.

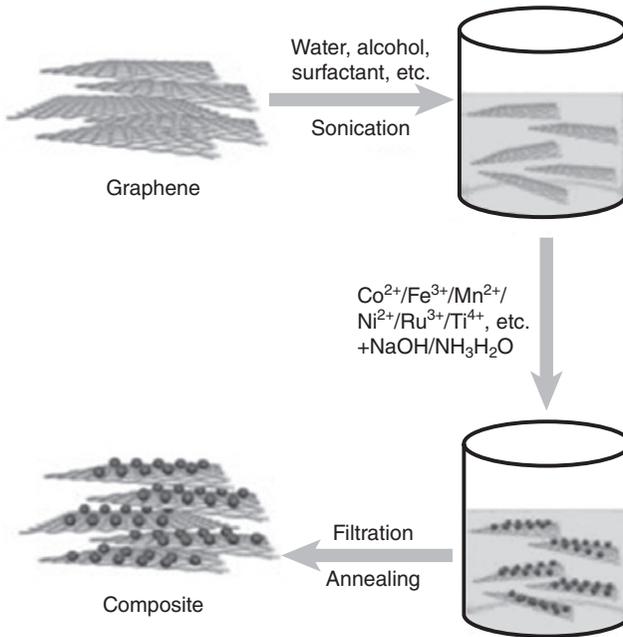
Second, it is vital to characterize the process of integration of complex nanostructures in a much more rigorous manner than is done at present, by shifting away from the 'proof-of-concept' experiments and towards quantitative assessment of the developed complex nanostructures. Recent advances in the development of GNSs and GO have demonstrated that both can serve as a perfect 2D support for anchoring metal or metal oxide nanoparticles in complex nanocomposites.¹⁶¹ In this regard, evaluating the interactions of different metal oxides with GNSs and GO, the coexistence of nanoparticle assemblies and individual nano-oxides and plotting

phase-like diagrams are significant in providing guidance for the development of manufacturing methods of these nanocomposites.

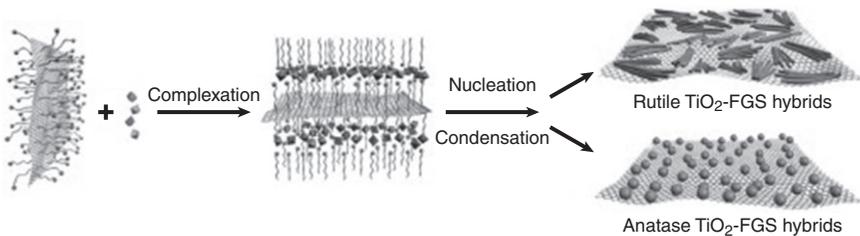
Third, understanding the kinetic factors and roles of thermal fluctuations in the formation of certain nanocomposites is equally important.¹⁶² As a result, so far there have been no reports that the defect-free structures and precisely controlled inter-particle spacing have been achieved during the preparation of nanocomposites. The employment of GNSs and GO as a support for different nanostructured composites provides a unique opportunity and a variety of practical solutions. For example, self-assembly of several types of semiconductor nanoparticles with different bandgaps on GNSs may create a stack of cascaded multiple *p-n* junctions with bandgaps matched to the solar spectrum, thereby reducing the heat loss due to carrier relaxation. This is particularly important for photovoltaic cells. Furthermore, the efficiency of photovoltaic devices may benefit from the ordering, orientation and close packaging of anisotropic rod-shaped semiconductor nanocomposites.

Fourth, employment of well-designed techniques, such as chemical *in situ* deposition, sol-gel processes and hydrothermal synthesis, which have been widely used in the preparation of a broad range of GNS/metal oxide composites, can open new opportunities for the development of an integrated supporting network for discrete metal nanoparticle applications in LIBs and ECs. The implementation of this strategy is schematically shown in Fig. 5.9.

In this approach, both GNSs and reduced GO are dispersed in aqueous or organic solvents by electrostatic stabilization and chemical functionalization. The presence of hydrophilic oxygen- and hydrogen-containing functional groups such as epoxides, hydroxides and carboxylic groups on the surface enables GO or reduced GO to be well dispersed.¹⁷ These scatterers enable the chemical reaction with metal ions from the precursors of inorganic and organic metal salts, which undergo hydrolysis or *in situ* redox reactions, to anchor them on the surface of GNS with multiple functionalities. After filtration and annealing, the developed nanocomposites are ready to use. Recently, there have been several successful reports of the homogeneous anchoring of Co_3O_4 ⁸⁰ and RuO_2 ¹²⁵ on the GNS surface. In both cases, the nanoparticles were within a 5–20 nm range. In contrast, the hydrous RuO_2 nanoparticles without GNS support tend to agglomerate and form larger particles with a size of hundreds of nanometers or even tens of micrometers.¹²⁵ The *in situ* growth of self-assembled anatase TiO_2 on GNS for increased Li^+ ion insertion has also been reported.⁸⁷ In this approach, anionic sulphate surfactants were used to assist the stabilization of GNS in aqueous solutions and to facilitate the self-assembly of anatase TiO_2 on GNS, as schematically presented in Fig. 5.10. This battery potentially offers long life and low cost, along with safety, all of which are critical to stationary



5.9 Schematic view of wet-chemistry approach to fabricating GNS/metal oxide nanocomposites. (Reprinted from Ref. 17 with permission from Elsevier Science)



5.10 Schematic view of anionic sulphate surfactant-mediated stabilization of graphene and growth of self-assembled TiO₂/few-layer graphene sheet hybrid nanostructures. (Reprinted from Ref. 17 with permission from Elsevier Science)

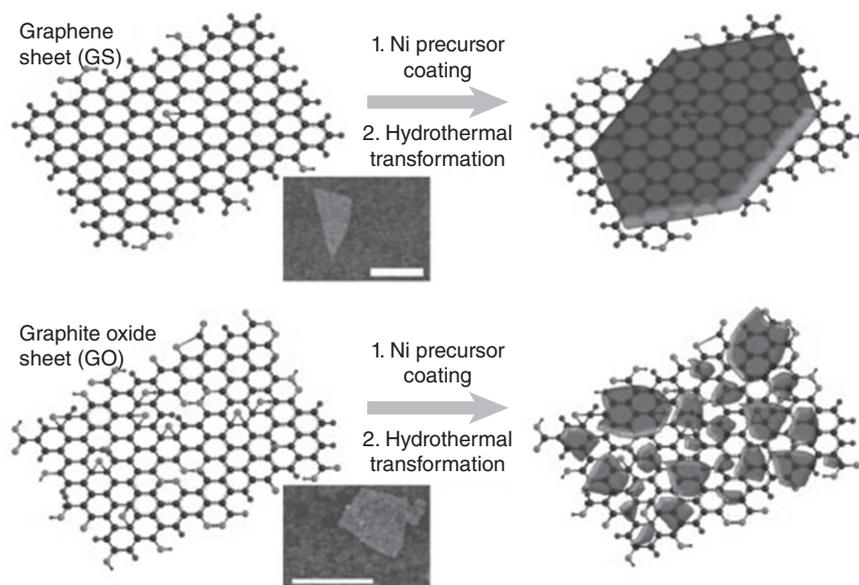
and vehicle applications. It can be emphasized that this approach can be extended to the production of other metal oxide nanostructures such as nanoneedles,¹²⁸ nanowires¹²⁹ and semiconductor/metal catalysts¹⁶³ on GNSs.

In another study, GNS/LiFePO₄ nanocomposites were prepared by the co-precipitation method. The reported capacity and cycle performance were substantially improved.¹²¹ Finally, a combination of bottom-up and top-down methods in assembly, orientation and patterning of metal oxide

nanoparticles on GNSs and GO may lead to large-area high-quality nanoparticle arrays. The self-organization of nanoparticles on GNS assisted by flow, external fields, confinement or photopatterning is also emerging as a strategy for the preparation of hierarchical, multifunctional composite nanostructures with programmable properties.

5.4.3 The role of oxygen contained in graphene

Hetero-atom doping to the graphitic framework leads to changes of structure with subsequent enhancement of the thermal and electrochemical properties because such doping usually changes the Fermi level.¹⁶⁴ Thus, the presence of many oxygen-containing functional groups on the edges and surface of both GNSs and reduced GO is one of the major advantages of graphene over CNTs. The latest results seem to suggest that these functional groups strongly influence the size, shape and distribution of metal oxide particles on the GNS. Due to well-defined redox reactions and the low costs of some hydroxides, they can be applied on the surface of GNSs and GO in order to increase specific capacitance as well as to make new nanocomposites. One example of such techniques is the development of single-crystalline $\text{Ni}(\text{OH})_2$ hexagonal nanosheets, which can be grown directly on GNSs, as graphically presented in Fig. 5.11.¹⁶⁵

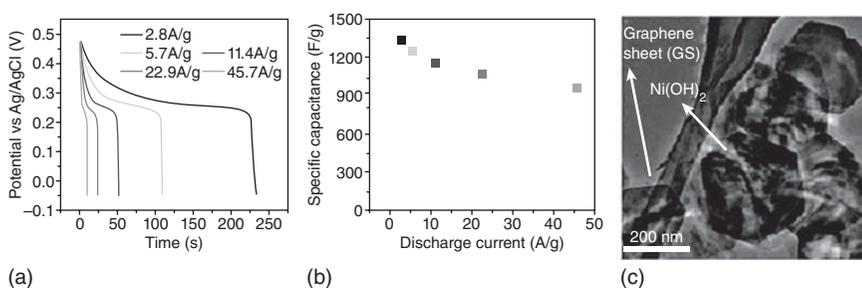


5.11 $\text{Ni}(\text{OH})_2$ nanocrystal growth on GNS (upper) and GO sheet (lower) with 5% and 20% oxygen, respectively. (Reprinted from Ref. 17 with permission from Elsevier Science)

It has been reported that these newly developed nanocomposites exhibited very high specific capacitance of $\sim 1335 \text{ F g}^{-1}$ (Fig. 5.12).¹⁶⁵ In contrast to GO–MnO₂ nanocomposites,¹²⁷ a simple physical mixture of pre-synthesized Ni(OH)₂ nanoplates and GNS displayed a lower specific capacitance.

This appeared to indicate that the interaction between GNS and nanoparticles is important and may affect the charge transport from the nanoparticles to the conducting graphene network. Experiments with securing highly-dispersed RuO₂ nanoparticles with a size less than 5 nm on the surface of GO revealed that the presence of oxygen plays an important role in the formation and anchoring of well-dispersed fine nanoparticles on a 2D graphene support.¹²⁵ In another example, it was found that GNS–Co(OH)₂ nanocomposites can be successfully synthesized by using Na₂S in water and isopropanol, in which the deposition of Co²⁺ and the reduction of GO occur simultaneously.¹⁶⁶ The specific capacitance of these nanocomposites was reported to be 972.5 F g^{-1} , which is substantially higher than each individual counterpart (137.6 and 726.1 F g^{-1} for GNS and Co(OH)₂, respectively). This fact again confirmed that nanocomposites exhibit a synergistic effect.

This example, together with the above-mentioned report on the development of GNS/Ni(OH)₂ nanosheets, suggests that, apart from the morphology, nanoparticle sizes and their crystallinity, the specific capacitance of nanocomposites is also strongly dependent on the oxygen content of the underlying GNS.¹⁶⁶ For instance, low oxygen content in GNS has resulted in weaker chemical interactions with coating species on the surface. This, in turn, enabled diffusion of the pre-coated small nanoparticles and their recrystallization into single-crystal nanoplates with a well-defined shape due to fewer functional groups and defects, as indicated in Fig. 5.11. In



5.12 (a) Galvanostatic discharge curves of Ni(OH)₂ grown on GNS at different discharge current densities; (b) average specific capacitance for Ni(OH)₂ grown on GNS at different discharge current densities; (c) TEM image of Ni(OH)₂ grown on GNS. (Reprinted from Ref. 165 with permission from The Royal Chemical Society)

contrast, the highly oxidized GO surface, possessing about 20 % of oxygen, with a high concentration of oxygen groups and defects interacts strongly with the pre-coated particles, offering a strong pinning force to the small particles that hinders diffusion and recrystallization and therefore results in irregular shaped nanocrystals.¹⁶⁵ This report also suggested that there are two methods for interfacial interactions of metal oxide nanoparticles with GO.¹⁶¹ They are as follows:

1. reactive chemisorption on functional groups (such as HO–C=O and –OH) that bridge metal centres with carboxyl or hydroxyl groups at oxygen-defect sites;
2. Van der Waals interactions between the pristine region of GNS and metal oxide nanoparticles.

Moreover, it should also be possible to control the particle size of metal oxide nanoparticles by varying and regulating the concentration of metal ions in a solution and the amount of the added graphene. All the above findings warrant further study in this area, including the development of the desired synthesis of novel GNS/metal oxide nanocomposites with controlled size, morphology and crystallinity using oxygen-defined GNSs as a carbon support for LIBs and ECs.

5.5 Development of three-dimensional conductive networks

5.5.1 Suppression of restacking of graphene

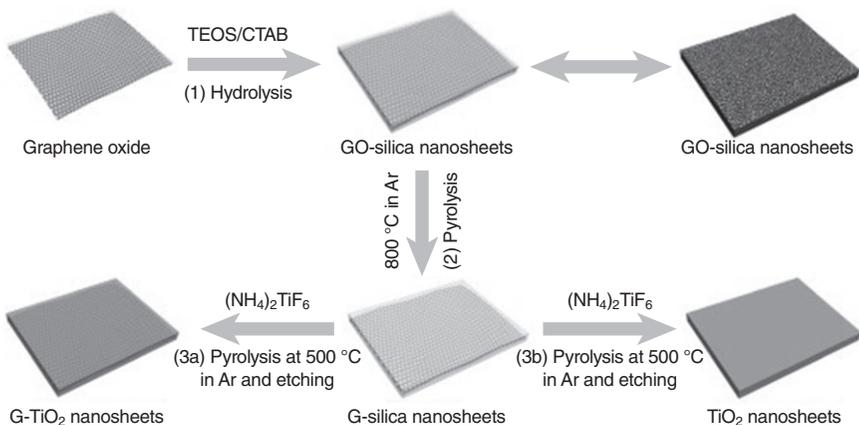
As has been discussed above, GNSs and GO as well as GNS/metal oxide nanocomposites have recently been synthesized by different template methods. In some cases, the newly-developed GNS/metal oxide nanostructures themselves can function as templates for growing novel hetero-structured materials and 3D conductive networks. These GNS/metal oxide nanostructures can be combined into core–sheath or sandwich-like layered configurations, which permit the formation of hetero-junctions within the 3D conductive networks, yielding specific functional properties and tunable, adjustable and efficient devices.

However, as has also been shown, the GNS/metal oxide nanostructures may suffer from the serious agglomeration and restacking after removal of suspension solvents owing to the existing Van der Waals forces between adjacent GNSs. If either restacking or agglomeration has occurred, this would inevitably lead to a substantial loss of effective surface area of nanocomposites within the 3D conductive network and, consequently, much poorer electrochemical properties than expected. Therefore, preventing developed GNSs as well as GNS/metal oxide nanostructures from

restacking has been considered as one of the key elements in improving the electrochemical performance of GNS-based materials in LIBs and ECs.¹⁷

Owing to the synergistic effect between GNS and metal oxide nanoparticles, metal oxide nanoparticles can be utilized as an effective separator of the adjacent GNSs. The loading of metal oxide fine particles can inhibit or decrease the possibility of serious agglomeration and restacking of graphene, thus subsequently increasing the available electrochemically-active surface area of graphene with a flexible and relatively porous structure. Some recent reports have suggested a sol-gel method of preparation of hydrous RuO_2 nanoparticles anchored on graphene,¹²⁵ in which nanosized RuO_2 serves as spacers to support GNS with an apparent increase in pore volume in this hetero-structure. Another report has shown the use of a polymeric binder during the preparation of RuO_2 nanostructures for supercapacitor applications.¹⁶⁷ The bottom-up approach, in which each GNS is fully separated by a mesoporous silica cell for the development of 2D sandwich-like mesoporous silica (GM-silica), has been proposed.¹⁴⁷ Such GM-silica sheets have served as a suitable, reliable platform for creating various 2D-based nanosheets, such as metal oxide sandwich-like nanostructures (Co_3O_4 , TiO_2), mesoporous carbon and carbon nitride.^{17,147-149} Figure 5.13 schematically illustrates the fabrication process of GNS/ TiO_2 -based nanosheets and titania nanosheets without graphene.^{17,149}

It has been acknowledged that sandwich-like GNS/ TiO_2 nanosheets exhibited a high rate capability and an excellent cycle performance, having great potential as a high-rate anode material for Li storage.¹⁴⁹ The results obtained so far showed that the GNS-based nanosheets fully separated by



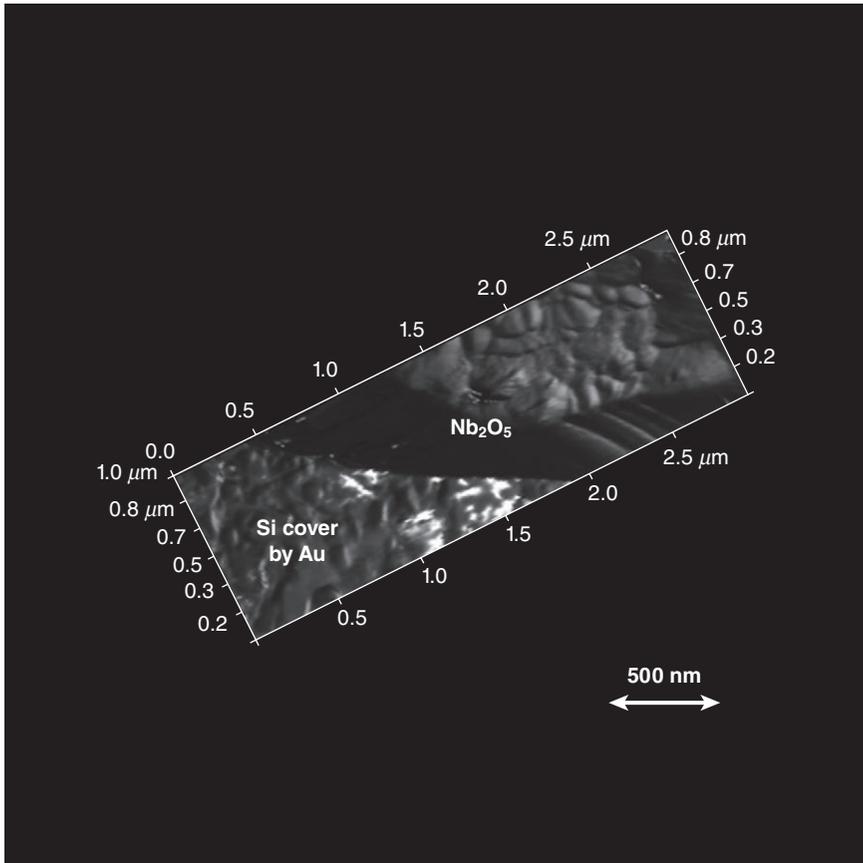
5.13 Fabrication of GNS-based titania nanosheets and TiO_2 nanosheets without graphene. (Reprinted from Ref. 17 with permission from Elsevier Science)

metal oxide nanoparticles not only increased the available active surface area which is essential for higher electrochemical activity, but could also significantly improve their electrochemical performance. Nevertheless, although scalable fabrication techniques employing GNS-based sandwich-like layered graphene/silicon anode hetero-structures have recently been investigated,¹⁶⁸ such limitations of graphene as low mass loading and poor scalability characteristics remain as challenges. These have to be overcome in order to achieve further commercialization of the reported GNS-based nanocomposites.

5.5.2 Suppression of volume change of semiconductor crystals

Effective conductivity between building elements of the modern LIBs and ECs is essential to their high efficiency and long-term stability. It is well-known that semiconductor metal oxide-based electrodes usually have inadequate electrical conductivity. Therefore, in engineering conductive 3D networks, responsive additives such as carbon black have to be added to optimize the electrical resistivity of the electrodes in their manufacturing, but these are not able to deliver energy in the charge–discharge process. Another approach to ensuring sufficient electrical conductivity of nanostructured semiconductor metal oxide electrodes is their intercalation by various metal ions, which is particularly effective, provided that the thickness of the layer is less than 20 nm.¹⁶⁹ Figure 5.14 clearly displays the difference in conductivity between the metallic and semiconductor oxide nanolayers. A conductive atomic force microscopy (AFM) image of a nanostructured Nb₂O₅ thin film deposited on Si substrate covered by Au has confirmed the huge difference in conductivity of two nanomaterials joined together. The Nb₂O₅ thin film appeared almost non-conductive in comparison with the conductive substrate.

Therefore, in order to increase the overall conductivity of the multilayered electrodes of electrochemical cells, the amount of additive ions has to be optimized and in each specific combination of nanomaterials it will be different. In this regard, modelling can help in designing the required electrode structure as, in addition to the percentage of intercalating ions, the texture and morphology of the developing layered electrodes also influence their conductivity. GNSs can also be used in designing and developing conductive 3D networks for the reason that they are different from the common conductive additives. GNS is not only a good electrically conductive carbon material, but also an electrochemically active component. Consequently, it is expected that GNSs will soon will be widely employed as conductive carbon constituents in multilayered semiconductor



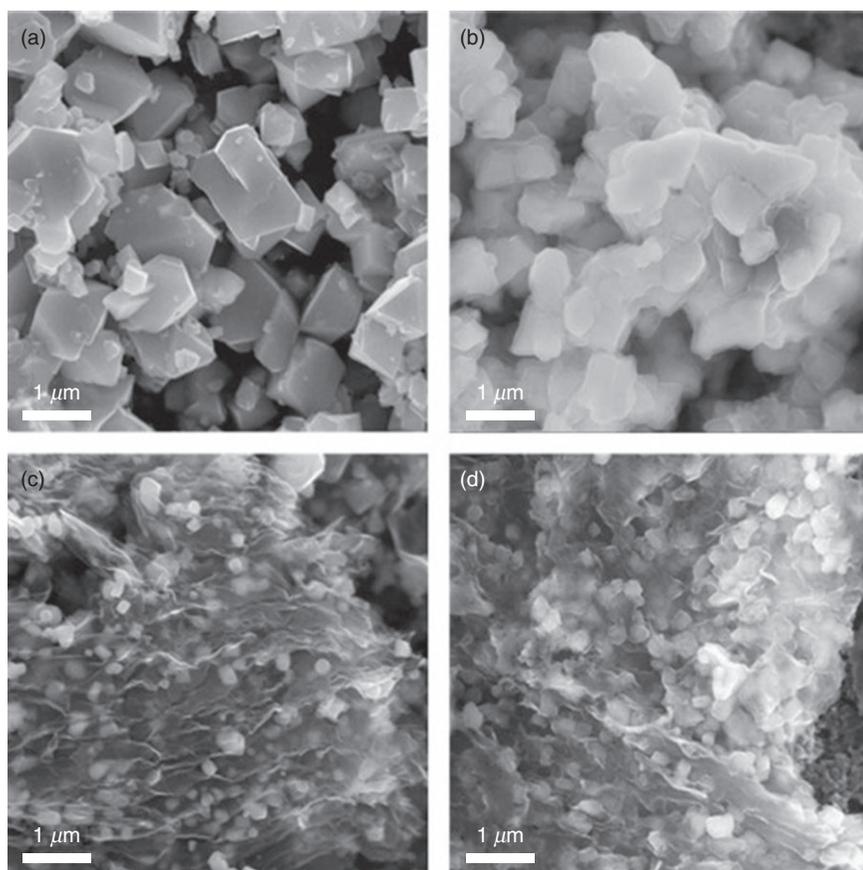
5.14 Conductive AFM image of nanostructured Nb₂O₅ thin film on Si substrate covered by Au.

metal oxide nano-electrodes to construct a 3D conductive network among metal oxide nanoparticles.¹⁵⁵

One powerful and accurate technique to examine the electrochemical behaviour and corresponding reactions on interfaces of the modern multi-layered LIBs and ECs is electrochemical impedance spectroscopy (EIS).¹⁷⁰ EIS can also assist in the comprehensive evaluation of phenomenological electrode–solution interactions and can distinguish between different contributions on the basis of their respective time constants. So far, EIS analysis has been used to access the combined resistance of electrodes, electrolyte and current collectors in the high-frequency range, charge transfer resistance with complex impedance plots, and the Warburg resistance in the lower frequency range, all of which are interpreted with the help of

candidates for the potential replacement of the current commercialized graphitic materials in high-energy electrodes in LIBs. However, these materials generally undergo severe structural and volume changes during Li insertion and removal, leading to the pulverization of their electrodes and, consequently, fast capacity loss.¹⁷¹ During recent years, various approaches have been adopted to address the above-mentioned challenges. However, the use of GNS with its excellent electrical conductivity and superb mechanical flexibility is emerging as one of the most appealing matrices for improving the performance of nanostructured semiconductor metal oxides. As has been discussed in the previous topics, GNSs can be considered as 2D building blocks for 3D conductive networks. Uniformly distributed metal oxide nanoparticles such as SnO_2 ,⁴¹ Co_3O_4 ,⁸¹ Mn_3O_4 ,¹¹² Fe_3O_4 ,¹³⁹ and Co_3O_4 ,¹⁴⁴ successfully anchored on the surface of GNS, or wrapped between GNS layers, or encapsulated by individual graphene sheets, have already been reported. These complex high-capacitive GNS/metal oxide nanocomposites allowed the suppression of the volume change of metal oxides. The designed samples of GNS-based 3D structures have exhibited a large elastic buffer space to accommodate the volume expansion/contraction of metal oxide nanoparticles and confine them during the Li insertion/extraction process.

It was also previously mentioned that these designed-to-application 3D structures have efficiently prevented the aggregation and cracking or crumbling of the electrode material upon cycling. In addition, they were able to retain the large overall electrode capacity, good cycling performance and high rate capability. One of the reported examples is a 3D structure based on GNS-wrapped Fe_3O_4 nanoparticles as an anode for high-performance LIBs.¹³⁹ Figure 5.16 illustrates SEM images of the developed 3D structure based on GNS and commercial Fe_3O_4 nanoparticles before and after 30 discharge–charge cycles. It was observed that the commercial Fe_3O_4 nanoparticles were isolated and dispersed well in the initial state (Fig. 5.16a). However, the changes in morphology and microstructure of Fe_3O_4 nanoparticles after such testing were clearly visible (Fig. 5.16b). The particles were agglomerated and became smaller with the average size decreasing from 735 to 428 nm, indicating the pulverization of the particles during cycling (Fig. 5.16c). On the other hand, no visual changes were indicated for GNS-based nanocomposite after testing (Fig. 5.16d). The Fe_3O_4 particles were still closely embedded between the GNS layers, and the surface morphology, surface-to-volume ratio and particle size were almost the same. The reported changes were to Fe_3O_4 particle sizes: 196 nm before and 213 nm after testing. These results confirmed the vital role of graphene in providing a flexible wrap of Fe_3O_4 particles, increasing surface-to-volume ratio, which has resulted in higher specific capacitance, and in its ability to accommodate the volume change during cycling.



5.16 SEM images of (a, b) commercial Fe_3O_4 particles and (c, d) GNS/ Fe_3O_4 nanocomposite before (a, c) and after (b, d) 30 discharge/charge cycles. (Reprinted from Ref. 17 with permission from Elsevier Science)

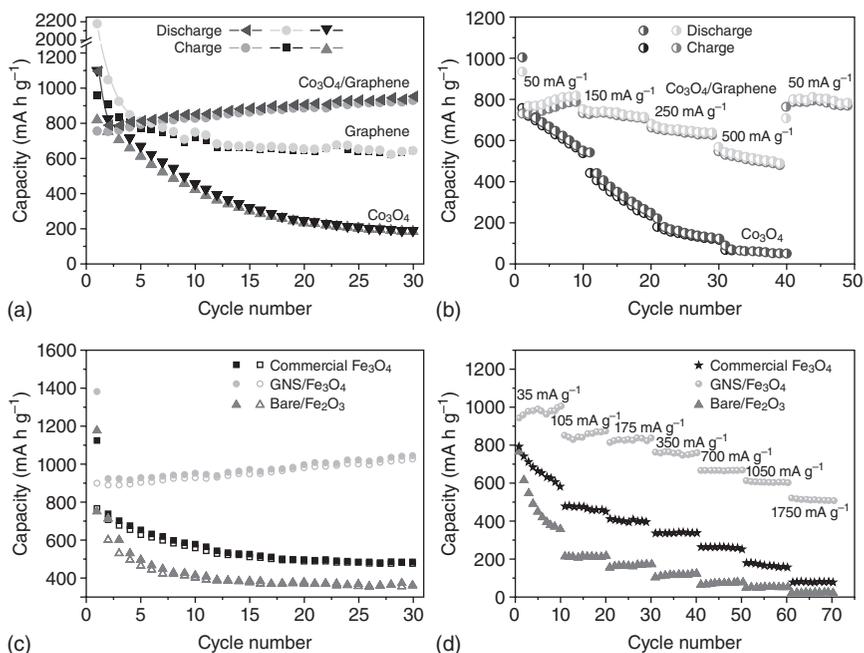
5.5.3 Improvement of electrochemical properties of LIBs and ECs

In the years since 2000, numerous studies have been focused on 2D semiconductor oxide materials as well as on graphene because of their remarkable physical, chemical, mechanical and electrochemical properties which are opening a new field for researchers in materials science, chemistry and physics, with the prospect of progressing new and diverse applications. For LIBs and ECs, the electrochemical properties are as important as the physical and chemical properties and, therefore, several reports have recently highlighted improvement in the electrochemical properties of GNS/metal oxide nanocomposites developed as electrode materials. Such semiconductors as SnO_2 , Fe_3O_4 , Co_3O_4 , RuO_2 and MnO_2 were used in these

nanocomposites owing to the synergistic effects. The electrochemical merits of GNS/metal oxide nanomaterials have been particularly addressed in comparison with their bulk oxide forms without the presence of graphene.

One of the major achievements associated with adopting newly-developed GNS/metal oxide nanocomposites is improvement in cycling performance. It is well-known that the Li-storage mechanism of metal oxides is based on either a Li^+ ion intercalation reaction or a Li conversion reaction. The major drawback of metal oxide materials is that their capacity decreases rapidly upon cycling, which is caused by a large volume change and/or by lower electrical conductivity. As a result of employing GNS/metal oxide nanocomposites, improvement in cycleability owing to the synergistic effect between graphene and metal oxides has been obtained. For example, Co_3O_4 nanoparticles, anchored on GNS, have shown much better cycling performance than graphene and Co_3O_4 .⁸¹ The reported reversible capacity of GNS and Co_3O_4 decreased from 955 to 638 mA h g^{-1} and from 817 to 184 mA h g^{-1} , respectively, up to 30 cycles. In contrast, the reversible capacity of the graphene/ Co_3O_4 composite slightly increased with cycling, reaching $\sim 935 \text{ mA h g}^{-1}$ after 30 cycles, as demonstrated in Fig. 5.17a. Another study also reported improvement in the cycling performance of ECs.¹²⁵ In this case, hydrous RuO_2 anchored on GNSs and graphene retained 97.9 % of the original capacity after 1000 cycles, which is a great improvement compared to a pure RuO_2 electrode ($\sim 42.0 \%$) and graphene (90.9 %).¹²⁵ This excellent electrochemical stability was attributed to the 2D carbon support and double-layer capacitance of GNS.

Another important GNS-based nanostructure is graphene-wrapped metal oxides, in which metal oxide particles are wrapped between adjacent graphene layers.¹³⁹ In this report, a graphene-wrapped Fe_3O_4 composite demonstrated a high reversible specific capacity of 1026 mA h g^{-1} after 30 cycles, which is significantly higher than that of commercial Fe_3O_4 (475 mA h g^{-1}) and bare Fe_2O_3 (359 mA h g^{-1}) with a rapid capacity fading, as displayed in Fig. 5.17c.¹³⁹ Moreover, it has recently been confirmed that flexible, graphene-encapsulated metal oxides, fabricated by electrostatic co-assembly between negatively charged GO and positively charged oxide nanoparticles, could effectively suppress the aggregation and accommodate the volume change of oxide nanoparticles upon cycling.¹⁴⁴ The resulting graphene-encapsulated Co_3O_4 nanoparticles exhibit a high reversible capacity of 1100 mA h g^{-1} in the initial cycle, and over 1000 mA h g^{-1} after 130 cycles. Such GNS-based 3D structures have a large elastic buffer space to accommodate the volume change and prevent the aggregation of metal oxide particles during Li insertion/extraction, and efficiently suppress the cracking or crumbling of the electrode materials during cycling.



5.17 (a) Cycling performance of graphene, Co_3O_4 and $\text{GNS}/\text{Co}_3\text{O}_4$ composite. (b) Rate capability of $\text{GNS}/\text{Co}_3\text{O}_4$ composite and Co_3O_4 at various current densities. (Reprinted from Ref. 17 with permission from the Elsevier Science)

All the above-mentioned examples suggest that designing conductive 3D GNS-based networks and nanostructures with an elastic flexible framework is beneficial for their electrochemical performance in LIBs and ECs. In the 3D framework small nanoparticles can be strongly bonded to GNS, allowing them to suppress their volume change, improve their electrical conductivity and contact with the electrolyte, and decrease the effective transport distance of Li^+ ions and electrons. Consequently, GNSs can not only facilitate the flexibility of nanocomposites, but also ensure improvement in the electrochemical properties of the developed structures.

Long-term stability and high rate capability at fast charge and discharge rates are also essential for LIBs and ECs in order to improve the performance of hybrid and electric vehicles as well as portable power tools.¹⁷² It is therefore expected that the next generation of nanostructured hybrid materials for these applications will have a higher reversible accommodation of Li at high rates compared to bulk materials due to the shortened distance of Li^+ ion and electron transport. However, the huge volume change and poor electrical conductivity of metal oxides during Li^+ insertion/extraction cycles inevitably result in rapid cracking and crumbling

of the electrode, leading to the fast capacity loss of metal oxides. Employment of newly-developed GNS/metal oxide nanocomposites can open a new opportunity for much better rate capability compared to bulk oxide electrodes.^{81–83,87,90–94} In all these cases, it was confirmed that GNS/metal oxide nanocomposites demonstrated better performance by inhibiting the large volume change and providing good electron conduction paths.

For instance, GNS/Co₃O₄ nanocomposite retained a reversible capacity of 800 mA h g⁻¹ at 50 mA g⁻¹, whereas the capacity of a Co₃O₄ electrode counterpart rapidly dropped to 541 mA h g⁻¹. Figure 5.17b shows the reversible capacity of the GNS/Co₃O₄ nanocomposite and Co₃O₄ at other rates: 715 and 239 mA h g⁻¹ at 150 mA g⁻¹, 631 and 122 mA h g⁻¹ at 250 mA g⁻¹, and 484 and 53 mA h g⁻¹ at 500 mA g⁻¹.⁸¹ In another example, GNS/Fe₃O₄ nanocomposite exhibited a much better rate performance compared to commercial Fe₃O₄ and bare Fe₂O₃ particles. In particular, when the rate reaches a value as high as 1750 mA g⁻¹, the capacity of the composite is still 520 mA h g⁻¹, 53 % of the initial capacity, while the capacities of Fe₃O₄ and Fe₂O₃ electrodes drop dramatically to 10 and 3 % of the initial capacity at such a high rate, as presented in Fig. 5.17d.¹³⁹ Other reports have highlighted very similar results in improvement of the rate capability for GNSe/SnO₂^{93,94} and GNS/Mn₃O₄¹¹² nanocomposites.

Considering the great achievements in the electrochemical performance of GNS/metal oxide nanocomposites used as electrodes of LIBs and ECs, it is highly likely that a future for such electrodes is commercially feasible through their further optimization and better design. All the research done so far has demonstrated substantial improvements in increased capacity/capacitance, rate capability, improved cycling stability and increased energy and power densities. However, in order to secure the acceptance of these nanocomposites by the different industries, several important challenges remain to be addressed. These are as follows:

- Large-scale, low-cost and simple production of graphene is one of the most important challenges.
- Control of the developed interface between GNS and metal nano-oxides is needed, as most of the electrochemical reactions and charge transfers occur on the interfaces. Better understanding of the surface chemistry of GNS/metal oxides interfaces is crucial for improving the rates of electrochemical interfacial reactions.
- Reproducibility in performance must be improved by smart design and control of the developing morphology and phase compositions of the semiconductor nano-oxides. This would lead to optimization of the structure–property relationships at the nanoscale.
- Considering such GNS properties as flexibility and light weight, much more attention should be dedicated to the technological progress of

portable, compact, ultrathin and even flexible energy storage devices for advanced thin and wearable electronics and wireless communications.

- Much better compatibility of the composites for use in the entire EC or LIB devices is needed, not just high performance of the nanocomposite electrodes.
- A major concern with GNS is their poor surface adhesion. Until GNS can be adequately protected and their integrity preserved, GNS/metal oxide nanocomposites will be limited to applications with low wear.

With continuous exploitation and improvements of all the above-mentioned aspects, it is evident that GNS/metal oxide nanocomposites for both LIBs and ECs will find their way in various practical applications such as in portable tools, personal electronics, wireless communications, electric vehicles, hybrid electric vehicles and plug-in hybrid electric vehicles, etc.

5.6 Nanostructured thermopower wave sources

As the demand for energy-efficient sources of power at the nanoscale for various applications has increased since 2000, scientists are dedicating their efforts to the development of micro- or nano-sized energy storage^{173–175} and harvesting^{176–180} systems which are capable of releasing energy at high rates. The motivation for this evolution has been based on the use of nano-scaled energy sources in such emerging activities as remote nanoscale sensor networks, flexible electronic devices, disposable medical diagnostics and micro-electromechanical systems.^{181–184} However, no reliable sources of power exist which are capable of direct conversion of the chemical energy to oscillating current at the nanoscale. One possible alternative to conventional power sources at the nanoscale is the utilization of nano-structured thermoelectric (TE) materials.^{185–188}

The ‘quality’ of TE as a material is characterized by its Seebeck coefficient, S , electrical conductivity, σ , and thermal conductivity, κ , which are combined in the thermoelectric figure of merit, $Z = S^2\sigma/\kappa$.¹⁸⁹ For nanostructured TE material development, the main target is, therefore, to maximize Z . However, the transport properties, S , σ and κ , usually vary with environmental conditions which results in a temperature-dependent function $Z(T)$. Thus, in any condition range, material with different properties has to be used in order to achieve a high figure of merit. Typically, nanostructured TE material is operated at a temperature difference of several hundred degrees. Under this condition, a pronounced climate profile will develop in the material, so that for a specific material the Z criterion will have an optimum high value only in a small spatial range. The spatially varying temperature profile together with the temperature-dependent material properties leads directly to the concept of local selection of the particular material or

composition which brings the highest overall efficiency or power output to the device. An efficiency improvement compared to homogeneous material, in certain cases up to 50–100 %, can be achieved by the use of functionally graded nanomaterials.¹⁹⁰

Initiation of the chemical decomposition releases heat that travels much faster along the nanotube than in the annulus, resulting in a reaction wave guided by the CNT. The coupled thermal diffusion and chemical reaction terms can be described using the following modified Fourier's Law equation with a non-linear source term to account for the chemical reaction:¹⁸⁷

$$\frac{\rho C_p \partial T_2}{M_w \partial t} = \chi \frac{\partial^2 T}{\partial x^2} - (Q k_0 y) e^{(-E_a/RT)} - G_0 \frac{4d_N}{d_M^2 - d_N^2} (T - T_2) \quad [5.5]$$

where G_0 is the interfacial conductance between the CNT and cyclotrimethylene-trinitramine (TNA), d_M is the outer diameter of the TNA–CNT system and d_N is the CNT diameter. The parameter χ is the thermal conductivity, ρ is the density, Q is the enthalpy of reaction, y is the molar concentration of reactive material, k_0 is the Arrhenius pre-factor, R is the universal gas constant, E_a is the activation energy of decomposition and C_p and M_w are the (molar) specific heat and molecular weight of the material, respectively. The second term on the right-hand side accounts for the thermal source of the decomposition reaction, with the mole fraction of unreacted material (y/y_0) decreasing in time and space (according to the spatial profile of T) according to

$$\frac{\partial y}{\partial t} = -(k_0 y) e^{(-E_a/RT)} \quad [5.6]$$

Considering heat transfer from the annulus and thermal diffusion, the equation for the temperature (T_2) evolution in the CNT can be as follows:¹⁸⁷

$$\frac{\rho C_{p2} \partial T_2}{M_{w2} \partial t} = \chi_2 \frac{\partial^2 T}{\partial x^2} + G_0 \frac{4}{d_N} (T - T_2) \quad [5.7]$$

where the subscript '2' refers to properties of the CNT. Equations 5.5–5.7 are solved using the following boundary conditions:

$$T_1(x, t = 0) = g \times e^{-x^2/W} + T_{\text{ambient}} \quad [5.8]$$

$$T_2(x, t = 0) = g \times e^{-x^2/W} + T_{\text{ambient}} \quad [5.9]$$

$$\frac{y}{y_0}(x = 0, t) = 1 \quad [5.10]$$

$\frac{y}{y_0}(x = 0, t) = 0.001$ (the last approximating a zero boundary condition) with the pulse width parameter $w = 2 \times 10^{-11} \text{ m}^2 \cdot \beta$. T_{ambient} is the ambient

temperature, assumed to be 298 K. The parameter grouping $\beta = (C_p E_a)/(-QR)$ is the inverse dimensionless adiabatic reaction temperature rise, which has proved to be important for determining wave characteristics. The function $T(x, t = 0)$ is a Gaussian pulse, offset by 298 K, to simulate initiation by a rapid pulse of heat. For instance, heat can be initiated from a laser or resistive filament. Here, g is the maximum initial temperature. From numerous simulations, it can be empirically determined that it must be greater than $0.16 \times \exp(0.37\beta)$ to commence a propagating reaction wave. Physically, the magnitude of the temperature initial condition must increase with β since that parameter is proportional to the specific heat and activation energy. More drive must be supplied in the initial pulse for larger values of β to overcome the specific heat and activation energy and increase the initial reaction rate sufficiently to sustain self-propagation. The initial condition for the composition of the material, y/y_0 , corresponds to a completely unreacted annulus, with the exception of the $x = 0$ boundary, which is almost entirely reacted so as to be consistent with the temperature condition, as is necessary for numerical stability. The boundaries of the system are assumed to be adiabatic, and the system is made to be sufficiently long that the wave is far from the boundaries.¹⁸⁷

Following Zeldovich's theory of thermal flame propagation,¹⁹¹ the system of equations can be scaled down to nanodimensions. A non-dimensional temperature $u = (R/E_a)T$, time $\tau = (-Qk_0R)/(C_p E_a)t$, and space $\xi = x[(\rho C_p/\chi M_w)(-Qk_0R/C_p E_a)]^{1/2}$ has been shown to appropriately scale the system and resulting reaction wave.¹⁸⁷ A conversion η can be defined $(M_w y)/\rho = 1 - \eta$. Other parameters of importance are the thermal diffusivities $\alpha = (\chi M_w/\rho C_p)$ of the annulus and of the nanotube, α_2 . The resulting equations are as follows:

$$\frac{\partial u}{\partial \tau} = \frac{\partial^2 u}{\partial \xi^2} + (1 - \eta)e^{-1/u} - \gamma_1(u - u_2) \tag{5.11}$$

$$\frac{\partial u_2}{\partial \tau} = \alpha_0 \frac{\partial^2 u_2}{\partial \xi^2} + \gamma_2(u - u_2) \tag{5.12}$$

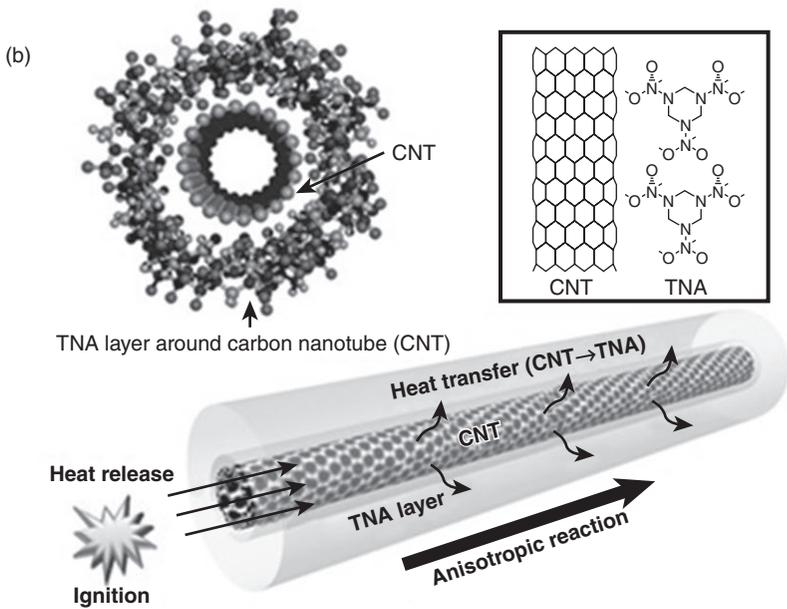
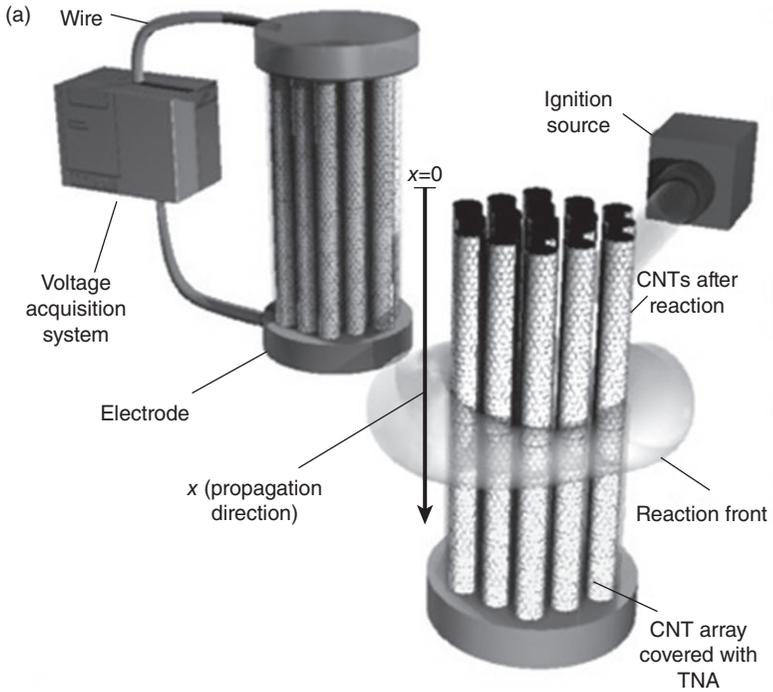
$$\frac{\partial \eta}{\partial \tau} = \beta(1 - \eta)e^{-1/u} \tag{5.13}$$

where $\alpha_0 = \alpha_2/\alpha$, $\gamma_1 = (4d_N/d_M^2 - d_N^2)(G_0\beta M_w/\rho C_p k_0)$ and $\gamma_2 = (4G_0\beta M_{w2})/(d_N\rho_2 C_{p,2}k_0)$. Interestingly, this shows that the only terms affected by the diameter of the thermal conduit or the fuel layer are the interfacial heat exchange terms, γ_1 and γ_2 . For β , α and α_2 , average values over the temperature range of 300–1700 K were used. Since β is the non-dimensionalized

adiabatic reaction temperature rise, the maximum temperature was iterated until a consistent average β of 10.6 for TNA was reached. Over the same range, α is $4.3 \times 10^{-8} \text{ m}^2/\text{s}$ and α_2 is $0.001 \text{ m}^2/\text{s}$. Depending on the concentration of defects, the thermal diffusivity of the nanotube, α_2 , may at least vary over an order of magnitude.¹⁸⁶ The value selected here was the median. Consequently, considering all the above-mentioned equations, the oscillatory behaviour of the thermopower waves can be modelled and analysed.

There have been several practical reports relating to experimental observations of thermopower wave oscillations by using different nanostructured materials.^{193–199} A typical structure of a thermopower wave generator based on a CNT array and a cross-section of CNT coupled with TNA and a nanostructured material with a high Seebeck coefficient is schematically presented in Fig. 5.18. In these devices, the thermopower waves are realized using TNA as a fuel around a shell of a multiwalled CNT array by a self-propagating exothermic reaction. These response waves induce a concomitant thermopower wave of high power density ($>7 \text{ kW/kg}$), resulting in an electrical current that travels along the same direction.¹⁸⁷ In such thermopower devices, the highly conductive CNT core allows the axial transportation of free electrons, which are generated via a large temperature gradient across the device. In these systems, the high thermal conductivity of the CNT array guarantees the continuation of the reaction and the propagation of the thermopower waves.

The main limitation of the works carried out at the beginning of the 21st century was the low voltage generated, which was generally in the order of 30–50 mV for masses in the range of several milligrams. The main reason for this was the relatively low Seebeck coefficient of CNTs ($80 \mu\text{V K}^{-1}$).^{193–195} Consequently, in order to increase the efficiency of thermopower wave generators, nanostructured materials such as Bi_2Te_3 and Sb_2Te_3 with their large respective Seebeck coefficients of 287 and $243 \mu\text{V K}^{-1}$ have been investigated.^{186,195} These nanomaterials can potentially replace CNTs in the next generations of thermopower sources. One of the main requirements of a thermopower source core material is high electrical conductivity. A higher electrical conductivity can increase the power output as it allows larger currents. This means that materials such as Si, even in its highly doped state, with a large Seebeck coefficient ($\sim 1500 \mu\text{V K}^{-1}$) are rendered inefficient due to their low electrical conductivity. On the other hand, both Bi_2Te_3 and Sb_2Te_3 have high electrically generated power. The electrical conductivity of Bi_2Te_3 is of the order of 10^5 S/m , while Sb_2Te_3 exhibits an electrical conductivity in the range of 5×10^3 – 10^4 S/m .¹⁹⁶ A high thermal current is also required to sustain the propagation of the thermopower waves. The thermal responses of Bi_2Te_3 and Sb_2Te_3 are low (1 and $2.5 \text{ W m}^{-1} \text{ K}^{-1}$, respectively).¹⁹⁷ In order to compensate for that, highly thermally conductive substrates such as Al_2O_3 with thermal conductivity of $20 \text{ W m}^{-1} \text{ K}^{-1}$ can be used to



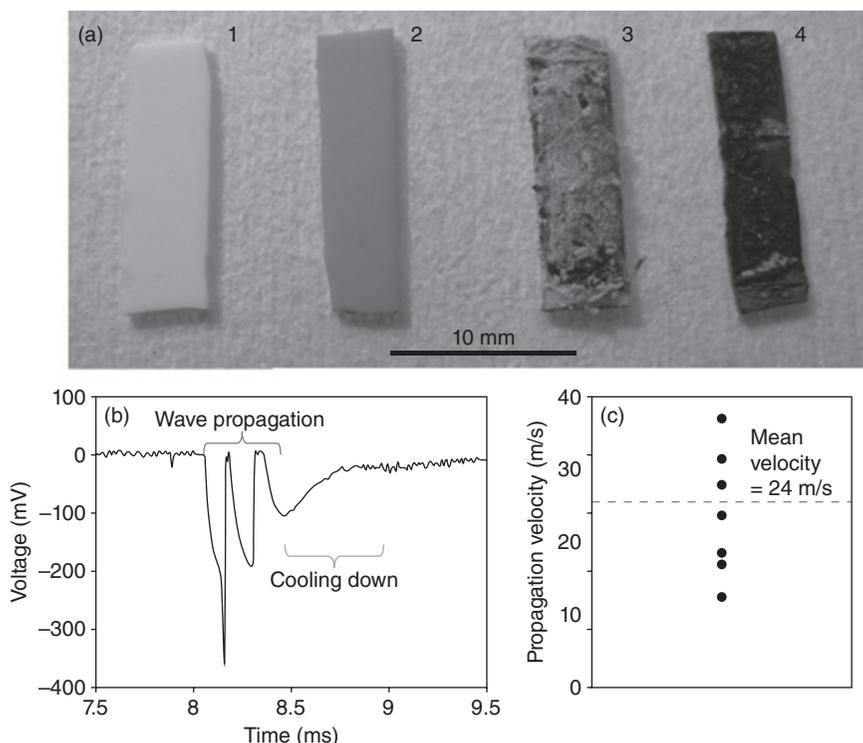
5.18 (a) Schematic view of a thermopower wave generator based on a CNT array. (b) Cross-section of CNT coupled with TNA and nanostructured materials with high Seebeck coefficient. (Reprinted from Ref. 187 with permission from the American Chemical Society)

achieve the desired thermally generated power.¹⁹⁷ Another advantage is the combination of these nanomaterials in one device as they represent *p*-(Sb₂Te₃) and *n*-type (Bi₂Te₃) semiconductors providing high output AC power.

Other materials which can be successfully utilized in the next generation of energy sources for different applications are nanostructured semiconductors ZnO¹⁹⁸ and MnO₂. ZnO, as a typical *n*-type semiconductor, appeared to be one of most outstanding candidates as the core thermoelectric material for thermopower-based energy sources. ZnO possesses a relatively high Seebeck coefficient (approximately $-360\mu\text{V K}^{-1}$ at 85 °C) which increases with temperature, a high electrical conductivity at elevated temperatures of above 300 °C (ZnO film resistance of 250 Ω at 300 °C, hence suitable for operation in thermopower wave sources), high thermal conductivity ($15\text{W m}^{-1}\text{K}^{-1}$ at 300 °C) and good chemical stability. Optical images of the ZnO samples used before and after the reaction are presented in Fig. 5.19a.¹⁹⁵ A typical thermopower voltage signal obtained across a sample of the fuel/ZnO/Al₂O₃ system is shown in Fig. 5.19b. The voltage profile exhibited two distinct regions: an initial phase during the wave propagation and a cooling down phase until the temperature across the ZnO film reached equilibrium (Fig. 5.19c). The initial reaction phase is a region of rising voltage as the wavefront spreads across the sample until all the combustion fuel is consumed. This is followed by a region of exponential decay. The moving temperature gradient resulted in voltages with peak magnitudes of up to 500 mV and oscillations with peak-to-peak amplitude of up to 400 mV. The power obtained from these devices can be as large as 1 mW.¹⁹⁷

Another very interesting example of a nanostructured material which has been recently investigated as a suitable candidate for thermoelectric wave sources is MnO₂.²⁰⁰ It was shown that coupling of solid fuel to the MnO₂ layers resulted in the highest output voltage (1.8 V) reported up to now for thermopower wave systems. Due to the high Seebeck coefficient, the reported output voltage was at least 300 % higher than any other previously reported thermopower wave system.²⁰⁰

Table 5.1 summarizes the performance of the nanostructured materials used up to now as thermopower wave sources. The results presented clearly display that the combination of the CNT, TNA and nanostructured thermoelectric materials increased the maximum output voltage compared to thermoelectric material based only on CNT. Observations obtained so far are combined and presented in Fig. 5.20, which compares different nanomaterials used on thermopower wave energy sources with the best available super-capacitors in terms of specific power, voltage and oscillation amplitudes. Axis Y in this figure is arbitrary. Analysis of the data presented shows that, although super-capacitors can exhibit higher rates of energy discharge, they are inefficient for long-term energy storage as they have a very high

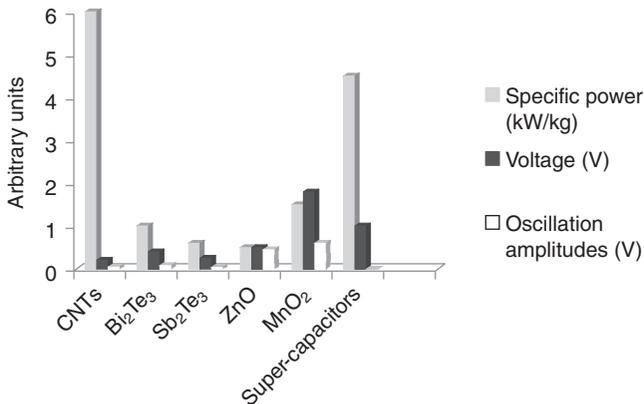


5.19 (a) Photo of the 1 – Al_2O_3 substrate, 2 – ZnO deposited on Al_2O_3 substrate, 3 – fuel/ZnO/ Al_2O_3 sample, 4 – sample after thermopower wave propagation. (b) Oscillatory thermopower voltage signal obtained using the fuel/ZnO/ Al_2O_3 device. (c) Reaction propagation velocities for the fuel/ZnO/ Al_2O_3 thermopower systems. (Reprinted from Ref. 194 with permission from the Royal Chemical Society)

Table 5.1 Nanostructured materials for thermopower wave sources

Output	CNT ¹⁸⁵	i_2Te_3 ¹⁸⁶	Sb_2Te_3 ¹⁹⁵	ZnO ¹⁹⁸	MnO_2 ²⁰⁰
Voltage (max)	210 mV	350 mV	200 mV	500 mV	1.80 V
Specific power (kW/kg)	4–7 kW/kg	1 kW/kg	0.6 kW/kg	0.5 kW/kg	1.5 kW/kg

self-discharge rate. Moreover, they are bulky and are capable of generating only DC power. In addition, thermopower wave systems can produce alternating voltages with concomitantly high specific power. They do not suffer from problems such as self-discharge and are much smaller in size. More work is underway in order to improve the efficiency as well as the specific



5.20 Comparative assessment of the specific power, output voltage and oscillation amplitudes for CNTs, nanostructured thermoelectric materials and best known super-capacitors.

power of the thermopower wave systems so that they can be a viable miniaturized energy generation technology.

5.7 References

1. M.S. Whittingham, Electrical energy storage and intercalation chemistry, *Science*, 192 (1976) 1126–1127.
2. J.M. Tarascon, M. Armand, Issues and challenges facing rechargeable lithium batteries, *Nature*, 414 (2001) 359–367.
3. A.S. Arico, P. Bruce, B. Scrosati, J.M. Tarascon, W. van Schalkwijk, Nanostructured materials for advanced energy conversion and storage devices, *Nat. Mater.*, 4 (2005) 366–377.
4. P. Simon, Y. Gogotsi, Materials for electrochemical capacitors, *Nat. Mater.*, 7 (2008) 845–854.
5. M.H. Liang, L.J. Zhi, Graphene-based electrode materials for rechargeable lithium batteries, *J. Mater. Chem.*, 19 (2009) 5871–5878.
6. J. Hou, Y. Shao, M.W. Ellis, R.B. Moore, B. Yi, Graphene-based electrochemical energy conversion and storage: fuel cells, supercapacitors and lithium ion batteries, *Phys. Chem. Chem. Phys.*, 13 (2011) 15384–15402.
7. W. Choi, I. Lahiri, R. Seelaboyina, Y.S. Kang, Synthesis of graphene and its applications: A review, *Crit. Rev. Solid State Mater. Sci.*, 35 (2010) 52–71.
8. Q. Cheng, J. Tang, J. Ma, H. Zhang, N. Shinya, L.C. Qin, Graphene and carbon nanotube composite electrodes for supercapacitors and ultra-high energy density, *Phys. Chem. Chem. Phys.*, 13 (2011) 17615–17624.
9. H.Q. Li, R.L. Liu, D.Y. Zhao, Y.Y. Xia, Electrochemical properties of an ordered mesoporous carbon prepared by direct tri-constituent co-assembly, *Carbon*, 45 (2007) 2628–2635.
10. Y.S. Hu, P. Adelhelm, B.M. Smarsly, S. Hore, M. Antonietti, J. Maier, Synthesis of hierarchically porous carbon monoliths with highly ordered microstructure

- and their application in rechargeable lithium batteries with high-rate capability, *Adv. Funct. Mater.*, 17 (2007) 1873–1878.
11. A. Mabuchi, K. Tokumitsu, H. Fujimoto, T. Kasuh, Charge-discharge characteristics of the mesocarbon microbeads heat-treated at different temperatures, *J. Electrochem. Soc.*, 142 (1995) 1041–1046.
 12. M. Pumera, Graphene-based nanomaterials and their electrochemistry, *Chem. Soc. Rev.*, 39 (2010) 4146–4157.
 13. S. Park, R.S. Ruoff, Chemical methods for production of graphenes, *Nat. Nanotechnol.*, 4 (2009) 217–224.
 14. D.R. Dreyer, S. Park, C.W. Bielawski, R.S. Ruoff, The chemistry of graphene oxide, *Chem. Soc. Rev.*, 39 (2010) 228–240.
 15. M. Pumera, Electrochemistry of graphene: new horizons for sensing and energy storage, *Chem. Rec.*, 9 (2009) 211–223.
 16. P. Dhiman, F. Yavari, X. Mi, H. Gullipalli, Y. Shi, P.M. Ajayan, N. Koratkar, Harvesting energy from water flow over graphene, *Nano Lett.*, 11 (2011) 3123–3127.
 17. Z.S. Wu, G. Zhou, L.C. Yin, W.C. Ren, F. Li, H.M. Cheng, Graphene/metal oxide composite materials for energy storage, *Nano Energy*, 1 (2012) 107–131.
 18. E. Yoo, J. Kim, E. Hosono, H. Zhou, T. Kuda, I. Honma, Graphene-based composites for electrochemical energy storage, *Nano Lett.*, 8 (2008) 2277–2282.
 19. G.X. Wang, X.P. Shen, J. Yao, J. Park, Graphene nanosheets for enhanced lithium storage in lithium ion batteries, *Carbon*, 47 (2009) 2049–2053.
 20. P. Guo, H.H. Song, X.H. Chen, Electrochemical performance of graphene nanosheets as anode material for lithium-ion batteries, *Electrochem. Commun.*, 11 (2009) 1320–1324.
 21. P.C. Lian, X.F. Zhu, S.Z. Liang, Z. Li, W.S. Yang, H.H. Wang, Large reversible capacity of high quality graphene sheets as an anode material for lithium-ion batteries, *Electrochim. Acta*, 55 (2010) 3909–3914.
 22. P.B. Amama, C. Lan, B.A. Cola, X. Xu, R.G. Reifengerger, T.S. Fisher, Electrical and thermal interface conductance of carbon nanotubes grown under direct current bias voltage, *J. Phys. Chem. C*, 112 (2008) 19727–19733.
 23. D.Y. Pan, S. Wang, B. Zhao, M.H. Wu, H.J. Zhang, Y. Wang, Z. Jiao, Li storage properties of disordered graphene nanosheets, *Chem. Mater.*, 21 (2009) 3136–3142.
 24. C.Y. Wang, D. Li, C.O. Too, G.G. Wallace, Electrochemical properties of graphene paper electrodes used in lithium batteries, *Chem. Mater.*, 21 (2009) 2604–2606.
 25. Z.S. Wu, W.C. Ren, L. Xu, F. Li, H.M. Cheng, Doped graphene sheets as anode materials with superhigh rate and large capacity for lithium ion batteries, *ACS Nano*, 5 (2011) 5463–5471.
 26. D.S. Su, R. Schlogl, Nanostructured carbon and carbon nanocomposites for electrochemical energy storage applications, *ChemSusChem*, 3 (2010) 136–168.
 27. N.A. Kaskhedikar, J. Maier, Lithium storage in carbon nanostructures, *Adv. Mater.*, 21 (2009) 2664–2680.
 28. G.G. Wallace, J. Chen, D. Li, S.E. Moulton, J.M. Razal, Nanostructured carbon electrodes, *J. Mater. Chem.*, 20 (2010) 3553–3562.
 29. H. Bai, C. Li, G.Q. Shi, Functional composite materials based on chemically converted graphene, *Adv. Mater.*, 3 (2011) 1089–1115.

30. M.H. Liang, L.J. Zhi, Graphene-based electrode materials for rechargeable lithium batteries, *J. Mater. Chem.*, 19 (2009) 5871–5878.
31. J.R. Dahn, T. Zheng, Y. Liu, J.S. Xue, Mechanisms for lithium insertion in carbonaceous materials, *Science*, 270 (1995) 590–593.
32. K. Sato, M. Noguchi, A. Demachi, N. Oki, M. Endo, A mechanism of lithium storage in disordered carbons, *Science*, 264 (1994) 556–558.
33. E. Yoo, J. Kim, E. Hosono, H.S. Zhou, T. Kudo, I. Honma, Large reversible Li storage of graphene nanosheet families for use in rechargeable lithium ion batteries, *Nano Lett.*, 8 (2008) 2277–2282.
34. C.Y. Wang, D. Li, C.O. Too, G.G. Wallace, Electrochemical properties of graphene paper electrodes used in lithium batteries, *Chem. Mater.*, 21 (2009) 2604–2606.
35. A. Abouimrane, O.C. Compton, K. Amine, S.T. Nguyen, Non-annealed graphene paper as a binder-free anode for lithium-ion batteries, *J. Phys. Chem. C*, 114 (2010) 12800–12804.
36. X. Liu, Y.S. Hu, J.O. Müller, R. Schlögl, J. Maier, D.S. Su, Composites of molecular-anchored graphene and nanotubes with multitubular structure: a new type of carbon electrode, *ChemSusChem*, 3 (2010) 261–265.
37. D. Pan, S. Wang, B. Zhao, M. Wu, H. Zhang, Y. Wang, Z. Jiao, Li storage properties of disordered graphene nanosheets, *Chem. Mater.*, 21 (2009) 3136–3142.
38. K. Xu, Electrolytes and interphasial chemistry in Li ion devices, *Energies*, 3 (2010) 135–154.
39. C. Uthaisar, V. Barone, Edge effects on the characteristics of Li diffusion in graphene, *Nano Lett.*, 10 (2010) 2838–2842.
40. T. Takamura, K. Endo, L. Fu, Y. Wu, K.J. Lee, T. Matsumoto, Identification of nano-sized holes by TEM in the graphene layer of graphite and the high rate discharge capability of Li-ion battery anodes, *Electrochim. Acta*, 53 (2007) 1055–1061.
41. S.M. Paek, E. Yoo, I. Honma, Enhanced cyclic performance and lithium storage capacity of SnO₂/graphene nanoporous electrodes with three-dimensionally delaminated flexible structure, *Nano Lett.*, 9 (2009) 72–75.
42. Z.S. Wu, W. Ren, L. Wen, L. Gao, J. Zhao, Z. Chen, G. Zhou, F. Li and H.M. Cheng, Graphene anchored with Co₃O₄ nanoparticles as anode of lithium ion batteries with enhanced reversible capacity and cyclic performance, *ACS Nano*, 4 (2010) 3187–3194.
43. S. Yang, G. Cui, S. Pang, Q. Cao, U. Kolb, X. Feng, J. Maier, K. Müllen, Fabrication of cobalt and cobalt oxide/graphene composites: towards high-performance anode materials for lithium ion batteries, *ChemSusChem*, 3 (2010) 236–239.
44. D. Wang, D. Choi, J. Li, Z. Yang, Z. Nie, R. Kou, D. Hu, C. Wang, L.V. Saraf, J. Zhang, I.A. Aksay, J. Liu, Self-assembled TiO₂-graphene hybrid nanostructures for enhanced Li-ion insertion, *ACS Nano*, 3 (2009) 907–914.
45. G. Wang, B. Wang, X. Wang, J. Park, S. Dou, H. Ahn, K. Kim, Sn/graphene nanocomposite with 3D architecture for enhanced reversible lithium storage in lithium ion batteries, *J. Mater. Chem.*, 19 (2009) 8378–8384.
46. S.L. Chou, J.Z. Wang, M. Choucair, H.K. Liu, J.A. Stride, S.X. Dou, Enhanced reversible lithium storage in a nanosize silicon/graphene composite, *Electrochem. Commun.*, 12 (2010) 303–306.

47. J.K. Lee, K.B. Smith, C.M. Hyner, H.H. Kung, Silicon nanoparticles-graphene paper composites for Li ion battery anodes, *Chem. Commun.*, 46 (2010) 2025–2027.
48. N. Zhu, W. Liu, M. Xue, Z. Xie, D. Zhao, M. Zhang, J. Chen, T. Cao, Graphene as a conductive additive to enhance the high-rate capabilities of electrospun $\text{Li}_4\text{Ti}_5\text{O}_{12}$ for lithium-ion batteries, *Electrochim. Acta*, 55 (2010) 5813–5818.
49. D. Choi, D. Wang, V.V. Viswanathan, I.T. Bae, W. Wang, Z. Nie, J.G. Zhang, G.L. Graff, J. Liu, Z. Yang, T. Duong, Li-ion batteries from LiFePO_4 cathode and anatase/graphene composite anode for stationary energy storage, *Electrochem. Commun.*, 12 (2010) 378–381.
50. L. Ji, H. Zheng, A. Ismach, Z. Tan, S. Xun, E. Lin, V. Battaglia, V. Srinivasan, Y. Zhang, Graphene/Si multilayer structure anodes for advanced half and full lithium-ion cells, *Nano Energy*, 1 (2012) 164–171.
51. C. Liu, F. Li, L.P. Ma, H.M. Cheng, Advanced materials for energy storage, *Adv. Mater.*, 22 (2010) 28–62.
52. R. Mukherjee, R. Krishnan, T.M. Lu, N. Koratkar, Nanostructured electrodes for high-power lithium ion batteries, *Nano Energy*, 1 (2012) 518–533.
53. L.L. Zhang, R. Zhou, X.S. Zhao, Graphene-based materials as supercapacitor electrodes, *J. Mater. Chem.*, 20 (2010) 5983–5992.
54. S.R.C. Vivekchand, C.S. Rout, K.S. Subrahmanyam, A. Govindaraj, C.N.R. Rao, Graphene-based electrochemical supercapacitors, *J. Chem. Sci.*, 120 (2008) 9–13.
55. Y. Wang, Z.Q. Shi, Y. Huang, Y.F. Ma, C.Y. Wang, M.M. Chen, Y.S. Chen, Supercapacitor devices based on graphene materials, *J. Phys. Chem. C*, 113 (2009) 13103–13107.
56. W. Lv, D.M. Tang, Y.B. He, C.H. You, Z.Q. Shi, X.C. Chen, C.M. Chen, P.X. Hou, C. Liu, Q.H. Yang, Low-temperature exfoliated graphenes: vacuum-promoted exfoliation and electrochemical energy storage, *ACS Nano*, 3 (2009) 3730–3736.
57. M.D. Stoller, S.J. Park, Y.W. Zhu, J.H. An, R.S. Ruoff, Graphene-based ultracapacitors, *Nano Lett.*, 8 (2008) 3498–3502.
58. Y.W. Zhu, S. Murali, M.D. Stoller, A. Velamakanni, R.D. Piner, R.S. Ruoff, Microwave assisted exfoliation and reduction of graphite, oxide for ultracapacitors, *Carbon*, 48 (2010) 2118–2122.
59. Y.W. Zhu, M.D. Stoller, W.W. Cai, A. Velamakanni, R.D. Piner, D. Chen, R.S. Ruoff, Exfoliation of graphite oxide in propylene carbonate and thermal reduction of the resulting graphene oxide platelets, *ACS Nano*, 4 (2010) 1227–1233.
60. D.W. Wang, F. Li, Z.S. Wu, W. Ren, H.M. Cheng, Electrochemical interfacial capacitance in multilayer graphene sheets: dependence on number of stacking layers, *Electrochem. Commun.*, 11 (2009) 1729–1732.
61. C.G. Liu, Z.N. Yu, D. Neff, A. Zhamu, B.Z. Jang, Graphene-based supercapacitor with an ultrahigh energy density, *Nano Lett.*, 10 (2010) 4863–4868.
62. J.R. Miller, R.A. Outlaw, B.C. Holloway, Graphene double-layer capacitor with ac line-filtering performance, *Science*, 329 (2010) 1637–1639.
63. A.V. Murugan, T. Muraliganth, A. Manthiram, Rapid, facile microwave-solvothermal synthesis of graphene nanosheets and their polyaniline nanocomposites for energy storage, *Chem. Mater.*, 21 (2009) 5004–5006.

64. A.P. Yu, I. Roes, A. Davies, Z.W. Chen, Ultrathin, transparent, and flexible graphene films for supercapacitor applications, *Appl. Phys. Lett.*, 96 (2010) 253105.
65. P.W. Sutter, J.I. Flege, E.A. Sutter, Epitaxial graphene on ruthenium, *Nat. Mater.*, 7 (2008) 406–411.
66. S. Gilje, S. Han, S. Wang, M. Wang, R.B. Kaner, A chemical route to graphene for device applications, *Nano Lett.*, 7 (2007) 3394–3398.
67. P. Dhiman, F. Yavari, X. Mi, H. Gullapalli, Y. Shi, P.M. Ajayan, N. Koratkar, Harvesting energy from water flow over graphene, *Nano Lett.*, 11 (2011) 3123–3127.
68. A.E. Rider, S. Kumar, S.A. Furman, K. Ostrikov, Self-organised Au nanoarrays on vertical graphenes: an advanced three-dimensional sensing platform, *Chem. Commun.*, 48 (2012) 2659–2661.
69. F. Bonaccorso, Z. Sun, T. Hasan, A.C. Ferrari, Graphene photonics and optoelectronics, *Nat. Photonics*, 4 (2010) 611–622.
70. X. Wang, L.J. Zhi, K. Müllen, Transparent, conductive graphene electrodes for dye-sensitized solar cells, *Nano Lett.*, 8 (2008) 323–327.
71. Y.Y. Dou, G.R. Li, J. Song, X.P. Gao, Nickel phosphide-embedded graphene as counter electrode for dye-sensitized solar cells, *Phys. Chem. Chem. Phys.*, 14 (2012) 1339–1342.
72. A.Y. Anderson, P.R.F. Barnes, J.R. Durrant, B.C.O. Regan, Quantifying regeneration in dye-sensitized solar cells, *J. Phys. Chem. C*, 115 (2011) 2439–2447.
73. J.M. Tarascon, M. Armand, Issues and challenges facing rechargeable lithium batteries, *Nature*, 414 (2001) 359–367.
74. P. Poizot, S. Laruelle, S. Grugéon, L. Dupont, J.M. Tarascon, Nano-sized transition-metal oxides as negative-electrode materials for lithium-ion batteries, *Nature*, 407 (2000) 496–499.
75. C.M. Park, J.H. Kim, H. Kim, H.J. Sohn, Li-alloy based anode materials for Li secondary batteries, *Chem. Soc. Rev.*, 39 (2010) 3115–3141.
76. J. Cabana, L. Monconduit, D. Larcher, M.R. Palacin, Beyond intercalation-based Li-ion batteries: the state of the art and challenges of electrode materials reacting through conversion reactions, *Adv. Mater.*, 22 (2010) E170–E192.
77. L.W. Ji, Z. Lin, M. Alcoutlabi, X.W. Zhang, Recent developments in nanostructured anode materials for rechargeable lithium-ion batteries, *Energy Environ. Sci.*, 4 (2011) 2682–2699.
78. L.H. Tang, Y. Wang, Y.M. Li, H.B. Feng, J. Lu, J.H. Li, Preparation, structure, and electrochemical properties of reduced graphene sheet films, *Adv. Funct. Mater.*, 19 (2009) 2782–2789.
79. S.M. Paek, E. Yoo, I. Honma, Enhanced cyclic performance and lithium storage capacity of SnO₂/graphene nanoporous electrodes with three-dimensionally delaminated flexible structure, *Nano Lett.*, 9 (2009) 72–75.
80. K.S. Novoselov, V.I. Falko, L. Colombo, P.R. Gellert, M.G. Schwab, K. Kim, A roadmap for graphene, *Nature*, 490 (2012) 192–200.
81. S.Q. Chen, Y. Wang, Microwave-assisted synthesis of a Co₃O₄-graphene sheet-on-sheet nanocomposite as a superior anode material for Li-ion batteries, *J. Mater. Chem.*, 20 (2010) 9735–9739.

82. H. Liu, Q. Zhao, Y. Li, Y. Liu, F. Lu, J. Zhuang, S. Wang, L. Jiang, D. Zhu, D. Yu, L. Chi, Field emission properties of large-area nanowires of organic charge-transfer complexes, *J. Am. Chem. Soc.*, 127 (2005) 1120–1121.
83. H. Kim, D.H. Seo, S.W. Kim, J. Kim, K. Kang, Highly reversible Co_3O_4 /graphene hybrid anode for lithium rechargeable batteries, *Carbon*, 49 (2011) 326–332.
84. B.J. Li, H.Q. Cao, J. Shao, G.Q. Li, M.Z. Qu, G. Yin, Co_3O_4 /graphene composites as anode materials for high-performance lithium ion batteries, *Inorg. Chem.*, 50 (2011) 1628–1632.
85. J. Zhu, Y.K. Sharma, Z. Zeng, X. Zhang, M. Srinivasan, S. Mhaisalkar, H. Zhang, H.H. Hng, Q. Yan, Cobalt oxide nanowall arrays on reduced graphene oxide sheets with controlled phase, grain size, and porosity for Li-ion battery electrodes, *J. Phys. Chem. C*, 115 (2011) 8400–8406.
86. B. Wang, Y. Wang, J. Park, H. Ahn, G. Wang, In situ synthesis of Co_3O_4 /graphene nanocomposite material for lithium-ion batteries and supercapacitors with high capacity and supercapacitance, *J. Alloys Compd.*, 509 (2011) 7778–7783.
87. D.H. Wang, D.W. Choi, J. Li, Z.G. Yang, Z.M. Nie, R. Kou, D.H. Hu, C.M. Wang, L.V. Saraf, J.G. Zhang, I.A. Aksay, J. Liu, Self-assembled TiO_2 -graphene hybrid nanostructures for enhanced Li-ion insertion, *ACS Nano*, 3 (2009) 907–914.
88. D.W. Choi, D.H. Wang, V.V. Viswanathan, I.T. Bae, W. Wang, Z.M. Nie, J.G. Zhang, G.L. Graff, J. Liu, Z.G. Yang, T. Duong, Li-ion batteries from LiFePO_4 cathode and anatase/graphene composite anode for stationary energy storage, *Electrochem. Commun.*, 12 (2010) 378–381.
89. S. Ding, J.S. Chen, D. Luan, F.Y.C. Boey, S. Madhavi, X.W. Lou, Graphene-supported anatase TiO_2 nanosheets for fast lithium storage, *Chem. Commun.*, 47 (2011) 5780–5782.
90. J. Yao, X.P. Shen, B. Wang, H.K. Liu, G.X. Wang, In situ chemical synthesis of SnO_2 -graphene nanocomposite as anode materials for lithium-ion batteries, *Electrochem. Commun.*, 11 (2009) 1849–1852.
91. L.S. Zhang, L.Y. Jiang, H.J. Yan, W.D. Wang, W. Wang, W.G. Song, Y.G. Guo, L.J. Wan, Mono dispersed SnO_2 nanoparticles on both sides of single layer graphene sheets as anode materials in Li-ion batteries, *J. Mater. Chem.*, 20 (2010) 5462–5467.
92. Z.F. Du, X.M. Yin, M. Zhang, Q.Y. Hao, Y.G. Wang, T.H. Wang, In situ synthesis of SnO_2 /graphene nanocomposite and their application as anode material for lithium ion battery, *Mater. Lett.*, 64 (2010) 2076–2079.
93. H. Kim, S.W. Kim, Y.U. Park, H. Gwon, D.H. Seo, Y. Kim, K. Kang, SnO_2 /graphene composite with high lithium storage capability for lithium rechargeable batteries, *Nano Res.*, 3 (2010) 813–821.
94. Z.Y. Wang, H. Zhang, N. Li, Z.J. Shi, Z.N. Gu, G.P. Cao, Laterally confined graphene nanosheets and graphene/ SnO_2 composites as high-rate anode materials for lithium-ion batteries, *Nano Res.*, 3 (2010) 748–756.
95. M. Zhang, D. Lei, Z.F. Du, X.M. Yin, L.B. Chen, Q.H. Li, Y.G. Wang, T.H. Wang, Fast synthesis of SnO_2 /graphene composites by reducing graphene oxide with stannous ions, *J. Mater. Chem.*, 21 (2011) 1673–1676.
96. X.D. Huang, X.F. Zhou, L.A. Zhou, K. Qian, Y.H. Wang, Z.P. Liu, C.Z. Yu, A facile one-step solvothermal synthesis of SnO_2 /graphene nanocomposite and

- its application as an anode material for lithium-ion batteries, *Phys. Chem. Chem. Phys.*, 12 (2011) 278–281.
97. P. Lian, X. Zhu, S. Liang, Z. Li, W. Yang, H. Wang, High reversible capacity of SnO₂/graphene nanocomposite as an anode material for lithium-ion batteries, *Electrochim. Acta*, 56 (2011) 4532–4539.
 98. X. Wang, X. Zhou, K. Yao, J. Zhang, Z. Liu, A SnO₂/graphene composite as a high stability electrode for lithium ion batteries, *Carbon*, 49 (2011) 133–139.
 99. S. Ding, D. Luan, F.Y.C. Boey, J.S. Chen, X.W. Lou, SnO₂ nanosheets grown on graphene sheets with enhanced lithium storage properties, *Chem. Commun.*, 47 (2011) 7155–7157.
 100. X. Zhu, Y. Zhu, S. Murali, M.D. Stoller, R.S. Ruoff, Reduced graphene oxide/tin oxide composite as an enhanced anode material for lithium ion batteries prepared by homogenous coprecipitation, *J. Power Sources*, 196 (2011) 6473–6477.
 101. B. Zhao, G. Zhang, J. Song, Y. Jiang, H. Zhuang, P. Liu, T. Fang, Bivalent tin ion assisted reduction for preparing graphene/SnO₂ composite with good cyclic performance and lithium storage capacity, *Electrochim. Acta*, 56 (2011) 7340–7346.
 102. B. Zhang, Q.B. Zheng, Z.D. Huang, S.W. Oh, J.K. Kim, SnO₂–graphene–carbon nanotube mixture for anode material with improved rate capacities, *Carbon*, 49 (2011) 4524–4534.
 103. X. Zhu, Y. Zhu, S. Murali, M.D. Stoller, R.S. Ruoff, Nanostructured reduced graphene oxide/Fe₂O₃ composite as a high-performance anode material for lithium ion batteries, *ACS Nano*, 5 (2011) 3333–3338.
 104. W. Zhou, J. Zhu, C. Cheng, J. Liu, H. Yang, C. Cong, C. Guan, X. Jia, H.J. Fan, Q. Yan, C.M. Li, T. Yu, A general strategy toward graphene/metal oxide core-shell nanostructures for high-performance lithium storage, *Energy Environ. Sci.*, 4 (2011) 4954–4961.
 105. M. Zhang, D.N. Lei, X.M. Yin, L.B. Chen, Q.H. Li, Y.G. Wang, T.H. Wang, Magnetite/graphene composites: microwave irradiation synthesis and enhanced cycling and rate performances for lithium ion batteries, *J. Mater. Chem.*, 20 (2010) 5538–5543.
 106. S.K. Behera, Enhanced rate performance and cyclic stability of Fe₃O₄–graphene nanocomposites for Li ion battery anodes, *Chem. Commun.*, 47 (2011) 10371–10373.
 107. J. Su, M. Cao, L. Ren, C. Hu, Nanocomposites with improved lithium storage and magnetism properties, *J. Phys. Chem. C*, 115 (2011) 14469–14477.
 108. J. Zhou, H. Song, L. Ma, X. Chen, Magnetite/graphene nanosheet composites: interfacial interaction and its impact on the durable high-rate performance in lithium-ion batteries, *RSC Adv.*, 1 (2011) 782–791.
 109. L. Ji, Z. Tan, T.R. Kuykendall, S. Aloni, S. Xun, E. Lin, V. Battaglia, Y. Zhang, Fe₃O₄ nanoparticles integrated graphene sheets for high-performance half and full lithium-ion cells, *Phys. Chem. Chem. Phys.*, 13 (2011) 7170–7177.
 110. B. Li, H. Cao, J. Shao, M. Qu, J.H. Warner, Superparamagnetic Fe₃O₄ nanocrystals/graphene composites for energy storage devices, *J. Mater. Chem.*, 21 (2011) 5069–5075.

111. B. Li, H. Cao, J. Shao, M. Qu, Enhanced anode performances of the Fe_3O_4 -Carbon-rGO three dimensional composite in lithium ion batteries, *Chem. Commun.*, 47 (2011) 10374–10376.
112. H.L. Wang, L.F. Cui, Y.A. Yang, H.S. Casalongue, J.T. Robinson, Y.Y. Liang, Y. Cui, H.J. Dai, Mn_3O_4 -graphene hybrid as a high-capacity anode material for lithium ion batteries, *J. Am. Chem. Soc.*, 132 (2010) 13978–13980.
113. C.-T. Hsieh, C.-Y. Lin, J.-Y. Lin, High reversibility of Li intercalation and de-intercalation in MnO-attached graphene anodes for Li-ion batteries, *Electrochim. Acta*, 56 (2011) 8861–8867.
114. I.R.M. Kottegoda, N.H. Idris, L. Lu, J.-Z. Wang, H.-K. Liu, Synthesis and characterization of graphene-nickel oxide nanostructures for fast charge-discharge application, *Electrochim. Acta*, 56 (2011) 5815–5822.
115. J. Hu, A. Ramadan, F. Luo, B. Qi, X. Deng, J. Chen, One-step molybdate ion assisted electrochemical synthesis of α - MoO_3 -decorated graphene sheets and its potential applications, *J. Mater. Chem.*, 21 (2011) 15009–15014.
116. B. Wang, X.-L. Wu, C.-Y. Shu, Y.-G. Guo, C.-R. Wang, Synthesis of CuO/graphene nanocomposite as a high-performance anode material for lithium-ion batteries, *J. Mater. Chem.*, 20 (2010) 10661–10664.
117. Y.J. Mai, X.L. Wang, J.Y. Xiang, Y.Q. Qiao, D. Zhang, C.D. Gu, J.P. Tu, CuO/graphene composite as anode materials for lithium-ion batteries, *Electrochim. Acta*, 56 (2011) 2306–2311.
118. J. Zhou, L. Ma, H. Song, B. Wu, X. Chen, Durable high-rate performance of CuO hollow nanoparticles/graphene-nanosheet composite anode material for lithium-ion batteries, *Electrochem. Commun.*, 13 (2011) 1357–1360.
119. C. Xu, X. Wang, L.C. Yang, Y.P. Wu, Fabrication of a graphene-cuprous oxide composite, *J. Solid State Chem.*, 182 (2009) 2486–2490.
120. B. Li, H. Cao, G. Yin, Y. Lu, J. Yin, Cu_2O /reduced graphene oxide composite for removal of contaminants from water and supercapacitors, *J. Mater. Chem.*, 21 (2011) 10645–10648.
121. Y. Ding, Y. Jiang, F. Xu, J. Yin, H. Ren, Q. Zhuo, Z. Long, P. Zhang, Preparation of nano-structured LiFePO_4 /graphene composites by co-precipitation method, *Electrochem. Commun.*, 12 (2010) 10–13.
122. G. Wang, J. Bai, Y. Wang, Z. Ren, J. Bai, Preparation and electrochemical performance of a cerium oxide-graphene nanocomposite as the anode material of a lithium ion battery, *Scr. Mater.*, 65 (2011) 339–342.
123. W. Zhou, J. Liu, T. Chen, K.S. Tan, X. Jia, Z. Luo, C. Cong, H. Yang, C.M. Li, T. Yu, Fabrication of Co_3O_4 -reduced graphene oxide scrolls for high-performance supercapacitor electrodes, *Phys. Chem. Chem. Phys.*, 13 (2011) 14462–14465.
124. J. Yan, T. Wei, W.M. Qiao, B. Shao, Q.K. Zhao, L.J. Zhang, Z.J. Fan, Rapid microwave-assisted synthesis of graphene nanosheet/ Co_3O_4 composite for supercapacitors, *Electrochim. Acta*, 55 (2010) 6973–6978.
125. Z.S. Wu, D.W. Wang, W. Ren, J. Zhao, G. Zhou, F. Li, H.M. Cheng, Anchoring hydrous RuO_2 on graphene sheets for high-performance electrochemical capacitors, *Adv. Funct. Mater.*, 20 (2010) 3595–3602.
126. A.K. Mishra, S. Ramaprabhu, Functionalized graphene based nanocomposites for supercapacitor application, *J. Phys. Chem. C*, 115 (2011) 14006–14013.

127. S. Chen, J.W. Zhu, X.D. Wu, Q.F. Han, X. Wang, Graphene oxide–MnO₂ nanocomposites for supercapacitors, *ACS Nano*, 4 (2010) 2822–2830.
128. Z.S. Wu, W.C. Ren, D.W. Wang, F. Li, B.L. Liu, H.M. Cheng, High-energy MnO₂ nanowire/graphene and graphene asymmetric electrochemical capacitors, *ACS Nano*, 4 (2010) 5835–5842.
129. J. Zhang, J. Jiang, X.S. Zhao, Synthesis and capacitive properties of manganese oxide nanosheets dispersed on functionalized graphene sheets, *J. Phys. Chem. C*, 115 (2011) 6448–6454.
130. Y. Qian, S. Lu, F. Gao, Preparation of MnO₂/graphene composite as electrode material for supercapacitors, *J. Mater. Sci.*, 46 (2011) 3517–3522.
131. Q. Cheng, J. Tang, J. Ma, H. Zhang, N. Shinya, L.C. Qin, Graphene and nanostructured MnO₂ composite electrodes for supercapacitors, *Carbon*, 49 (2011) 2917–2925.
132. J. Yan, Z. Fan, T. Wei, W. Qian, M. Zhang, F. Wei, Fast and reversible surface redox reaction of graphene–MnO₂ composites as supercapacitor electrodes, *Carbon*, 48 (2010) 3825–3833.
133. H. Huang, X. Wang, Graphene nanoplate–MnO₂ composites for supercapacitors: a controllable oxidation approach, *Nanoscale*, 3 (2011) 3185–3191.
134. G. Yu, L. Hu, M. Vosgueritchian, H. Wang, X. Xie, J.R. McDonough, X. Cui, Y. Cui, Z. Bao, Solution-processed graphene/MnO₂ nanostructured textiles for high-performance electrochemical capacitors, *Nano Lett.*, 11 (2011) 2905–2911.
135. Z. Fan, J. Yan, T. Wei, L. Zhi, G. Ning, T. Li, F. Wei, Asymmetric supercapacitors based on graphene/MnO₂ and activated carbon nanofiber electrodes with high power and energy density, *Adv. Funct. Mater.*, 21 (2011) 2366–2375.
136. B. Wang, J. Park, C.Y. Wang, H. Ahn, G.X. Wang, Mn₃O₄ nanoparticles embedded into graphene nanosheets: Preparation, characterization, and electrochemical properties for supercapacitors, *Electrochim. Acta*, 55 (2010) 6812–6817.
137. Y.P. Zhang, H.B. Li, L.K. Pan, T. Lu, Z. Sun, Capacitive behavior of graphene–ZnO composite film for supercapacitors, *J. Electroanal. Chem.*, 634 (2009) 68–71.
138. J. Wang, Z. Gao, Z. Li, B. Wang, Y. Yan, Q. Liu, T. Mann, M. Zhang, Z. Jiang, Green synthesis of graphene nanosheets/ZnO composites and electrochemical properties, *J. Solid State Chem.*, 184 (2011) 1421–1427.
139. G.M. Zhou, D.W. Wang, F. Li, L.L. Zhang, N. Li, Z.S. Wu, L. Wen, G.Q. Lu, H.M. Cheng, Graphene-wrapped Fe₃O₄ anode material with improved reversible capacity and cyclic stability for lithium ion batteries, *Chem. Mater.*, 22 (2010) 5306–5313.
140. J.S. Chen, Z. Wang, X.C. Dong, P. Chen, X.W. Lou, Graphene-wrapped TiO₂ hollow structures with enhanced lithium storage capabilities, *Nanoscale*, 3 (2011) 2158–2161.
141. W. Lv, F. Sun, D.-M. Tang, H.-T. Fang, C. Liu, Q.-H. Yang, H.-M. Cheng, A sandwich structure of graphene and nickel oxide with excellent supercapacitive performance, *J. Mater. Chem.*, 21 (2011) 9014–9019.
142. Y. Sun, X. Hu, W. Luo, Y. Huang, Self-assembled hierarchical MoO₃/graphene nanoarchitectures and their application as a high-performance anode material for lithium-ion batteries, *ACS Nano*, 5 (2011) 7100–7107.

143. H. Liu, W. Yang, Ultralong single crystalline V_2O_5 nanowire/graphene composite fabricated by a facile green approach and its lithium storage behavior, *Energy Environ. Sci.*, 4 (2011) 4000–4008.
144. S.B. Yang, X.L. Feng, S. Ivanovici, K. Müllen, Fabrication of graphene-encapsulated oxide nanoparticles: towards high-performance anode materials for lithium storage, *Angew. Chemie Int. Ed.*, 49 (2010) 8408–8411.
145. J.Z. Wang, C. Zhong, D. Wexler, N.H. Idris, Z.X. Wang, L.Q. Chen, H.K. Liu, Graphene-encapsulated Fe_3O_4 nanoparticles with 3D laminated structure as superior anode in lithium ion batteries, *Chem. Eur. J.*, 17 (2011) 661–667.
146. D. Chen, G. Ji, Y. Ma, J.Y. Lee, J. Lu, Graphene-encapsulated hollow Fe_3O_4 nanoparticle aggregates as a high-performance anode material for lithium ion batteries, *ACS Appl. Mater. Interfaces*, 3 (2011) 3078–3083.
147. S.B. Yang, X.L. Feng, L. Wang, K. Tang, J. Maier, K. Müllen, Graphene-based nanosheets with a sandwich structure, *Angew. Chemie Int. Ed.*, 49 (2010) 4795–4799.
148. S.B. Yang, X.L. Feng, X.C. Wang, K. Müllen, Graphene-based carbon nitride nanosheets as efficient metal-free electrocatalysts for oxygen reduction reactions, *Angew. Chemie Int. Ed.*, 50 (2011) 5339–5343.
149. S.B. Yang, X.L. Feng, K. Müllen, Sandwich-like, graphene-based titania nanosheets with high surface area for fast lithium storage, *Adv. Mater.*, 23 (2011) 3575–3579.
150. D.H. Wang, R. Kou, D. Choi, Z.G. Yang, Z.M. Nie, J. Li, L.V. Saraf, D.H. Hu, J.G. Zhang, G.L. Graff, J. Liu, M.A. Pope, I.A. Aksay, Ternary self-assembly of ordered metal oxide–graphene nanocomposites for electrochemical energy storage, *ACS Nano*, 4 (2010) 1587–1595.
151. Y. Qiu, K. Yan, S. Yang, L. Jin, H. Deng, W. Li, Synthesis of size-tunable anatase TiO_2 nanospindles and their assembly into anatase/titanium oxynitride/titanium nitride/graphene nanocomposites for rechargeable lithium ion batteries with high cycling performance, *ACS Nano*, 4 (2010) 6515–6526.
152. Y. Zou, Y. Wang, NiO nanosheets grown on graphene nanosheets as superior anode materials for Li-ion batteries, *Nanoscale*, 3 (2011) 2615–2620.
153. A. Yu, H.W. Park, A. Davies, D.C. Higgins, Z. Chen, X. Xiao, Free-standing layer-by-layer hybrid thin film of graphene- MnO_2 nanotube as anode for lithium ion batteries, *J. Phys. Chem. Lett.*, 2 (2011) 1855–1860.
154. C.X. Guo, M. Wang, T. Chen, X.W. Lou, C.M. Li, A hierarchically nanostructured composite of MnO_2 /conjugated polymer/graphene for high-performance lithium ion batteries, *Adv. Energy Mater.*, 1 (2011) 736–741.
155. N. Zhu, W. Liu, M.Q. Xue, Z.A. Xie, D. Zhao, M.N. Zhang, J.T. Chen, T.B. Cao, Graphene as a conductive additive to enhance the high-rate capabilities of electrospun $Li_4Ti_5O_{12}$ for lithium-ion batteries, *Electrochim. Acta*, 55 (2010) 5813–5818.
156. Y. Shi, L. Wen, F. Li, H.M. Cheng, Nanosized $Li_4Ti_5O_{12}$ /graphene hybrid materials with low polarization for high rate lithium ion batteries, *J. Power Sources*, 196 (2011) 8610–8617.
157. N. Li, G. Liu, C. Zhen, F. Li, L.L. Zhang, H.M. Cheng, Battery performance and photocatalytic activity of mesoporous anatase TiO_2 nanospheres/graphene composites by template-free self-assembly, *Adv. Funct. Mater.*, 21 (2011) 1717–1722.

158. H. Liu, P. Gao, J. Fang, G. Yang, $\text{Li}_3\text{V}_2(\text{PO}_4)_3$ /graphene nanocomposites as cathode material for lithium ion batteries, *Chem. Commun.*, 47 (2011) 9110–9112.
159. G. Wang, T. Liu, Y. Luo, Y. Zhao, Z. Ren, J. Bai, H. Wang, Preparation of Fe_2O_3 /graphene composite and its electrochemical performance as an anode material for lithium ion batteries, *J. Alloys Compd.*, 509 (2011) L216–L220.
160. J. Yan, Z.J. Fan, T. Wei, W.Z. Qian, M.L. Zhang, F. Wei, Fast and reversible surface redox reaction of graphene– MnO_2 composites as supercapacitor electrodes, *Carbon*, 48 (2010) 3825–3833.
161. P.V. Kamat, Graphene-based nanoarchitectures. Anchoring semiconductor and metal nanoparticles on a two-dimensional carbon support, *J. Phys. Chem. Lett.*, 1 (2010) 520–527.
162. Y.J. Min, M. Akbulut, K. Kristiansen, Y. Golan, J. Israelachvili, The role of interparticle and external forces in nanoparticle assembly, *Nat. Mater.*, 7 (2008) 527–538.
163. Y.Y. Liang, H.L. Wang, H.S. Casalongue, Z. Chen, H.J. Dai, TiO_2 nanocrystals grown on graphene as advanced photocatalytic hybrid materials, *Nano Res.*, 3 (2010) 701–705.
164. X. Wang, X. Li, L. Zhang, Y. Toon, P.K. Weber, H. Wang, J. Guo, H. Dai, N-doping of graphene through electrothermal reactions with ammonia, *Science*, 324 (2009) 768–771.
165. H.L. Wang, J.T. Robinson, G. Diankov, H.J. Dai, $\text{Ni}(\text{OH})_2$ nanoplates grown on graphene as advanced electrochemical pseudocapacitor materials, *J. Am. Chem. Soc.*, 132 (2010) 3270–3271.
166. S. Chen, J.W. Zhu, X. Wang, One-step synthesis of graphene-cobalt hydroxide nanocomposites and their electrochemical properties, *J. Phys. Chem. C*, 114 (2010) 11829–11834.
167. S. Sopic, M.K. Rokovic, Z. Mandic, Preparation and characterisation of RuO_2 /polyaniline/polymer binder composite electrodes for supercapacitor applications, *J. Electrochem. Sci. Eng.*, 2 (2012) 41–52.
168. L. Ji, H. Zheng, A. Ismach, Z. Tan, S. Xun, E. Lin, V. Battaglia, V. Srivasan, Graphene/Si multilayer structure anodes for advanced half and full lithium-ion cells, *Nano Energy*, 1 (2012) 164–171.
169. S. Balendhran, J.Z. Ou, M. Bhaskaran, S. Sriram, S. Ippolito, Z. Vasic, E. Kats, S. Bhargava, S. Zhuiykov, K. Kalantar-zadeh, Atomically thin layers of MoS_2 via a two step thermal evaporation – exfoliation method, *Nanoscale*, 4 (2012) 461–466.
170. F. Fabregat-Santiago, G. Garcia-Belmonte, I. Mora-Sero, J. Bisquert, Characterisation of nanostructured hybrid and organic solar cells in impedance spectroscopy, *Phys. Chem. Chem. Phys.*, 13 (2011) 9083–9118.
171. M.S. Wittingham, Lithium batteries and cathode materials, *Chem. Rev.*, 104 (2004) 4271–4301.
172. B. Kang, G. Ceder, Battery materials for ultrafast charging and discharging, *Nature*, 458 (2009) 190–193.
173. A.W.C. Van der Berg, C.O. Arean, Materials for hydrogen storage: current research trends and perspectives, *Chem. Commun.*, 6 (2008) 668–681.
174. J.H. Song, J. Zhou, Z.L. Wang, Piezoelectric and semiconducting coupled power generating process of a single ZnO belt/wire: A technology for harvesting electricity from the environment, *Nano Lett.*, 6 (2006) 1656–1662.

175. Y. Qin, X.D. Wang, Z.L. Wang, Microfibre–nanowire hybrid structure for energy scavenging, *Nature*, 451 (2008) 809–813.
176. Z.P. Shao, S.M. Haile, J. Ahn, P.D. Ronney, Z.L. Zhan, S.A. Barnett, A thermally self-sustained micro solid-oxide fuel-cell stack with high power density, *Nature*, 435 (2005) 795–798.
177. M. Strasser, R. Aigner, C. Lauterbach, T.F. Sturm, M. Franosch, G. Wachutka, Micromachined CMOS thermoelectric generators as on-chip power supply, *Sens. Actuators A: Phys.*, 114 (2004) 362–370.
178. P.D. Mitcheson, E.M. Yeatman, G.K. Rao, A.S. Holmes, T.C. Green, Energy harvesting from human and machine motion for wireless electronic devices, *Proc. IEEE*, 96 (2008) 1457–1486.
179. D.P. Arnold, Review of microscale magnetic power generation, *IEEE Trans. Magn.*, 43 (2007) 3940–3951.
180. G.K. Mor, O.K. Varghese, M. Paulose, K. Shankar, C.A. Grimes, A review on highly ordered, vertically oriented TiO₂ nanotube arrays: fabrication, material properties and solar energy applications, *Sol. Energy Mater. Sol. Cells*, 90 (2006) 2011–2075.
181. K.A. Cook-Chennault, N. Thambi, A.M. Sastry, Powering MEMS portable devices – A review of non-regenerative and regenerative power supply systems with special emphasis on piezoelectric energy harvesting systems, *Smart Mater. Struct.*, 17 (2008) 043001.
182. S. Kerzenmacher, J. Ducree, R. Zengerle, F. von Stetten, Energy harvesting by implantable abiotically catalyzed glucose fuel cells, *J. Power Sources*, 182 (2008) 1–17.
183. P. Yager, T. Edwards, E. Fu, K. Helton, K. Nelson, M.R. Tam, B.H. Weigl, Microfluidic diagnostic technologies for global public health, *Nature*, 442 (2006) 412–418.
184. H. Klauk, U. Zschieschang, J. Pflaum, M. Halik, Ultralow-power organic complementary circuits, *Nature*, 445 (2007) 745–748.
185. W. Choi, S. Hong, J.T. Abrahamson, J.H. Han, C. Song, N. Nair, S. Baik, M.S. Strano, Chemically driven carbon-nanotube-guided thermopower waves, *Nat. Mater.*, 9 (2010) 423–429.
186. S. Walia, R. Weber, K. Latham, P. Petersen, J.T. Abrahamson, M.S. Strano, K. Kalantar-zadeh, Oscillatory thermopower waves based on Bi₂Te₃ films, *Adv. Funct. Mater.*, 21 (2011) 2072–2079.
187. J.T. Abrahamson, W. Choi, N.S. Schinenbach, J. Park, J.H. Han, M.P. Walsh, K. Kalantar-zadeh, M.S. Strano, Wavefront velocity oscillations of carbon-nanotube-guided thermopower waves: nanoscale alternative current sources, *ACS Nano*, 5 (2011) 367–375.
188. H.J. Goldsmid, in D.M. Rowe (ed.), *CRC Handbook of Thermoelectricity*, 1995, CRC Press, Boca Raton, New York, 19–25.
189. R.R. Heikes, R.W. Ure Jr, in: R.R. Heikes, R.W. Ure Jr (Eds), *Thermoelectricity: science and engineering*, 1961, Interscience Publishers, New York, 1–6.
190. E. Müller, Č. Drašar, J. Schilz, W.A. Kaysser, Functionally graded materials for sensor and energy applications, *Mater. Sci. Eng. A*, 362 (2003) 17–39.
191. Y.B. Zeldovich, D.A. Frank-Kamenskii, The theory of thermal flame propagation, *Zh. Fiz. Khim.*, 12 (1938) 100–105.
192. P. Kim, L. Shi, A. Majumdar, P.L. McEuen, Thermal transport measurements of individual multiwalled nanotubes, *Phys. Rev. Lett.*, 87 (2001) 215502.

193. C.H. Yu, L. Shi, Z. Yao, D.Y. Li, A. Majumdar, Thermal conductance and thermopower of an individual single-wall carbon nanotube, *Nano Lett.*, 5 (2005) 1842–1846.
194. J.T. Abrahamson, N. Nair, M.S. Strano, Modelling the increase in anisotropic reaction rates in metal nanoparticle oxidation using carbon nanotubes as thermal conduits, *Nanotechnology*, 19 (2008) 195701–195708.
195. S. Walia, R. Weber, S. Sriram, M. Bhaskaran, K. Latham, S. Zhuiykov, K. Kalantar-zadeh, Sb₂Te₃ and Bi₂Te₃ based thermopower wave sources, *Energy Environ. Sci.*, 4 (2011) 3558–3564.
196. B. Lv, S.B. Hu, W. Li, X. Di, L.H. Feng, J.Q. Zhang, L.L. Wu, Y.P. Cai, B. Li, Z. Lei, Preparation and characterization of Sb₂Te₃ thin films by co-evaporation, *Int. J. Photoenergy*, vol. 2010, 476589.
197. W. Wang, X. Yan, B. Poudel, Y. Ma, Q. Hao, J. Yang, G. Chen and Z. Ren, Chemical synthesis of anisotropic nanocrystalline Sb₂Te₃ and low thermal conductivity of the compacted dense bulk, *J. Nanosci. Nanotechnol.*, 8 (2008) 452–456.
198. S. Walia, R. Weber, S. Balendhran, D. Yao, J.T. Abrahamson, S. Zhuiykov, M. Bhaskaran, S. Sriram, M.S. Strano, K. Kalantar-zadeh, ZnO based thermopower wave sources, *Chem. Commun.*, 48 (2012) 7462–7464.
199. Q.H. Wang *et al.*, Understanding and controlling the substrate effect on graphene electron-transfer chemistry via reactivity imprint lithography, *Nat. Chem.*, 4 (2012) 724–732.
200. S. Walia, S. Balendhran, P. Yi, D. Gao, S. Zhuiykov, M. Pannirselvam, R. Weber, M.S. Strano, M. Bhaskaran, S. Sriram, K. Kalantar-zadeh, MnO₂-based thermopower wave sources with exceptionally large output voltages, *J. Phys. Chem. C*, 117 (2013) 9137–9142.

DOI: 10.1533/9781782422242.267

Abstract: The chapter reviews recent developments in nanostructured semiconductor composites for solar cells. It begins by describing the operating principle of the photovoltaic cell and the strategic potential of nanostructured semiconductors in photovoltaics. The chapter then discusses structured transparent electron conductors, semiconductor quantum dot absorbers and dye-sensitized solar cells.

Key words: photovoltaics, structured transparent electron conductors, semiconductor quantum dot absorbers, solar cells, dye-sensitized solar cells.

6.1 Operating principle of a liquid-junction photovoltaic cell

The field of photovoltaics has made steady theoretical and technological progress since the discovery of photo-induced current by French physicist Alexandre Becquerel in 1839. Global warming and the impending exhaustion of fossil fuels are placing increased demands on sustainable energy, in particular energy harvested from sunlight.

Given that the world's requirement for energy is predicted to reach ~28 Terawatt (TW) by 2050,¹ in order to meet such high usage, alternative energy sources, for example solar energy conversion and others, will have to reach the TW scale. Greenhouse gas emissions, increasing production costs of non-renewable fossil fuels and unreliable geopolitical constraints have also underscored the increasing need to develop alternative efficient energy sources. One area that continues to attract a lot of interest is the advancement of solar cells. The focus of solar energy utilization has predominantly been on electricity (photovoltaics²) and hydrogen generation (water splitting³⁻⁵). Most photovoltaic systems absorb energy from the sun to convert it into an electrical signal.⁶ In the years since 2000, significant progress in the enhancing of the performance of such systems has been made⁷ and today they are one of the most promising alternative sources of energy.⁸

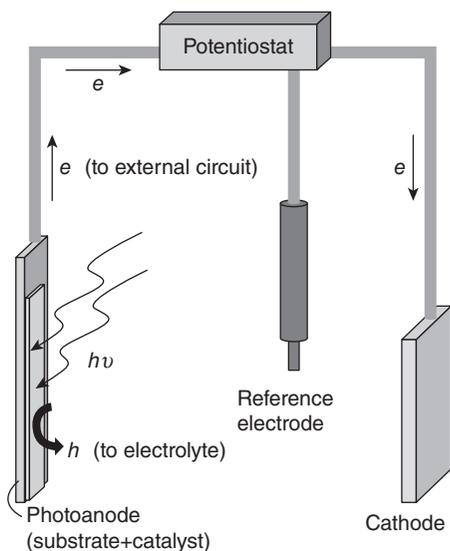
This is particularly important for Australia as the country is blessed with high sunlight activity all year around in many areas. Photovoltaic systems produce electricity directly from sunlight in one step, avoiding the problems

of other alternative energy sources, and have already proven to be reliable power suppliers for various satellite systems, hot-water appliances and portable devices.⁹ Due to the maturity of the silicon industry, approximately 80 % of the solar market is dominated by technology based on Si, which is an indirect gap semiconductor and requires Si wafers thicker than 200 μm to function well as a solar cell.¹⁰ On the other hand, thin-film technologies such as CdTe and CuInGaSe₂ use direct bandgap compound semiconductors.^{11,12} Although substantial progress has been achieved in the development of thin films based on these materials with thickness in the range 1–3 μm , there are potential limitations in materials availability and higher cost at the TW scale.¹⁰

To put things in perspective with regard to the status and potential benefits of each type of modern technology for solar cell fabrication, Plate XIX (see colour section between pages 232 and 233) summarizes the best obtained laboratory cell efficiencies for the different available technologies at the end of 2010.¹⁰ This chart clearly shows that the best Si-based solar cells boast 27 % efficiency while the most proficient thin-film solar cells are in the 20 % range. Triple junction solar cells have reached up to 41 % efficiency, and the most superior organic and emerging inorganic solar cells reach between 8 and 11 %.¹³ It is therefore evident that further progress in reaching the set TW target is inseparably connected with the development of ‘smart’ nanostructured materials with improved solar energy conversion. This can be achieved not only by selecting an acceptable compromise between the efficiencies of the newly-developed materials and their manufacturing costs, but also by careful selection of appropriate technologies for improved solar cells.

To understand where the improvements can be made, let’s consider a process of solar energy conversion in detail. A schematic illustration of the mechanism of solar-to-electric signal conversion is presented in Fig. 6.1. Generally speaking, the liquid-junction photovoltaic cell consists of a photo-anode, a counter electrode cathode and a reference electrode. As clearly shown in Fig. 6.1, upon the exposure of the photovoltaic cell to the sun, the photo-anode adsorbs energy ($h\nu$) from the solar radiation to create electrons (e^-) and holes (h^+). The photo-generated electrons are driven naturally or by the application of an external bias voltage to an underlying conducting substrate to generate a *photo-current*. At the same instant, photo-generated holes are scavenged by the surrounding electrolyte and carried to the cathode where they recombine with the electrons and complete the circuit. Voltage and the current flow are typically expressed with respect to a reference electrode.

The effectiveness of solar cells is in converting solar energy to electricity. This depends on the efficiency of the cell. Consequently, a vast majority of research effort has been focused on the development of novel materials for photo-anodes.



6.1 Schematic interpretation of a liquid-junction-based photovoltaic cell. (Reprinted from Ref. 93 with permission of the Electrochemical Society)

The ideal materials of a photo-anode should:

- absorb light from a substantial part of the solar spectrum efficiently;
- provide high surface-to-volume area for maximum light absorption;
- effectively utilize the absorbed energy to produce maximum electron-hole pairs;
- facilitate rapid transport of the charges;
- preferably be inexpensive and easily available;
- be non-corrosive and non-toxic;
- be stable in the electrolyte for a long period of time.

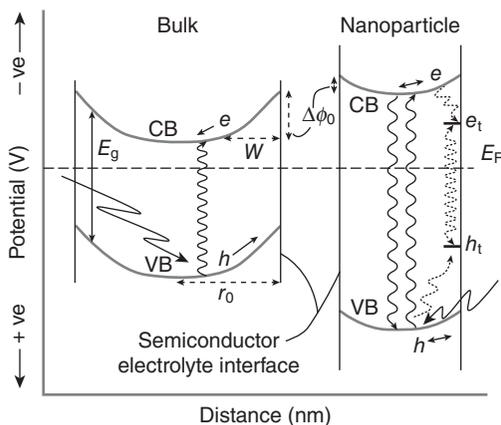
There are many materials which have been utilized as possible candidates for photo-anodes. These include organic,¹⁴ semiconductor oxides^{6,15} and polymer-based composites.^{14,16} Among them, nanostructured semiconductor oxides have attracted considerable interest as they can satisfy most of the above-mentioned requirements for photo-anodes.

In an ideal defect-free semiconductor, the electrons would be distributed in such a way that they occupy energy levels in a completely filled band (valence band), which is separated from a higher-positioned conduction band. The gap between these two bands is called bandgap (E_g).¹⁷ An ideal semiconductor can absorb light from any portion of the solar spectrum depending upon the size of the gap. One possible way to manipulate the bandgap is simply to change the particle size of the semiconductor.^{11,18} This

process is called the size quantization effect and is schematically presented in Fig. 6.2.¹⁰ The effects of quantization were monitored using photo-electrochemical techniques and were observed in several semiconductor oxides.¹⁹

Atomic vacancies can create irregularities (defects) in the semiconductor lattice structure. The defects are represented as energy states (referred to as trap sites) within the bandgap and also alter the electronic properties of the semiconductor to make it an *n*-type or *p*-type semiconductor. These traps will delay or prevent the electrons from moving to the external circuit. The e^-h^+ pair can also undergo recombination resulting in a decrease in photocurrent generation (the dotted lines in the nanoparticle shown in Fig. 6.3 represent possible routes for e^-h^+ recombination). Thus, defects play a vital role in controlling the photo-electrochemical activity of a semiconductor.^{20,21}

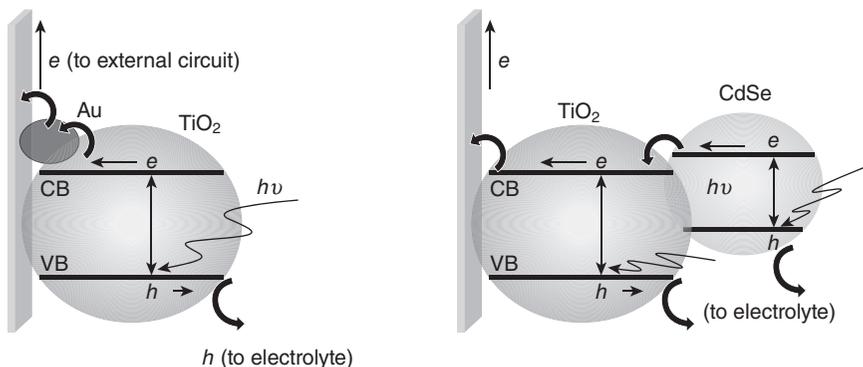
When the semiconductor makes contact with an electrolyte, usually an electrical double layer is formed as a result of this contact. This electrical double layer causes deformation of the bandgap at the semiconductor surfaces. The direction of this deformation depends upon the nature of the defects (*n*- or *p*-type). This process is called band bending, and it is graphically represented in Fig. 6.2 for an *n*-type semiconductor. On the other hand,



$$\Delta\phi = \left(\frac{\kappa T}{6e}\right) \left(\frac{r - (r_0 - W)}{L_D}\right) \left(1 + \frac{2(r_0 - W)}{r}\right)$$

$\Delta\phi$ = potential difference
 κ = Boltzmann constant
 r_0 = radius of the particle
 W = width of the depletion layer
 L_D = Debye length

6.2 Energy diagram of a semiconductor bulk and nanoparticle showing physical charges (quantization effect) and details of various electron processes that occur under illumination. (Reprinted from Ref. 10 with permission of the Electrochemical Society)



TiO₂-Au composite
 • Reduces charge recombination

(a)

TiO₂-CdSe composite
 • Reduces charge recombination
 • Improves light harvesting

(b)

6.3 The steps involved in the transport of photo-generated electrons from the semiconductor to the substrate via Au nanoparticles. Favourable energies are essential for charge transport (a). The scheme to improve the solar to electric conversion using CdS deposited on TiO₂ (b). (Reprinted from Ref. 93 with permission of the Electrochemical Society)

the extent of band bending depends on numerous factors (applied potential, doping level of semiconductor, etc.) and influences e⁻-h⁺ pair separation. The external voltage can change the extent of band bending.²² Control of charge flow in the case of nanoparticulate films is also achieved by the application of a suitable bias voltage.¹⁷

6.2 Nanostructured semiconductors as solar harvesting materials: strategic potential of inorganic semiconductors in photovoltaics

The recent thrust in designing semiconductor nanostructured assemblies for solar cell applications has increased interest in understanding the dynamics and kinetic details of interfacial electron and hole transfer.²³⁻²⁷ Simultaneously, most of the photovoltaic research efforts have been focused on net photo-conversion efficiency, whereas understanding of various electron-transfer steps at the fundamental level is still lacking. Early studies have shown that photogenerated electrons and holes in a semiconductor nanoparticle can be transferred across the interface in picoseconds.²⁸⁻³⁷

One possible way to boost the efficiency of the photocatalytic reaction is to couple semiconductor nanoparticles to noble-metal co-catalysts.³⁸⁻⁴⁸

Specifically, noble-metal co-catalysts enhance the quantum yield of the photo-induced electron-transfer process as follows:

- improving charge separation within the semiconductor particle;
- discharging photo-generated electrons across the interface;
- providing a redox pathway with low over-potential.

Utilization of nanostructured semiconductors and inorganic nanoparticles in photovoltaics has the following three aims:⁴⁹

1. Exploitation of semiconductors with high strategic potential, which have large absorption coefficients but relatively low diffusion length (L_{diff}) of photo-generated charge carriers. For this purpose, very low local absorber layer thicknesses (d_{local}) have to be employed and/or new concepts of defect passivation have to be implemented. The challenge is to determine the appropriate preparation techniques for absorbers with high strategic potential, materials combinations suitable for charge-selective contacts, and morphologies for photon management offer the potential to minimize recombination losses, resistive losses and optical losses in solar cells.⁵⁰
2. Extension of the strategic potential of semiconductors by implementing strategies of efficient light trapping with nanostructures which reduce the amount of absorber material required. For example, pillars with length of the order of μm and average diameters and distances of several 100 nm can lead to quite efficient light trapping. An increase in the path length of incident solar radiation by up to a factor of 73 was measured recently in Si nanowire solar cells,⁵¹ which is above even the randomized scattering limit.⁵² Another example is CdSe nanopillars.⁵³ These have been embedded in an ordered matrix of porous alumina and contacted with a CdTe layer embedding the CdSe nanopillars in the top region of the solar cell.
3. Reduction of processing costs and energy pay-back time of solar cells by reducing processing temperatures and/or by applying printable absorbers from suspensions of absorber nanoparticles.⁵⁴ For instance, metal nanoparticles can be printed on substrates and transformed into absorbing semiconductor layers by oxidation, selenization or sulphurization. This has been demonstrated for metal nanoparticles of Cu and In, which were printed and subsequently selenized into a CuInSe₂ absorber.⁵⁵ Another example is the printing of semiconductor nanoparticles and their sintering onto layers and crystallites. Nanoparticle layers of CdTe and CdSe have been deposited by spin-casting, resulting in solar cells with an energy conversion efficiency (η) \approx 3% after annealing in air.⁵⁶ Nanocrystal and nanoring inks of CuInSe₂ have been proposed recently for the development of low-cost solar cells.⁵⁷

A very promising route is the use of specific properties of semiconductor particles with quantum confinement which can be realized by solution-casting of colloidal quantum dots (QDs).⁵⁸

Semiconductor QDs have been successfully employed in the operation of solar cells. Moreover, they provide the advantage of slowing the relaxation time of hot charge carriers.^{54,59} This is because in QDs the quasi-continuous conduction and valence energy bands of a bulk semiconductor are replaced by a discrete electronic structure. The spacing between these discrete energy levels is such that the possible relaxation processes that can occur are limited – creating what is known as a phonon bottleneck and allowing only slower multi-phonon emission. Specifically, choosing PbSe QDs offers certain advantages over other materials. For example, the large Bohr radius (46 nm) of PbSe allows the synthesis of a wide array of PbSe particles in the quantum size regime. Furthermore, using PbSe QDs not only allows them to achieve strong quantum confinement but also helps electronic coupling to nearby electron-accepting materials because their electronic wave function extends in space beyond the QD particle.

6.3 Principles of inorganic solid-state nanostructured solar cells

The maximum theoretical power-conversion efficiency of a single-junction solar cell device is approximately ~32%.⁶⁰ The main deviation from this ideal limit occurs through the loss-in-potential, which can be closely defined for the highly efficient solar cells as the difference between the optical bandgap of the photoactive semiconductor divided by the charge of an electron, and the open-circuit voltage (V_{OC}). Most semiconductors of the highest strategic potential produced at relatively low temperatures possess very low values of L_{diff} . In order to minimize recombination losses in the solar cell absorber, the local absorber layer thickness has to be minimized to $d_{local} < L_{diff}$. However, it is often the case that only a small fraction of the sunlight can be absorbed at very low values of d_{local} considering that the optical absorption length (α^{-1}) can be much larger than d_{local} at a given wavelength (λ). It is therefore evident that to increase the efficiency of the solar cells, the absorber layer thickness has to be increased to an effective absorber layer thickness (d_{eff}) by folding the surface on which the absorber layer is deposited.⁶¹ The ratio between the extended internal surface area and the external surface area is the so-called roughness factor (F_R). In this regard, dye-sensitized solar cells (DSSCs)^{62–70} represent an extreme example since d_{local} corresponds to the thickness of only one layer of dye molecules and F_R should be of the order of 1000. One recent breakthrough in the development of nanoporous semiconductors for DSSCs was reported in

1991, where the nanoporous TiO_2 film with very high surface area, utilized in DSSCs, exhibited $\sim 9\%$ efficiency.⁷¹

Because high densities of electronic defect states are available for both excess electrons and excess holes in nanoporous semiconductors, the development of charge-selective contacts and suppression of recombination are critical in inorganic nanostructured solar cells. For instance, it has been proposed to sandwich an ultrathin (10–20 nm) pyrite layer between large-gap electron and hole conductors as in a p–i–n structure for pyrite-based solar cells.⁷² In the p–i–n concept, a relatively thick undoped absorber layer is contacted by very thin highly doped *p*-type and *n*-type nanostructured semiconductor layers. This concept has been further developed for a-Si:H solar cells to minimize the recombination losses and improve the collection efficiency of photo-generated charge carriers which is strongly enhanced by drift in the electrical field of a p–i–n structure (drift length $L_{\text{drift}} \gg L_{\text{diff}}$).⁷³ Recent publications confirmed that this consideration has successfully played a dominating role in the use of Schottky barriers in QD solar cells.⁷⁴

Plate XXa (see colour section between pages 232 and 233) schematically represents an inorganic solid-state solar cell with *ultrathin nanocomposite absorber*.⁴⁹ This principle aims to increase L_{diff} of the bare absorber material to an effective diffusion length L_{eff} , being a characteristic of the nanocomposite which was recently confirmed by nanocomposite absorber based on TiO_2 and In_2O_3 .⁷⁵ The main idea in this approach is to divide photo-generated electrons and holes locally to distances larger than the overlap of their wave functions and to decrease by this means their recombination probability. The influence of the limiting charge-selective contact is minimized by forming it at an external interface of the nanocomposite absorber.⁷⁵

Another concept for nanostructured inorganic solar cells, often called *extremely thin absorber solar cell*, utilizes the need for an extremely thin absorber being contacted between transparent electron and hole conductors and being folded within a transparent matrix.⁴⁹ This method is graphically presented in Plate XXb. Based on such an approach, d_{local} should be significantly larger than the tunnelling length (d_{tunnel}) in order to avoid shunts between the transparent electron and hole conductors.

The last concept, graphically presented in Plate XXc, is called *depleted-hetero-junction colloidal QD solar cells*.⁷⁶ The efficiency in such solar cells can be enhanced by high exciton diffusion lengths, which can be reached by the surface passivation of QDs with adequate surfactants. Moreover, the average distance between QDs should be low enough for sufficient transport of separated charge, but at the same time large enough to preserve specific electronic states of QDs.

Requirements for achieving high photo-currents in inorganic nanostructured solar cells are: the right combinations of different length scales (reflected by d_{tunnel} , L_{diff} , L_{drift} , d_{local} , d_{eff} , L_{eff} , α^{-1} and λ) as well as

appropriate combinations of nanomaterials in charge-selective heterojunctions. These ensure the minimization of losses in the photo-voltage due to potential drops and recombination at interfaces.⁷⁷

6.4 Structured transparent electron conductors

6.4.1 Nanostructures based on TiO₂

The first and the second generations of solar cells were predominantly based on solid-state junction devices, for which Si was the most common material and the most abundantly used commercially. In these solar cells, the processes of light absorption, charge generation, separation and transport were utilized by the same material. However, a new emerging class of solar cells represents new concepts for light harvesting and charge collection as briefly described in the previous section. These new approaches rely heavily on the development of a new class of polycrystalline nanostructured materials, which can provide new solutions for old problems. So far, excitonic solar cells have been very promising to be more efficient.⁷¹ In this type of cell, the typical physicochemical processes of light absorption, exciton creation and separation, charge injection, charge transport and collection are assigned to different parts of the cell, and the cell is composed of different materials which are optimized for the specific task.⁶² One of the most promising and extensively investigated semiconductor nanomaterial, providing substantial improvement in the performance of the new generation of solar cells, is TiO₂.^{32,34,54,59,62,78–92} Polycrystalline TiO₂ is a remarkable semiconductor with an average measured bandgap of 3.05 eV, which makes it photoactive in the UV portion of solar spectrum. However, the UV portion of the solar spectrum accounts for just ~3% of the total energy radiated by the sun. Therefore, in order to fabricate an efficient photovoltaic cell, there are three directions that researchers are currently pursuing:

1. improve photo-current generation by minimizing charge recombination across the bandgap;
2. develop nanomaterials that can absorb light from visible and IR portions of the light spectrum;
3. develop nanomaterials that satisfy both of the above criteria.

From the non-stoichiometric point of view, most of the physical and electrochemical properties of TiO₂ relevant to solar energy conversion have been comprehensively summarized in a recent monograph.²² One of the interesting properties of TiO₂ is the fact that it can be oxidized and reduced within a single phase, leading to the formation or removal of point defects that are thermodynamically reversible. Defect disorder therefore plays a critical role in the reactivity and photo-reactivity of TiO₂²² and,

consequently, assessing the developed nanostructures of TiO₂ and their photo-reactivity in the next generation of solar cells is essential. Table 6.1 provides a few examples of recently developed TiO₂-based semiconductor nanocomposites for use in photo-anodes.

The incident photon-to-current conversion efficiency (IPCE) in Table 6.1 is calculated using the following equation:⁹³

$$IPCE(\%) = \frac{1240 \times I_{sc} (\text{A/cm}^2)}{\lambda(\text{nm}) \times I_{inc} (\text{W/cm}^2)} \times 100 \quad [6.1]$$

where I_{sc} is short circuit current and I_{inc} is incident light power.

The IPCE values from Table 6.1 indicate that in general the developed composite materials can out-perform semiconductors. The mechanisms of charge generation and separation, and the path of transport for representative composites belonging to some of the categories listed in Table 6.1 are schematically displayed in Fig. 6.3. It is clearly shown that a metal can be deposited over a semiconductor to synthesize a composite that improves

Table 6.1 Examples of semiconductor based photo-anode nanocomposites

Composite materials	Examples	IPCE	Application	Ref.
Semiconductor and metal	TiO ₂	5%	Minimize charge recombination, improve photocurrent	89
	TiO ₂ -Au	28%		
	TiO ₂ -Pt	27%		
Semiconductor and dye	TiO ₂	60%	Dye improves the ability of the photoanode to absorb light from visible and IR regions	79
	TiO ₂ -	80%		
	Ru-based dye			
Semiconductor with another semiconductor	TiO ₂	5%	Depending on the particle size of the CdSe component, different sections of visible light can be absorbed	80
	TiO ₂ -CdSe	16%		
Doped semiconductor and dye	TiO ₂	28%	While the TiO ₂ alone is not photoactive in the visible, the addition of dye to the doped TiO ₂ makes it photoactive in the visible	81
	N-doped TiO ₂	14%		
	N-doped	28%		
	TiO ₂ -Ru-CBB ^a			

^aRu-CBB: cisdithiocyanato-bis(2,2'-bipyridyl-4,4'-dicarboxylate)-ruthenium (II).

charge separation by decreasing recombination. Figure 6.3a, for instance, displays the mechanism of charge transfer from a TiO_2 conduction band to the collecting substrate via a Au nanoparticle. There is great potential for the employment of this method to decrease recombination in a semiconductor.

An alternative approach, graphically presented in Fig. 6.3b, is to deposit a second semiconductor over the TiO_2 . In this case, CdSe can be used, as this semiconductor has a small bandgap ($E_g \sim 1.6\text{--}2.7\text{ eV}$). CdSe absorbs visible light to generate e–h pairs. The bandgaps of CdSe and TiO_2 are located in such a way that photo-generated electrons from the conduction band of CdSe are injected into the conduction band of TiO_2 and collected at the substrate. The advantage of this procedure is that both TiO_2 and CdSe can absorb light from different portions of the solar spectrum, consequently improving the overall efficiency of the solar-to-electric conversion process.

There are few mature technologies available for the development of efficient nanostructured TiO_2 . Traditionally, nanoporous layers of TiO_2 for DSSCs were prepared by screen printing or by the so-called ‘doctor blade technique’.⁹⁴ The network of interconnected TiO_2 nanoparticles was formed by the subsequent sintering in air at temperatures of about 450°C . During this process, the organic molecules were burned out and necks were formed between the TiO_2 nanoparticles during the sintering process. Nevertheless, a disadvantage of this technique arose from difficulty in controlling the preferential orientation of TiO_2 nanoparticles. An alternative process for efficient preparation TiO_2 nanoparticles is electrophoretic deposition (EPD).⁹⁵ EPD has been shown to provide improved benefits in solar cell technologies. Up to now, it is one of the most selective processes, because deposition occurs only at positions on a substrate where the substrate conductivity is the highest. Another advantage of EPD is that layer morphology and connection of nanoparticles by subsequent sintering can be adjusted separately. For example, it has been reported that TiO_2 nanoparticles were preferentially orientated after EPD at lower temperatures⁹⁶ and the average coordination number of TiO_2 nanoparticles was increased by pressing.⁹⁷

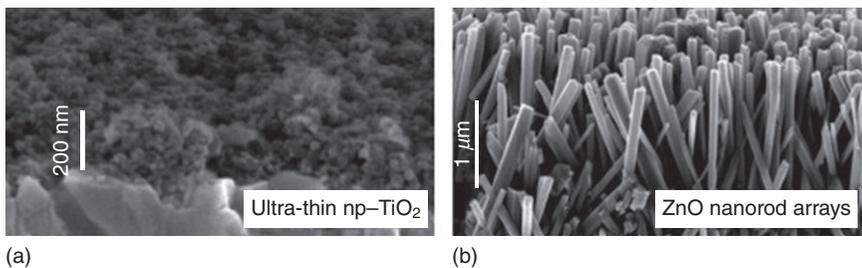
Unlike evaporation, sputtering, chemical vapour deposition and some other of wet chemical processes, the materials utilization rate in EPD is better than 90 %, partly owing to selectivity and partly because there is extensive know-how on the re-use and recycling of EPD chemistries. A further advantage of EPD is the excellent thickness control over a wide range. In terms of processing conditions, it is a low-temperature atmospheric process that allows the fabrication of 3D nanometre scale or nanometre planar structures with great precision and control.

Sol–gel processing under controlled humidity has been widely used for the preparation of porous TiO_2 as a substrate for solar cells, reported creating extremely thin absorber.⁹⁸ TiO_2 nanoparticles were dipped in

suspensions and ultrathin nanoporous TiO₂ layers were prepared as shown in Fig. 6.4a.^{99,100} Spraying of nanoparticles can be also a suitable alternative for large-scale processing. By using TiO₂ nanoparticles with relatively large diameter of about 100 nm in sol-gel processing, more open porous structures with relatively large pore sizes have been obtained.¹⁰¹ It has also been reported that a high degree of light scattering has been reached for microcrystalline TiO₂ layers deposited by spray pyrolysis from Ti-isopropoxide in isopropanol solution.¹⁰² The successful combination of micro- and nanostructured TiO₂ will be advantageous for any future development of solar cell substrates attached with ultrathin nanocomposite absorber.

TiO₂ nanotubes can be developed by utilizing anodization in fluorine-containing electrolytes. Reports relating to TiO₂ nanotubes can be found in some of the recent reviews.^{103,104} There are also recently published reports outlining the potential of TiO₂ nanotube arrays for DSSCs.^{105,106} The diffusion length of electrons injected into TiO₂ nanotubes was in the order of 100 μm.¹⁰⁶ It was illustrated that the tube diameters, their morphology, wall thickness and lengths can be successfully controlled by the components and their concentrations in the electrolyte and by the anodization conditions. There are also rapid techniques producing TiO₂ nanotubes by breakdown anodization, which may become of interest for large-scale applications.¹⁰⁷ However, it should be noted that dense and homogeneous Ti layers deposited on a transparent conductive oxide layer are required for the development of TiO₂ nanotubes, and this would give rise to the need for adequate deposition techniques. TiO₂ nanotube arrays may become of great interest for inorganic nanostructured solar cells due to their open structure and relatively low value of F_R .

One of the highest photo-conversion efficiencies (~7.12%) obtained for hierarchically structured TiO₂ has been reported for TiO₂ nanotubes prepared by a combination of a two-step electrochemical anodization com-



6.4 SEM images of cross-sections of an ultrathin nanoporous TiO₂ layer (a) and an array of ZnO nanorods (b). The plane of the cross-section was tilted. (Reprinted from Ref. 49 with permission from Elsevier Science)

bined with a hydrothermal process as schematically displayed in Fig. 6.5.¹⁰⁸ Efficiency was further enhanced to 7.75 % upon exposure to O₂ plasma.⁶²

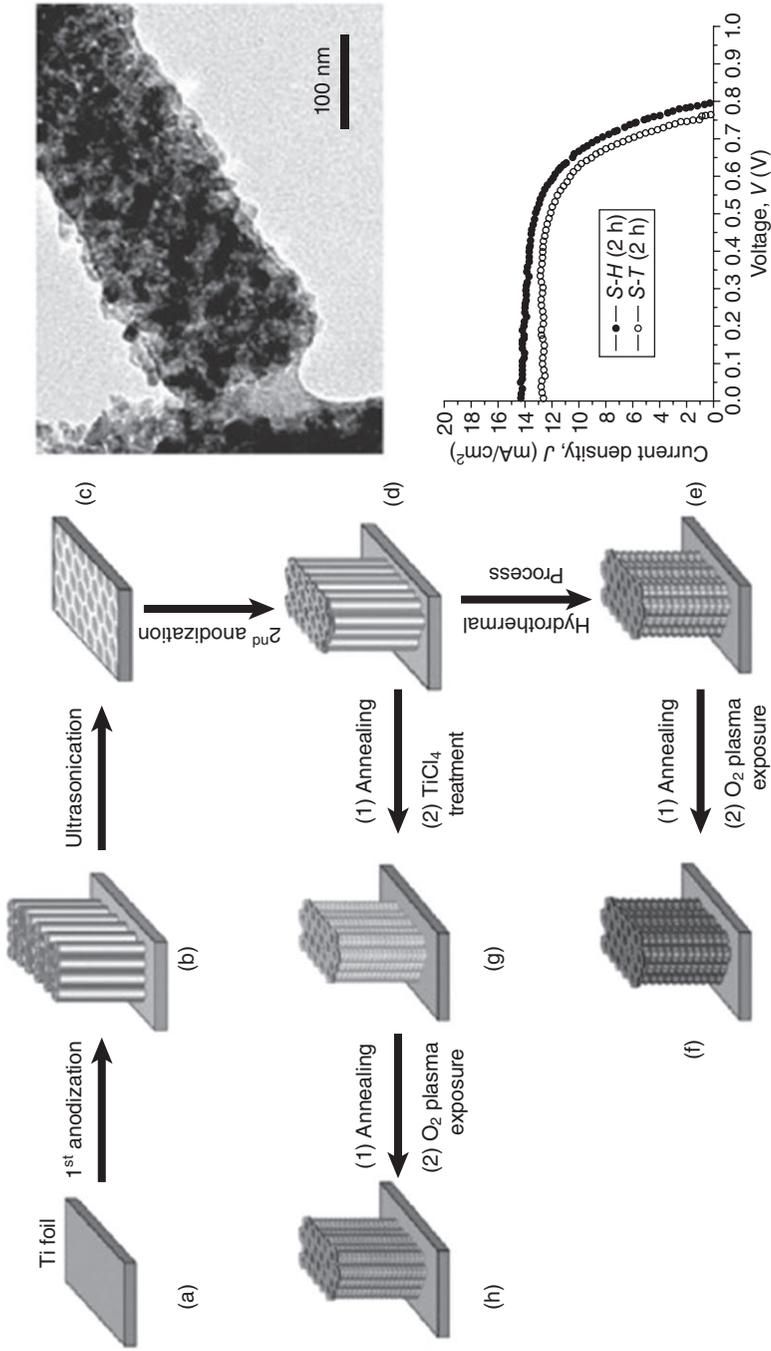
Intercalation of the developed nanostructures by various cations such as H⁺ and Li⁺ has recently been considered as an effective means to increase the overall conductivity of nanostructured materials thereby enhancing their performance.¹⁰⁹ With regard to TiO₂ nanotubes, cationic intercalation caused reduction of Ti⁴⁺ sites which, in turn, resulted in a substantial increase in the photocurrent.⁶² Some of the recent achievements have relied on the ability to fabricate nanotubes on various substrates (Al₂O₃, glass, conducting glass, plastics, etc.),¹¹⁰ which paved the way for further development of flexible structures on high-temperature-resistant (polyamide) substrate.^{111,112} This fact opened up the potential to tailor both the morphology and the shape of nanotubes on the flexible plastic substrates in order to enhance the optical density of the sensitized layer.^{113,114} Figure 6.6 depicts schematically the growth of nanotubes on different substrates.⁶²

6.4.2 ZnO nanorod array

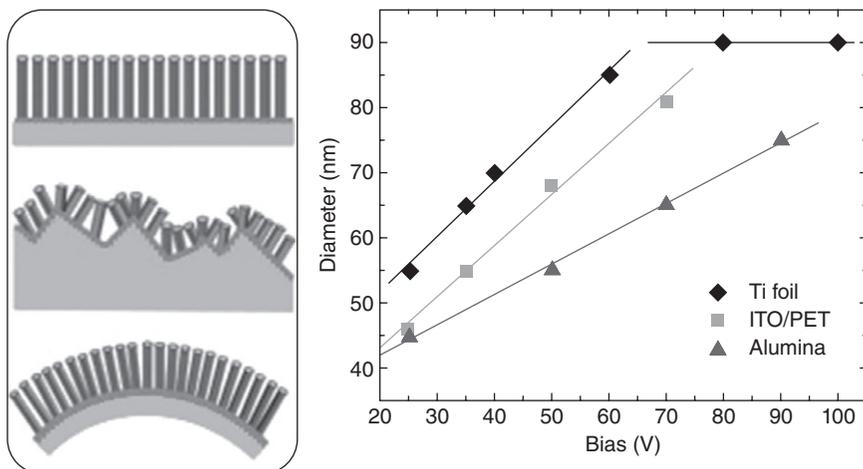
Zinc oxide (ZnO) is semiconductor with a large bandgap (~3.37 eV for the bulk at room temperature) and large exciton binding energy (~60 meV). ZnO is one of the most important transparent conductive oxides in thin-film photovoltaic, and it can be doped up to high free carrier concentrations with electron drift mobility of the order of 10 cm²/Vs.¹¹⁵ In the years since 2000, ZnO has been extensively explored in the fields of electronics and optoelectronics.¹¹⁶ In particular, due to its excellent stability at elevated temperatures, ZnO has been considered as a very promising semiconductor for high-temperature thermo-electrical applications and solar cells.^{117,118} For example, Fig. 6.4b shows an SEM image of wet-chemically prepared ZnO nanorod arrays, which have been considered as very promising substrates for η -solar cells. Well-defined morphologies of crystalline nanostructures of ZnO have been achieved using very different preparation techniques.^{119,120}

For instance, ZnO nanorods can be fabricated by electrochemical preparation.¹²¹ This technique allows a relatively wide variation of parameters, for example by controlling the compact ZnO substrate,¹²² the concentration of ions during electrochemical deposition¹²³ or the concentration of added anions in the solutions.¹²⁴ The tailoring of diameters and lengths of ZnO nanowires has a great influence on the light scattering with and without extremely thin absorber layers.¹²⁵ Alternatively, ZnO nanostructures prepared by EDS at low temperature have shown high measured quantum efficiency in photoluminescence.¹²⁶

As far as photo-conversion efficiency is concerned, excitonic solar cells provide higher surface-to-volume ratio in comparison to single-junction cells. This ratio can be increased by enhancing dye uptake and consequently



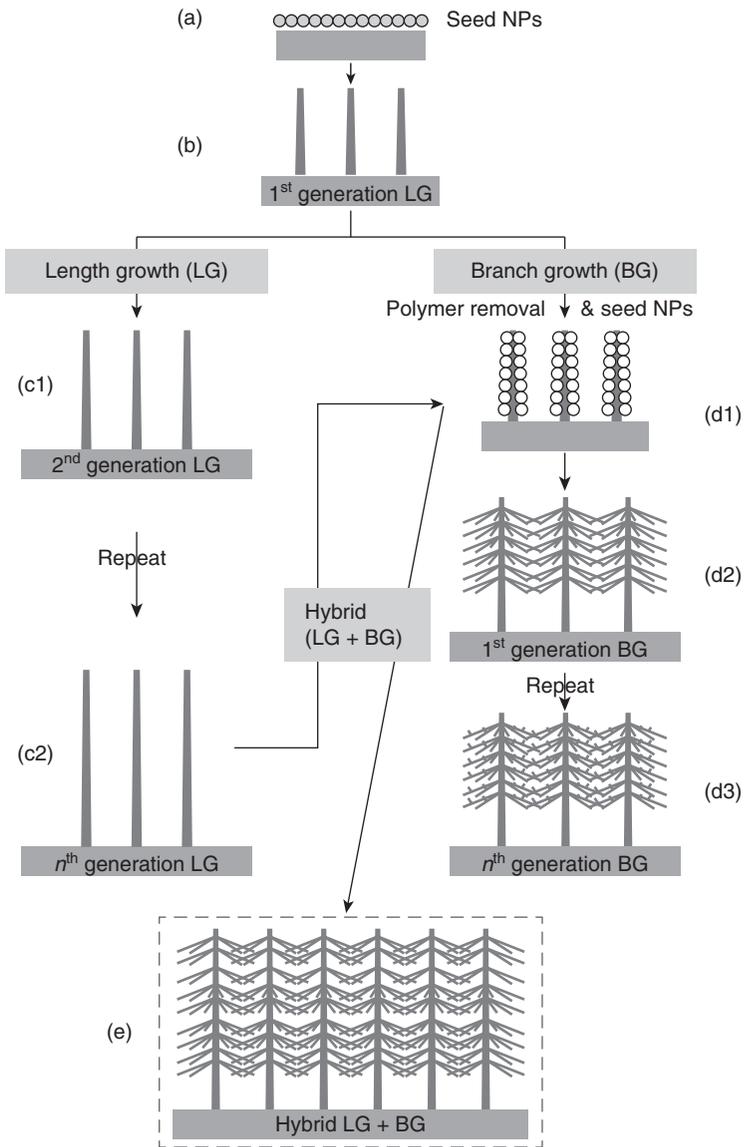
6.5 Scheme of the development of hierarchically structured TiO₂ nanotubes via a combination of two-step anodization and hydrothermal treatment (from a to f). (Upper right) TEM images of two-step anodized TiO₂ nanotube with hydrothermal treatment. (Lower right) reported J - V characteristics. (Reprinted from Ref. 62 with permission of the Electrochemical Society)



6.6 Graphical illustration of the scheme of nanotubes grown on different substrates. Top to bottom: smooth substrate (conducting glass); rough substrate (polycrystalline alumina); flexible substrate (plastic sheet). Pore size as a function of the applied voltage on different substrates, namely, alumina, ITO/PET and Ti foil. Solid lines are linear fits of the experimental data. (Reprinted from Ref. 62 with permission from Elsevier Science)

improving optical density. Recently, various strategies have been utilized to enhance the surface-to-volume ratio, such as ZnO nanowires coupled with dendrite-like branched structure,¹²⁷ mixture of nanowires and nanoplates^{128,129} and ‘nano-forest’ comprising high-density, long-branched ‘tree-like’ multigenerated hierarchical ZnO nanowire photo-anodes.^{62,130} This last approach is schematically presented in Fig. 6.7.

Hybrid cells based on a combination of nanowires and nanoplates have been tailored to take advantage of both the high surface area provided by nanoplates and the improved electron transport along a nanowire network.⁶² Solar cells built from branched nanowires showed photocurrents of 1.6 mA/cm², internal quantum efficiencies of 70 % and overall efficiencies of 0.5 %. Solar cells constituted from appropriate hybrid morphologies showed photocurrents of 3 mA/cm² and overall efficiencies of 1.1 %, while both the nanowire and hybrid cells showed larger open-circuit voltages compared to nanoplate cells.¹²⁹ Moreover, it has been confirmed that further enhancement of photo-conversion efficiency can be obtained by exploiting ZnO and TiO₂ nanonetworks. The nanonetworks demonstrated three-fold enhancement of efficiency compared to a nanowire photo-anode with the same thickness. Cell efficiency of 1.6 % was obtained in 1.5 μm thick photo-anode.¹³¹ The reported improvement was attributed to the increased



6.7 Schematic view of two routes for hierarchical ZnO nanowires hydrothermal growth. Length growth (LG) (a–b–c), branched growth (BG) (a–b–d), and hybrid (a–b–c–d–e). (Reprinted from Ref. 62 with permission from Elsevier Science)

dye uptake of the mixed network, with respect to nanowire array. In the case of nano-forest geometry, the efficiency increase was attributed to greatly enhanced surface area, and reduced charge recombination was achieved by providing direct conduction pathways along the crystalline ZnO 'nano-tree' multigeneration branches.

It has also been reported that shape- and size-selective ZnO nanorods may be fabricated by a microwave-assisted chemical bath deposition method, where the diameters of ZnO nanorods can be varied systematically over hundreds of nanometres.¹³² The employment of spray pyrolysis enabled relatively large diameters of ZnO nanorods to be obtained on substrate from ZnCl₂ solution at temperatures above 500 °C.¹³³ Due to the local extension of space charge regions, control of the free carrier concentration in ZnO nanorod is vital for nanostructured solar cell applications.¹³⁴ It has been shown that the free electron concentration in electrochemically grown ZnO nanorods decreased strongly from more than 10¹⁹ cm⁻³ to about 10¹⁸ cm⁻³ after annealing.¹³⁵ However, the exact control of the free carrier concentration in wet-chemically prepared ZnO nanorods seems still challenging. Therefore, despite numerous efforts to improve the new fabrication methods of ZnO nanostructures for solar cells, the highest reported photo-conversion efficiency for ZnO-based DSSCs is still 7.5%.¹³⁶ This was achieved by application of a hierarchically assembled network comprising sub-micrometer sized clusters of small nanoplates and application of a compact buffer layer inhibiting electron back reaction.

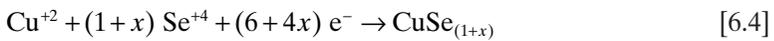
6.4.3 Emerging CuIn_xGa_{1-x}(Se_yS_{1-y})₂ thin-film solar cells

Recent reports have also focused on the development of different emerging nanostructured thin films for solar cells. Despite the fact that the laboratory results obtained so far have been considered to be outstanding and several companies with different process approaches have rushed to scale the existing technologies, there is still a gap between the small cell efficiencies of 20%¹³⁷ and the large module efficiencies which are between 10 and 12%. This is partly due to the complex nature of the quaternary material and somewhat due to the difficulties inherent in scaling up the expensive vacuum-based CdTe and CuInGaSe₂ (CIGS) deposition approaches that were adapted in the early 1990s during the research and development phase of this material system. Consequently, there is a drive to identify lower cost processing methods for CIGS film growth with the ability to yield high-efficiency solar cells at high yield.

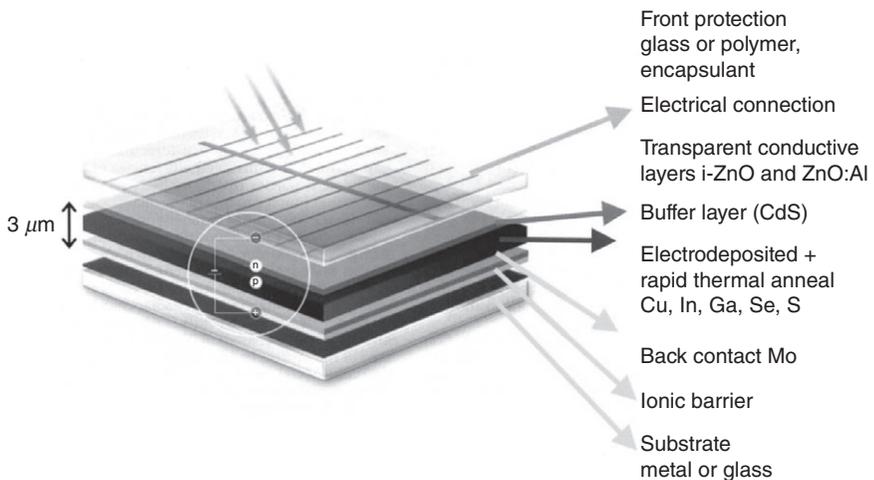
This drive has recently produced a report where roll-to-roll EPD-based CIGS technology was discussed.¹⁰ The EPD step of the process has the capability to control the Cu/(In+Ga) and Ga/(In+Ga) metal ratios reliably. Based on this technology, CIGS layers were formed by EPD of precursor

CIGS layers that were later converted to high-quality chalcopyrite through rapid thermal annealing (RTA) as graphically presented in Fig. 6.8. Solar cells were fabricated in a roll form and then cut and sorted for module manufacturing. Large area solar cell efficiencies of over 12 % were demonstrated using this technology. Modules with 10 % efficiency and 1 m² area were fabricated.

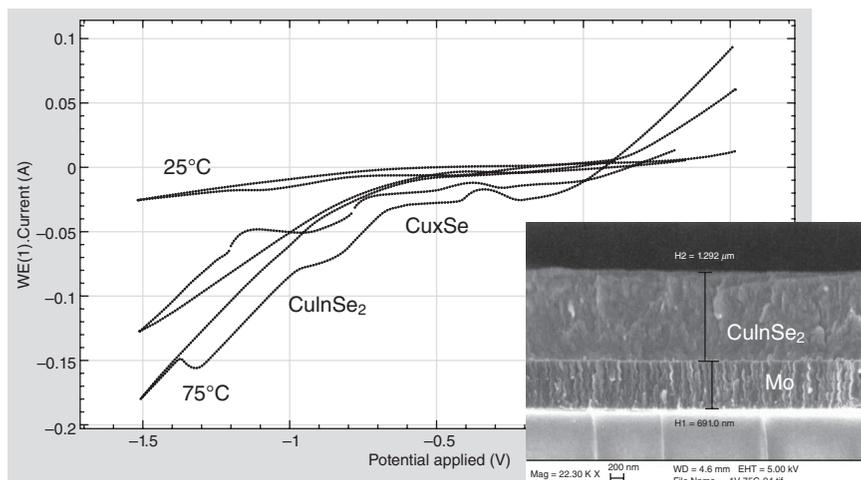
The same report¹⁰ has highlighted challenges in the fabrication of CuInSe₂, CuInS₂ and CuInGaSe₂ by EPD. Co-deposition of the CuInSe₂ precursor layer in a citrate solution without organic additives was also investigated. Figure 6.9 illustrates the voltammetric data and the SEM image of the cross-section of the microstructure obtained.¹⁰ At the initial stages of film growth, Cu-rich Se phases form during deposition. An alternative report suggested that Cu-rich phases facilitate the incorporation of Se and the formation of CuInSe₂ by the following mechanism:¹³⁸



As a result, the incorporation of In in the CuInSe₂ film is facilitated by the formation of CuSe phases. This mechanism results in a non-uniform composition of the precursor film CuInSe₂ layer with a Cu₂Se layer next to the Mo interface. Both the compositional non-uniformities and the modular



6.8 Schematic view of the thin film CuInGaSe₂ solar cell. (Reprinted from Ref. 10 with permission of the Electrochemical Society)



6.9 Cyclic voltammograms of a Mo electrode in a solution containing 5 mM CuSO_4 , 15 mM InSO_4 , and 10 mM SeO_2 , sodium citrate solution at pH 2.5 and 25 °C and 75 °C. Inset: cross-section of the resulting deposit at -1.3V vs MSE and 75 °C. (Reprinted from Ref. 10 with permission of the Electrochemical Society)

microstructure make it difficult to electrodeposit the CuInSe_2 material from simple complex chemistries.

Another report has recently confirmed that the electroplating bath technique has capability to deposit InSe as well as GaSe layers that can be successfully used for the preparation of Ga-containing precursors and CIGS layers.¹³⁹ However, the development of specialized electrolytes with long-term stability and the ability to control the crucially important $\text{Cu}/(\text{In}+\text{Ga})$ and $\text{Ga}/(\text{Ga}+\text{In})$ molar ratios is of utmost importance for the successful application of electrochemistry to CIGS film growth. Reproducibility with minimal thickness variations and the slightest surface roughness of all layers has been found to be critical for a well-controlled absorber.¹⁴⁰

Surface roughness and thickness control are highly influenced by nucleation and growth of In on Cu. Fast interdiffusion was observed between the electroplated Cu and In and a CuIn_2 alloy phase formed during In deposition at room temperature.¹⁴⁰ The alloy formation is believed to promote a conformal deposition of a few In monolayers; the fast interdiffusion counterbalances the In deposition and lowers the In content at the surface. The 3D island growth is believed to be delayed until a threshold value of In content is reached at the surface. The time when this threshold value is reached depends on the In deposition rate and the grain size and the diffusivity of the Cu.

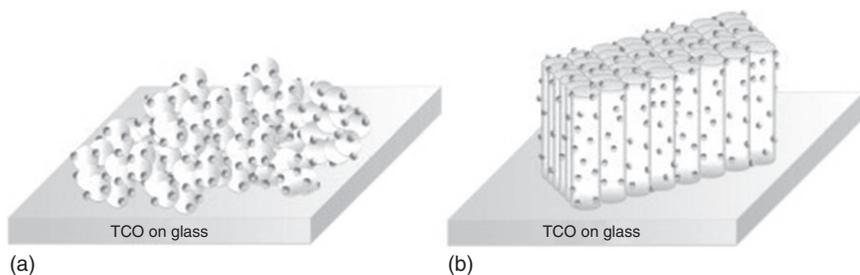
6.5 Semiconductor quantum dot absorbers

6.5.1 Sensitization and charge separation with quantum dots

Exciton wave function can be confined in semiconductor nanocrystals of low dimension so that the energy levels of the electron and hole are shifted, resulting in increased bandgap (quantum confinement).¹⁴¹ Consequently, the use of semiconductor nanocrystals of low dimension, which are also known as QDs, as light harvesters for the third generation of solar cells has attracted great interest in the scientific community due to specific features of these materials. It has been proven that QDs have adsorption spectra tuneable from the visible to the near infrared region by changing their sizes. They can be produced by available low-cost techniques and both multi-exciton generation by a single photon¹⁴² and the presence of intraband transitions¹⁴³ have been claimed. This should, in principle, allow Queisser–Shockley limit to be overcome.¹⁴⁴ Among semiconductor materials for QDs, special attention has been given to CdSe, PbS, CdS, PbSe during last few years. PbS and PbSe especially are of great interest due to their large electron and hole radius. The tuneability of the electronic states of QDs together with their solution-based preparation make them very interesting as potential absorbers in inorganic nanocomposite solar cells. In fact, the sensitization of various wide-bandgap metal oxides with PbS, CdS, Ag₂S, Sb₂S₃ and Bi₂S₃ QDs was demonstrated more than 15 years ago.¹⁴⁵ Electron injection from CdSe QDs into TiO₂ has been investigated, for example, by surface photo-voltage.¹⁴⁶ Charge-selective type II tunnelling structures based on QDs have also been established for closely packed CdTe and CdSe nanocrystals¹⁴⁷ and proven directly by surface photo-voltage spectroscopy.¹⁴⁸

Unfortunately, the reported performance of QDs employed up to now in DSSCs is relatively inefficient if compared with the performance of solar cells. Nevertheless, QD-based solar cells provide for photo-electrochemical systems not directly comparable with those of solar cells: the electrolyte as well as the counter electrode has to be changed, in order to make them compatible in terms of both chemical stability and electron transport.¹⁴⁹ In order to improve the performance of QDs in solar cells, the use of 1D metal oxide semiconductors has recently been proposed for photovoltaic applications as graphically represented in Fig. 6.10.⁶²

Due to the highly promising features of QDs, great effort is currently being devoted to improvement in the assembling of devices integrating QDs in 1D-based photo-anodes. Sensitization of metal oxide-based photo-anodes with QDs can be achieved by both *in situ* (direct generation of QDs on photo-anode surface) and *ex situ* (anchoring of preformed QDs) techniques. Polydisperse nanocrystals are obtained using the *in situ* technique,



6.10 Semiconductor QDs on TiO₂ nanoplates (a) and TiO₂1D nanostructures (b). (Reprinted from Ref. 62 with permission from Elsevier Science)

while monodisperse colloidal QDs are linked to the metal oxide surface by means of *ex situ* techniques. The choice of sensitization method has a great impact on the performance of the cell¹⁵⁰ as well as the choice of both counter electrode and electrolyte.

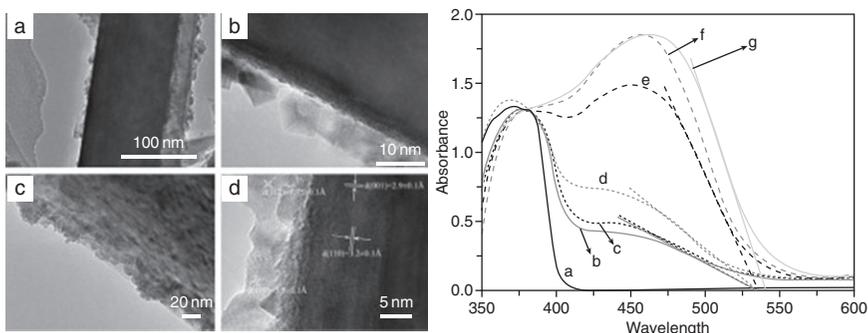
In the vast majority of recently published reports dedicated to the use of semiconductor 1D structures, the authors claim superior performances attributed to an improved electron transport provided by these structures. However, despite all these efforts, the best performances have still been obtained through the use of nanoparticulate films.⁶² One interesting recent example is the anchoring of different sized CdSe-QDs to sensitize TiO₂ films, composed of either nanoplates or nanotubes. As a result, the reported IPCE values have been increased from 35 % to 45 % (with 3 nm CdSe), when nanoplates were substituted by nanotubes.^{11,113} The next step was the sanitation of *successive ion layer absorption and reaction* (SILAR) technique TiO₂ nanoplates and nanotubes¹¹⁴ attached with CdS. Comparison of the devices obtained demonstrated the superior performance of TiO₂ nanotube photo-anodes. In particular, more than a two-fold increase in IPCE value was found for TiO₂ nanotubes (55 % vs 26 %), attributed to better charge separation and transport provided by the nanotubes, while a corresponding increase of about 20 % was displayed in the photo-current density (6.18 mA/cm² vs 5.14 mA/cm²). All investigations have demonstrated a strong correlation between particle sizes and the maximum IPCE observed and confirmed that the lower the QDs diameter the higher the IPCE.⁶²

A ZnO-nanorod/CdTe-QD/CdSe-QD/CuSCN system has recently shown that the related charge-selective layer systems can be incorporated directly into solar cells.¹⁵¹ Collective electronic states are formed in the close-packed ensembles of nanocrystals. This fact has been demonstrated for dense layers of PbSe-QDs packed closely in a plane using scanning tunnelling microscopy¹⁵² or for dense layers of CdSe-QDs using optical methods.¹⁵³

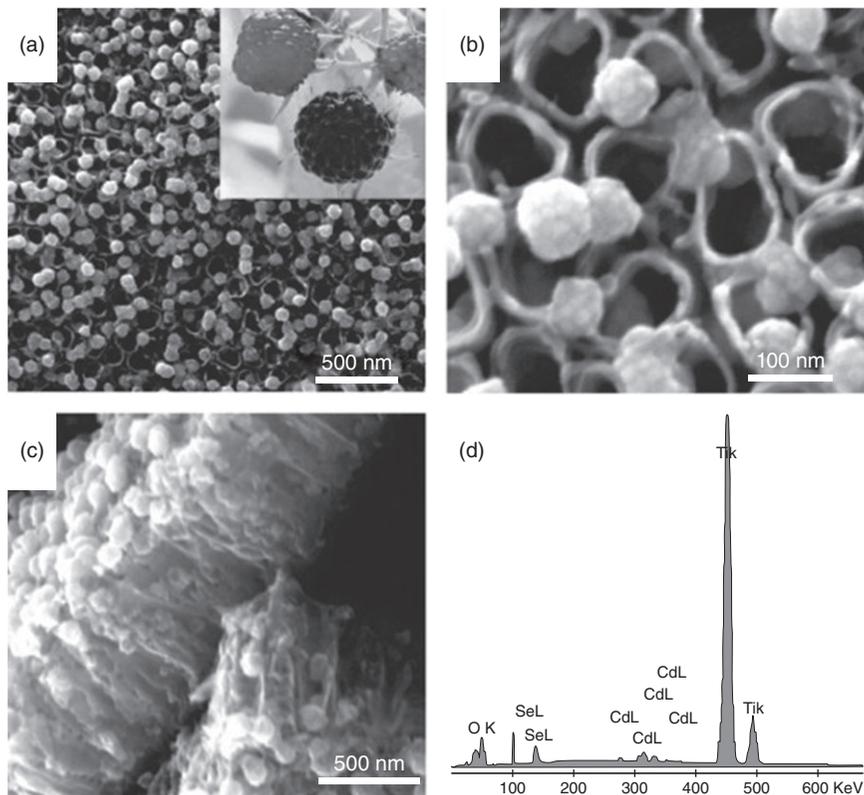
Figure 6.11 depicts transmission electron microscopy (TEM) images as well as diffuse reflectance absorption spectra for bare TiO_2 nanorod film and the TiO_2 nanorod after being subjected to several cycles of a chemical bath deposition process for incorporation of CdS.⁶² In this device, a remarkable 1.91 % photo-conversion efficiency was obtained by sensitizing with CdS rutile TiO_2 nanorods prepared by a hydrothermal method.¹⁵⁴ It is noteworthy that the phenomenon of ‘saturation’ occurring after a certain number of depositions of QDs was observed, as evidenced in the absorption spectra of CdS-sensitized TiO_2 nanorods, where the optical density did not increase any further after nine cycles of the chemical bath deposition.

Another approach represents the use of pre-synthesized CdTe-QDs.¹⁵⁵ Short circuit current density of 6 mA/cm^2 on a TiO_2 nanotube array was reported. A substantial increase of up to 13.0 mA/cm^2 in photo-current density can be further obtained by a sequential deposition of CdS and CdSe on the TiO_2 nanotube array, which is higher than the single contribution provided by the two QDs.

An original configuration with ‘mulberry-like’ structured CdSe-QDs as sensitizers for TiO_2 nanotubes has been recently proposed,¹⁵⁶ and appropriate scanning electron microscopy (SEM) with energy dispersive X-ray (EDX) analyses for such a structure are presented in Fig. 6.12. The new structures developed may reach a remarkable photocurrent density of 16 mA/cm^2 in a three-electrode set-up. This notable photo-response has been ascribed to the multilevel absorption of the ‘mulberry-like’ CdSe



6.11 (Left) TEM images under different magnifications of CdS-sensitized TiO_2 nanorod (a, b and c); HRTEM image CdS QDs coated TiO_2 nanorods: (a), (b) and (c) TEM image. (d) HRTEM image. (Right) Diffuse reflectance absorption spectra of a bare TiO_2 -nanorod film (curve a) and the TiO_2 -nanorod films after introduction of one cycle (curve b), three cycles (curve c), five cycles (curve d), seven cycles (curve e), nine cycles (curve f) and 11 cycles (curve g) of the chemical bath deposition process for incorporation of CdS. (Reprinted from Ref. 62 with permission from Elsevier Science)



6.12 SEM analysis of 'mulberry-like' CdSe cluster anchored on TiO₂: (a) and (b) top view at different magnifications; (c) cross-section view; (d) EDX analysis (0.98% atomic CdSe percentage was identified). SEM analyses show the coverage of TiO₂, quite homogeneous along the main axis of TiO₂ tubes and the hierarchical structure of CdSe nanoclusters. (Reprinted from Ref. 62 with permission from Elsevier Science)

architecture, as well as to decreased exciton recombination dynamics courtesy of the 3D multi-junction between the nanoclusters and TiO₂ nanotubes.

6.5.2 PbS and PbSe quantum dot layers

It has been reported that the quantum confinement effect contributes to the extension of the photovoltaic potential of low-bandgap semiconductors such as PbS or PbSe (bandgaps are about 0.41¹⁵⁷ and 0.27 eV¹⁵⁸ for PbS and PbSe, respectively) by shifting their bandgap to an optimal value for high energy conversion efficiency. A Schottky diode-like solar cell structure

comprising a layer of PbSe-QDs almost 200 nm thick and a Mg contact gave a solar energy conversion efficiency of 1.1 % ($I_{SC} = 12 \text{ mA/cm}^2$, $V_{OC} = 0.25 \text{ V}$) at AM1.5, and the infrared power-conversion efficiency of 3.6 % was confirmed.⁵⁷ The development of a depleted Schottky junction with the PbSe-QD layer was vital for obtaining large drift lengths (10 μm for holes and 1 μm for electrons) in comparison to the much lower diffusion lengths.¹⁵⁹ Correlations between V_{OC} and the bandgap of the PbSe-QDs as well as between V_{OC} and the metal work function of the metal forming the Schottky contact to the QD layer have been impressively demonstrated and, consequently, $I_{SC} > 21 \text{ mA/cm}^2$ and $\eta = 2.1 \%$ at AM1.5 were reached.¹⁶⁰ A very similar result was observed for PbSe-QD layers deposited on a 20 nm thick PEDOT:PSS layer and coated with a Ca contact.¹⁶¹ The value of V_{OC} increased with a decrease in diameter of the PbSe-QDs and with the introduction of the PEDOT:PSS layer, while $I_{SC} = 21.9 \text{ mA/cm}^2$, $V_{OC} = 0.24 \text{ V}$, fill factor (FF) = 45.5 % and $\eta = 2.4 \%$ were reached for a particle diameter of 4.5 nm and $d_{\text{eff}} < 100 \text{ nm}$.¹⁶¹

The average distance between PbSe-QDs or PbS-QDs has been reduced by ethanedithiol treatment linking neighbouring QDs.¹⁶² This measure resulted in an increase in hole mobility by one order of magnitude, while the concentration of free holes in the PbSe-QD layer decreased strongly to the order of 10^{16} cm^{-3} . In an advanced design consisting of a $\text{SnO}_2\text{:F/TiO}_2\text{/PbS-QD/Au}$ system, values of $\eta = 3.5 \%$ ($V_{OC} = 0.54 \text{ V}$, $I_{SC} = 10.5 \text{ mA/cm}^2$) were obtained at AM1.5¹⁶³ and have been increased even further to $\eta = 5.1 \%$.¹⁶⁴ This is the largest reported value obtained for a solar cell based on QDs. In an ITO/ZnO/PbS-QD/Au system, a value of $\eta \approx 3 \%$ has been reported.¹⁶⁵ The advanced design of solar cells with PbSe- and PbS-QDs contains the elements also used in the concepts discussed above.¹⁶⁶ As a result of all these developments, it has been envisaged that energy conversion efficiencies above 6–10 % will be reached in the near future after optimization of photon management.

6.5.3 Passivation and interface conditioning with quantum dot layers

The development of QDs has also opened new opportunities for local passivation concepts in solar cells. In a clear example, nanocrystals can be passivated by applying core–shell hetero-structures,¹⁶⁷ by the right choice of linker molecules¹⁶⁸ or by introducing specific electron donor or acceptor molecules.¹⁶⁹ A passivation concept for large contact areas involving local modulation of QDs of different size and/or capping remains a challenge. The energy level alignment of QDs of a given diameter can be tuned by varying the molecular dipoles of adsorbed molecules. This was demonstrated for TiO_2 sensitized with CdS-QDs coated with different benzenthio

derivates.⁴⁹ It is probable that surface conditioning of QDs assists in substituting Au contacts in Schottky junction-based QD solar cells.

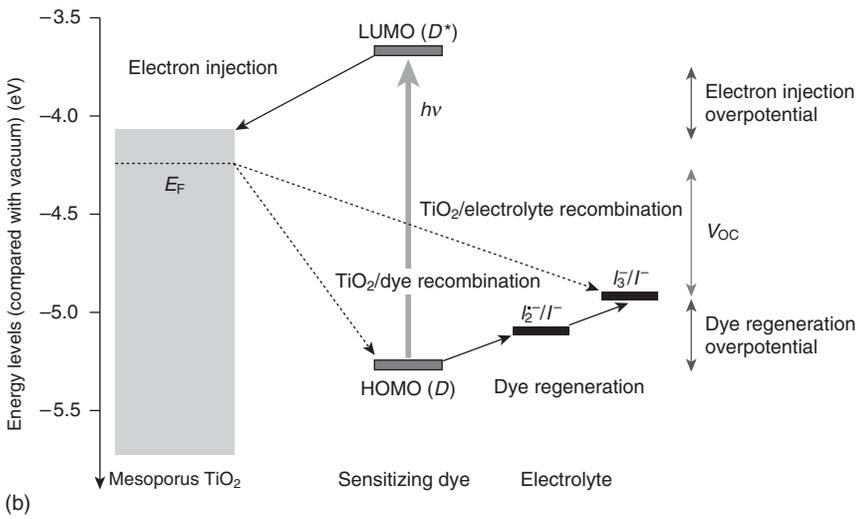
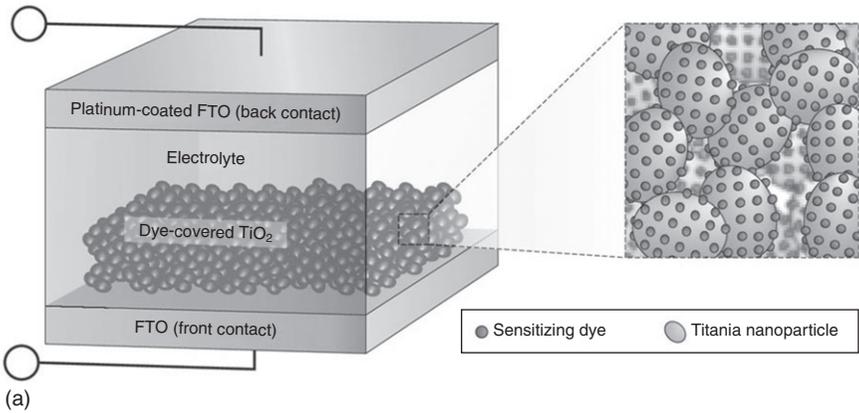
The application of QDs in solar cells may enable the development of solar cells with energy conversion efficiencies above the Shockley–Queisser¹⁷⁰ limit (for solar cells with a single bandgap). The great potential of QDs for large solar energy conversion efficiency as well as possible configurations of QD solar cells have been recently discussed.¹⁷¹ However, a great deal of technological development and fundamental research is needed to generate exploration of specific physical effects, such as the extraction of hot charge carriers, multi-exciton generation or electronic transport in mini-bands of QDs, possible in future high-efficiency solar cells. It is emphasized that relatively high quantum efficiencies may be achieved by multi-exciton generation in semiconductor QDs.¹⁷²

6.6 Dye-sensitized solar cells (DSSCs)

6.6.1 TiO₂-based dye-sensitized solar cells

DSSCs are unique compared with almost all other types of solar cells in that electron transport, light absorption and hole transport are each handled by different materials in the cell.^{6,60,65,83} The development of DSSCs is attractive simply because they can be manufactured from cheap materials that do not need to be highly purified and can be printed at low cost.^{22,71} Since the 1990s and early 2000s, one of the most popular materials utilized in different designs of DSSC has been semiconductor polycrystalline TiO₂ possessing wide bandgap. Historically, the power-conversion efficiency of DSSCs quickly reached ~10% in late 1990s, but progress was then slower with only ~11.5% being claimed by the late 2000s.¹⁷³ However, during the last few years alternative nanostructured semiconductors and technologies for their preparation have been reported, which will be discussed in the following paragraphs.

A typical schematic diagram of a DSSC and its operation is presented in Fig. 6.13a.⁶⁰ One of the major differences between DSSCs and conventional photovoltaic cells is the essential lack of a built-in electric field throughout most of the DSSCs. The majority of conventional solar cells are based on a *p–n* semiconductor junction,¹⁷⁰ which results in a built-in electric field (the space charge layer). The purpose of this field is to separate photo-generated electrons and holes before they recombine. This electric field may also be established by a semiconductor–electrolyte junction (the photo-electrochemical cell) or by a semiconductor–metal junction (such as a Schottky diode). The width of the field is inversely proportional to the square root of the semiconductor doping density; for semiconductors used in solar cells, it is typically hundreds of nanometres.⁶⁵



6.13 (a) Liquid-based DSSCs comprise a transparent conducting oxide (such as fluorine-doped tin oxide, FTO) on glass, a nanoparticle photoanode (such as titania) covered in a monolayer of sensitizing dye, a hole-conducting electrolyte and a Pt-coated, FTO-coated glass back-contact. (b) Energy level and device operation of DSSCs; the sensitizing dye absorbs a photon (energy $h\nu$), the electron is injected into the conduction band of the metal oxide (titania) and travels to the front electrode (not shown). The oxidized dye is reduced by the electrolyte, which is regenerated at the counter-electrode (not shown) to complete the circuit. V_{oc} is determined by the Fermi level (E_F) of titania and the redox potential (I_3/I^-) of the electrolyte. (Reprinted from Ref. 60 with permission of the Nature Publishing Group)

Figure 6.13b displays a basic energy diagram of DSSC operation. The system contains a wide-bandgap semiconductor electrode (TiO_2), a dye that is attached to the semiconductor, a redox electrolyte and a counter electrode (the specific materials are discussed later). Upon illumination of the DSSC, an electron is injected from the dye into the semiconductor film. Following the injection, a hole is transferred to the redox electrolyte, thus generating the dye. The injected electrons must cross the semiconductor layer and reach the conductive substrate, while the oxidized ions diffuse towards the counter electrode where they are reduced to their original state by the electron travelling through the external wire. Consequently, while there is no net charge in the system, electrons flow through the external wire.⁶⁰

The processes involved in the operation of the DSSC are quite efficient. In particular, the initial charge separation, i.e. the electron injection, is an ultrafast, efficient process.¹⁷⁴ However, to obtain the fairly high optical density that is required for effective solar energy conversion, it is necessary to use the high surface area of semiconductor electrodes¹⁷⁵. These electrodes consist of nanosized conductor colloids which are sintered onto a transparent substrate. The sintering process forms electrical contact between the various colloids and between the colloids and the substrate.¹⁷⁶ Electrodes have a porous geometry and a very large surface area. For example, when 10–20 nm colloids are used, the surface area of a 10 μm thick electrode is approximately 1000 times greater than the substrate area.¹⁷⁷ Consequently, in this figure, the transport issues regarding both the photo-injected electron and the electrolyte ions are represented by different shades.

There are several important issues regarding the efficiency of the cell operation that must not be ignored. The geometry of the nanoporous electrodes imparts special characteristics that differentiate these electrodes from their compact analogues. These porous electrodes are strongly influenced by the following factors: the open structure of the electrodes that permits electrolyte penetration through the entire electrode; the small size of the individual colloidal particles that cannot support a high space charge; and the low inherent conductivity of the semiconductor with respect to the penetrating electrolyte. These inherent properties of the nanoporous electrodes have several implications for the functioning of DSSCs:^{50,178}

- Transient electric fields generated upon illumination are neutralized under steady-state conditions, although they may be an important factor in transient measurements.
- Charge carrier motion through the TiO_2 occurs primarily via diffusion rather than drift.
- The activity of the electrolyte ions may change upon charge accumulation in the solid nanoporous electrode, thus being different in the dark and under illumination.

- Systems without excess supporting electrolyte, such as some solid-state versions of the DSSC, may not be able to efficiently neutralize the field generated by photo-induced charge separation, leading to enhanced charge recombination.

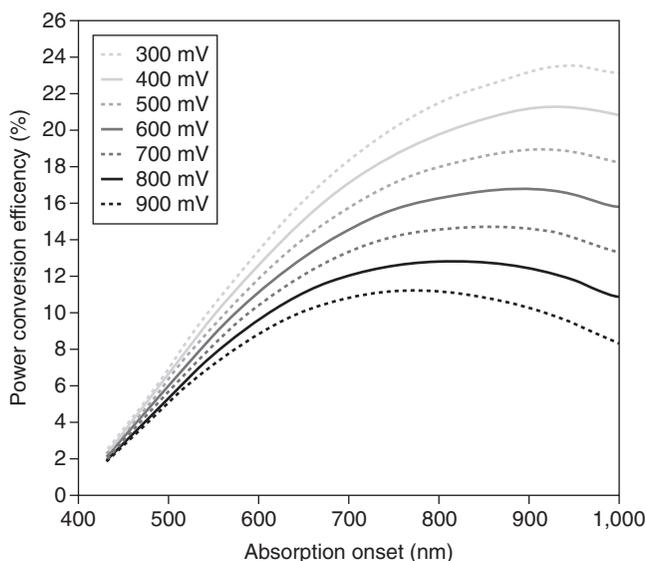
As in any other photovoltaic system, the performance of DSSCs is limited by the recombination process. In short, during the operation of a DSSC, the injected electrons diffuse through the TiO_2 film towards the conducting substrate, while the oxidized ions move in the opposite direction to be regenerated at the counter electrode. The porous geometry that permits electrolyte contact through the entire electrode also provides a high surface area for the recombination of the photo-injected electrons with the holes in the dye layer or reducible species in the electrolyte.¹⁷⁹ The small size of the individual particles in the nanoporous electrode, screened by the interpenetrating electrolyte, cannot support an appreciable space charge.¹⁸⁰ Thus, in contrast to a conventional photovoltaic cell, where the space charge layer prevents the majority of the charge from reaching the surface, there is usually no energy barrier in the semiconductor to prevent electrons from being back-injected into the dye or electrolyte. Other factors must dominate the recombination in the DSSC.

Although the use of a combination of electrolyte and dye-coated TiO_2 has been proven to be successful, new approaches to the development of all solid-state DSSCs (ss-DSSCs)^{23,69} or use of the embedded graphene as a counter electrode for DSSCs^{181,182} have recently emerged. Nevertheless, despite all the latest advances, it has to be admitted that at present the power-conversion efficiencies of ss-DSSCs have been far below the efficiencies of their counterparts that use liquid electrolytes. The best performing ss-DSSCs to date use spiro-OMeTAD as hole-transporting material (HTM) and sintered nanoparticle-based mesoporous TiO_2 films as photo-anodes.¹⁸³ The highest efficiency of such reported ss-DSSCs was obtained when the thickness of the mesoporous TiO_2 films was about $2\ \mu\text{m}$, five times thinner than the thickness needed for sufficient light absorption.^{184–186} Incomplete filling of the mesoporous TiO_2 films with HTMs has been identified as a major factor limiting the performance of ss-DSSCs when the thickness of the TiO_2 films is beyond $2\ \mu\text{m}$.^{187–191} For instance, the pore filling fraction (i.e. volume fraction of the pores filled by the HTMs) of spiro-OMeTAD is more than 60 % for a $2\text{--}3\ \mu\text{m}$ thick film^{189,190} but drops to $\sim 20\text{--}40\%$ as the film thickness increases to $8\text{--}11\ \mu\text{m}$.¹⁹⁰ The ineffective filling of the pores in thick TiO_2 films with spiro-OMeTAD causes low hole injection efficiency from the dye cation to spiro-OMeTAD, short recombination lifetime of charge carriers and poor hole transport through spiro-OMeTAD.^{190,191} Although considerable effort has been made to improve the pore filling, effective

filling of thick nanoparticle-based mesoporous TiO_2 films with HTMs remains a challenging task.^{192–194}

One of the latest approaches to solving the difficulties of filling sensitized films with solid HTMs is to replace the sintered nanoparticle-based mesoporous TiO_2 film with vertically ordered nanostructures. Recently, much effort has been devoted to developing vertically ordered nanostructures for DSSCs.^{195–200} Such structures provide a direct pathway for electron transport and therefore reduce the probability of electron recombination. Moreover, the ordered structures provide a straight channel for filling the pores of the sensitized film with electrolytes. Despite the considerable amount of effort, synthesizing vertically ordered nanostructures with a sufficiently high internal surface area that can be used as photo-anodes for DSSCs remains a challenge. Consequently, DSSCs based on such photo-anodes, to date, have suffered from low internal surface area and thus insufficient dye loading, resulting in low efficiencies.^{195–198,201,202}

It was a reasonable assumption⁶⁰ that an over-potential of only 200 mV may be sufficient for hole regeneration, thus allowing for power-conversion efficiencies of more than 20 %, as graphically presented in Fig. 6.14. Significant recombination rates, coupled with difficulty in achieving high levels of pore-filling in thicker films, means that ss-DSSCs currently work best at a

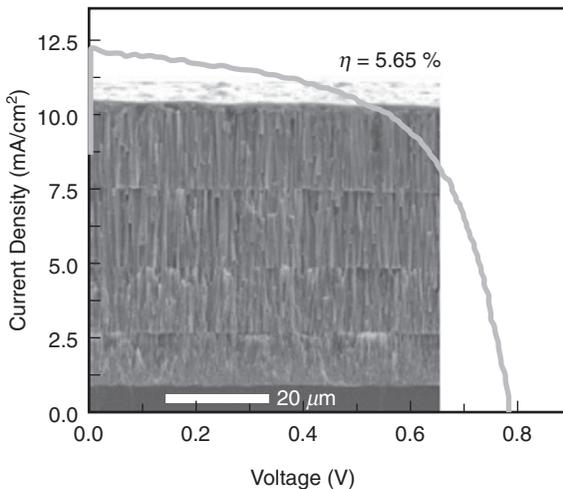


6.14 Maximum obtained power-conversion efficiencies versus absorption onset for various loss-in-potentials. (Reprinted from Ref. 60 with permission of the Nature Publishing Group)

thickness of only a few micrometers.²⁰³ The biggest issues for newly developed ss-DSSCs are their incomplete light harvesting and lower internal quantum efficiency, which together result in current densities that are lower than conventional liquid-based DSSCs.

Recent scientific reports, however, provide confidence that improvement in donor-pi-acceptor dyes, careful control over the *p*-dopant²⁰⁴ and fabrication of high-efficiency ss-DSSCs using multilayer TiO₂-coated ZnO nanowire arrays sensitized with Z907 dye as the photo-anode and spiro-OMeTAD as the solid-state HTM²⁰⁵ can increase the efficiency of DSSCs to over ~5.5%. Figure 6.15, for example, gives a SEM image of the developed structure and obtained efficiency for ss-DSSC TiO₂-coated ZnO nanowire arrays.²⁰⁵ In this ss-DSSC the straight channel between the vertically aligned nanostructures combined with a newly developed multistep HTM filling process allowed effective filling of the sensitized film to a thickness of up to 50 μm with spiro-OMeTAD. The resulting ss-DSSCs yield an average power-conversion efficiency of 5.65%.²⁰⁵

In most of the reported results for the development of new ss-DSSC, solid hole conductors are almost exclusively fabricated through solution-deposition techniques. However, pore-filling can never be complete through such procedures because there is space left when the solvent evaporates.²⁰⁶ The pore-filling fraction, which is defined as fraction of porous volume taken by the hole conductors,⁶⁰ can be as high as 60–80% with small-



6.15 SEM image of the structure and reported obtained efficiency of solid-state dye-sensitized solar cells based on TiO₂-coated ZnO nanowire arrays. (Reprinted from Ref. 205 with permission of the American Chemical Society)

molecule hole conductors, and pores are generally uniformly filled throughout the entire film thickness. Improving the pore-filling fraction is an important strategy for reducing recombination and might be achieved by infiltrating hole conductors from the melt.²⁰⁷

6.6.2 WO_3 - and Nb_2O_5 -based dye-sensitized solar cells

DSSCs have attracted a great deal of attention among researchers of photovoltaic devices because they provide the following advantages:

- require mostly abundant materials from earth;
- offer respectable efficiencies;
- low level of requirement for high-temperature material processing;
- offer simplicity of cell assembly.

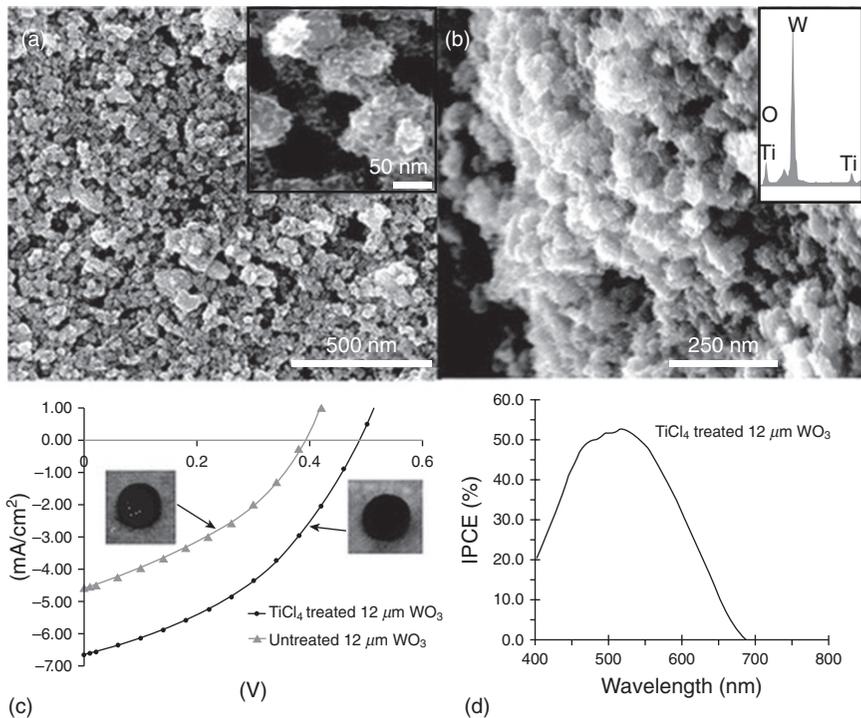
Therefore, they represent an excellent potential for many applications. The operating mechanism of the standard DSSC was explained in the previous section. The best reported efficiency of DSSCs based on TiO_2 is approaching ~12%.⁶⁰ While the vast majority of DSSC research is focused on further development of TiO_2 -based DSSCs, other semiconductor oxides have also been studied as adequate alternatives,⁶⁴ most notably ZnO-based DSSCs, which have achieved 5% conversion efficiency.^{133–136,208} ZnO is a wide-bandgap material with a similar band structure to TiO_2 and comparable electron injection dynamics.^{125,128}

Another semiconductor material which has been demonstrating great potential as photo-anode in ss-DSSCs is WO_3 .⁶³ WO_3 is a transition metal oxide with wide bandgap that is commonly observed in a range from 2.6–3.1 eV²⁰⁹ for most of its crystal phases, which responds to the blue–UV region of the light spectrum. Although its bandgap energy is relatively narrower than that of TiO_2 , WO_3 itself is an extremely stable material that can endure most harsh environments, such as exposure to strong acids, and with a proven history of effective and efficient absorption and chemisorption in different gaseous sensors.²¹⁰ The carrier mobility of WO_3 is also reported to be within the range of TiO_2 .²¹¹ Moreover, modern technologies facilitate the preparation of WO_3 in various nanoforms – from nanoplates to nanowires. Variation of suitable WO_3 nanostructures for specific design of ss-DSSCs allows optimization of suitable surface-to-volume ratio for maximum dye loading. Other reported properties of WO_3 were comprehensively covered in some of the latest reviews.^{212,213}

One approach to the design of WO_3 -based DSSCs is coating WO_3 with TiO_2 for a more active oxide surface which favours the dye adsorption. It is important that the open current voltage V_{oc} should be larger because the excited electrons can now be injected to the more negative conduction band of TiO_2 and then step down to the conduction band of WO_3 . Coating the

WO₃ nanoparticle surface with TiO₂ was followed by treating the sample using aqueous TiCl₄ solution at the elevated temperature of 70 °C.⁶³ The resulting surface morphology of TiCl₄-treated WO₃ has been improved, as shown in Fig. 6.16a. It was reported that the modifications occurred in the whole bulk of the thin film, and the strong presence of Ti element was confirmed by EDX analysis (Fig. 6.16b).⁶³

It has been reported that the performance of a 12 μm treated WO₃ DSSC reached an overall efficiency of 1.46%.⁶³ While Fig. 6.16c displays the improvement in *J-V* characteristics made by the TiCl₄ treatment, Fig. 6.16d exhibits that the quantum ability of the WO₃ DSSC has also been enhanced by the treatment, as the peak efficiency approached 55% and a broader peak range of 460–570 nm was observed. However, the TiCl₄-treated WO₃ DSSC still performs in the lower end compared with the standard TiO₂-



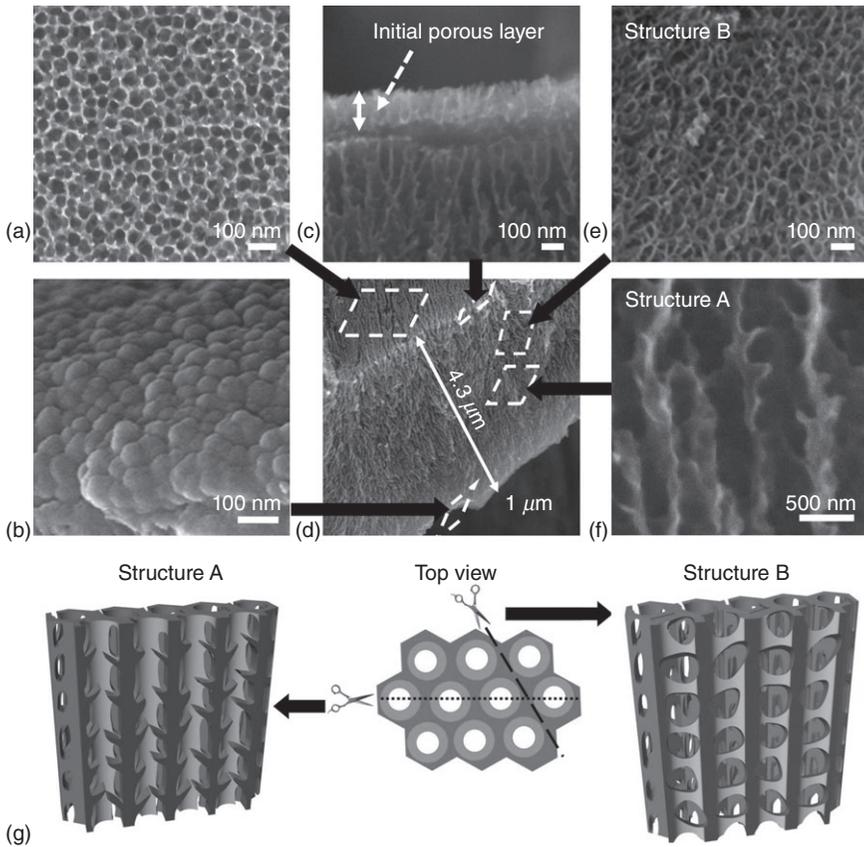
6.16 (a) Top view of the TiCl₄-treated WO₃ film and the magnified view as inset. (b) Cross-section view of the film with inset – EDX showing presence of Ti element. (c) *J-V* characteristics of the treated 12 μm WO₃ DSSC in comparison with the untreated one and their corresponding physical photo-images. (d) IPCE for the TiCl₄-treated 12 μm WO₃ DSSC. (Reprinted from Ref. 63 with permission of the American Chemical Society)

based DSSCs because the TiO_2 coating did not form a complete shell structure to entirely insulate the WO_3 surface. Therefore, the charge recombination level within the cell could still be very high.

Another remarkable semiconductor, which can be considered as an alternative to widely used TiO_2 for ss-DSSCs, is Nb_2O_5 . Potentially, nanostructured Nb_2O_5 can be an even more suitable candidate for ss-DSSCs than TiO_2 and other semiconductors.^{63,213} It has wider bandgap ($\sim 3.4\text{--}4.0\text{ eV}$) and higher conduction band,²¹⁴ comparable electron injection efficiency²¹⁵ and better chemical stability.²¹⁶ In most of reports dedicated to the development of Nb_2O_5 for ss-DSSCs published so far, Nb_2O_5 nanostructures were represented as nanoparticles, nanorods and nanofibre networks. Unfortunately, their photo-conversion efficiencies and photo-currents have not reached the levels reported for similar ss-DSSCs based on nanostructured TiO_2 owing to reduction in their dye-loading sites.^{217,218} It was found that the larger lattice dimensions of orthorhombic Nb_2O_5 , compared to anatase TiO_2 , create a major challenge for optimization of the Nb_2O_5 morphology for ss-DSSCs.²¹⁶

Nevertheless, a breakthrough was reported recently in the development of Nb_2O_5 crisscross nanoporous networks with a thickness of $\sim 4.0\ \mu\text{m}$. This nanoporous network was fabricated using a novel anodization method at elevated temperatures.²¹⁹ In brief, anodization intervals from 30–240 min resulted in Nb_2O_5 films comprising 1.5–6.0 μm thick nanoporous structures. After anodization, the sample was annealed in air at a temperature of 440°C for 20 min, with a slow ramp up and down rate of $1^\circ\text{C}/\text{min}$. Three main factors concerning the prevention of the formation of porous layers thicker than 500 nm during Nb anodization have been considered.^{220,221} The first is the high chemical dissolution rate of the porous layer caused by fluoride ions in the electrolytes. The second is the development of a thick barrier layer on the bottom of the pores, which inhibits further ion diffusion and growth of the porous layer. In order to increase the layer thickness up to several micrometers, ethylene glycol was utilized as the solvent instead of water. This reduced the chemical dissolution effect on the porous layer.²²¹ The third is the enhancement of the ion diffusion rate. This was achieved by optimization of the electrolyte temperature at 50°C , thereby enhancing the growth rate of the porous layer.²²² SEM images of the final structure of the developed Nb_2O_5 crisscross nanoporous network are presented in Fig. 6.17, where Figs 6.17a and 6.17b are the top and bottom views, respectively, of the Nb_2O_5 porous network. The obtained thickness of the porous Nb_2O_5 layer was $\sim 4.0\ \mu\text{m}$ after approximately 120 min of anodization.

The Nb_2O_5 crisscross nanoporous network represents a stratified structure consisting of several different regions. A bulky porous layer of $\sim 100\text{--}200\ \text{nm}$ thickness can be observed on top (Figs 6.17c and 6.17d). This layer, with similar morphology and thickness to previously-reported anodized



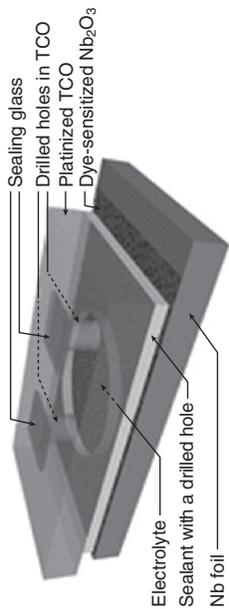
6.17 SEM images of Nb_2O_5 nanoporous network: (a) top view of the nanoporous network; (b) bottom view of the nanoporous network; (c) cross-section view of the top of the nanoporous network; (d) cross-sectional view of the Nb_2O_5 network indicating the thickness of the film; (e) cross-section of the network from a different angle; (f) higher magnification of cross-section view of nanoporous network; (g) three-dimensional schematic of the different cross-sectional views of nanoporous network.

NbO_2 structures, could be the initial porous layer formed at the beginning of the anodization process. The absence of a barrier layer underneath this initial layer provides further evidence for an enhancement of the ion diffusion rate created by our unique anodization method at an elevated temperature. The top morphologies of both upper and underneath layers were very similar, except that the side walls of the upper layer are thinner and the pores less ordered.²¹⁹ From the SEM images, this in-between layer appears to be made up of compressed vein-like nanostructured networks,

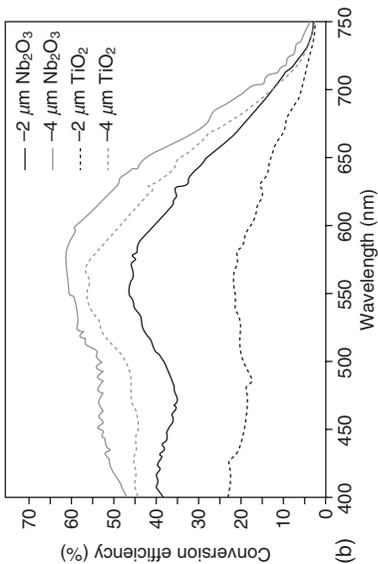
which are connected to each other via lateral openings. The top view schematic of the in-between layer is shown in Fig. 6.17g. If the layer is sectioned along the dotted line or any parallel lines, 'Structure A', demonstrating the 'nano-veins' morphology, can be observed (Fig. 6.17f). These 'nano-veins' have internal diameters ranging from 30–60 nm, whereas the 'nano-vein' valve diameters are typically reduced in diameter from ~40 to 80 % of the veins' original internal diameters.²¹⁹ The valves are the residuals grown from the internal walls, possibly due to the chemical dissolution caused by fluoride ions in the electrolytes.

Another type of nanostructure also observed in the cross-sectional SEM image (Fig. 6.17e), designated as 'Structure B', can be obtained mathematically by cutting a layer along the dashed line in Fig. 6.17g. This configuration consists of compressed pore networks with dispersed distribution. From the high-resolution TEM images, this crisscross nanoporous network can provide excellent directional pathways for electron transfer in addition to enhanced surface area, which fulfils the prerequisites for developing highly efficient ss-DSSCs.

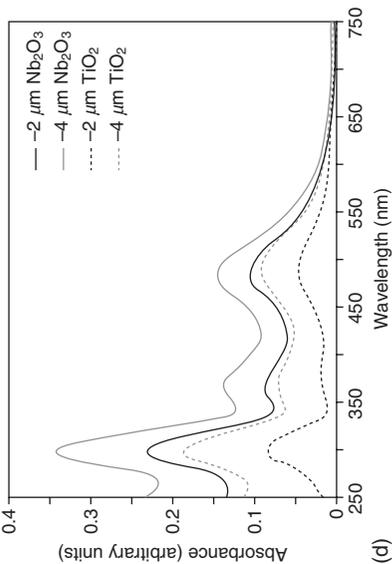
Two Nb₂O₅ crisscross nanoporous networks with thickness of ~2.0 and ~4.0 μm were assembled into ss-DSSCs, as graphically represented in Fig. 6.18a, and their IPCE has been tested. The results obtained were compared to the IPCE of the ss-DSSC based on nanostructured anatase TiO₂ with the same thickness. The combined results are displayed in Fig. 6.18b.²¹⁹ The IPCE spectrum of the dye-loaded 4 μm thick Nb₂O₅ nanoporous network reveals two broad peaks in a wide wavelength range (400–750 nm). The centre of the first peak is at 450 nm with a peak magnitude of 52.4 %, while the second peak is at 575 nm with 61.1 % conversion efficiency. Significant photo-conversion capabilities can also be observed for wavelengths up to 750 nm. The results obtained confirmed that it is possible to create ss-DSSCs based on sophisticatedly accomplished nanostructured Nb₂O₅. It is evident that the developed Nb₂O₅ crisscross nanoporous network is superior to any other Nb₂O₅ nanostructures for ss-DSSCs reported so far. More importantly, the ss-DSSC based on the 4.0 μm thick Nb₂O₅ crisscross nanoporous network exhibited approximately 20 % better efficiency compared to the ss-DSSC based on TiO₂ nanotube arrays with a similar thickness. This enhancement becomes more evident for the 2 μm thick Nb₂O₅ nanoporous network, which surprisingly provided almost 100 % improvement in efficiency compared with a TiO₂ nanotube array. This appeared to suggest that this noteworthy enhancement in the conversion efficiency could be primarily due to the sophisticated surface area of the Nb₂O₅ nanoporous networks. The 2 and 4 μm thick Nb₂O₅ nanoporous networks have a greater surface area by factors of 100 and 45 %, respectively, in comparison to the equivalent TiO₂ nanotube arrays according to the dye coverage characterization provided in Figs 6.18c and 6.18d.



(a)



(b)



(d)

Sample	Dye coverage (nmol/cm ²)	Absorbance at 534 nm
-2 μm Nb ₂ O ₃	52.3	0.059
-4 μm Nb ₂ O ₃	73.7	0.084
-2 μm TiO ₂	25.1	0.029
-4 μm TiO ₂	50.0	0.058

(c)

Consequently, the results presented above are just the first attempts at the development of efficient and effective ss-DSSCs based on nanostructured Nb₂O₅. These results justify the necessity for further research focusing on optimization of the Nb₂O₅ nanoporous network structure. The next obvious step could be to increase the thickness of the photo-anode while maintaining a high degree of photo-conversion efficiency. In this regard, the electrochemical anodization method at elevated temperatures has proven to be an effective process in fabricating porous morphologies. This nanoporous network offers superior dye-loading sites, excellent continuous and directional pathways for electron transfer, as well as enhanced productive electron lifetimes. Up to now, a Nb₂O₅ nanoporous network with a thickness of ~4.0 μm has been achieved.²¹⁹ The advantages of this nanoporous network, together with the wide bandgap and high conduction band edge of Nb₂O₅, could make it an ideal material for the creation of photo-anodes for highly efficient ss-DSSCs. The demonstrated conversion efficiency of 4.1 % from a ~4.0 μm thick Nb₂O₅ photo-anode is about 50 % higher than that of a TiO₂ nanotube array with a similar thickness.²¹⁹ The 4.1 % efficiency achieved is lower than the 15 % value which justifies commercialization but creates real research and development opportunities to enhance performance by synthesizing thicker porous structures as well as utilizing front-side illumination by realizing these structures on transparent conductive substrates.

6.7 Future trends in technological development

By the end of 21st century, the world's energy requirements will be four times what they are at present,²²³ and it is inevitable that solar cells will play



6.18 Characteristics of the DSSCs fabricated using crystalline Nb₂O₅ nanoporous networks and anatase TiO₂ nanotube arrays. (a) Configuration of the DSSC fabricated incorporating the Nb₂O₅ nanoporous network. (b) IPCE spectra of DSSCs fabricated using Nb₂O₅ nanoporous networks and TiO₂ nanotube arrays of various thicknesses. IPCE was calculated using the relation $IPCE \% = 100hcj(\lambda)/e\lambda P(\lambda)$, where h denotes the Planck constant, c the velocity of light, e the electron charge, λ the wavelength, $j(\lambda)$ the photocurrent density at λ and $P(\lambda)$ the power density of light at λ . (c) Table of dye coverage details for the Nb₂O₅ nanoporous networks and TiO₂ nanotube arrays. N3 dye attached on Nb₂O₅ nanoporous networks and TiO₂ nanotube arrays was desorbed by immersing the samples in a 10 mM KOH solution. The concentration of the desorbed dye determined by UV-vis spectroscopy was used to calculate the dye coverage in the samples. (d) UV-vis absorption spectra of N3 dye desorbed from Nb₂O₅ nanoporous networks and TiO₂ nanotube arrays of various thicknesses. (Reprinted from Ref. 219 with permission of the American Chemical Society)

a much more significant role in satisfying the world's growing energy demands in the near future. The ultimate goal of any development of highly efficient solar cell technology is to achieve the maximum possible photo-conversion with the great prospect of commercialization based on the potential for long-term functional stability with reasonably cost-effective manufacturing. In order to deliver this goal, solar cell technology must not only be efficient and inexpensive, but also acceptable and beneficial in use compared to conventional fossil fuel technologies and able to compete favourably against incumbent photovoltaic technologies. Several recent major advances in the design of dyes and electrolytes for DSSCs have led to record power-conversion efficiencies. Donor- π -acceptor dyes absorb much more strongly than commonly employed Ru-based dyes, thereby allowing most of the visible spectrum to be absorbed in thinner films. Light-trapping strategies are also improving photon absorption in thin films. New Co-based redox couples are making it possible to obtain higher open-circuit voltages, leading to a new record power-conversion efficiency of 12.3%. Solid-state hole conductor materials also have the potential to increase open-circuit voltages and are making ss-DSSCs more adaptable. Engineering of the interface between the titania and the hole transport material is being used to reduce recombination and thus attain higher photo-currents and open-circuit voltages. The combination of these strategies promises to provide much more efficient and stable solar cells, paving the way for large-scale commercialization.

The latest advances in the design of dyes and electrolytes for DSSCs and functionally structured nanomaterials for ss-DSSCs have led to their increased efficiency of around 14%. This has subsequently provided substantial incentive to the development of laboratory-scale devices with efficiency greater than 15%.^{224,225} One of the greatest opportunities for improving the overall competence of all type of DSSCs is to reduce the energy gap of the dyes, thus providing more light to be adsorbed in the spectral range of 650–940 nm. However, from the practical point of view, to develop such a dye that strongly absorbs all the way from 350–940 nm is an extremely challenging task. Usually, the spectral width of the dye and the peak absorption coefficient are inversely related to each other. Therefore, the most promising strategies reported so far for harvesting of the whole spectrum are the employment of a combination of visible- and near-infrared-absorbing dyes⁶⁰ and improvement of performance of the solar cells through better engineering of their hetero-interfaces.²²⁶

The increase in the photo-conversion efficiency values since year 2000 has been relatively slow compared to the previous decade. This indirectly gave the impression that the performance of the newest DSSCs is near its peak, which has to be partially justified considering that the conventional iodide- and Ru-based DSSCs have a realistic maximum possible efficiency

of little more than 13%.²²⁵ On the other hand, the loss-in-potential can certainly be inevitably reduced to 500 mV by closer matching of the energy levels at the hetero-junction, employing more strongly adsorbing dyes in thinner films. By reducing the recombination losses, it is possible to obtain efficiencies as high as ~19% with dye capable of absorbing out to 920 nm.⁶⁰

It has to be admitted that, although there have been substantial initial studies relating to the development of ss-DSSCs, a complete understanding of the overall lifetimes and degradation mechanisms of ss-DSSCs based on newly-created composite nanomaterials would justify further detailed investigation.²²⁷

EDS for solar cells is an active area of modern research, and it has been shown to provide improved benefits in several solar technologies. For Si solar cell contacts, EDS metal contacts result in 1–2% improvement in the solar cell efficiency.⁹³ This is probably due to a lower processing temperature with better yield than screen printing, improved contact resistance, lower overall resistance and the ability to fabricate small contacts that reflect the sunlight less. It is expected that EDS will become a game changer through its ability to reduce manufacturing costs to less than \$0.50/W, making solar energy affordable to the public.

An alternative course to achieve efficient light harvesting is by appropriately engineering the cell. In this regard, the development of organic photovoltaic cells – particularly those based on polymers – has attracted considerable attention in recent years, owing to their low cost and potentially high power-conversion efficiencies.^{228,229} Recent progress in the development of polymer solar cells has improved power-conversion efficiencies from 3% to almost 9%. Based on semiconducting polymers, these solar cells are fabricated from solution-processing techniques and have unique prospects for achieving relatively inexpensive solar energy harvesting, owing to their material and manufacturing advantages. The potential applications of polymer solar cells are broad, ranging from flexible solar modules and semi-transparent solar cells in windows, to building applications and even photon recycling in liquid-crystal displays.

The most advanced polymer solar cells are those based on polymer–fullerene systems, whose power-conversion efficiencies are now approaching 10%.²²⁹ Fullerene derivatives have become the standard *n*-type molecules for use in polymer solar cells owing to their strong electronegativity and high electron mobility.

Alternatives to glass water-tolerant DSSCs have recently emerged due to unique features of their technology.²³⁰ However, sputtered transparent conducting oxides on plastic are still relatively expensive, less transparent and possess higher resistance than the same nanomaterials deposited on glass. As a consequence, this design of ss-DSSCs has been less efficient so far. Further improvements in performance and cost-effective approaches

need to be developed in future in order for these ss-DSSCs to be competitive with glass-based ss-DSSCs.^{231–234}

In the past, the co-sensitization of the Ru metal complex dyes was considered to be challenging owing their low molar extinction coefficients.⁶⁰ However, the employment of organic dyes may provide a possible solution to this problem. Organic dyes possess substantially higher molar extinction coefficients than the Ru metal complex dyes, which in turn require smaller surface areas. As a result, it is possible to co-sensitize thinner DSSCs without significantly reducing light harvesting in any portion of the spectrum.²³³

All the recent advances in the development of solar cells technology outlined above indicate that, although rapid progress in photovoltaic research has already provided substantial positive growth, the main challenge now faced by the industry is to develop techniques for storing the energy harvested during the day for use at night. Only then will solar energy rise to take its place as a major provider of sustainable energy.

6.8 References

1. M.I. Hoffert *et al.*, Energy implications of future stabilization of atmospheric CO₂ content, *Nature*, 395 (1998) 881–884.
2. K. Kalyanasundaram, M. Grätzel, Photovoltaic performance of injection solar cells and other applications of nanocrystalline oxide layers, *J. Chem. Sci.*, 109 (1997) 447–469.
3. T. Bak, J. Nowotny, M. Rekas, C.C. Sorrell, Photo-electrochemical hydrogen generation from water using solar energy. Materials-related aspects, *Int. J. Hydrogen Energy*, 27 (2002) 991–1022.
4. M. Fisher, Review of hydrogen production with photovoltaic electrolysis system, *Int. J. Hydrogen Energy*, 11 (1986) 495–501.
5. A. Fujishima, K. Honda, Electrochemical photolysis of water at a semiconductor electrode, *Nature*, 49 (1972) 37–38.
6. M. Grätzel, Photoelectrochemical cells, *Nature*, 414 (2001) 338–344.
7. G. Hodes, A. Zaban, Nanocrystalline solar cells, in H. Hahn, G. Wilde (eds), *Nanostructured Materials*, 2009, Elsevier, Oxford, 232–269.
8. R.W. Miles, Photovoltaic solar cells: choice of materials and production methods, *Vacuum*, 80 (2006) 1090–1097.
9. R. Kapadia, Z. Fan, K. Takei, A. Javey, Nanopillar photovoltaics: Materials, processes, and devices, *Nano Energy*, 1 (2012) 132–144.
10. H. Deligianni, S. Ahmed, L.T. Romankiw, The next frontier: electrodeposition for solar cell fabrication, *ECS Interface*, 4 (2011) 47–53.
11. Z.A. Peng, X.G. Peng, Formation of high-quality CdTe, CdSe, and CdS nanocrystals using CdO as precursor, *J. Am. Chem. Soc.*, 123 (2001) 183–184.
12. R. Narayanan, M. Deepa, A.K. Srivastava, Nanoscale connectivity in a TiO₂/CdSe quantum dots/functionalized graphene oxide nanosheets/Au nanoparticles composite for enhanced photoelectrochemical solar cell performance, *Phys. Chem. Chem. Phys.*, 14 (2012) 767–778.

13. F. Fabregat-Santiago, G. Garcia-Belmonte, I. Mora-Sero, J. Bisquert, Characterization of nanostructured hybrid and organic solar cells, *Phys. Chem. Chem. Phys.*, 13 (2011) 9083–9118.
14. G.A. Chamberlain, Organic solar cells: a review, *Sol. Cells*, 8 (1983) 47–83.
15. G.K. Mor, O.K. Varghese, M. Paulose, K. Shankar, C.A. Grimes, A review on highly ordered, vertically oriented TiO₂ nanotube arrays: fabrication, material properties, and solar energy applications, *Sol. Energy Mater. Sol. Cells*, 90 (2006) 2011–2075.
16. X.Y. Deng, L.P. Zheng, C.H. Yang, Y.F. Li, G. Yu, Y. Cao, Polymer photovoltaic devices fabricated with blend MEHPPV and organic small molecules, *J. Phys. Chem. B*, 108 (2004) 3451–3456.
17. J. Singh, *Semiconductor Devices: An Introduction*, 2nd ed., 1994, McGraw-Hill Companies, New York.
18. K.F. Lin, H.M. Cheng, H.C. Hsu, L.J. Lin, W.F. Hsieh, Band gap variation of size-controlled ZnO quantum dots synthesized by sol–gel method, *Chem. Phys. Lett.*, 409 (2005) 208–211.
19. T. Torimoto, S. Nagakubo, M. Nishizawa, H. Yoneyama, Photo-electrochemical properties of size-quantized CdS thin films prepared by an electrochemical method, *Langmuir*, 14 (1998) 7077–7081.
20. D.S. Zhang, J.A. Downing, F.J. Knorr, J.L. McHale, Room-temperature preparation of nanocrystalline TiO₂ films and the influence of surface properties on dye-sensitized solar energy conversion, *J. Phys. Chem. B*, 110 (2006) 21890–21898.
21. Y. Hamasaki, S. Ohkubo, K. Murakami, H. Sei, G. Nogami, Photoelectrochemical properties of anatase and rutile films prepared by the sol–gel method, *J. Electrochem. Soc.*, 141 (1994) 660–663.
22. J. Nowontny, *Oxide Semiconductors for Solar Energy Conversion: Titanium Dioxide*, 2012, CRC Press, New York, 394.
23. V.C. Tung, J.H. Huang, J. Kim, A.J. Smith, C.W. Chu, J. Huang, Towards solution processed all-carbon solar cells, *Energy Environ. Sci.*, 5 (2012) 7810–7818.
24. G.D. Scholes, G.R. Fleming, A. Olaya-Castro, R. van Grondelle, Lessons from nature about solar light harvesting, *Nat. Chem.*, 3 (2011) 763–774.
25. F.M. Pesci, A.J. Cowan, B.D. Alexander, J.R. Durrant, D.R. Klug, Charge carrier dynamics on mesoporous WO(3) during water splitting, *J. Phys. Chem. Lett.*, 2 (2011) 1900–1903.
26. W.H. Leng, P.R.F. Barnes, M. Juozapavicius, B.C. O'Regan, J.R. Durrant, Electron diffusion length in mesoporous nanocrystalline TiO(2) photoelectrodes during water oxidation, *J. Phys. Chem. Lett.*, 1 (2010) 967–972.
27. A. Thibert, F.A. Frame, E. Busby, M.A. Holmes, F.E. Osterloh, D.S. Larsen, Sequestering high-energy electrons to facilitate photocatalytic hydrogen generation in CdSe/CdS nanocrystals, *J. Phys. Chem. Lett.*, 2 (2011) 2688–2694.
28. K.R. Gopidas, M. Bohorquez, P.V. Kamat, Photoelectrochemistry in semiconductor particulate systems. 16. Photophysical and photochemical aspects of coupled semiconductors. Charge-transfer processes in colloidal CdS-TiO₂ and CdS-AgI systems, *J. Phys. Chem.*, 94 (1990) 6435–6440.
29. M.A. Fox, B. Lindig, C.C. Chen, Transients generated upon photolysis of colloidal TiO₂ in acetonitrile containing organic redox couples, *J. Am. Chem. Soc.*, 104 (1982) 5828–5829.

30. C. Arbour, D.K. Sharma, C.H. Langford, Electron trapping in colloidal TiO₂ photocatalysts: 20ps to 10ns kinetics, in V. Balzani, S. Campagna (eds), *Photochemistry and Photophysics of Coordination Compounds*, 1987, Springer Verlag Berlin, 277–283.
31. D.P.J. Colombo, R.M. Bowman, Femtosecond diffuse reflectance spectroscopy of TiO₂ powders, *J. Phys. Chem.*, 99 (1995) 11752–11756.
32. N. Serpone, D. Lawless, R. Khairutdinov, E. Pelizzetti, Subnanosecond relaxation dynamics in TiO₂ colloidal sols (particle sizes $R_p = 1\text{--}13.4\text{ nm}$). Relevance to heterogeneous photocatalysis, *J. Phys. Chem.*, 99 (1995) 16655–16661.
33. D.P.J. Colombo, K.A. Rousal, J. Saeh, D.E. Skinner, R.M. Bowman, Femtosecond study of the size-dependent charge carrier dynamics in ZnO nanocluster solutions, *Chem. Phys. Lett.*, 232 (1995) 207–214.
34. D.P.J. Colombo, R.M. Bowman, Does interfacial charge transfer compete with charge carrier recombination? Femtosecond diffuse reflectance investigation of TiO₂ nanoparticles, *J. Phys. Chem.*, 100 (1996) 18445–18449.
35. A. Furube, T. Asahi, H. Masuhara, H. Yamashita, M. Anpo, Femtosecond diffuse reflectance spectroscopy on some standard TiO₂ powder catalysts, *Chem. Lett.*, 35 (1997) 735–736.
36. J.H. Hodak, I. Martini, G.H. Hartland, Spectroscopy and dynamics of nanometer-sized noble metal particles, *J. Phys. Chem. B*, 102 (1998) 6958–6967.
37. P.A. Sant, P.V. Kamat, Inter-Particle Electron Transfer between size-quantized CdS and TiO₂ semiconductor nanoclusters, *Phys. Chem. Chem. Phys.*, 4 (2002) 198–203.
38. A. Henglein, Small-particle research: Physicochemical properties of extremely small colloidal metal and semiconductor particles, *Chem. Rev.*, 89 (1989) 1861–1873.
39. A. Henglein, Physicochemical properties of small metal particles in solution: ‘Microelectrode’ reactions, chemisorption, composite metal particles, and the atom-to-metal transition, *J. Phys. Chem.*, 97 (1993) 5457–5471.
40. P.V. Kamat, Photophysical, photochemical and photocatalytic aspects of metal nanoparticles, *J. Phys. Chem. B*, 106 (2002) 7729–7744.
41. A. Kudo, Y. Miseki, Heterogeneous photocatalyst materials for water splitting, *Chem. Soc. Rev.*, 28 (2009) 253–278.
42. M. Matsumura, Y. Saho, H. Tsubomura, Photocatalytic hydrogen production from solutions of sulfite using platinized cadmium sulfide powder, *J. Phys. Chem.*, 87 (1983) 3807–3808.
43. Z. Jin, Q. Li, X. Zheng, C. Xi, C. Wang, H. Zhang, L. Feng, H. Wang, Z. Chen, Z. Jiang, Surface properties of Pt-CdS and mechanism of photocatalytic dehydrogenation of aqueous alcohol, *J. Photochem. Photobiol. A*, 71 (1990) 85–96.
44. Y. Nosaka, K. Yamaguchi, A. Kuwabara, H. Miyama, R. Baba, A. Fujishima, Colloidal CdS-Pt photocatalyst stabilized by pendant viologen polymer for photoinduced electron transfer and hydrogen evolution, *J. Photochem. Photobiol. A*, 64 (1992) 375–382.
45. J. Yoshimura, A. Kudo, A. Tanaka, K. Domen, K. Maruya, T. Onishi, H₂ evolution caused by electron transfer between different semiconductors under visible light irradiation, *Chem. Phys. Lett.*, 147 (1988) 401–404.
46. V.N. Parmon, Photoproduction of hydrogen – An overview of modern trends, *Adv. Hydrogen Energy*, 8 (1990) 801–813.

47. T. Uchihara, H. Abe, M. Matsumura, H. Tsubomura, Photocatalytic hydrogen evolution from aqueous solutions of sodium sulfite using platinum-loaded $\text{CdS}_{1-x}\text{Se}_x$ mixed crystal powder, *Bull. Chem. Soc. Jpn.*, 62 (1989) 1042–1046.
48. T. Uchihara, M. Matsumura, A. Yamamoto, H. Tsubomura, Effect of platinum loading on the photocatalytic activity and luminescence of cadmium sulfide powder, *J. Phys. Chem.*, 93 (1989) 5870–5874.
49. T. Dittrich, A. Belaidi, A. Ennaoui, Concepts of inorganic solid-state nanostructured solar cells, *Sol. Energy Mater. Sol. Cells*, 95 (2011) 1527–1536.
50. P.V. Kamat, Manipulation of charge transfer across semiconductor interface. A criterion that cannot be ignored in photocatalyst design, *J. Phys. Chem. Lett.*, 3 (2012) 663–672.
51. E. Garnett, P. Yang, Light trapping in silicon nanowire solar cells, *Nano Lett.*, 10 (2010) 1082–1087.
52. E. Yabionovitch, Statistical ray optics, *J. Opt. Soc. Am.*, 72 (1982) 899–907.
53. Z. Fan *et al.*, Three-dimensional nanopillar-array photovoltaics on low-cost and flexible substrates, *Nat. Mater.*, 8 (2009) 648–653.
54. P.V. Kamat, Capturing hot electrons, *Nat. Chem.*, 2 (2010) 809–810.
55. J. Ungelenk, V. Haug, A. Quintilla, E. Ahiswede, CnInSe_2 low-cost thin-film solar cells made from commercial elemental metallic nanoparticles, *Physica Status Solidi (RRL)*, 4 (2010) 58–60.
56. I. Gur, N.A. Fromer, M.I. Geier, A.P. Alivisatos, Air-stable all-inorganic nanocrystal solar cell processed from solution, *Science*, 310 (2005) 462–465.
57. Q. Guo, S.J. Kim, M. Kar, W.M. Shafarman, R.W. Birkmire, E.A. Stach, R. Agrawal, H.W. Hillhouse, Development of CuInSe_2 nanocrystal and nanoring inks for low-cost solar cells, *Nano Lett.*, 8 (2008) 2982–2987.
58. G.I. Koleilat, L. Levina, H. Shukla, S.H. Myrskog, S. Hinds, A.G. Pattantyus-Abraham, E.H. Sargent, Efficient, stable infrared photovoltaics based on solution-cast colloidal quantum dots, *ACS Nano*, 2 (2008) 833–840.
59. R. Narayanan, M. Deepa, A.K. Srivastava, Nanoscale connectivity in a TiO_2/CdSe quantum dots/functionalized graphene oxide nanosheets/Au nanoparticles composite for enhanced photoelectrochemical solar cell performance, *Phys. Chem. Chem. Phys.*, 14 (2012) 767–778.
60. B.E. Hardin, H.J. Snaith, M.D. McGehee, The renaissance of dye-sensitized solar cells, *Nat. Photonics*, 6 (2012) 162–169.
61. M.I. Asghar *et al.*, Review of stability for advanced dye solar cells, *Energy Environ. Sci.*, 3 (2010) 418–426.
62. A. Vomiero, I. Concina, E. Comini, C. Soldano, M. Ferroni, G. Faglia, G. Sberveglieri, One-dimensional nanostructured oxides for thermoelectric applications and excitonic solar cells, *Nano Energy*, 1 (2012) 372–390.
63. H. Zheng, Y. Tachibana, K. Kalantar-zadeh, Dye-sensitized solar cells based on WO_3 , *Langmuir*, 26 (2010) 19148–19152.
64. J.J. Jasieniak, J. Seifert, J. Jo, T. Mates, A.J. Heeger, A solution-processed MoO_x anode interlayer for use within organic photovoltaic devices, *Adv. Funct. Mater.*, 22 (2012) 2594–2605.
65. B.E. Hardin *et al.*, High excitation transfer efficiency from energy relay dyes in dye-sensitized solar cells, *Nano Lett.*, 10 (2010) 3077–3083.
66. J. Melas-Kyriazi *et al.*, The effect of hole transport material pore filling on photovoltaic performance in solid-state dye-sensitized solar cells, *Adv. Eng. Mater.*, 1 (2011) 407–414.

67. Y.Y. Dou, G.R. Li, J. Song, X.P. Gao, Nickel phosphide-embedded graphene as counter electrode for dye-sensitized solar cells, *Phys. Chem. Chem. Phys.*, 14 (2012) 1339–1342.
68. A.Y. Anderson, P.R.F. Barnes, J.R. Durrant, B.C. O'Regan, Quantifying regeneration in dye-sensitized solar cells, *J. Phys. Chem. C*, 115 (2011) 2439–2447.
69. I. Chung, B. Lee, J. He, R.P.H. Chang, M.G. Kanatzidis, All-solid-state dye-sensitized solar cells with high efficiency, *Nature*, 486 (2012) 486–490.
70. X. Wang, L. Zhi, K. Mullen, Transparent, conductive graphene electrodes for dye-sensitized solar cells, *Nano Lett.*, 8 (2008) 232–327.
71. B. O'Regan, M. Gratzel, A low cost high efficiency solar cell based on dye sensitized colloidal TiO₂ films, *Nature*, 353 (1991) 737–740.
72. A. Ennaoui, S. Fiechter, Ch. Pettenkofer, N. Alonso-ante, K. Bükler, M. Bronold, Ch. Höpfner, H. Tributsch, Iron disulfide for solar energy conversion, *Sol. Energy Mater. Sol. Cells*, 29 (1993) 289–370.
73. J. Drechsel, B. Männig, F. Kozłowski, M. Pfeiffer, K. Leo, H. Hoppe, Efficient organic solar cells on a double p–i–n architecture using doped wide-gap transport layers, *Appl. Phys. Lett.*, 86 (2005) 244102-1–244102-3.
74. K.W. Johnston, A.G. Pattantyus-Abraham, J.P. Clifford, S.H. Myrskog, S. Hoogland, H. Shukla, E.J.D. Klem, L. Levina, E.H. Sargent, Efficient Schottky-quantum-dot photovoltaics: The roles of depletion, drift and diffusion, *Appl. Phys. Lett.*, 92 (2008) 122111-1–122111-3.
75. C. Herzog, A. Belaidi, A. Ogacho, Th. Dittrich, Inorganic solid state solar cell with ultra-thin nanocomposite absorber based on nanoporous TiO₂ and In₂S₃, *Energy Environ. Sci.*, 2 (2009) 962–964.
76. A.G. Pattantyus-Abraham, I.J. Kramer, A.R. Barkhouse, X. Wang, G. Konstantatos, R. Debnath, L. Levina, I. Rabe, M.K. Nazeeruddin, M. Grätzel, E.H. Sargent, Depleted-heterojunction colloidal quantum dot solar cells, *ACS Nano*, 4 (2010) 3374–3380.
77. K. Shankar, X. Feng, C.A. Grimes, Enhanced harvesting of red photons in nanowire solar cells: Evidence of resonance energy transfer, *ACS Nano*, 3 (2009) 788–794.
78. N.J. Cherepy, G.P. Smestad, M. Grätzel, J.Z. Zhang, Ultrafast electron injection: implications for a photoelectrochemical cell utilizing an anthocyanin dye-sensitized TiO₂ nanocrystalline electrode, *J. Phys. Chem. B*, 101 (1997) 9342–9351.
79. M.K. Nazeeruddin, P. Pechy, T. Renouard, S.M. Zakeeruddin, R. Humphry-Baker, P. Comte, P. Liska, L. Cevey, E. Costa, V. Shklover, L. Spiccia, G.B. Deacon, C.A. Bignozzi, M. Grätzel, Engineering of efficient panchromatic sensitizers for nanocrystalline TiO₂-based solar cells, *J. Am. Chem. Soc.*, 123 (2001) 1613–1624.
80. I. Robel, V. Subramanian, M.K. Kuno, P.V. Kamat, Quantum dot solar cells. Harvesting light energy with CdSe nanocrystals molecularly linked to mesoscopic TiO₂ films, *J. Am. Chem. Soc.*, 128 (2006) 2385–2393.
81. T. Lindgren, J.M. Mwabora, E. Avendano, J. Jonsson, A. Hoel, C.G. Granqvist, S.E. Lindquist, Photoelectrochemical and optical properties of nitrogen doped titanium dioxide films prepared by reactive DC magnetron sputtering, *J. Phys. Chem. B*, 107 (2003) 5709–5716.
82. M.G. Thomas, H.N. Post, R. DeBlasio, Photovoltaic systems: an end-of-millennium review, *Prog. Photovoltaics*, 7 (1999) 1–19.

83. M. Grätzel, Dye-sensitized solid-state heterojunction solar cells, *MRS Bull.*, 30 (2005) 23–27.
84. C. Chou, Y. Lin, R. Yang, K. Liu, Preparation of TiO₂/NiO composite particles and their applications in dye-sensitized solar cells, *Adv. Power Techn.*, 22 (2011) 31–42.
85. N. Chandrasekharan, P.V. Kamat, Improving the photoelectrochemical performance of nanostructured TiO₂ films by adsorption of gold nanoparticles, *J. Phys. Chem. B*, 104 (2000) 10851–10857.
86. V. Subramanian, E.E. Wolf, P.V. Kamat, Semiconductor–metal composite nanostructures. To what extent do metal nanoparticles improve the photocatalytic activity of TiO₂ films?, *J. Phys. Chem. B*, 105 (2001) 11439–11446.
87. K. Sayama, S. Tsukagoshi, K. Hara, Y. Ohga, A. Shinpou, Y. Abe, S. Suga, H. Arakawa, Photoelectrochemical properties of J aggregates of benzothiazole merocyanine dyes on a nanostructured TiO₂ film, *J. Phys. Chem. B*, 106 (2002) 1363–1371.
88. C. Nasr, P.V. Kamat, S. Hotchandani, Photoelectrochemistry of composite semiconductor thin films. Photosensitization of the SnO₂/TiO₂ coupled system with a ruthenium polypyridyl complex, *J. Phys. Chem. B*, 102 (1998) 10047–10056.
89. V. Subramanian, E.E. Wolf, P.V. Kamat, Influence of metal/metal–ion concentration on the photocatalytic activity of TiO₂–Au composite nanoparticles, *Langmuir*, 19 (2003) 469–474.
90. N.R. de Tacconi, M. Mrkic, K. Rajeshwar, Photoelectrochemical oxidation of aqueous sulfite on Ni–TiO₂ composite film electrodes, *Langmuir*, 16 (2000) 8426–8431.
91. N.R. de Tacconi, C.A. Boyles, K. Rajeshwar, Surface morphology/composition and photoelectrochemical behavior of metal–semiconductor composite films, *Langmuir*, 16 (2000) 5665–5672.
92. R. Zhu, C.Y. Jiang, B. Liu, S. Ramakrishna, Highly efficient nanoporous TiO₂–polythiophene hybrid solar cells based on interfacial modification using a metal-free organic dye, *Adv. Mater.*, 21 (2009) 994–1000.
93. V. Subramanian, Nanostructured semiconductor composites for solar cells, *The Electrochem. Soc. Interface*, 16 (2007) 32–36.
94. L. Hu, S. Dai, J. Weng, S. Xiao, Y. Sui, Y. Huang, S. Chen, F. Kong, X. Pan, L. Liang, K. Wang, Microstructure design of nanoporous TiO₂ electrodes for dye-sensitized solar cell modules, *J. Phys. Chem. B*, 111 (2007) 358–362.
95. L. Grinis, S. Dor, A. Ofir, A. Zaban, Electrophoretic deposition and compression of titania nanoparticle films for dye-sensitized solar cells, *J. Photochem. Photobiol. A: Chem.*, 198 (2008) 52–59.
96. S. Tirosh, Th. Dittrich, A. Ofir, L. Grinis, A. Zaban, Influence of ordering in porous TiO₂ layers on electron diffusion, *J. Phys. Chem. B*, 110 (2006) 16165–16168.
97. A. Ofir, S. Dor, L. Grinis, A. Zaban, Th. Dittrich, J. Bisquert, Porosity dependence of electron percolation in nanoporous TiO₂ layers, *J. Chem. Phys.*, 128 (2008) 064703-1–064703-9.
98. S.A. Gavrilov, A.A. Dronov, V.I. Shevyakov, A.N. Belov, E.A. Poltoratskii, Ways to increase the efficiency of solar cells with extremely thin absorption layers, *Nanotech. Russ.*, 4 (2009) 237–243.

99. P. Zabel, Th. Dittrich, M. Funes, E.N. Durantini, L. Otero, Charge separation at Pd-porphyrin/TiO₂ interfaces, *J. Phys. Chem. C*, 113 (2009) 21090–21096.
100. C. Sahin, Th. Dittrich, C. Varlikli, S. Icli, M.Ch. Lux-Steiner, Role of side groups in pyridine and bipyridine ruthenium dye complexes for modulated surface photovoltage in nanoporous TiO₂, *Sol. Energy Mater. Sol. Cells*, 94 (2010) 686–690.
101. G. Larramona, C. Chone, A. Jacob, D. Sakakura, B. Delatouche, D. Pere, X. Cieren, M. Nagino, R. Bayon, Nanostructured photovoltaic solar cell of the type titanium dioxide, cadmium sulfide thin coating, and copper thiocyanate showing high quantum efficiency, *Chem. Mater.*, 18 (2006) 1688–1696.
102. R. Könenkamp, L. Dloczik, K. Ernst, C. Olesch, Nanostructures for solar cells with extremely thin absorbers, *Physica E*, 14 (2002) 219–223.
103. C.A. Grimes, G.K. Mor, *TiO₂ Nanotube Arrays: Synthesis, Properties and Applications*, 2009, Springer, Dordrecht, Heidelberg, London, New York.
104. A. Chicov, P. Schmuki, Self-ordering electrochemistry: a review on growth and functionality of TiO₂ nanotubes and other self-aligned MOx structures, *Chem. Commun.*, 23 (2009) 2791–2808.
105. G.K. Mor, K. Shankar, M. Paulose, O.K. Varghese, C.A. Grimes, Use of highly-ordered TiO₂ nanotube arrays in dye-sensitized solar cells, *Nano Lett.*, 6 (2006) 215–218.
106. J.R. Jennings, A. Chicov, L.M. Peter, P. Schmuki, A.B. Walker, Dye sensitized solar cells based on oriented TiO₂ nanotube arrays: transport, trapping, and transfer of electrons, *J. Am. Chem. Soc.*, 130 (2008) 13364–13372.
107. R. Hahn, T. Stergiopoulos, J.M. Macak, D. Tsoukleris, A.G. Kontos, S.P. Albu, D. Kim, A. Chicov, J. Kunze, P. Falaras, P. Schmuki, Efficient solar energy conversion using TiO₂ nanotubes produced by rapid breakdown anodization – a comparison, *Phys. Status Solidi (RRL)*, 1 (2007) 135–137.
108. M. Ye, X. Xin, C. Lin, High efficiency dye-sensitized solar cells based on hierarchically structured nanotubes, *Nano Lett.*, 11 (2011) 3214–3220.
109. B.H. Meekins, P.V. Kamat, Got TiO₂ nanotubes? Lithium ion intercalation can boost their photoelectrochemical performance, *ACS Nano*, 3 (2009) 3437–3446.
110. V. Galstyan, A. Vomiero, E. Comini, G. Faglia, G. Sberveglieri, TiO₂ nanotubular and nanoporous arrays by electrochemical anodization on different substrates, *RSC Advances*, 1 (2011) 1038–1044.
111. A. Vomiero, V. Galstyan, A. Braga, I. Concina, M. Brisotto, E. Bontempi, G. Sberveglieri, Flexible dye sensitized solar cells using TiO₂ nanotubes, *Energy Environ. Sci.*, 4 (2011) 3408–3413.
112. V. Galstyan, A. Vomiero, I. Concina, A. Braga, M. Brisotto, E. Bontempi, G. Faglia, G. Sberveglieri, Vertically aligned TiO₂ nanotubes on plastic substrates for flexible solar cells, *Small*, 7 (2011) 2437–2442.
113. A. Kongkanand, K. Tvrđy, K. Takechi, M. Kuno, P.V. Kamat, Quantum dot solar cells. Tuning photoresponse through size and shape control of CdSe–TiO₂ architecture, *J. Am. Chem. Soc.*, 130 (2008) 4007–4015.
114. D.R. Baker, P.V. Kamat, Photosensitization of TiO₂ nanostructures with CdS quantum dots: particulate versus tubular support architectures, *Adv. Funct. Mater.*, 19 (2009) 805–811.

115. A.B. Djurišić, A.M.C. Ng, X.Y. Chen, ZnO nanostructures for optoelectronics: Material properties and device applications, *Prog. Quant. Electron.*, 34 (2010) 191–259.
116. Z.L. Wang, Zinc oxide nanostructures: growth, properties and applications, *J. Physics: Condensed Matter.*, 16 (2004) R829–R858.
117. T. Tsubota, M. Ohtaki, K. Eguchi, H. Arai, Thermoelectric properties of Al-doped ZnO as a promising oxide material for high-temperature thermoelectric conversion, *J. Mater. Chem.*, 7 (1997) 85–90.
118. A. Valdes *et al.*, Solar hydrogen production with semiconductor metal oxides: new directions in experiment and theory, *Phys. Chem. Chem. Phys.*, 14 (2012) 49–70.
119. B. Cao, W. Cai, From ZnO nanorods to nanoplates: chemical bath deposition and surface-related emissions, *J. Phys. Chem. C*, 112 (2008) 680–685.
120. Q. Zhang, C.S. Dandeneau, X. Zhou, G. Cao, ZnO nanostructures for dye-sensitized solar cells, *Adv. Mater.*, 21 (2009) 4087–4108.
121. T. Pauporte, D. Lincot, Heteroepitaxial electrodeposition of zinc oxide on gallium nitride, *Appl. Phys. Lett.*, 75 (1998) 3817–3819.
122. J. Elias, R. Tena-Zaera, C. Lévy-Clément, Electrodeposition of ZnO nanowires with controlled dimensions for photovoltaic applications: role of buffer layer, *Thin Solid Films*, 515 (2007) 8553–8557.
123. R. Tena-Zaera, J. Elias, G. Wang, C. Lévy-Clément, Role of chloride ions on electrochemical deposition on ZnO nanowire arrays from O₂ reduction, *J. Phys. Chem. C*, 111 (2007) 16706–16711.
124. J. Elias, R. Tena-Zaera, C. Lévy-Clément, Effect of the chemical nature of the anions on the electrodeposition of ZnO nanowire arrays, *J. Phys. Chem. C*, 112 (2008) 5736–5741.
125. R. Tena-Zaera, J. Elias, C. Lévy-Clément, ZnO nanowire arrays: optical scattering and sensitization to solar light, *Appl. Phys. Lett.*, 93 (2008) 233119-1–233119-3.
126. J. Chen, L. Aé, C. Aichele, M.Ch. Lux-Steiner, High internal quantum efficiency ZnO nanorods prepared at low temperature, *Appl. Phys. Lett.*, 92 (2008) 161906-1–161906-3.
127. J.B. Baxter, E.S. Aydil, Dye-sensitized solar cells based on semiconductor morphologies with ZnO nanowires, *Sol. Energy Mater. Sol. Cells*, 90 (2006) 607–622.
128. A. Vomiero, I. Concina, M.M. Natile, E. Comini, G. Faglia, M. Ferroni, I. Kholmanov, G. Sberveglieri, ZnO/TiO₂ nanonetwork as efficient photoanode in excitonic solar cells, *Appl. Phys. Lett.*, 95 (2009) 193104.
129. A. Yella, H.W. Lee, H.N. Tsao, C. Yi, A.K. Chandiran, M.K. Nazeeruddin, E.W.G. Diau, C.Y. Yeh, S.M. Zakeeruddin, M. Grätzel, Porphyrin-sensitized solar cells with cobalt (II/III) – based redox electrolyte exceed 12 percent efficiency, *Science*, 334 (2011) 629–634.
130. S.H. Ko, D. Lee, H.W. Kang, K.H. Nam, J.Y. Yeo, S.J. Hong, C.P. Grigoropoulos, H.J. Sung, Nanoforest of hydrothermally grown hierarchical ZnO nanowires for a high efficiency dye-sensitized solar cell, *Nano Lett.*, 11 (2011) 666–671.
131. G.K. Mor, O.K. Varghese, M. Paulose, K. Shankar, C.A. Grimes, A review on highly ordered, vertically oriented TiO₂ nanotube arrays: Fabrication, material

- properties, and solar energy applications, *Sol. Energy Mater. Sol. Cells*, 90 (2006) 2011–2075.
132. V.R. Shinde, T.P. Gujar, T. Noda, D. Fujity, A. Vinu, M. Grandcolas, J. Ye, Growth of shape- and size-selective zinc oxide nanorods by a microwave-assisted chemical bath deposition method: effect on photocatalysis properties, *Chem. Eur. J.*, 16 (2010) 10569–10575.
 133. M. Krunks, A. Katerski, T. Dedova, I. Oja Acik, A. Mere, Nanostructured solar cell based on spray pyrolysis deposited ZnO nanorod array, *Sol. Energy Mater. Sol. Cells*, 92 (2008) 1016–1019.
 134. J. Tornow, K. Schwarzburg, Transient electrical response of dye-sensitized ZnO nanorod solar cells, *J. Phys. Chem. C*, 111 (2007) 8692–8698.
 135. I. Mora-Seró, F. Fabragat-Santiago, B. Denier, J. Bisquert, R. Tena-Zaera, J. Elias, C. Lévy-Clément, Determination of carrier density of ZnO nanowires by electrochemical techniques, *Appl. Phys. Lett.*, 89 (2006) 203117-1–203117-3.
 136. N. Memarian, I. Concina, A. Braga, S.M. Rozati, A. Vomiero, G. Sberveglieri, Hierarchically assembled ZnO nanocrystallites for high-efficiency dye-sensitized solar cells, *Angew. Chemie – Int. Ed.*, 50 (2011) 12321–12325.
 137. I. Repins, M.A. Contreras, B. Egaas, C. DeHart, J. Scharf, C.L. Perkins, B. To, R. Noufi, 19.9 %-efficient ZnO/CdS/CuInGaSe₂ solar cell with 81.2 % fill factor, *Prog. in Photovoltaics: Res. Appl.*, 16 (2008) 235–239.
 138. O. Roussel, O. Ramdani, E. Chassaing, P.P. Grand, M. Lamirand, A. Etcheberry, O. Kerrec, J.F. Guillemoles, D. Lincot, First stages of CuInSe₂ electrodeposition from Cu(II)-In(III)-Se(IV) acidic solutions on polycrystalline Mo films, *J. Electrochem. Soc.*, 155 (2008) D141–D147.
 139. S. Aksu, J. Wang, B.M. Basol, Electrodeposition of In–Se and Ga–Se thin films for preparation of CIGS solar cells, *Electrochem. Solid-State Lett.*, 12 (2009) D33–D35.
 140. Q. Huang, K. Reuter, S. Amhed, L. Deligianni, L.T. Romankiw, S. Jaime, P.P. Grand, V. Charrier, Electrodeposition of indium on copper for CIS and CIGS solar cell applications, *J. Electrochem. Soc.*, 158 (2009) D57–D61.
 141. I. Kang, W. Wise, Electronic structure and optical properties of PbS and PbSe quantum dots, *J. Opt. Soc. Am. B*, 14 (1997) 1632–1646.
 142. A. Shabaev, A.L. Efros, A.J. Nozik, Multiexciton generation by a single photon in nanocrystals, *Nano Lett.*, 6 (2006) 2856–2863.
 143. A. Luque, A. Martí, A.J. Nozik, Solar cells based on quantum dots: multiple exciton generation and intermediate bands, *MRS Bull.*, 32 (2007) 236–241.
 144. S. Rühle, M. Shalom, A. Zaban, Quantum-dot-sensitized solar cells, *Phys. Chem. Chem. Phys.*, 11 (2010) 2290–2304.
 145. R. Vogel, P. Hoyer, H. Weller, Quantum-sized PbS, Ag₂S, Sb₂S₃, and Bi₂S₃ particles as sensitizers for various nanoporous wide-bandgap semiconductors, *J. Phys. Chem.*, 98 (1994) 3183–3188.
 146. I. Mora-Sero, J. Bisquert, Th. Dittrich, A. Belaidi, A.S. Susha, A.L. Rogach, Photosensitization of TiO₂ layers with CdSe quantum dots: correlation between light absorption and photoinjection, *J. Phys. Chem. C*, 111 (2007) 14889–14892.
 147. D. Gross, A.S. Susha, T.A. Klar, E. da Como, A.L. Rogach, J. Feldmann, Charge separation in type II tunneling structures of close-packed CdTe and CdSe nanocrystals, *Nano Lett.*, 8 (2008) 1482–1485.

148. D. Gross, I. Mora-Seró, Th. Dittrich, A. Belaidi, C. Mauser, A.J. Houtepen, E. da Como, A.L. Rogach, J. Feldmann, Charge separation in type II tunneling multilayered structures of CdTe and CdSe nanocrystals directly proven by surface photovoltage spectroscopy, *J. Am. Chem. Soc.*, 132 (2010) 5981–5983.
149. T.Z. Markus, S. Itzhakov, Y.I. Alkotzer, D. Cahen, G. Hodes, D. Oron, R. Naaman, Energetics of CdSe quantum dots adsorbed on TiO₂, *J. Phys. Chem. C*, 115 (2011) 13236–13241.
150. I. Mora-Seró, S. Giménez, F. Fabregat-Santiago, R. Gomez, Q. Shen, T. Toyoda, J. Bisquert, Recombination in quantum dot sensitized solar cells, *Acc. Chem. Res.*, 42 (2009) 1848–1857.
151. D. Gross *et al.*, Charge separation in type II tunnelling multilayered structures of CdTe and CdSe nanocrystals directly proven by surface photovoltage spectroscopy, *J. Am. Chem. Soc.*, 132 (2010) 5981–5983.
152. L. Jdira, P. Liljeroth, E. Stoffels, D. Vanmaekelbergh, S. Speller, Size-dependent single-particle energy levels and interparticle Coulomb interactions in CdSe quantum dots measured by scanning tunnelling spectroscopy, *Phys. Rev. B*, 73 (2006), 115305-1–115305-6.
153. M.V. Artemyev, U. Woggon, H. Jaschinski, L.I. Gurinovich, S.V. Gaponenko, Spectroscopic study of electronic states in an ensemble of close-packed CdSe nanocrystals, *J. Phys. Chem. B*, 104 (2000) 11617–11621.
154. H. Chen, W. Fu, H. Yang, P. Sun, Y. Zhang, L. Wang, W. Zhao, X. Zhou, H. Zhao, Q. Jing, X. Qi, Y. Li, Photosensitization of TiO₂ nanorods with CdS quantum dots for photovoltaic devices, *Electrochim. Acta*, 56 (2010) 919–924.
155. X.F. Gao, H.B. Li, W.T. Sun, Q. Chen, F.Q. Tang, L.M. Peng, CdTe quantum dots-sensitized TiO₂ nanotube array photoelectrodes, *J. Phys. Chem. C*, 113 (2009) 7531–7535.
156. H. Zhang, X. Quan, S. Chen, H. Yu, N. Ma, ‘Mulberry-like’ CdSe nanoclusters anchored on TiO₂ nanotube arrays: a novel architecture with remarkable photoelectrochemical performance, *Chem. Mater.*, 21 (2009) 3090–3095.
157. R.B. Schoolar, J.R. Dixon, Optical constants of lead sulfide in the fundamental absorption edge region, *Phys. Rev.*, 137 (2A) (1965) 667–670.
158. W.W. Scanlon, Recent advances in the optical and electronic properties of PbS, PbSe, PbTe and their alloys, *J. Phys. Chem. Solids*, 8 (1959) 423–428.
159. K.W. Johnston, A.G. Pattantyus-Abraham, J.P. Clifford, S.H. Myrskog, S. Hoogland, H. Shukla, E.J.D. Klem, L. Levina, E.H. Sargent, Efficient Schottky-quantum-dot photovoltaics: the roles of depletion, drift and diffusion, *Appl. Phys. Lett.*, 92 (2008) 122111-1–122111-3.
160. J.M. Luther, M. Law, Q. Song, C.L. Perkins, M.C. Beard, A.J. Nozik, Structural, optical, and electrical properties of self-assembled films of PbSe nanocrystals treated with 1,2-ethanedithiol, *ACS Nano*, 2 (2008) 271–280.
161. C.-Y. Kuo, M.-S. Su, Y.-C. Hsu, H.-N. Lin, K.-H. Wei, An organic hole transport layer enhances the performance of colloidal PbSe quantum dot photovoltaic devices, *Adv. Funct. Mater.*, 20 (2010) 3555–3560.
162. E.J.D. Klem, H. Shukla, S. Hinds, D.D. MacNeil, L. Levina, E.H. Sargent, Impact of dithiol treatment and air annealing on the conductivity, mobility, and hole density in PbS colloidal quantum dot solids, *Appl. Phys. Lett.*, 92 (2008) 212105-1–212105-3.

163. R. Debnath, M.T. Greiner, I.J. Kramer, A. Fischer, J. Tang, D.A.R. Barkhouse, X. Wang, L. Levina, Z.-H. Lu, E.H. Sargent, Depleted-heterojunction colloidal quantum dot photovoltaics employing low-cost electrical contacts, *Appl. Phys. Lett.*, 97 (2010) 023109-1–023109-3.
164. A.G. Pattantyus-Abraham, I.J. Kramer, A.R. Barkhouse, X. Wang, G. Konstantatos, R. Debnath, L. Levina, I. Rabe, M.K. Nazeeruddin, M. Grätzel, E.H. Sargent, Depleted-heterojunction colloidal quantum dot solar cells, *ACS Nano*, 4 (2010) 3374–3380.
165. J.M. Luther, J. Gao, M.T. Lloyd, O.E. Semonin, M.C. Beard, A.J. Nozik, Stability assessment on a 3% bilayer PbS/ZnO quantum dot heterojunction solar cell, *Adv. Mater.*, 22 (2010) 3704–3707.
166. M. Brumer, A. Kigel, L. Amirav, A. Sashchiuk, O. Solomesch, N. Tessler, E. Lifshitz, PbSe/PbS and PbSe/PbSe_{1-x} core/shell nanocrystals, *Adv. Funct. Mater.*, 15 (2005) 1111–1116.
167. I. Mora-Seró, Th. Dittrich, A.S. Susha, A.L. Rogach, J. Bisquert, Large improvement of electron extraction from CdSe quantum dots into a TiO₂ thin layer by N3 dye coadsorption, *Thin Solid Films*, 516 (2008) 6994–6998.
168. I. Mora-Seró, S. Giménez, T. Moehl, F. Fabregat-Santiago, T. Lana-Villareal, R. Gómez, J. Bisquert, Factors determining the photovoltaic performance of a CdSe quantum dot sensitized solar cells: the role of the linker molecule and of the counter electrode, *Nanotechnology*, 19 (2008) 424007-1–424007-7.
169. M. Shalom, S. Rühle, I. Hod, S. Yahav, A. Zaban, Energy level alignment in CdS quantum dot sensitized solar cells using molecular dipoles, *J. Am. Chem. Soc.*, 131 (2009) 9876–9877.
170. W. Shockley, H.J. Queisser, Detailed balance limit of efficiency of *p-n* junction solar cells, *J. Appl. Phys.*, 32 (1961) 510–519.
171. A.J. Nozik, Quantum dot solar cells, *Physica E*, 14 (2002) 115–120.
172. V.I. Klimov, Detailed-balance power conversion limits of nanocrystal-quantum-dot solar cells in the presence of carrier multiplication, *Appl. Phys. Lett.*, 89 (2006) 123118.
173. C.Y. Chen *et al.*, Highly efficient light-harvesting ruthenium sensitizer for thin-film dye-sensitized solar cells, *ACS Nano*, 3 (2009) 3103–3109.
174. L. Rehm, G.L. McLendon, Y. Nagasawa, K. Yoshihara, J. Moser, M. Grätzel, Femtosecond electron-transfer dynamics at a sensitizing dye–semiconductor (TiO₂) interface, *J. Phys. Chem.*, 100 (1996) 9577–9578.
175. A. Hagfeldt, M. Grätzel, Molecular photovoltaics, *Acc. Chem. Res.*, 33 (2000) 269–277.
176. S. Yang, D. Prendergast, J.B. Neaton, Tuning semiconductor band edge energies for solar photocatalysis via surface ligand passivation, *Nano Lett.*, 12 (2012) 383–388.
177. J. Kavan, M. Grätzel, S.E. Gilbert, C. Klemenz, H.J. Scheel, Electrochemical and photoelectrochemical investigation of single-crystal anatase, *J. Am. Chem. Soc.*, 118 (1996) 6716–6723.
178. A. Zaban, A. Meier, B.A. Gregg, Electric potential distribution and short-range screening in nanoporous TiO₂ electrodes, *J. Phys. Chem. B*, 101 (1997) 7985–7990.
179. G. Oskam, B.V. Bergeron, G.J. Meyer, P.C. Searson, ChemInform abstract: pseudohalogens for dye-sensitized TiO₂ photoelectrochemical cells, *J. Phys. Chem.*, 105 (2001) 6867–6873.

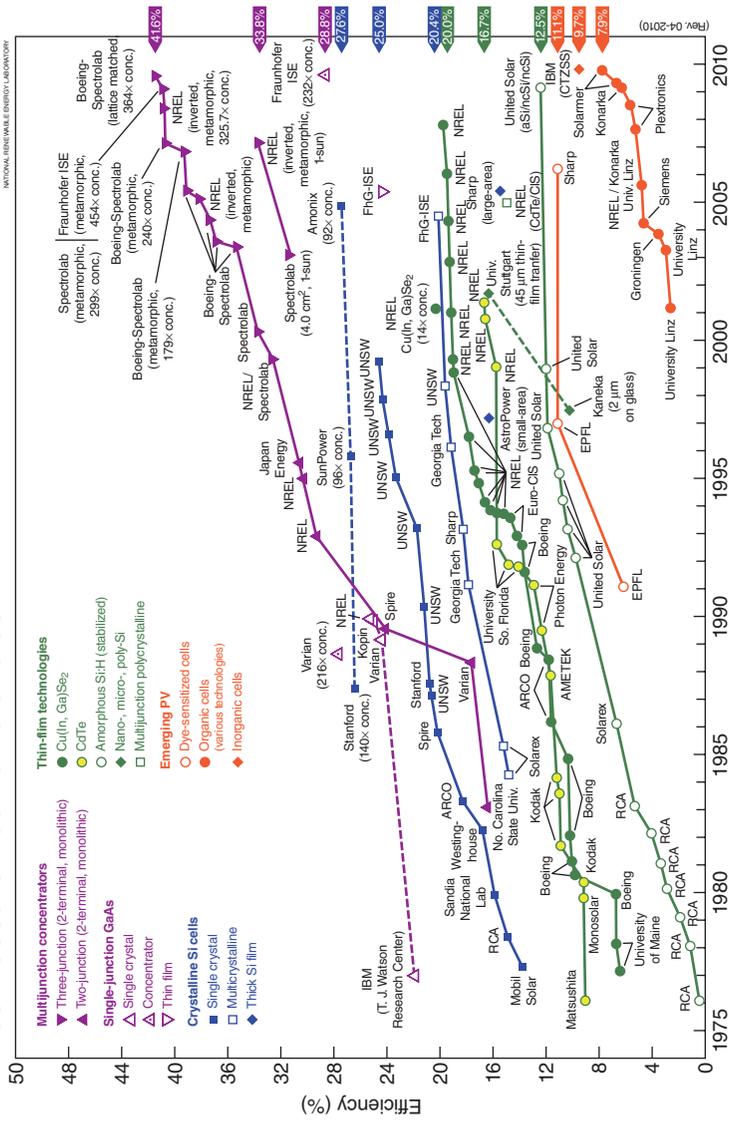
180. F.S. Cai, J. Chen, R.S. Xu, Porous acetylene-black spheres as the cathode materials of dye-sensitized solar cells, *Chem. Lett.*, 35 (2006) 1266–1267.
181. X. Miao, S. Tongay, M.K. Petterson, K. Berke, A.G. Rinzler, B.R. Appleton, A.F. Hebard, High efficiency graphene solar cells by chemical doping, *Nano Lett.*, 12 (2012) 2745–2750.
182. Y.Y. Dou, G.R. Li, J. Song, X.P. Gao, Nickel phosphide-embedded graphene as counter electrode for dye-sensitized solar cells, *Phys. Chem. Chem. Phys.*, 14 (2012) 1339–1342.
183. J. Burschka, A. Dualeh, F. Kessler, E. Baranoff, N.-L. Cevey-Ha, C. Yi, M.K. Nazeeruddin, M. Grätzel, Tris(2-(1*H*-pyrazol-1-yl)pyridine)cobalt(III) as p-type dopant for organic semiconductors and its application in highly efficient solid-state dye-sensitized solar cells, *J. Am. Chem. Soc.*, 133 (2011) 18042–180045.
184. L. Schmidt-Mende, S.M. Zakeeruddin, M. Grätzel, Efficiency improvement in solid-state-dye-sensitized photovoltaics with an amphiphilic ruthenium-dye, *Appl. Phys. Lett.*, 86 (2005) 013504.
185. H.J. Snath, A.J. Moule, C. Klein, K. Meerholz, R.H. Friend, M. Grätzel, Efficiency enhancements in solid-state hybrid solar cells via reduced charge recombination and increased light capture, *Nano Lett.*, 7 (2007) 3372–3376.
186. H.J. Snath, L. Schmidt-Mende, Advances in liquid-electrolyte and solid-state dye-sensitized solar cells, *Adv. Mater.*, 19 (2007) 3187–3200.
187. L. Schmidt-Mende, M. Grätzel, TiO₂ pore-filling and its effect on the efficiency of solid-state dye-sensitized solar cells, *Thin Solid Films*, 500 (2006) 296–301.
188. J.E. Kroeze, N. Hirata, L. Schmidt-Mende, C. Orizu, S.D. Ogier, K. Carr, M. Grätzel, J.R. Durrant, Parameters influencing charge separation in solid-state dye-sensitized solar cells using novel hole conductors, *Adv. Funct. Mater.*, 16 (2006) 1832–1838.
189. H.J. Snath, H.-B. Robin, C. Peter, C. Ilkay, M.Z. Shaik, M. Grätzel, Charge collection and pore filling in solid-state dye-sensitized solar cells, *Nanotechnology*, 19 (2008) 424003–424015.
190. I.K. Ding, N. Tétreault, J. Brilllet, B.E. Hardin, E.H. Smith, S.J. Rosenthal, F. Sauvage, M. Grätzel, M.D. McGehee, Pore-filling of Spiro-OMeTAD in solid-state dye sensitized solar cells: quantification, mechanism, and consequences for device performance, *Adv. Funct. Mater.*, 19 (2009) 2431–2436.
191. J. Melas-Kyriazi, I.K. Ding, A. Marchioro, A. Punzi, B.E. Hardin, G.F. Burkhard, N. Tétreault, M. Grätzel, J.-E. Moser, M.D. McGehee, The effect of hole transport material pore filling on photovoltaic performance in solid-state dye-sensitized solar cells, *Adv. Energy Mater.*, 1 (2011) 407–414.
192. I.K. Ding, J. Melas-Kyriazi, N.-L. Cevey-Ha, K.G. Chittibabu, S.M. Zakeeruddin, M. Grätzel, M.D. McGehee, Deposition of hole-transport materials in solid-state dye-sensitized solar cells by doctor-blading, *Org. Electron.*, 11 (2010) 1217–1222.
193. T. Leijtens, I.K. Ding, T. Giovenzana, J.T. Bloking, M.D. McGehee, A. Sellinger, Hole transport materials with low glass transition temperatures and high solubility for application in solid-state dye-sensitized solar cells, *ACS Nano*, 6 (2012) 1455–1462.
194. M. Juozapavicius, B.C. O'Regan, A.Y. Anderson, J.V. Grazulevicius, V. Mimaite, Efficient dye regeneration in solid-state dye-sensitized solar cells fabricated with melt processed hole conductors, *Org. Electron.*, 13 (2012) 23–30.

195. X. Feng, K. Shankar, O.K. Varghese, M. Paulose, T.J. Latempa, C.A. Grimes, Vertically aligned single crystal TiO₂ nanowire arrays grown directly on transparent conducting oxide coated glass: synthesis details and applications, *Nano Lett.*, 8 (2008) 3781–3786.
196. B. Liu, E.S. Aydil, Growth of oriented single-crystalline rutile TiO₂ nanorods on transparent conducting substrates for dye-sensitized solar cells, *J. Am. Chem. Soc.*, 131 (2009) 3985–3990.
197. C. Xu, P. Shin, L. Cao, D. Gao, Preferential growth of long ZnO nanowire array and its application in dye-sensitized solar cells, *J. Phys. Chem. C*, 114 (2010) 125–129.
198. C. Xu, P.H. Shin, L. Cao, J. Wu, D. Gao, Ordered TiO₂ nanotube arrays on transparent conductive oxide for dye-sensitized solar cells, *Chem. Mater.*, 22 (2010) 143–148.
199. O.K. Varghese, M. Paulose, C.A. Grimes, Long vertically aligned titania nanotubes on transparent conducting oxide for highly efficient solar cells, *Nat. Nanotechnol.*, 4 (2009) 592–597.
200. X. Xin, J. Wang, W. Han, M. Ye, Z. Lin, Dye-sensitized solar cells based on a nanoparticle/nanotube bilayer structure and their equivalent circuit analysis, *Nanoscale*, 4 (2012) 964–969.
201. M. Wang, J. Bai, F. Le Formal, S.-J. Moon, L. Cevey-Ha, R. Humphry-Baker, C. Grätzel, S.M. Zakeeruddin, M.J. Grätzel, Solid-state dye-sensitized solar cells using ordered TiO₂ nanorods on transparent conductive oxide as photoanodes, *Phys. Chem. C*, 116 (2012) 3266–3273.
202. J.S. Bendall, L. Etgar, S.C. Tan, N. Cai, P. Wang, S.M. Zakeeruddin, M. Grätzel, M.E. Welland, An efficient DSSC based on ZnO nanowire photo-anodes and a new D- π -A organic dye, *Energy Environ. Sci.*, 4 (2011) 2903–2908.
203. L. Schmidt-Mende, J.E. Kroeze, J.R. Durrant, M.K. Nazeeruddin, M. Grätzel, Effect of hydrocarbon chain length of amphiphilic ruthenium dyes on solid-state dye-sensitized photovoltaics, *Nano Lett.*, 5 (2005) 1315–1320.
204. J. Burschka *et al.*, Tris(2-(1H-pyrazol-1-yl)pyridine)cobalt(III) as p-type dopant for organic semiconductors and its application in highly efficient solid-state dye-sensitized solar cells, *J. Am. Chem. Soc.*, 133 (2011) 18042–18045.
205. C. Xu, J. Wu, U.V. Desai, D. Gao, High-efficiency solid-state dye-sensitized solar cells based on TiO₂-coated ZnO nanowire arrays, *Nano Lett.*, 12 (2012) 2420–2424.
206. H.J. Snaith *et al.*, Charge collection and pore filling in solid-state dye-sensitized solar cells, *Nanotechnology*, 19 (2008) 424003.
207. J. Melas-Kyriazi *et al.*, The effect of hole transport material pore filling on photovoltaic performance in solid-state dye-sensitized solar cells, *Adv. Eng. Mater.*, 1 (2011) 407–414.
208. K. Keis, E. Magnusson, H. Lindström, S.E. Lindquist, A. Hagfeldt, A 5 % efficient photoelectrochemical solar cell based on nanostructured ZnO electrodes, *Sol. Energy Mater. Sol. Cells*, 73 (2002) 51–58.
209. E. Washizu, A. Yamamoto, Y. Abe, M. Kawamura, K. Sasaki, Optical and electrochromic properties of RF reactively sputtered WO₃ films, *Solid State Ionics*, 165 (2003) 175–180.
210. M.H. Yaacob, M. Breedon, K. Kalantar-zadeh, W. Wlodarski, Absorption spectral response of nanotextured WO₃ thin films with Pt catalyst towards H₂, *Sens. Actuators B: Chem.*, 137 (2009) 115–120.

211. M. Gillet, K. Aguir, C. Lemire, E. Gillet, K. Schierbaum, The structure and electrical conductivity of vacuum-annealed WO₃ thin films, *Thin Solid Films*, 467 (2004) 239–246.
212. C. Santato, M. Ulmann, J. Augustynski, Photoelectrochemical properties of nanostructured tungsten trioxide films, *J. Phys. Chem. B*, 105 (2001) 936–940.
213. H. Zheng, J.Z. Ou, M.S. Strano, R.B. Kaner, A. Mitchell, K. Kalantah-zadeh, Nanostructured tungsten oxide – properties, synthesis, and applications, *Adv. Funct. Mater.*, 21 (2011) 2175–2196.
214. A. Le Viet, R. Jose, M.V. Reddy, B.V.R. Chowdari, S. Ramakrishna, Nb₂O₅ photoelectrodes for dye-sensitized solar cells: Choice of the polymorph. *J. Phys. Chem. C*, 114 (2010) 21795–21800.
215. V. Thavasi, V. Renugopalakrishnan, R. Jose, S. Ramakrishna, Controlled electron injection and transport at materials interfaces in dye sensitized solar cells, *Mater. Sci. Eng. R-Reports*, 63 (2009) 81–99.
216. R. Jose, V. Thavasi, S. Ramakrishna, Metal oxides for dye-sensitized solar cells. *J. Am. Ceram. Soc.*, 92 (2009) 289–301.
217. P.V. Kamat, Photoinduced transformations in semiconductor-metal nanocomposite assemblies, *Pure Appl. Chem.*, 74 (2002) 1693–1706.
218. M.D. Wei, Z.M. Qi, M. Ichihara, H.S. Zhou, Synthesis of single-crystal niobium pentoxide nanobelts, *Acta Mater.*, 56 (2008) 2488–2494.
219. J.Z. Ou, R.A. Rani, M.H. Ham, Y. Zhang, H. Zheng, S. Sriram, M. Bhaskaran, K. Latham, S. Zhuiykov, R.B. Kaner, K. Kalantar-zadeh, Elevated temperature anodized Nb₂O₅: a photoanode material with exceptionally large photoconversion efficiencies, *ACS Nano*, 5 (2012) 4045–4053.
220. I. Sieber, H. Hildebrand, A. Friedrich, P. Schmuki, Formation of self-organized niobium porous oxide on niobium, *Electrochem. Commun.*, 7 (2005) 97–100.
221. J. Choi, J.H. Lim, J. Lee, K.J. Kim, Porous niobium oxide films prepared by anodization-annealing-anodization, *Nanotechnology*, 18 (2007) 055603.
222. M. Paulose *et al.* Anodic growth of highly ordered TiO₂ nanotube arrays to 134 um in length, *J. Phys. Chem. B*, 110 (2006) 16179–16184.
223. S. Wenham, Towards highly efficient solar cells, *Nat. Photonics*, 6 (2012) 136–137.
224. K. Kalyanasundaram, M. Grätzel, Applications of functionalized transition metal complexes in photonic and optoelectronic devices, *Coord. Chem. Rev.*, 177 (1998) 347–414.
225. H.J. Smith, Estimating the maximum attainable efficiency in dye-sensitized solar cells, *Adv. Funct. Mater.*, 20 (2010) 13–19.
226. A.S. Zoolfakar, R.A. Rani, A.J. Morfa, S. Balendhran, A.P. O’Mullane, S. Zhuiykov, K. Kalantar-zadeh, Enhancing the current density of electrodeposited ZnO-Cu₂O solar cells by engineering their heterointerfaces, *J. Mater. Chem.*, 22 (2012) 21767–21775.
227. M.I. Asgar *et al.*, Review of stability for advanced dye solar cells, *Energy Environ. Sci.*, 3 (2010) 418–426.
228. F.J. Uribe-Romo, W.R. Dichtel, Polymers stripped down, *Nat.: Chem.*, 4 (2012) 244–245.
229. G. Li, R. Zhu, Y. Yang, Polymer solar cells, *Nat.: Photonics*, 6 (2012) 153–161.
230. C. Law *et al.*, Water-based electrolytes for dye-sensitized solar cells. *Adv. Mater.*, 22 (2010) 4505–4509.

231. W. Gaynor, G.F. Burkhard, M.D. McGehee, P. Peumans, Smooth nanowire/polymer composite transparent electrodes, *Adv. Mater.*, 23 (2011) 2905–2910.
232. B.E. Hardin *et al.*, Laminating solution-processed silver nanowire mesh electrodes onto solid-state dye-sensitized solar cells, *Org. Electron.*, 12 (2011) 875–879.
233. J.J. Cid, Molecular cosensitization for efficient panchromatic dye-sensitized solar cells, *Angew. Chem. Int. Ed.*, 119 (2007) 8510–8514.
234. Q. Zhang, G. Cao, Nanostructured photoelectrodes for dye-sensitized solar cells, *Nano Today*, 6 (2011) 91–109.

Best research-cell efficiencies



(Ref. 04-2010)

Plate XIX (Chapter 6) Efficiency of the best laboratory solar cells summarized by the National Renewable Energy Laboratory in Golden, Colorado. (Reprinted from Ref. 10 with permission of the Electrochemical Society)

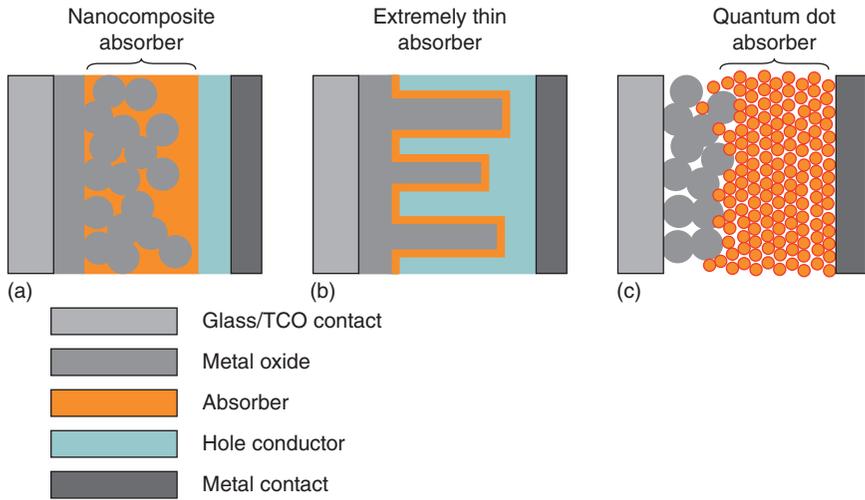


Plate XX (Chapter 6) Schematic cross-sections of inorganic nanostructured solar cells: (a) with ultrathin nanocomposite absorber; (b) extremely thin absorber; (c) quantum dot absorber. (Reprinted from Ref. 49 with permission from Elsevier Science)

Nanostructured semiconductor composites for solid oxide fuel cells (SOFCs)

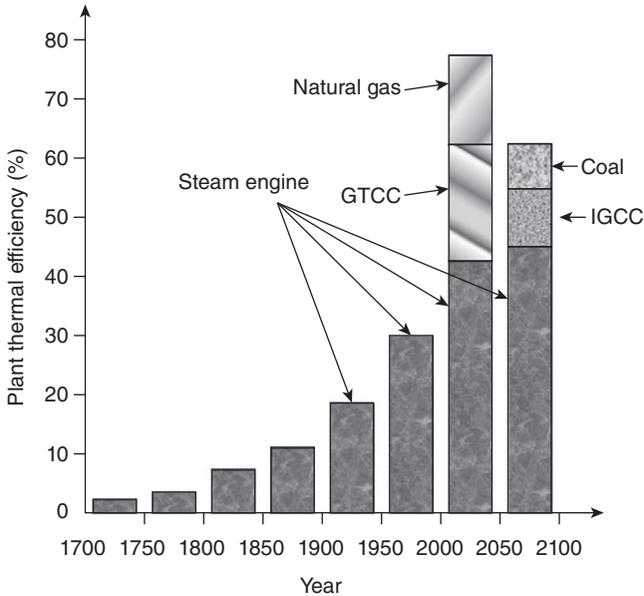
DOI: 10.1533/9781782422242.321

Abstract: The chapter describes modern nanomaterials and designs for solid oxide fuel cells (SOFCs), including cathode, anode, interconnect and electrolyte materials. The chapter then discusses the trend towards miniaturization and lowering of the operating temperatures of SOFCs. It then describes new advances and tools for rational SOFC material design. The chapter concludes with future SOFC applications and markets.

Key words: solid oxide fuel cells (SOFC), miniaturization of SOFC, low-temperature SOFC.

7.1 Introduction to materials and designs for solid oxide fuel cells (SOFCs)

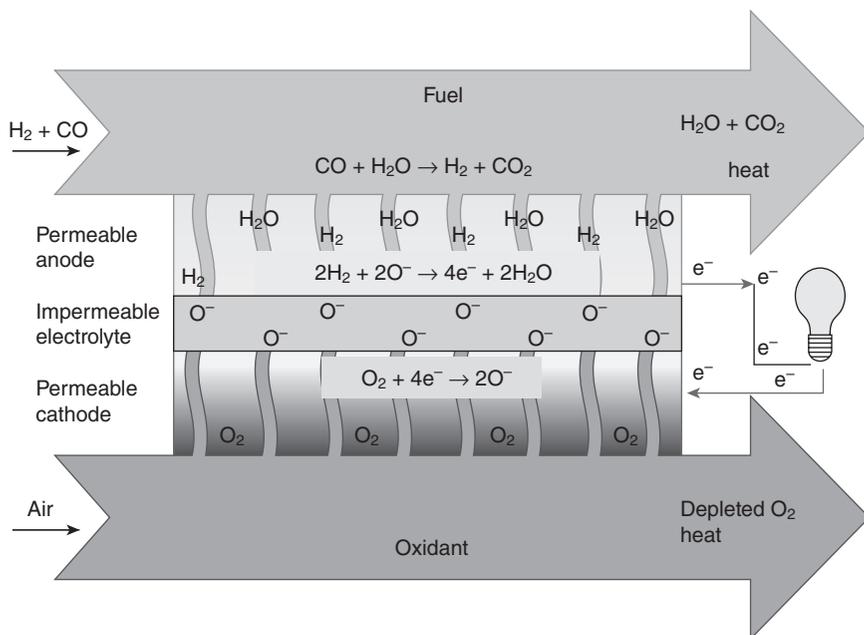
Energy demand has increased substantially over the last few decades due to the growth of various industries, economies and countries. However, since the beginning of the 21st century the efficiency provided by the different power supplies has been insufficient. Nowadays, to secure a stable power supply while reducing the impact of CO₂ emissions on the environment, a rational combination of renewable and other energy sources with advanced power grids based on centralized power sources, such as thermal power generation, is required. Therefore, enhancement of the overall efficiency of thermal power generation is essential. Moreover, to conserve energy sources, it is also important to make full use of fossil fuels via the widespread use of ultra-high-efficiency thermal power systems. Figure 7.1 graphically represents the gradual improvement in the overall performance of various power suppliers since the 18th century when the steam engine was discovered.¹ Historically, from this era and through the peak years of the Brayton–Rankine combined cycle with gas turbines (GT) and steam turbines (ST), the drive was to maximize power generation capability by continuously increasing operating temperature and pressure. Nonetheless, the discovery of the gas turbine combined cycle (GTCC) and solid oxide fuel cells (SOFCs), which can be combined in the triple cycle, allowed the upscaling of the the reported efficiency. Some of the recent industrial reports confirm that the triple combined cycle integrated with SOFCs located upstream of the GTCC can reach productivity of 63%.² Since



7.1 Plant thermal efficiency (%) vs year – the historical transformation of power generation efficiency.

SOFCs are placed in a high-pressure area upstream of the GT combustor, they must have a robust structure, and hence tubular ceramic SOFCs are suitable for this purpose. By cascading the energy from fossil fuels (including coal) in three stages (SOFC, GT and ST), the system is capable of generating power with extremely high efficiency compared with other existing heat engines.

The SOFC is a high-temperature electrochemical device that converts the chemical energy in fuels (such as hydrogen, methane, butane or even gasoline and diesel) into electrical energy by exploiting the natural tendency of oxygen and hydrogen to react offering the potential for clean and efficient power generation. By controlling the means by which such a reaction occurs and directing the reaction through a device, it is possible to harvest the energy given off by the reaction.³⁻⁵ Fuel cells are simple devices, containing no moving parts and only four functional component elements: cathode, electrolyte, anode and interconnect.⁶⁻¹⁰ SOFC technology dominates competing fuel cell technologies because of the ability of SOFCs to use currently available fossil fuels, thus reducing operating costs. Alternative fuel cell technologies (e.g. molten carbonate, polymer electrolyte, phosphoric acid and alkali) require hydrogen as their fuel. Widespread use of such fuel cells would require a network of hydrogen suppliers, similar to our familiar gas stations. Figure 7.2 schematically displays the operating



7.2 Principle of operation of a solid oxide fuel cell. (Reprinted from Ref. 11 with permission from The Electrochemical Society)

principle of the SOFC.¹¹ The SOFC is constructed with two porous electrodes which sandwich an electrolyte. Air flows along the cathode. When an oxygen molecule contacts the cathode/electrolyte interface, it catalytically acquires four electrons from the cathode and splits into two oxygen ions. The oxygen ions diffuse into the electrolyte material and migrate to the other side of the cell where they detect the anode (also called the ‘fuel electrode’). The oxygen ions encounter the fuel at the anode/electrolyte interface and react catalytically, giving off water, CO₂, heat and – most importantly – electrons.

The electrons travel through the anode to the external circuit and back to the cathode, providing a source of useful electrical energy in an external circuit. Provided that both fuel and oxygen are supplied continuously, these electrochemical reactions generate electricity continuously. Although electrode reactions and overall SOFC reaction have been summarized,^{12,13} it must be stressed that the SOFC was first conceived following the discovery of solid electrolytes in 1899 by Nernst.¹⁴ The measured potential difference (E) of the SOFC is therefore determined by the well-known Nernst equation:¹⁵

$$E = \bar{i}_i \frac{RT}{4F} \ln \left(\frac{(pO_2)_A}{(pO_2)_F} \right) \quad [7.1]$$

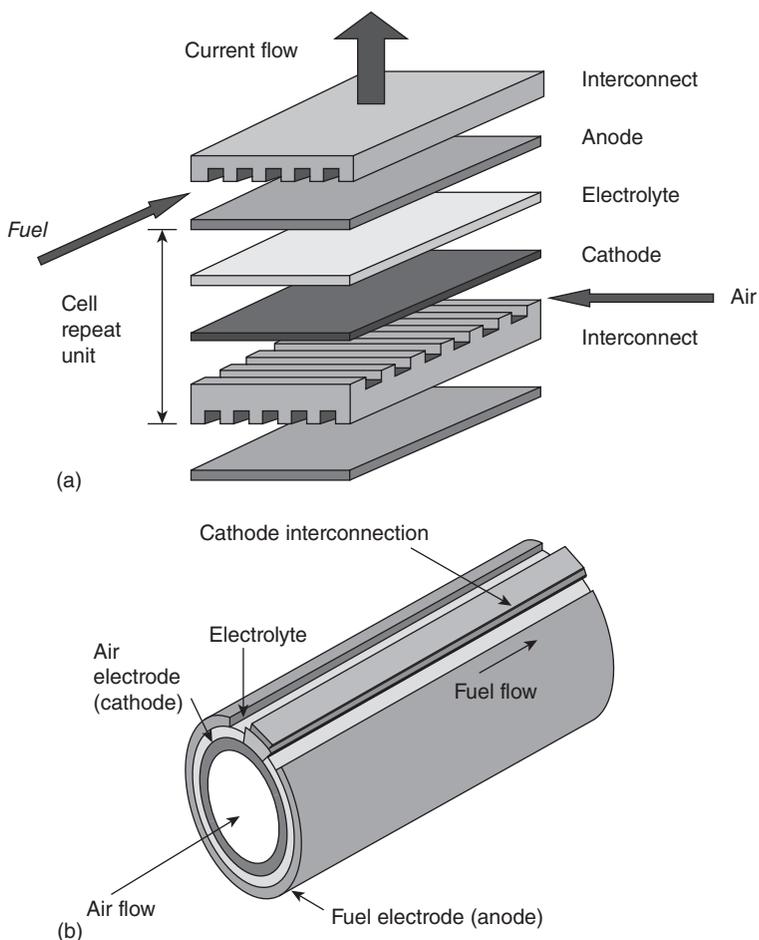
where \bar{t}_i is the average ionic transference number (ionic conductivity/total conductivity = $\sigma_i / (\sigma_i + \sigma_e)$, where σ_i , σ_e , are ionic and electronic conductivities, respectively) of oxygen ions in electrolyte, T is the operating temperature, R is the gas constant, F is the Faraday constant, $(pO_2)_A$ is the oxygen activity on the air side, and $(pO_2)_F$ is the oxygen activity on the fuel side. In the case without any external circuit, the potential difference E corresponds to the open-circuit voltage (OCV). For instance, OCV of $\sim 1.0\text{V}$ can be calculated for an SOFC operating at working temperature of 800°C with air and room temperature-humidified hydrogen as oxidant and fuel, respectively. Under cell operating conditions, i.e. when a current passes through it, a fingerprint characteristic of fuel cells is the relationship between voltage (V) and current density (I).^{11,16}

High efficiency and fuel adaptability are not the only advantages of SOFCs. SOFCs are attractive as energy sources because they are clean, reliable and almost entirely non-polluting. Since there are no moving parts and the cells are therefore vibration-free, the noise pollution associated with power generation is also eliminated. Typically, a single SOFC could only produce around 1.0V OCV. Therefore, to generate a reasonable voltage, SOFCs are not operated as single units but rather as an array of units of a 'stack', with interconnections joining the anodes and cathodes of adjacent units. Usually, the anode is made of Ni/yttria-stabilized zirconia (YSZ) cermet, the electrolyte is made of YSZ and the cathode is electronically conductive perovskite Sr-doped LaMnO_3 (LSM) or other perovskite nanomaterials.¹⁷

Two possible design configurations for SOFCs have emerged: a planar design (Fig. 7.3a) and a tubular arrangement (Fig. 7.3b).¹ In the planar design, the components are assembled in flat stacks, with air and fuel flowing through channels built into the cathode and anode. In the tubular design, components are assembled in the form of a hollow tube, with the cell constructed in layers around a tubular cathode; air flows through the inside of the tube.

7.2 Nanostructured cathode materials

Although the operating concept of SOFCs is relatively simple, the selection of materials for the individual components represents enormous challenges. Each material must have the electrical properties required to perform its function in the cell. There must be sufficient chemical and structural stability to enable fabrication and operation at high temperatures. The fuel cell needs to run at high temperatures in order to achieve sufficiently high current densities and power output; operation at up to 1000°C is possible using the most common electrolyte material YSZ. Reactivity and interdiffusion between the components must be as low as possible. The thermal



7.3 Typical configuration of planar design (a) and tubular design (b) of SOFC. (Reprinted from Ref. 1 with permission from the Elsevier Science)

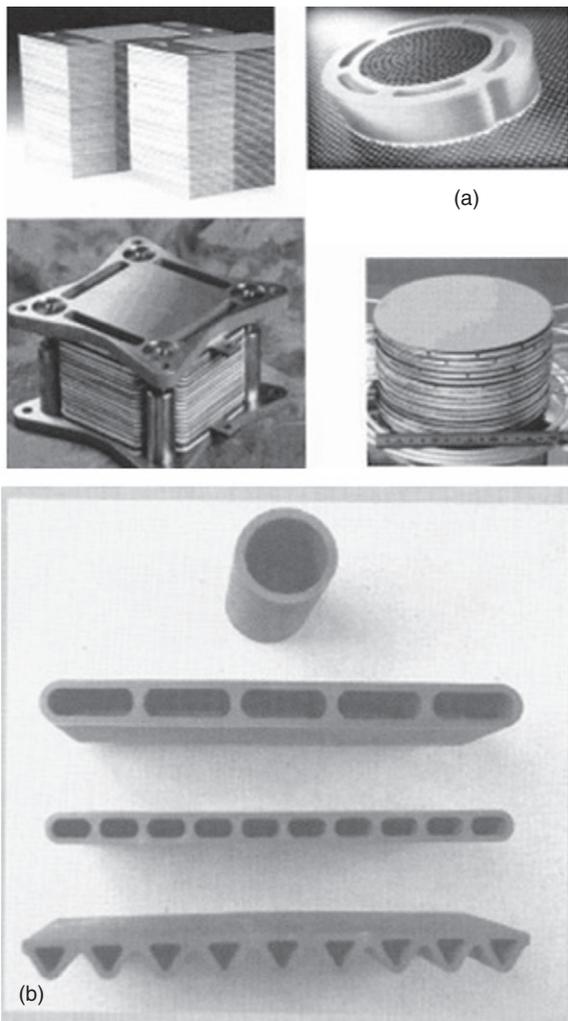
expansion coefficients of the components must also be as close to one another as possible in order to minimize the thermal stresses which may lead to cracking and mechanical failure. The air side of the cell must operate in an oxidizing atmosphere and the fuel side must operate in a reducing atmosphere. The temperature and atmosphere requirements drive the materials selection for all the other components.¹⁸⁻²³

The electrodes, which support the electrochemical reactions, play a vital role in determining the performance and durability of these devices. Effective electrode materials must balance a spectrum of criteria, including cost, thermal and chemical stability, electronic conductivity and catalytic activity.

A number of successful electrode materials have been identified; the most widely adopted constituents are composite structures providing electronic, ionic and gas phase percolation, which promote electrochemical activity throughout the bulk of the electrode. The contiguous contact of electronic, ionic and gas phases at so-called triple phase boundaries (TPBs) provides a direct indication of the electrochemical activity of the electrode. Improvements in tomography techniques have allowed SOFC electrode microstructures to be characterized in three dimensions, giving unprecedented access to a wealth of microstructural information on the nature of triple phase contact and percolation. With improved availability of advanced tomographic techniques, fuel cell developers are increasingly equipped to link processing routes to electrode microstructure and, in turn, electrochemical performance, such that the intelligent engineering of SOFC electrodes is becoming a reality.²⁴⁻²⁶

In terms of stack design, most development has been focused on planar and tubular design cells, each of these systems having a number of interesting variations. For example, the planar SOFC may be in the form of a circular disk fed with fuel from the central axis, or it can be in the form of a square plate fed from the edges. The tubular SOFC might be of a large diameter (>15 mm), or of a much smaller diameter (<5 mm), the so-called microtubular cells. In addition, tubes may be flat and joined together to achieve higher power density and easily printable surfaces for depositing the electrode layers. Figure 7.4 illustrates typical planar cell stacks (a) and tubular cell bundle (b), respectively.¹¹

One of the inherent advantages of tubular cell bundles is that the air and the fuel are naturally isolated because the tubes are closed at one end. However, in the case of planar cell stacks, an effective seal must be provided to isolate air from the fuel. It is imperative that the seal has a thermal expansion match to the fuel cell components; it must be electrically insulating and it must be thermochemically stable under the operational conditions of the stack. Also, the seal should exhibit no deleterious interfacial reactions with other cell components; it needs to be stable under both high-temperature oxidizing and reducing operational conditions, be created at a low enough temperature to avoid damaging cell components (under 850 °C for some materials), and not migrate or flow from the designated sealing region during sealing or cell operation. In addition, it is essential that the sealing system is able to withstand thermal cycling between the cell operating temperature and room temperature. A number of different sealing approaches are under development, including rigid, bonded seals (e.g. glass-ceramics and brazes), compliant seals (e.g. viscous glasses) and compressive seals (e.g. mica-based composites); multiple sealants may also be used in any given stack design between different cell components. Successful development of sealing materials and concepts for planar SOFCs is probably the



7.4 Illustration of the planar cell stacks design (a) and an alternative tubular geometry design being developed by Siemens (b). (Reprinted from Ref. 11 with permission from The Electrochemical Society)

most important issue for the long-term performance stability and lifetime of planar SOFC stacks and hence for their eventual commercialization at competitive costs.

The single biggest advantage of tubular cells over planar cells is that they do not require any high-temperature seals to isolate oxidant from the fuel, and this makes the performance of tubular cell stacks very stable over long periods of time (several years). However, their areal power density is much

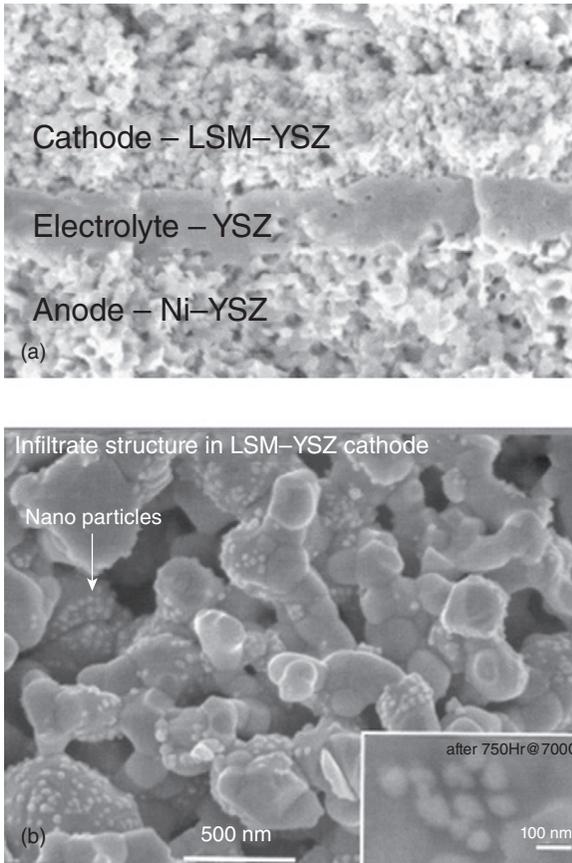
lower (about 0.2 W cm^{-2}) compared to planar cells (up to 2 W cm^{-2} for single cells and at least 0.5 W cm^{-2} for stacks), and manufacturing costs are higher. The volumetric power density is also lower for tubular cells than for planar cells. To increase the power density and reduce the physical size and the cost of tubular SOFC stacks, equivalent tubular geometry cells, as illustrated in Fig. 7.4b, are under development by Siemens.¹¹ Such alternate geometry cells combine all the advantages of the tubular SOFCs, such as not requiring high-temperature seals, with the provision of higher area and volumetric power densities. The performance of these new design cells is higher than that of cylindrical tubular cells, but still lower than that of anode-supported planar cells.

Taking into account all influential factors affecting the performance of the SOFC and its manufacturing costs, the main directions of further improvements in the performance of SOFCs can be summarized as follows:

- *Development of better performing cathodes.* Cathodes perform several roles within a SOFC: reduction of molecular oxygen, transport of charged species to the electrolyte and distribution of the electrical current associated with the oxygen reduction reaction. The cathode must meet all the above requirements and be porous in order to allow oxygen molecules to reach the electrode/electrolyte interface. In some designs (e.g. tubular), the cathode contributes over 90 % of the cell's weight and therefore provides structural support for the cell.^{5,27} Therefore, development of alternative cathode composite nanomaterials that function effectively is a vital step in the realization of technologically viable SOFCs capable of being efficient at intermediate temperatures.^{28–31}
- *Lowering the operating temperature for SOFCs.* SOFC operation at high temperatures ($800\text{--}1000^\circ\text{C}$) means that the components of the stack need to be mainly ceramic. A tubular or box section design is commonly used which results in low volumetric power density. For smaller scale operations, there is a strong trend to move to lower operating temperatures ($500\text{--}750^\circ\text{C}$), where a wider range of materials can be used, allowing cheaper fabrication costs and longer stability of the SOFC.^{12,32,33} However, there is no consensus as to the optimal operating temperature of SOFCs for the time being.
- *Structural and dimensional modifications of YSZ as the electrolyte of SOFC.* As the electrolyte in SOFC is exposed to both oxidizing (air side) and reducing species (fuel side) at high temperatures, successful long-term SOFC stability requires that electrolytes have the following properties:
 - sufficient ionic conductivity;
 - superior stability;
 - dense structure.

- *Search for alternative high-performing electrolytes.* The search for alternative solid electrolyte materials has been an active research area for many years.³⁴ At present, several promising candidates as alternatives to YSZ have emerged: gadolinia-doped ceria (GDC)³⁵ and LaGaO₃-based structures.³⁶
- *Miniaturization of SOFCs.* The large energy densities of SOFCs and the versatility in fuel used, i.e. not limited to hydrogen, have generated interest in the deployment of micro-SOFCs (μ -SOFCs) for mobile power generation in the lower 1–500W range.³⁷ Foreseeable applications include portable electronic devices (which are now powered by rechargeable batteries), vehicle power supplies and auxiliary power units.^{38,39}
- *Improvement of interconnect long-term stability.* The interconnect (also called bipolar plate) in planar fuel cells performs the vital roles of separating the fuel from air, collecting the current from the electrodes, conducting the electrical current between each layer of the stack, distributing reactant gas evenly across the face of each electrode and providing mechanical support to the SOFC and stack structure.⁴⁰
- *Direct utilization of liquid fuels in SOFCs for portable applications.* High operating temperature (500–1000 °C) of SOFCs has two consequences: high efficiency and fuel flexibility. A variety of fuels can be reformed within the cell stack (internal reforming) or through a separate fuel reformer (external reforming). This flexibility allows the use of fuels such as biogas, liquid hydrocarbon fuels and landfill gas and enables SOFCs to be especially suited to standalone and remote applications.

Since all the above factors are equally important, let's consider them in detail. In order for SOFCs to reach their commercial potential, the materials and processing must also be cost-effective. The first successful SOFC used Pt as both the cathode and the anode, but fortunately less expensive alternatives are available now. Today, the most commonly used cathode material is LaMnO₃, a *p*-type perovskite. Typically, it is doped with rare earth elements (e.g. Sr, Ce, Pr) to enhance its conductivity. Most often it is doped with Sr and referred to as LSM (La_{1-x}Sr_xMnO₃). The conductivity of these perovskites is all electronic (no ionic conductivity), a desirable feature since the electrons from the open circuit flow back through the cell via the cathode to reduce the oxygen molecules, forcing the oxygen ions through the electrolyte. In addition to being compatible with YSZ electrolytes, it has the further advantage of having adequate functionality at intermediate fuel cell temperatures (about 700 °C), allowing it to be used with alternative electrolyte compositions. Any reduction in operating temperature reduces operating costs and expands the materials selection, creating an opportunity for additional cost savings. Figure 7.5 displays scanning electron microscopy



7.5 SEM images of the typical cross-section of the planar SOFC (a) and infiltrated cathode (b), respectively. (Reprinted from Ref. 27 with permission from The Electrochemical Society)

(SEM) images of the typical cross-section of the planar SOFC (Fig. 7.5a) and infiltrated LSM-YSZ cathode (Fig. 7.5b), respectively.²⁷

Figure 7.5 clearly shows that nanostructured cathode material has a very complex structure. This is probably because the cathode process is extremely versatile with multiple potential series and parallel mechanistic steps. An example of this is given in Fig. 7.6a for a relatively simple case of oxygen reduction at a Pt/YSZ interface.²⁹ Multiple reactions occurring at TPBs confirmed that, a rational design process for higher performing cathodes demands a more fundamental understanding, and this requires the quantification of the various conditions for cathode polarization: electrocatalytic reduction (activation polarization), ionic and electronic conduction (ohmic polarization), and gas diffusion (concentration polarization).²⁷ In this

regard, microstructure plays a critical role in quantifying cathode performance. Figure 7.6b provides a 3D image of the reconstruction of Siemens SOFC cathode nanomaterial, obtained from a series of sequential SEM images.²⁷ Phase contrasting allows for identification of each phase. This, in turn, allows for quantification of the critical parameters necessary to determine the sources of cathode polarization. By quantifying the phase boundaries, it was possible to calculate the TPB length and surface area, and later to determine the fundamental reactions which occur at each feature of the structure. Therefore, by integrating calculation with measurements of the reaction rates and fundamental rate constant, with quantified micro- and nanostructures of the measured cathode materials, and comparing to electrochemical measurements, a fundamental and rational based approach to cathode development can provide the framework for further reductions in cathode polarization and ultimately optimization of the SOFC operating temperature.^{41,42}

There are a few notable reviews dedicated to the overview of the performance of the different cathode materials.^{13,41–43} Most of the properties of the perovskite-type oxide materials considered in these reviews are summarized in Table 7.1.

As the length of the TPB correlates well with the interfacial resistances to electrochemical oxidation of fuel at the anode⁴⁴ and reduction of oxygen at the cathode,^{45–48} in order to improve the cathode performance in the SOFC it is necessary to extend the TPB and to increase the number of active reaction sites. This can be achieved by developing materials with a higher mixed ionic–electronic conductivity and optimizing the nanostructure of electrodes.

Nanostructured materials for SOFC electrodes possess significantly higher surface areas and have already displayed superior electrochemical properties.⁴⁹ There are different processes involved in preparation of nanostructured electrodes for SOFCs. For example, chemical vapour deposition (CVD) has been used in fabrication of functionally graded composite cathodes.⁴⁸ Nanostructures were graded in terms of both structures and composition. Results in this report highlighted that nanostructured electrodes substantially reduce the cathode/electrolyte interfacial polarization resistance ($0.17 \Omega \text{cm}^2$). The power density of an anode-supported cell consisting of Sr-doped samarium cobaltite (SSC) and $\text{Ce}_{0.8}\text{Sm}_{0.2}\text{O}_{1.9}$ cathode and Ni– $\text{Ce}_{0.8}\text{Sm}_{0.2}\text{O}_{1.9}$ anode reached 0.375Wcm^{-2} at 600°C while the long-term stability of these electrodes is still waiting to be reported.

Another example is a wet impregnation method, which has shown promise in recent years. This method was used for preparation of nanostructured electrodes with reported high performance.^{50,51} An additional report⁵² has also demonstrated that adding LaCoO_3 (LSCo) to LSM–YSZ cathode by the infiltration method had a dramatic impact on the

Table 7.1 Perovskite-type oxide materials: thermal expansion coefficient (TEC), electronic (σ_e), and ionic conductivities (σ_i) in air

	TEC ($\times 10^{-6} \text{K}^{-1}$)	T ($^{\circ}\text{C}$)	σ_e (S cm^{-1})	σ_i (S cm^{-1})
$\text{La}_{0.8}\text{Sr}_{0.2}\text{MnO}_3$	11.8	900	300	5.93×10^{-7}
$\text{La}_{0.7}\text{Sr}_{0.3}\text{MnO}_3$	11.7	800	240	–
$\text{La}_{0.6}\text{Sr}_{0.4}\text{MnO}_3$	13	800	130	–
$\text{Pr}_{0.6}\text{Sr}_{0.4}\text{MnO}_3$	12	950	220	–
$\text{La}_{0.8}\text{Sr}_{0.2}\text{CoO}_3$	19.1	800	1220	–
$\text{La}_{0.6}\text{Sr}_{0.4}\text{CoO}_3$	20.5	800	1600	0.22
$\text{La}_{0.8}\text{Sr}_{0.2}\text{FeO}_3$	12.2	750	155	–
$\text{La}_{0.5}\text{Sr}_{0.5}\text{FeO}_3$	–	550	352	–
	–	800	369	0.205
$\text{La}_{0.6}\text{Sr}_{0.4}\text{FeO}_3$	16.3	800	129	5.6×10^{-3}
$\text{Pr}_{0.5}\text{Sr}_{0.5}\text{FeO}_3$	13.2	550	300	–
$\text{Pr}_{0.8}\text{Sr}_{0.2}\text{FeO}_3$	12.1	800	78	–
$\text{La}_{0.7}\text{Sr}_{0.3}\text{Fe}_{0.8}\text{Ni}_{0.2}\text{O}_3$	13.7	750	290	–
$\text{La}_{0.8}\text{Sr}_{0.2}\text{Co}_{0.8}\text{Fe}_{0.2}\text{O}_3$	20.1	600	1050	–
$\text{La}_{0.8}\text{Sr}_{0.2}\text{Co}_{0.2}\text{Fe}_{0.8}\text{O}_3$	15.4	600	125	–
$\text{La}_{0.6}\text{Sr}_{0.4}\text{Co}_{0.8}\text{Mn}_{0.2}\text{O}_3$	18.1	500	1400	–
$\text{La}_{0.6}\text{Sr}_{0.4}\text{Co}_{0.8}\text{Fe}_{0.2}\text{O}_3$	21.4	800	269	0.058
$\text{La}_{0.6}\text{Sr}_{0.4}\text{Co}_{0.2}\text{Fe}_{0.8}\text{O}_3$	15.3	600	330	8×10^{-3}
$\text{La}_{0.4}\text{Sr}_{0.6}\text{Co}_{0.2}\text{Fe}_{0.8}\text{O}_3$	16.8	600	–	–
$\text{La}_{0.8}\text{Sr}_{0.2}\text{Co}_{0.2}\text{Fe}_{0.8}\text{O}_3$	14.8	800	87	2.2×10^{-3}
$\text{La}_{0.8}\text{Sr}_{0.2}\text{Co}_{0.8}\text{Fe}_{0.2}\text{O}_3$	19.3	800	1000	4×10^{-2}
$\text{La}_{0.6}\text{Sr}_{0.4}\text{Co}_{0.9}\text{Cu}_{0.1}\text{O}_3$	19.2	700	1400	–
$\text{Pr}_{0.8}\text{Sr}_{0.2}\text{Co}_{0.2}\text{Fe}_{0.8}\text{O}_3$	12.8	800	76	1.5×10^{-3}
$\text{Pr}_{0.7}\text{Sr}_{0.3}\text{Co}_{0.2}\text{Mn}_{0.8}\text{O}_3$	11.1	800	200	4.4×10^{-5}

Composition	TEC ($\times 10^{-6} \text{K}^{-1}$)	T ($^{\circ}\text{C}$)	σ_e (S cm^{-1})	σ_i (S cm^{-1})
$\text{Pr}_{0.6}\text{Sr}_{0.4}\text{Co}_{0.8}\text{Fe}_{0.2}\text{O}_3$	19.69	550	950	–
$\text{Pr}_{0.4}\text{Sr}_{0.6}\text{Co}_{0.8}\text{Fe}_{0.2}\text{O}_3$	21.33	550	600	–
$\text{Pr}_{0.7}\text{Sr}_{0.3}\text{Co}_{0.9}\text{Cu}_{0.1}\text{O}_3$	–	700	1236	–
$\text{Ba}_{0.5}\text{Sr}_{0.5}\text{Co}_{0.8}\text{Fe}_{0.2}\text{O}_3$	20	500	30	–
$\text{Sm}_{0.5}\text{Sr}_{0.5}\text{CoO}_3$	20.5	700 ~ 900	>1000	–
$\text{LaNi}_{0.6}\text{Fe}_{0.4}\text{O}_3$	11.4	800	580	–
$\text{Sr}_{0.9}\text{Ce}_{0.1}\text{Fe}_{0.8}\text{Ni}_{0.2}\text{O}_3$	18.9	800	87	0.04

performance, but forming a mixed Sr-doped $\text{LaCo}_{0.2}\text{Mn}_{0.8}\text{O}_3$ had no effect. Mixed conductivity at the TPB may explain the improved performance. It has also been demonstrated that the impregnation of nanosized particles, forming connected networks, into SOFC electrodes led to considerable improvement in overall functioning.⁵³ Impedance analysis of the impregnated electrode suggests that the particular morphology of the nanostructured pore-wall coating minimizes the rate-limiting step in the oxygen reduction reaction within LMS-YSZ cathodes.

Although the wet impregnation method has been shown to be an effective technique to achieve the desired morphology; which has been reflected by high performance, the durability of these nanostructures over long periods at high temperatures remains a big concern. Basically, the nanostructured particles tend to aggregate at a high temperature and, consequently, catalytic activity decreases with operating time. Moreover, it should be stressed that nanomaterials synthesized by different methods usually have very different nanostructures and properties. For cathode materials with the same composition, the nanostructures prepared by a sol–gel or glycine–nitrate combustion method as a rule have much smaller grain size and higher active surface area compared with those prepared by a conventional solid-phase reaction, thus leading to better SOFC performances. However, the feasibility of scale-up and cost of these processes must be taken into account when considering incorporation into practical applications.¹³

In addition, the selection of an appropriate fabrication technique for LSM preparation depends on the SOFC design. For example, at Siemens Westinghouse a tubular cell design is being developed.¹¹ The cell is constructed by extruding a cathode tube and building the rest of the cell around it. Another example is the approach taken by NexTech Materials, where several planar cell designs are being investigated; the cathode is designed as the bottom supporting layer, and fabricated with tape casting techniques using nanoscale particles.⁵⁰ In both cases, the challenge is to sinter the cathode adequately, often by co-sintering with the other components, while maintaining sufficient interconnected porosity. Improving the performance of the existing cathode materials can also be achieved through optimization of processing, composition and microstructure. Work on the optimization of interfacial properties and stability is also necessary for stack development. However, more fundamental studies on the reaction mechanisms and the kinetics of oxygen reduction in SOFC cathodes are highly desirable and the work should be intensified in the near future.

7.3 Electrolytes for SOFCs

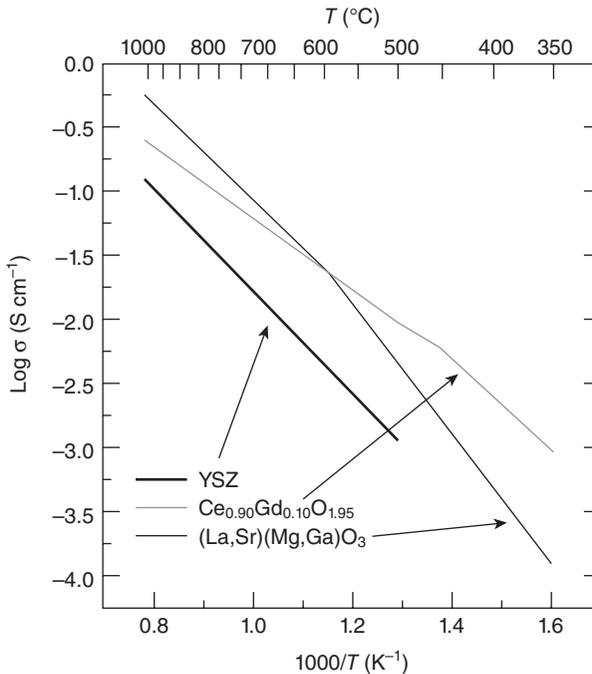
In the schematic representation of the SOFC, shown in Fig. 7.2, the electrolyte is exposed to both oxidizing (air side) and reducing species (fuel side) at high temperatures. Therefore, once the molecular oxygen has been converted to oxygen ions, it must migrate through the electrolyte to the fuel side of the cell. In order for such migration to occur, the electrolyte must possess high ionic conductivity and no electrical conductivity. It should be fully dense to prevent short circuiting of reacting gases through it, and it must also be as thin as possible to minimize resistive losses in the cell. As with the other materials, it needs to be chemically, thermally and structur-

ally stable across a wide temperature range. Its coefficient of thermal expansion should be compatible with the coefficients of thermal expansion of the anode and cathode of the SOFC. In addition, for long-term stability of the SOFC, it is essential for the electrolyte to have an ionic transference number close to unity,¹⁵ i.e. the electronic conductivity of electrolyte must be sufficiently lower in order to provide high energy conversion efficiency.

There are several typical candidate materials:³⁴ YSZ, gadolinium-doped cerium oxide (GDC), (La,Sr)(Mg,Ga)O₃ (LSMG) and doped Bi₂O₃. Of these, the first two are the most promising. Bi₂O₃-based materials have a high oxygen ion conductivity and lower operating temperature (less than 800 °C), but do not offer enough crystalline stability at high temperature to be broadly useful.⁶ It may seem straightforward to design an oxide ion conductor by simply adding more dopants to increase the oxygen vacancy concentration. This strategy, however, might not be valid in many cases because factors such as vacancy ordering, dopant segregation and compatibility with other SOFC components must be taken into consideration. The most suitable material that satisfies the requirements of the SOFC electrolyte is YSZ.¹⁵ Ytria serves the dual purpose of stabilizing zirconia into the cubic structure at high temperatures and also providing oxygen vacancies at the rate of one vacancy per mole of dopant. A typical dopant level is 10 mol% yttria.^{4,54} A plot of ionic conductivity as a function of temperature for the most common SOFC electrolyte materials is presented in Fig. 7.7. In this figure, YSZ has shown the lowest ionic conductivity. Nevertheless, so far this is the only material that has been demonstrated to provide long-term stability under SOFC operating conditions up to 80000 h at $T = 1000$ °C.

Grain boundary conduction is very important for YSZ⁵⁵ and, since the grain boundary contribution increases with decreasing temperature, it is particularly important for lowering of SOFC operating temperatures. For example, for YSZ produced by several different methods, the fraction of the total resistance due to grain boundary resistance is negligible at 900 °C, but increases to ~0–40 % at 700 °C, and then further to ~10–65 % at 500 °C.³⁴ Grain boundary transport becomes especially important for nanostructured materials due to their high proportion of grain boundary area. For example, processing YSZ to produce grain sizes less than 10 nm resulted in conductivities which were 50 % higher than those of materials with larger grain sizes.⁵⁶ Thus, the benefits of small particle sizes in reducing processing temperatures must be balanced against increased grain boundary resistance, particularly at lower operating temperatures.

In order for YSZ to be used at the lower temperatures, a typical approach to minimize ohmic loss is to decrease the thickness of YSZ. A thin, dense film of YSZ electrolyte (approximately 40 μm thick) needs to be applied to the cathode substrate. A reliable method to engage the electrolyte, known as electrochemical vapour deposition, offers high purity and a high level of



7.7 Conductivity as a function of temperature for YSZ, GDC and LSMG.

process control. Electrochemical vapour deposition overcomes the problem of depositing a dense film onto a porous substrate by passing oxygen through the inside of the cathode tube while chlorides of Zr and Y are passed along the outside. They react at the tube surface to form YSZ and, because the reaction comes to the surface from both sides, the porosity is closed off. Once the porosity is closed off, the electrolyte deposition continues, but now the oxygen diffuses through the growing YSZ layer to react with the chlorides, thereby ensuring a highly dense electrolyte layer. While the process is effective, it can be relatively expensive and capital-intensive, and it requires excellent quality control.⁴

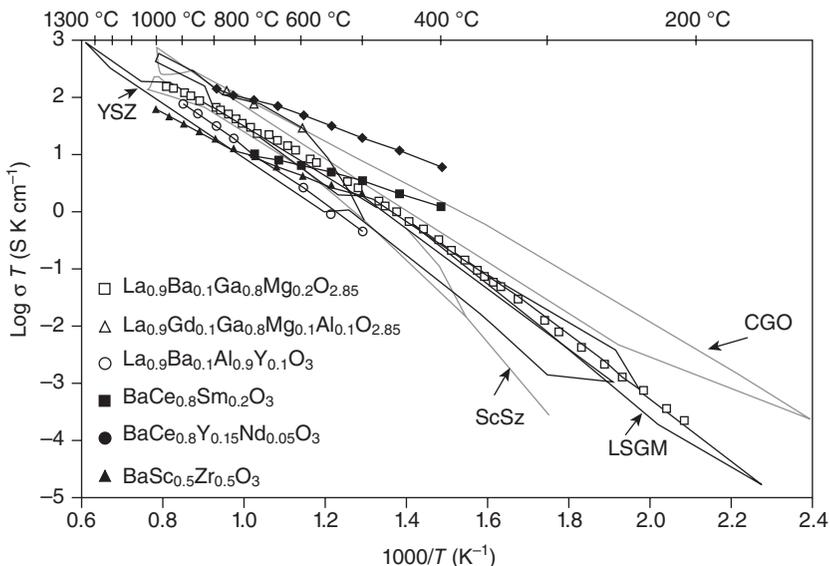
Alternative electrolyte deposition methods that show promise are spray and dip coating followed by sintering. Colloidal suspensions of YSZ are applied in thin layers of at least 20 μm , using nanosize (5–10 nm) particles in order to meet the critical requirement of low porosity. Through careful engineering of the particle size distribution and dispersions, these deposition techniques are likely to replace electrochemical deposition.⁶

Cerium oxide (ceria) has also been considered as a possible electrolyte. Its advantage is that it has high ionic conductivity in air, but it can operate effectively at much lower temperatures (under 700 °C). This temperature

range significantly broadens the choice of materials for the other components, which can be made of much less expensive and more readily available materials. The problem is that this electrolyte is susceptible to reduction on the anode (fuel) side. At low operating temperatures (500–700 °C), grain boundary resistance is a significant impediment to ionic conductivity. Efforts are underway to develop compositions which address these problems.⁸ Like zirconia, ceria forms the fluorite structure and is a common electrolyte material for SOFCs. In comparison to zirconia, ceria has a higher conductivity, particularly at low temperatures, and a lower polarization resistance.⁵⁷ The primary disadvantage of ceria is electronic conduction at low oxygen partial pressures.^{57,58} Like zirconia, ceria is doped to increase conductivity and, also like zirconia, the highest conductivity occurs for ions with the lowest size mismatch, which for cerium is Gd and Sm.^{34,59} The conductivity of the most widely used ceria-based electrolyte, $\text{Ce}_{1-x}\text{Gd}_x\text{O}_2$ (CGO) has been investigated.^{60–63} Below 600 °C, the conductivities of CGO are consistently higher than those of YSZ or scandia-stabilized zirconia (ScSZ). Similar to zirconia, the conductivity increases with increasing dopant concentration to a maximum (e.g. 0.20–0.25 Gd⁶⁴) and then decreases. The range of conductivities for $\text{Ce}_{0.9}\text{Gd}_{0.1}\text{O}_2$ and $\text{Ce}_{0.8}\text{Gd}_{0.2}\text{O}_2$ are similar, and $\text{Ce}_{0.9}\text{Gd}_{0.1}\text{O}_2$ has been shown to have better stability than $\text{Ce}_{0.8}\text{Gd}_{0.2}\text{O}_2$ at low oxygen partial pressure. Performance of the electrolyte at low oxygen partial pressures is important, so both compositions are used.⁶⁵

The existence of two differently-sized cation sites in the perovskite structure expands the range of possible dopants. For example, although Sr and Mg are the most common dopants for LaGaO_3 , the La site can also be doped with Ba⁶⁶ or Gd.⁶⁷ Doping with Ba, rather than Sr, affects the octahedral tilt angle, which reduces the activation energy, such that at high temperatures the conductivity of $\text{La}_{0.9}\text{Ba}_{0.1}\text{Ga}_{0.8}\text{Mg}_{0.2}\text{O}_{2.85}$ is lower than that of $\text{La}_{0.9}\text{Sr}_{0.1}\text{Ga}_{0.8}\text{Mg}_{0.2}\text{O}_{2.85}$ (LSGM), but the reverse is the case at lower temperatures.⁶⁶ The conductivities of $\text{La}_{0.9}\text{Ba}_{0.1}\text{Ga}_{0.8}\text{Mg}_{0.2}\text{O}_{2.85}$ and other perovskite materials are shown in Fig. 7.8.³⁴ Other La-based perovskites, including LaScO_3 -, LaInO_3 - and LaYO_3 -based materials, are oxygen ion conductors⁵⁸ and thus potential electrolyte materials. Due to the lower cost of Al relative to Ga, LaAlO_3 -based materials are particularly attractive as electrolytes for SOFCs.³⁴ Although the stability of aluminates is quite good, their conductivity is lower than other potential materials (e.g. $\text{La}_{0.9}\text{Ba}_{0.1}\text{Al}_{0.9}\text{Y}_{0.1}\text{O}_3$ in Fig. 7.8).

Proton-conducting or mixed-ion-conducting oxides have been investigated as electrolytes in fuel cells.⁶⁸ One of the advantages of such fuel cells is that, since hydrogen is transported through the electrolyte, the fuel is not diluted with water vapour. The most common proton-conducting oxide is BaCeO_3 , which has been doped with various oxides, including those of Sr, Nd⁶⁹ and Yb,⁷⁰ for use in SOFCs. Figure 7.8 demonstrates that the



7.8 Conductivity of perovskite oxides in air. (Reprinted from Ref. 34 with permission from Elsevier Science)

conductivity of neodymium–yttria co-doped BaCeO_3 is particularly high. Other proton-conducting oxides for potential application in solid oxide fuel cells include $\text{BaSc}_{0.5}\text{Zr}_{0.5}\text{O}_3$,⁷¹ $(\text{La},\text{Pr})_{0.9}\text{Ba}_{1.1}\text{GaO}_{3.95}$ and $\text{Nd}_{0.9}\text{Ba}_{1.1}\text{GaO}_{3.95}$.³⁴

7.4 Nanostructured anode materials

The anode (the fuel electrode) must meet most of the same requirements as the cathode for electrical conductivity, thermal expansion compatibility and porosity, and needs to be an excellent catalyst for the oxidation of the fuel. The reducing conditions combined with electrical conductivity requirements make metals attractive candidate materials.²⁵ So far most of developments of anode materials have been focused on Ni owing to its abundance and affordability.⁷² However, its thermal expansion ($13.3 \times 10^{-6}/\text{C}$ compared with $10 \times 10^{-6}/\text{C}$ for YSZ) is too high to pair it in pure form with YSZ; moreover, it tends to sinter and close off its porosity at typical operating temperatures. These problems have been solved by making the anode out of a Ni–YSZ composite. The YSZ provides structural support for separated Ni particles, preventing them from sintering together while matching the thermal expansions. Adhesion of the anode to the electrolyte is also improved.⁴

Anodes are applied to the fuel cell through powder technology processes. Either a slurry of Ni is administered over the cell and then YSZ is deposited

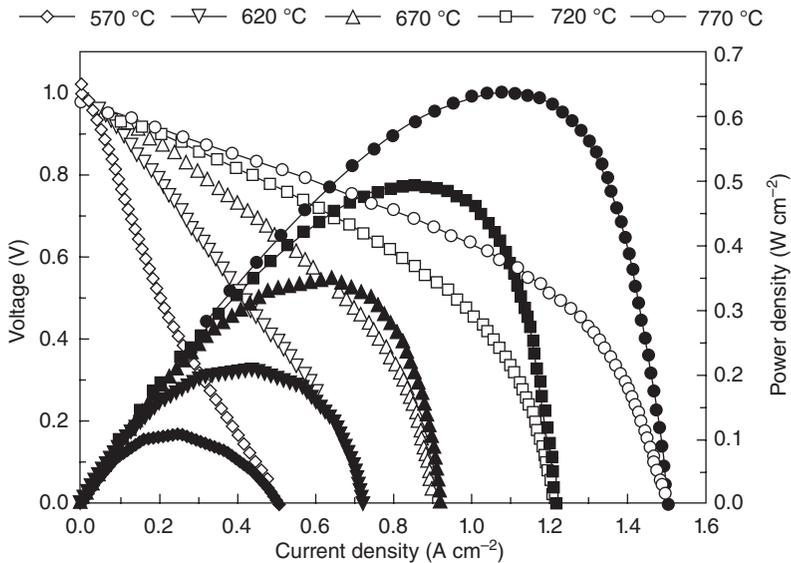
by electrochemical vapour deposition, or a Ni–YSZ slurry is applied and sintered. More recently NiO–YSZ slurries have been used, the NiO being reduced to particulate Ni in the firing process. In order to maintain porosity, pore regulators such as starch, carbon or thermosetting resins are added. These burn out during firing and leave pores behind. There are a number of problems associated with this approach. First, the process tends to form tortuous porosity pathways that reduce the transport efficiency of reacting gases through the anode. Second, there is an increased likelihood of cracking on firing because of the thinness of the interior solid structure left behind. Third, there are environmental issues in relation to the burning of the pore formers. For these reasons, recent research is investigating the possibility of a freeze-drying approach to forming porous structures without the use of fillers. The slurry is applied through a simple dipping process and then freeze-dried; the resulting ice is then sublimed out of the unfired structure. The resulting pore structure – neatly aligned because of the way water crystallizes – allows efficient flow of gases to and from the electrolyte/anode interface. The fineness of the pore structure is easily controlled by adjusting the solids content (and therefore water content) of the slurry.⁹

Other choices of material are under investigation.^{73–75} Although Ni–YSZ is currently the anode material of choice and the freeze-drying process solves most of the identified problems, Ni still has a disadvantage: it catalyses the formation of graphite from hydrocarbons. The deposition of graphite residues on the interior surfaces of the anode reduces its usefulness by destroying one of the main advantages of SOFCs, namely their ability to use unreformed fuel sources.

Cu–cerium oxide anodes are being studied as a possible alternative.⁵ Cu is an excellent electrical conductor, but a poor catalyst of hydrocarbons; cerium oxide is used as the matrix in part because of its high hydrocarbon oxidation activity. A composite of the two thus has the advantage of being compatible with cerium oxide electrolyte fuel cells. Initial results using a wide range of hydrocarbon fuels are very promising.

Incorporating oxide-based catalysts is an approach that has been tried to overcome the limitations of the Ni-based anodes in directly utilizing hydrocarbons, and it has fulfilled some of the requirements. It was reported that a catalytic layer of Ru–CeO₂/CeO₂–ZrO₂/Ru–CeO₂ used on the top of the conventional Ni-based anode.²⁵ Ceria is well-known catalyst, and might be expected to increase the activity of the anode for the electrochemical oxidation of methane. The catalytic layer allows internal reforming of isooctane without coking (carbon deposition) and yields stable power densities (0.3–0.6 W cm⁻²) (as graphically presented in Fig. 7.9²⁵).

This concept of using a bi-layer anode is interesting, even though the catalytic layer possessed lower gas permeation and higher electronic resistance. Another cerium dioxide-based anode is a Cu–CeO₂ composite, used



7.9 Electrochemical performance of SOFC with $\text{Ba}_{0.5}\text{Sr}_{0.5}\text{Co}_{0.8}\text{Fe}_{0.2}\text{O}_{3-\sigma}$ as the cathode, $\text{Sm}_{0.15}\text{Ce}_{0.85}\text{O}_{2-\sigma}$ (SDC) as the electrolyte ($\sim 20\ \mu\text{m}$) and Ni-SDC as the anode ($\sim 700\ \mu\text{m}$), with air and room temperature humidified H_2 . (Reprinted from Ref. 25 with permission from Nature Publishing group)

as the SOFC anode for the direct oxidation of hydrocarbon fuels. In contrast to Ni, Cu is not an active catalyst for carbon formation. The addition of CeO_2 provides active catalytic sites. However, sintering of Cu at high cell operating temperatures has limited its use in practical SOFCs.⁷⁶ Moreover, the conditions under which such anodes could be used for direct hydrocarbon oxidation can be a potential problem for their widespread application, whilst their long-term performance in terms of deactivation from carbon deposition is another concern. The development of such anodes is a very active area of current research.

7.5 Interconnects for SOFCs

Just as an internal combustion engine relies on several cylinders to provide enough power to be useful and effective, so too can excess fuel cells be used in combination in order to generate enough voltage and current. This means that the cells must be connected together and a mechanism for collection of electrical current needs to be provided, hence the need for interconnects. The interconnect functions as the electrical contact to the cathode, ensuring air and fuel separation within the cell stack while protecting it from the reducing atmosphere of the anode.

The high operating temperature of the cells combined with severe environments means that interconnects must meet the most stringent requirements of all the cell components: 100 % electrical conductivity, no porosity (to avoid mixing of fuel and oxygen), thermal expansion compatibility and inertness with respect to the other fuel cell components. It will be exposed simultaneously to the reducing environment of the anode and the oxidizing atmosphere of the cathode.

Interconnects serve various vital functions in SOFC stacks. They provide electrical connection between the anode of one individual cell and the cathode of the neighbouring one, and act as physical barrier to avoid any contact between the reducing and the oxidizing atmospheres. The criteria for the interconnect materials are the most stringent of all cell components. In general terms, the interconnect has to meet the following demands:^{1,77,78}

- excellent electrical conductivity – the acceptable area-specific resistance (ASR) level is considered to be below $0.1 \Omega \text{cm}^2$;
- adequate stability in terms of dimensions, microstructure, chemistry and phases at operating temperature around 800°C in both oxidizing and reducing atmospheres during 40000 h (service lifetime);
- excellent imperviousness to oxygen and hydrogen to prevent direct combination of oxidant and fuel during operation;
- coefficient of thermal expansion (CTE) matching those of electrodes and electrolyte, around $10.5 \times 10^{-6} \text{K}^{-1}$, so that the thermal stresses developed during start-up and shut-down could be minimized;
- no reaction or interdiffusion between interconnect and its adjoining components;
- excellent oxidation, sulphidation and carbon cementation resistance;
- adequate strength and creep resistance at elevated temperatures;
- low cost, as well as ease of fabrication and shaping.

In general, there are only two approaches in developing interconnect materials for SOFCs, i.e. ceramics and metallic alloys. Interconnects can be applied to the anode by plasma spraying after which the entire cell is co-fired. Any reduction in component costs (either raw materials or processing) directly translates into improved energy affordability. The strong economic incentive to use traditional metals for interconnect is driving the development of intermediate- and low-temperature SOFCs. At operating temperatures in the $900\text{--}1000^\circ\text{C}$ range, interconnects made of Ni base alloys such as Inconel® 600 are possible.¹⁰ At or below 800°C , ferritic steels can be used. At even lower temperatures (below 700°C), it becomes possible to use stainless steels, which are comparatively inexpensive and readily available.⁸

7.5.1 Lanthanum chromites as interconnects

The traditional material used for the SOFC interconnect is LaCrO_3 for high-temperature applications ($\sim 1000^\circ\text{C}$).^{1,77} Firstly, this material exhibits a remarkably high electric conductivity under SOFC operating conditions compared with typical ceramics,⁷⁹ and the conductivity can be improved significantly by doping with Mg, Sr or Ca. Secondly, the melting point of LaCrO_3 is $2783 \pm 20\text{K}$, and the material could remain stable at both the cathode and anode environment.⁸⁰ Thirdly, average CTE of LaCrO_3 is $9.5 \times 10^{-6}\text{K}^{-1}$, which is quite close to the CTE of YSZ ($10.5 \times 10^{-6}\text{K}^{-1}$).

Many properties of LaCrO_3 will be improved accordingly by means of appropriate doping, which has been summarized in a recent review.⁷⁷ In terms of mechanical strength, Mg doping is less effective than that of Ca and Sr, and the strengths of Sr-doped LaCrO_3 (LSC) are generally better than those of Ca-doped LaCrO_3 . In terms of CTE, at the same dopant level, LSC has higher CTE than Ca-doped LaCrO_3 , which makes LSC closer to YSZ. In conductivity, Ca-doped LaCrO_3 is higher than that doped by Sr; nevertheless, both of them are much higher than undoped LaCrO_3 . In relation to Cr evaporation, the activity of CrO_3 in $\text{La}_{0.84}\text{Sr}_{0.16}\text{CrO}_3$ (5.5×10^{-6}) is lower than that for $\text{La}_{0.79}\text{Ca}_{0.21}\text{CrO}_3$ (3×10^{-4}), indicating that Sr is more effective in reducing the CrO_3 activity.¹

On the other hand, certain weaknesses of LaCrO_3 have been reported.⁸¹ They are as follows:

- LaCrO_3 is a *p*-type semiconductor, and its conductivity decreases with decreasing oxygen partial pressure as LaCrO_3 becomes oxygen deficient.
- compared with typical engineering materials, La, being a rare-earth element, is expensive.
- LaCrO_3 is a ceramic material, and processing methods are limited which results in limitations as to the geometry of interconnect that can be fabricated.
- LaCrO_3 is difficult to sinter to a high relative density, so the processing of a hermetic LaCrO_3 layer is quite difficult, which is the most significant drawback.

To achieve full densification, two options can be considered: (i) a conventional liquid-phase sintering process can be used to promote densification; (ii) firing LaCrO_3 between Cr_2O_3 plates (sandwich configuration) in conjunction with fast heating and cooling schedule improves the densification process.⁸² These factors undoubtedly added manufacturing complexity and costs are inevitably incurred. Because of these weaknesses of LaCrO_3 , significant research efforts have been dedicated to finding an alternative material.

7.5.2 Metallic alloys as interconnect

For a YSZ SOFC operating at about 1000°C, the material of choice is LaCrO₃ doped with a rare earth element (Ca, Mg, Sr, etc.) to improve its conductivity.^{1,77} Ca-doped CrO₃ is also being considered because it has better thermal expansion compatibility, especially in reducing atmospheres.²⁷

Reduction of the operating temperature of the SOFC down to 600–800°C opens an opportunity for metallic materials to be potential replacements for LaCrO₃ as interconnect. They can be successfully employed as interconnect because of their advantages compared with high-temperature LaCrO₃.⁸³

- Metallic materials have high mechanical strength. Interconnect in anode-supported SOFCs also acts as a mechanical support for ceramic parts and as a constructional connection to the external inlets and outlets. In some cases, interconnect has been designed with extra channels for distributing the gas in co-, cross- and/or counter-flow configurations. Traditional LaCrO₃ could not fulfil this requirement.
- Metallic materials have high thermal conductivity, which could eliminate the presence of thermal gradient both along the interconnect plane and across the components.
- Metallic materials have high electronic conductivity, thereby decreasing in resistance of the cell and increasing output.
- Ease of fabrication, low cost and ready availability. It should be pointed out that almost all the candidate alloys typically contain Cr and/or Al (Si is a third possibility, but much less used) to provide oxidation resistance by forming oxide scales of Cr₂O₃ and Al₂O₃, respectively. For the chromia formers, there should be enough Cr in the alloys to form a continuous oxide scale and to effectively provide oxidation resistance under SOFC operating conditions.¹ The Al content in these alloys should be kept to a minimum to avoid formation of a continuous alumina layer, considering the insulating nature of alumina scales.⁸³

Cr-based alloys

At very high temperature (900–1000°C), Cr-based oxide dispersion strengthened (ODS) alloys were used to replace LaCrO₃. A typical alloy is Ducrolloy (Cr–5Fe–1Y₂O₃) which was specifically designed by Plansee Company to match the CTE of other SOFC components.⁸⁴ Some other Cr-based ODS alloys include: Cr–5Fe–1.3La₂O₃, Cr–5Fe–0.5CeO₂, Cr–5Fe–0.3Ti–0.5Y₂O₃ and others.

The reason for choosing Cr-based (chromia formation) alloys is because chromia has high conductivity compared to other oxides.⁷⁷ However, due to its high Cr content, Cr poisoning of the cathode and excessive chromia

growth are inevitable. Apart from that, ODS alloys are more difficult and costly to fabricate.¹ Since melting can affect the dispersion of the oxides, these techniques are powder metallurgy based and designed to produce near-net-shape components. For example, a powder metallurgy technique for directly producing sheets of interconnects has been reported; however, the cost of the alloy was still quite high.⁴⁰

Fe-Cr-based alloys

To fabricate a continuous chromia layer, the substrate alloy should have sufficient Cr content. The critical minimum Cr content has been summarized in literature⁸³ and is approximately 20–25 % in order to ensure the formation of a protective, continuous Cr₂O₃ scale. Note that low Cr content (5 % and 10 %) has also been used as interconnect. However, the oxidation resistance was reduced significantly when lowering the Cr content.⁸⁵ Low-Cr steels (<5 % Cr) consist of nearly pure Fe oxide accompanied by internal oxide precipitates of Cr₂O₃ and/or FeCr₂O₄ spinels. With increasing Cr content, the scales become richer in spinel and chromia, which is accompanied by a decrease of the scale growth rate. Nominal composition of Fe-Cr-based alloys is shown in Table 7.2.⁴⁰

Stainless steels are usually divided into four groups.⁸³

1. ferritic steels;
2. austenitic steels;
3. martensitic steels; and
4. precipitation hardening steels.

Among these, usually the ferritic stainless steels are the most promising candidates for SOFC interconnect applications because of their body-centred cubic structure, which makes the CTE quite close to that of other SOFC materials. In addition, the processing methods of this type of alloys are quite simple.⁸⁶ However, the effect of substrate impurities, Si and Al, on the performance of interconnect must not be neglected, especially Si, which could form a continuous layer between substrate and scale. Pacific Northwest National Lab (PNNL) has systematically investigated the (Mn,Co)₃O₄-coated SUS430 alloy (≈0.5 wt pct Si), showing that ASR will increase sharply at 4000 h due to the formation of continuous silica layer. Accordingly, SUS 441, with the addition of Nb and Ti based on SUS430, has also been tested. The results demonstrated that ASR is quite low even for bare metal, because Nb tied up Si to prevent the formation of a SiO₂ layer at the scale/metal interface.¹

During SOFC stack operation, the interconnect will face a reducing environment on the anode side and an oxidizing one on the cathode side. Therefore, exposure tests in air, to an H₂O + H₂ gas mixture simulating the

Table 7.2 Nominal composition of Fe-based alloys⁴⁰

Alloy	Concentration (wt %)										
	Fe	Cr	Mn	Mo	W	Si	Al	Ti	Y	Zr	La
Fe-10Cr	Bal	10	<0.02			<0.1					
1.4724	Bal	13					1				
SUS 430	Bal	16-17	0.2-1.0			0.4-1.0	≤0.2				
Fe-17Cr-0.2Y	Bal	17							0.2		
1.4016	Bal	17									
Ferrotherm (1.4742)	Bal	17-18	0.3-0.7			0.8-0.9	0.9-1.0				
Fe-18Cr-9W	Bal	18		9							
Fe-20Cr-7W	Bal	20		7		0.3	0.6			0.3	
Fe-20Cr	Bal	20	<0.02			<0.1					
ZMG 232	Bal	21-22	0.5			0.4	0.1-0.2			0.2	0.04
AL 453	Bal	22	0.3			0.3	0.6	0.02		0.3	0.1
Fe22CrMoTiY	Bal	22	0.1	2		<0.05	<0.05	0.3	0.4		
1.4763(446)	Bal	24-26	0.7-1.5	≤0.05		0.4-1		<0.05			
FeCrMn(LaTi)	Bal	16-25	?					?			?
Fe-Cr-Mn	Bal	16-25	?								
Fe-25Cr-DIN 50049	Bal	25	0.3			0.7		0.01			
Fe-25Cr-0.1Y-2.5Ti	Bal	25						2.5	0.1		

anode side service gas, and to air/H₂ gas dual atmosphere simulating real operating conditions have been carried out in various reports. In the H₂ + H₂O gas mixture, the chromia morphology is slightly modified and the adhesion of the scale is improved. In the dual atmosphere, the scales formed in air contained Fe-rich spinel or Fe₂O₃ nodules, which were not present in the alloys exposed to air on both sides. This suggests that the mobility of Fe is accelerated by hydrogen at the anode side.^{1,40,87}

Ni–Cr-based alloys

Ni–Cr-based alloys, compared with Fe–Cr-based alloys, have always demonstrated better oxidation resistance and satisfactory scale electrical conductivity. In order to obtain a continuous chromia layer, only 15 % Cr was needed to establish a reasonable resistance to hot corrosion, which is lower than Fe–Cr-based alloys, and the optimum content was 18–19 %. Also, Ni-based alloys are mechanically stronger. Nominal compositions of Ni-based alloy are shown in Table 7.3.⁴⁰

Most Ni–Cr-based alloys exhibited excellent oxidation resistance in moist hydrogen, growing a thin scale that was dominated by Cr₂O₃ and (Mn,Cr,Ni)₃O₄ spinels or Cr₂O₃.⁸⁸ Therefore, it could be used as clad metal or plated layer in the anode side.⁸⁹ In air oxidation, high Cr containing alloys, such as Haynes 230 and Hastelloy S, formed a thin scale mainly comprising Cr₂O₃ and (Mn,Cr,Ni)₃O₄ spinel during high temperature exposure. On the other hand, low Cr containing alloys, such as Haynes 242, developed a thick double-layer scale consisting of a NiO outside layer above a chromia-rich substrate, raising concern over its oxidation resistance for interconnect applications.^{1,40,77,88}

7.6 Miniaturisation of SOFCs

Miniaturization of SOFCs is one of the major directions in their development at the beginning of the 21st century. SOFCs have shown great potential because, depending on type of fuel cells, they can be utilized not only for the production of stationary energy but also for mobile applications for vehicle and portable electronics.¹¹ Polymer electrolyte fuel cells (PEFCs) have been demonstrated to be the most suitable for mobile applications.²⁰ The scaling-down factor is an important issue for compact, portable applications. Miniature SOFCs are predicted to have significant market penetration because of the expectation that they can produce energy densities per volume and specific energy per weight significantly larger compared to state-of-the-art rechargeable Li-ion and Ni metal hybrid batteries and also larger than PEFCs, especially when hydrocarbon fuels are used.⁹⁰ Considering the speed of the development of modern electronic devices and the

Table 7.3 Nominal composition of Ni-based alloys for SOFC interconnect applications⁴⁰

Alloy	Concentration (wt %)										
	Ni	Cr	Fe	Co	Mn	Mo	Nb	Ti	Si	Al	Al
Inconel 600	Bal	14–16	6–9		0.4–1			0.2–0.4	0.2–0.5		0.2
ASL 528	Bal	16	7.1		0.3				0.3		0.2
Haynes R-41(Rene 14)	Bal	19	5	11	0.1	10		3.1	0.5		1.5
Inconel 718	Bal	22	18	1	0.4	1.9					
Haynes 230	Bal	22–26	3	5	0.5–0.7	1–2					0.3
Hastelloy X	Bal	24	19	1.5	1.0	5.3					
Inconel 625	Bal	25	5.4	1.0	0.6	5.7					
Nicrofer 6025HT	Bal	25	9.5		0.1	0.5			0.5		0.15
Hastelloy G-30	Bal	30	1.5	5	1.5	5.5	1.5	1.8	1		

energy demand created by the expansion of their functionalities, it is envisaged that even updated modern rechargeable batteries will not be capable of matching this demand in the foreseeable future without changing their size. Therefore, compact SOFCs could provide an alternative to satisfy this growing demand. In principle, it is possible to scale-down the size of the whole device to micrometer level without affecting the overall SOFC efficiency. This is because direct conversion of chemical energy into electrical output energy does not suffer from the restrictions on thermodynamic efficiency associated with conventional thermomechanical energy production methods.

One of the substantial prerequisites for the use of SOFCs in mobile applications is the decrease of their operating temperature down to 350–600 °C.⁹¹ This temperature range will open opportunities for new and unique architectures, materials and technologies in the manufacture of miniaturized SOFCs. Two basic successful designs of miniaturized SOFCs for portable application at lower temperatures have been reported so far: microtubular SOFC and thin-film μ -SOFC.^{12,27,33} The first design allows scaling-down the size of the SOFC at the millimeter range, whereas the second design was prepared on Si substrates at the sub-millimeter range by using microfabrication technologies.

7.6.1 Microtubular SOFCs

Based on a recent review of the microtubular SOFC design,⁹² the main limiting factor for employing SOFCs in portable power production was the high operating temperature. Another report described the development of a microtubular SOFC stack based on YSZ tubes with wall thickness of 0.2 mm and an internal diameter of just 2 mm.⁹³ Such a design can successfully withstand rapid temperature cycling between 400 and 800 °C at a rate of ~ 200 °C/min without failure. The stack was a robust design with high efficiency. Another report demonstrated tolerance of thermal cycling at a much higher heating/cooling rate of 4000 °C/min.⁹⁴ These promising findings have boosted research activity towards the miniaturization of SOFC design in order to improve processing of the cell's elements and advance the materials' performance.

The most customary microtubular SOFC stack design is a heat exchanger-like arrangement with a bundle of microtubular SOFCs with hydrogen flowing inside each cell and air flowing outside the cells. In the contrast to the planar SOFC, where appropriate sealing is vital, tubular SOFCs only need sealing at the junction with cells and manifolds. It has to be admitted that, owing to very small dimensions, microtubular SOFCs need to be sealed more accurately than their larger counterparts. So far the most promising electrolyte material remains YSZ due to its toughness and because the CTE

is compatible with the other cell materials. YSZ can be deposited or extruded and can also be co-extruded with other functionally graded materials. Microtubes of various electrolytes such as GDC and Sr- and Mg-doped La have also been extruded.⁹⁵

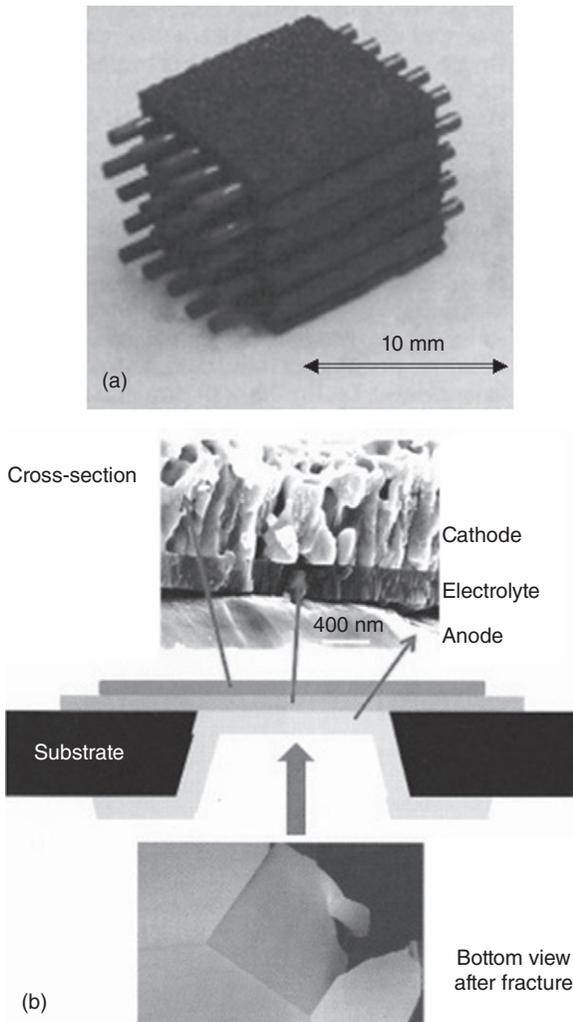
An alternative to the extrusion procedure – electrophoretic deposition (EPD) – has recently been proposed for fabrication of the elements of microtubular SOFCs.⁹⁶ EPD is a very versatile technique which displayed several advantages for fabrication of multilayers for SOFCs.⁹⁷ An example of a microtubular SOFC is presented in Fig. 7.10a.³⁷ This SOFC consisted of 25 microtubular cells with a diameter of 0.8 mm in a 5×5 configuration. The tubular cells were based on anode-supported GDC electrolyte and stored in a porous $\text{La}_{0.6}\text{Sr}_{0.4}\text{Co}_{0.2}\text{Fe}_{0.8}\text{O}_3$ (LSCF) matrix. The electrode area of the single bundle was about 5 cm^2 . The demonstrated efficiency obtained for a single microtubular cell of 0.8 mm in diameter increased from 350 mW cm^{-2} at 550°C , with hydrogen as fuel,⁹⁸ to more than 1.0 W cm^{-2} upon improvement of the anode microstructure.⁹⁹ Consequently, the overall power density for a stack of three bundles with fuel manifolds, each bundle having five microtubular cells, was about 2.0 W cm^{-3} at 550°C .¹⁰⁰ Further improvement is on its way and will be based on the use of bi-layer electrolytes to block the electronic conductivity of GDC.¹⁰⁰

More research directed at the improvement of the microtubular SOFC must concentrate on enhancing of the electrochemical performance of the stack, reducing polarization losses at the electrodes and improving the stack design. In this regard, alternative materials and manufacturing techniques can open new possibilities for improvement in cell performance and efficiency.

7.6.2 Thin-film μ -SOFCs

Thin-film μ -SOFCs based on Si substrates with sub-millimeter scale lateral dimensions are very promising for use in portable electronic devices operating at low temperatures. Modern state-of-the-art microfabrication techniques allow, in principle, the building of a thin-film design SOFC on a single chip with other electronic circuits, enabling extended, remote operation of portable electronic devices.¹⁰¹ Integration of the thin-film materials into the development of 3D structures will open new opportunities to improve SOFC performance.

Considering the number of reports dedicated to the development of thin-film μ -SOFCs and fabrication of the entire device on one substrate, it can be concluded that, although the reported results are promising, the market penetration of these devices is still fragmentary. A maximum power density of 140 mW cm^{-2} at 575°C has been reported for SOFCs based on YSZ electrolyte using hydrogen as fuel.¹⁰² In this SOFC, a porous Pt cathode layer



7.10 Typical configuration of the microtubular design (a) and the planar design (b) of SOFC. (Reprinted from Ref. 37 with permission from the Electrochemical Society)

was deposited on the YSZ electrolyte side and a porous NiO–YSZ thin film on the porous Ni side to boost the anode TPB. These layers were fabricated by pulsed laser deposition. The approach of using Ni substrate for μ -SOFCs fabrication has also been reported.¹⁰²

Another example of a μ -SOFC design, where a conventional dual-chamber configuration was used, is shown in Fig. 7.10b.³⁷ In this μ -SOFC design, the dense free-standing electrolyte membrane acts as an air/fuel barrier and as mechanical support for anode and cathode thin films.¹⁰³

However, from a practical point of view, the most important problem to be resolved in near future for the fabrication of μ -SOFCs is their thermomechanical stability. Residual tensile or compressive stresses deriving from thermal expansion mismatch with the substrate can lead to buckling and/or failure of the free-standing membrane even at relatively low temperatures. It was found that the deposition technique affects the residual stress in the electrolyte films.¹⁰⁴ Therefore, only a larger thickness/area ratio allowed such stress to be reduced. However, at the same time this μ -SOFC design was less efficient from the electrochemical point of view.

A different report has described ultra-thin μ -SOFCs fabricated by lithography and etching techniques.¹⁰⁵ In this μ -SOFC design, YSZ films as thin as 50 nm were deposited by RF sputtering on a silicon wafer with porous Pt films for both anode and cathode, which were fabricated by DC sputtering. The reported power density for ultra-thin YSZ electrolyte film was 130 mW cm^{-2} at 350°C , which was excellent for such a low temperature. In addition, an extra GDC layer between the YSZ and cathode films increased the power output to 200 mW cm^{-2} at 350°C , reaching 400 mW cm^{-2} at 400°C .

For μ -SOFC systems to become competitive in the market place, their materials and fabrication technologies need to be improved. A system comprising not only a μ -SOFC device but also a gas-processing unit for fuel reforming and post combustion, together with a suitable thermal management system, would represent such improvement.³⁷

One of the biggest challenges for thin-film μ -SOFC development is boosting the materials performance. For the time being, both electrolyte membrane and electrodes with low over-potentials, especially cathode, have not reached their optimum performance. For example, some improvement can be achieved in ionic conductivity of the polycrystalline films when depositing epitaxially-ordered electrolyte films.³⁷ This will also have a beneficial effect on thermomechanical reliability. It has recently been discovered that epitaxially-grown Sm-doped ceria (SDC) single crystals are stable in low-oxygen partial-pressure environments, while similar polycrystalline films were dramatically unstable.¹⁰⁵ In addition, further selection and fabrication of the cathode could be the crucial factors in the successful development of μ -SOFCs.

7.7 Low-temperature SOFCs

The key technical issue that has limited the deployment and wide industrial acceptance of SOFCs is their high operating temperature, resulting in higher systems costs and performance degradation rates. Further complications associated with the high operating temperature of SOFCs are slow start-up and shut-down cycles and high maintenance costs. Considerable efforts have been applied since 2000 for the improvement of SOFCs

performance by reducing their operating temperatures to the intermediate temperature (IT) range of 650–800 °C. In this IT range, metallic interconnections, can be used as an alternative to the ceramic components, and fabrication costs can be reduced. If the operating temperature for miniaturized SOFCs can be further reduced to below 600 °C, both radiation heat transfer and sintering rates exponentially decrease, resulting in much lower insulation cost and improved overall SOFC performance.^{18,33,91}

Moreover, if the operating temperature can be reduced further to less than ~350 °C, cheap stainless steel interconnects, elastomeric/polymeric seals and other alternative materials can be utilized with a high rate of success.⁹¹ In addition, rapid start-up and repeated thermal cycling from ambient to operating temperature become possible. All these factors are critical for the portable and transportation applications of SOFCs. A clear example is proton-exchange membrane fuel cells (PEMFCs), which were much preferred to SOFCs due to their low operating temperature of ~100 °C, even though PEMFCs require hydrogen fueling.

Apart from the reduction costs, lowering the SOFC operating temperature can help in bringing their performance up to the theoretical optimum efficiency. For example, the maximum theoretical efficiency of an SOFC using CO as fuel increases from 63 % at 900 °C to 81 % at 350 °C.⁹¹ However, it should be noted that lower operating temperature does not automatically result in higher system efficiency due to possible cell polarization losses. Therefore, the difference between the attained and the theoretical efficiencies increases as the operating temperature decreases. Overall efficiency depends on thermodynamics (attained voltage relative to the theoretical open-circuit potential and fuel use) and kinetics (polarization losses) during operation.³⁶ One example of improvement in SOFC performance is graphically presented in Plate XXIIa (see colour section between pages 232 and 233).⁹¹ The increase in overall SOFC efficiency was achieved by fabricating a bi-layered structure of 50 nm thick YSZ and 50 nm thick GDC. This structure has obtained a peak power density of ~400 mW cm⁻² at 400 °C and has demonstrated small polarization loss at such low temperatures.¹⁰⁴ Plate XXIIb schematically illustrates the power output of LT-SOFCs from a single cell to a module design and the approximate power requirements of a variety of portable and mobile applications.⁹¹

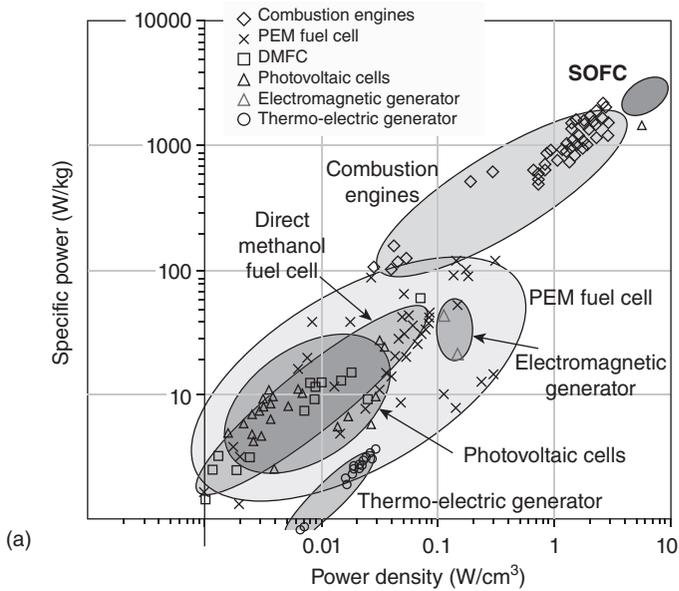
The total thickness of the LT-SOFC in the demonstrated cells was about 0.5 mm, and the expected interconnect thickness is 1.5 mm. Thus, based on areal power density of 2 W cm⁻², the stack volumetric power density and the gravimetric power density are ~10 W cm⁻³ and ~3 kW/kg, respectively.⁹¹ Figure 7.11 provides a comparison of the specific obtained power of an LT-SOFC with various energy conversion devices. For example, it is seen that the developed LT-SOFC exceeded an internal combustion engine in power density (Fig. 7.11a).⁹¹ Moreover, with liquid hydrocarbon fueling, SOFCs and

internal combustion engines have essentially the same specific energy, that of the fuel (~ 1 kWh/kg).¹⁰⁶ As a result, since the LT-SOFC has essentially the same power and energy density as an internal combustion engine (Fig. 7.11b), it could potentially transform the automotive sector as, for example, a range extender for plug-in hybrid electric vehicles (PHEVs) operating on conventional fuels. The corresponding 10 kW stack would only be a small cube of 10 cm per edge, as shown in Fig. 7.11b. However, it must be noted that other reports have claimed achievable power densities of ~ 2 W cm⁻², albeit at 800 °C with YSZ-based cells.^{107,108} However, these laboratory-scale button-cell results do not directly translate to full-scale stack performance because of numerous parasitic losses such as cell–interconnect interfacial resistances, thermal gradients and higher fuel use. Nevertheless, this demonstrates the potential of this technology if these losses can be addressed.

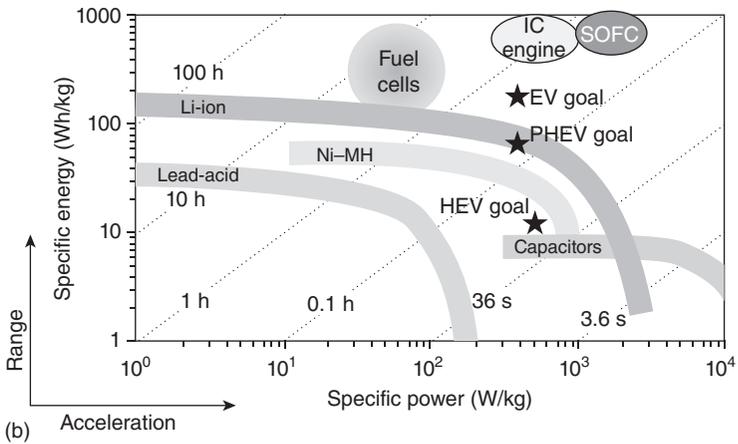
For portable and transportation applications, volumetric and gravimetric power densities are key performance metrics. Issues relating to fueling of SOFCs are highly dependent on the operating temperature and the electrode materials used. Lowering the operating temperature to the IT range has an impact on the efficiency of internal reforming, the propensity of carbon formation to occur and the extent to which impurities such as sulphur interact with the anode. The steam reforming (oxygenolysis) of hydrocarbons is a well-established process used on an industrial scale for the production of hydrogen.¹² The reaction is presented below in (7.2) and results in the formation of a mixture of CO and H₂ (syngas). Further reaction via water gas shift (WGS), as shown below in (7.3), converts CO and steam into more H₂. During internal reforming, these two reactions occur simultaneously, the equilibrium composition of the gas dictated by temperature and pressure. The CO and H₂ produced are subsequently electrochemically oxidized by the O²⁻ ions at the anode (7.3 and 7.4):



Figure 7.12 depicts the thermodynamically predicted composition of a system supplied with methane over a range of temperatures for three different steam-to-carbon (S/C) ratios.¹² Although the thermodynamically predicted composition may not be realized for lower temperatures owing to kinetic limitations, at a higher temperature range, relevant to IT-SOFC operation, kinetics are fast and the predictions are a reasonable indicator of the actual fuel composition. The amount of solid-phase carbon expected to form is also displayed.



(a)



(b)

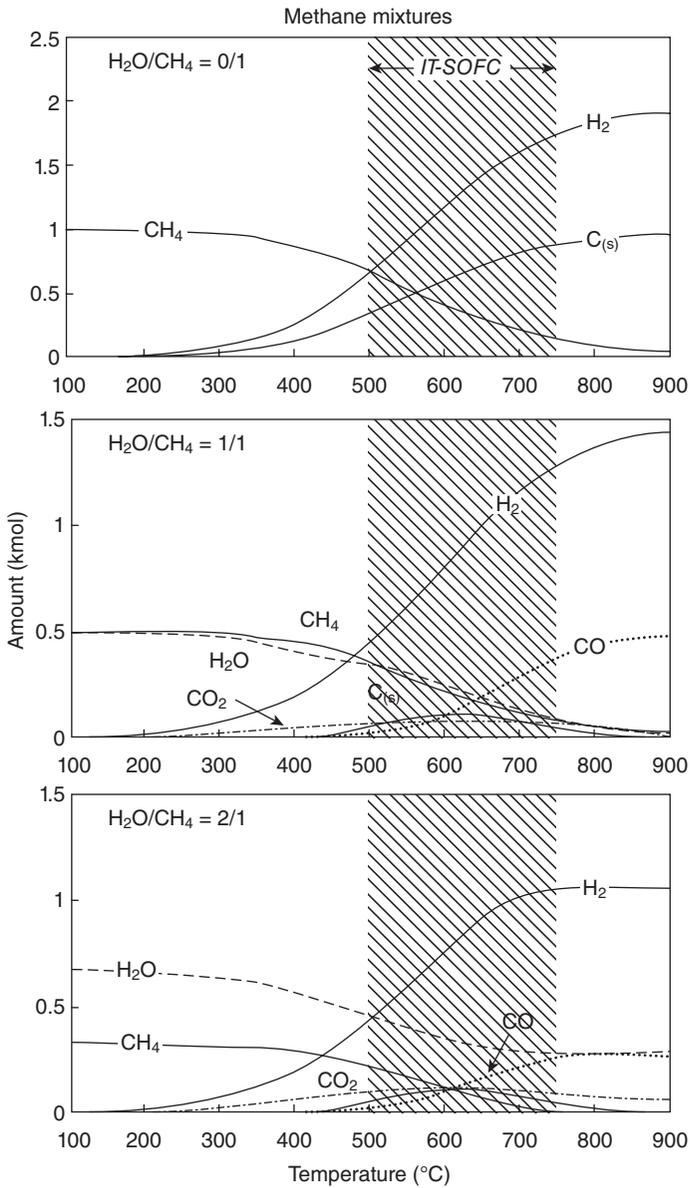
7.11 (a) Comparison of specific power of the present $\sim 2\text{W}/\text{cm}^2$ SOFC at 650°C compared with various energy conversion devices as a function of power density. (b) Ragone plot (specific energy versus specific power) for various energy devices compared with the present SOFC conductivity of perovskite oxides in air. (Reprinted from Ref. 91 with permission from *Science*)

The temperature and steam content both have a strong effect on the formation of carbon, as shown by Fig. 7.12. Operating dry (i.e. with no initially added steam), carbon formation becomes progressively worse with increasing temperature, whereas an S/C of 2 or more results in complete suppression of carbon.¹² Between these bounds (S/C = 1), carbon formation is predicted to be highest in the IT range. In practice, an S/C ratio of between 2 and 3 is used to safely avoid carbon deposition. However, excessive addition of steam can lower the system efficiency due to fuel dilution and the energy required to raise the steam. The lowest temperature at which an SOFC can effectively achieve internal reforming is contentious. The reforming reaction will occur at an appreciable rate over an appropriate catalyst, given an ample supply of steam at temperatures above $\sim 500^\circ\text{C}$. Direct coupling of the reforming reaction to the anode of the IT-SOFC then allows the oxidation of the hydrogen-rich reformat at the anode, shifting the equilibrium of the reforming reaction in such a way that a high conversion of hydrocarbon fuels can be achieved, even at operating temperatures down to 500°C . Moreover, since the reforming reaction is strongly endothermic ($\Delta H = +206\text{kJ mol}^{-1}$), cooling of the cell will occur, lowering the requirement for additional air cooling, reducing the parasitic air blower load and increasing net system efficiency. A small external pre-reformer may also be needed to convert higher hydrocarbons to methane before fuel enters the stack.

As was mentioned previously, various contaminants in the fuel interact with SOFC elements and degrade cell performance. Sulphur is a particular 'poison' for Ni-containing anodes even at very low concentrations of few ppm.¹⁰⁹ Desulphurizers are therefore commonly used to remove sulphur, though this adds to the complexity, cost and maintenance burden of the system. The interaction of sulphur (typically in the form of H_2S) with the anode is complex. Increasing temperature tends to lessen the degrading effect of sulphur on performance. However, steam and hydrogen content, oxide ion flux to the anode surface and the metallic and electrolyte material composition all have an effect.

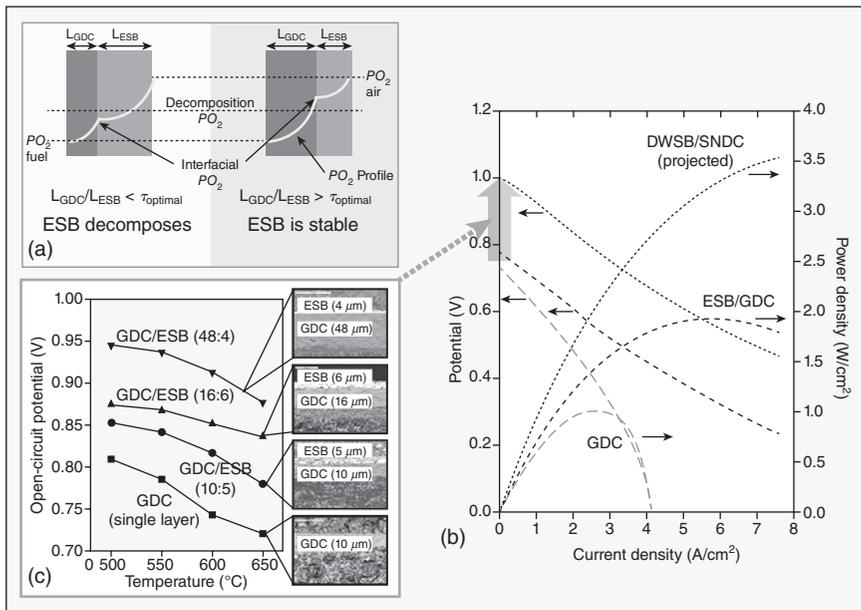
7.8 Toward further performance increase of SOFCs at lower temperatures

Although the developed LT-SOFCs ($\sim 650^\circ\text{C}$) with high power density are already suitable for numerous stationary applications, significant increases in power density and reductions in temperature are achievable by further optimizing the bi-layer thicknesses to increase optimal performance, incorporating electrodes with even greater conductivity, and engineering infiltrated nanostructured catalytically active electrodes. One feasible approach is optimization of the electrolyte layers for enhancement of



7.12 Thermodynamic predictions of the equilibrium composition for methane fed at different temperatures and steam-to-carbon ratios. The combined CH₄ + H₂O input amount is 1 kmol in each case. (Reprinted from Ref. 12 with permission from the Royal Chemical Society)

optimal performance without increasing ASR. Although the optimal reported LT-SOFC performance was increased to $\sim 2\text{W cm}^{-2}$ with addition of the bi-layer,¹¹⁰ the full theoretical value was not achieved because neither the total nor the relative thickness was optimized. As the thickness of mixed ionic and electronic conducting (MIEC) electrolytes, such as GDC, is decreased, the electronic leakage current increases, resulting in lower performance. Consequently, there is an optimum thickness in terms of trade-off between reducing ASR with thinner electrolytes and increasing optimal performance with thicker electrolytes.¹¹¹ Figure 7.13 illustrates the



7.13 (a) Schematic of ceria/bismuth oxide bi-layer concept demonstrating the effect of relative thickness on interfacial oxygen partial pressure and ESB stability. (b) Current-voltage behaviour (left y axis) and power density (right y axis) for SOFCs with GDC single-layer --- and ESB/GDC bi-layer ---- electrolytes at 650°C using 90 standard cubic centimetre per minute of 3% wet H_2 (anode side)/dry air (cathode side). With ESB/GDC bi-layer electrolyte, a power density of $\sim 2\text{W/cm}^2$ at 650°C was achieved because of higher performance and reduced cathodic polarization. By controlling total thickness and thickness ratio of more conductive DWBS/SNDC bi-layer electrolyte, the projected maximum power density is $\sim 3.5\text{W/cm}^2$ under the same conditions. (c) Effect of total thickness and thickness ratio of bi-layered electrolyte on OCP. OCP increases as total thickness and ESB/GDC thickness ratio increase and as temperature decreases, indicating the potential to achieve theoretical OCP at these temperatures. (Reprinted from Ref. 91 with permission from *Science*)

development of a new functionally graded ceria-bismuth oxide bi-layered electrolyte for an IT-SOFC (Fig. 7.13a) with measured $C-V$ characteristics (Fig. 7.13b) and the effect of total thickness variations in order to achieve the optimal power density (Fig. 7.13c).⁹¹

Based on two decades of research on the fundamentals of ion conduction,¹¹² the highest conductivity solid oxide electrolyte with a co-doped stabilized Bi_2O_3 [$\text{Dy}_{0.08}\text{W}_{0.04}\text{Bi}_{0.88}\text{O}_{1.56}$ (DWSB)] has been reported.¹¹³ In fact, at 350 °C, the ASR of 10 μm thick DWSB was only $0.6 \Omega\text{cm}^2$, low enough for SOFC operation at this temperature. DWSB has higher conductivity compared with erbia-stabilized Bi_2O_3 (by a factor of 1.9)¹¹³ and Sm–Nd-doped ceria (SNDC) has higher conductivity compared to GDC (by a factor of 1.4),¹¹⁴ and these characteristics can be used to increase their respective thicknesses with no impact on the electrolyte ASR at a temperature of 650 °C. It has been reported that an IT-SOFC can achieve $\sim 2 \text{Wcm}^{-2}$ by employing approximately 14 μm thick ESB/GDC (4:10 ratio) electrolyte.¹¹⁰ Increasing this to 21 μm thick DWSB/SNDC (7.5:13.5 ratio) would significantly increase optimal performance with no change in ASR, as shown in Fig. 7.13b. Furthermore, considering the 12-fold higher conductivity of DWSB compared with SNDC at 650 °C, increasing the DWSB thickness from 7.5 to 22.5 μm adds less than 9 % to the ohmic ASR, while significantly increasing total bi-layer thickness to 36 μm , relative (22.5:13.5 ratio) Bi_2O_3 thickness.⁹¹ As a result, increasing the optimal performance to 1 V without increasing the total polarization would have a significant effect on maximum power density, as projected for DWSB/SNDC.⁹¹

At lower temperatures, the ceria-based electrolytes have a wider electrolytic domain (the region where ionic conductivity dominates over electronic), and the Bi_2O_3 -based electrolytes have higher thermodynamic stability under reducing conditions. Therefore, obtaining theoretical open-circuit potential (OCP) using DWSB/SNDC bi-layers at lower temperatures can be achieved with both thinner total electrolyte layer and higher relative Bi_2O_3 thicknesses, further reducing ohmic resistance as temperature decreases. In fact, the Bi_2O_3 decomposition P_{O_2} decreases from $10^{-11.9}$ atm at 650 °C to $10^{-22.1}$ atm at 350 °C.⁹¹ The latter is comparable to typical anode-fuel P_{O_2} s and, as such, it is possible that DWSB could be used as a single layer at 350 °C to take advantage of both its low ASR and unity transference number (thus obtaining theoretical OCP).

The second feasible approach is the optimization of electrode microstructure to compensate for thermal activation. Exponentially decreasing area-specific electrode reaction rates (activation polarization) with decreasing temperature can be compensated by shifting the effective particle diameter of the catalytic phase from the micro (10^{-6}) to the nano (10^{-9}) regime, dramatically increasing 3D TPB density [$(10^{-6}/10^{-9})^3 = 10^9$], and thus proportionally reducing activation polarization.⁹¹ Moreover, it is

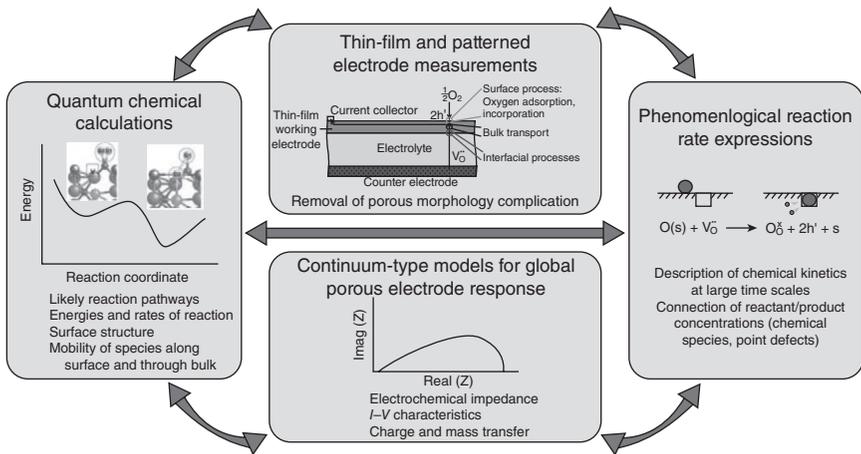
the reduced operating temperature that makes these nanostructured electrodes stable against coarsening, the primary performance degradation mechanism.

However, this particle size reduction must be done without negatively impacting percolation of the ionic/electronic and gas phase conduction paths that contribute to the electrode's ohmic and concentration polarizations, respectively. Consequently, nanostructured cathodes have been fabricated by infiltration of precursor solutions into porous ionic–electronic conducting scaffolds.¹¹⁵ For example, a recent report¹¹⁶ has demonstrated that infiltrated LSM in nanofibre YSZ scaffolds effectively decreased cathodic polarization from 70 to 90% compared with a conventionally mixed LSM–YSZ cathode. Moreover, infiltration has also been demonstrated to result in low polarization and stability at temperatures below 600°C.⁵⁰ To reduce the temperature to below 600°C, a multifaceted, multidisciplinary approach is required to deconvolute the multiple mechanistic contributions to electrode polarization, including catalytic, solid-state and pore transport contributions. By combining focused ion beam and SEM to quantify the cathode microstructure (in terms of morphology and porosity for gas diffusion, solid-phase surface area for gas adsorption/surface diffusion, and TPBs for the charge transfer reaction) with electrochemical impedance spectroscopy (EIS), it was possible to obtain direct logarithmic relationships between charge-transfer resistance and TPB length in typical random porous electrode structures.¹¹⁷ Kinetic rate constants and mechanistic results were obtained and demonstrated that cathode materials such as LSM have facile dissociative adsorption of O₂ and are rate-limited by the lattice incorporation step, whereas LSCF has rapid incorporation and is limited by oxygen surface coverage.¹¹⁸ These kinetic mechanistic measurements combined with the microstructure-polarization results provide the ability to rationally design and optimize the composition and microstructure of electrodes for LT operation.

7.9 Rational SOFC material design: new advances and tools

7.9.1 Continuum modeling

In optimization of SOFC design, in order to predict values of the experimentally measurable parameters, such as exchange current density and ASR of a cell, coupled continuum and phenomenological models can be used.^{15,38,119,120} These provide a means to understand the rates of charge and mass transfer processes in detail and predict them in a variety of circumstances. Figure 7.14 graphically illustrates the interdependence of models



7.14 Interdependence of models at different length and timescale and characterization techniques for the rational study and design of SOFC materials. (Reprinted from Ref. 38 with permission from the Elsevier Science)

at different lengths and timescales for the rational study of SOFC materials.³⁸

In turn, these models can predict the behaviour of materials or the performance of fuel cells under various conditions when the phenomenological parameters are known. For example, continuum models have been successfully applied to various aspects of electrode operation,¹²¹ from the global response of porous mixed conducting electrodes^{122,123} to the performance of heterogeneous composite electrodes described using particle/resistor networks¹²⁴ and homogenized treatment,¹²⁵ and to detailed reaction rates or intermediate steps of surface and interfacial processes.¹²⁶ Moreover, continuum models can link calculations indirectly to the experimental measurements, thus providing a means of verifying their predictions. For instance, these set-ups can be used to predict the performance of fuel cells from materials properties derived from simulations, including the molecular level reaction sequence, rate-limiting steps, detailed defect structures, surface structures and phenomenological parameters (e.g. surface-adsorbed oxygen concentration¹⁵), some of which may not be readily accessible from experiments.

Furthermore, a model conformal to electrode geometry is required to examine the effect of the microstructure on the performance of a porous electrode. Therefore, these phenomenological/continuum models have been successfully used with cells consisting of thin-film/patterned electrodes. As described in detail elsewhere,¹²⁷ these models have been used to predict potential and defect distribution in a thin-film working electrode with

current collectors of different geometries (strips, grids and circular pads), the critical spacing between current collectors to minimize the effect of sheet resistance on performance, and the relative contributions from competing bulk and TPB pathways of a patterned electrode under cathodic polarization.

The reactions on both cathode and anode are quite complex, often involving adsorption, dissociation and reduction/oxidation of gas molecules, transport of adsorbed surface species and participation of point defects (e.g. oxygen vacancies and electrons/electron holes). An electrochemical driving force may not only alter the concentrations of surface species within a mixed conductor, but also change their energies. Further, the composition and structure of an active electrode surface may be different from those of the bulk phase due to surface elemental segregation.¹²⁸ As a consequence of this, the linkage of electrochemical response with detailed surface properties and reaction mechanisms is quite a challenge and continues to be an important research pursuit.

7.9.2 Quantification of the microstructure effect

The 3D porosity and morphology of the electrode are critical factors influencing its performance. Other important factors include the exposed catalyst surface area, facility of gas transport through pores, resistance to ionic and electronic transport through solid phase and length of TPB lines. Plates XXIa and XXIb (see colour section between pages 232 and 233) provide a schematic diagram of charge and mass transport, specifically in the solid phase, highlighting the complexity of these processes.³⁸ There have been several strategies dedicated to the improvement and optimization of the electrode microstructure, including the formation of composite electrodes, functionally graded microstructures and infiltration of active electrode phases on electrolyte scaffolds. Optimization of the electrodes is a very difficult task because many of the important features compete with one another; for example, surface area may increase at the expense of gas-phase diffusion.¹⁵

Modelling of electrode reactions and interactions with gaseous environments at high temperatures at the microlevel^{129,130} has been proven to be a useful tool for understanding electrode performance. Another model type for mixed ionic–electronic conducting electrodes is based upon porous electrode theory¹²² and uses homogenized microstructural parameters and linear irreversible thermodynamics in reaction rates. 3D reconstruction by FIB/SEM¹³¹ and phase-sensitive X-ray computed tomography is a recent and promising development, providing high-resolution microstructural details of the structures of porous electrodes. The information obtained has been used in homogenized models for performance prediction.

One of the latest approaches to the modelling of SOFCs is based on the use of 3D reconstructions as the domain for electrochemical simulations using the lattice-Boltzmann method or the finite element method.¹³² The former has been applied primarily in the anode using models developed for Ni patterned electrodes, gas diffusion and ionic transport. The last has been activated and applied to an LSCF cathode using effective linear irreversible thermodynamic parameters (not detailed reaction rates) based on surface exchange and tracer diffusion coefficients. Recent results in such modelling are presented in Plate XXIc.³⁸ The figure shows the results for the simulation of the electrochemical response of 3D porous electrodes reconstructed by X-ray computed tomography.

While simulations conformal to the reconstructed electrode microstructures constitute a powerful computational framework, some challenges still remain. They are as follows:

- 3D reconstructions may require extensive and skilled FIB/SEM or synchrotron work.
- Simulations deployed on the actual porous structures need sophisticated numerical methods and, depending on the complexity of phenomena modelled, can require very complicated constitutive equations and/or parameter determination.¹⁵ Such simulations can corroborate the accuracy of homogenized models and, when homogenized models break down, provide the most accurate and detailed means of simulation.
- The detailed microstructure may also be able to act as a sort of well-defined electrode in and of itself: the *a priori* digital representation of explicit microstructural geometry might allow fundamental study.³⁸

Nevertheless, the ultimate goal is to use 3D geometry for numerical simulation of the performance of SOFC electrodes in engineering design, in conjunction with detailed, mechanistic, non-linear phenomenological rate expressions serving as boundary conditions¹³³ and informed by parameters derived from patterned or porous electrodes.³⁸

7.9.3 New directions and future perspectives

One important modern direction in modelling is to exploit nanostructures and nano-architectures derived from a variety of templates in order to transcend some of the difficulties facing materials development for energy applications. Specifically, the use of nanomaterials as electrode materials and catalysts expands their extended surface area dramatically.^{119,120} Nanostructured thin-film catalysts are the only practical materials found and reported so far.¹²⁰ The support is a thin monolayer of an oriented array of organic whiskers, less than 1 μm tall and $30 \times 55 \text{ nm}$ in cross-section. It is

applied to a roll-good substrate (a material made by a roll-to-roll process) with a number density of 30–40 whiskers per square micrometer, and then magnetron sputter-coated with catalyst thin films. Modelling of such hierarchical 3D nanoporous architectures may dramatically enhance the rates of charge and mass transfer processes while improving the mechanical integrity and robustness. These nanostructured electrodes and interfaces are known for increased numbers of active sites for electrochemical reactions, extremely high surface-to-volume ratio, reduced length of ion diffusion to active sites and greater flexibility in surface modification for catalysis and electrocatalysis.¹³⁴

Another important new direction is the development of a predictive multiscale computational framework, through rigorous validation at each scale by carefully designed experiments under *in situ* conditions, for the rational design of better structured materials for a new generation of SOFCs. These new SOFCs can be powered by readily available fuels. While significant progress has been made in developing SOFC materials, in probing and mapping electrode surface species relevant to electrode processes, and in unravelling some of the mechanisms of the electrode processes, many challenges still remain to bridge the gaps between models at different scales or between theoretical predictions and experimental observations. Only when the detailed mechanisms of the rate-limiting steps are clearly understood and verified will it be possible to rationally design better-structured nano- and micromaterials.

All the above-mentioned developments illustrate that the level and quality of fundamental research in the field need to continue unabated. Particularly beneficial would be a clear comprehension of the surface area and activity loss mechanisms, and insight into the causes of durability loss associated with the ageing mechanisms and with externally and internally generated impurities. It is vital to perform well-designed experiments at each scale under *in situ* conditions in order to validate and perfect the predictability of the individual models at different scales. Linking the global performance or functionality of a 3D porous electrode with the *local* structure, composition and morphology of nanostructured surfaces and interfaces remains a grand challenge.³⁸ Validation and integration of information collected from different scales are critical to developing a computational framework across multiple scales for the rational design of materials with exceptional functionality.

7.10 SOFC applications and markets

Forty years have passed since the first successful demonstration of a SOFC. Through ingenuity, materials science and micro- and nanotechnologies, extensive research and commitment to developing alternative energy

sources, that seed of an idea has germinated and is about to bloom into a viable, robust energy alternative. Materials development will certainly continue to make SOFCs increasingly affordable, efficient and reliable.

The US government is taking a proactive role in expediting the technology through the Solid State Energy Conversion Alliance (SECA), which is coordinated by the Department of Energy and Pacific Northwest National Laboratory. The technical goal is to develop mass-producible, modular SOFC units capable of 3–10 kW at a price of \$400/kW. The SECA's approach is to develop industrial collaborations and to extend the financial support for technical research. In this regard, analysts expect that the overall market for fuel cell technology could reach \$115 billion by the year 2015. The market share that will belong to SOFCs is unclear but will surely be significant, as SOFCs are targeted for use in three energy applications: stationary energy sources, transportation and military applications.²

Stationary installations would be the primary or auxiliary power sources for such facilities as homes, office buildings, industrial sites, ports and military installations. They are well-suited for mini-power-grid applications at places like universities and military bases. According to the SECA, worldwide demand for electricity is expected to double by 2030. SOFC technology is ideal for such an expansion, since much of the anticipated demand is expected to come from growing economies with minimal infrastructure. SOFCs can be positioned on-site, even in remote areas; on-site location makes it possible to match power generation to the electrical demands of the site.

Stationary SOFC power generation is no longer just a hope for the future. Siemens Westinghouse has tested several prototype tubular systems, with excellent results. Meanwhile, in Australia, Ceramic Fuel Cells Pty Ltd has been operating prototype planar fuel cell plants since 2001 and it is expected to be ready with market-entry products in 2013.

In the transportation sector, SOFCs are likely to find applications in both trucks and automobiles. In diesel trucks, they will probably be used as auxiliary power units to run electrical systems, for example, air conditioning and on-board electronics. Such units would preclude the need to leave diesel trucks running at rest stops, thereby leading to savings in diesel fuel expenditures and a significant reduction in both diesel exhaust and truck noise. Meanwhile, automobile manufacturers have invested at least \$4.5 billion in fuel cell research (not all SOFC).¹¹ There are an estimated 600 million vehicles worldwide, 75 % of which are personal automobiles, and the number is expected to grow by 30 % by 2015.²¹ With more stringent environmental restrictions in the US and European Union, automobile manufacturers are under growing time pressure to bring non-polluting cars to the market place. SOFCs are attractive prospects because of their ability to use readily available, inexpensive fuels.

Market penetration in the near future will be dependent on fuel flexibility and thermal cycling. How best to use SOFC fuel flexibility depends on desired fuel choice and operating temperature for a particular application. For stationary distributed generation applications, the ability to internally reform natural gas with conventional Ni–YSZ cermet anodes at $\geq 700^\circ\text{C}$ has been well-demonstrated.⁹¹ Unfortunately, at lower temperatures Ni–YSZ anodes experience performance degradation due to carbon coking and sulphur poisoning as well as Ni oxidation to NiO during thermal cycling.¹³⁵ However, CeO₂-based anodes are utilized and have been demonstrated to increase both coking and sulphur tolerance as well as the ability to operate directly on hydrocarbon fuels.⁹¹

All-ceramic anodes are also being developed (e.g. La_{0.4}Sr_{0.6}Ti_{1-x}Mn_xO₃ and Sr₂Mg_{1-x}Mn_xMoO_{6- δ})¹³⁶ because they do not undergo metal/metal-oxide phase transition (e.g. Ni/NiO) during thermal cycling. They also exhibit enhanced coking and sulphur tolerance, but to date have lower performance due to insufficient electronic conductivity and/or low electrocatalytic hydrocarbon oxidation activity.

Regardless, as temperature is reduced, the tendency toward coking can be compensated by a higher degree of external reforming. The DWSB/SNDC bi-layer electrolyte makes SOFC operation down to $\sim 350^\circ\text{C}$ feasible if appropriate electrodes are developed. Although these temperatures would require a thermally integrated external fuel reformer, the overall system efficiency should still be higher than PEMFCs using hydrocarbons as the source of H₂.⁹¹

Finally, SOFCs are of great interest to the military as they can be installed and established on-site in remote locations. They are quiet and non-polluting. Moreover, the use of fuel cells could significantly reduce deployment costs: 70 % by weight of the material that the military moves is nothing but fuel.

7.11 References

1. J. Wu, X. Liu, Recent development of SOFC metallic interconnect, *J. Mater. Sci. Technol.*, 26 (2010) 293–305.
2. Y. Kobayashi, T. Kabata, K. Tomida, Y. Ando, M. Nishiura, N. Mataka, Extremely high-efficiency thermal power system-solid oxide fuel cell (SOFC) triple combined-cycle system, *Mitsubishi Heavy Ind. Tech. Rev.*, 48 (2011) 9–15.
3. J. Weissbart, R. Ruka, A solid electrolyte fuel cell, *J. Electrochem. Soc.*, 109 (1962) 723–726.
4. S.C. Singhal, Science and technology of solid-oxide fuel cells, *MRS Bull.*, 25 (2000) 16–21.
5. S. Park, J.M. Vohs, R.J. Gorte, Direct oxidation of hydrocarbons in a solid-oxide fuel cell, *Nature*, 404 (2000) 265–267.

6. J.-H. Liou, P.-J. Liou, T.-S. Sheu, Physical properties and crystal chemistry of bismuth oxide solid solution, *Proc. Symp. Processing and Characterization of Electrochemical Materials and Devices*, Indianapolis, 25–28 April 1999, 3–10. *Ceram. Trans.* 109.
7. M.M. Seabaugh, S.L. Swartz, W.J. Dawson, Developing colloidal fabrication processes for YSZ solid electrolyte membranes, *Proc. Symp. Processing and Characterization of Electrochemical Materials and Devices*, Indianapolis, 25–28 April 1999, 21–30. *Ceram. Trans.* 109.
8. J.M. Ralph, J.A. Kilner, B.C.H. Steele, Improving Gd-doped ceria electrolytes for low temperature solid oxide fuel cells, *Proc. Symp. New Materials for Batteries and Fuel Cells*, San Francisco, 5–8 April 1999, 309–314.
9. J.-W. Moon, H.-J. Hwang, M. Awano, K. Maeda, Preparation of NiO-YSZ tubular support with radially aligned pore channels, *Mater. Lett.*, 57 (2003) 1428–1434.
10. Y. Matsuzaki, I. Yasuda, Dependence of SOFC cathode degradation by chromium-containing alloy on compositions of electrodes, *J. Electrochem. Soc.*, 148 (2001) A126–A131.
11. S.C. Singhal, Solid oxide fuel cells, *The ECS Interface*, 16 (2007) 41–44.
12. D.J.L. Brett, A. Atkinson, N.P. Brandon, S.J. Skinner, Intermediate temperature solid oxide fuel cells, *Chem. Soc. Rev.*, 37 (2008) 1568–1578.
13. C.-W. Sun, R. Hui, J. Roller, Cathode materials for solid oxide fuel cells: a review, *J. Solid State Electrochem.*, 14 (2010) 1125–1144.
14. R.M. Ormerod, Solid oxide fuel cells, *Chem. Soc. Rev.*, 32 (2003) 17–28.
15. S. Zhuikov, *Electrochemistry of Zirconia Gas Sensors*, 2007, CRC Press, Boca Raton, 297.
16. T. Zawodzinski Jr., A. Wieckowski, S. Mukerjee, M. Neurock, Integrated theoretical and experimental studies of fuel cell electrocatalysts, *The ECS Interface*, 16 (2007) 37–41.
17. J. Suntivich, H.A. Gasteiger, N. Yabuuchi, H. Nakanishi, J.B. Goodenough, Y. Shao-Horn, Design principles for oxygen-reduction activity on perovskite oxide catalysts for fuel cells and metal-air batteries, *Nat.: Chem.*, 3 (2011) 546–550.
18. E.A. Artukhin, Optimum planning of experiments in the identification of heat-transfer processes, *J. Eng. Phys. Thermophys.*, 56 (1989) 256–260.
19. H.J. Choi, S.M. Jung, J.M. Seo, D.W. Chang, L. Dai, J.B. Baek, Graphene for energy conversion and storage in full cells and supercapacitors, *Nano Energy*, 1 (2012) 534–551.
20. A. Boudghene Stambouli, E. Traversa, Solid oxide fuel cells (SOFCs): a review of an environmentally clean and efficient source of energy, *Ren. Sustain. Energy Rev.*, 6 (2002) 433–455.
21. N.Q. Minh, Solid oxide fuel cell technology – features and application, *Solid State Ionics*, 174 (2004) 271–277.
22. J.Z. Ou, S. Balendhran, M.R. Field, D.G. McCulloch, A.S. Zoolfakar, R.A. Rani, S. Zhuikov, A.P. O’Mullane, K. Kalantar-zadeh, The anodized crystalline WO₃ nanoporous network with enhanced electrochromic properties, *Nanoscale*, 4 (2012) 5980–5988.
23. A.J. McEvoy, Thin SOFC electrolytes and their interfaces – a near-term research strategy, *Solid State Ionics*, 132 (2000) 159–165.

24. Z.P. Shao, S.M. Halle, A high-performance cathode for the next generation of solid-oxide fuel cells, *Nature*, 431 (2004) 170–173.
25. Z.L. Zhan, S.A. Barnett, An octane-fueled solid oxide fuel cell, *Science*, 308 (2005) 844–847.
26. A. Atkinson *et al.*, Advanced anodes for high-temperature fuel cells, *Nat.: Mater.*, 3 (2004) 17–27.
27. E.D. Wachsman, S.C. Singhal, Solid oxide fuel cells: commercialization, research, and challenges, *The ECS Interface*, 18 (2009) 38–43.
28. J.W. Kim, A.V. Virkar, K.Z. Fung, K. Mehta, S.C. Singhal, Polarization effects in intermediate temperature, anode-supported solid oxide fuel cells, *J. Electrochem. Soc.*, 146 (1999) 69–78.
29. J. Nowotny, T. Bak, M.K. Nowotny, C.C. Sorrell, Charge transfer at oxygen/zirconia interface at elevated temperature, *Adv. Appl. Ceramics*, 104 (2005) 154–164.
30. D. Gostovic, N.J. Vito, K.A. O'Hara, K.S. Jones, E.D. Wachsman, Microstructure and connectivity quantification of complex composite electrode three-dimensional networks, *J. Am. Ceram. Soc.*, 94 (2011) 620–627.
31. J.M. Ralph, A.C. Schoeler, M. Krumpelt, Materials for lower temperature SOFC, *J. Mater. Sci.*, 36 (2001) 1161–1172.
32. B.C.H. Steele, Material science and engineering: the enabling technology for the commercialization of fuel cell systems, *J. Mater. Sci.*, 36 (2001) 1053–1068.
33. L. Fan, C. Wang, B. Zhu, Low temperature ceramic fuel cells using all nano composite materials, *Nano Energy*, 1 (2012) 631–639.
34. J.W. Fergus, Electrolytes for solid oxide fuel cells, *J. Power Sources*, 162 (2006) 30–40.
35. M. Mogensen, N.M. Sammes, G.A. Tompsett, Physical, chemical and electrochemical properties of pure and doped ceria, *Solid State Ionics*, 129 (2000) 63–94.
36. B.C.H. Steele, A. Heinzl, Materials for fuel-cell technologies, *Nature*, 414 (2001) 345–352.
37. E. Traversa, Toward the miniaturization of solid oxide fuel cells, *The ECS Interface*, 18 (2009) 49–52.
38. M. Liu, M.E. Lynch, K. Blinn, F.M. Alamgir, Y.M. Choi, Rational SOFC material design: new advances and tools, *Mater. Today*, 14 (2011) 543–546.
39. G.A. Tomsett, C. Finnerty, K. Kendall, T. Alston, N.M. Sammes, Novel applications for micro-SOFCs, *J. Power Sources*, 86 (2000) 376–384.
40. J.W. Fergus, Metallic interconnects for solid oxide fuel cell, *Mater. Sci. Eng. A*, 397 (2005) 271–283.
41. P.R. Shearing, D.J.L. Brett, N.P. Brandon, Towards intelligent engineering of SOFC electrodes: a review of advanced microstructural characterization techniques, *Int. Mater. Rev.*, 55 (2010) 347–363.
42. J. Richter, P. Holtappels, T. Graule, T. Nakamura, L.J. Gauckler, Materials design for perovskite SOFC cathodes, *Monatsh. Chem.*, 140 (2009) 985–999.
43. S.J. Skinner, Recent advances in Perovskite-type materials for solid oxide fuel cell cathodes, *Int. J. Inorg. Mater.*, 3 (2001) 113–121.

44. C.W. Sun, Z. Xie, C.R. Xia, H. Li, L.Q. Chen, Investigations of mesoporous CeO₂-Ru as a reforming catalyst layer for solid oxide fuel cells, *Electrochem. Commun.*, 8 (2006) 833–838.
45. A. Endo, S. Wada, C.J. Wen, H. Komiyama, K. Yamada, Low overvoltage mechanism of high ionic conducting cathode for solid oxide fuel cell, *J. Electrochem. Soc.*, 145 (1998) L35–L37.
46. Y. Liu, S.W. Zha, M.L. Liu, Novel nanostructured electrodes for solid oxide fuel cells fabricated by combustion chemical vapor deposition (CVD), *Adv. Mater.*, 16 (2004) 256–260.
47. M. Mamak, G.S. Metraux, S. Petrov, N. Coombs, G.A. Ozin, M.A. Green, Lanthanum strontium manganite/yttria-stabilized zirconia nanocomposites derived from a surfactant assisted, co-assembled mesoporous phase, *J. Am. Chem. Soc.*, 125 (2003) 5161–5175.
48. Y.J. Leng, S.H. Chan, Q.L. Liu, Development of LSCF-GDC composite cathodes for low-temperature solid oxide fuel cells with thin film GDC electrolyte, *Int. J. Hydrogen Energy*, 33 (2008) 3808–3817.
49. M. Antonetti, G.A. Ozin, Promises and problems of mesoscale materials chemistry or why meso?, *Chem. Eur. J.*, 10 (2004) 28–41.
50. J.M. Vohs, R.J. Gorte, High-performance SOFC cathodes prepared by infiltration, *Adv. Mater.*, 21 (2009) 943–956.
51. S.P. Jiang, A review of wet impregnation – An alternative method for the fabrication of high performance and nano-structured electrodes of solid oxide fuel cells, *Mater. Sci. Eng. A*, 418 (2006) 199–210.
52. Y. Huang, J.M. Vohs, R.J. Gorte, An examination of LSM-LSCo mixtures for use in SOFC cathodes, *J. Electrochem. Soc.*, 153 (2006) A951–A955.
53. T.Z. Shoklapper, H. Kurokawa, C.P. Jacobson, S.J. Visco, L.C. DeJonghe, Nanostructured solid oxide fuel cell electrodes, *Nano Lett.*, 7 (2007) 2136–2141.
54. S. Zhuiykov, Development of dual sulfur oxides and oxygen solid state sensor for ‘in-situ’ measurements, *Fuel*, 79 (2000) 1255–1265.
55. X. Guo, J. Maier, Grain boundary blocking effect in zirconia: a Schottky barrier analysis, *J. Electrochem. Soc.*, 148 (2001) E121–E126.
56. X. Xin, Z. Lu, Z. Ding, X. Huang, Z. Liu, X. Sha, Y. Zhang, W. Su, Synthesis and characteristics of nanocrystalline YSZ by homogeneous precipitation and its electrical properties, *J. Alloys Compd.*, 425 (2006) 69–75.
57. B. Dalslet, P. Blennow, P.V. Hendriksen, N. Bonanos, D. Lybye, M. Mogensen, Assessment of doped ceria as electrolyte, *J. Solid State Electrochem.*, 10 (2006) 547–561.
58. V.V. Kharton, F.M.B. Marques, A. Atkinson, Transport properties of solid oxide electrolyte ceramics: a brief review, *Solid State Ionics*, 174 (2004) 135–149.
59. H. Yahiro, K. Eguchi, H. Arai, Electrical properties and reducibilities of ceria-rare earth oxide systems and their application to solid oxide fuel cell, *Solid State Ionics*, 36 (1989) 71–75.
60. V.V. Kharton, F.M. Figueiredo, L. Navarro, E.N. Naumovich, A.V. Kovalevsky, A.A. Yaremchenko, A.P. Viskup, A. Carneiro, F.M.B. Marques, J.R. Frade, Ceria-based materials for solid oxide fuel cells, *J. Mater. Sci.*, 36 (2001) 1105–1117.
61. S. Wang, T. Koyabashi, M. Dokiya, T. Hashimoto, Electrical and ionic conductivity of Gd-doped ceria, *J. Electrochem. Soc.*, 147 (10) (2000) 3606–3609.

62. E. Jud, L.J. Gauckler, The effect of cobalt oxide addition on the conductivity of $\text{Ce}_{0.9}\text{Gd}_{0.1}\text{O}_{1.95}$, *J. Electroceram.*, 15 (2005) 159–166.
63. A. Sin, Yu. Dubitsky, A. Zaopo, A.S. Aricò, L. Gullo, D. La Rosa, S. Siiracusano, V. Antonucci, C. Oliva, O. Ballabio, Preparation and sintering of $\text{Ce}_{1-x}\text{Gd}_x\text{O}_{2-x/2}$ nanopowders and their electrochemical and EPR characterization, *Solid State Ionics*, 175 (2004) 361–366.
64. D.J. Seo, K.O. Ryu, S.B. Park, K.Y. Kim, R.-H. Song, Synthesis and properties of $\text{Ce}_{1-x}\text{Gd}_x\text{O}_{2-x/2}$ solid solution prepared by flame spray pyrolysis, *Mater. Res. Bull.*, 41 (2006) 359–366.
65. S. Wang, H. Inaba, H. Tagawa, M. Dokiya, T. Hashimoto, Nonstoichiometry of $\text{Ce}_{0.9}\text{Gd}_{0.1}\text{O}_{1.95-x}$, *Solid State Ionics*, 107 (1998) 73–79.
66. J.W. Stevenson, T.R. Armstrong, D.E. McCready, L.R. Pederson, W.J. Weber, Processing and electrical properties of alkaline earth-doped lanthanum gallate, *J. Electrochem. Soc.*, 144 (10) (1997) 3613–3620.
67. M. Kajitani, M. Matsuda, M. Miyake, Effect of Al doping on crystal structure and electrical conduction properties of $\text{LaGa}_{0.9}\text{Mg}_{0.1}\text{O}_{2.95}$ perovskite compound, *Solid State Ionics*, 178 (2007) 355–358.
68. T. Schober, Applications of oxidic high-temperature proton conductors, *Solid State Ionics*, 162–163 (2003) 277–281.
69. E. Gorbova, B.V. Zhuravlev, A.K. Demin, S.Q. Song, P.E. Tsiakaras, Charge transfer properties of $\text{BaCe}_{0.88}\text{Nd}_{0.12}\text{O}_{3-\delta}$ co-ionic electrolyte, *J. Power Sources*, 157 (2006) 720–723.
70. H. Taherparvar, J.A. Kilner, R.T. Baker, M. Sahibzada, Effect of humidification at anode and cathode in proton-conducting SOFCs, *Solid State Ionics*, 162–163 (2003) 297–303.
71. T. Kobayashi, H. Watanabe, M. Hibino, T. Yao, Electrical conductivity of $\text{Ba}_{1-x}\text{La}_x\text{Sc}_{1-y}\text{Zr}_y\text{O}_{3-\delta}$ with defective perovskite structure, *Solid State Ionics*, 176 (2005) 2439–2443.
72. M. Cimenti, J.M. Hill, Direct utilization of liquid fuel cells in SOFC for portable applications: challenges for the selection of alternative anodes, *Energies*, 2 (2009) 377–410.
73. J.C. Ruiz-Morales, D. Marrero-López, J. Canales-Vázquez, J.T.S. Irvine, Symmetric and reversible solid oxide fuel cells, *RSC Adv.*, 1 (2011) 1403–1414.
74. M. Andersson, H. Paradis, J. Yuan, B. Sundén, Review of catalyst materials and catalytic steam reforming reactions in SOFC anodes, *Int. J. Energy Res.*, 35 (2011) 1340–1350.
75. J.W. Fergus, Oxide anode materials for solid oxide fuel cells, *Solid State Ionics*, 177 (2006) 1529–1541.
76. E.P. Murray, T. Tsai, A direct-methane fuel cell with a ceria based anode, *Nature*, 400 (1999) 649–651.
77. J.W. Fergus, Lanthanum chromite-based materials for solid oxide fuel cell interconnects, *Solid State Ionics*, 171 (2004) 1–15.
78. S. Fontana, R. Amendola, S. Chevalier, P. Piccardo, G. Caboche, M. Vivani, R. Molins, M. Sennour, Metallic interconnects for SOFC: Characterisation of corrosion resistance and conductivity evaluation at operating temperature of differently coated alloys, *J. Power Sources*, 171 (2007) 652–662.
79. N. Ming, Ceramic fuel cells, *J. Am. Ceram. Soc.*, 76 (1993) 563–588.
80. F. Tietz, Thermal expansion of SOFC materials, *Ionics*, 5 (1999) 129–139.

81. W.Z. Zhu, S.C. Deevi, Development of interconnect materials for solid oxide fuel cells, *Mater. Sci. Eng. A*, 348 (2003) 227–243.
82. W.Z. Zhu, S.C. Deevi, Opportunity of metallic interconnects for solid oxide fuel cells: a status on contact resistance, *Mater. Res. Bull.*, 38 (2003) 957–972.
83. Z. Yang, K. Weil, D. Paxton, J. Stevenson, Selection and evaluation of heat-resistant alloys for SOFC interconnect applications, *J. Electrochem. Soc.*, 150 (2003) A1188–A1201.
84. W.Z. Zhu, S.C. Deevi, Opportunity of metallic interconnects for solid oxide fuel cells: a status on contact resistance, *Res. Bull.*, 38 (2003) 957–972.
85. S. Geng, J. Zhu, M. Brady, H. Anderson, X. Zhou, Z. Yang, A low-Cr metallic interconnect for intermediate-temperature solid oxide fuel cells, *J. Power Sources*, 172 (2007) 775–781.
86. W. Qu, L. Jian, D. Ivey, J. Hill, Yttrium, cobalt and yttrium/cobalt oxide coatings on ferritic stainless steels for SOFC interconnects, *J. Power Sources*, 157 (2006) 335–350.
87. Z. Yang, M.S. Walker, P. Singh, J.W. Stevenson, T. Norby, Oxidation behavior of ferritic stainless steels under SOFC interconnect exposure conditions, *J. Electrochem. Soc.*, 151 (2004) B669–B678.
88. Z. Yang, G. Xia, J. Stevenson, Evaluation of Ni-Cr-Base alloys for SOFC interconnect applications, *J. Power Sources*, 160 (2006) 1104–1110.
89. L. Chen, Z. Yang, B. Jha, G. Xia, J. Stevenson, Clad metals, roll bonding and their applications for SOFC interconnects, *J. Power Sources*, 152 (2005) 40–45.
90. U.P. Muecke, D. Beckel, A. Bernard, A. Bieberle-Hutter, S. Graf, A. Infortuna, P. Muller, J.L.M. Rupp, J. Schneider, L.J. Gauckler, Micro solid oxide fuel cells on glass ceramic substrates, *Adv. Funct. Mater.*, 18 (2008) 3158–3168.
91. E.D. Wachsman, K.T. Lee, Lowering the temperature of solid oxide fuel cells, *Science*, 334 (2011) 935–939.
92. V. Lawlor, S. Griesser, G. Buchinger, A.G. Olabi, S. Cordiner, D. Meisser, Review of the micro-tubular solid oxide fuel cell: Part I. Stack design issues and research activities, *J. Power Sources*, 193 (2009) 387–399.
93. T. Alston, K. Kendall, M. Palin, M. Prica, P. Windibank, SOFC reactor for domestic cogeneration, *J. Power Sources*, 71 (1998) 271–274.
94. W. Bujalski, C.M. Dikwal, K. Kendall, Cycling of three solid oxide fuel cell types, *J. Power Sources*, 171 (2007) 96–100.
95. Y. Du, N.M. Sammes, G.A. Tompsett, D. Zhang, J. Swan, M. Bowden, Extruded tubular strontium- and magnesium-doped lanthanum gallate, gadolinium-doped ceria, and yttria-stabilized zirconia electrolytes, mechanical and thermal properties, *J. Electrochem. Soc.*, 150 (2003) A74–A78.
96. P. Sarkar, L. Yamarte, H. Rho, L. Johanson, Anode-supported tubular micro-solid oxide fuel cell, *Int. J. Appl. Ceram. Technol.*, 4 (2007) 103–108.
97. F. Bossa, R. Polini, E. Traversa, Electrophoretic deposition of dense Sr- and Mg-doped LaGaO₃ electrolyte films on porous La-doped ceria for intermediate temperature solid oxide fuel cells, *Fuel Cells*, 8 (2008) 344–350.
98. T. Suzuki, Y. Funahashi, T. Yamaguchi, Y. Fujishiro, M. Awano, Anode-supported micro tubular SOFCs for advanced ceramic reactor system, *J. Power Sources*, 171 (2007) 92–95.

99. T. Suzuki, Y. Funahashi, T. Yamaguchi, Y. Fujishiro, M. Awano, Performance of the micro-SOFC module using submillimeter tubular cells, *J. Electrochem. Soc.*, 156 (2009) B318–B321.
100. T. Yamaguchi, S. Shimizu, T. Suzuki, Y. Fujishiro, M. Awano, Evaluation of micro LSM-supported GDC/ScSZ bilayer electrolyte with LSM–GDC activation layer for intermediate temperature-SOFCs, *J. Electrochem. Soc.*, 155 (2008) B423–B426.
101. J.L. Hertz, H.L. Tuller, Electrochemical characterization of thin films for a micro-solid oxide fuel cell, *J. Electroceram.*, 13 (2004) 663–668.
102. S. Kang, P.C. Su, Y.I. Park, Y. Saito, F.B. Prinz, Thin-film solid oxide fuel cells on porous nickel substrates with multistage nanohole array, *J. Electrochem. Soc.*, 153 (2006) A554–A559.
103. C.D. Baertsch, K.F. Jensen, J.L. Hertz, H.L. Tuller, S.T. Vengallatore, S.M. Spearling, M.A. Schmidt, Fabrication and structural characterization of self-supporting electrolyte membranes for a micro solid-oxide fuel cell, *J. Mater. Res.*, 19 (2004) 2604–2615.
104. H. Huang, M. Nakamura, P.C. Su, R. Fasching, Y. Saito, F.B. Prinz, High-performance ultrathin solid oxide fuel cells for low-temperature operation, *J. Electrochem. Soc.*, 154 (2007) B20–B24.
105. S. Sanna, V. Esposito, D. Perfolesi, A. Orsini, A. Tebano, S. Licoccia, G. Balestrino, E. Traversa, Fabrication and electrochemical properties of epitaxial samarium-doped ceria films on SrTiO₃-buffered MgO substrates, *Adv. Funct. Mater.*, 19 (2009) 1713–1719.
106. S.F.J. Flipsen, Power sources compared: The ultimate truth?, *J. Power Sources*, 162 (2006) 927–934.
107. S. de Souza, S.J. Visco, L.C. Dejonghe, Thin-film solid oxide fuel cell with high performance at low-temperature, *Solid State Ionics*, 98 (1997) 57–61.
108. A.V. Virkar, J. Chen, C.W. Tanner, J.W. Kim, The role of electrode microstructure on activation and concentration polarizations in solid oxide fuel cells, *Solid State Ionics*, 131 (2000) 189–198.
109. M. Gong, X. Liu, J. Trembly, C. Johnson, Sulfur-tolerant anode materials for solid oxide fuel cell application, *J. Power Sources*, 168 (2007) 289–298.
110. J.S. Ahn, D. Pergolesi, M.A. Camaratta, H. Yoon, B.W. Lee, K.T. Lee, D.W. Jung, E. Traversa, E.D. Wachsman, High-performance bilayered electrolyte intermediate temperature solid oxide fuel cells, *Electrochem. Commun.*, 11 (2009) 1504–1507.
111. K.L. Duncan, K.T. Lee, E.D. Wachsman, Dependence of open-circuit potential and power density on electrolyte thickness in solid oxide fuel cells with mixed conducting electrolytes, *J. Power Sources*, 196 (2011) 2445–2451.
112. E.D. Wachsman, Effect of oxygen sublattice order on conductivity in highly defective fluorite oxides, *J. Europ. Ceram. Soc.*, 24 (2004) 1281–1285.
113. D.W. Jung, K.L. Duncan, E.D. Wachsman, Effect of total dopant concentration and dopant ratio on conductivity of (DyO_{1.5})_x–(WO₃)_y–(BiO_{1.5})_{1–x–y}, *Acta Mater.*, 58 (2010) 355–363.
114. S. Omar, E.D. Wachsman, J.C. Nino, Appl. Phys. Letters, Higher ionic conductive ceria-based electrolytes for solid oxide fuel cells, *Appl. Phys. Lett.*, 91 (2007) 144106.

115. T.Z. Sholklapper, H. Kurokawa, C.P. Jacobson, S.J. Visco, L.C. De Jonghe, Nanostructured solid oxide fuel cell electrodes, *Nano Lett.*, 7 (2007) 2136–2141.
116. M.J. Zhi, N. Mariani, R. Gemmen, K. Gerdes, N.Q. Wu, Nanofiber scaffold for cathode of solid oxide fuel cell, *Energy Environ. Sci.*, 4 (2011) 417–420.
117. J.R. Smith, J.R. Smith, A. Chen, D. Gostovic, D. Hickey, D. Kundinger, K.L. Duncan, R.T. De Hoff, K.S. Jones, E.D. Wachsman, Evaluation of the relationship between cathode microstructure and electrochemical behavior for SOFCs, *Solid State Ionics*, 180 (2009) 90–98.
118. E.N. Armstrong, K.L. Duncan, D.J. Oh, J.F. Weaver, E.D. Wachsman, Determination of surface exchange coefficients of LSM, LSCF, YSZ, GDC constituent materials in composite SOFC cathodes, *J. Electrochem. Soc.*, 158 (2011) B492–B499.
119. K. Lai, B.J. Koepfel, K.S. Choi, K.P. Recknagle, X. Sun, L.A. Chick, V. Korolev, M. Khaleel, A quasi-two-dimensional electrochemistry modelling tool for planar solid oxide fuel cells stacks, *J. Power Sources*, 196 (2011) 3204–3222.
120. M.K. Debe, Electrocatalyst approaches and challenges for automotive fuel cells, *Nature*, 486 (2012) 43–51.
121. J. Fieg, Solid oxide fuel cell cathodes: polarization mechanisms and modelling of the electrochemical performance, *Ann. Rev. Mater. Res.*, 33 (2003) 361–382.
122. S.B. Adler, J.A. Lane, B.C.H. Steele, Electrode kinetics of porous mixed-conducting oxygen electrodes, *J. Electrochem. Soc.*, 143 (1996) 3554–3564.
123. A.V. Virkar, J. Chen, C.W. Tanner, J.-W. Kim, The role of electrode microstructure on activation and concentration polarizations in solid oxide fuel cells, *Solid State Ionics*, 131 (2000) 189–198.
124. S. Sunde, Calculation of conductivity and polarization resistance of composite SOFC electrodes from random resistor networks, *J. Electrochem. Soc.*, 142 (1995) L50–L52.
125. P. Costamagna, P. Costa, V. Antonucci, Micro-modelling of solid oxide fuel cell electrodes, *Electrochim. Acta*, 43 (1998) 375–394.
126. A.M. Svensson, S. Sunde, K. Nissancioglu, Mathematical modeling of oxygen exchange and transport in air – Perovskite–YSZ interface regions: I. reduction of intermediately adsorbed oxygen, *J. Electrochem. Soc.*, 144 (1997) 2719–2732.
127. M.E. Lynch, M.L. Liu, Investigation of sheet resistance in thin-film mixed-conducting solid oxide fuel cell cathode test cells, *J. Power Sources*, 195 (2010) 5155–5166.
128. S.P. Simner, M.D. Anderson, M.H. Engelhard, J.W. Stevenson, Degradation mechanisms of La-Sr-Co-Fe-O₃ SOFC cathodes, *Electrochem. Solid State Lett.*, 9 (2006) A478–A481.
129. S. Zhuiykov, Mathematical Modelling of YSZ-based potentiometric gas sensors with oxide sensing electrodes – Part I: Model of interactions of measuring gas with sensor, *Sens. Actuators B, Chem.*, 119 (2006) 456–465.
130. S. Zhuiykov, Mathematical Modeling of YSZ-based potentiometric gas sensors with oxide sensing electrodes – Part II: Complete and numerical models for analysis of sensor characteristics, *Sens. Actuators B, Chem.*, 120 (2007) 645–656.

131. J.R. Wilson, W. Kobsiriphat, R. Mendoza, H.-Y. Chen, J.M. Hiller, D.J. Miller, K. Thornton, P.W. Voorhees, S.B. Adler, S.A. Barnett, Three-dimensional reconstruction of a solid-oxide fuel-cell anode, *Nat.: Mater.*, 5 (2006) 541–544.
132. J. Joos, T. Carrarob, M. Enderc, B. Rügerd, A. Webere, E. Ivers-Tiffée, Detailed microstructure analysis and 3D simulations of porous electrodes, *ECS Trans.*, 35 (2011) 2357–2368.
133. D.S. Mebane, M. Liu, Classical, phenomenological analysis of the kinetics of reactions at the gas-exposed surface of mixed ionic electronic conductors, *J. Solid State Electrochem.*, 10 (2006) 575–580.
134. Z. Bao, M.R. Weatherspoon, S. Shian, Y. Cai, P.D. Graham, S.M. Allan, G. Ahmad, M.B. Dickerson, B.C. Church, Z. Kang, H.W. Abernathy, C.J. Summers, M. Liu, K.H. Sandhage, Chemical reduction of three-dimensional silica micro-assemblies into microporous silicon replicas, *Nature*, 446 (2007) 172–175.
135. C.W. Sun, U. Stimming, Recent anode advances in solid oxide fuel cells, *J. Power Sources*, 171 (2007) 247–260.
136. Y.H. Huang, R.I. Dass, Z.L. Xing, J.B. Goodenough, Double perovskites as anode materials for solid-oxide fuel cells, *Science*, 312 (2006) 254–257.
137. L. Fan, C. Wang, B. Zhu, Low temperature ceramic fuel cells using all nano composite materials, *Nano Energy*, 1 (2012) 631–639.

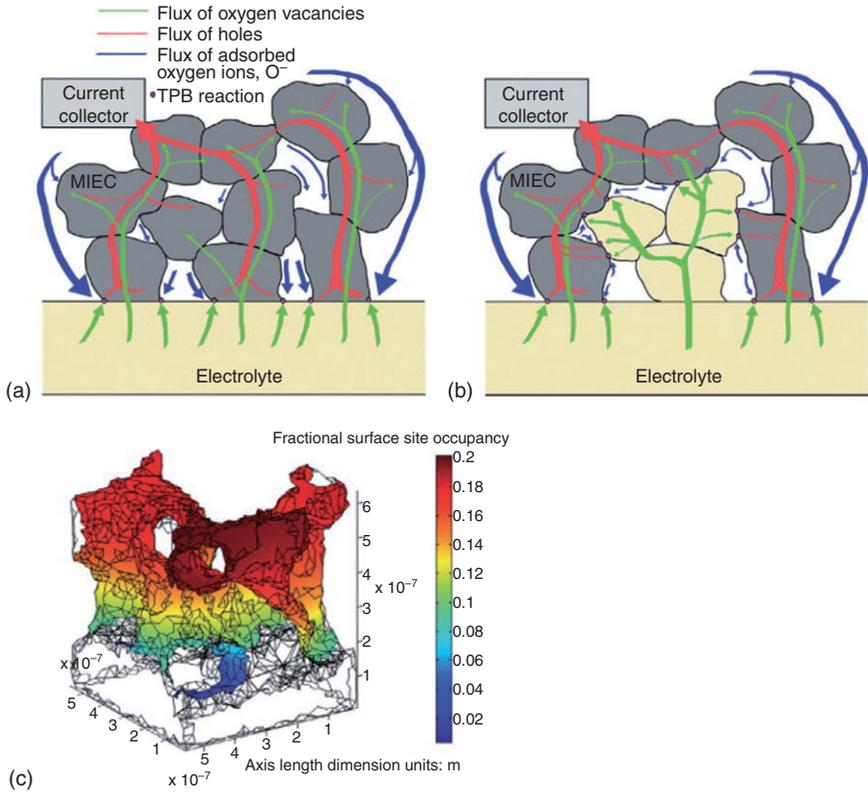


Plate XXI (Chapter 7) Schematic diagram of charge and mass transport within and on the surface of (a) a single-phase mixed conducting porous electrode and (b) a composite (mixed conductor + electrolyte) porous electrode. (c) Initial 3D FEM simulation of adsorbed oxygen species on the surface and at the TPBs of a porous LSM electrode. (Reprinted from Ref. 38 with permission from Elsevier Science)

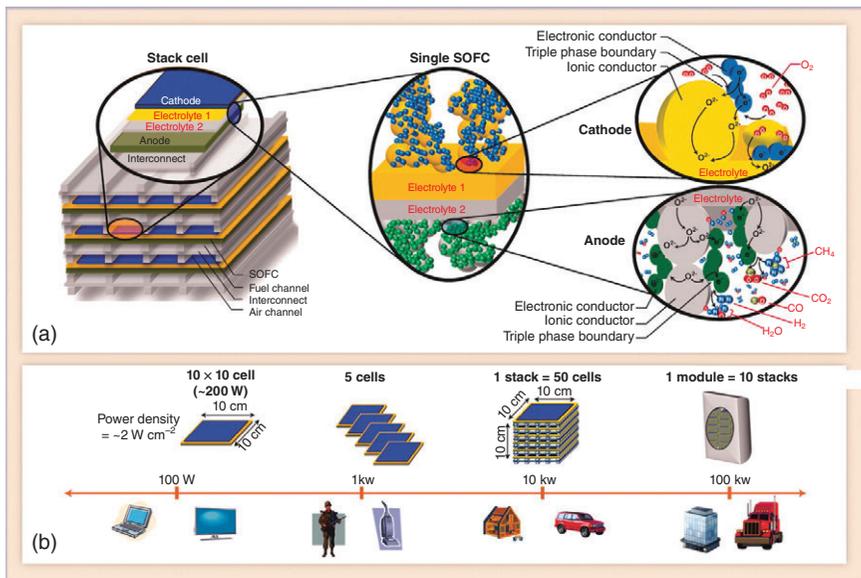


Plate XXII (Chapter 7) (a) Schematic diagrams of structure of high-performance LT-SOFCs from low magnification (stack) to high magnification (nano/microstructured electrodes). Functionally graded bismuth oxide (electrolyte 1) / ceria (electrolyte 2) bi-layered electrolytes effectively reduce ohmic polarization at lower temperatures. Carefully controlled nanostructured electrodes by infiltration provide highly extended reaction sites compensating exponentially reduced oxygen reaction kinetics at cathode and allow use of hydrocarbon fuels at anode at reduced temperatures. (b) Estimation of power output with LT-SOFCs from a single cell to a module (upper) and schematic diagram of power requirements according to various applications (lower). On the basis of demonstrated high power density ($\sim 2\text{W}/\text{cm}^2$ at 650°C) of the state-of-the-art LT-SOFC, a 10 cm by 10 cm planar cell corresponds to $\sim 200\text{W}$ power output. A stack of 50 planar cells with interconnects (10 cm by 10 cm) can provide 10 kW, and a module consisting of 10 stacks can provide 100 kW. (Reprinted from Ref. 91 with permission from *Science*)

DOI: 10.1533/9781782422242.374

Abstract: This chapter reviews the applications of various semiconductor nanocrystals utilized in environmental sensors, including pH, dissolved oxygen (DO), dissolved organic carbon (DOC) and dissolved metal ion sensors. The chapter then discusses the modification of semiconductor nanocrystals for sensing electrodes, and conductivity measurements and the modern trend towards the improvement of antifouling resistance for solid-state water quality sensors.

Key words: solid-state environmental sensors, nanostructured semiconductor sensing electrodes, antifouling technologies, doping semiconductor nanocrystals

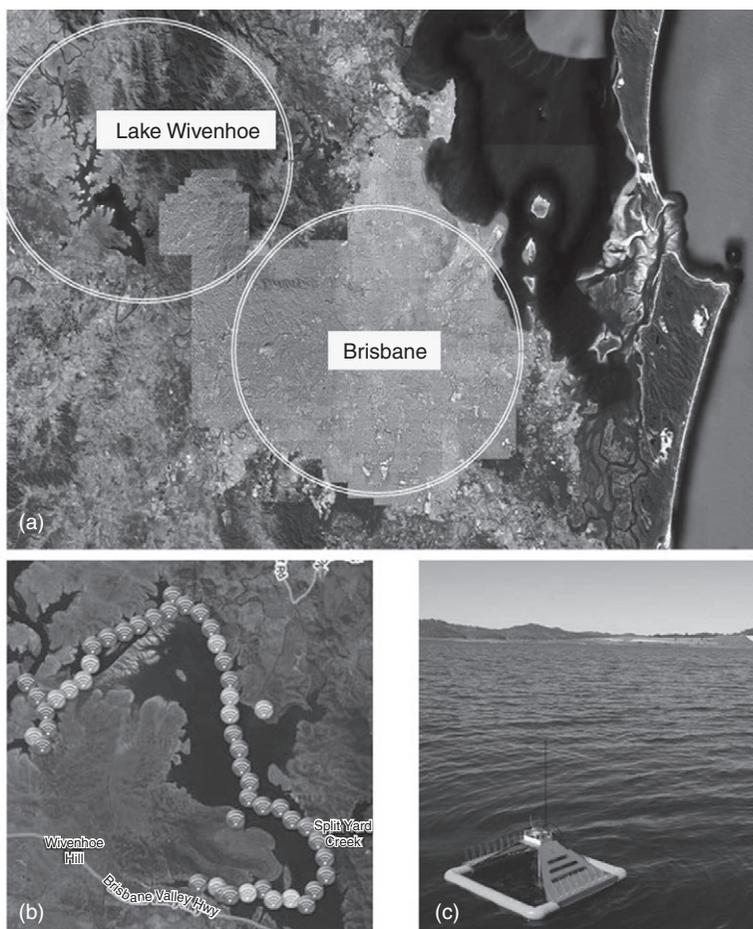
8.1 Solid-state pH sensors

Water is becoming increasingly valued in society, especially in Australia where the nation has experienced extended droughts over the last decades. This has resulted in a general decline in the level of water in rivers, estuaries and surface collection dams, with increasing concern over the deteriorating water quality of ecosystems supported by these waters. Managing various ecological systems, as well as the potable water drinking supply, will need to be supported by appropriate levels of monitoring, and one way to quickly determine the health status of a body of water is by measuring its main parameters such as pH, dissolved oxygen (DO), conductivity, turbidity, etc. To solve increasing water pollution problems, complicated continuous on-line monitoring and multistage treatment processes are required. In this regard, portable, inexpensive, reliable, robust and accurate solid-state water quality sensors are needed.

On the other hand, in Australia, Water Authorities now require on-line information about water quality on a much larger scale. As a result of this, traditional methods of water quality analysis, where people collect samples of water at various locations and at different points in time, then return to laboratory for subsequent analysis, are not efficient. Today, water quality analysis requires constant monitoring of the different parameters in the major catchments. This creates a new paradigm in water quality sensing as the information has to be collected and eventually transferred wirelessly over a certain period of time. Consequently, when the accurate measurement of such water quality parameters as pH, DO, conductivity, turbidity,

etc. is mandatory at different depths and at high spatial resolution and the measuring instruments have to be part of wireless distributed sensor networks, miniature, solid-state, cheap sensors would likely be the most preferable option.^{1,2}

Another complication arises from the fact that the area of the main water catchments of Australia's major cities, where water quality must be established and maintained, is comparable with the area of capital cities. For example, Fig. 8.1a illustrates a real satellite image of one Australian capital



8.1 Satellite image of the Australian city of Brisbane and its major water catchment (Lake Wivenhoe) (a), installed distributed wireless sensors network on Lake Wivenhoe (b) with an example of the sensor node (c). (Reprinted from Ref. 141 with permission from Elsevier Science)

city – Brisbane, which has a population of over two million inhabitants – and its major water catchment – Lake Wivenhoe. This image clearly shows that monitoring of the water quality is needed on a complex lake profile over an area of approximately 250 km², which requires large-scale sensing and hundreds of reliable and miniature sensors incorporated into a distributed wireless sensors network (Fig. 8.1b). This network has already been installed on the lake and each node of the network (Fig. 8.1c) has a capacity to incorporate between six and eight sensors set up at different depths. However, experience shows that, as the number of sensors and nodes in a wireless network grows, the amount of data increases tremendously and hence not all of it can be utilized. As a result, a new generation of sensor networks includes cheap on-device data storage, which can store an abundance of data and transfer only the requested data representing the information people desire from the network, rather than referral to a traditional database. This area undoubtedly requires much more progress if such sensors are to become widespread.

Although modern laboratory testing of water quality is sufficiently accurate, research into the development of miniature, robust, inexpensive water quality sensors has recently pointed out that solid-state sensors using metal oxide sensing electrodes (SEs) are a better choice for dealing with a fast-changing, large range of DO concentrations, turbidity and pH, which cannot be covered by contemporary, time-consuming laboratory analytical methods.^{3–5} Moreover, the lack of reliable and miniature sensors with high antifouling resistance capable of being deployed in the next generation of sensor networks has been identified as a major limiting factor in implementing real-time on-line spatially distributed water quality monitoring.⁶ However, based on the latest research results, there is no doubt that over the next decade solid-state sensors will become the prevalent technology for obtaining information about rapid changes in diversified aqueous environments.

The development of single or multisensor assemblies will enable the fabrication of larger and more complex of sensor parts as well as improving structural efficiency and design flexibility, optimizing materials compatibility, maximizing sensor properties and reducing cost. Unfortunately, it has to be admitted that ‘the advances in sensor development have not kept pace with the advances in materials’.⁷ Today, new sensor materials often require totally new methods, processes and approaches. Traditional solid-state sensor materials or improved versions of them usually require just improved concepts within typical manufacturing processes to reach new levels of performance. Such improvements may be achieved in the sensor development process itself, or through the development of special procedures for employing a traditional method. These facts are directly related to the development of chemical solid-state sensors in general and metal oxide film-based sensors in particular.

However, a newly emerging trend can be dated from the end of the last century. In this trend, the nanostructured semiconductor oxide-based SEs and reference electrodes (REs) are gradually replacing SE (REs) made of noble metals in chemical sensor structures. Thanks to a new approach in the screening of potential candidates for SE (RE) use, based on combinatorial and high-throughput development of sensing materials,^{8,9} this trend continues its growth in the 21st century at a rate faster than ever before. Recent advances in the development of solid-state water quality sensors with nanostructured metal oxide SEs have confirmed that solid-state sensors based on thick/thin-film SEs are capable of measuring pH,¹⁰⁻⁴⁶ DO⁴⁷⁻⁶⁵ and dissolved metal ions in water.⁶⁶⁻⁸³ The progress has already resulted in a number of highly successful sensors. It is evident that the high catalytic activity of nanostructured SEs is due to several factors: high surface-to-volume ratio, orientation of nanostructures in SE and/or different population of the crystal edges located on prismatic and pyramidal parts of nanocrystals.⁸⁴

Doping of the base nanostructured oxide-SE by materials with high catalytic activity (noble metal nanostructures and other nano-oxides) has been considered as an effective method of changing the electrocatalytic activity and improving the properties of oxide-SEs for various chemical sensors.^{47,84-88} It should be noted that the defect disorder of doped oxide-SEs has led to the formation of donor levels located in the upper part of the energy gap of the semiconductor film-SE which are primarily responsible for the observed improvement in the properties.⁸⁹ However, the origin of these effects is difficult to rationalize, mainly due to incomplete information concerning the oxide's phase purity, surface composition and surface orientation, all of which can, in principle, alter the electrocatalytic behaviour of the doped nanostructured semiconductor-SE.

For instance, RuO₂ has recently been considered as one of the most promising candidates among other semiconductor film-SEs for reliable pH and DO sensors. This fact has unequivocally been supported by a large number of publications during the last few years. Up to the present time, RuO₂, as an electronically conductive oxide of rutile structure, has been included in the important class of electrode materials, mainly based on its practical application in electrocatalysis.^{19,90,91} In an aqueous environment, water dissociates into OH⁻ groups and proton species. Considering the basic rules of defect chemistry, one may expect that incorporation of protons into a RuO₂ lattice would result in the formation of Ru vacancies (required for charge compensation) or the removal of oxygen vacancies. The catalytic activity of nanostructured semiconductor oxides in various reactions in water generally increases with decreasing surface oxygen binding energy and, in the general case, this reaction cannot be attributed to difficulties of DO separation from the surface. It is natural to assume that the oxygen

binding energy is a measure of cation reactivity of oxide-forming elements. An inverse relationship exists between oxygen binding energy with catalyst surface area and cation reactivity, where decreases in binding energy with surface area correspond with increasing cation reactivity and, hence, the relatively high catalytic activity of oxides. So far, most attempts at doping RuO₂ with nanostructured oxides such as TiO₂,^{20,92} Co₃O₄,⁹³ NiO,^{90,94,95} Ta₂O₅,^{87,96} ZrO₂,⁹⁷ La₂O₃,⁶⁰ and CeO₂⁹⁸ have shown that it is practically impossible to predict the exact sensing properties and behaviours of the doped RuO₂-SEs. The aim of those fragmented improvements was mainly to improve the high catalytic activity of the composite oxides, predominantly for electrocatalysis.⁹⁹ From these studies, it was clearly concluded that the activity of modified materials differs from that of the undoped RuO₂-SEs.¹⁰⁰ The large surface-to-volume ratio of these nanomaterials and small active size of SEs meant that these SEs could provide a unique opportunity to sense the environment in nanoscale spaces such as those found in a living cell or even a cell nucleus.

Through intelligent design of chemical molecular recognition events between receptor and analyte at the surface of a nanocrystal or nanowire, coupled with large electrical responses to these events, it has proven possible to develop a wealth of new highly selective and sensitive pH and DO sensors as well as E-tongues capable of monitoring heavy metals in drinking water and detecting bacteria and traces of organics in recycled water. However, for the time being the available data is insufficient to outline the development trend conclusively, and progress in using this data is slow because of a lack of knowledge in relation to the actual structure at the functional-group level. The situation regarding the use of RuO₂ for sensors is even worse since most of the above-mentioned studies were focused only on the catalytic activity of oxygen, and not on the electrochemical behaviour of the doped RuO₂-SE. Taking this into account, it needs to be stressed that the comprehensive characterization of the nanostructured SE material is a complex task and requires a combination of microscopic, diffraction, spectroscopic and electrochemical measurement methods.

8.1.1 Modification of semiconductor nanocrystals for pH sensing electrodes

In general terms, the pH of a solution can be considered as a measurement of its acidity.² Distilled water is neutral and therefore has a pH of 7.0. Traditionally, pH has been assessed by means of the well-known pH glass electrode invented by W.S. Hughes in 1922. In fact, this was the first recorded chemical sensor. In this sensor, the pH of a solution was detected through chemical exchange signals in a thin glass membrane. This breakthrough was followed by a stream of other types of sensors for identifying a variety of

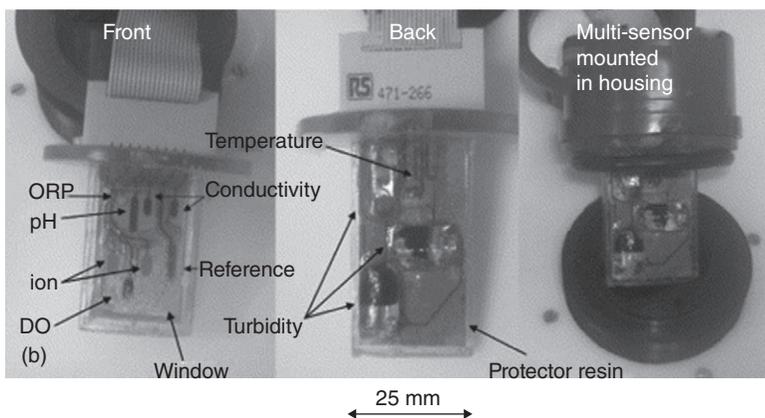
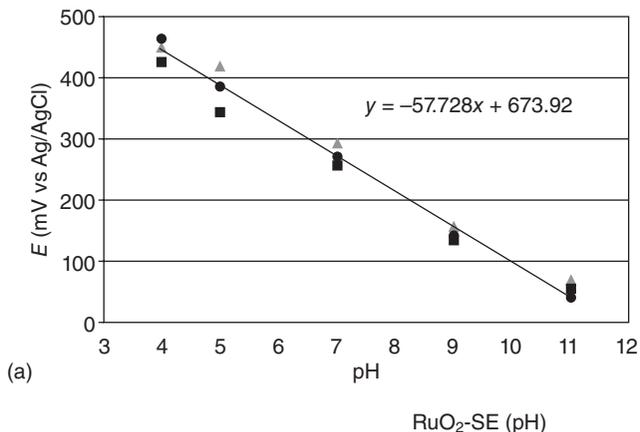
chemicals from oxygen to glucose. Developments in the semiconductor microelectronics industry led to the development in the 1980s of miniaturized circuits and sensor arrays that were able to exploit signal pattern recognition for differentiating various chemicals and biochemicals. Around this time, nanochemistry and defect chemistry were beginning to produce myriad examples of nanocrystals and nanowires with controlled size and shape and with surfaces that could be chemically modified allowing them to function as new sensor platforms for monitoring chemical and biochemical contaminants in water, air and food, as well as having biomedical and security applications. In fact, the first review concerning semiconductor oxides that can be successfully used as SEs for pH sensors was published in 1984.¹⁸ Since this publication, a number of researchers attentively and enthusiastically pursued the idea of using thick/thin-film nanostructured semiconductor oxides as pH-sensitive SEs. Moreover, since the 1990s, nanotechnology and doping techniques have inspired the next step in pH sensor development as the demand for small, reliable and inexpensive solid-state pH sensors has increased. Although the pH glass electrode still remains the most commercially successful sensor, the aim of modern research is to create a long-lasting robust miniature pH sensor insensitive to most of the dissolved interfering ions compared to the fragile pH glass electrode, which shows significant interference from F^- ions.²⁷ Another aim is to develop a built-in antifouling feature for SEs to prevent biofouling.

Table 8.1 summarizes the latest developments in film metal oxide semiconductor-SEs reported up to now for planar solid-state pH sensors. Even a brief analysis of the data presented in this table confirms that significant progress has recently been made on the RuO_2 -based pH sensors. The RuO_2 -SE demonstrates one of the highest sensitivities to pH of all the semiconductor oxides, along with high accuracy and less interference due to dissolved ions in water. Over the last few years, CMSE and SSN TCP Laboratories of CSIRO (Australia) have been working on the development and improvement of water quality sensors based on various RuO_2 -based nanostructures, focusing on the fundamental issues as well as potential applications. This research has been inspired by the pioneering work of the Spanish group who used Ru-containing pastes for the SEs of their solid-state multisensors.^{4,12,56} Figure 8.2a illustrates typical pH sensitivity for SEs based on Ru-containing paste while Fig. 8.2b shows multisensor set-up for simultaneous measurement of pH, DO, conductivity, turbidity and water temperature.⁴ The thickness of the RuO_2 -SE was generally less than $10\mu m$. The established Nernstian slope for such a SE was approximately $57.72 mV/pH$. The intercept at pH 0 provided an apparent standard electrode potential (E^0) of about $640 \pm 10 mV$ vs $Ag/AgCl, Cl^-$ -RE.

Reasonable agreement was obtained between the Nernstian slopes and E^0 values for the different RuO_2 -SEs of the sensors. The curve closely

Table 8.1 Characteristics of metal oxides as pH-sensitive electrodes¹⁴¹

SE material	Sensitivity (mV/pH)	pH range	Accuracy (±mV)	Interference	Redox interference (±mV)	Reference
IrO ₂	59.8	2.0–10.0	2	Cl ⁻ , Br ⁻ , I ⁻	20	18, 21, 30
Ta ₂ O ₅	49.3	3.0–10.0	30	F ⁻	70	18
TiO ₂	55.0	2.0–12.0	15	F ⁻	100	18, 20
TiO ₂ nanotube-Ti	54.5	2.0–12.0	15	-	-	33
PtO ₂	46.7	5.0–10.0	4	I ⁻	100	18
OsO ₂	51.2	2.9–11.0	15	-	200	11, 18
SnO ₂	46.6	4.0–10.0	65	-	-	18
RhO ₂	68.2	2.0–12.0	1	Br ⁻ , I ⁻	100	18, 25
RuO ₂	61.8	2.0–12.0	30	I ⁻ , Br ⁻	100	4, 12, 16, 17, 19, 20, 43
Nanostructured RuO ₂	58.0	2.0–13.0	5	Br ⁻	90	5, 6, 23, 27, 39
Pt-doped RuO ₂	61.0	2.0–13.0	5	Br ⁻	100	45
Cu ₂ O-doped RuO ₂	41.0	2.0–12.0	6	Cl ⁻	8	7, 10
WO ₃	40.7	2.0–12.0	7	I ⁻	-	26
Na _{0.9} Mo ₆ O ₁₇	76.3	4.0–9.0	10	K ⁺ , Na ⁺ , Li ⁺	10	38
Ce _{0.8} Sm _{0.2} O _{1.9-x}	39.9	3.0–10.0	4	-	-	31
Li _{3x} La _{2/3-x} 1/3-2xTiO ₃	47.0	2.0–11.0	10	-	Temperature-dependent	32, 36
α-PbO ₂ ; β-PbO ₂	59.2	1.0–12.0	-	NH ₄ ⁺	-	34, 35
Co ₃ O ₄	35.0	2.0–12.0	15	I ⁻	-	37
ZnO	43.6	4.0–12.0	4	-	-	45, 46



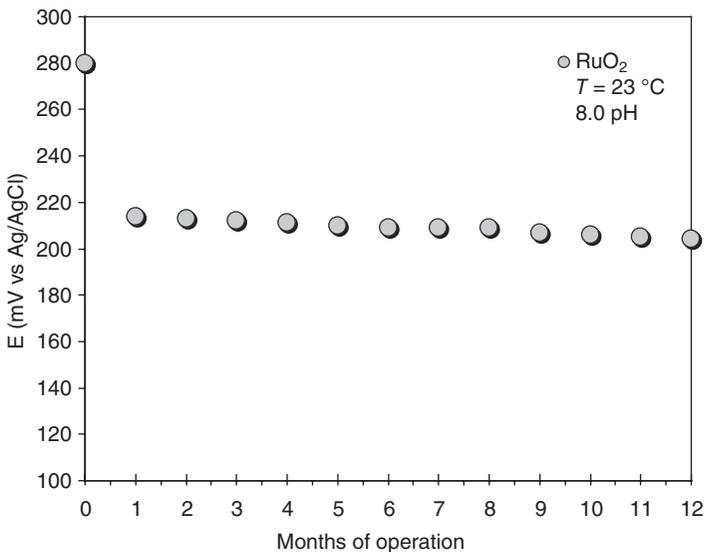
8.2 (a) Voltage variations vs pH for SE based on Ru-containing electrode paste. (b) Set of planar water quality sensors. (Reprinted from Ref. 4 with permission from Elsevier Science)

followed a straight line. However, the standard deviation of the output voltage was experimentally found to be $\pm 30\text{--}50\text{mV}$ in the entire pH measurement range. This is apparently due to the presence of Pb, Ca, Mn and Si in the Ru-containing electrode paste.¹⁰¹ In fact, it was reported that these pastes contain only $\sim 24\text{ mol \%}$ of Ru.¹⁰² It was also published that the commercial Ru-containing electrode pastes used as SE in pH sensors partially responded to the presence of halides, sulphate, bromide and carbonate anions in water.¹⁰¹ Apparently, this was mainly caused by the presence of Pb in the available pastes. As a consequence of this, in order to improve adhesion, selectivity and SE reliability, alternative SE nanostructures have been proposed. Although nanostructured RuO₂-SEs and Pt-doped RuO₂-SEs have exhibited similar sensitivity to pH

measurement, they extended the pH range from 2.0 to 13.0.^{5,47} A big improvement ($\pm 2\text{ mV}$) was also recorded in reproducibility of results between different days when measurements were carried out. This was probably due to the nanofabricated structure and morphology of the $\text{RuO}_2\text{-SE}$. Results of pH measurements taken with a pure Pt-SE revealed that the angle of the Nernstian slope for the Pt-SE is less than the angle of the Nernstian slope for the $\text{RuO}_2\text{-SE}$.⁴⁷ Thus, it was concluded that the nanostructured $\text{RuO}_2\text{-SE}$ possesses a better sensitivity along with a complete pH measurement range.

So far, results from long-term stability testing have revealed that the lifetime of the solid-state pH sensor based on the nanostructured $\text{RuO}_2\text{-SE}$ is greater than 24 months; further testing of the long-term stability is still in progress. This is also a big improvement compared to the published six months lifetime for a thick-film SE based on Ru-containing pastes.⁴ Recently declared results regarding the long-term stability of pH measurement using a CSIRO sensor based on a nanostructured $\text{RuO}_2\text{-SE}$ at 23°C and pH 8.0 are shown in Fig. 8.3.

Substantial voltage drift during the first month of testing was due to H^+ transport through the SE, which is governed by H_2 trapping at the trap sites existing at the grain boundaries or micropores of the nanostructured SE,⁴⁷ as well as being due to heterogeneous oxidation of the developed SE within the first week of its exposure to aqueous environment.⁵⁴ The complexity of

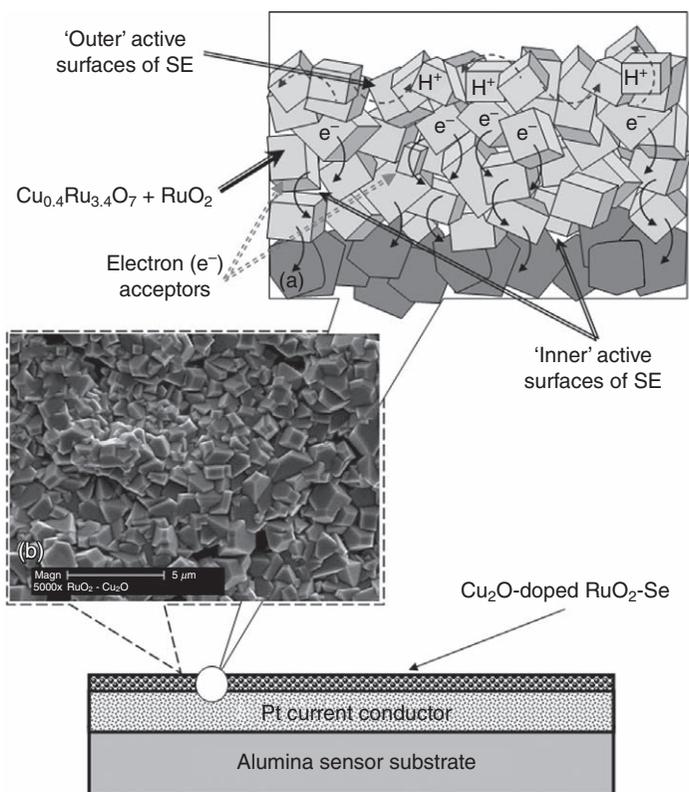


8.3 Long-term stability of pH measurement by multisensor based on nanostructured $\text{RuO}_2\text{-SE}$. (Reprinted from Ref. 6 with permission from IOP Publishing)

the developed morphology of the 20 mol % Cu_2O -doped RuO_2 -SE is schematically shown in Fig. 8.4.⁵⁴ It was found that in the developed $\text{Cu}_{0.4}\text{Ru}_{3.4}\text{O}_7 + \text{RuO}_2$ -SE structure, both 'inner' and 'outer' active surfaces of the complex oxide structures are taking part in electrochemical reactions and consequently enhancing the sensing properties of the SE.^{54,57} Therefore, in order to stabilize the sensor's response from the practical point of view, all newly-developed sensors must be conditioned in water for at least three weeks before any meaningful results of the pH measurements can be obtained.⁶

Thus, two results in the development of sensors have been found to be important:

1. Freshly prepared RuO_2 -SEs are affected by the slow non-random voltage drift responsible for the diffusion of H^+ ions through the structure of the complex SEs and neglecting the effects of the other ions.



8.4 A cross-sectional view of the sensor substrate featuring a 20 mol% Cu_2O -doped RuO_2 -SE showing a SEM image of the surface of SE (b) and tortuous paths of charge carriers to the Pt current conductor (a). (Reprinted from Ref. 54 with permission from Elsevier Science)

Drift is significant for the first six days and is stabilized only after 15–20 days with negligible drift afterwards.

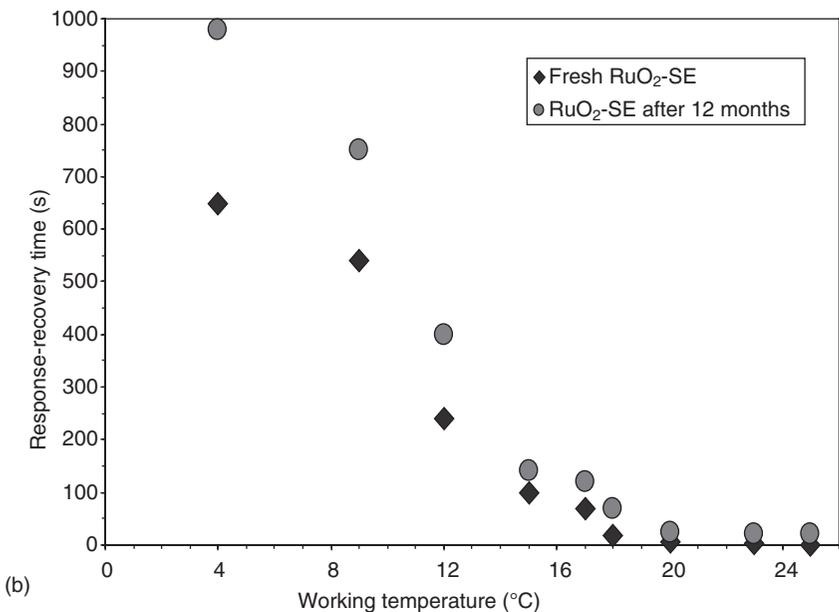
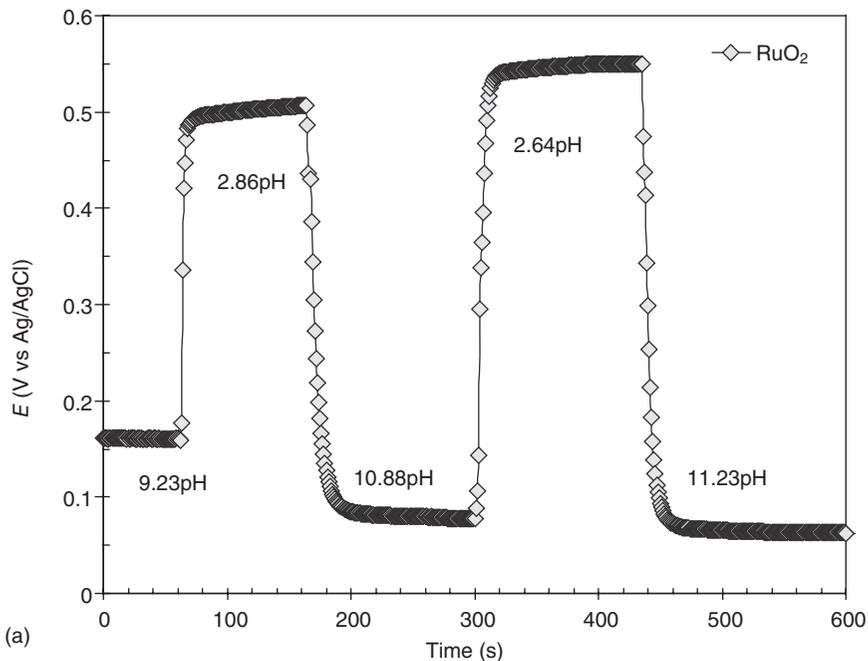
- Active sites for oxygen reduction are not limited to the triple boundaries, but extend to the RuO₂-SE surfaces.^{54,57} After voltage stabilization, the output signal remained stable during the following months of testing, displaying a standard drift of around ± 1.5 mV/month.

Typical dynamic characteristics of a solid-state pH sensor based on nanostructured RuO₂-SEs at different pH levels at a temperature of 23 °C are presented in Fig. 8.5a.⁵ The average response time (T_{90}) for pH changes made by acid-base titration was within ± 2 s, which is faster than the response time of less than 6 s reported for similar sensors with SEs based on Ru-containing pastes.⁴ Although the absolute voltage value for pH measurements drifted lower with time, the response time remained at only a few seconds during all experiments. Bearing in mind that the measurement of pH changes is required not only in warm, but also in cold water, dynamic characteristics of the RuO₂-SE were also studied at low temperatures. The results of these tests confirmed that the operating temperature does influence the response and recovery rate. It was experimentally determined that the response and recovery time decreases with the drop in temperature.

The response time for a solid-state pH sensor based on a nanostructured RuO₂-SE vs working temperature is presented in Fig. 8.5b.⁶ It is clearly revealed in this figure that, as the water temperature cools to about 9 °C, the response/recovery time increases to approximately 8–10 min. However, the response time improves with the increase in working temperature. For instance, T_{90} improves from 8–10 min to about 3–5 min at a temperature of 12 °C. Nevertheless, the recovery rate remains slow. All the above results indicate that, due to the nature of water quality monitoring (24 h per day; 7 days per week), even such a sluggish response/recovery rate of the sensor at low temperatures should allow adequate information in relation to changes in water quality to be obtained and analysed.

8.1.2 Doping semiconductor nanocrystals

Since year 2000 it has been clearly shown through the development of numerous sensors that selective doping of the nanostructured SEs of water quality sensors is an attractive and essential method for further improvement in their performance and functionalization. In practice, nanostructured semiconductor SEs can be doped in various ways, such as intercalation of electron donors or acceptors, substitution doping, encapsulation in the lattice, molecular adsorption and covalent sidewall functionalization.^{10,20,33,47,49,52,54,57} Studies of doped semiconductor SEs of the sensors



8.5 (a) Dynamic characteristics of nanostructured $\text{RuO}_2\text{-SE}$ in aqueous solution vs a Ag/AgCl-RE at changes in pH of the solution at a temperature of 23°C . (Reprinted from Ref. 5 with permission from Elsevier Science). (b) Response time for sensor based on $\text{RuO}_2\text{-SE}$ vs water temperature. (Reprinted from Ref. 6 with permission from IOP Publishing)

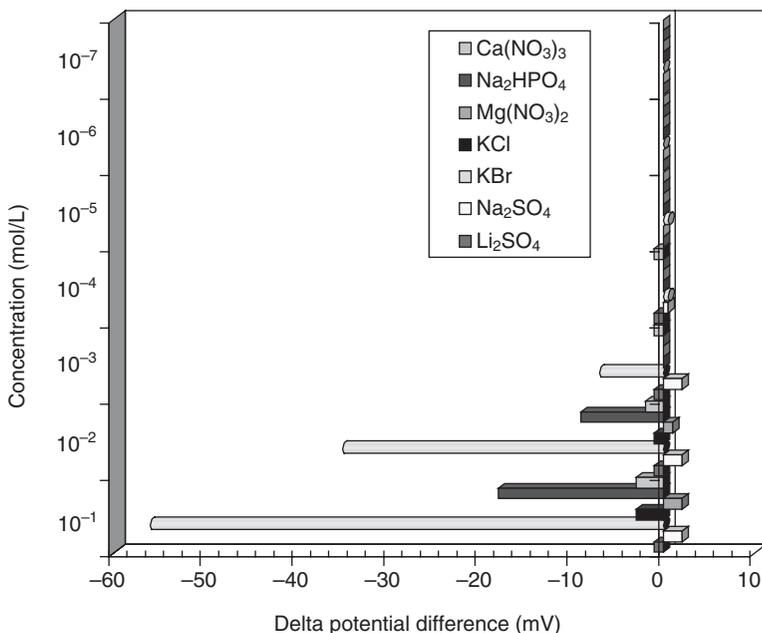
include electrical measurement of individual SEs on sensors, electrochemical and spectral investigation of doped SEs in the solutions, and thin-film characteristics such as transport properties.¹⁰³ Doping modifies the charge distribution in the band structure and changes the Fermi level position, as was established in Chapter 1,^{104–106} therefore, the electrochemical properties will be varied.

Most of the nanostructured semiconductor oxides with high electronic conductivities have shown some oxygen deficiency and corresponding variation (reduction) in the oxidation state of the predominant metal. This is due to their slightly non-stoichiometric composition.⁸⁴ In fact, doping can not only change slightly or significantly the stoichiometry of the oxide, but it can also develop complex and/or mixed valence oxides with completely different electrochemical properties. Therefore, the search for a stable dopant which possesses high enough binding energy, yet will not affect the electronic and transport properties of the base semiconductor nano-oxide, is a very challenging task.

For example, in recent CSIRO developments aimed at improving water quality sensors properties, nanostructured Ta₂O₅, La₂O₃,⁶⁰ Cu₂O,^{10,49,54} and ZnO^{52,55} dopants for RuO₂-SEs have been investigated. Intensive variations and manipulations with different oxides, including their sizes and molar concentrations, revealed that the greatest improvement was achieved when Cu₂O and ZnO dopants were utilized in SE fabrication. Optimization of the molar percentage of the dopant in the RuO₂ nanostructure has led to the conclusion that typically the maximum advance in the sensing and antifouling properties of the SE can be attributed to the fact that the base semiconductor oxide represents nanoparticles with dimensions of 500–900 nm and the dopant is generally an oxide with dimensions from 20–50 nm.^{10,55} As the analyte in most cases represents multicomponent systems, selectivity has been considered as one of the most important sensor characteristics.

Investigation of the interference effects of various dissolved salts on the sensor measurement potential in aqueous solutions has been performed using the fixed interference method.¹⁰ Interference testing of a sensor based on 20 mol % ZnO-RuO₂-SE using solutions containing Li⁺, Na⁺, SO₄²⁻, K⁺, Na⁺, Br⁻, Cl⁻, Mg²⁺, NO₃⁻ and Ca²⁺ ions, at concentrations from 10⁻⁷–10⁻¹ mol/L and a temperature range of 11–30 °C were involved in this analysis. Figure 8.6 illustrates the means by which a 20 mol % ZnO-doped RuO₂-SE can improve selectivity of the solid-state sensor in a temperature range 11–30 °C.⁵²

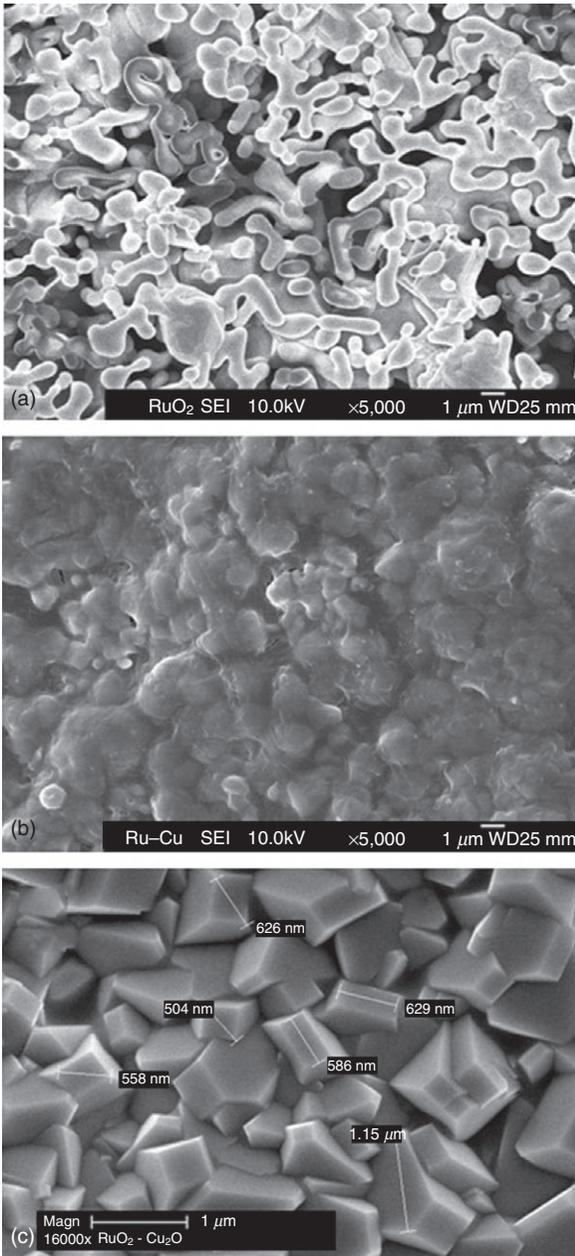
Delta potential difference is defined as the difference between the sensor's potential difference measurements in an aqueous test solution containing none of the dissolved salts and the solution containing dissolved salts. The results obtained demonstrate that the solid-state sensor based on



8.6 Interference testing of the solid-state sensor based on sub-micron 20 mol% ZnO-doped RuO₂-SE at a temperature range of 11–30°C. (Reprinted from Ref. 52 with permission from Elsevier Science)

20 mol % ZnO-doped RuO₂-SE is not susceptible to the most common ions, with the exception of KBr. Only one Br⁻ ion exhibited cross-sensitivity to 20 mol % ZnO-doped RuO₂-SE in the high concentration range of 10⁻²–10⁻¹ mol/L, whereas at the low concentration range of 10⁻⁷–10⁻² mol/L, no effect on the sensor's potential difference was observed. One possible explanation of this cross-sensitivity is the likelihood that heterogeneous oxidation enhances the concentration of bromide at the SE surface.⁵⁷ This cross-sensitivity must be taken into consideration when the industrial sensor prototype is manufactured – a simple correction factor may be proposed which considers the rate of change of the SE response as a function of KBr concentration.

Apart from changes in adsorption/desorption dynamics, doping can also modify the structure and morphology of SEs. For example, Fig. 8.7 depicts SEM images of the different RuO₂-based SEs of a water quality sensor.¹⁰ Notably, the undoped nanostructured RuO₂-SE (Fig. 8.7a) has a relatively porous structure,⁶¹ which could easily accumulate heavy biofouling during long-term measurements. In extreme cases, for example, the assessment of water quality parameters in sewage, biofouling can completely cover the surface of undoped RuO₂-SE (as clearly presented in Fig. 8.7b), causing a



8.7 SEM images of (a) undoped RuO₂-SE (reprinted from Ref. 61 with permission from Elsevier Science) (b) undoped RuO₂-SE after three months in sewerage environment and (c) 20 mol% Cu₂O-doped RuO₂-SE. (Reprinted from Ref. 10 with permission from Elsevier Science)

total loss of the sensor's functionality. On the other hand, 20 mol % Cu_2O -doping (Fig. 8.7c) can not only decrease the porosity of the doped complex $\text{Cu}_{0.4}\text{Ru}_{3.4}\text{O}_7 + \text{RuO}_2\text{-SE}$ down to practically zero, but can also enhance the surface-to-volume ratio, resulting in improvement in the sensor's sensitivity and its antifouling resistance.¹⁰

8.2 Electrochemical dissolved oxygen (DO) sensors

8.2.1 Galvanic and polarographic sensor technologies

DO is the term describing the amount of oxygen dissolved in a unit volume of water and has been considered as one of the most important parameters of water quality. It usually varies from 0.5–8.0 ppm. In water quality applications, such as aquaculture (including fish farming) and waste water treatment, the level of DO must be kept relatively high (7.0–8.0 ppm). For aquaculture, if the DO level falls too low the fish will suffocate. In sewage treatment, bacteria decompose the solids. If the DO level is too low, the bacteria will die and decomposition ceases. In contrast, if the DO level is too high, energy is wasted in aeration of the water. With industrial applications, including boilers, the make-up water must have low DO levels to prevent corrosion and boiler scale build-up, which inhibits heat transfer. Although DO is displayed as mg/L or ppm, DO sensors do not measure the actual amount of oxygen in water, but instead evaluate the partial pressure of oxygen in water. Oxygen pressure is dependent on both the salinity (pH) and the temperature. Therefore, both pH and DO are interconnected and changes in one parameter will inevitably affect the other.

There are two fundamental techniques for measuring DO: galvanic and polarographic. Both sensors use an electrode system where the DO reacts with the cathode to produce current. If the electrode materials are selected to keep the difference in potential between the cathode and anode at -0.5V or greater, an external potential is not required and the system is called galvanic. Provided that an external voltage is applied, the system is called polarographic. The comparison of these two methods is as follows:

- Galvanic probes are more stable and accurate at low DO levels than polarographic probes.
- Galvanic probes often operate several months without electrolyte or membrane replacement, resulting in lower maintenance cost.
- Polarographic probes need to be recharged after several weeks of heavy use.

Galvanic DO sensors consist of two electrodes, an anode and a cathode, which are both immersed in electrolyte (inside the sensor body). In the sensor, an oxygen-permeable membrane separates the anode and cathode

from the water being measured. As oxygen diffuses across the membrane, it interacts with the sensor's internals to produce an electrical current, which usually represents the sensor output measured in mV. Galvanic DO sensors are designed to allow higher pressure to be applied on the membrane and, consequently, more oxygen is able to diffuse across the membrane to create the current. This is achieved by passing the current across a thermistor (a resistor that changes output with temperature), which corrects for membrane permeability errors due to temperature change. In other words, increasing permeability at higher temperature allows more oxygen to diffuse into the sensor, even though the oxygen pressure has not changed. This would give a falsely high DO reading if the thermistor was not used. To represent sensor output in ppm or mg/L, the temperature of the water must be known. As a result, a separate temperature sensor can be used or one can be built into the sensor. This device is independent from the thermistor connected between the anode and cathode to compensate for membrane permeability variations due to temperature change. Since the partial pressure of DO is a function of the temperature of the sample, the DO sensor must be calibrated at the sample temperature or the sensor's meter must automatically compensate for varying sample temperature. The reading of a DO sensor should also be corrected for the amount of salt in the sample. Oxygen saturation based on temperature, salinity and solubility of solutes as a function of temperature are presented in Tables 8.2 and 8.3,¹⁴¹ respectively.

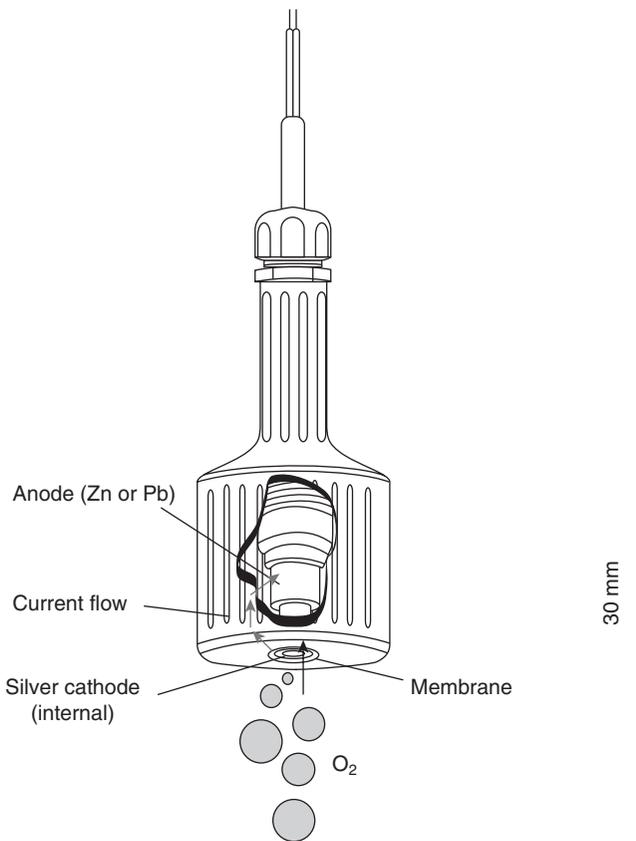
Amongst electrochemical sensors, amperometric Clark cells have conventionally been used in most applications.¹⁰⁷ A typical example of such a sensor is schematically displayed in Fig. 8.8. This type of sensor monitors the oxygen reduction current, which is controlled by the oxygen flux resulting from diffusion across the gas-permeable membrane separating the cell from the solution. This flux is proportional to the DO concentration (Fick's

Table 8.2 Oxygen saturation based on temperature and salinity¹⁴¹

Temperature (°C)	Salinity (ppt)					
	0 ppt	9 ppt	18.1 ppt	27.1 ppt	36.1 ppt	45.2 ppt
0	14.62 ppm	13.73	12.89	12.10	11.36	10.66
10	11.29	10.66	10.06	9.49	8.96	8.45
20	9.09	8.62	8.17	7.75	7.35	6.96
25	8.26	7.85	7.46	7.08	6.72	6.39
30	7.56	7.19	6.85	6.51	6.20	5.90
40	6.41	6.12	5.84	5.58	5.32	5.08

Table 8.3 Solubility of solutes as a function of temperature (mg of solutes per litre of water)¹⁴¹

Solute	Temperature (°C)					
	0	20	40	60	80	100
O ₂	69	43	31	14	0	
CO ₂	3350	1690	970	580		
NaCl	357 000	360 000	366 000	373 000	384 000	398 000
KCl	276 000	340 000	400 000	455 000	511 000	567 000



8.8 Schematic view of the solid-state DO sensor. (Reprinted from Ref. 139 with permission from Elsevier Science)

law). In the typical Clark cell, the cathode is a hydrogen electrode and carries a negative potential with respect to the anode.

Electrolyte surrounds the electrode pair and is contained by the membrane. With no oxygen, the cathode becomes polarized with hydrogen and resists the flow of current. When oxygen passes through the membrane, the cathode is depolarized and electrons are consumed. The cathode electrochemically reduces the oxygen to hydroxyl ions:



The anode reacts with the product of the depolarization with a corresponding release of electrons:



The electrode pair permits current to flow in direct proportion to the amount of oxygen entering the system. The magnitude of the current gives a direct measure of the amount of oxygen entering the sensor. Because all of the oxygen entering the sensor is chemically consumed, the partial pressure of oxygen in the electrolyte is zero. Therefore, a partial pressure gradient exists across the membrane and the rate of oxygen entering the sensor is a function of the partial pressure of oxygen in the water being measured. However, in many applications the oxygen consumption of the Clark cells is not negligible in comparison to the oxygen self-diffusion in the sample and therefore reliable and stable sensing signals are not obtained in unstirred or small volumes. In general, these problems may be solved by using electrochemical potentiometric sensors which, based on their definition, are non-oxygen-consuming.¹⁰⁸

8.2.2 Electrochemical potentiometric DO sensors

The techniques most commonly used for DO detection are as follows:

- titrimetric method using Winkler titration;¹⁰⁹
- optical methods of analysis (luminescence methods);¹¹⁰
- colourimetry;¹¹¹
- electrochemical techniques.¹¹²

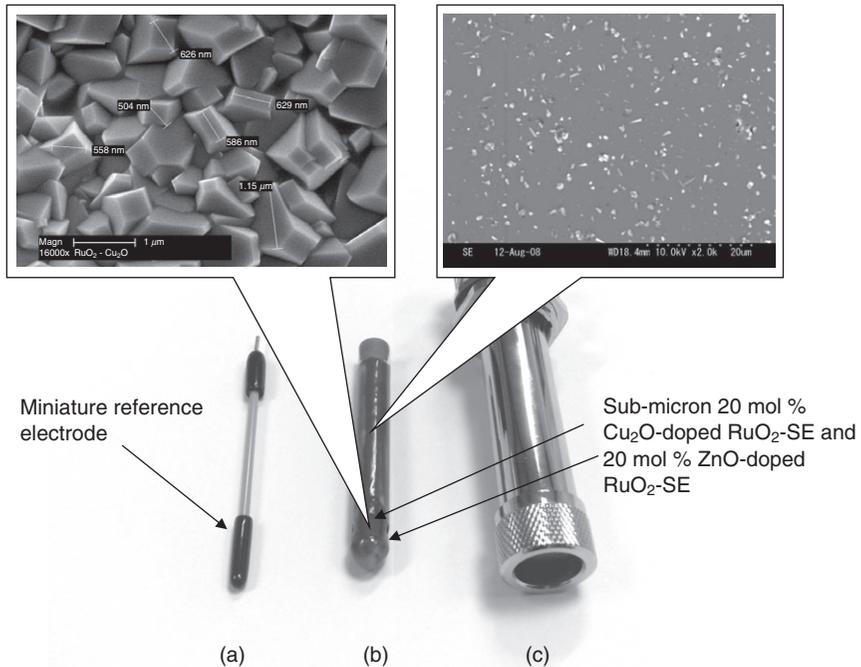
The luminescence measuring technique has been used for DO detection in the concentration range 0.20–20 mg/L and up to now has been adopted as a standard technique by the US Environmental Protection Agency (USEPA).¹¹¹ Although all of the above-mentioned techniques are highly sensitive, if DO measurement is required at high spatial resolution, then miniature, robust electrochemical sensors with high antifouling resistance would probably be the best option for implementation in wireless sensor networks.⁴⁹ Because direct DO measurements at different locations at high

spatial resolution can be relatively expensive, ongoing monitoring using miniaturized economical potentiometric sensors will provide an alternative method of assessing and evaluating various aqueous environments.

In this context, several concepts leading toward the development of highly-sensitive electrochemical sensors based on nanostructured metal oxides have been proposed since 2000.^{5,6,14,16,27,64,71,74–76} Among semiconductor metal oxide-SEs investigated to date, doped nanostructured RuO₂ has been considered as one of the most promising SE materials for potentiometric electrochemical DO sensors.^{52,54,55} It has been confirmed that selective doping of RuO₂ by another semiconductor nano-oxide can facilitate the formation of mixed oxides.^{49,52,55,60,61,65} The development of a sub-micron complex oxide SE matrix modifies the lattice, resulting in enhanced properties of the sensor, such as higher sensitivity to the measuring parameter and better selectivity.⁶⁴ In addition, the doping may lead to totally different physicochemical properties of the SE.¹¹³ Moreover, successful doping of a RuO₂-SE can not only change the major sensor characteristics, but also improve its antifouling resistance,^{49,61} which is critical for most practical applications.¹¹⁴ A typical example of a tubular electrochemical sensor for simultaneous measurement of pH and DO is presented in Fig. 8.9. In this sensor, a nanostructured 20 mol % ZnO-doped RuO₂-SE is used for DO measurement and a nanostructured 20 mol % Cu₂O-doped RuO₂-SE is utilized for pH measurement. A miniaturized Ag/AgCl, Cl⁻-RE has been assembled within the alumina sensor assembly.

Considering doped semiconductors, the fundamental deviations in the electronic structure of doped mixed oxide-SEs commonly result in the formation of donor levels located on the upper part of the bandgap of the semiconductor SE. These donor levels are largely responsible for the significant advance in properties.¹⁰ The dopant not only acts as a charge donor, but also transforms the structure of the nano-oxide and supplies excess carriers to the conductivity band which, in turn, increases the conductivity.¹⁰⁶ The use of donor nano-oxides will generate electronic defects in the nanostructure which maximize the influence of adsorbates on the conductivity. All of these aspects have contributed to the advances in the sensitivity, selectivity and stability characteristics of the sensors.

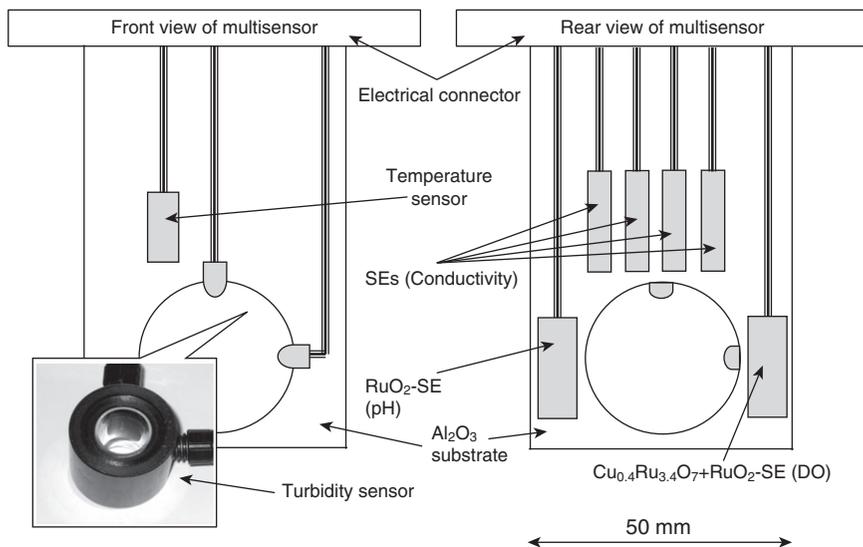
In order to investigate the surface area of 20 mol % ZnO-doped RuO₂-SE structures, atomic force microscopy (AFM) measurements have been completed. Plate XXIII (see colour section between pages 232 and 233) shows 2D and 3D AFM images of the surface of a 20 mol % ZnO-doped RuO₂-SE sintered at 800 °C with appropriate analysis. AFM measurements were carried out at scan rate of 1 Hz and scan size of 1000 nm. The AMF analysis conducted confirmed that in the complex SE structure the distance between the highest and lowest points is within the 100–400 nm range and the height of the major grains varies between 30 and 50 nm. The minimum recorded



8.9 Water quality sensor elements: (a) Ag/AgCl, Cl^- reference electrode; (b) alumina sensor assembly covered by ceramic protective layer and attached with Cu_2O -doped RuO_2 -SE and ZnO -doped RuO_2 -SE, respectively; (c) stainless steel protective sheet and housing of the probe with built-in filter.

grain diameter was 26.44 nm and the maximum was 95.15 nm. The 3D AFM image of the SE surface and analysis of the depth of the measured scan size also suggested only a very small percentage of deviation in the depth of the sample. The actual measured active surface area for SE sintered at 800°C was 7110.596 nm^2 and was much bigger than that of the measured active surface area of 2955.119 nm^2 for a similar SE sintered at 900°C . The AFM results obtained have confirmed 'better structured' and uniformly distributed morphology of the 20 mol % ZnO -doped RuO_2 -SE sintered at 800°C .

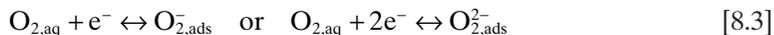
Due to the very small active areas of nanostructured SEs, they can be successfully utilized not only in tubular bulk sensors but also in planar miniature multisensor assemblies. A typical example of such a multisensor is schematically displayed in Fig. 8.10.⁶ This integrated water quality multisensor employs a nanostructured RuO_2 -SE for pH and a $\text{Cu}_{0.4}\text{Ru}_{3.4}\text{O}_7 + \text{RuO}_2$ -SE for DO measurements. The multisensor is capable of recording pH, DO, conductivity, temperature and turbidity of the measuring aqueous solutions. Extensive experimental studies have concluded that it is preferable to utilize a nanostructured RuO_2 -SE for pH measurement and



8.10 Schematic view of both sides of the integrated water quality monitoring multisensor. (Reprinted from Ref. 6 with permission from IOP Publishing)

a $\text{Cu}_{0.4}\text{Ru}_{3.4}\text{O}_7 + \text{RuO}_2\text{-SE}$ for DO measurement on the same sensor substrate.^{5,10,49,52,55,61}

If electrochemical reactions of DO measurement by a semiconductor SE are to be considered, it should be noted that in a solid-state nanostructured semiconductor SE, any solid surface forms surface groupings (the surface imperfections), by the reaction of coordinatively- or valence-unsaturated surface atoms on the bare surface with DO molecules. For the following one-electron oxygen reduction process



it is expected from the Nernst equation that the open-circuit potential will be as follows:

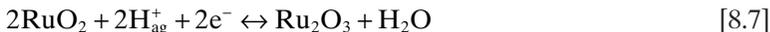
$$E = E_0 + \frac{RT}{F} \ln \left(\frac{\text{O}_{2,\text{aq}}}{\text{O}_{2,\text{ads}}^-} \right) \quad [8.4]$$

Here, $\text{O}_{2,\text{ads}}^-$ denotes the activity of adsorbed superoxide ions and the other parameters have their standard meanings.⁶⁴ The sensing performance of DO sensors with attached thick-film microstructured TiO_2 -coated $\text{RuO}_2\text{-SE}$ ^{4,12} and thin-film nanostructured $\text{RuO}_2\text{-SE}$ ^{5,6,64,65} was measured in standard buffer solutions, in which DO concentration was regulated by pumping a N_2/O_2 gas mixture with various fixed O_2 concentrations through the buffer solution. Although the changes of DO concentration in water achieved by

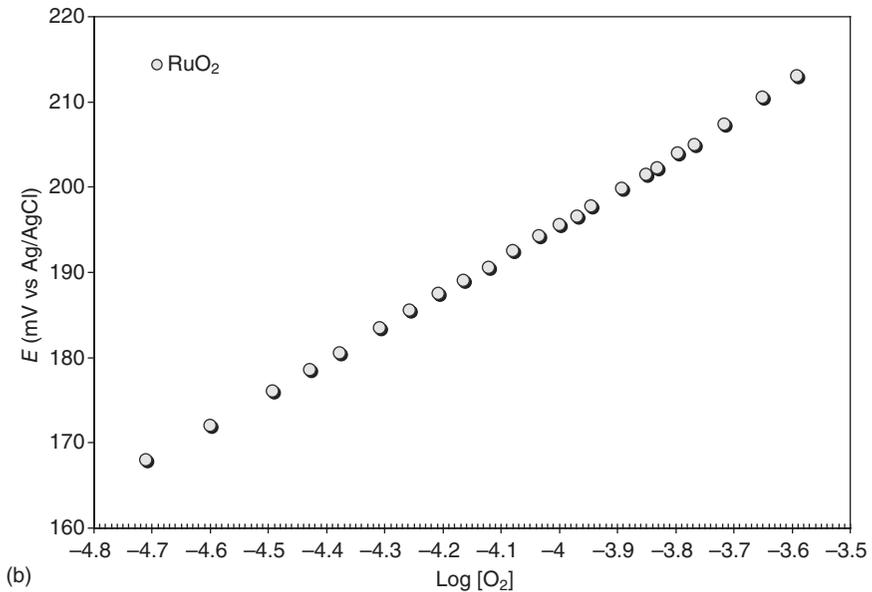
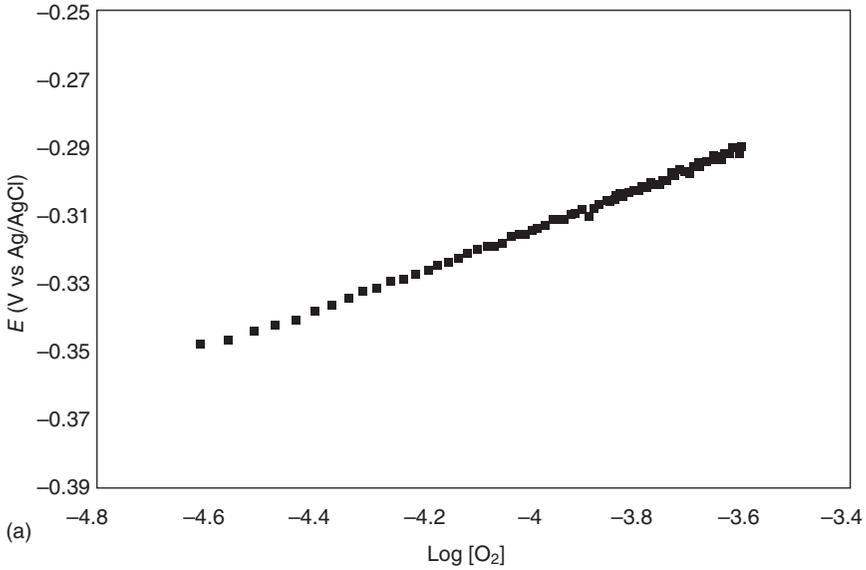
this method are time-consuming, this approach keeps the pH of the solution intact. DO sensors with attached RuO₂-SEs were conditioned in the buffer solution for at least two hours before the measurement. A linear response was obtained in output voltage variation for all RuO₂-SEs vs an Ag/AgCl,Cl⁻-RE with DO detection limits from 0.5–8.0 ppm (log[O₂], -4.71–-3.59) in water, as clearly illustrated in Fig. 8.11.^{4,6}

In this figure, it is shown that the straight line confirms the fast electrode reaction (8.3) involving one electron per oxygen molecule. This could be attributed to superoxide O₂⁻ ions at the surface electrode reaction.⁶⁵ The output voltage was stable with a Nernstian slope of -59.4 mV/decade⁴ and -41 mV/decade⁶⁴ and produced negligible drift during the testing period. Standard deviations of the output voltage were found to be around ± 5 mV in the entire DO measuring range. Further improvement in DO sensitivity has been achieved when the nanostructured RuO₂ was doped with ~10–20 mol % of Cu₂O or ZnO nano-oxides. In this case, the DO sensitivity increased up to -47.4 mV/decade for 10 mol % Cu₂O^{10,49} and -48.6 mV/decade for 10 mol % ZnO.^{52,55} Although the main purpose of doping RuO₂ with nanostructured Cu₂O or ZnO was the development of high antifouling resistance,⁶¹ it also served well for increasing DO sensitivity and improving the selectivity of the DO sensor.

Nevertheless, it was also experimentally determined that, although the gas flow controllers had a constant gas-mixture pumping rate (~100 cm³/min) during all experiments, a deviation of ±1.5 mV in DO measurement did still occur.⁶⁴ This suggested that, apart from the fast electrode reaction (8.3), other much slower electrode processes are possibly also involved in DO measurement using a nanostructured RuO₂-SE in strong alkaline solutions. It has to be noted that this slight deviation of the measured potential difference from a straight line indicates that the OH⁻ ions are possibly involved through, for example, heterogeneous dissolution of the SE according to:



whereby the reduced components (Ru₂O₃, RuO₄) are enriched as a layer at the surface.⁵² This indicates a supporting influence of OH⁻ ions in the kinetics of the oxygen adsorption reaction (8.1). All the above-mentioned results indicated that chemical structure and electronic band complex for the electrode surface layer have an influence on the DO measurement and that the RuO₂-SE is affected by heterogeneous oxidation, which has recently been verified by X-ray photoelectron spectroscopy (XPS) surface analysis.⁵⁴



8.11 (a) Voltage response of the potentiometric TiO₂-coated RuO₂ electrode as a function of the logarithm of the DO concentration in water at 25°C. (Reprinted from Ref. 4 with permission from Elsevier Science) (b) Nanostructured RuO₂-SE at a temperature of 23°C. (Reprinted from Ref. 6 with permission from IOP Publishing)

8.3 Conductivity measurements

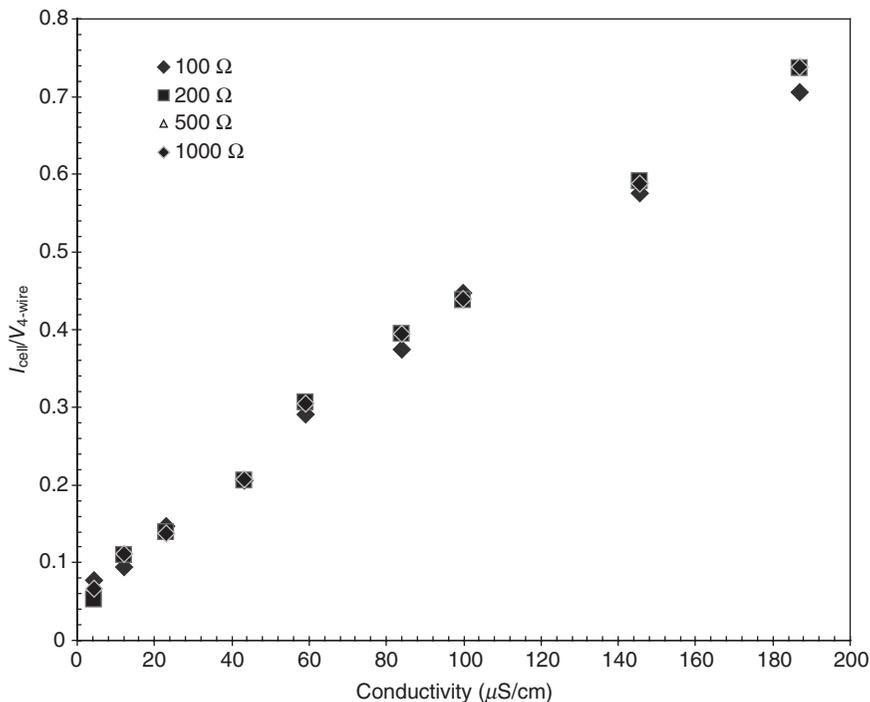
Conductivity is a measurement of the ability of an aqueous solution to transfer an electrical current. The current is carried by ions and therefore the conductivity increases with the concentration of ions present in solution, their mobility and the temperature of the water. Conductivity measurements are related to ionic strength. However, this is not a qualitative exercise (i.e. it is not known which ions are present). Resistance, which is an electrical calculation expressed in Ω , is the inverse of conductivity. Traditionally, conductivity sensors have been used for the determination of water quality in the following applications:¹¹⁵

- Mineralization: this is commonly called total dissolved solids. Total dissolved solids information is used to determine the overall ionic effect in a water source. Certain physiological effects on plants and animals are often affected by the number of available ions in water.
- Noting variation or changes in natural water and waste waters quickly.
- Estimating the sample size necessary for other chemical analysis.
- Determining the amounts of chemical reagents or treatment chemical to be added to the water sample.

Elevated dissolved solids can generate ‘mineral tastes’ in drinking water. Corrosion or encrustation of metallic surfaces by water high in dissolved solids causes problems with industrial equipment and boilers, as well as domestic plumbing, hot water heaters, toilet flushing mechanisms, faucets, washing machines and dishwashers.

There are two types of solid-state sensor which can be used to measure conductivity: those with two SEs or those with four SEs.⁴ In the latest CSIRO development four working Pt/Ag/Pd-SEs were used on the sensor substrate as presented in Fig. 8.10.⁶ Conductivity measurements by multi-sensor revealed that by using ‘a four SEs system’ and 3V p/p square wave at 500 Hz, the sensor is capable of measuring conductivity from $\sim 5 \mu\text{S}/\text{cm}$ (de-ionized water) up to $200 \mu\text{S}/\text{cm}$ with acceptable accuracy. On the other hand, published results concerning utilization of different serigraphic Ru-containing pastes for conductivity measurements⁴ showed that the lowest measured conductivity was only $500 \mu\text{S}/\text{cm}$. CSIRO SEs have proved to be much more sensitive, possibly due to the metallic nature of the SEs and their superior resistance compared to SEs based on Ru-containing pastes. Use of inexpensive metallic Pt/Ag/Pd alloy as SEs in an integrated water quality multisensor provided significant improvement, specifically towards the low conductivity range ($5\text{--}200 \mu\text{S}/\text{cm}$). Results of these measurements are presented in Fig. 8.12.⁶

In these assessments, the sensor cell is effectively a four-wire resistance unit. I_{cell} is the AC current that flows through the cell when 3V p/p at 500 Hz



8.12 Multisensor response as a function of conductivity in 5–200 $\mu\text{S/cm}$ range at a temperature of 20 °C for Pt/Ag/Pd-SEs. (Reprinted from Ref. 6 with permission from IOP Publishing)

is applied to the two-wire electrodes. $V_{4\text{wire}}$ is the RMS AC voltage which appears across the four-wire electrodes when 3 V p/p at 500 Hz is applied. The X-axis in Fig. 8.12 is a set of known conductivity solutions measured in $\mu\text{S/cm}$ by a calibrated commercial conductivity meter. The range 5–1200 $\mu\text{S/cm}$ has been considered as the most interesting conductivity range for potable water and other recycled water applications. The measured characteristic was linear and stable over numerous cycles of measurement with no significant hysteresis effect. Moreover, due to the absence of units in the published conductivity measurements graph,⁴ it was impossible to directly compare the results obtained for our Pt/Ag/Pd-SE with the previously published results for a SE based on Ru-containing pastes. In addition, substantial improvement in the response time was obtained for the Pt/Ag/Pd-SE. The response time of the developed conductivity sensor based on the Pt/Ag/Pd-SE to the conductivity changes was approximately 1–3 s at a temperature of 20 °C compared to about 2 min for the similar sensor based on Ru-containing pastes.⁴

8.4 Antifouling technologies for solid-state water quality sensors

Biofouling is a serious problem that costs, for example the shipping industry, more than \$200 billion per annum.¹¹⁶ The accumulation of bio-organisms such as algae, mussels and barnacles increases the object water resistance and, consequently, fuel consumption. This means additional costs for shipping companies and increased CO₂ emissions. With regard to environmental water quality sensors, biofouling makes these sensors non-operational within a very short period of time. Therefore there is a tremendous interest in the development of antifouling technologies using nanoscale materials, especially in water quality sensors, where doping of a semiconductor SE by another nanoscale semiconductor oxide can yield improvement of the sensor's characteristics and likewise increase the SE's antifouling resistance. Tailoring nanostructured SEs of water quality sensors for high antifouling resistance has been one of the main priorities of the advance of water quality sensors in the 21st century.^{47,59} Many bio-organisms in fresh and marine environments adhere to the components of any deployed instruments, and the growth of this biological material on the sensor is known as biofouling. This results in the need for expensive and frequent maintenance unless the sensor's SEs are protected from this process. Resistance to the accumulation of biofouling is identified as antifouling and therefore there is a strong demand for the development of antifouling strategies applicable for electrochemical solid-state sensors.¹¹⁷

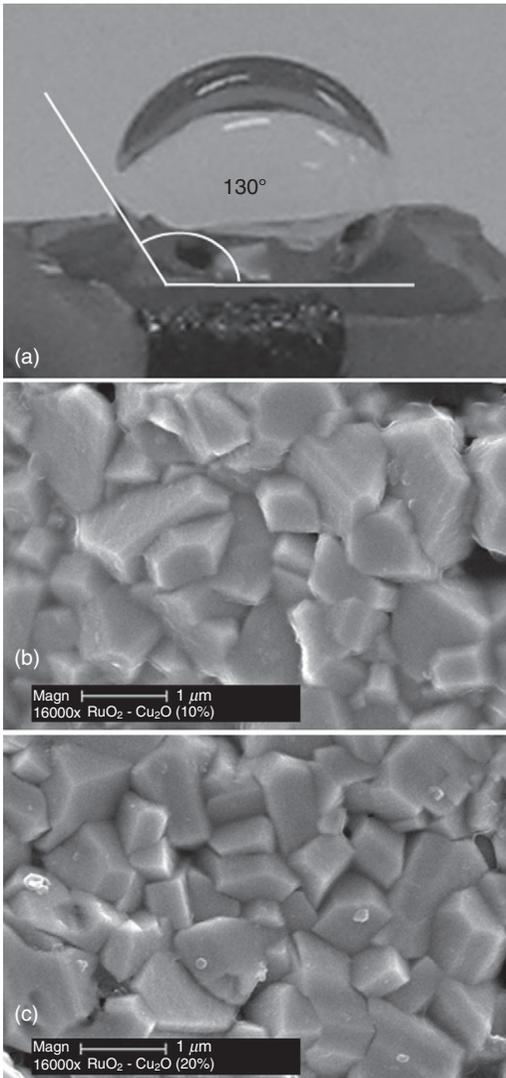
In the past, antifouling was achieved by the use of coatings containing strong biocides.¹¹⁴ However, due to their ecological consequences, many of these biocides have been prohibited and thus a new generation of novel antifouling strategies is under development. In this context, several proposals for improvement of the antifouling resistance of electrochemical sensors, based on nanostructured metal oxides, have recently been put forward.¹¹⁸⁻¹²⁴ The study of and copying of natural mechanisms is known as 'bio-mimicry', and researchers are increasingly investigating and adopting a biomimetic approach for antifouling. This is largely due to the need to develop innovative approaches to a problem that has yet to be controlled comprehensively by any environmentally benign antifouling technologies. The recurring theme of combining surface chemistry and surface topographies has been identified as an area where the most significant advances in the new antifouling technologies will be generated and accomplished.¹¹⁴ Notably, the majority of biomimetic surfaces have surface features at single length scales and predominantly have species-specific antifouling effects.^{123,124}

Since year 2000, the development of multiple scales of topography has been a tangible step toward the modification of the sensor's SE materials.¹²¹ The bio-inspired development of multiple-scale surfaces is exemplified by

the production of hierarchically wrinkled surfaces with multiple length scales ranging from nanometers to millimetres.¹²³ Another approach for the improvement of the antifouling resistance of the sensor's SE is based on the development of nanostructured SE materials possessing super-hydrophobic properties.^{119,120,122} Most super-hydrophobic surfaces have more extreme effects in terms of settlement and the attachment of bio-materials.¹¹⁹ Although little is still understood and recognized regarding the properties of super-hydrophobic surfaces of nanostructured complex oxide SEs in the aqueous environment, the most important factor associated with super-hydrophobic surfaces may not be minimizing adhesion, but rather reducing the scale of roughness.¹¹⁴

An alternative novel antifouling strategy is based on the development of complex oxide nanostructured SEs with improved morphologies. This can be achieved by doping the base nano-oxide with a small amount of another nano-oxide possessing high antifouling properties. Since nanostructured Cu_2O is a well-known antifouling agent used in commercial marine paints for biofouling prevention,¹²⁵⁻¹²⁹ it has been utilized for doping RuO_2 -based SEs in CSIRO research.¹⁰ As described in the previous sections, nanostructured RuO_2 with a rutile structure has been extensively tested and is considered to be one of the most promising SE materials for solid-state pH and DO sensors. It has been recently reported that the electrochemical solid-state DO sensor based on a nanostructured Cu_2O -doped RuO_2 -SE can provide improved DO sensitivity and selectivity, with acceptable response and recovery rates for environmental monitoring.⁴⁹ The increase in antifouling resistance has been achieved by Cu_2O doping with the development of a $\text{Cu}_{0.4}\text{Ru}_{3.4}\text{O}_7 + \text{RuO}_2$ complex oxide.^{10,61} Although both 10 and 20 mol % Cu_2O -doped RuO_2 -SEs have similar morphology and microstructure,¹⁰ it has also been determined that a solid-state DO sensor based on a ~20 mol % Cu_2O -doped RuO_2 -SE has exhibited superior antifouling resistance to a similar DO sensor based on a 10 mol % Cu_2O -doped RuO_2 -SE.⁶¹ Figure 8.13 provides SEM images at the same scale of the unaffected areas of both 10 and 20 mol % Cu_2O -doped RuO_2 -SEs after a three-month trial in a sewage environment.^{54,61}

Figure 8.13a depicts a water droplet on the surface of the $\text{Cu}_{0.4}\text{Ru}_{3.4}\text{O}_7 + \text{RuO}_2$ with a water contact angle of 130° , confirming the super-hydrophobic nature of the $\text{Cu}_{0.4}\text{Ru}_{3.4}\text{O}_7 + \text{RuO}_2$ -SE and the presence of a large number of hydroxyl groups on its surface.¹³⁰ It is evident from these SEM images that there is not much difference in the grain size distribution between the 10 and 20 mol % Cu_2O -doped RuO_2 -SEs. However, a very thin layer (~10–50 nm) of biofouling has been observed on the main grains and grain boundaries of the 10 mol % Cu_2O -doped RuO_2 -SE (Fig. 8.13b). On the other hand, there were no observations of similar biofouling deposits on the main grains and grain boundaries of the 20 mol % Cu_2O -doped



8.13 (a) Water droplet on nanostructured 20mol% Cu₂O-doped RuO₂-SE indicating super-hydrophobic property of its surface. (Reprinted from Ref. 54 with permission from Elsevier Science), SEM images of 10 mol% Cu₂O-doped RuO₂-SE with some deposits of biofouling (b); 20 mol% Cu₂O-doped RuO₂-SE (c) with no apparent biofouling on the SE grain boundaries. (Reprinted from Ref. 61 with permission from Elsevier Science)

RuO₂-SE (Fig. 8.13c). All these observations suggest that an effective improvement in biofouling resistance can be achieved by ~20 mol % Cu₂O doping of the RuO₂-SE, promising a long-term biofouling resistance of the SE. These results have also shown that relative improvement in antifouling resistance can be achieved with much smaller amounts of Cu₂O in the SE structure compared to the amounts of Cu₂O pigment particles in commercial antifouling paints (~80 mol %).^{131,132}

8.5 Solid-state turbidity sensors

ISO 7021-1999 Standards describes turbidity as the reduction of transparency of a liquid caused by the presence of undissolved matter.¹³³ Turbidity is used as a measure of colloidal and suspended matter in water systems. These materials often react with chlorine disinfectant, therefore, in potable water supplies turbidity is carefully controlled to ensure that disinfectant levels and public health are properly maintained.^{134–137} Turbidity is especially important for recycled water, when potable substitution is involved. In addition to these health concerns, turbidity is also an aesthetic parameter, as consumers expect a sparkling clear water supply. Turbidity can vary from a river full of mud and silt, where it would be impossible to see through the water (high turbidity), to a spring or drinking water which appears to be completely clear (low turbidity). Turbidity can be caused by the following:

- silt, sand and mud;
- bacteria and other germs;
- chemical precipitations.

It is vital to measure the turbidity of domestic water supplies, as those supplies often undergo some type of water treatment which can be affected by the turbidity. For example, during the wet season when mud and silt are washed into rivers and dumps, high turbidity can rapidly block filters and eventually prevent them from working efficiently. Where chlorination of water takes place, even quite low turbidity can prevent the chlorine from killing microorganisms in the water. Some treatment systems, such as sedimentors, coagulators and gravel pre-filters, are designed to remove turbidity. However, it is important for operators of both large and small treatment systems to know how well these systems are operating. Consequently, turbidity measurements of water before and after each part of the system can provide the controller with valuable information, especially when maintenance and/or cleaning is required.

CSIRO turbidity sensors using solid-state components and utilizing a common electronics module have recently been developed. Although there are plenty of turbidity measuring instruments currently available on the market, most of these are expensive and not directly compatible

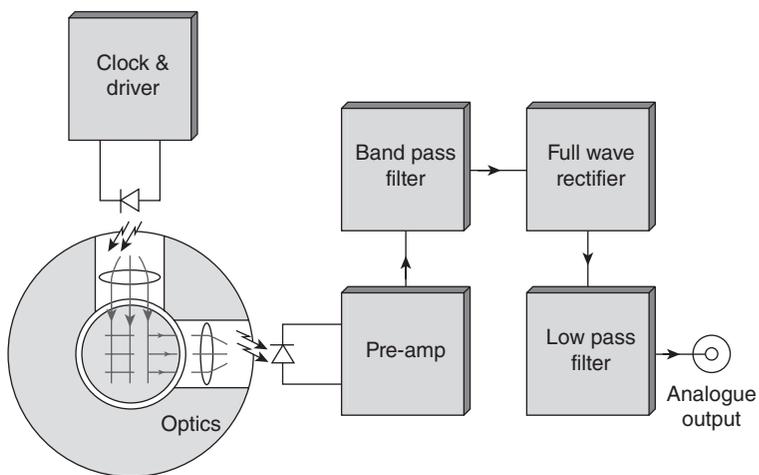
with wireless distributed sensor networks. Consequently, CSIRO has developed a custom turbidity sensor optimized for network and multisensor applications. An example of a turbidity sensor incorporated into a multisensor assembly is given in Fig. 8.10 above. Figure 8.14 provides further information in relation to turbidity signal conditioning used in the inexpensive CSIRO sensor.

Every turbidity sensor, regardless of its optical configuration, must be calibrated with a known standard. This is the reference to which the measured values are compared. The most widely used measurement unit for turbidity is the FTU (formazin turbidity unit). This unit can be used for all turbidity sensors which employ formazin ($C_2H_4N_2$) as the calibration standard. The USEPA uses formazin, but states its measuring units as nephelometric turbidity units (NTU).

For drinking water suppliers, the following guidelines should be taken into account:

- Drinking water should have a turbidity of 5 NTU or less. Turbidity of more than 5 NTU would be noticed by users and may cause rejection of the supply.
- Wherever drinking water is chlorinated, turbidity should be less than 5 NTU and preferably less than 1 NTU for chlorination to be effective.

Therefore, development of a turbidity sensor capable of accurate measurement of both high and low turbidity is essential in water quality analysis. A multisensor incorporated turbidity sensor has already been reported by



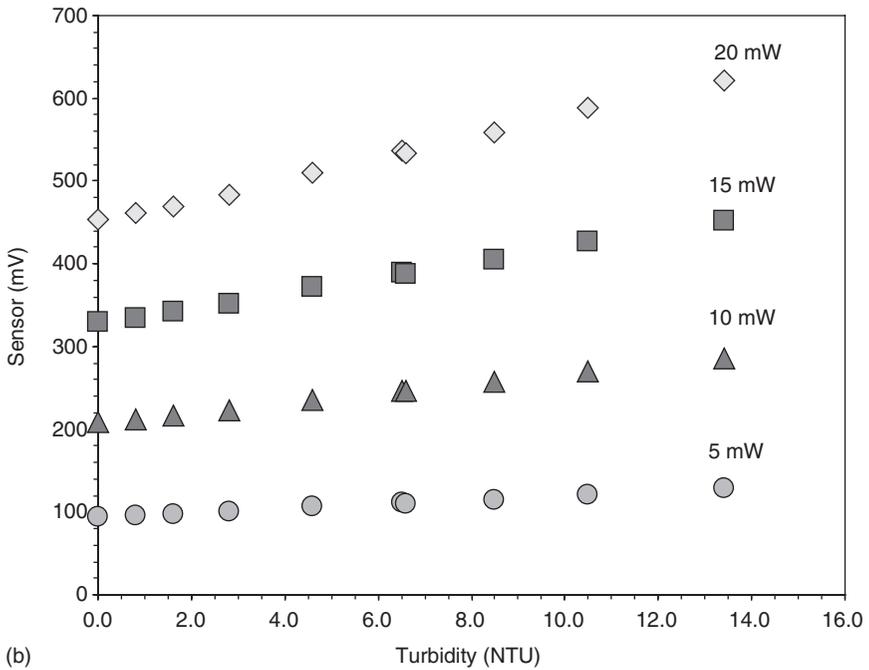
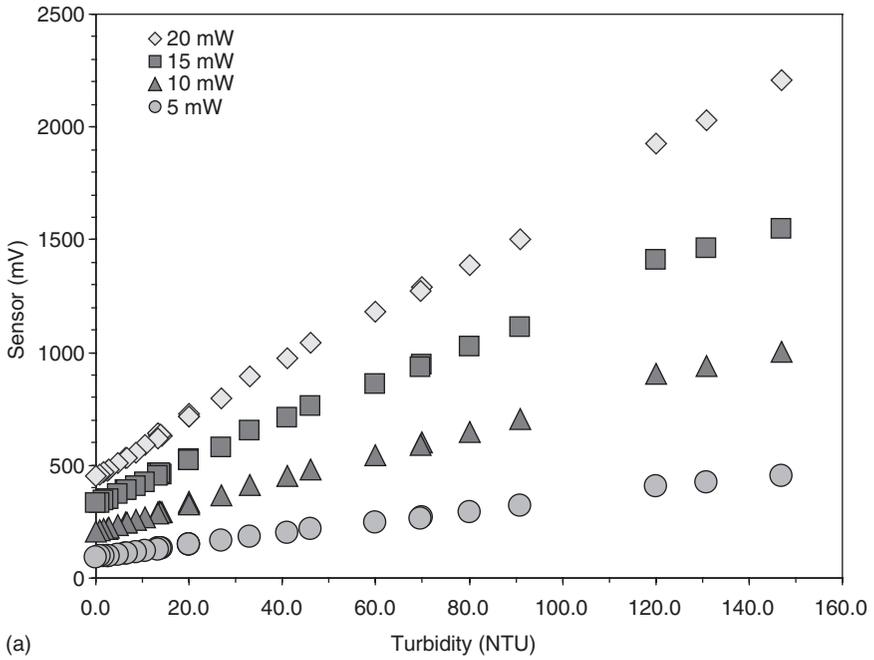
8.14 Turbidity signal conditioning of inexpensive CSIRO turbidity sensor for multisensor application. (Reprinted from Ref. 141 with permission from Elsevier Science)

the Spanish research group.⁴ CSIRO used a similar 90-degree scattering optical method in its turbidity sensor. It allows small standalone or flow-through cells to be mounted on either a multisensor or as part of an on-line flow-through manifold system, as illustrated in Fig. 8.14. The electronics of the sensor has been simplified to reduce the manufacturing cost and keep it at less than \$150. Figure 8.15 shows some data for the low- and high-turbidity range for the CSIRO sensor at 23°C.⁶ It has a resolution of 0.1 NTU and can measure in the range 1–2000 NTU with reasonable linearity. Figure 8.15a provides turbidity measurement data in the 1.0–150 NTU range and Fig. 8.15b is a magnified section covering 1.0–13.0 NTU turbidity measurements. The light source is an infra-red light-emitting diode (IR LED) with a collimating lens system and a photodiode detector. Power to the LED has been changed sequentially during turbidity measurement in order to demonstrate the output signal intensity.

There is clearly a linear relationship between turbidity and output sensor mV for both low and high turbidity ranges. Biofouling from a contaminated source has been an ongoing issue during the use of the turbidity sensor in industrial applications requiring frequent maintenance. Therefore, turbidity sensors of an alternative design should be applied in order to minimize the impact of frequent calibrations. One approach commonly employed is the use of an automatic intermittent wiper. Another is to exploit the mildly toxic properties of Cu corrosion products by installing a Cu annulus around the window area of the sensor. In the case of the cylindrical cell, it may be worth revisiting the original concept with a glass tube. This would isolate the LEDs and photodiodes from the test medium and open up the possibility of a linear cleaning cycle using a plunge/piston device. Non-linearity of the turbidity output is usually affected by the absorption of incident light. An additional detector in line with the LED may be used to measure absorption and apply a correction to the displayed turbidity. This would be most easily implemented in the cylindrical cell. In fact, all sensor modifications should be tested to the requirements of the ISO Standard 15839-2003 outlining performance testing requirements for water quality sensors.¹³⁸

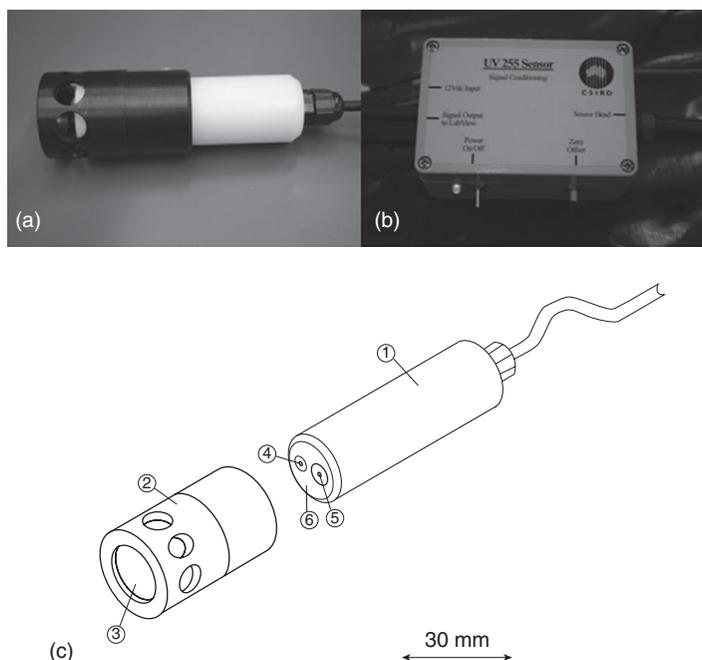
8.6 Solid-state dissolved organic carbon (DOC) sensors

Dissolved organic carbon (DOC) is generally defined as organic matter that is able to pass through a filter which removes material between 0.70 and 0.22 μm in size. Determining the concentration of DOC in an aqueous solution, such as a sample of waste water or potable water, is important in diverse fields including pollution abatement and industrial processing situations.¹³⁹ This is particularly valuable to Australia as a prolonged



8.15 Measurements of high (a) and low (b) turbidity ranges at 23°C. (Reprinted from Ref. 6 with permission from IOP Publishing)

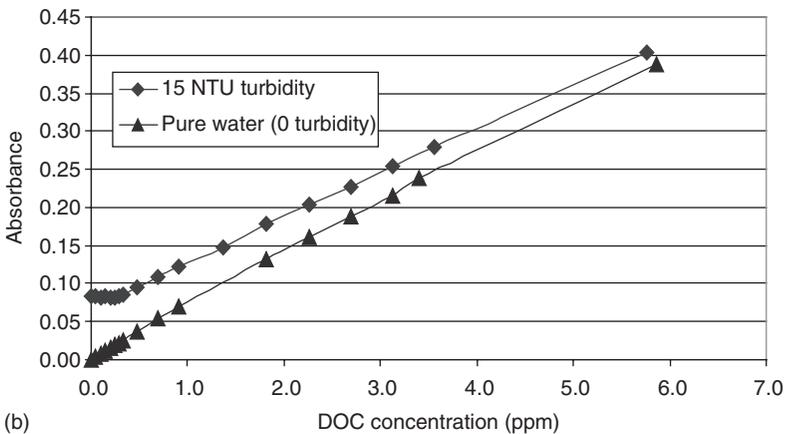
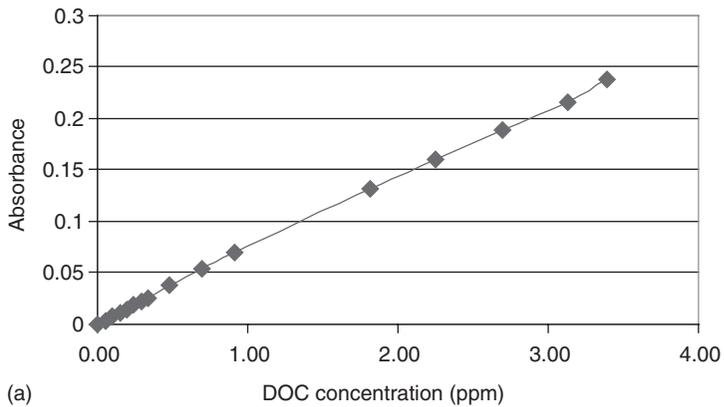
drought since 2000 has resulted in increased adoption of recycled water to alleviate the environmental strain. CSIRO recently finished development of an inexpensive hand-held device for monitoring traces of DOC in aqueous solutions.¹⁴⁰ The patented DOC sensor has an innovative design based on an UV255 LED as the light source, a reflecting mirror and an UV-sensitive photodiode as detector. A general view of the hand-held device together with the signal conditioning box and a diagram showing the main components is given in Fig. 8.16.¹⁴¹ The main body (1) incorporates a UV255 LED (4) as the light source and a UV photodiode (5) as the detector in the housing (6), whilst the outer sleeve (2) houses a glass reflecting mirror (3). Sensor 1 has a front-surface mirror, whereas sensor 2 has a back-surface mirror. The front-surface mirror can be a cheaper glass whilst the back-surface mirror has to be UV-grade quartz. The mirror at the base of the movable sleeve reflects the UV signal back to the photodiode and is secured to the sensor body using a plastic screw, which homes into a captive position each time the sleeve is refitted (this ensures that the path length of the absorption cell is constant). The UV photodiode has a current output



8.16 Sensor with fixed outer sleeve (a), signal conditioning box (b) and diagram showing main components of the sensor (c). (Reprinted from Ref. 141 with permission from Elsevier Science)

which the pre-amp converts to a voltage, and the AC signal is filtered and rectified to produce an analogue output voltage that is proportional to transmission intensity.

Laboratory trials revealed that the new hand-held device exhibited a good linear absorbance with DOC from 5 to ~100 ppm, as illustrated in Fig. 8.17a.¹⁴¹ However, the most interesting results were obtained at the ppb level, where the sensor's detection limit was established at ~10 ppb of DOC.¹⁴⁰ $C_8H_5KO_4$ was used for calibration purposes. Some tests were conducted on water taken from CSIRO laboratory taps and some on recycled water from the Melbourne Hunt Club site. Samples were measured with



8.17 (a) Absorbance of DOC detected by a hand-held UV255 sensor in water at 20°C. (b) Effect of turbidity on absorbance of newly-developed hand-held UV255 sensor. (Reprinted from Ref. 141 with permission from Elsevier Science)

the DOC sensor and compared with values obtained when measured using a commercially available UV-Vis spectrometer. Very good correlation was found as presented in Table 8.4.¹⁴¹

However, during field trials it was also established that turbidity does affect absorbance readings and therefore provides a false 'high' concentration. Rise in turbidity (from 0 to 15 NTU) increases absorbance and requires compensation. Possible use of a 20 wavelength system (Fig. 8.17b) could alleviate errors. Consequently, if DOC has to be measured in high-turbidity solutions such as waste water, the testing solution has to pass through a 1 µm filter prior to measurement. Therefore, the best analysis of the water can be achieved if the hand-held DOC sensor is used in conjunction with the turbidity sensor.

8.7 Solid-state dissolved metal ion sensors

Modern environmental monitoring requires simultaneous on-site measurements not only of major water quality parameters (pH, DO, conductivity, turbidity, temperature, etc.) but also a number of different dissolved chemical species. Heavy metals in surface water systems can be from natural or anthropogenic sources. At the beginning of the 21st century, anthropogenic inputs of metals exceed natural inputs. Excess of heavy metals in the surface water may pose a health risk to humans and to the environment. The EPA and World Health Organization (WHO) set maximum contaminant levels in drinking water supplied to municipal population.¹⁴¹ When a standard or guideline is exceeded in the municipal or community water system, the local authority is required to take proper action to improve water quality level including treating the water through filtration or aeration, blending water from several sources to reduce contaminants, including inorganic chemicals such as metals, salts and minerals.

These substances occur naturally in geological structures or are sometimes caused by mining, industrial and agricultural activities. Based on

Table 8.4 Correlation of DOC measurements between the hand-held DOC sensor and commercial spectrometer¹⁴¹

Water type	Hand-held sensor Calculated from std additions curve DOC (ppm)	Commercial spectrometer DOC (ppm)
Recycled – Hunt Club	25.2	23.1
Tap – Lab G.07	2.16	2.0
Drinking fountain	0.25	0
Tap – Lab 1.61	3.06	3.0

WHO recommendations, all dissolved metals in raw water should be monitored at least four times in a year. Usually raw water comes from sources such as lakes, reservoirs and streams and groundwater. The raw water will go through some processes in the water treatment plant, such as coagulation or flocculation, sedimentation, filtration, stabilization, fluoridation, chlorination and finally, before allowing water to be used in the residential area, water will be tested for a few contaminants again. This is to ensure that the drinking water distributed is safe for public consumption. Based on EPA and WHO recommendations, the acceptable values of different dissolved metals in untreated and drinking waters are presented in Table 8.5.¹⁴¹ It has to be noted that the WHO guidelines have been strengthened since 2000 toward lower acceptable concentration levels of the major dissolved metals. For example, the legal acceptable limit for lead (Pb) in drinking water has been decreased from 0.05 ppm in 1995 to 0.01 ppm in 2010.

A classic approach to this problem is to use a selective solid-state sensor for each chemical species, and many solid-state sensors for detection of dissolved heavy metals have been developed to date. However, in complex aqueous solutions, sensors tend to lose their own specificity and their response is no longer directly related to the concentration of the species for which they have been designed, as they are influenced by the presence of other species.¹⁴² As an alternative, multicomponent analysis is an analytical procedure allowing the extraction of qualitative and quantitative information from an array of non-selective sensors matched with a suitable data analysis procedure.^{71,76} Multicomponent analysis provides a sensor array model from a calibration dataset, which should be large enough to cover the concentration range of each species and to cope with non-linearity in the sensor responses.

Table 8.5 WHO guidelines for acceptable values of metal content in raw water and in drinking water after treatment¹⁴¹

N/N	Contaminant and unit of measurement	Acceptable value in raw water	Acceptable value in drinking water
1	Arsenic (mg/L)	0.01	0.01
2	Cadmium (mg/L)	0.003	0.003
3	Lead (mg/L)	0.05	0.01
4	Chromium (mg/L)	0.05	0.05
5	Zinc (mg/L)	3.00	3.00
6	Copper (mg/L)	1.0	1.0
7	Mercury (total) (mg/L)	0.001	0.001
8	Magnesium (mg/L)	150	150

Many data analysis techniques can be utilized to disentangle the information from sensor array outputs; they can be grouped into four classes: chemometrics, artificial neural networks, non-linear least squares and exotic methods (such as genetic algorithms or multidimensional splines). During the last few years, the potential ability to perform measurements of concentrations of a number of chemical species in complex solutions has resulted in a number of devices called 'Electronic tongue' (E-tongue) for monitoring dissolved metal ions in complex solutions.^{67–83}

The E-tongue is an analytical measuring device comprising an array of potentiometric chemical solid-state sensors with relatively low selectivity, albeit high sensitivity to several components of a solution (cross-sensitivity), and an advanced data processing engine such as pattern recognition or multivariate calibration.⁸² Since 2000, most E-tongues have proven to be very promising devices for rapid and precise simultaneous monitoring of dissolved heavy metals in different complex solutions.^{81,83} So far, the most promising SE materials for construction of an E-tongue for a particular application are the chalcogenide glass SE for monitoring Ag^+ , Tl^+ , Cu^{2+} , Pb^{2+} , Cd^{2+} , Hg^{2+} , Fe^{3+} , Cr(VI) , the crystalline SE for monitoring Fe^- , Cl^- , Br^- , I^- , CN^- , CNC^- and the PVC plasticized SE for monitoring K^+ , NH_4^+ , Ca^{2+} , NO_3^- , Na^+ , Mg^{2+} , Cl^- , Zn^{2+} , CO_3^{2-} , SO_4^{2-} , NO_2^- . Table 8.6 summarizes the technical characteristics of these electrodes.¹⁴¹

Unfortunately, very limited information with regard to the design of E-tongues is available in recent publications, as they have not yet reached the level of industrial acceptance. Most of the published data represent measurements performed in different laboratories and under various conditions. Consequently, further development is required in order to re-design available E-tongues to fit most industrial requirements. Figure 8.18 shows an example of a potentiometric E-tongue using a sequential injection analysis (SIA) flow system and an array of ion-sensitive electrodes (ISEs).^{143,144}

It is clearly presented in Fig. 8.18 that the modern E-tongue is a complex system requiring further modification. However, the results obtained so far indicate that the E-tongue is capable of simultaneously measuring dissolved Cd^{2+} , Pb^{2+} and Cu^{2+} even at sub-micromolar level, as illustrated in Fig. 8.19. Some inaccuracy, however, was observed for the Cd^{2+} monitoring, especially at the lower concentration levels.¹⁴³ This could be attributable to the strong interfering effect that Pb^{2+} and Cu^{2+} ions had on the Cd^{2+} sensor, as already evaluated in the sensor characterization stage. Nevertheless, the determination of Cd^{2+} at the sub-micromolar level was still possible. In order to improve the results and reduce the dispersion observed, a more selective Cd^{2+} sensor would be needed. Another option would be to enlarge the sensor array, incorporating sensors with different properties or replicating the sensors in order to increase the available information. Aside from the external test set, an extra comparison employing synthetic samples was also

Table 8.6 Characteristics of solid-state electrodes of modern E-tongues for analysis of dissolved metals in complex solutions¹⁴¹

Primary ion	Working range (mol/L)	Detection limit (mg/L)	Electrode response slope (mV/pX)	Working pH range	Interfering ions
Chalcogenide glass electrodes					
Ag ⁺	10 ⁻⁷ -1	0.01	58 ± 2	0-9	-
Tl ⁺	10 ⁻⁶ -10 ⁻¹	0.2	40 ± 10	1-11	Ag ⁺ , Hg ²⁺
Cu ²⁺	10 ⁻⁷ -1	0.006	28 ± 2	0-7	Ag ⁺ , Hg ²⁺
Pb ²⁺	5 × 10 ⁻⁷ -1	0.01	28 ± 2	2-7	Ag ⁺ , Hg ²⁺
Cd ²⁺	5 × 10 ⁻⁷ -1	0.05	27 ± 2	1-7	Ag ⁺ , Hg ²⁺ , Pb ²⁺ , Cu ²⁺
Hg ²⁺	10 ⁻⁶ -10 ⁻¹	0.02	*	0-2	Ag ⁺
Fe ³⁺	10 ⁻⁵ -10 ⁻²	0.06	**	0-2	Ag ⁺ , Hg ²⁺
Cr (VI)	10 ⁻⁷ -10 ⁻⁴	0.006	***	0-2	Ag ⁺ , Hg ²⁺
Crystalline electrodes					
F ⁻	10 ⁻⁶ -10 ⁻¹	0.02	-(58 ± 2)	4-7	-
Cl ⁻	10 ⁻⁵ -1	0.35	-(58 ± 2)	0-12	S ²⁻ , Br ⁻ , I ⁻
Br ⁻	5 × 10 ⁻⁶ -1	0.4	-(58 ± 2)	0-12	S ²⁻ , I ⁻
I ⁻	5 × 10 ⁻⁷ -1	0.06	-(58 ± 2)	0-12	S ²⁻
CN ⁻	10 ⁻⁶ -10 ⁻²	0.03	-(57 ± 3)	12-14	S ²⁻ , I ⁻
CNS ⁻	10 ⁻⁶ -10 ⁻¹	0.06	-(57 ± 3)	2-10	S ²⁻ , I ⁻

PVC plasticized electrodes

K ⁺	5×10^{-6} -0.5	0.2	55 ± 3	1-9	NH ₄ ⁺
NH ₄ ⁺	5×10^{-4} -0.5	9	55 ± 3	0-8.5	K ⁺
Ca ²⁺	5×10^{-5} -0.1	2	27 ± 2	4.5-9.5	Ba ²⁺
NO ₃ ⁻	2×10^{-6} -0.2	0.1	-(54 ± 4)	1-10	Cl ⁻
Na ⁺	5×10^{-5} -0.1	1	54 ± 3	2-8.5	K ⁺
Mg ²⁺	5×10^{-5} -0.1	1	27 ± 2	4.5-9.5	Ca ²⁺
Ca ²⁺ + Mg ²⁺ (water hardness)	10^{-4} - 10^{-1}	6	25 ± 3	4.5-9.5	NH ₄ ⁺ , Ba ²⁺
Cl ⁻	5×10^{-5} -0.5	1.75	-(57 ± 2)	4-9	NO ₂ ⁻ , CNS ⁻ , Sal ⁻
CO ₃ ²⁻	10^{-5} -0.5	0.6	-(27 ± 2)	7-9	-
SO ₄ ²⁻	10^{-4} -0.5	9.5	-(26 ± 2)	3-8.5	Cl ⁻ , Br ⁻ , CO ₃ ²⁻ , OH ⁻
Zn ²⁺	5×10^{-5} -0.1	3.2	50 ± 3	5-7.5	Cu ²⁺ , Pb ²⁺
NO ₂ ⁻	10^{-4} -0.1	2.4	-(40 ± 7)	5.5-8.5	F ⁻ , Br ⁻ , Cl ⁻

* depending on primary ion concentration electrode response slope is equal to:

10^{-6} - 10^{-4} mol/L (30 ± 10) mV/pX

10^{-4} - 10^{-2} mol/L (45 ± 10) mV/pX

** depending on primary ion concentration electrode response slope is equal to:

10^{-5} - 10^{-4} mol/L (20 ± 10) mV/pX

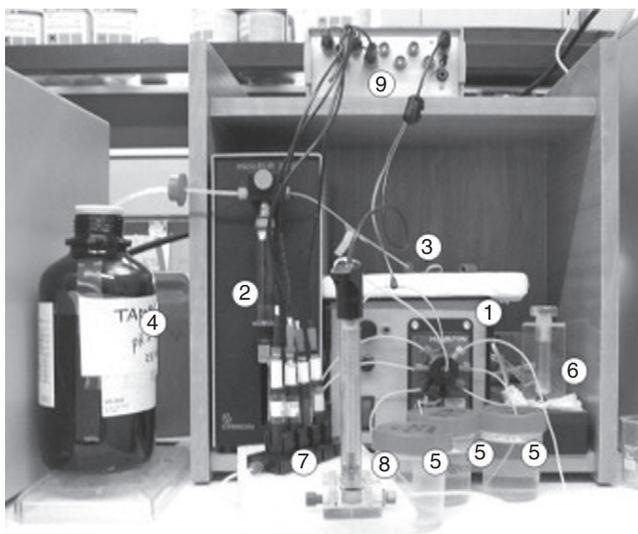
10^{-4} - 10^{-3} mol/L (35 ± 10) mV/pX

10^{-3} - 10^{-2} mol/L (50 ± 10) mV/pX

*** depending on primary ion concentration electrode response slope is equal to:

10^{-7} - 10^{-6} mol/L (30 ± 10) mV/pX

10^{-6} - 10^{-4} mol/L (60 ± 10) mV/pX

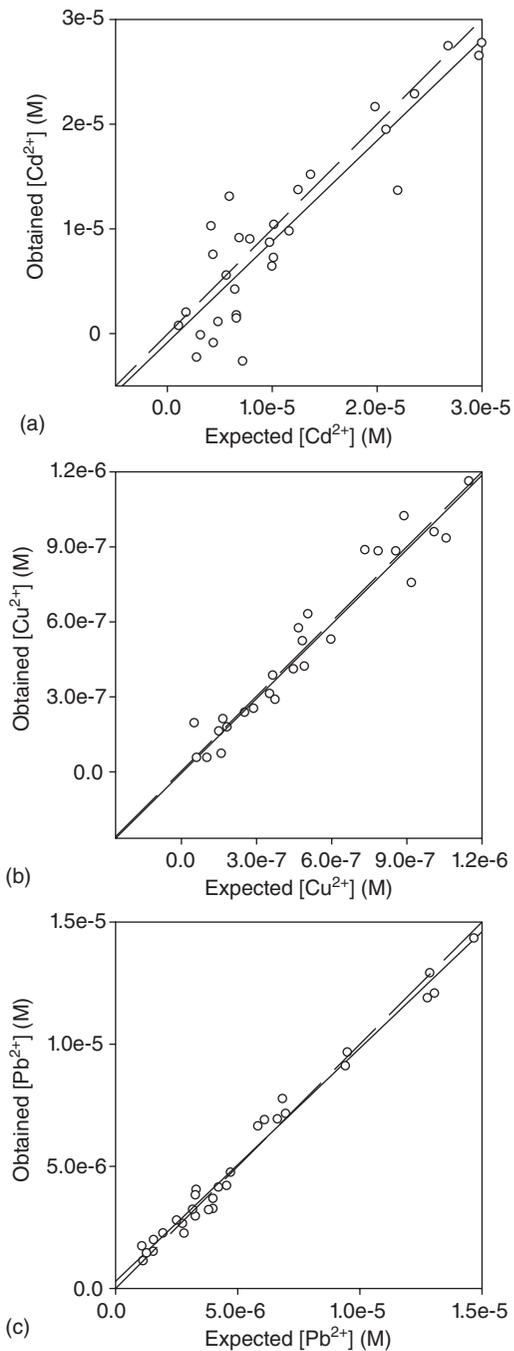


8.18 Potentiometric E-tongue using sequential injection analysis flow system used in this work. (1) 8-way valve; (2) automatic microburette; (3) holding coil; (4) buffer reservoir; (5) stock solutions of metals; (6) mixing cell; (7) ISEs array; (8) reference electrode; (9) multipotentiometer. (Reprinted from Ref. 143 with permission from the Elsevier Science)

performed. These samples were processed using the SIA system, their signals acquired, and then interpolated in the response model generated. Samples used in this validation process were eight synthetic mixtures prepared manually under laboratory conditions with arbitrary concentrations of the three metals in the final range considered. The general sensitivity trend is satisfactory, with slopes and intercepts close to 1.0 and 0.0 and with correlations also being highly significant. Again, Cd^{2+} metal is the species with limited performance, especially with a somewhat poorer correlation, which does require further improvement.

8.8 Future trends

This chapter has surveyed modern solid-state sensors for water quality monitoring and trends in their development. Although miniature, inexpensive water quality sensors reported to date have shown excellent sensing performances, generally they remain as prototypes used in laboratory studies to explore new possibilities in water sensing. Despite promising performance in controlled laboratory conditions, these sensors have yet to be tested for long-term stability and antifouling resistance, which are prerequisites to industry acceptance.



8.19 Comparison of obtained vs expected results provided by the proposed E-tongue for the test samples (those not participating in training) for Cd^{2+} (a), Cu^{2+} (b) and Pb^{2+} (c) ions. (Reprinted from Ref. 143 with permission from Elsevier Science)

The results presented above testify that structural and morphological modifications of nanostructured complex oxide SEs have real potential to improve various sensor characteristics, such as selectivity, sensitivity, response and recovery rates, and to design SEs for chemical sensors with desirable consumer properties. An analysis of current research dedicated to the development of new complex oxide SEs shows that an understanding of the nature and mechanism of various processes responsible for improvement of the sensor characteristics remains a priority, and no doubt more findings will be made in years to come.⁸ Consequently, although the addition of the second phase to the SE by doping seems to be a reasonable approach for achieving better selectivity and sensitivity, the process for choosing the dopant becomes a challenge owing to the lack of basic understanding. The particular properties of the grain boundaries and segregation layers of the complex nano-oxides with respect to their ionic and electronic defect concentrations offer many possibilities to modify the transport behaviour and electrochemical characteristics of SEs and their interfaces.⁵⁴ Decreasing the crystalline size into the nanometer range is a straightforward method to prepare SE materials with properties that are dominated by their interfaces, i.e. by surface and space charges. A great deal of the present interest lies in the development of new techniques for preparation, analysis and fine tuning of nanostructured materials. Therefore, based on the information given above, it has become evident that increasing efforts in basic studies for better understanding of the sensing mechanisms is essential for making progress in developing solid-state chemical water quality sensors acceptable for practical use.

It is necessary to admit that no universal solution exists for simultaneous optimization of all sensors characteristics. Basically, an improvement of one parameter is often accompanied by worsening of another.⁸⁴ Therefore, one should always seek a compromise in the development of multisensor designs for synchronic measurement of various water quality parameters. The combination of atomic-scale resolution of surface modification techniques with high lateral resolution offers a great chance for understanding and optimization of the electrochemistry of nanostructured SE interfaces.

Thus, further development of new solid-state chemical sensors for environmental monitoring is likely to be focused on even higher levels of performance and reliability. Hopefully, new device concepts and advances in nanotechnologies based on improved theoretical understanding of both surface processes and mechanisms on the complex oxide interfaces will result in stable, inexpensive devices with enhanced characteristics capable of meeting stringent industrial demands.

All the presented examples of the design and characteristics of sensors have highlighted that the solid-state chemical sensors for environmental monitoring based on nanostructured complex oxide SEs need to be further

modernized to have specific *built-in* features (like antifouling resistance in water quality sensors) to ensure their high sensing characteristics and long-term stability. In this regard, electrochemical solid-state sensors based on metal oxide nanostructures offer several advantages. These devices are comparatively simple in design, inexpensive in mass-production and exhibit high sensitivities and detection limits. It is clear that the microstructure and interfacial properties of nanostructured SEs need to be optimized in order to enhance the sensing performance. Turbidity, conductivity, DOC and dissolved metal ions measurements have revealed that these instruments are capable of measuring both high and low ranges with reasonable linearity. Planar, thin- and thick-film sensors based on complex oxide nanostructures are expected to reinforce their place in the environmental monitoring market owing to their chemical robustness and potential for implementation in wireless sensor networks. Thus, careful screening and selection of the appropriate semiconductor oxide and its dopant for the developing SE material must be completed in order to improve and optimize desirable sensor properties. Furthermore, future developments of antifouling technologies must incorporate multiple defence strategies to achieve high antifouling resistance against multiple species.

Finally, although the individual and multicomponent sensors reviewed have been shown to be an excellent sensing platform for environmental control in the new generation of wireless sensor networks, all of these instruments have yet to be tested in the field to demonstrate that they are suitable for use by industry.

Consequently, the development of a new generation of environmental sensors based on nanostructured semiconductor SEs is inseparably connected with the development of wireless sensor networks. This joint research area will continue to benefit from the latest contributions from various disciplines, such as analytical and inorganic chemistry, materials science and nanotechnology, electrical, RF and computer engineering, nanofabrication and packaging, and many other disciplines. However, implementation of the positive results of this joint research will be dependent on system design and integration aspects, successful interdiscipline collaborations and transfer of the sensor networks concepts from laboratory demonstrations to diverse end-use applications. In this regard, field tests of the laboratory prototypes of sensors combined with integrated wireless sensor networks should be commenced as early as possible in joint research process.¹⁴⁵

8.9 References

1. G.W. McLaughlin, K. Braden, B. Franc, G.T.A. Kovacs, Microfabricated solid-state dissolved oxygen sensor, *Sens. Actuators B: Chem.*, 83 (2002) 138–142.

2. S. Zhuiykov, Integrated multilayered 'electronic tongue' for *in-situ* water quality monitoring, in K. Ertud, I. Mirza (eds), *Water Quality: Physical, Chemical and Biological Characteristics*, 2010, Nova Science, New York, 71–96.
3. A. Lynggaard-Jensen, Trends in monitoring of waste water systems, *Talanta*, 50 (1999) 707–716.
4. R. Martínez-Mañez, J. Soto, E. García-Breijo, L. Gil, J. Ibáñez, E. Gadea, A multisensor in thick-film technology for water quality control, *Sens. Actuators B: Chem.*, 120 (2005) 589–595.
5. S. Zhuiykov, Morphology and sensing characteristics of nanostructured RuO₂ electrodes for integrated water quality monitoring sensors, *Electrochem. Comm.*, 10 (2008) 839–843.
6. S. Zhuiykov, D. O'Brien, M. Best, Water quality assessment by integrated multi-sensor based on semiconductor RuO₂ nanostructures, *Meas. Sci. Technol.*, 20 (2009) 095201.
7. S. Zhuiykov, *Electrochemistry of Zirconia Gas Sensors*, 2007, CRC Press, Boca Raton, 297.
8. R.A. Potyrailo, V.M. Mirsky, Combinatorial and high-throughput development of sensing materials: the first 10 years, *Chem. Rev.*, 108 (2008) 770–813.
9. G. Korotcenkov, Metal oxides for solid-state gas sensors: What determines our choice? *Mater. Sci. Eng. B*, 139 (2007) 1–23.
10. S. Zhuiykov, E. Kats, D. Marney, Potentiometric sensor using sub-micron Cu₂O-doped RuO₂ sensing electrode with improved antifouling resistance, *Talanta*, 82 (2010) 502–507.
11. A. Bratov, N. Abramova, A. Ipatov, Recent trends in potentiometric sensor arrays – A review, *Anal. Chim. Acta*, 678 (2010) 149–159.
12. R. Martinez-Manez, J. Soto, E. Garcia-Breijo, L. Gil, J. Ibanez, E. Llobet, An 'electronic tongue' design for the qualitative analysis of natural waters, *Sens. Actuators B: Chem.*, 104 (2005) 302–307.
13. S.S. Walia, R. Weber, K. Latham, S. Zhuiykov, K. Kalantar-zadeh, Sb₂Te₃ and Bi₂Te₃ based thermopower wave sources, *Energy Environ. Sci.*, 4 (2011) 3558–3564.
14. S. Zhuiykov, Development of ceramic electrochemical sensor based on Bi₂Ru₂O_{7+x}-RuO₂ sub-micron oxide sensing electrode for water quality monitoring, *Ceramics Int.*, 36 (2010) 2407–2413.
15. S. Zhuiykov, Hydrogen sensor based on a new type of proton conductive ceramic, *Int. J. Hydrogen Energy*, 21 (1996) 749–759.
16. J.K. Atkinson, A.W.J. Cranny, W.V. Glasspool, J.A. Mihell, An investigation of the performance characteristics and operational lifetimes of multi-element thick film sensor arrays used in the determination of water quality parameters, *Sens. Actuators B: Chem.*, 54 (1999) 215–231.
17. X.-J. Huang, Y.-K. Choi, Chemical sensors based on nanostructured materials, *Sens. Actuators B: Chem.*, 122 (2007) 659–671.
18. A. Fog, R.P. Buck, Electronic semiconducting oxides as pH sensors, *Sens. Actuators B: Chem.*, 5 (1984) 137–146.
19. P. Kurzweil, Precious metal oxides for electrochemical energy converters: Pseudocapacitance and pH dependence of redox processes, *J. Power Sources*, 190 (2010) 189–200.

20. L.A. Pocrifka, C. Goncalves, P. Grossi, P.C. Colpa and E.C. Pereira, Development of RuO₂-TiO₂ (70–30) mol% for pH measurements, *Sens. Actuators B: Chem.*, 113 (2006) 1012–1016.
21. C. Angelinetta, S. Trasatti, Lj.D. Atanososka, R.T. Atanasoski, Surface properties of RuO₂ + IrO₂ mixed oxide electrodes, *J. Electroanal. Chem.*, 214 (1986) 535–546.
22. Y. Takasu, Y. Marakami, Design of oxide electrode with large surface area, *Electrochim. Acta*, 45 (2000) 4135–4141.
23. H.N. McMurray, P. Douglas, D. Abbot, Novel thick-film pH sensors based on ruthenium dioxide-glass composites, *Sens. Actuators B: Chem.*, 28 (1995) 9–15.
24. T.M. Pan, M.D. Huang, C.W. Lin, Thin Sm₂TiO₅ film electrolyte-insulator-semiconductor for pH detection and urea biosensors, *J. Electrochem. Soc.*, 157 (2010) J275–J280.
25. W. Vonau, J. Gabel, H. Jahn, Potentiometric all solid-state pH sensors, *Electrochim. Acta*, 50 (2005) 4981–4987.
26. W.-D. Zhang, B. Xu, A solid-state pH sensor based on WO₃-modified vertically aligned multiwalled carbon nanotubes, *Electrochem. Comm.*, 11 (2009) 1038–1041.
27. B. Xu, W.-D. Zhang, Modification of vertically aligned carbon nanotubes with RuO₂ for a solid-state pH sensor, *Electrochim. Acta*, 55 (2010) 2859–2864.
28. L. Telli, B. Brahimi, A. Hammouche, Study of a pH sensor with MnO₂ and montmorillonite-based solid-state internal reference, *Solid State Ionics*, 128 (2000) 255–259.
29. S. Nakayama, K. Onishi, T. Asahi, Y. Lin Aung, S. Kuwata, Response characteristics of all-solid-state pH sensor using Li₅YSi₄O₁₂ glass, *Ceram. Int.*, 35 (2009) 3057–3060.
30. W.-D. Huang, H. Cao, S. Deb, M. Chiao, J.C. Chiao, A flexible pH sensor based on the iridium oxide sensing film, *Sens. Actuators A: Phys.*, 169 (2011) 1–11.
31. P. Shuk, K. V. Ramanujachary, M. Greenblatt, pH sensors with samarium stabilized ceria membrane, *Solid State Ionics*, 85 (1996) 257–263.
32. Cl. Bohnke, J.-L. Fourquet, Impedance spectroscopy on pH-sensors with lithium lanthanum titanate sensitive material, *Electrochim. Acta*, 48 (2003) 1869–1878.
33. R. Zhao, M. Xu, J. Wang, G. Chen, A pH sensor based on the TiO₂ nanotube array modified Ti electrode, *Electrochim. Acta*, 55 (2010) 5647–5651.
34. A. Eftekhari, pH sensor based on deposited film of lead oxide on aluminum substrate electrode, *Sens. Actuators B: Chem.*, 88 (2003) 234–238.
35. F. Tedjar, L. Zerroual, 'All solid' pH sensor, *Sens. Actuators B: Chem.*, 2 (1990) 215–217.
36. Q.N. Pham, C. Bohnke, J. Emery, O. Bohnke, F. Le Berre, M.-P. Crosnier-Lopez, J.-L. Fourquet, P. Florian, A new perovskite phase Li_{2x}Ca_{0.5-x}TaO₃: Li⁺ ion conductivity and use as pH sensor, *Solid State Ionics*, 176 (2005) 495–504.
37. L. Qingwen, L. Guoan, S. Youqin, Response of nanosized cobalt oxide electrodes as pH sensors, *Anal. Chim. Acta*, 409 (2000) 137–142.
38. P. Shuk, K. V. Ramanujachary, M. Greenblatt, Molybdenum oxide bronzes as pH sensors, *Electrochim. Acta*, 41 (1996) 2055–2058.

39. S.H. Kwon, O.K. Kwon, J.H. Kim, S.J. Jeong, S.W. Kim, S.W. Kang, Improvement of the morphological stability by stacking RuO₂ on Ru thin films with atomic layer deposition, *J. Electrochem. Soc.*, 154 (2007) H773–H777.
40. R.D. Prien, The future of chemical in situ sensors, *Marine Chem.*, 107 (2007) 422–432.
41. E. Bakker, E. Pretsch, Nanoscale potentiometry, *Trends Anal. Chem.*, 27 (2008) 612–618.
42. J. Zosel, H. Kaden, G. Peters, M. Hoffmann, P. Rudisch, L. Jakel, G. Lauchner, A. Grodrian, U. Guth, Continuous long-term monitoring of ruminal pH, *Sens. Actuators B: Chem.*, 144 (2010) 395–399.
43. Y.H. Liao, J.C. Chou, Preparation and characteristics of ruthenium dioxide for pH array sensors with real-time measurement system, *Sens. Actuators B: Chem.*, 128 (2008) 603–612.
44. W. Vonau, W. Oelbner, U. Guth, J. Henze, An all-solid-state reference electrode, *Sens. Actuators B: Chem.*, 144 (2010) 368–373.
45. Y.S. Chiu, C.T. Lee, pH sensor investigation on various-length photoelectrochemical passivated ZnO nanorod arrays, *J. Electrochem. Soc.*, 158 (2011) J282–J285.
46. X. Qiu, R. Tang, S.J. Chen, H. Zhang, W. Pang, H. Yu, pH measurements with ZnO based surface acoustic wave resonator, *Electrochem. Comm.*, 13 (2011) 488–490.
47. S. Zhuiykov, Morphology of Pt-doped RuO₂ nanocomposites and their application in water quality monitoring sensors, *Sens. Actuators B: Chem.*, 136 (2009) 248–256.
48. A. Bonastre, R. Ors, J.V. Capella, M.J. Fabra, M. Peris, In-line chemical analysis of wastewater: present and future trends, *Trends Anal. Chem.*, 24 (2005) 128–138.
49. S. Zhuiykov, D. Marney, E. Kats, K. Kalantar-zadeh, Potentiometric solid-state sensor for DO measurement in water using sub-micron Cu_{0.4}Ru_{3.4}O₇ + RuO₂ sensing electrode, *Sens. Actuators B: Chem.*, 153 (2011) 312–320.
50. J. Goschnick, I. Koromczi, M. Frietsch, I. Kiselev, Water pollution recognition with the electronic nose KAMINA, *Sens. Actuators B: Chem.*, 106 (2005) 182–186.
51. K.T. Lau, S. Edwards, D. Diamond, Solid-state ammonia sensor based on Berthelot's reaction, *Sens. Actuators B: Chem.*, 98 (2004) 12–17.
52. S. Zhuiykov, E. Kats, V. Plashnitsa, N. Miura, Toward selective electrochemical 'E-tongue' potentiometric DO sensor based on sub-micron ZnO-RuO₂ sensing electrode, *Electrochim. Acta*, 56 (2011) 5435–5442.
53. W. Bourgeois, J.E. Burgess, R.M. Stuetz, On-line monitoring of wastewater quality: a review, *J. Chem. Technol. Biotechnol.*, 76 (2001) 337–348.
54. S. Zhuiykov, Effect of heterogeneous oxidation on electrochemical properties of tailored Cu_{0.4}Ru_{3.4}O₇ + RuO₂ sensing electrode of potentiometric DO sensor, *Mater. Lett.*, 65 (2011) 3219–3222.
55. S. Zhuiykov, V. Plashnitsa, N. Miura, Effect of ZnO doping on morphology and electrochemical properties of sub-micron RuO₂ sensing electrode of DO sensor, *Mater. Lett.*, 65 (2011) 991–994.
56. R. Martinez-Manez, J. Soto, J. Lizondo-Sabater, E. Garcia-Breijo, L. Gil, J. Ibanez, I. Alcaina, S. Alvarez, New potentiometric dissolved oxygen sensors in thick film technology, *Sens. Actuators B: Chem.*, 101 (2004) 295–301.

57. S. Zhuiykov, K. Kalantar-zadeh, Development antifouling of electrochemical solid-state DO sensors based on nanostructured $\text{Cu}_{0.4}\text{Ru}_{3.4}\text{O}_7 + \text{RuO}_2$ sensing electrode, *Electrochim. Acta*, 73 (2012) 105–111.
58. H. Kohler, W. Gopel, Mixed valent tungsten oxides: new electrode materials for the potentiometric detection of dissolved oxygen at temperatures below 35 °C, *Sens. Actuators: B: Chem.*, 4 (1991) 345–354.
59. S. Yao, M. Wang, Electrochemical sensor for dissolved carbon dioxide measurement, *J. Electrochem. Soc.*, 149 (2002) H28–H32.
60. S. Zhuiykov, D. Marney, E. Kats, Investigation electrochemical properties of $\text{La}_2\text{O}_3\text{-RuO}_2$ thin-film sensing electrode used in sensors for analysis of complex solutions, *Int. J. Appl. Ceram. Technol.*, 8 (2011) 1192–1200.
61. S. Zhuiykov, E. Kats, D. Marney, K. Kalantar-zadeh, Improved antifouling resistance of electrochemical water quality sensors based on Cu_2O -doped RuO_2 sensing electrode, *Prog. Org. Coating*, 70 (2011) 67–73.
62. M. Sosna, G. Denuault, R.W. Pascal, R.D. Prien, M. Mowlem, Development of a reliable microelectrode dissolved oxygen sensor, *Sens. Actuators B: Chem.*, 123 (2007) 344–351.
63. G.W. McLaughlin, K. Braden, B. Franc, G.T.A. Kovacs, Microfabricated solid-state dissolved oxygen sensor, *Sens. Actuators B: Chem.*, 83 (2002) 138–148.
64. S. Zhuiykov, Potentiometric detection DO in water by ceramic sensor based on sub-micron RuO_2 sensing electrode, *Ionics*, 15 (2009) 693–701.
65. S. Zhuiykov, *In-situ* FTIR study of oxygen adsorption on nanostructured RuO_2 thin-film electrode, *Ionics*, 15 (2009) 507–512.
66. S.H. Hong, M.W. Lee, D.S. Lee, J.M. Park, Monitoring of sequencing batch reactor for nitrogen and phosphorus removal using neutral networks, *Biochem. Eng. J.*, 35 (2007) 365–370.
67. M.M. Hassaniien, K.S. Abou-El-Sherbini, G.A.E. Mostafa, A novel tetrachlorothallate (III)-PVC membrane sensor for the potentiometric determination of thallium (III), *Talanta*, 59 (2003) 383–392.
68. M.R. Ganjali, P. Norouzi, F. Faridbod, M. Ghorbani, M. Adib, Highly selective and sensitive chromium (III) membrane sensors based on a new tridentate Schiff's base, *Anal. Chim. Acta*, 569 (2006) 35–41.
69. M.F. Bergamini, D.P. dos Santos, M. Valnice Boldrin Zanoni, Development of a voltametric sensor for chromium (VI) determination in wastewater sample, *Sens. Actuators B: Chem.*, 123 (2007) 902–908.
70. A. Mimendia, A. Legin, A. Merkoci, M. deValle, Use of Sequential Injection Analysis to construct a potentiometric electronic tongue: Application to the multidetermination of heavy metals, *Sens. Actuators B: Chem.*, 146 (2010) 420–426.
71. G. Verrelli, L. Francioso, R. Paolesse, P. Siciliano, C. Di Natale, A. D'Amico, A. Logrieco, Development of silicon-based potentiometric sensors: Towards a miniaturized electronic tongue, *Sens. Actuators B: Chem.*, 123 (2007) 191–197.
72. R.T. Masserini, K.A. Fanning, A sensor package for the simultaneous determination of nanomolar concentrations of nitrite, nitrate and ammonia in seawater by fluorescent detection, *Marine Chem.*, 68 (2000) 323–333.
73. Y.G. Mourzina, J. Schubert, W. Zander, A. Legin, Y.G. Vlasov, H. Luth, M.J. Schining, Development of multisensory systems based on chalcogenide thin

- film chemical sensors for the simultaneous multicomponent analysis of metal ions in complex solutions, *Electrochim. Acta*, 47 (2001) 251–258.
74. Y.G. Mourzina, M.J. Schoning, J. Schubert, W. Zander, A.V. Legin, Y.G. Vlasov, H. Luth, Copper, cadmium and thallium thin film sensors based on chalcogenide glasses, *Anal. Chim. Acta*, 433 (2001) 103–110.
 75. L. Lvova, E. Martinelli, E. Mazzone, A. Pede, R. Paolesse, C. Di Natale, A. D'Amico, Electronic tongue based on an array of metallic potentiometric sensors, *Talanta*, 70 (2006) 833–839.
 76. A. Legin, A. Rudnitskaya, Y. Vlasov, C. Di Natale, E. Mazzone, A. D'Amico, Application of electronic tongue for qualitative and quantitative analysis of complex liquid media, *Sens. Actuators B: Chem.*, 65 (2000) 232–234.
 77. A.V. Legin, A.M. Rudnitskaya, Yu.G. Vlasov, C. Di Natale, F. Davide, A. D'Amico, Tasting of beverages using an electronic tongue, *Sens. Actuators B: Chem.*, 44 (1997) 291–296.
 78. A. Legin, A.M. Rudnitskaya, Y. Vlasov, C. Di Natale, E. Mazzone, A. D'Amico, Application of electronic tongue for qualitative and quantitative analysis of mineral water and wine, *Electroanalysis*, 11 (1999) 814–820.
 79. A.M. Rudnitskaya, A. Ehlert, A. Legin, Yu. Vlasov, S. Buttgenbach, Multisensor system on the basis of an array of non-specific chemical sensors and artificial neural networks for determination of inorganic pollutants in model groundwater, *Talanta*, 55 (2001) 425–431.
 80. A. Legin, A. Rudnitskaya, D. Clapham, B. Seleznev, K. Lord, Yu. Vlasov, Electronic tongue for pharmaceutical analytics—quantification of tastes and masking effects, *Anal. Bioanal. Chem.*, 380 (2004) 36–45.
 81. A.V. Legin, D.O. Kirsanov, V.A. Babain, A.V. Borovoy, R. Herbst, Cross-sensitive rare-earth metal sensors based on bidentate neutral organophosphorus compounds and chlorinated cobalt dicarbollide, *Anal. Chim. Acta*, 572 (2006) 243–247.
 82. A.V. Legin, V.A. Babain, D.O. Kirsanov, O.V. Mednova, Cross-sensitive rare earth metal sensors based on extraction systems, *Sens. Actuators B: Chem.*, 131 (2008) 29–36.
 83. A. Rudnitskaya, A. Legin, B. Seleznev, D. Kirsanov, Yu. Vlasov, Detection of ultra-low activities of heavy metal ions by an array of potentiometric chemical sensors, *Microchim. Acta*, 163 (2008) 71–80.
 84. G. Korotcenkov, Gas response control through structural and chemical modification of metal oxide films: state of the art and approaches, *Sens. Actuators B: Chem.*, 107 (2005) 209–232.
 85. S. Zhuiykov, Carbon monoxide detection at low temperatures by semiconductor sensor with nanostructured Au-doped CoOOH films, *Sens. Actuators B: Chem.*, 129 (2008) 431–441.
 86. J. Rossmeisl, Z.W. Qu, H. Zhu, G.J. Kroes, J.K. Nørskov, Electrolysis of water on oxide surfaces, *J. Electroanal. Chem.*, 607 (2007) 83–89.
 87. C. Carrara, J. Munera, E.A. Lombardo, L.M. Cornaglia, Kinetic and stability studies of Ru/La₂O₃ used in the dry reforming of methane, *Top. Catal.*, 51 (2008) 98–106.
 88. J. Ribeiro, F.L.S. Purgato, K.B. Kokoh, J.M. Leger, A.R. de Andrade, Application of Ti/RuO₂-Ta₂O₅ electrodes in the electrooxidation of ethanol and derivants: reactivity versus electrocatalytic efficiency, *Electrochim. Acta*, 53 (2008) 7845–7851.

89. J. Nowotny, T. Bak, M.K. Nowotny, L.R. Sheppard, TiO₂ surface active sites for water splitting, *J. Phys. Chem.*, 110 (2006) 18492–18495.
90. H. Ma, C. Liu, J. Liao, Y. Su, X. Xue, W. Xing, Study of ruthenium oxide catalyst for electrocatalytic performance in oxygen evolution, *J. Mol. Catal. A: Chem.*, 247 (2006) 7–13.
91. K. Joudkazis, J. Joudkazyte, R. Vilkauskaitė, B. Sebek, V. Jasulaitienė, Oxygen evolution on composite ruthenium and nickel oxides electrode, *Chimija*, 19 (2008) 1–6.
92. J.R. Osman, J.A. Crayston, A. Pratt, D.T. Richens, RuO₂-TiO₂ metal oxides prepared from the hydrolysis of the metal alkoxides, *Mater. Chem. Phys.*, 110 (2008) 256–262.
93. M.V. Makarova, J. Jirkovsky, M. Klementova, I. Jirka, K. Macounova, P. Krtil, The electrocatalytic behavior of Ru_{0.8}Co_{0.2}O_{2-x} – the effect of particle shape and surface composition, *Electrochim. Acta*, 53 (2008) 2656–2664.
94. K. Macounova, M. Makarova, J. Jirkovsky, J. Frans, P. Krtil, Parallel oxygen and chlorine evolution on Ru_{1-x}Ni_xO_{2-y} nanostructured electrodes, *Electrochim. Acta*, 53 (2008) 6126–6134.
95. K. Macounova, M. Makarova, P. Krtil, Oxygen evolution on nanocrystalline RuO₂ and Ru_{0.9}Ni_{0.1}O_{2-δ} electrodes – DEMS approach to reaction mechanism determination, *Electrochem. Comm.*, 11 (2009) 1865–1868.
96. J. Ribeiro, M.S. Moats, A.R. De Andrade, Morphological and electrochemical investigation of RuO₂-Ta₂O₅ oxide films prepared by the Pechini-Adams method, *J. Appl. Electrochem.*, 38 (2008) 767–775.
97. J. Wang, W. Zhu, X. He, S. Yang, Catalytic wet air oxidation of acetic acid over different ruthenium catalysts, *Catal. Comm.*, 9 (2008) 2163–2167.
98. P. Nowakowski, S. Villain, K. Aguir, J. Guerin, A. Kopia, J. Kusinski, F. Guinnetin, J.-R. Gavarri, Microstructure and electrical properties of RuO₂-CeO₂ composite thin films, *Thin Solid Films*, 518 (2010) 2801–2807.
99. A. Pintar, J. Batista, T. Tisler, Catalytic wet-air oxidation of aqueous solutions of formic acid, acetic acid and phenol in a continuous-flow trickle-bed reactor over Ru/TiO₂ catalysts, *Appl. Catal. B: Environ.*, 84 (2008) 30–41.
100. Y. Takasu, Y. Marakami, Design of oxide electrodes with large surface area, *Electrochim. Acta*, 45 (2000) 4135–4141.
101. R.H. Labrador, J. Soto, R. Martinez-Manez, C. Coll, A. Benito, J. Ibanez, E. Garcia-Breijo, L. Gil, An electrochemical characterization of thick-film electrodes based on RuO₂-containing resistive pastes, *J. Electroanal. Chem.*, 611 (2007) 175–180.
102. J. Soto, R.H. Labrador, M.D. Marcos, R. MatinezManez, C. Coll, E. Garcia-Breijo, L. Gil, A model for the assessment of interfering processes in Faradic electrodes, *Sens. Actuators B: Chem.*, 142 (2008) 56–60.
103. L. Hu, D.S. Hecht, G. Gruner, carbon nanotube thin films: fabrication, properties and applications, *Chem. Rev.*, 110 (2010) 5790–5844.
104. N.P. Zaretskyi, L.I. Menshikov, A.A. Vasiliev, On the origin of sensing properties of the nanostructured layers of semiconducting metal oxide materials, *Sens. Actuators B: Chem.*, 170 (2012) 148–157.
105. M. Zhao, H. Peng, J. Hu, Z. Han, Effect of Cobalt doping on the microstructure, electrical and ethanol-sensing properties of SmFe_{1-x}Co_xO₃, *Sens. Actuators B: Chem.*, 129 (2008) 953–957.

106. L.M. Li, Z.F. Du, T.H. Wang, Enhanced sensing properties of defect-controlled ZnO nanotetrapods arising from aluminum doping, *Sens. Actuators B: Chem.*, 147 (2010) 165–169.
107. A.F. Albantov, A.L. Levin, New functional possibilities for amperometric dissolved oxygen sensors, *Biosens. Bioelectron.*, 9 (1994) 515–520.
108. G. Alberti, A. Carbone, R. Palombari, Oxygen potentiometric sensors based on thermally stable solid state proton conductors: a preliminary investigation in the temperature range 150–200 °C, *Sens. Actuators B: Chem.*, 86 (2002) 150–154.
109. M.L. Hitchman, *Measurement of Dissolved Oxygen (Chemical Analysis)*, Vol. 49, John Wiley & Sons, NY, 1978, 195–210.
110. *Annual Book of ASTM Standards*, D 888-09, vol. 11.01, 2009, ASTM, West Conshohocken.
111. P. Sahoo, R. Ananthanarayanan, N. Malathi, M.P. Rajiniganth, N. Murali, P. Swaminathan, Pulsating potentiometric titration technique for assay of dissolved oxygen in water at trace level, *Anal. Chim. Acta*, 669 (2010) 17–21.
112. S. Quintar de Guzman, O.M. Baudino, V.A. Cortinez, Design and evaluation of an electrochemical sensor for determination of dissolved oxygen in water, *Talanta*, 34 (1987) 551–556.
113. X.-J. Huang, Y.-K. Choi, Chemical sensors based on nanostructured materials, *Sens. Actuators B: Chem.*, 122 (2007) 659–671.
114. A.J. Scardino, R. de Nys, Mini review: Biomimetic models and bioinspired surfaces for fouling control, *Biofouling*, 27 (2011) 73–86.
115. Y.C. Wu, W.F. Koch, Absolute determination of electrolytic conductivity for primary standard KCl solutions from 0 to 50 °C, *J. Solution Chem.*, 20 (1991) 39–49.
116. F. Natalio *et al.*, Vanadium pentoxide nanoparticles mimic vanadium haloperoxidases and thwart biofilm formation, *Nat. Nanotechnol.*, 7 (2012) 530–535.
117. N. Aldred, A. Scardino, A. Cavaco, R. de Nys, A.S. Clare, Attachment strength is a key factor in the selection of surfaces by barnacle syprids (*Balanus Amphitrite*) during settlement, *Biofouling*, 26 (2010) 287–299.
118. K. Anselme, P. Davidson, A.M. Popa, M. Giazzon, M. Liley, L. Ploux, The interaction of cells and bacteria with surfaces structured on the nanometre scale, *Acta Biomater.*, 6 (2010) 103824–103846.
119. J. Genser, K. Efimenko, Recent development in superhydrophobic surfaces and their relevance to marine fouling: a review, *Biofouling*, 22 (2006) 339–360.
120. A. Marmur, Super-hydrophobicity fundamentals: implications to biofouling prevention, *Biofouling*, 22 (2006) 107–115.
121. A.J. Scardino, H. Zhang, D.J. Cookson, R.N. Lamb, R. de Nys, The role of nano-roughness in antifouling, *Biofouling*, 25 (2009) 757–767.
122. T.L. Sun, L. Feng, X.F. Gao, L. Jiang, Bioinspired surfaces with special wettability, *Acc. Chem. Res.*, 38 (2005) 644–652.
123. K. Efimenko, M. Rackaitis, E. Manias, A. Vaziri, L. Mahadevan, L. Genzer, Nested self-similar wrinkling patterns in skins, *Nat. Mater.*, 4 (2005) 293–297.
124. F. Natalio, R. Andre, A.F. hartog, B. Stroll, K.P. Jochum, R. Wever, W. Tremel, Vanadium pentoxide nanoparticles mimic vanadium haloperoxidases and thwart biofilm formation, *Nat. Nanotechnol.*, 7 (2012) 530–535.
125. M. Pérez, G. Blustein, M. García, B. del Amo, M. Stupak, Cupric tannate: A low copper antifouling pigment, *Prog. Org. Coat.*, 55 (2006) 311–315.

126. H. Okamura, T. Watanabe, I. Aoyama, M. Hasobe, Toxicity evaluation of new antifouling compounds using suspension-cultured fish cells, *Chemosphere*, 46 (2002) 945–951.
127. E. Lindner, Failure mechanism of copper antifouling coatings, *Int. Biodeterior. Biodegrad.*, 24 (1988) 247–253.
128. F. Cassé, G.W. Swain, The development of microfouling on four commercial antifouling coatings under static and dynamic immersion, *Int. Biodeterior. Biodegrad.*, 57 (2006) 179–185.
129. L. Wu, L. Tsui, N. Swami, G. Zangari, Photoelectrochemical stability of electrodeposited Cu₂O films, *J. Phys. Chem. C*, 114 (2010) 11551–11556.
130. Z. Guo, W. Kiu, B. Su, Superhydrophobic surfaces: from natural to biomimetic to functional, *J. Colloid Interface Sci.*, 353 (2011) 335–355.
131. S. Kill, C.E. Weinell, M.S. Pedersen, K. Dam-Johanensen, Analysis of self-polishing antifouling paints using rotary experiments and mathematical modelling, *Ind. Eng. Chem. Res.*, 40 (2001) 3906–3920.
132. M. Srinivasan, G.W. Swain, Managing the use of copper-based antifouling paints, *Environ. Manag.*, 39 (2007) 423–441.
133. ISO Standard ISO 7027:1999, *Water quality – determination of turbidity*, 1999, ISO, Geneva, 11p.
134. W.F. McCoy, B.H. Olson, Relationship among turbidity, particle counts and bacteriological quality within water distribution lines, *Water Res.*, 20 (1986) 1023–1029.
135. L. Shu, L. Qiaa, G. Wu, L.H. Chen, X. Wu, Polymeric turbidity sensor fabricated by laser direct writing, *Meas. Sci. Technol.*, 22 (2011) 075403.
136. S.B. Mitchell, D.M. Lawler, J.R. West, J.S. Couperthwaite, Use of continuous turbidity sensor in the prediction of fine sediment transport in the turbidity maximum of the Trent Estuary, UK, *Estuar. Coast Shelf Sci.*, 58 (2003) 645–652.
137. P.D. Wass, S.D. Marks, J.W. Finch, G.J.L. Leeks, J.K. Ingram, Monitoring and preliminary interpretation of in-river turbidity and remote sensed imagery for suspended sediment transport studies in the Humber catchment, *Sci. Total Environ.*, 194–195 (1997) 263–283.
138. ISO Standard ISO 15839:2003, *Water quality – On-line sensors/analysing equipment for water – Specifications and performance tests*, 2003, ISO, Geneva, 30p.
139. D.O. Hessen, J.L. Carroll, B. Kjeldstad, A.A. Korosov, L.H. Pettersson, D. Pozdnyakov, K. Sørensen, Input of organic carbon as determinant of nutrient fluxes, light climate and productivity in the Ob and Yenisey estuaries, *Estuar. Coast Shelf Sci.*, 88 (2010) 53–62.
140. S. Zhuiykov, B. Sexton, P. Hoobin, M. Best and D. Marney, Hand-held device for monitoring dissolved organics in fresh and recycled water on ppb levels, *14th Int. Symp. Olfaction and Electronic Noses (ISOEN 2011)*, New York, 2–5 May 2011, 213.
141. S. Zhuiykov, Solid-state sensors monitoring parameters of water quality for the next generation of wireless sensor networks, *Sens Actuators B: Chem.*, 161 (2012) 1–20.
142. C. Di Natale, A. Macagnano, F. Davide, A. D’Amico, A. Legin, Y. Vlasov, A. Rudnitskaya, B. Selezenev, Multicomponent analysis on polluted waters by means of an electronic tongue, *Sens. Actuators B: Chem.*, 44 (1997) 423–428.

143. A. Mimendia, A. Legin, A. Merkoçi, M. del Valle, Use of Sequential Injection Analysis to construct a potentiometric electronic tongue: Application to the multidetermination of heavy metals, *Sens. Actuators B: Chem.*, 146 (2010) 420–426.
144. R. Cartas, A. Mimendia, A. Legin, M. del Valle, Two analyte calibrations from the transient response of a single potentiometric sensor employed with the SIA technique, *Talanta*, 80 (2010) 1428–1435.
145. R.A. Potyrailo, C. Surman, N. Nagraj, A. Burns, Materials and transducers toward selective wireless gas sensing, *Chem. Rev.*, 111 (2011) 7315–7354.

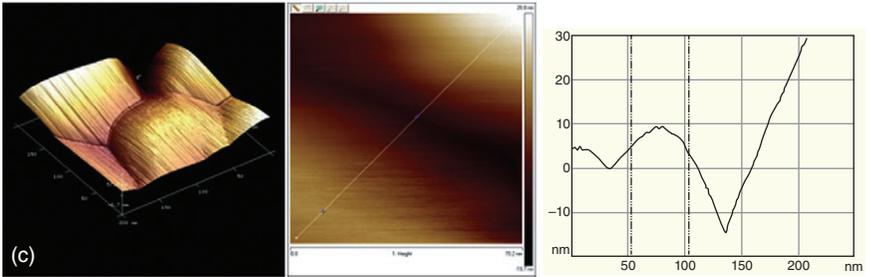
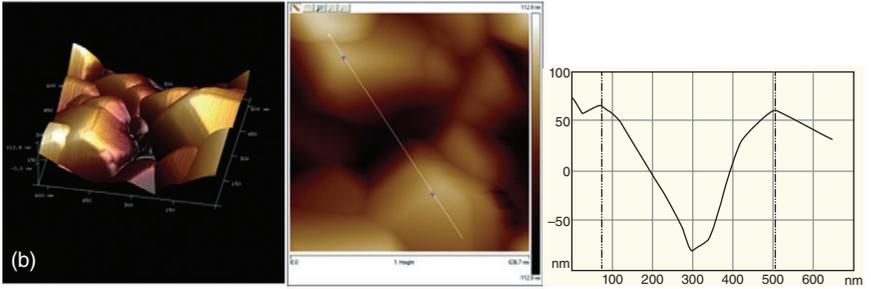
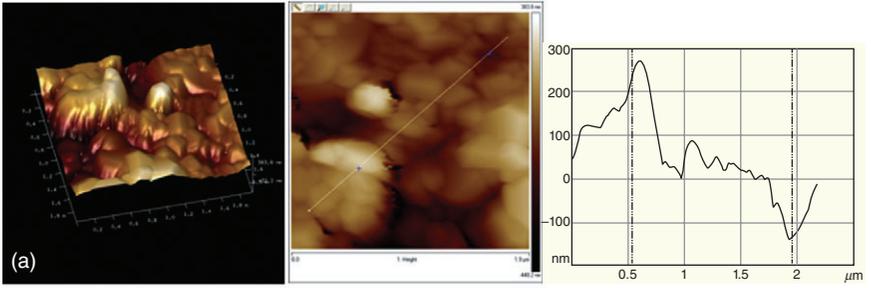


Plate XXIII (Chapter 8) AFM 2D and 3D images of the surface of 20 mol% ZnO-doped RuO₂-SE sintered at 800°C: (a) low magnification; (b) analysis of grain depths; (c) high magnification.

-
- acceptor, 16
 impurities, 12
- acetylcholinesterase (AChE), 126–9
 hydrolysis and electrochemical
 oxidation of ATC, 127
- activation polarisation, 330–1
- all-ceramic anodes, 365
- alternate geometry cells, 328
- alternating current (AC) power
 generation, 67
- amperometric Clark cells, 390–2
- anatase, 163
- anodisation method, 299
- antifouling technologies
 solid-state water quality sensors,
 401–3
- area-specific resistance (ASR), 341
- artificial neural networks, 411
- atomic force microscopy (AFM),
 393
- band theory, 39–43
 characteristic feature, 39–40
 valence band, 41–3
 validity, 40–1
- bi-layer anode, 339–40
- biofouling, 401
- Bloch's method *see* collective electron
 method
- Born-von Karman condition, 20
- boson, 31
- Brayton-Rankine combined cycle,
 321–2
- brookite, 163
- cantilevers, 114–18
- carbon nanotubes (CNT), 213–15,
 248
 environmental sensors, 124–9
 AChE enzyme, 126–9
 OP and OPH pesticides detection,
 124–6
 functional structures, 118–24
 development and production of
 electrochemical sensors, 122
 electrodes, 121
 functionalisation schemes, 120
 web layers, 122
- catalyst patterning, 56–7
- ceria *see* cerium oxide
- cerium oxide, 336–7
- chalcogenide, 148–62
 exfoliated MoS₂ flakes spectra,
 155
 experimental set-up, 153
 MoS₂ flakes Raman spectra, 156
 MoS₂ monolayer transistor local gate
 control, 157
 MoS₂ photoswitching, 161
 MoS₂ room-temperature electrical
 characteristic, 159
 TiS₂ nanosheets, 150
 TiS₂ nanosheets linear and
 absorption spectra, 151
- chemical defect, 3
- chemical exfoliation, 142, 144
- chemical sensors, 115–18
 NW-based E-nose system., 118
 semiconductor gas sensors, 116

- chemical vapour deposition (CVD), 51–2, 142, 332
- chemometrics, 411
- CIGS technology, 283–4
- coefficient of thermal expansion (CTE), 341
- collective electron method, 24
- concentration polarisation, 330–1
- conduction band, 16, 23–4
- conductive atomic force microscopy (C-AFM), 184
- conductivity, 398
 - measurements, 398–400
 - multisensor response as function of conductivity in 5–200 $\mu\text{S}/\text{cm}$ range, 399
 - SEM images of Cu_2O -doped RuO_2 -SE with and without biofouling, 400
- continuum modelling, 359–61
 - length, timescale and characterisation techniques for SOFC materials, 360
- conventional dual-chamber configuration, 350–1
- core shell nanowires, 64–5
 - hetero-structure types, 65
- Cr-based alloys, 343–4
- crystal shape, 75–6
 - NW and NB position on bonding pad, 78
 - SnO_2 films deposited by spray pyrolysis, 77
- CSIRO sensor, 382
- Cu-cerium oxide anodes, 339
- current sensing force spectroscopy atomic force microscopy (CSFS-AFM), 184, 186
- degree of disorder, 6
- delta potential difference, 386–7
- density functional theory (DFT), 219
- depleted-hetero-junction colloidal QD solar cells, 274
- desulphurisers, 355
- dilute magnetic semiconductor (DMS), 62
- dip coating, 336
- direct current (DC) power generation, 67
- dissolved organic carbon (DOC), 405, 407
- dissolved oxygen (DO), 374
- donor, 16
 - impurities, 12
- dopant atoms, 59
- doping, 8, 377
 - oxide nanowires, 63–4
 - semiconductor nanocrystals, 384, 386–9
 - ZnO nanowires, 60–3
 - temperature-dependent magnetisation curve, 62
- drift, 7
- dual atmosphere, 346
- Ducrolloy, 343
- dye-sensitised solar cells (DSSC), 273, 291–303
 - TiO_2 -based dye-sensitized solar cells, 291–7
 - maximum obtained power-conversion efficiencies vs absorption onset, 295
 - schematic diagram of DSSC and its operation, 292
 - SEM image and based on TiO_2 -coated ZnO nanowire arrays, 296
 - WO_3 and Nb_2O_5 -based dye-sensitised solar cells, 297–303
 - DSSCs fabricated using crystalline Nb_2O_5 nanoporous networks, 302–3
 - SEM images of Nb_2O_5 nanoporous network, 300
 - TiCl_4 -treated WO_3 film EDX analysis, J-V characteristics and IPEC, 298
- E-tongue, 378, 411
- edge dislocation, 5

- eigenfunctions, 19–22, 26–8
 - energy level broadening in a crystal lattice, 21
- eigenvalues, 19–22, 26–8
 - energy level broadening in a crystal lattice, 21
- electric field, 9–10
 - field strength dependence of conductivity, 10
- electrical conductivity, 6–12
 - influencing factors, 6–10
 - electric field, 9–10
 - impurities, 8–9
 - light, 10
 - temperature, 7–8
 - types, 10–12
- electrocatalysis, 377–8
- electrochemical anodisation, 278–9
- electrochemical capacitors (EC)
 - composites graphene/semiconductor nanocrystals, 229–37
- electrochemical properties
 - improvement, 243–7
 - cycling performance and rate capability, 245
 - graphene performance, 222–4
 - chemically modified graphene, 224
 - prospects of using graphene, 225–8
 - ultrathin and transparent GNS, 227
- electrochemical deposition (ED), 54
- electrochemical dissolved oxygen (DO) sensors, 389–97
- electrochemical potentiometric DO sensors, 392–7
 - schematic view of integrated water quality monitoring multisensor, 395
 - voltage response of potentiometric TiO₂-coated RuO₂ and nanostructured RuO₂-SE, 397
 - water quality sensor elements, 394
- galvanic and polarographic sensor technologies, 389–92
 - oxygen saturation based on temperature and salinity, 390
 - schematic view of solid-state DO sensor, 391
 - solubility of solutes as function of temperature, 391
- electrochemical impedance spectroscopy (EIS), 359
- electrochemical potentiometric DO sensors, 392–7
- electrochemical sensors, 119
- electrochemical vapour deposition, 335–6
- electrode additive, 221–2
- electrode stability, 72
- electrolytes, 334–8
- electron
 - energy level, 15–17
 - patterns in M⁺ and R⁻ ions, 15
 - injection, 293
- electron-injection layer (EIL), 107
- electronic conductivity, 11
- electronic noses (e-noses), 115
- electronic tongues (e-tongues), 115
- electrophoretic deposition (EPD), 277, 349
- elementary excitation, 42
- energy dispersive X-ray (EDX) analysis, 288
- energy harvesting
 - based on piezoelectric nanostructures, 66–9
 - AC-type charge generation in V-ZnO-based nanogenerators, 68
 - complexity of inverted layered organic solar cells, 70
 - DC-type output charge generation, 68
- energy level
 - electrons and holes, 15–17
 - patterns in M⁺ and R⁻ ions, 15

- energy spectrum
 - finite crystal lattice, 24–30
 - free electron behaviour in a semi-infinite crystal, 25
 - infinite crystal lattice, 17–24
 - hole, 23–4
 - one-dimensional model of a crystal lattice, 17
 - three-dimensional lattice, 22–3
- environmental sensors
 - semiconductor nanocrystals, 374–417
 - antifouling technologies for solid-state water quality sensors, 401–3
 - conductivity measurements, 398–400
 - electrochemical dissolved oxygen (DO) sensors, 389–97
 - future trends, 414, 416–17
 - solid-state dissolved metal ion sensors, 409–14
 - solid-state dissolved organic carbon (DOC) sensors, 405–9
 - solid-state pH sensors, 374–89
 - solid-state turbidity sensors, 403–5
 - enzyme bio-sensors, 119
 - exciton, 12–15, 286
 - external quantum efficiency (EQE), 195
 - extremely thin absorber solar cell, 274
 - extrinsic semiconductor, 8
- fabrication technique, 334
- Fe-Cr-based alloys, 344–6
- Fermi-Dirac distribution function, 31–3
 - schematic diagram, 33
- Fermi energy, 32
- Fermi level, 32
 - position, 37–9
 - temperature dependence, 39
- fermion, 31
- Fick's law, 390–2
- field-effect transistor (FET), 96–100
 - current-voltage characteristics, 98
 - current vs. bias and gate voltage, 99
- field emission tip, 101–2
- finite element method, 362
- fixed defect, 5
- fixed interference method, 386
- flexible molecular-scale electronic devices, 111–14
 - C12 device, 113
 - schematic diagram, 112
- formazin turbidity unit (FTU), 404
- fossil fuel technology, 304
- four SEs system, 398
- free electrons, 12–15
- free holes, 12–15
- freeze-drying approach, 339
- Frenkel exciton, 13
- Frenkel mechanism, 11
- gadolinium-doped cerium oxide (GDC), 335
- galvanic sensor technologies, 389–92
- Ga₂O₃ nanowires, 63
- gas turbines (GT), 321–2
- genetic algorithms, 411
- geno-sensors, 119
- glass electrodes, 379
- grain boundary conduction, 335
- graphene
 - anodes, 218–19
 - nanocrystals in lithium ion batteries and electrochemical capacitors, 229–37
 - anionic sulphate surfactant-mediated stabilisation, 234
 - graphene/metal oxide nanocomposites preparation, 229
 - mass production approach, 231
 - multifunctionalities, 232–5
 - oxygen role, 235–7
 - structural models, 229–32
 - wet-chemistry approach, 234
- nanostructure for energy storage, 213–54
- nanostructured thermopower wave sources, 247–54
- fuel/ZnO/Al₂O₃ thermopower system, 253

- materials, 253
- specific power, output voltage and oscillation amplitudes
 - assessment for CNT, 254
- thermopower wave generator, 251
- performance in electrochemical capacitors, 222–4
- chemically modified graphene, 224
- performance in lithium ion batteries, 213–22
 - anodes, 218–19
 - d*-spacing, charge capacity
 - relationship and charge/discharge cycle performance, 216
 - electrode additive, 221–2
 - heterogeneous hybrids, 219–21
 - irreversible and reversible storage, 217
 - power *vs.* specific energy for various energy storage devices, 214
- physical and chemical properties, 139–40
 - schematic diagram, 141
- potential applications, 145–8
- prospects in lithium ion batteries and electrochemical capacitors, 225–8
 - ultrathin and transparent GNS, 227
- synthesis, 140, 142–5
 - chemical reduction routine, 144
 - schematic diagram, 142
 - thermal reduction methods, 143
- three-dimensional conductive networks, 237–47
 - restacking suppression, 237–9
- graphene-based electronics, 146
- graphene-based heterogeneous hybrids, 219–21
 - schematic diagram, 220
- graphene-based optoelectronics, 146
- graphene-filled polymer composites, 146
- graphene/metal oxides interface, 147
- graphene nanosheet (GNS), 215–17, 218–19, 225–7, 229–37
- ground-state exciton, 14
- hetero-atom doping, 235
- high operating temperature, 341
- hole
 - energy level, 15–17
 - patterns in M^+ and R^- ions, 15
 - energy spectrum, 23–4
- hole-blocking layer (HBL), 107
- hole-transporting material (HTM), 294
- hybrid cells, 281
- hybrid materials, 119
- hydrolysis, 233
- hydrothermal process, 55, 279
- immuno-sensors, 119
- impedance analysis, 333
- impurity, 8–9
 - absorption, 2
- in situ* redox reactions, 233
- incident photon-to-current conversion efficiency (IPCE), 276
- Inconel, 341
- infiltration method, 332–3
- infra-red light-emitting diode (IR-LED), 405
- In_2O_3 nanowires, 64
- inorganic solid-state nanostructured solar cells, 273–5
- intermediate temperature, 352
- intermittent contact atomic force microscopy (IC-AFM), 184
- intrinsic absorption, 2
- intrinsic defects *see* native defects
- intrinsic semiconductor, 7
- ion-sensitive electrodes (ISE), 411
- ionic conductivity, 11
- ISO 7021-1999, 403
- ISO 15839-2003, 405
- lanthanum chromites, 342
- lattice-Boltzmann method, 362

- light, 10
- light-emitting diode (LED), 104–9
 - current density-voltage (J - V) characteristics, 108
 - p -GaN/ n -ZnO nanorod hetero-junction device, 106
- liquid-junction photovoltaic cell
 - operating principle, 267–71
 - energy diagram of semiconductor bulk and nanoparticle physical charges, 270
 - photo-generated electrons
 - transport from semiconductor to substrate, 271
 - schematic interpretation of liquid junction-based photovoltaic cell, 269
- lithium
 - conversion reaction, 227
 - insertion/extraction reaction, 228
- lithium-alloy reaction, 228
- lithium ion batteries (LIB)
 - composites graphene/semiconductor nanocrystals, 229–37
 - electrochemical properties
 - improvement, 243–7
 - cycling performance and rate capability, 245
 - graphene performance, 213–22
 - anodes, 218–19
 - d -spacing, charge capacity and charge/discharge cycle performance, 216
 - electrode additive, 221–2
 - heterogeneous hybrids, 219–21
 - irreversible and reversible storage, 217
 - power vs. specific energy for various energy storage devices, 214
 - prospects of using graphene, 225–8
 - ultrathin and transparent GNS, 227
- local electron, 24
- logic gate, 102
 - ZnO nanorod logic devices, 103
- longitudinal super-lattice nanowire, 66
- luminescence measuring technique, 392–3
- macroscopic defect, 2
- metal nano-oxides
 - crystallographic structure, 75–9
 - crystal shape, 75–6
 - surface stoichiometry (disordering), 76–9
- metal oxide semiconductor systems doping, 58–66
 - calculated potential distributions
 - in channel regions, 61
 - nanoscale metal oxide heterostructures, 64–6
 - oxide nanowires, 63–4
 - parameters, 59–60
 - ZnO nanowires, 60–3
- metal oxide sensing electrodes, 376
- metallic alloys, 343–6
 - Cr-based alloys, 343–4
 - Fe-Cr-based alloys, 344–6
 - nominal composition of Fe-based alloys, 345
 - Ni-Cr-based alloys, 346
 - nominal composition of Ni-based alloys for SOFC interconnect applications, 347
- microscopic defect, 2–3, 4
- microstructure effect
 - quantification, 361–2
- mixed-ion-conducting oxides, 337–8
- molybdenum trioxide (MoO_3), 167–73
 - charge carrier mobility, 172
 - crystalline phases, 168
 - drain current vs. gate voltage characteristics, 172
 - exfoliated nanosheets Raman spectra, 171
 - exfoliated nanosheets STM, 169
- MoS_2 nanosheet, 154–62
- Mott exciton, 13
- multi-walled carbon nanotubes (MWCNT), 143–4
- multidimensional splines, 411

- multiscale computational framework, 363
- multiscales topography, 401–2
- n*-type conductivity, 12–17
- n*-type semiconductor, 9, 34–5
- nano-veins morphology, 301
- nanostructured anode materials, 338–40
 - electrochemical performance of SOFC, 340
- nanostructured cathode materials, 324–34
 - oxygen reduction reaction and FIB/SEM 3D reconstruction of SOFC, 331
 - perovskite-type oxide materials, 333
 - planar cell stacks design and alternative tubular geometry design, 327
 - SEM images of cross-section of planar SOFC and infiltrated cathode, 330
- nanostructured semiconductor composites
- solar cells, 267–306
 - dye-sensitised solar cells (DSSC), 291–303
 - future trends in technological development, 303–6
 - operating principle of liquid-junction photovoltaic cell, 267–71
 - principles of inorganic solid-state nanostructured solar cells, 273–5
 - semiconductor quantum dot absorbers, 286–91
 - strategic potential of inorganic semiconductors in photovoltaics, 271–3
 - structured transparent electron conductors, 275–85
- solid oxide fuels cells (SOFCs), 321–65
 - electrolytes for SOFCs, 334–8
 - further performance increase of SOFCs at lower temperatures, 355–9
 - interconnects for SOFCs, 340–6
 - low-temperature SOFCs, 351–5
 - materials and cell designs, 321–4
 - miniaturisation of SOFCs, 346, 348–51
 - nanostructured anode materials, 338–40
 - nanostructured cathode materials, 324–34
 - rational SOFC material design
 - new advances and tools, 359–63
 - SOFC applications and markets, 363–5
- native defects, 1
- native point defects, 5
- nephelometric turbidity unit (NTU), 404
- Nernst equation, 323, 395
- Nernstian slopes, 379–80
- network node, 376
- NexTech Materials, 334
- Ni-Cr-based alloys, 346
- niobium pentoxide (Nb_2O_5), 178–87
 - bandgap energies, 180
 - conduction and valence bands position, 179
 - CSFC-AFM set-up and principle, 185
 - 1D nanostructural development
 - mechanism, 181
 - microstructured and quasi-2D nanoflakes, 188
 - sol-gel/exfoliation approach, 182
 - structural characteristics, 181
 - XPS measurement and EDS analysis of nanosheets, 183
- noble-metal co-catalysts, 271–2
- non-linear least squares, 411
- O_2 electro-catalysis, 73
- ohmic polarisation, 330–1
- open circuit potential (OCP), 358
- open circuit voltage (OCV), 324

- optoelectronics, 102–14
 - emitter, laser and waveguide, 102–4
 - switching device concept, 105
 - ZnO NW, 104
- flexible molecular-scale electronic devices, 111–14
- light-emitting diode, 104–9
- polarisation-dependent photodetector, 109–10
- organophosphate (OP) pesticide detection, 124–6
 - schematic diagram, 125
- organophosphorous hydrolase (OPH) pesticide detection, 124–6
 - schematic diagram, 125
- oxide nanowires, 63–4
- oxygen
 - role in graphene, 235–7
 - Ni(OH)₂ growth on GNS, 236
 - Ni(OH)₂ nanocrystal growth on GNS and GO sheet, 235
- oxygenolysis, 353
- p*-type conductivity, 12–17
- p*-type semiconductor, 9, 34–5
- particle size reduction, 359
- phase-sensitive X-ray computed tomography, 361
- phonon bottleneck, 273
- photo-anode, 269
- photo-conversion efficiency, 279, 280
- photo-current, 268
- photo-voltage spectroscopy, 286
- phototransistor, 158
- photovoltaic system, 294
- piezoelectric properties, 115
- plug-in hybrid electric vehicles (PHEVs), 353
- polarisation-dependent photodetector, 109–10
 - polarised detection, 110
- polarographic sensor technologies, 389–92
- polyaniline (PANI), 127–8
- polymer electrolyte fuel cells (PEFC), 346
- Poole's law, 10
- pore-filling fraction, 296–7
- porous electrode theory, 361
- powder technology processes, 338–9
- proton-conducting oxides, 337–8
- proton-exchange membrane fuel cells (PEMFCs), 352
- quantum confinement, 286
- quantum dot (QD), 4–5, 106–7, 273
- quantum wells (QW), 4–5
- quasi-particles, 42
- Queisser-Shockley limit, 286
- rapid thermal annealing (RTA), 284
- reference electrodes (RE), 377
- resonators, 114–18
 - resonating Ga₂O₃ NW, 114
- rutile, 163
- scanning electron microscopy (SEM), 287, 329–30, 361
- scanning tunnelling microscopy (STM), 287
- Schottky diode-like solar cell, 289–90
- Schottky mechanism, 11
- selected-area electron diffraction (SAED), 191
- self-consistent field method, 31
- semiconductor
 - band theory, 39–43
 - crystals electrical conductivity, 6–12
 - crystals order and disorder, 1–6
 - defects properties, 4–6
 - defects types, 1–4
 - microstructural defects, 3
 - electrons and holes, 1–47
 - energy harvesting based on piezoelectric nanostructures, 66–9
 - energy spectrum
 - finite crystal lattice, 24–30
 - infinite crystal lattice, 17–24

- metal oxide semiconductor systems
 - doping, 58–66
- n*- and *p*-type conductivity
 - mechanism, 12–17
- nanocrystal structural and chemical modification, 50–84
- nanocrystals in lithium ion batteries and electrochemical capacitors, 229–37
 - graphene/metal oxide
 - nanocomposites preparation, 229
 - mass production approach, 231
 - structural models, 229–32
- nanostructure for energy storage, 213–54
- nanostructured based electronic devices and functional structures, 95–129
 - carbon nanotubes (CNT), 118–24
 - carbon nanotubes (CNT) for environmental sensors, 124–9
 - novel nanoscale devices, 95–6
 - optoelectronics, 102–14
 - resonators and cantilevers, 114–18
 - tunable electronic device, 96–102
- nanostructured thermopower wave sources, 247–54
- physical electrochemistry, 69–79
 - characterisation of nanostructured metal oxides, 74
 - crystallographic structure of metal nano-oxides, 75–9
 - current flow dependence applied to electrolysis cell, 72
 - technological demand, 71–4
- solution-phase material growth, 53–5
- state-of-the-art characterisation techniques, 43–7
 - analytical techniques with their typical applications and detection limits, 44–6
- statistics, 31–9
 - local states, 35–6
- structural and electrochemical properties, 79–84
 - grain size decrease influence on sensor parameters, 82
 - small size ordered nanoparticles, 83
 - structural engineering utilisation and implementation, 80
- three-dimensional conductive networks, 237–47
 - volume change suppression, 239–43
- two-dimensional nanocrystals, 139–198
 - chalcogenide semiconductor nanocrystal, 148–62
 - graphene, 139–40
 - impact of combining with three-dimensional structure, 196–8
 - impact on science and industry, 140–8
 - molybdenum trioxide, 167–73
 - niobium pentoxide, 178–87
 - tantalum pentoxide, 187, 189–91
 - titanium dioxide, 162–7
 - tungsten trioxide, 173–8
 - zinc oxide, 191, 193–6
- vapour-phase material growth, 51–3
- vertical and horizontal alignment strategies, 55–8
 - catalyst patterning, 56–7
 - substrate lattice matching, 57–8
 - template alignment, 58
- semiconductor-electrolyte junction, 291
- semiconductor-metal junction, 291
- semiconductor nanocrystals
 - environmental sensors, 374–417
 - antifouling technologies for solid-state water quality sensors, 401–3
 - conductivity measurements, 398–400
 - electrochemical dissolved oxygen (DO) sensors, 389–97
 - future trends, 414, 416–17
 - solid-state dissolved metal ion sensors, 409–14

- solid-state dissolved organic carbon (DOC) sensors, 405–9
- solid-state pH sensors, 374–89
- solid-state turbidity sensors, 403–5
- semiconductor quantum dot absorbers, 286–91
- passivation and interface
 - conditioning with quantum dot layers, 290–1
- PbS and PbSe quantum dot layers, 289–90
- sensitisation and charge separation
 - with quantum dots, 286–9
- SEM analysis of CdSe cluster anchored on TiO₂, 289
- semiconductor QDs on TiO₂ nanoplates and TiO₂ nanostructures, 287
- TEM images under different magnifications of CdS-sensitized TiO₂ nanorod, 288
- sequential injection analysis (SIA), 411
- Shockley surface, 29–30
- size quantization effect, 270
- Sn₂O₃ nanowires, 64
- sol-gel technique, 54, 277–8
- solar cell technology, 304
- solar cells
 - nanostructured semiconductor composites, 267–306
 - dye-sensitized solar cells (DSSC), 291–303
 - future trends in technological development, 303–6
 - operating principle of liquid-junction photovoltaic cell, 267–71
 - principles of inorganic solid-state nanostructured solar cells, 273–5
 - semiconductor quantum dot absorbers, 286–91
 - strategic potential of inorganic semiconductors in photovoltaics, 271–3
 - structured transparent electron conductors, 275–85
 - solid electrolyte interface (SEI), 219
 - solid oxide fuels cells (SOFCs)
 - continuum modelling, 359–61
 - interdependence of models at different length and timescale and techniques, 360
 - electrolytes, 334–8
 - conductivity as function of temperature for YSZ, GDC and LSMG, 336
 - conductivity of perovskite oxides in air, 338
 - further performance increase of SOFCs at lower temperatures, 355, 357–9
 - ceria/bismuth oxide bi-layer concept, 357
 - interconnects, 340–6
 - lanthanum chromites, 342
 - metallic alloys, 343–6
 - low-temperature, 351–5
 - specific power of -2W/cm² SOFC at 650C vs various energy conversion devices, 354
 - thermodynamic predictions of equilibrium composition for methane fed, 356
 - materials and cell designs, 321–4
 - plant thermal efficiency (%) vs year, 322
 - principle operation, 323
 - typical configuration of planar and tubular design, 325
 - microtubular, 348–9
 - typical configuration of microtubular and planar design, 350
 - miniaturisation, 346, 348–51
 - microtubular SOFCs, 348–9
 - thin-film μ -SOFCs, 349–51
 - nanostructured semiconductor composites, 321–65
 - low-temperature SOFCs, 351–5
 - nanostructured anode materials, 338–40

- nanostructured cathode materials, 324–34
- SOFC applications and markets, 363–5
- rational SOFC material design new advances and tools, 359–63
 - microstructure effect quantification, 361–2
 - new directions and future perspectives, 362–3
- solid-state dissolved metal ion sensors, 409–14
- modern E-tongues for analysis of dissolved metals in complex solutions, 412–13
- obtained vs expected results by proposed E-tongue for test samples, 415
- potentiometric E-tongue using sequential injection analysis flow system, 414
- WHO guidelines for acceptable values of metal content in raw and drinking water, 410
- solid-state dissolved organic carbon (DOC) sensors, 405, 407–9
 - absorbance of hand-held UV255 sensor in water and turbidity effect, 408
 - DOC measurements from hand-held sensor and commercial spectrometer, 409
 - sensor with fixed outer sleeve signal conditioning box and main components, 407
- Solid State Energy Conversion Alliance (SECA), 364
- solid-state pH sensors, 374–89
 - doping semiconductor nanocrystals, 384, 386–9
 - interference testing of solid-state sensor, 387
 - SEM images of undoped RuO₂-Se and Cu₂O-doped RuO₂-SE, 388
 - satellite image of Australian city of Brisbane and its major water catchment, 375
 - semiconductor nanocrystals
 - modification for pH sensing electrodes, 378–84
 - characteristics of metal oxides as pH-sensitive electrodes, 380
 - cross-sectional view of sensor substrate, 383
 - long-term stability of pH measurement by multisensor, 382
 - nanostructured RuO₂-SE vs Ag/AgCl-RE and response time vs water temperature, 385
 - voltage variations vs pH and set of planar water quality sensors, 381
 - solid-state turbidity sensors, 403–5
 - measurements of high and low turbidity ranges at 23°C, 406
 - turbidity signal conditioning of inexpensive CSIRO turbidity sensor, 404
 - solid-state water quality sensors, 401–3
 - solution-deposition techniques, 296–7
 - solution-phase material growth, 53–5
 - sonochemical method, 55
 - spin, 31
 - spray coating, 336
 - spray pyrolysis, 278
 - steam-to-carbon ratios, 353
 - structural defect, 3
 - structure-independent property, 1–2
 - structure-sensitive property, 1–2
 - structured transparent electron conductors, 275–85
 - emerging CuIn_xGa_{1-x}(Se_yS_{1-y})₂ thin-film solar cells, 283–5
 - cyclic voltammograms of Mo electrode, 285
 - schematic view of thin film CuInGaSe₂ solar cell, 284
 - nanostructures based on TiO₂, 275–9
 - examples of semiconductor based photo-anode nanocomposites, 276
 - graphical illustration of nanotubes grown on different substrates, 281

- scheme of TiO₂ nanotubes via two-step anodisation hydrothermal treatment, 280
 - SEM images of cross-sections of ultrathin nanoporous layer and ZnO nanorods, 278
- Zinc oxide (ZnO) nanorod array, 279, 281–3
 - routes for hierarchical ZnO nanowires hydrothermal growth, 282
- substrate lattice matching, 57–8
 - metal oxide film with transient layer, 57
- successive ion layer absorption and reaction (SILAR) technique, 287
- surface roughness, 285
- surface stoichiometry, 76–9
- surface Tamm level, 16
- surface valence band, 30
- surfactant-assisted growth, 54–5

- Tamm surface, 29–30
- tantalum pentoxide (Ta₂O₅), 187, 189–91
 - high-density array nanorods, 190
 - phase diagrams, 192–3
- temperature, 7–8
 - dependence types of electrical conductivity, 8
- template alignment, 58
- template-assisted synthesis, 54
- thermal cycling, 365
- thermal flame propagation, 249
- thermodynamically irreversible defect, 5
- thermodynamically reversible defect, 5
- thermopower wave oscillations, 250
- thermopower wave sources, 247–54
 - fuel/ZnO/Al₂O₃ thermopower system, 253
 - materials, 253
 - specific power, output voltage and oscillation amplitudes assessment for CNT, 254
 - thermopower wave generator, 251
 - thickness control, 285
- thin-film μ -solid oxide fuels cells, 349–51
- TiS₂ nanosheet, 149–51
- titanium dioxide (TiO₂), 162–7
 - liquid junction dye operation or QD-sensitized solar cell, 165
 - oxidation and reduction processes, 166
 - photocatalytic activation, 164
 - potential applications, 167
- transmission electron microscopy (TEM), 288
- triple phase boundaries (TPB), 326
- tubular cell bundles, 326–7
- tunable electronic device, 96–102
- tungsten trioxide (WO₃), 173–8
 - growth directions along different unit-cell axes, 178
 - Li⁺ intercalation for thin and thick nanosheets, 177
 - sheet thickness, 175
 - single layer monoclinic formation via exfoliation process, 174
- turbidity, 403

- ultrasonic cleavage, 143
- ultrathin nanocomposite absorber, 274
- ultraviolet (UV), 275
- US Environmental Protection Agency (USEPA), 392–3

- valence band, 16, 23–4, 41–3
- vapour-liquid-solid process (VLS), 51
- vapour-phase material growth, 51–3
 - experimental set-up, 53
 - thermal furnace synthesis system, 52
- vapour-solid process (VS), 52
- vertical electronic device, 100–1
 - VSG FET, 101
- vertical surrounding gate field-effect transistor (VSG-FET), 100
- voltage drift, 382–3

- water, 374
- water gas shift (WGS), 353
- water quality analysis, 374–5
- wet impregnation method, 332–3
- Winkler titration, 392
- wireless sensors network, 376
- World Health Organisation (WHO), 409

- X-ray computed tomography, 362
- X-ray photoelectron spectroscopy (XPS), 396

- yttria-stabilised zirconia (YSZ), 335

- zinc oxide (ZnO), 191, 193–6
 - nanohelix structural uniformity, 193
 - nanorod array, 279, 281–3
 - nanowire dye-sensitised cell, 195
 - nanowires, 103–4
 - doping, 60–3
 - temperature-dependent magnetisation curve, 62
 - photoluminescence of nanowire diameters, 194